



A11103 387964

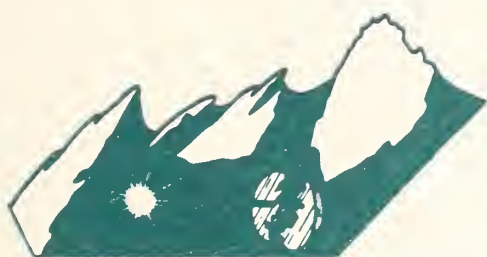


NIST  
PUBLICATIONS

NIST SPECIAL PUBLICATION **775**

U.S. DEPARTMENT OF COMMERCE/National Institute of Standards and Technology

# Laser Induced Damage in Optical Materials: 1988



*BOULDER DAMAGE SYMPOSIUM*



STP 1099

QC

100

.U57

No. 775

1989

C.2

# NATIONAL INSTITUTE OF STANDARDS & TECHNOLOGY

## Research Information Center

Gaithersburg, MD 20899



The National Institute of Standards and Technology<sup>1</sup> was established by an act of Congress on March 3, 1901. The Institute's overall goal is to strengthen and advance the Nation's science and technology and facilitate their effective application for public benefit. To this end the Institute conducts research to assure international competitiveness and leadership of U.S. industry, science and technology. NIST work involves development and transfer of measurements, standards and related science and technology, in support of continually improving U.S. productivity, product quality and reliability, innovation and underlying science and engineering. The Institute's technical work is performed by the National Measurement Laboratory, the National Engineering Laboratory, the National Computer Systems Laboratory, and the Institute for Materials Science and Engineering.

### *The National Measurement Laboratory*

Provides the national system of physical and chemical measurement; coordinates the system with measurement systems of other nations and furnishes essential services leading to accurate and uniform physical and chemical measurement throughout the Nation's scientific community, industry, and commerce; provides advisory and research services to other Government agencies; conducts physical and chemical research; develops, produces, and distributes Standard Reference Materials; provides calibration services; and manages the National Standard Reference Data System. The Laboratory consists of the following centers:

- Basic Standards<sup>2</sup>
- Radiation Research
- Chemical Physics
- Analytical Chemistry

### *The National Engineering Laboratory*

Provides technology and technical services to the public and private sectors to address national needs and to solve national problems; conducts research in engineering and applied science in support of these efforts; builds and maintains competence in the necessary disciplines required to carry out this research and technical service; develops engineering data and measurement capabilities; provides engineering measurement traceability services; develops test methods and proposes engineering standards and code changes; develops and proposes new engineering practices; and develops and improves mechanisms to transfer results of its research to the ultimate user. The Laboratory consists of the following centers:

- Computing and Applied Mathematics
- Electronics and Electrical Engineering<sup>2</sup>
- Manufacturing Engineering
- Building Technology
- Fire Research
- Chemical Engineering<sup>3</sup>

### *The National Computer Systems Laboratory*

Conducts research and provides scientific and technical services to aid Federal agencies in the selection, acquisition, application, and use of computer technology to improve effectiveness and economy in Government operations in accordance with Public Law 89-306 (40 U.S.C. 759), relevant Executive Orders, and other directives; carries out this mission by managing the Federal Information Processing Standards Program, developing Federal ADP standards guidelines, and managing Federal participation in ADP voluntary standardization activities; provides scientific and technological advisory services and assistance to Federal agencies; and provides the technical foundation for computer-related policies of the Federal Government. The Laboratory consists of the following divisions:

- Information Systems Engineering
- Systems and Software Technology
- Computer Security
- Systems and Network Architecture
- Advanced Systems

### *The Institute for Materials Science and Engineering*

Conducts research and provides measurements, data, standards, reference materials, quantitative understanding and other technical information fundamental to the processing, structure, properties and performance of materials; addresses the scientific basis for new advanced materials technologies; plans research around cross-cutting scientific themes such as nondestructive evaluation and phase diagram development; oversees Institute-wide technical programs in nuclear reactor radiation research and nondestructive evaluation; and broadly disseminates generic technical information resulting from its programs. The Institute consists of the following divisions:

- Ceramics
- Fracture and Deformation<sup>3</sup>
- Polymers
- Metallurgy
- Reactor Radiation

<sup>1</sup>Headquarters and Laboratories at Gaithersburg, MD, unless otherwise noted; mailing address Gaithersburg, MD 20899.

<sup>2</sup>Some divisions within the center are located at Boulder, CO 80303.

<sup>3</sup>Located at Boulder, CO, with some elements at Gaithersburg, MD.

# Laser Induced Damage in Optical Materials: 1988

---

Proceedings of a Symposium sponsored by:

National Institute of Standards and Technology  
(formerly National Bureau of Standards)  
American Society for Testing and Materials  
Defense Advanced Research Project Agency  
Department of Energy

October 26-28, 1988

NIST, Boulder, Colorado 80303

Edited by:

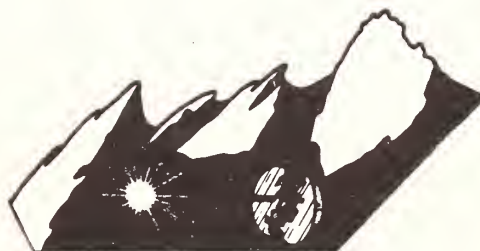
Harold E. Bennett  
Naval Weapons Center  
China Lake, California 93555

Arthur H. Guenther  
Los Alamos National Laboratory  
Los Alamos, New Mexico 87545

Brian E. Newnam  
Los Alamos National Laboratory  
Los Alamos, New Mexico 87545

M.J. Soileau  
University of Central Florida  
Orlando, Florida 32816

**NOTE:** As of 23 August 1988, the National Bureau of Standards (NBS) became the National Institute of Standards and Technology (NIST) when President Reagan signed into law the Omnibus Trade and Competitiveness Act.



**BOULDER DAMAGE SYMPOSIUM**



**UNITED STATES**

**DEPARTMENT OF COMMERCE**, Robert A. Mosbacher, Secretary  
**NATIONAL INSTITUTE OF STANDARDS**  
**AND TECHNOLOGY**, Raymound G. Kammer, Acting Director

Issued October 1989

Library of Congress Catalog Card Number: 89-600787

National Institute of Standards and Technology  
Special Publication 775, 576 pages (Oct. 1989)  
CODEN: NBSAV

U.S. GOVERNMENT PRINTING OFFICE  
WASHINGTON: 1989

---

For sale by the Superintendent of Documents, U.S. Government Printing Office, Washington, DC 20402-9325



## Foreword

The Proceedings contain the papers presented at the Twentieth Symposium on Optical Materials for High-Power Lasers held at the National Institute of Standards and Technology in Boulder, Colorado, on October 26-28, 1988. The Symposium was jointly sponsored by the National Institute of Standards and Technology, the American Society for Testing and Materials, the Defense Advanced Research Project Agency, and the Department of Energy. The Symposium was attended by over 210 scientist from the United States, the United Kingdom, France, Canada, People's Republic of China, Japan, the Federal Republic of Germany, Lithuania, and the Soviet Union. It was divided into sessions devoted to the following topics: Materials and Measurements, Mirrors and Surfaces, Thin Films, and finally, Fundamental Mechanisms. The Symposium Co-Chairmen were Dr. Harold E. Bennett of the Naval Weapons Center, Dr. Arthur H. Guenther of the Air Force Weapons Laboratory, Dr. Brian E. Newnam of the Los Alamos National Laboratory, and Dr. M. J. Soileau of the University of Central Florida. They also served as editors of this report.

The editors assume full responsibility for the summary article which contains an overview of the Symposium. The manuscripts of the papers presented at the Symposium have been prepared by their authors, and questions pertaining to their content should be addressed to those authors. The interested reader is referred to the bibliography at the end of the summary article for general references to the literature of laser damage studies. The Twenty-First Annual Symposium on this topic was held in Boulder, Colorado, November 1-3, 1989. A concerted effort will be made to ensure closer liaison between the practitioners of high-peak power and the high-average power community.

The principal topics to be considered as contributed papers in 1989 do not differ drastically from those enumerated above. We expect to hear more about improved scaling relations as a function of pulse duration, area, and wavelength, and to see a continuing transfer of information from research activities to industrial practice. New sources at shorter wavelengths continue to be developed, and a corresponding shift in emphasis to short wavelength and repetitively pulsed damage problems is anticipated, particularly in the RF free-electron laser pulse format. Fabrication and test procedures will continue to be developed, particularly in the thin film areas. New materials, diamond and diamond-like, for example, and the implication of thermal conductivity on damage modelling will undoubtedly be emphasized.

The purpose of these symposia is to exchange information about optical materials for high-power lasers. The editors will welcome comment and criticism from all interested readers relevant to this purpose, and particularly relative to our plans for the Twenty-First Annual Symposium.

H.E. Bennett, A.H. Guenther,  
B. E. Newnam, and M. J. Soileau  
Co-Chairmen

#### Disclaimer

Certain papers contributed to this publication have been prepared by non-NIST authors. These papers have not been reviewed or edited by NIST; therefore, the National Institute of Standards and Technology accepts no responsibility for comments or recommendations contained therein.

Certain commercial equipment, instruments, and materials are identified in this publication in order to explain the experimental procedure adequately. Such identification in no way implies approval, recommendation, or endorsement by the National Institute of Standards and Technology, nor does it imply that the equipment, instruments, or materials identified are necessarily the best available for the purpose.

## CONTENTS

	Page
FOREWORD .....	iii
H.E. Bennett, A.H. Guenther, B.E. Newnam, and M.J. Soileau	
DISCLAIMER .....	iv
NIST WELCOME .....	xiii
Aaron A. Sanders, NIST-Boulder	
SYMPOSIUM WELCOME .....	xv
Brian E. Newnam, Los Alamos National Laboratory	
OPENING COMMENTS - 20TH ANNUAL DAMAGE SYMPOSIUM .....	xix
Arthur H. Guenther, Los Alamos National Laboratory	
SUMMARY OF MEETING .....	1
H.E. Bennett, A.H. Guenther, B.E. Newnam, and M.J. Soileau	
1. Introduction .....	1
2. Overview .....	2
3. Acknowledgments .....	8
4. References .....	9

## MATERIALS AND MEASUREMENTS

Multiple Shot Intrinsic Bulk Damage in KBr at 532 nm .....	12
R. Thomas Casper, Scott C. Jones, and Peter Braunlich	
Laser Heating of Free Electrons and the Mechanism of Intrinsic Laser Breakdown in Wide-Gap Optical Materials at 1064 nm .....	22
X. A. Shen, Scott C. Jones, and Peter Braunlich	
Optical Measurements at PMS Electro-Optics .....	34
Ramin Lalezari and Scott Knollenberg	
The Art of Optical Scatter Measurement .....	42
Thomas A. Leonard	
Are 1 Meter Square Calcium Fluoride Laser Windows Possible? .....	48
C. William King	
Radiation Damage in Barium Fluoride Detector Materials .....	49
P. W. Levy, J. A. Kierstead, and C. L. Woody	

Optical Damage in Glass from Focused Nanosecond Radiation .....	61
Evaldas K. Maldutis, Stanislovas K. Balickas and Silvinas V. Sakalauskas	
The Non-Destructive Prediction of Laser Damage .....	62
S. E. Clark and D. C. Emmony	
Repetitively Pulsed Beam Diagnostics for Large Laser Optics Damage .....	73
D. B. Nichols, D. J. Morris, W. B. Shepherd T. M. Donovan, J. L. Stanford, C. D. Marrs, and C. F. Zahnow	
Emergence of "Consensus Standards" in Laser Damage Acceptance	
Testing of Production Nd:YAG Laser Optics .....	74
S. C. Seitel, E. A. Teppo, and J. W. Arenberg	
Optical Breakdown in Particle Suspension .....	75
Kamjou Mansour, M. J. Soileau, and E. W. Van Stryland	
Colloidal Materials as Optical Filtering Media .....	76
Kent J. Kogler, R.G. Pastor, R.L. Burton, R.A. Spence, and N.P. Murarka	
Structural Damage and Analysis of the Nova Final Focusing Lenses .....	87
John H. Pitts	
Photoconductivity Study of Charge-Producing Defects in $\text{CaF}_2$ .....	92
Robert M. O'Connell and C. Denton Marrs	
Laser-Induced Changes in the Electrical Performance of Silicon	
MOS Device Structures .....	105
Chen-Zhi Zhang, Steve E. Watkins, Rodger M. Walser, and Michael F. Becker	
A Multi-Facet XUV Aluminium Mirror for the FEL .....	114
Marion L. Scott	
Measurement of the Three Photon Absorption Cross Section and	
Intrinsic Optical Breakdown of KI at 532 nm .....	118
Lin Simpson, X. A. Shen, Scott C. Jones Peter Braunlich, and Paul Kelly	



## SURFACES AND MIRRORS

Damage to Silver Coatings from High Average Power 1- $\mu$ m Laser .....	122
V. Sanders, L. Jolin, and S. Salazar	
Investigation of the Effect of Surface Finish on the Damage Threshold of Nd:Cr:GSGG Slabs .....	128
D. W. Mordaunt and D. E. Maguire	
Surface Damage Thresholds of Fluoride Crystals: Dependence on Surface Quality and Irradiation Mode .....	133
S. Petzoldt, A. P. Elg, J. Reif, and E. Matthias	
Laser-Induced Surface Ablation and Optical Damage of ZnS Crystals Caused by Single-and Multiple-Pulse Laser Irradiation .....	140
H. F. Arlinghaus, W. F. Galaway, D. M. Gruen, and L. L. Chase	
Substrate Cleaning in Vacuum by Laser Irradiation .....	152
Tilak Raj, D. E. McCready, and C. K. Carniglia	
Cavity Ringdown Measurements of High-Reflection Mirrors at 1.06 $\mu$ m .....	166
L. John Jolin, Virgil R. Sanders, and Thomas P. Turner	
Radiation Effects in Mirror Substrate Materials .....	175
E. J. Friebele, J. A. Ruller, and P. L. Higby	
Laser Polished Fused Silica Surfaces: Absorption Data .....	176
Alan F. Stewart and Arthur H. Guenther	
The Detection, Removal and Effect on Damage Thresholds of Cerium Impurities on Fused Silica .....	183
R. C. Estler, N. S. Nogar, and R. A. Schmell	
Laser Damage of YAG Surfaces .....	189
T. McMin, S. Seitel, and M. Babb	
Damage Mechanism on Metal Mirrors Induced by CO <sub>2</sub> Laser .....	211
K. Yoshida, M. Yamanaka, S. Nakai, Y. Tsunawaki, H. Okamoto, K. Motoba, S. Aramaki, and K. Ohta	

Optical Characteristics of ZnSe Coated Copper Mirror for High Power CO <sub>2</sub> Laser .....	212
K. Yoshida, M. Yamanaka, S. Nakai, Y. Tsunawaki, H. Okamoto, K. Motoba, S. Aramaki, and K. Ohta	

## THIN FILMS

Parasitic Oscillation Suppression Coatings for Slab Lasers and Their Optical Damage .....	213
M. A. Acharekar, D. P. McCarthy, D. A. Dobberpuhl, and H. W. Willhite	
Absorption and Damage Threshold of Dielectric Reflectors at 193 nm .....	232
T. Izawa, Y. Ishiwata, I. Hashimoto, H. Shikakura, Y. Owadano, Y. Matsumoto, and M. Yano	
The Response of Multilayer Dielectric Coatings to Low Fluence UV Light Exposure .....	233
J. Early, V. Sanders, and W. Leamon	
Thermal Imaging Studies of Laser Irradiated Coated Optical Surfaces .....	245
Alan F. Stewart, Adam Rusek, and Arthur H. Guenther	
Effect of n-on-1 Laser Treatment on Damage Threshold of Selected Optical Coatings .....	259
John G. Wilder and Ian M. Thomas	
Two Layer Broadband AR Coating .....	265
Ian M. Thomas	
Scanning Tunneling Microscopy Study of the Effects of Pulsed High Power Laser Irradiation on Carbon, Silicon Carbide, and Gold Surfaces .....	266
Wigbert Siekhaus, Thomas Beebe, and Markus Schildbach	
Tarnishing Measurements of Al <sub>2</sub> O <sub>3</sub> Overcoated Silver Mirrors .....	267
W. D. Kimura, Q. D. Appert, P. N. Arendt, V. E. Sanders, and M. L. Scott	
The Formation of Laser-Induced Ripple Structures .....	273
N.C. Kerr, S. E. Clark, and D. C. Emmony	
Sputter Etching of Coating Substrates for Improved Laser Damage of AR Coatings .....	286
K. Yoshida, H. Yoshida, S. Nakai, and M. Ohtani	

Ultra-Precision Grinding of Optical Materials .....	287
Y. Namba	
Laser-Induced Electrical Parameter Degradation in Silicon Photodiodes .....	288
Steve E. Watkins, Chen-Zhi Zhang,	
Rodger M. Walser, and Michael F. Becker	
Stress Reduction of Ion-Beam-Sputtered Mixed-Oxide Coatings by Baking .....	311
B. J. Pond, J. I. DeBar, C. K. Carniglia, and Tilak Raj	
Laser Damage Thresholds of Dielectric Multilayers Produced by Reactive Ion Plating Deposition .....	320
Karl H. Guenther, Kamjou Mansour, Paul Sachdeva,	
Harald Schink, and Francis J. Boero	
Damage Threshold Dependence on Film Thickness .....	321
Wu Zhouling, Fan Zhengxiu, and Wang Zhijiang	
Optical Properties of Metal-Oxide Thin Films: Influence of Microstructure .....	328
Kim F. Ferris, Michael R. Thompson, Gregory J. Exarhos,	
Wendy S. Frydrych, Charles B. Duke, and Nancy J. Hess	
Smoothing of Optical Surfaces with Dielectric Thin Films Produced by Reactive Ion Plating Deposition .....	339
Francis J. Boero, Russell A. Chipman, and Karl H. Guenther	
Measurement of Thermal Expansion Coefficients of Optical Thin Films .....	348
Wu Zhouling, Tang Jinfa, and Shi Baixuan	
Second Harmonic Generation and Laser Damage Threshold of Deuterated L-Arginine Phosphate Monohydrate Crystal .....	356
Takatomo Sasaki, Atsushi Yokotani, Kana Fujioka,	
Kunio Yashida, Tatsuhiko Yamanaka, and Sadao Nakai	
Free Vibration Pulse Laser-Induced Damage in Optical Thin Films .....	361
Fan Zhengxiu, Jin Linfa, and Luo Miaohong	
Ion-Beam Sputtered MgF <sub>2</sub> and CaF <sub>2</sub> Thin Films .....	366
M.F. Dafoe, B.J. Pond, C.K. Carniglia, and T. Raj	
Localization of Absorption Losses in Optical Coatings .....	377
Wu Zhouling and Fan Zhengxiu	

Measurement of Weak Absorption in Optical Coatings by Means of Photothermal Deflection Technique .....	385
Wu Zhouling, Tang Jinfa, and Shi Baixun	

## FUNDAMENTAL MECHANISMS

Recent Work in the Theory of Laser-Induced Damage in Solids .....	390
V. M. Kenkre, V. I. Kovanis, J. K. McIver, and A. H. Guenther	
Variation, Variability and Differences in the Measurement of Laser- Induced Damage Thresholds .....	398
R. M. Wood and R. J. Chad	
The Consequence of Doping Optical Materials with D <sub>2</sub> O .....	399
J. B. Franck, J. O. Porteus, L. F. Johnson, J. M. Pentony, W. N. Faith, and H. Angus Macleod	
Some Studies of Thin Film Distributed Bragg Reflectors .....	400
K. L. Lewis, I. T. Muirhead, A.M. Pitt, A. G. Cullis, and G. M. Williams	
Laser-Induced Damage of Dielectric Systems with Gradual Interfaces at 1.064 $\mu\text{m}$ .....	414
D. Ristau, H. Schink, F. Mittendorf, J. Akhtar, J. Ebert, and H. Welling	
Measurements of Pulse Damage Thresholds of AR Coated CdTe 10.6 $\mu\text{m}$ .....	427
J. G. Grimm, R. S. Eng, C. Freed, N. W. Harris, and R.G. O'Donnell	
Microcomputer Finite Difference Modeling of Laser Heating and Melting .....	440
J. O. Porteus	
Accumulated Surface Damage on ZnS Crystals Produced by Closely Spaced Pairs of Picosecond Laser Pulses .....	455
L. L. Chase and H. W. H. Lee	
1053-nm High-Field Effect in Monomeric and Polymeric Conjugated Systems .....	462
M. Guardalben, A. Bevin, K. Marshall, A. Schmid, and F. Kreuzer	



Thermally Induced Phase-Retardance Degradation in Laser-Irradiated Liquid Crystal Cells .....	470
Claude A. Klein, Terry A. Dorschner, Douglas S. Hobbs, and Daniel P. Resler	
Fundamental Mechanisms of Laser-Induced Damage in Transparent Solids: Up-to-Date Status of Research and Understanding .....	486
A. A. Manenkov	
The Theory of Inclusion-Initiated Laser Damage in Optical Materials: The Thermal Explosion Mechanism .....	502
M. F. Koldunov, A. A. Manenkov, and I. L. Pokotilo	
Experimental Investigation on the Role of Wavelength in the Laser Conditioning Effect .....	516
J.W. Arenberg and D.W. Mordaunt	
APPENDIX I. List of Attendees .....	520



NIST Welcome

Aaron A. Sanders  
National Institute of Standards and Technology  
Boulder, Colorado 80303

It is my pleasure to welcome you to Boulder and the National Institute of Standards and Technology, formerly the National Bureau of Standards. Since I will be telling you later about the changes associated with the new name, I will not take the time now to further discuss this excepting to assure you that the same work associated with NBS will continue uninterrupted in NIST.

We are especially pleased with the long relationship of NIST and this symposium, now in its 20th year. The information exchanged and documented through this conference has, we believe, become the major exchange and documentation of information in this important area of laser-induced damage in optical materials. In this regard we believe this symposium has played an important service to the development and use of lasers and laser systems throughout the world and we are pleased to have had a small part in this accomplishment. I have only been associated with the symposium since the early 1970's and in an official capacity only since the later 1970's. During this period I have been pleased to see the symposium maintain and build a truly international flavor and indeed its relevance by continually addressing new topics of interest to the research community. We have also, each year, experienced a growth in the number of quality papers. Much of the success of course is due to the hard work of our co-chairmen, both past and present, and indeed we all owe them our thanks.

As you know, the main part of NIST is located in Gaithersburg, Maryland, with the facilities here at Boulder being only a small part and about 500 people. The Group for which I am responsible is the Optical Electronic Metrology Group and is a group of about 45 people. We conduct research in laser measurements and standards, optical fiber, integrated optics, optical fiber sensors, and components for optical communications. Our work has been growing, due to new monies from the Congress and we expect additional growth in the next few years, especially in the area of optical communications. During this year we are putting in a chemical beam epitaxial system which will allow us to make multiple quantum wells, III-V integrated optic structures and long wavelength (1.3 and 1.55 micrometer) laser diodes and detectors. We will be using these facilities for our work in standards and measurement methods of these components. Our work in laser standards has been especially synergistic with the work of interest here at this symposium. Over the years we have developed a number of calorimeters used as national standards and have provided traceable measurement services to many of you during this period. We also, over a decade ago, developed a national standard

for measuring a few hundred kilowatts of cw laser power and are still providing measurement support with this system, although we have subsequently turned this system over to the Air Force. We are currently working on a national standard capable of measuring a few megawatts of cw power. Of additional interest may be our work on the measurement of fast laser pulses. We are pursuing both detector development, and both all optical and electro-optical sampling methods.

Standards are of course also very important in your work -- both physical standards such as measurement of power/energy, beam profile, pulse characteristics, etc. and procedural standards and measurement methods. We, of course, here at NIST work principally in development of physical standards, but we are very happy to and do participate in consensus standard-making bodies such as ASTM, ANSI, EIA, IEEE, etc. when we can make a contribution.

I hope your stay here in Boulder will be a pleasant one. If there is anything either I or my staff can do, please let me know.

Thank you and welcome.



## Symposium Introduction and Projections for Future Research

Brian E. Newnam  
Los Alamos National Laboratory  
Los Alamos, New Mexico 87545

On behalf of the Symposium Steering Committee of Drs. Harold Bennett, Arthur Guenther, M.J. Soileau, and myself, I am pleased to welcome you to the 20th Annual Symposium on Optical Materials for High-Power Lasers. It is always a pleasure to return to Boulder, Colorado, and the excellent facilities of the National Institute of Standards and Technology.

Before projecting into the future, I have a status report about the Proceedings of recent Boulder Damage Symposia and announcements about the planned activities for this meeting. In the last few years, the timely publication of the conference Proceedings has been a matter of concern, but we believe that we finally have the matter under control. I am glad to say that the 1985 Proceedings were mailed this summer, and copies of the 1986 Proceedings are available at the registration desk for last year's attendees. The 1987 Proceedings are about to be published, although the manuscripts of a number of the papers are not included because they were not available to us on time. Nevertheless, we do encourage delinquent authors to send in late manuscripts, which will be included in the following year's publication. A deadline of January 15 has been set for delivery of your manuscripts to enable us to publish this year's proceedings within the year. To contribute to early publication, we co-chairmen will remain in Boulder an extra morning after this symposium to summarize and document the technical highlights for inclusion with the proceedings.

Since this conference is sponsored by organizations of the U.S. Government, I am obligated to comment on the elegant clocks given to each registrant as a special conference memento. These are intended for your offices (not your homes) to advertise and promote these annual symposia.

Regarding the social events, do plan on attending the wine and cheese festival this evening. Also, you are invited to a special Banquet tomorrow evening to formally celebrate this Twentieth Laser Damage Symposium. As our after-dinner speaker, we are pleased to welcome back our colleague in damage, Dr. Jack Marburger. Although Jack is known to many of us for his definitive work on self focusing during the 1970's, he is now the very competent President of the State University of New York at Stony Brook.

Now, I wish to take this opportunity to discuss one topic that offers special opportunities for present and future research in the area of laser damage. This is the survival and performance of the optical components of free-electron lasers, known as FELs, which are now beginning to proliferate. First demonstrated by John Madey's group at Stanford University in 1977, this class of lasers was not of concern when research on the

causes of laser damage began at the end of the 1960's. For the last ten years, research centers in a number of countries have focused on the subtleties of FEL physics and experimental demonstrations. With continued developments, these lasers have the potential to have very high wall-plug efficiency, even up to 40% when energy-recovery schemes can be used. Major goals of present FEL research and development are: (1) high-average power operation at visible and near-infrared wavelengths, and (2) extension of the short-wavelength operating limit into the vacuum ultraviolet.

Briefly, the optical gain of an FEL is due to the stimulated emission from pulses of relativistic (1 MeV to 1 GeV) electrons passing through a magnetic undulator. The length of the undulator can range from  $<1$  to  $>10$  m, and the mirrors of an FEL optical resonator are precisely spaced so that the optical pulses overlap the train of picosecond electron pulses. Present FEL dimensions can be quite large, but there is a great desire to compress all FEL dimensions to reduce the necessary electron energy. This should make FELs cheaper and more attractive for a host of applications.

In contrast with the relatively limited spectral range of operation of most other lasers, the inherently broad tunability of FELs requires use of many classes of optically transparent and reflective materials. Recent experiences with the near-infrared FELs operating at Los Alamos and Stanford University have shown that optical damage to the mirrors, intracavity optical elements, and output windows limits the output power. Since FELs operate in essentially the lowest-order spatial mode in the resonator with the beam waist centered in the undulator, the mirrors generally have to be spaced far enough apart to reduce the incident beam intensity below the threshold for damage or significant thermal distortion. This contradicts the desire for compact resonators, so the need for maximum mirror damage resistance is obvious. One resonator design to increase the beam divergence in the resonators uses metal-coated, intracavity hyperboloidal reflectors at grazing incidence angles from  $80^\circ$  to  $88^\circ$ . This allows the end mirrors, which may have paraboloidal or ellipsoidal surfaces, to be moved in closer to the beam waist which is located near the center of the undulator. Likewise, intracavity elements such as output couplers and diffraction gratings experience lower intensities with this configuration.

In addition to highlight intensities, the FEL optics must operate in the presence of several other radiation hazards. First, high-energy radiation, gamma rays, x-rays, and neutrons, are produced by collisions of the electron beam with the various materials in the beam line. These create color centers in dielectric materials associated with impurities or structural changes even in pure materials. Second, optical harmonics of the fundamental laser wavelength, generated by the oscillatory motion of the electrons in the undulator, extend into the vacuum ultraviolet. These photons can produce color centers, too. Third, at the very high-peak powers associated with the picosecond micropulses, stimulated Raman scattering and self focusing may produce phase distortion in window materials. Finally, thermal distortion must be considered as the lowest order threat, especially in high-average power devices.

Of the above, vacuum-ultraviolet induced degradation of multilayer dielectric mirrors has been most problematic in FEL oscillators. For example, FEL researchers at the University of Paris found that titania-silica reflectors degraded after only a moderate exposure to ultraviolet synchrotron radiation in the ACO storage-ring FEL. Loss of oxygen from the coatings and carbon contamination were responsible. Similarly, the operating lifetime of the storage-ring FEL at Novosibirsk, USSR, has been limited by mirror degradation caused by VUV synchrotron radiation. VUV-induced degradation has also been observed in laser gyro reflectors. In this case, the He-Ne laser plasma radiates several lines below 100 nm, resulting in a slow deterioration in the titania/silica mirror reflectance. At this year's conference, Jim Early and Virgil Sanders of Los Alamos will present experimental data on the rate of degradation versus UV dose for a number of multilayer coating combinations. Apparently, certain materials, such as hafnium oxide, and optimized coating processes are more resistant to UV degradation. More work on this problem by members of the laser damage community could be very fruitful.

Although multilayer dielectric mirrors can be produced with very high reflectance and are very convenient as transmissive output couplers, metal mirrors have survived best in FEL oscillators operating in the visible and infrared. Also, certain metals have a broad range of high reflectance which allows for continuous tuning of the FEL wavelength. However, for future high-average power FELs, the absorption of metal reflectors is still too large, and the resultant thermal loading could cause excessive surface distortion. One potential solution to this problem may be operation at cryogenic temperatures. At the 1981 Boulder Damage Symposium, Don Decker and V. Hodgkin of the Naval Weapons Center presented evidence that absorption of silver surfaces does indeed exhibit the predicted temperature dependence, decreasing from the values at 300 K to a factor of 5 lower at 77 K. However, with repeated thermal cycling, the absorption values were not reproducible, indicating that some surface restructuring was occurring. With such a high potential impact on laser power handling capability cryogenic metal mirrors should be pursued seriously.

Looking forward into the future, FEL technology will extend into the extreme ultraviolet below 100 nm. This will require resonator mirrors with adequately high reflectance both to minimize roundtrip losses and to control surface figure distortion due to absorption. Over the 30-100 nm and 10-14 nm spectral ranges, these requirements may be satisfactorily met by the multifaceted metal mirror design that I first described here during the 1985 Symposium. This year, Marion Scott will give a poster paper that describes Los Alamos progress to implement this design into a nine-faceted aluminum retroreflector that attained a measured reflectance of 89% at 58.4 nm. This is a factor of 3 higher reflectance than previously attained by any other mirror operating in this wavelength region. This work may lead to practical devices, but I do recommend that some of you try to devise other new mirror concepts for the XUV.

In summary, FELs pose a number of challenging problems for the optical and laser damage community. Since there is a wide array of potential applications awaiting these devices,<sup>1-4</sup> it is important that damage-resistant optical elements be developed to further FEL utilization.

- [1] Deacon, D.A.G.; De Angelis, A., eds. Applications of Free Electron Lasers, in Nucl. Inst. and Methods in Phys. Res. A239, No. 3(1984).
- [2] Deacon, D.A.G.; Newnam, B.E., eds. Free-Electron Laser Applications in the Ultraviolet, Opt. Soc. Am., Washington, DC; OSA Tech. Digest Series, Vol. 4; 1984.
- [3] Morin, P. "FEL Applications in the UV," Synchrotron Radiation News 1, 11; 1988.
- [4] Deacon, D.A.G.; Haglund, Jr., R.F.; Newnam, B.E.; Schlossberg, H., eds. Special Issue on Physics of Free-Electron-Laser Applications, J. Opt. Soc. Am. B, 6, May, 1989.



## OPENING COMMENTS - 20TH ANNUAL DAMAGE SYMPOSIUM

Arthur H. Guenther  
Los Alamos National Laboratory  
Los Alamos, NM 87545

Good morning and welcome to Boulder. This is truly a pleasure for all of us to be back here celebrating our 20th year at this venue. We thought it might be appropriate to share with you some of the background of this series of conferences. Some of this may be old news to a few of you, but I am sure much of this information will be new because of the longevity of this symposium. A review will point out why we are meeting here at the Boulder Laboratories of the National Institute of Standards and Technology, known as the National Bureau of Standards until recently. As you all know, laser action was first demonstrated in 1960 and their application exploded on the commercial market shortly thereafter. The language of commerce to many people is standards, standards of definitions, of tests, of performance specifications. When one purchases something, one needs to describe its characteristics and have both the supplier and the buyer agree on what the terminology means. That happens to be the business, in part, of standards. The National Institute of Standards and Technology has in its charter a responsibility to interact with standards committees in promulgating standards through certain procedures.

Back in those early days, the ASTM, the American Society for Testing and Materials, was involved in developing standards for the burgeoning laser industry. It formed a committee, a subcommittee of its Fl electronics committee, in the mid-sixties and it started to attack laser problems of slope efficiency, beam divergence and other quantities that were important to laser manufacturers and purchasers at that time. The committee consisted of buyers and suppliers, while government people were represented either by the Institute of Standards and Technology or people from the DoD or DoE. The objective of the group activities was to address the standards that were being proposed, tested, and evaluated. We found that when we got together to develop standards, we could not agree among ourselves what parameters should be measured as well as how they should be measured. We decided it would be appropriate to have what would be called a mini-symposium to discuss the physics of the issues under question.

You must realize that standards are supposed to measure the quantity or object under test. Standards should not depend on the operator of the test or instruments used in the test or anything like that, they need to be test object sensitive. It is necessary to develop standards that have a good foundation based on an understanding of the physical and engineering principals that are behind the operative definition and the test procedures. Because of the newness of the field of lasers we had to start with definitions and data reduction methods. A series of round-robin tests was organized to insure that we were measuring the sample under test and not the performer of the test!

We were quite successful in holding several mini-symposiums on selected subjects like beam divergence, slope efficiency, crystal orientation, roughness, etc. Damage came along as an issue that was, of particular interest, in those early days of rather impure materials and great variability in what you could buy in the commercial sector. So it was decided in 1969 to hold a little mini-symposium that would discuss the physics of damage and then write our standard. We thought that would be the end of the subject. At that early meeting, I think there were thirty-five people. We found out that we knew even less than we thought we did when we went into the meeting. That is how this conference started. The proceedings of the first meeting were published by ASTM. However, few have seen it since the distribution was more limited than the subsequent proceedings, published as NBS Special Publications.

The history we have just reviewed explains why, in fact, we are here in Boulder at the Boulder Laboratories of the what was then the National Bureau of Standards. The meeting logo features the Flatiron mountains surrounding the Boulder Laboratories and is symbolic of the important role played by the National Institute of Standards and Technology in these meetings (Fig. 1).

The following figures contain some interesting statistics. Some of the early chairmen of the ASTM sub-committees include Johnnie Meyers, who now runs KIGER and makes optical and laser materials; Haynes Lee, who presently is executive director of the Laser Institute of America; John Detrio, who is at the University of Dayton Research Institute; and me (Fig. 2). One thing that is sure is that we have out-lived the sub-committee on lasers of the ASTM. The ASTM is still the sponsor of this conference because they, in fact, put one of their reference numbers on our proceedings and distribute the proceedings, not only here in the United States, but also in Europe. I think this participation has a lot to do with why we have had good foreign representation at this conference.

In 1969, Alex Glass and I took it upon ourselves to write up and put the proceedings together. A major player in attracting some of the speakers was Martin Stickley who was at that early meeting. As the meeting progressed and grew we needed additional help and were pleased to add Hal Bennett from the Naval Weapons Center and Brian Newnam from Los Alamos to the committee as co-chairmen. Alex was moving to the corporate aspect of lasers. We also added Dave Milam as a representative from Livermore and said goodbye to Alex as co-chairman. Alex, in fact, still acts as our treasurer, so he can maintain a connection with this particular meeting.

The co-chairmen primarily represented the DoD and the DoE, which had large programmatic interests in the damage question. We were starting to see a tremendous influx from the academic community and felt that it would be necessary to start bringing in some young blood to stimulate those guys who were becoming old war horses in this business. Thus, we added M.J. Soileau as a co-chairman last year to represent the academic community. All of these people have made significant contributions to this conference over the years. Aaron Sanders of the Boulder Laboratories is coordinator for

this meeting. Over the years we have had sponsorship from those organizations that are listed in the proceedings. We have had additional support from organizations such as the Naval Weapons Center and the Air Force Weapons Laboratory. They provide in-kind services by which we were able to bring in staff personnel to help us operate the meeting. Last, Dave Milam is moving on to other areas at Lawrence Livermore National Laboratory and is being replaced by some virile new blood the very capable Lloyd Chase. Good-bye Dave, welcome Lloyd.

How has the meeting grown? As the chart shows, we have grown to about eighty papers this year and about 210 participants. I will be honest with you; one of the goals that we set for ourselves was to review the technical content of what has gone on at Boulder for twenty years. We found it necessary to only have two of those reviews this year. We will have the other two reviews next year because of lack of time due to the large number of papers submitted this year. There has been a healthy growth in both attendance and participation. Many of us feel the present level is about correct, since we don't want to go to multiple sessions and wish to have the meeting remain informal and conducive to discussion and openness (Fig. 3).

You might find the nations that have been involved in this conference over the last 20 years interesting. They are listed in the attendance lists at the back of our proceedings. I went through those attendance lists and checked off the participating countries. Of the more than 900 papers that have been presented in the first twenty years, about fifteen percent were from countries other than the United States. By the end of this meeting, we will probably have 3,000 participants over the twenty years and about seven percent from countries outside of the United States (Fig. 4).

What has been happening at the meeting? The graph represents a percentage of the total papers that were divided up among the four areas into one of which we try to place each contribution (Fig. 5). The areas include fundamental mechanisms, which concern primarily the interaction of light with optical media: mirrors and surfaces, which involve reflectivity, scattering, polishing techniques; thin films, which is self explanatory; and bulk materials and measurements, which covers new materials and the measurement of those properties important in the damage process. In the beginning there was no work on thin films, and everybody was interested in getting impurities or platinum inclusions out of laser glass. Issues like that generated a need for a data base, and that is why in the early years most of the papers dealt with materials and measurement issues. Mirrors and surfaces have been of fairly constant interest, as have fundamental mechanisms. We really do try to understand. A lot of the early papers in this particular area dealt with self focusing in materials and high-power effects such as multiphoton processes and their theoretical analysis. But as you have seen, we have realized that the area with the most leverage for improvement in optical performance of systems is in the thin films area. This area has grown to be the major portion of the meeting at the present time. The drivers in the early days were high-power issues because of ICF, the Inertial Confinement Fusion program of the DOE, and the high-energy area by the DoD. Commercial spin-off

abounded and still does -- with the added benefit of education and basic research by the university community. Just think of how many graduate students presented their results here at Boulder. (Including one of the current conference co-chairs!).

Looking through the index from the first meeting in 1969, I noticed that at least one person who gave a paper at the first meeting is at this meeting, and that is Dave Edwards (Fig. 6). He is going to give a paper later this week. Our first foreign participant is Jon Davit, an individual from CGE in France. CGE was a prime developer of high-power glass laser systems at that time. We move on five years later and there is self-focusing. Jack Marburger, a major contributor in that area, will be our banquet speaker on Thursday night (Figs. 7 and 8). This summary starts to give you an indication of some of the people involved and some of those people who are still coming to this meeting.

Let us move on to our glorious Tenth. In the tenth symposium, measurement of absorption characteristics and bulk material properties were big players. On the second page of contents it is interesting to note: Dave Milam, Brian Newnam, Art Guenther, Hal Bennett, and if you look down at the bottom, there is M.J. Soileau, all present co-chairmen and all are found on one page of the index of that particular year (Figs. 9 and 10). And if we go on to our fifteenth, John Detrio, gave a presentation on ASTM, and John is here at this particular meeting (Figs. 11, 12, 13, and 14, Laser Induced Damage in Optical Materials: 1983, NBS Special Publication No. 688). If we go on, we see what happened just five years ago. You are going to hear more in depth discussion of the surface and mirrors and fundamental mechanism areas during the review papers at this conference.

It is interesting to note that at that particular meeting there was a report of round-robin experiments involving damage testing of thin films, fifteen years after the meeting started and we were now at least at a round-robin test. And by the way, it was interesting that a lot of these people went to Liechtenstein to discuss this subject, and we published reports on our deliberations in a special issue of Applied Optics. There were several papers at that meeting that dealt with the measurements of damage at seven to nine different laboratories throughout the world to try to see how well we understood the damage process and if we could agree on levels.

At our tenth, we had a logo contest and that was the logo that was drawn up by Jerry Bettis then at the Air Force Weapons Lab, now at Rocketdyne. He is here in the audience. We were a lot more staid bunch of people at that time, as you can tell from the next figure (Fig. 15). Anyhow, we did put a sheet which described its significance, in the proceedings of our tenth meeting (Fig. 16). You will remember from the first slide I showed, that these are the flatiron mountains, and we are doing a little damage down here at the foothills of the flatirons, and that is the logo of the Boulder Damage Symposium.



We sent out announcements to people and suggested to them how they should prepare their abstracts to be published in the program. One of the examples I would like to share with you says that a solution to laser induced surface damage was found. I will not tell you who the authors are yet, but the abstract says

ever since roughness assisted laser breakdown reared its jagged head, the attempts to explain the effects have gone through ups and downs. In the particularly heated attack on the problem, samples were flame polished and then tested. Although there was some improvement in threshold, people tended to gloss over our results. We attempted to dig out the answer by etching some test samples, but we only managed to magnify the depth of the difficulty. We also tried to cover the problem up by using thin film overcoats, but even the laser beam saw through that ruse.

So we have tried a new approach, which we reported in another paper. We made numerous measurements and gathered mountains of data on height distributions in the expectation that essential features would stand out. Analyses of the data included determining slope distributions, since we were obviously searching for new slants on the problem. This method, in which detail analysis of large quantities of data would cause proper relationships to surface and suggest themselves, is called the auto-correlation approach. So if I were to say we were successful, the answer would be simplicity itself. The problem is that standard components have surfaces. Surface damage is not possible if there is no surface to damage. This realization immediately suggested the proper solution, as is well known, a piece of material in the shape of Mobius strip has two faces, but only one surface. Edges do not count here, therefore make an optical component in the shape of a Mobius strip and radiate the face that has no surface. Our paper discusses how to accomplish this new twist in optics and technology.

That was written by A. Anonymous and U.N. Known of Bedlam Agriculture and Technical School that is in Bedlam, New York 10023. It really was the work of Dick House at the Weapons Laboratory who was a student at that particular time. I guess he had nothing better to do than to write comic literature for us to enjoy. But anyhow one of the things that we did at the tenth was to do an index of all the papers and divide them up by abstract, subjects titles, authors, and by year (Fig. 17). It is our intention, if possible, to try and put out a twenty- year index at the end of this particular meeting. Let us go on, we were so successful with our logo we even ended up on the cover of Applied Optics (Fig. 18). These ties are golden now and becoming collectors items. Through the use of this logo, we try to promulgate the meetings' identity, location and importance.

With that foundation -- watch our next 20 years! Thank you, all of you, ( without you there would be no meeting) you have truly advanced our understanding and aroused our awareness of the importance of laser-induced damage studies. Come back for our twentieth anniversary meeting next year.



Figure 1. Flatiron mountains overlooking the Boulder Laboratories (right center) served as the logo for the 1969 Damage Symposium.



# BOULDER DAMAGE SYMPOSIUM MOVERS

## ASTM Committee F-1 Chairmen

Johnny Meyers, Haynes Lee  
Art Guenther, John Detrio

## Chairmen

1969 A. J. Glass, A. H. Guenther (C.M. Stickley)  
1979 add H. E. Bennett and B. E. Newnam  
1981 add D. Milam, good--bye A. J. Glass  
1987 add M. J. Soileau  
1988 add L. Chase, good--bye D. Milam

## Coordinator

Aaron A. Sanders

## Treasurer

A. J. Glass

## Sponsors

AFOSR, ASTM, DARPA, DOE (LANL, LLNL), NIST (NBS) ONR

Figure 2. Boulder Damage Symposium movers.

# Boulder Damage Symposium Participation Indicates Strong Interest in Laser Damage Research

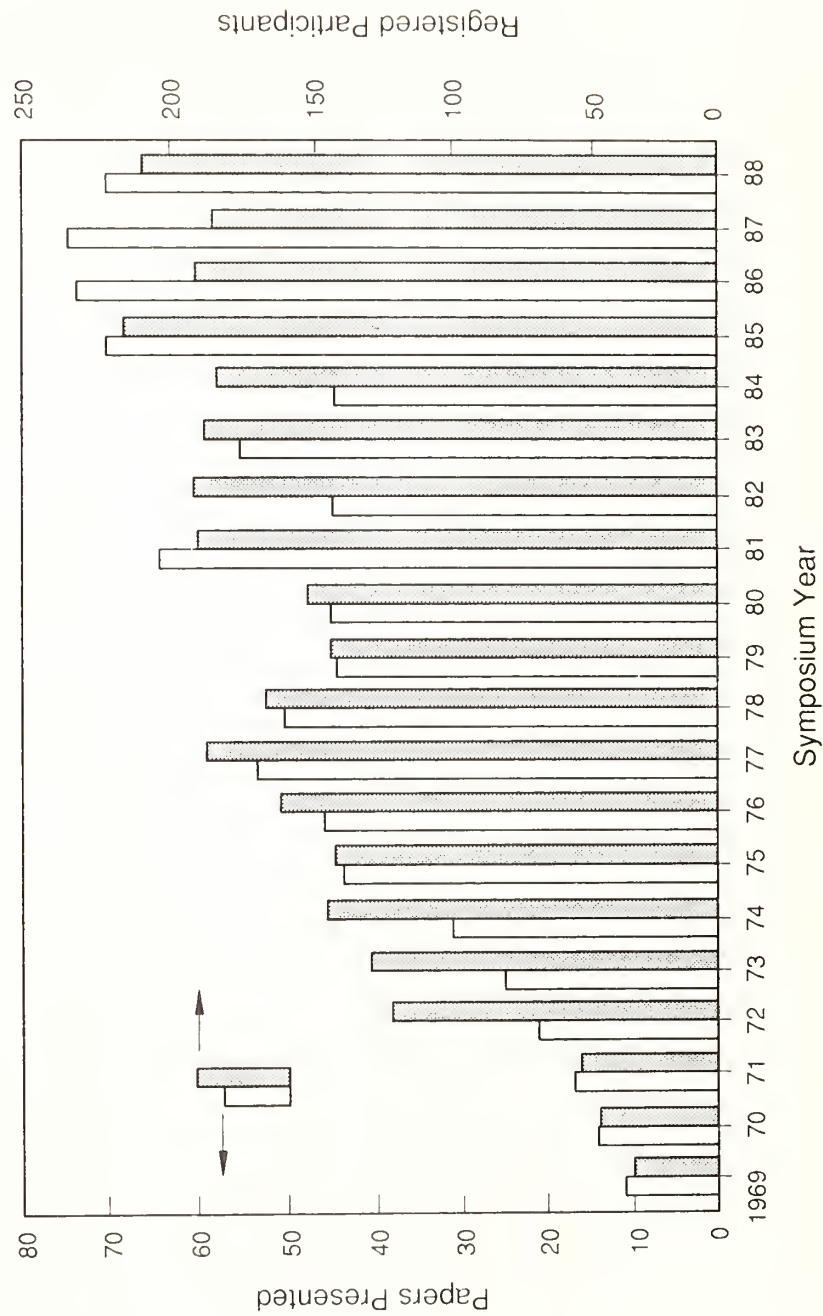


Figure 3. Boulder Damage Symposia participation/presentations--  
1969 through 1988.

# NATIONS PARTICIPATING IN THE BOULDER DAMAGE SYMPOSIA

1969 - 1988

AUSTRALIA	JAPAN
BRAZIL	LIECHTENSTEIN
CANADA	NETHERLANDS
DENMARK	PEOPLES REPUBLIC
FEDERAL REPUBLIC	OF CHINA
OF GERMANY	SWEDEN
FRANCE	TAIWAN
GREAT BRITAIN	UNITED STATES OF AMERICA
INDIA	UNION OF SOUTH AFRICA
ISRAEL	UNION OF SOVIET
	SOCIALIST REPUBLICS

- OF THE >900 PAPERS PRESENTED IN OUR FIRST 20 YEARS, ~135 (15%) WERE FROM COUNTRIES OTHER THAN THE USA.
- OF THE >2800 PARTICIPANTS IN OUR FIRST 19 YEARS, ~200 (7%) WERE FROM COUNTRIES OTHER THAN THE USA.

Figure 4. Nations participating in the Boulder Damage Symposia--  
1969 through 1988.

# THE TOPICAL EMPHASIS IN LASER DAMAGE RESEARCH HAS EVOLVED AT THE BOULDER DAMAGE SYMPOSIA

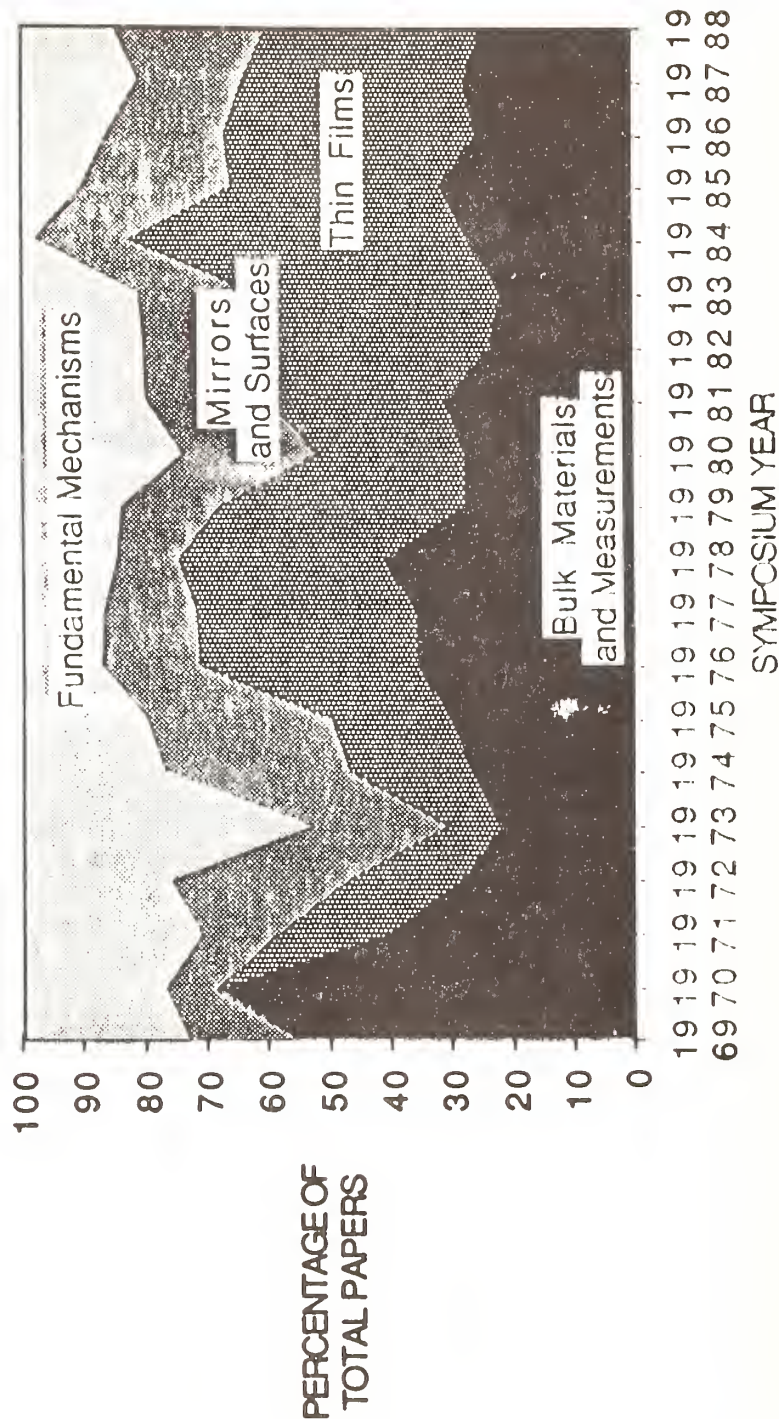


Figure 5. The topical emphasis in laser damage research has evolved at the Boulder Damage Symposia.

# BOULDER DAMAGE SYMPOSIUM 1969

Laser-Damage Mechanisms in Transparent Dielectrics—E. S. BLISS . . .	
Discussion . . . . .	
Laser-Beam Self-Focusing and Glass Damage Caused by Electrostrictively Driven Acoustic Waves—EDWIN L. KERR . . .	
Discussion . . . . .	
Non-Destructive Damage Studies of Ruby Laser Rods—E. CHICKLIS, J. SCHWARTZ, AND CARL A. PITHA . . . . .	
Discussion . . . . .	
Applications of Electron Spin Resonance to Study of Damage in Glass Lasers—C. S. NAIMAN AND E. CHICKLIS . . . . .	
Surface-Damage Threshold Measurements for Several Laser Glasses —J. E. SWAIN . . . . .	
Discussion . . . . .	
Damage-Threshold Testing of Laser Glass at Owens-Illinois —H. A. LEE . . . . .	
Laser-Induced Damage in Glass—C. G. YOUNG AND R. F. WOODCOCK . . .	
Discussion . . . . .	
Laser Damage in Optical Glasses—J. DAVIT . . . . .	
Discussion . . . . .	
Self-Focusing in Glass—FRED W. QUELLE . . . . .	
Glass-Laser-Materials Testing at Naval Research Laboratory —JOHN M. McMAHON . . . . .	
Discussion . . . . .	
Diagnostics and Evidence of Pre-Catastrophic Damage in Transparent Solids—DAVID F. EDWARDS, Y. D. DANKLER, JON D. MASSO, AND C. V. CHEN . . . . .	
Discussion . . . . .	
General Discussion . . . . .	

Figure 6. Contents of 1969 Boulder Damage Symposium.



# BOULDER DAMAGE SYMPOSIUM 1973

Opening Remarks . . . . .	A. H. Guenther
The ARPA Program on Optical Surface and Coating Science . . . . .	C. M. Stickley

## SELF-FOCUSING

Nonlinear Refractive Index Measurements in Laser Media . . . . .	A. Owyang
Self-Focusing in Yttrium Aluminum Garnet and Optical Glasses . . . . .	A. Feldman, D. Horowitz, & R. M. Waxler
A Rational Definition of Index Nonlinearity in Self-Focusing Media . . . . .	A. J. Glass
Self-Focusing of Very Powerful Laser Beams . . . . .	B. R. Suydam
Homogeneity Requirements for Minimizing Self-Focusing Damage . . . . .	J. Marburger, A. Jokipii, A. Glass, & J. Trenholme
Self-Focusing and Saturation in Disk Amplifiers . . . . .	K. A. Brueckner & J. E. Howard
Damage Control in a 100 GW High Power Laser System (Abstract only) . . . . .	J. Tillotson, B. Guscott, & K. Moncur

## SURFACE DAMAGE

Low Scatter Finishing of Optical Elements . . . . .	W. P. Barnea
Laser Surface Damage Studies on Several Glasses . . . . .	N. L. Boling, G. Dube', & M. D. Crisp
Some Aspects of Surface Damage That Can Be Explained With Linear Optics . . . . .	M. D. Crisp
Damage in Lithium Iodate With and Without Second Harmonic Generation . . . . .	C. R. Giuliano & D. Y. Tseng
Laser Surface Damage Studies at Bendix . . . . .	P. Braunlich, J. Carrico, B. Rosenblum, & A. Schmid
Effects of Laser Flux on GaAs . . . . .	J. L. Smith
Carrier Effects Observed in Laser-Induced Damage In A Silicon Junction Photodetector . . . . .	J. F. Giuliani

## OPTICAL COATING DAMAGE

The Role of Coating Defects in Laser-Induced Damage to Thin Films . . . . .	L. G. DeShazer, B. E. Newnam, & K. M. Leung
The Role of Inclusions and Linear Absorption in Laser Damage to Dielectric Mirrors . . . . .	D. Milam, R. A. Bradbury, & M. Bass
Time Resolution of Laser-Induced Damage to Thin Films . . . . .	N. Alyassini, J. H. Parke, & L. G. DeShazer

Figure 7. Contents of 1973 Boulder Damage Symposium.



#### DAMAGE TO INFRARED COMPONENTS

Investigation of Pulsed CO Laser Damage in Coated Metal Mirrors and Dielectric-Coated Windows . . . . .	S. Holmes & P. Kraatz
Pulsed CO <sub>2</sub> Laser Damage Studies of Windows and Window Coatings . . . . .	A. I. Braunstein, V. Wang, M. Braunstein, J. E. Rudisill, & J. Wada
Pulsed CO <sub>2</sub> Laser Damage Studies of Metal and Dielectric Coated Mirrors . . . . .	V. Wang, A. Braunstein, M. Braunstein, J. E. Rudisill, & J. Y. Wada
Damage Threshold in 10.6 $\mu$ m Laser Materials . . . . .	J. Davitt
Radiation-Induced Damage to NaCl by 10.6 $\mu$ m Fractional Joule, Nanosecond Pulses . . . . .	W. H. Reichelt & E. E. Stark, Jr.
A Study of 10.6 $\mu$ m Laser-Induced Damage in Alkali Halide Crystals . . . . .	H. Posen, J. Bruce, J. Comer, & A. Armington
Surface and Coating Absorption Measurement With An Alphaphone . . . . .	E. L. Kerr

#### THEORY AND FUNDAMENTAL PROPERTIES

Photoelastic Constants of Infrared Transmitting Materials . . . . .	B. Bendow & P. D. Gianino
Checks of Multi-Phonon Absorption Theory . . . . .	R. Hellwarth
Theory of Material Failure in Crystals Containing Infrared Absorbing Inclusions . . . . .	C. J. Duthler & M. Sparks
Surface Damage by Laser-Induced Collective Electron Oscillations . . . . .	R. A. Shatas, L. M. Narducci, J. L. Smith, H. C. Meyer, & S. S. Mitra
Studies of Intrinsic Optical Breakdown . . . . .	D. W. Fradin & M. Bass
Laser-Induced Surface Damage in Proustite (Ag <sub>3</sub> AsS <sub>3</sub> ) at 1.06 $\mu$ m and 0.694 $\mu$ m . . . . .	C. R. Giuliano & D. Y. Tseng
Spectral Emittance Measurements on Several Crystalline Samples . . . . .	D. L. Stierwalt
A Sensitive Interferometric Null Method for Measuring Stress-Induced Birefringence . . . . .	G. Birnbaum & E. Cory

Figure 8. Contents of 1973 Boulder Damage Symposium (contd.).

# BOULDER DAMAGE SYMPOSIUM 1978

## INTRODUCTORY REMARKS

DDE Welcome--Presentation of Awards to Drs. Guenther and Glass.....	C. M. Stickley
Defense ARPA Welcome.....	H. V. Winsor
Symposium Welcome.....	A. J. Glass

## MEASUREMENT OF ABSORPTION CHARACTERISTICS

Discussion of a Theory of Analysis of Rate Calorimetry which Includes Coating Absorption....	N. C. Fernelius and G. T. Johnston
Absorption Coefficient of NaF by Attenuated Total Reflection Spectroscopy.....	D. L. Burdick
Laser Calorimetric Measurement of Two Photon Absorption.....	M. Bass, E. W. Van Stryland, and A. F. Stewart
A Comparison of Bulk and Surface Absorptions in NaCl and KCl between 9.2 and 10.8 $\mu\text{m}$ .....	H. Vora, M. C. Dhmer, and T. G. Stoebe
A 1.06 $\mu\text{m}$ Laser Absorption Calorimeter for Optical Coatings.....	T. H. Allen, J. H. Apfel, and C. K. Carniglia
Measured Thin Film Absorption at the Air-film Interface, the Film Bulk, and the Film-substrate Interface.....	P. A. Temple, D. L. Decker, T. M. Donovan, and J. W. Bethke
Photoacoustic Spectroscopy Studies of Thin Film Coatings on Laser Windows.....	N. C. Fernelius and D. A. Walsh

## BULK MATERIAL PROPERTIES

Piezo-optical Coefficients of Some Neodymium Doped Laser Glasses and Single Crystals of $\text{CaF}_2$ , $\text{BaF}_2$ , and $\text{SrF}_2$ .....	R. M. Waxler, A. Feldman, and D. Horowitz
Refractive Index of Strontium Fluoride.....	M. J. Dodge
The Development of Fluorides for High Power Laser Optics.....	J. F. Ready, H. Vora, R. A. Skogman, K. M. Leung, and E. Bernal G.
Optical Properties of KCl Forged between Optically Polished Dies.....	R. H. Anderson and J. M. Bennett
Bulk Optical Properties of Fine Grained Forged Calcium Fluoride.....	R. H. Anderson, R. A. Skogman, J. F. Ready, and J. M. Bennett
CW Laser Damage in AR Coated Alkaline Earth Fluorides at 3.8 $\mu\text{m}$ .....	J. A. Detrio and R. D. Petty
Lattice Absorption, Phonon Assignments, and Image Spoiling Properties of CVD ZnS in the Infrared.....	C. Klein, B. Di Benedetto, R. Donadio, T. Kohane, and J. Pappis
Laser Induced Damage in Fluoride Glasses: A Status Report.....	S. E. Stokowski, D. Milam, and M. J. Weber
Liquids for High Repetition Rate Glass Laser Systems J. M. Rinefierd, S. D. Jacobs, D. C. Brown, J. A. Abate, O. Lewis, and H. Applebaum.....	

Figure 9. Contents of 1978 Boulder Damage Symposium.

#### MIRRORS AND SURFACES

- Physical and Optical Properties of Surfaces Generated by Diamond-Turning on an Advanced Machine  
D. L. Decker and D. J. Grandjean.....
- Optical and Metallurgical Characterization of Molybdenum Laser Mirrors  
S. M. Wong, G. Krauss, and J. M. Bennett.....
- 1064 nm Laser Damage Thresholds of Polished Glass Surfaces as a Function of Pulse Duration and Surface Roughness  
D. Milam.....
- Large Giant and Free-running Laser Pulse Energy and Power Densities through Optical Fibers  
M. J. Landry.....

#### THIN FILM DAMAGE

- Ultraviolet Damage Resistance of Laser Coatings  
B. E. Newnam and D. H. Gill.....
- Multithreshold Evaluation of 100-nsec Pulsed Laser Damage to Coating Materials at 2.7 and 3.8  $\mu$ m Wavelengths  
J. D. Porteus, T. M. Donovan, J. L. Jernigan, and W. N. Faith.....
- Multithreshold Damage Measurements on  $As_2S_3$ ,  $As_2Se_3$ , and NaF at HF and DF Wavelengths  
T. M. Donovan, J. D. Porteus, J. L. Jernigan, and E. J. Ashley.....
- TEM Investigation of Effects of a Barrier Layer on Damage to 1.064  $\mu$ m AR Coatings  
C. K. Carniglia, J. H. Apfel, G. B. Carrier, and D. Milam.....
- Optical Techniques for the Determination of Pulsed Laser Damage in Thin Films  
T. W. Walker, A. H. Guenther, and P. E. Nielsen.....
- A Statistical Analysis of Absorptive Laser Damage in Dielectric Thin Films  
A. B. Budgor and K. F. Luria-Budgor.....

#### COATING MATERIALS AND DESIGN

- New Coating Materials for IR Laser Optical Components  
R. C. Pastor, J. A. Harrington, L. E. Gorre, and R. K. Chew.....
- Improved  $PbF_2$  Coatings for the Infrared  
P. Baumeister, G. P. Arnold, and D. F. Edwards.....
- Graded Index Coatings of Cubic Thallium Iodide (TlI) and Lead Fluoride ( $PbF_2$ )  
T. J. Moravec and R. A. Skogman.....
- Simple Expressions for Calculating the Effect of Volume or Interface Absorption in Thin Films on the Performance of High Reflectance or Antireflectance Multilayer Coatings  
H. E. Bennett and D. K. Burge.....
- Simplified Description of Dielectric Reflectors  
M. Sparks and M. Flannery.....
- Electric Fields near Coated Surfaces: Application to Damage Protection  
H. B. Rosenstock.....

#### BREAKDOWN PHENOMENA

- Computer Simulation of Laser Damage Morphology in the Alkali Halides  
P. Kelly, D. Ritchie, P. Bräunlich, and A. Schmid.....
- The Relative Role of the Impact and Multiphoton Ionization Mechanisms in Laser Induced Damage of Transparent Dielectrics  
B. G. Gorshkov, A. S. Epifanov, and A. A. Manenkov.....
- Theory of Laser Damage in Dielectric Solids  
S. Brawer and W. L. Smith.....
- Laser Induced Damage in Semiconductors  
Yu. K. Danileiko, A. A. Manenkov, and A. V. Sidorin.....
- Frequency Dependence of Breakdown Fields in Single-Crystal NaCl and KCl  
M. J. Soileau, M. Bass, and E. W. Van Stryland.....
- Investigation of the Surface Breakdown Mechanism in IR-optical Materials  
V. I. Kovalev and F. S. Fatzulloev.....

Figure 10. Contents of 1978 Boulder Damage Symposium (contd.).

CONTENTS		Page
Foreword.....	H. E. Bennett, A. H. Guenther, D. Milam, and B. E. Newnam	111
Disclaimer.....		111
Memoriam.....		iv
Symposium Welcome.....	A. H. Guenther	ix
Welcome on Behalf of the ASTM.....	J. A. Detrio	xxi
Summary of Meeting.....	H. E. Bennett, A. H. Guenther, D. Milam, and B. E. Newnam	1
1.0 Introduction.....		1
2.0 Principal Conclusions.....		2
2.1 Materials and Measurements.....		2
2.2 Surfaces and Mirrors.....		4
2.3 Thin Films.....		4
2.4 Fundamental Mechanisms.....		6
3.0 Summary of Papers.....		7
3.1 Materials and Measurements.....		8
3.2 Surfaces and Mirrors.....		12
3.3 Thin Films.....		16
3.4 Fundamental Mechanisms.....		22
4.0 Recommendations for the Future.....		26
5.0 Acknowledgments.....		27
6.0 References.....		28
<u>Materials and Measurements</u>		
Studies of Optical and Mechanical Properties of Heavy-Metal Fluoride Glasses.....	B. Bendow, D. K. Burge, H. E. Bennett, L. H. Johnston, and J. J. Mecholsky	30
Optical Properties of Infrared Transmitting Glasses.....	S. S. Mitra	51
Optical and Mechanical Properties of Water Clear ZnS.....	R. J. Harris, G. A. Graves, D. V. Dempsey, P. R. Greason, M. E. Gangl, D. B. O'Quinn, and M. J. Lefebvre	52
Laser Damage in Plastics at the Frank J. Seiler Research Laboratory (FJSRL).....	R. M. O'Connell, T. T. Saito, T. F. Deaton, K. E. Siegenthaler, J. J. McNally, and A. A. Shaffer	59
Increase in the Optical Damage Threshold of Cellulose Acetate.....	M. A. Acharekar	70
Strehl Ratio Measurements of Laser Damaged Plastics.....	B. W. Mullins and B. A. Richert	80
Damage Thresholds of Fused Silica, Plastics and KDP Crystals Measured with 0.6-ns 355-nm Pulses.....	M. C. Staggs and F. Rainer	84

Figure 11. Contents of 1983 Boulder Damage Symposium.

Strengthening CsI Crystals for Optical Applications.....	91
W. W. Durand, B. G. Koepke, and W. W. Gerberich	
Strengthening of Calcium Fluoride.....	101
C. B. Willingham, M. A. Spears, G. A. Graves, and W. L. Knecht	
Investigation of Window Materials for Repetitively Pulsed CO <sub>2</sub> Lasers.....	106
J. S. Goela, R. L. Taylor, M. J. Lefebvre, P. E. Price, Jr., and M. J. Smith	
Laser Induced Bulk Damage in SiO <sub>2</sub> at 1.064, 0.532 and 0.355 $\mu$ m.....	128
L. D. Merkle, N. Koumvakalis, and M. Bass	
Bulk Absorption Measurements Using Prism-Shaped Samples for Laser Calorimetry.....	135
P. A. Temple and D. P. Arndt	
<u>Surfaces and Mirrors</u>	
Inherent Mechanical Damage in Diamond Machined Optical Surfaces.....	140
H. H. Hurt and D. L. Decker	
Optical Properties of Diamond-Machined Metal Surfaces and Their Relationship to Physical and Chemical Surface Perfection.....	147
D. L. Decker, H. H. Hurt, J. O. Porteus, and D. J. Grandjean	
The Effect of Surface Finish on the Laser-Induced Damage Thresholds of Gold-Coated Copper Mirrors.....	157
R. M. Wood, P. Waite, and S. K. Sharma	
Thermally Induced Effects on the Infrared Reflectance of Metal Mirrors.....	164
V. A. Hodgkin and D. L. Decker, and H. H. Hurt	
Single-Shot, Cumulative and PRF Dependent Laser-Induced Damage Thresholds.....	174
R. M. Wood, P. Waite, and S. K. Sharma	
Damage Threshold of Fused Silica at 3 $\omega_0$ .....	179
J. F. Mengue and D. Friart	
Round-Robin Testing of Low-Scatter Optics.....	183
J. M. Bennett and W. Kent Stowell	
Light Scattering Characteristics of Some Metal Surfaces--A Smoothing Effect?.....	202
J. R. McNeil, L. J. Wei, J. Casstevens, W. C. Herrmann, Jr., and J. C. Stover	
Light Scattering from Surfaces with Microroughness and Static Density Variations in the Bulk Dielectric Permittivity.....	211
J. M. Elson	
Surface Finish Measurements on Low Scatter Laser Mirrors and Roughness Standards.....	220
J. M. Bennett, K. H. Guenther, and P. G. Wierer	
The Effects of Slope Error on the Imaging Quality of a Mirror as the Ratio of Surface Perturbation Depth to Wavelength Approaches Zero.....	236
H. E. Bennett and D. K. Burge	

Figure 12. Contents of 1983 Boulder Damage Symposium (contd.).

# Thin Films

1.06 Micron Laser Damage of Thin Film Optical Coatings - a Round Robin Experiment Involving Various Pulse Lengths and Beam Diameters.....	241
K. H. Guenther and T. W. Humpherys, J. Balmer, J. R. Bettis, E. Casparis, J. Ebert, M. Eichner, A. H. Guenther, E. Kiesel, R. Kuehnel, D. Milam, W. Ryseck, S. C. Seitel, A. Stewart, H. Weber, H. P. Weber, G. Wirtenson, and R. M. Wood	
Measurements of the Dependence of Damage Thresholds on Laser Wavelength, Pulse Duration, and Film Thickness.....	268
F. Rainer, C. L. Vercimak, D. Milam, C. K. Carniglia, and T. Tuttle Hart	
A Fundamental Approach Towards Improved Optical Coatings.....	277
K. L. Lewis and J. A. Savage	
Development of RF-Sputtered Laser Coatings at Burleigh Northwest.....	287
D. Lunt	
Comparison of Optical Coatings Deposited by Novel Physical and Chemical Techniques.....	292
F. J. Wodarczyk, D. R. Strauss, and A. B. Harker	
Optical Characterization of Low-Scatter, Plasma-Deposited Thin Films.....	302
W. D. Partlow, W. J. Choyke, and J. M. Bennett, and R. M. Silva	
Optical Properties of Ion-Beam Sputtered TiO <sub>2</sub> Films.....	311
H. Demiryont, D. B. Kerwin, and J. R. Sites	
Improvement of the Damage Threshold of High Reflectivity Multidielectric Coatings at 1.06 μM.....	317
B. Geenen, A. Malherbes, J. Guerin, D. Boisgard, D. Friart, and F. Garaude	
Phase Shift Variations on HEL Mirrors.....	322
T. A. Leonard and J. S. Loomis	
A Review of UV Coating Material Properties.....	329
M. L. Scott	
Recent Damage Results for Antireflection Coatings at 355 nm.....	340
T. Tuttle Hart, C. K. Carniglia, F. Rainer, and M. C. Staggs	
Recent Damage Results on High Reflector Coatings at 355 nm.....	347
C. K. Carniglia, T. Tuttle Hart, F. Rainer, and M. C. Staggs	
Alumina/Silica Multilayer Coatings for Excimer Lasers.....	354
S. R. Foltyn and L. J. Jolin	
Photothermal Deflection Microscopy of HR and AR Coatings.....	360
W. C. Mundy, J. E. L. Ermshar, P. D. Hanson, and R. S. Hughes	
Laser Damage in Porous-Silica Antireflection Films.....	372
W. H. Lowdermilk, J. G. Widler, N. J. Brown C. A. Gunderson, D. Milam, F. Rainer, and M. C. Staggs	
Defect Damage Precursors in Visible-Wavelength Mirrors.....	378
C. D. Marrs, J. O. Porteus, and J. R. Palmer	
Characterization of Micron-Sized, Optical Coating Defects by Photothermal Deflection Microscopy.....	385
J. A. Abate, A. W. Schmid, M. J. Guardalben, D. J. Smith, and S. D. Jacobs	

Figure 13. Contents of 1983 Boulder Damage Symposium (contd.).



Experimental Observation and Computer Simulation of the Microstructure of Vapor Deposited Thin Films.....	393
K. H. Guenther	
A Wide Spectrum Antireflective Coating for Silica Optics and Its Damage Resistance at 350 nm.....	407
B. E. Yoldas, D. P. Partlow, and H. D. Smith	
Plasma Deposited Inorganic Thin Films for Optical Applications.....	417
W. D. Partlow and J. V. R. Heberlein	
<u>Fundamental Mechanisms</u>	
Laser-Induced Emission and Laser Damage of Optical Components.....	423
D. B. Nichols, D. J. Morris, M. P. Bailey, and R. B. Hall	
Charge Emission and Related Precursor Events Associated with Laser Damage.....	429
M. F. Becker, F. E. Domann, A. F. Stewart, and A. H. Guenther	
Predamage Threshold Electron Emission From Insulator and Semiconductor Surfaces.....	442
W. J. Siekhaus, J. H. Kinney, and D. Milam	
Laser Induced Damage of a Thin Film With an Absorbing Inclusion: Thermal Considerations of Substrates and Absorption Profiles.....	448
M. R. Lange, J. K. McIver, and A. H. Guenther	
Laser Damage Threshold Predictions Based on the Effects of Thermal and Optical Properties Employing a Spherical Impurity Model.....	454
M. R. Lange, J. K. McIver, and A. H. Guenther	
Analytical Model for Evaluating Transient, Steady-State, Coating Damage Threshold, Optical Distortion, and Axial Gradient for Externally Cooled Laser Mirrors.....	466
J. R. Palmer	
"A Comprehensive Analytical Theory for Unifying Pulsed and Continuous Wave Laser Damage on Metal Mirrors, Encompassing the Relationship of Small Spot to Large Spot Size Damage on Metal Mirrors".....	483
J. R. Palmer	
Catastrophic versus Microscopic Damage: Applicability of Laboratory Measurements to Real Systems.....	493
S. R. Foltyn and L. J. Jolin	
Toward Improved Accuracy in Limited-Scale Pulsed Laser Damage Testing via the "Onset Method".....	502
S. C. Seitel and J. O. Porteus	
The Effects of Self-Focusing on Laser Induced Breakdown.....	513
W. E. Williams, M. J. Soileau, and E. W. Van Stryland	
Simple Direct Measurements of $n_2$ .....	522
W. E. Williams, M. J. Soileau, and E. W. Van Stryland	
Refractive Index of Ternary and Quaternary Compound Semiconductors Below the Fundamental Absorption Edge: Linear and Nonlinear Effects.....	532
B. Jensen and A. Torabi	
APPENDIX I List of Attendees.....	551

Figure 14. Contents of 1983 Boulder Damage Symposium (contd.).

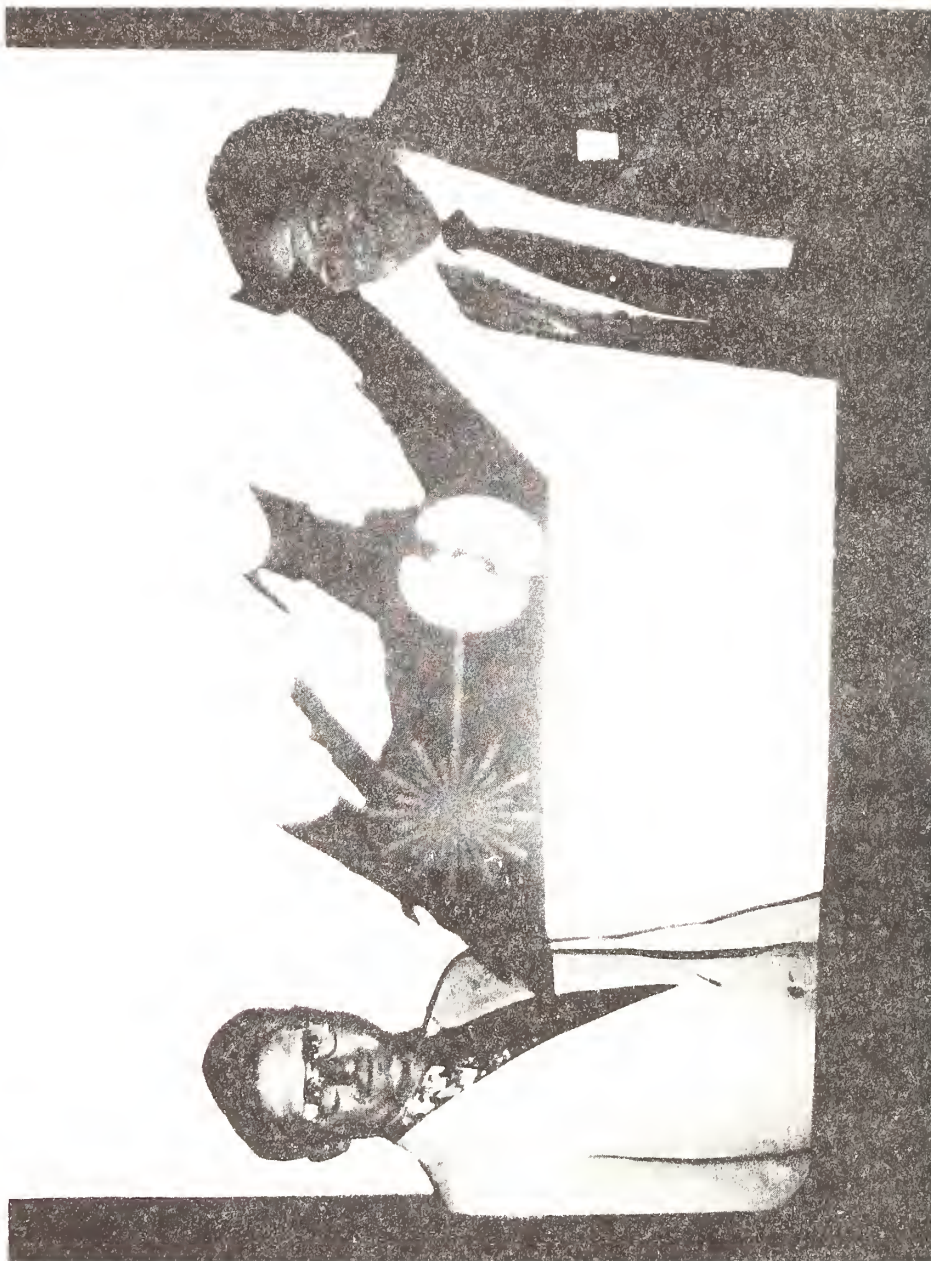
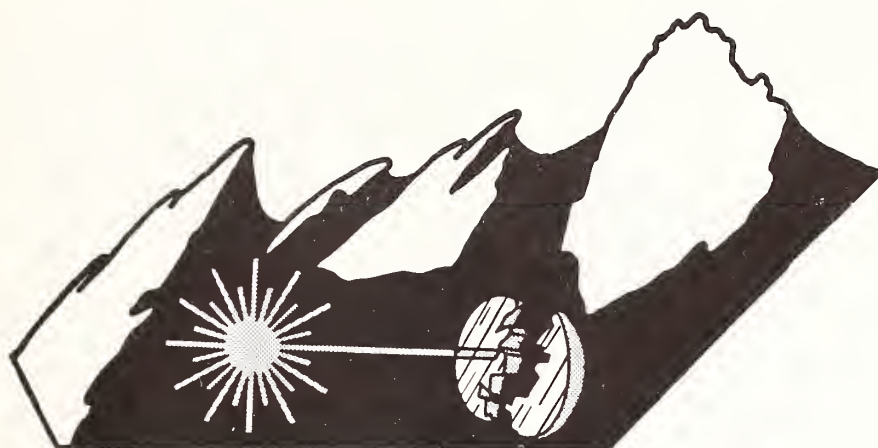


Figure 15. Major J. R. Bettis, left, (USAF), U.S. Naval Academy, winner of the logo contest, shown with co-Chairman A. H. Guenther.



## ***BOULDER DAMAGE SYMPOSIUM***

In commemoration of our tenth anniversary meeting and in expectation of its continuance, the organizers of this meeting decided that it would be appropriate to establish a logo which could be used to highlight the symposium and its future correspondence and publications. Thus a contest was held during this meeting, with the ground rules that the logo must be simple, and easily recognizable as representing the subject of the symposium. After a difficult time of evaluating over 30 entries, the organizers of the conference selected the logo you see decorating this our tenth anniversary proceedings. It was submitted by Major J. R. Bettis (USAF) of the US Naval Academy. Jerry is well known to the participants of this conference for his many technical presentations and stimulating demeanor. He now has made a contribution of another sort, one we are sure is as important and lasting.

Figure 16. Logo selected at tenth anniversary meeting to be used to highlight future symposia.

# Index Of Papers Laser Induced Damage In Optical Materials Symposia: --- 1969 - 1978

SYMPOSIUM SPONSORED BY:  
National Bureau of Standards  
American Society for Testing and Materials  
Office of Naval Research  
Department of Energy  
Defense Advanced Research Project Agency

Edited By:

ARTHUR H. GUENTHER  
Air Force Weapons Laboratory  
Kirtland Air Force Base, New Mexico 87117

ALEXANDER J. GLASS  
Lawrence Livermore National Laboratories  
Livermore, California 94550

WITH SINCERE APPRECIATION  
FOR THE ASSISTANCE OF:

Martha Adamson  
Mary Flannery  
Georgianna Hillyer  
Janet Hodges  
Margaret Putnam  
Margaret Ruiz

ABSTRACT  
KEY

SUBJECT

PERMUTED  
TITLE

AUTHORS

ABSTRACTS  
BY YEAR



Published By:  
AIR FORCE WEAPONS LABORATORY KIRTLAND AFB, NEW MEXICO 87117

Figure 17. Cover page for Index of Papers (1969-1978) categorized by abstracts, subjects, titles, authors, and year.



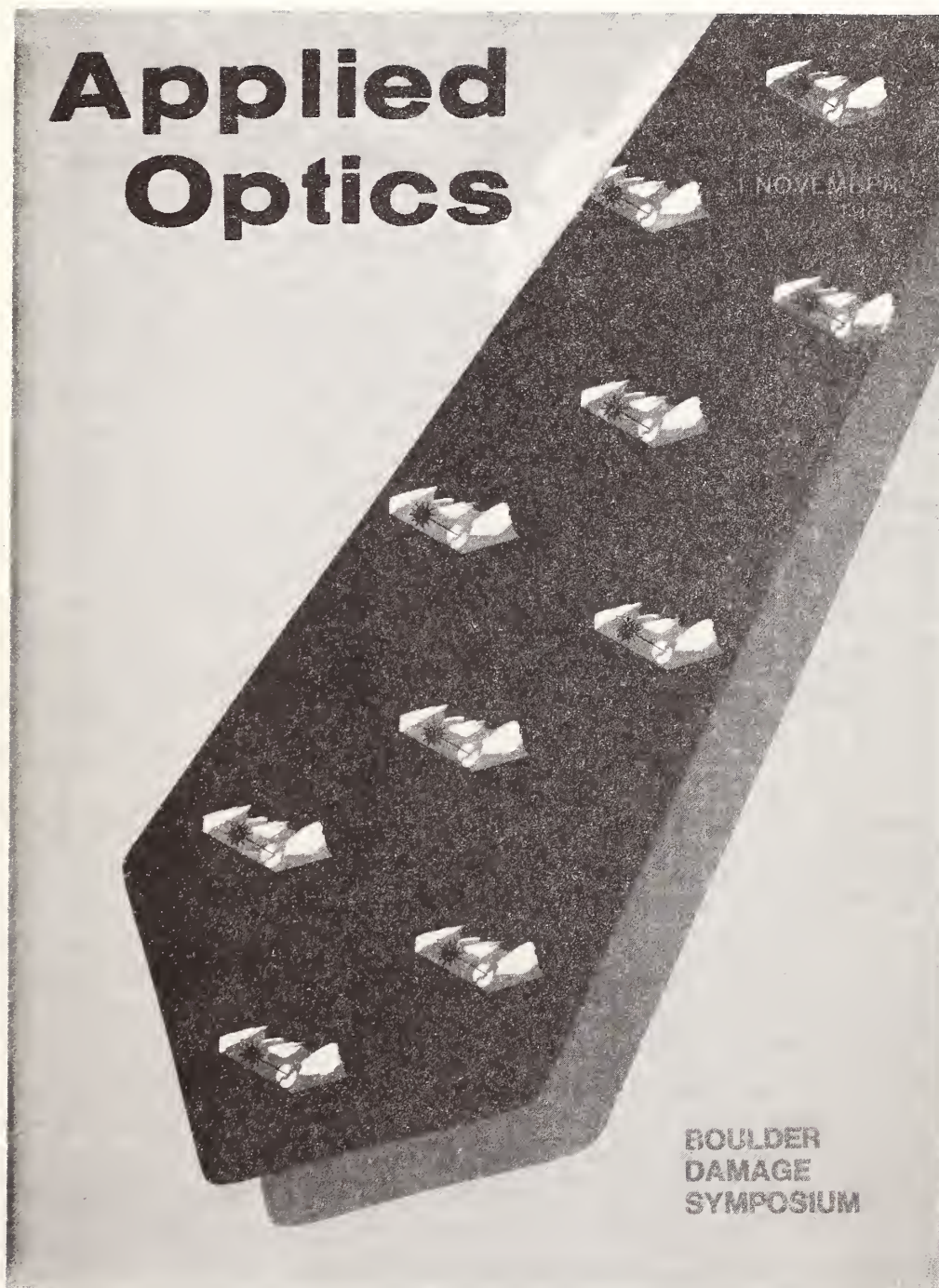


Figure 18. Cover of Applied Optics, 1 November 1984, depicting Boulder Damage Symposium logo on commemorative tie.





Laser-Induced Damage in Optical Materials  
Twentieth ASTM Symposium  
October 26-28, 1988

The Twentieth Annual Symposium on Optical Materials for High Power Lasers (Boulder Damage Symposium) was held at the National Institute of Standards and Technology in Boulder, Colorado, October 26-28, 1988. The Symposium was held under the auspices of the ASTM Committee F-1, Subcommittee on Laser Standards, with the joint sponsorship of NIST, the Defense Advanced Research Project Agency, and the Department of Energy. Over 210 scientists attended the Symposium, including representatives from the United States, the United Kingdom, France, Canada, the People's Republic of China, Japan, Federal Republic of Germany, Lithuania, and the Soviet Union. The Symposium was divided into sessions concerning Materials and Measurements, Surfaces and Mirrors, Thin Films, and Fundamental Mechanisms. As in previous years, the emphasis of the papers presented at the Symposium was directed toward new frontiers and new developments. Particular emphasis was given to materials for high-power apparatus. The wavelength range of prime interest was from 10.6  $\mu\text{m}$  to the uv region. Highlights included surface characterization, thin film-substrate boundaries, and advances in fundamental laser-matter threshold interactions and mechanisms. Harold E. Bennett of the Naval Weapons Center, Arthur H. Guenther of the Los Alamos National Laboratory, Brian E. Newnam of the Los Alamos National Laboratory, and M. J. Soileau of the University of Central Florida were co-chairmen of the Symposium. The Twenty-First Annual Symposium is scheduled for November 1-3, 1989, at the National Institute of Standards and Technology, Boulder, Colorado.

Key Words: laser damage; laser interaction; optical components; optical fabrication; optical materials and properties; thin film coatings.

## 1. Introduction

The Twentieth Annual Symposium on Optical Materials for High Power Lasers (Boulder Damage Symposium) was held, as in previous years, at the National Institute of Standards and Technology in Boulder, Colorado, October 26-28, 1988. The Symposium was held under the auspices of the ASTM Committee F-1, Subcommittee on Laser Standards, with the joint sponsorship of NIST, the Defense Advanced Research Projects Agency, and the Department of Energy. Over 210 scientists attended the Symposium, including representatives from the United States, the United Kingdom, France, Canada, People's Republic of China, Japan, Federal Republic of Germany, Lithuania, and the Soviet Union. The Symposium was divided into sessions concerning Materials and Measurements, Surfaces and Mirrors, Thin Films, and finally, Fundamental Mechanisms. In all, approximately 75 technical presentations were made. Harold E. Bennett of the Naval Weapons Center, Arthur H. Guenther of the Los Alamos National Laboratory, Brian E. Newnam of the Los Alamos National Laboratory, and M. J. Soileau of the University of Central Florida were co-chairmen of the Symposium. Alexander J. Glass of Lawrence Livermore National Laboratory is Conference Treasurer and Aaron A. Sanders of the National Institute of Standards and Technology acts as Conference Coordinator.

The purpose of these symposia is to exchange information about optical materials for high-power lasers. The authors welcome comments and criticism from all interested readers relevant to this purpose and particularly relative to our plans for the Twenty First Annual Symposium, scheduled for November 1-3, 1989 at the National Institute of Standards and Technology, Boulder, Colorado.

## 2. Overview

At this the 20th Boulder Damage Symposium, the conference hit an all-time high in number of presented papers, approaching 80 in number with well over 200 participants. This led to numerous contributions in the categories that we historically have applied to this meeting, materials and measurements, surfaces and mirrors, thin films, and fundamental mechanisms. Our objective in this section is to give the reader a sense of the emphasis and general concerns of this year's symposium. Although we do not review all of the excellent work presented, some highlights are touched upon briefly.

### Materials and Measurements

In the area of materials and measurements a series of papers dealt with the subject of multi-pulse or multi-exposure damage both from the theoretical and experimental standpoint. A principle conclusion of these papers was the importance of the development of F-centers in dielectric materials and the temperature dependance of their production. Aspects relating to multi-photon absorption were considered as well. Laser heating of free electrons as a mechanism for elevating local temperatures was emphasized in several presentations.

Another area covered the production and in some cases the system oriented use of very large size optics, whether it be the potential for fabricating 1-meter diameter calcium fluoride windows or the operational performance of 80 centimeter diameter beam splitters in short pulse, high peak power, inertial confinement fusion systems. Such beam splitters seem to suffer mechanical degradation thought to be related to stimulated Brillouin scattering in these systems. This meeting has always addressed issues from evaluating the most fundamental potential of various materials, to their production and employment in science, to their fabrication and use in systems. We therefore span the whole gamut of material applications.

This year we saw a continual proliferation of automated damage testing facilities with extended wave-length capability including a new facility at 10.6 microns. Perhaps one of the most significant aspects of this section dealt with an attempt to standardize the damage testing procedures and nomenclature (a development which could effectively enhance commercial transaction relating to optical materials and components). Other areas included the performance of optical materials in adverse environments, including space and high energy ionizing particles. Finally, the performance of silicon photo-diodes and optical limiters and their potential utilization was covered in a few select papers.

A subject that has seen a lot of continuing interest at this series of meetings concerns multiple irradiation -- on one hand relating to accumulation of damage (measured absorption) thus reducing the damage threshold and increasing the extent of damage, or on the other hand conditioning (reducing absorption by bleaching, annealing, etc.) thus damage thresholds. At this meeting we heard a number of papers that dealt with this subject in a more quantitative way, i.e. measuring the increase of absorption in materials as a result of repeated irradiation at high intensities and in measuring the decreased absorption as a result of multiirradiation at lower intensities. Another area that has been of continuing interest is the search for a means to monitor pre-damage as an indicator in an effort to better understand the operative mechanisms relating to damage.

As relates to material property measurements talks were given that showed encouraging results, for example, in monitoring the production of free carriers by multi-photon processes arising from defects. This was accomplished by monitoring the heating of selected sites on surfaces using classical optical techniques.

A suggestion by Maldutis was that increases in absorption caused by multiple pulse effects can lead to thermal self-focusing. This in turn can lead to a reduction in damage threshold of sites subjected to multiple pulse irradiation. In Maldutis' paper, one interesting confirmation of our understanding is that color centers accumulate with numbers of pulses and that the accumulation corresponds exactly with the reduced damage threshold. He showed by the measurement of transient increase in temperature and computer assisted deconvolution that the size of absorption and size of damage have a fairly good correlation.

This year the materials and measurements saw an emphasis on ultra-violet radiation correlated with the study of accumulative damage. One of the specific U.V. developments this year was a new process for producing one meter sized optics, for example calcium fluoride, reported by Harshaw. A slab process using single crystal orientations looks to be scalable to very large sizes.

Progress on the new nonlinear material L-arginine phosphate is an important new development. It is an exciting new material that has been known for some time in the literature and which may offer some distinctive advantage in second harmonic generation and optical parametric oscillators. The results presented at this meeting shows that this material can also exhibit greatly improved laser-induced damage resistance compared to materials that are more traditionally used in these applications. The material is simply grown in very large sizes using very inexpensive techniques. The emergence of this second harmonic generating material in parametric oscillators will receive more attention in years to come.

## Surfaces and Mirrors

Numerous papers presented at this year's symposium covering several areas of historical interest. Real advances were reported as well as some good rules of thumb that can be applied to laser induced damage. One area of particular interest related to the polishing, grinding, or treatment of optical surfaces. We heard Professor Namba report on ultra precision grinding at sub-micron accuracies indicating that he is continuing the development of new machining and fabrication techniques based upon his early work with float polishing.

Sputter etching of substrates prior to coating was reported as an excellent means of removing contamination. In addition, we heard continued reports on the beneficial aspects of laser treatment of fused silica surfaces in reducing surface absorption. Papers again reported impurities that were retained by the surfaces from the grinding compounds, mostly ceria and titania.

Desorption by lasers as a substrate cleaning technique and improved adhesion of coatings (surface activation) were covered in several papers. Most notably were the beneficial or deleterious aspects of either normal water or heavy water on surfaces. In apparent violation of conventional wisdom that water is always bad, it was shown that one can actually increase the damage threshold of material by exposing it to different amounts of water. Thin film coatings were proposed for smoothing surfaces prior to the deposition of mirror-like surfaces.

New techniques employing cavity ring down for measuring very high reflectivities were presented. These are increasingly necessary in the expanding and important field of free electron laser optics. Optical design techniques using multi-faceted or grazing angle of incidence for reflecting surfaces in the XUV region were proposed and showed great promise as a means of overcoming or at least alleviating short wave length damage concerns!

A particularly important area reported on at this meeting was the cleaning of surfaces in-situ using laser radiation. There is an obvious benefit to any in-situ technique as it offers the possibilities of being coupled with other process variables that improve film deposition such as laser assisted film deposition. Although laser cleaning can improve bad surfaces and increase laser damage threshold surfaces, if you have surfaces which exhibit nearly intrinsic properties, laser cleaning does not improve the damage threshold measurably.

A study of the importance of scatter by particulates was reported. This area has been largely neglected at this meeting because there has not been a convenient theory to explain or correlate scatter and damage. This is another case where experimental data is not available or where scatter from poor surfaces masks that from particulates.



## Thin Films

As is usually the case, the contributions in the thin film area were the greatest in number at the meeting, being roughly one-third. Presentations this year reflect similar interest as discussed in other categories of the meeting proper. Multi-pulse damage, the performance of materials in adverse environments and in particular short-wave lengths. In fact, considerable progress has been made in the damage resistance of coated elements from 148 nanometers to 308 nanometers.

Several design tricks to improve the damage resistance in coated optics were presented. Keith Lewis discussed the use of distributed Bragg reflectors as a potential mechanism for improving the damage resistance of multilayers at the expense of some optical performance. This was an extension of his previously reported attempts to place the intense field within one of the materials and not at the boundaries where one might expect adsorption or other weaknesses to be present.

Another paper, which reported improvements in damage resistance, concerned the use of gradual or changing refractive index interfaces by the simultaneous deposition of two coating materials. The same ruse of co-evaporation was utilized in ion sputtering of mixed oxides to produce a stress reduction in the films. Performance of these were rather nicely correlated with the deposition process.

From this work on ion sputtering one noted, with great pleasure, still another new deposition technique which promises, at least at this stage, to afford a truly significant advance in thin film damage resistance. The technique generally falls under the category of plasma assisted chemical vapor deposition. The author indicated that he was borrowing from fiber optics processors, by applying the particular technique of microwave excitation of a plasma which deposits material of high quality on the inside of a cylinder. The most significant result of this early work was that film adsorption as low as  $10^{-7}$  was observed, which is at least  $10^5$  lower than what has been reported before. Initial indications of greatly improved damage resistance in the 40 to 50 joule per square centimeter range were reported. These are certainly preliminary numbers, and we are all anticipating additional varification of this approach, and also hope to learn whether or not this process can be applied to other geometrical surfaces.

There is no question that thin films continues to be the area of principal concentration, because of the potential leverage for improvement and the limitations it places on system design at the present time. Most thin film coatings are still produced in the industry in a way that is not very different from the way in which they have been produced in the pre-laser days. There have been refinements and improvements perhaps in vacuum systems and procedures but few real fundamental changes. This year we saw quite an emphasis on trying to use techniques that were developed for other technologies such as the fiber optic industry and the electronics industry. Techniques like plasma assisted depositions, chemical vapor depositions, ion plating techniques, and various other



techniques have been developed and refined in other technologies, where the economic drivers are much larger than they are in the optics area. Groups are now trying to exploit those advances and apply them to thin film optical coatings.

The reemergence of metal coatings as important in laser systems was noted because of the advent, and finally the working, of free electron lasers. These lasers require coatings or optics that have large bandwidths. With these wideband width systems one now has to go back to materials like thin films of silver with broad spectrum reflectance to satisfy FEL requirements. FELs also have some peculiar needs in the sense that they both have cw and pulsed formats. The output of these devices include high average powers from many picosecond pulses.

One of the most significant advances in the thin film area related to the ultraviolet and the vacuum ultra violet, where the development of reflectances above 85% at 58.4 and 30.4 nanometers was reported using in-situ ultra-high vacuum deposited aluminum. One of the pleasant surprises was that the optical constants are in fact more favorable than we had been led to believe by previous work. We now have better values of the optical constants for pure aluminum in this region of the spectrum than were available previously.

Another area that received notice was the effective reflectance of coatings in laser systems. There is a problem of optimism on the part of designers as to the values that they hope to obtain for reflectance of coatings. There was a very interesting paper by Newnam and Saunders on the reflectance values measured by the ring down cavity technique for "typical" and the best coatings that they could obtain at 1.6 micrometers. The best they obtained was a 99.97% for titanium oxide/silicon dioxide. The gold coating they employed had an effect reflectance of 97.68%, which shows one should not be too optimistic about the anticipated reflectance of coatings.

The transient effect of increased absorption by ultra violet radiation at 350 nanometers and the absorption being measured at 1 micrometer was demonstrated. This is important for many systems, such as free electron lasers. There was evidence of a significant recovery after the radiation stopped, but residual absorption still remained.

Likewise, there was evidence given by the Japanese on the aging of lithium or lanthanum fluoride films after storage. It was presupposed that the lithium fluoride was actually becoming oxidized with time. The Japanese also showed that sputter etching of substrates is effective in removing impurities. They observed 2 to 3 times higher damage threshold for AR coatings on these treated surfaces. They consider sputter etch a more convenient process than the argon fluoride laser radiation treatments (also found to remove impurities).

We would like to add a note of encouragement to those people in coatings research that are trying some nontraditional, nonoptical techniques for depositing coatings. There is more than 40 or 50 years of history using traditional technique, so it will take some time we believe to completely transition those new approaches to acceptable coatings for optics. But we think it is important that those techniques that have proved to work so well in other areas be examined very carefully and with some patience. Relative to that point, ion plating technology, which has been developed in the last year or two, appears to be producing moderate damage thresholds. There is some concern that chamber contaminants may be causing problems. Such problems will have to be overcome before these coatings can emerge from the average performance category. However, this is one of those technologies that is in its infancy, and should be pursued for optimization and capability!

#### Fundamental Mechanisms

As was customary, the meeting concluded with a most free-wheeling discussion on issues of fundamental mechanisms relating to the interaction of intense light with matter. This session was initiated with a review by M.J. Soileau of the 20 years of discussions and presentations relating to this field. As previously indicated and expected, one of the underlying threads throughout the conference dealt with multi-pulse phenomena. There was considerable theoretical exposition on this issue treating both high and low intensity irradiation, that is, accumulation of damage versus conditioning as annealing of damage. The relative independence of individual pulses from a thermal standpoint, depending upon their pulse width relative to their separation, materials, optical, thermal and thermomechanical properties as well as design, are all factors which effect damage. Interestingly, at this meeting there was more than the normal emphasis on the chemical aspects of laser-material interactions. This was certainly evident in discussions of laser interactions with monomeric and polymeric conjugates as well as liquid crystals. The use of these classes of materials continues to grow in the high power community.

An interesting perspective was presented by Professor Manenkov of the Institute of General Physics in Moscow on the relative importance of impact ionization or of avalanche as an intrinsic process. Professor Manenkov reviewed the work of his group over the past decade or so. It has been directed primarily toward producing a detailed model of laser induced breakdown in optical material going away from the previous one or two parameter models that have been invoked to try to describe this extremely complicated process. He reviewed the incorporation of not only laser parameters into the model, but basic material properties and non-equilibrium material properties, as well as multi-photon mechanisms to describe laser-induced breakdown in transparent dielectrics. He then moved on to defects, particularly as they play a role in polymeric optic materials. This is an area of considerable activity in the Soviet Union.

Continuing on with the subject of organic materials, emphasis was given at this meeting to liquid crystals and polymeric materials of similar structures. These materials are starting to see greater and greater use in optical systems of all kinds, particularly

large optical systems and the presentations at this meeting are indicative of their increased application. Organics offer great opportunity for use including improved nonlinear materials for a variety of applications. Presentations at this meeting on this subject presage future importance of organic materials.

One-on-one damage effects in dielectric materials are much better understood than m-on-1 effects. We heard about accumulative damage even for pulses as short as picoseconds. In addition, some models discussed the importance of thermal cracking and thermal explosion of particulates as an important source of damage. An analysis of major damage to a cracked large optic at the Livermore National Laboratory was given. By examining the data and the damaged sites concluded that stimulated Brillouin scattering was responsible for major cracks oriented along polarization axis. They suggested that to avoid this problem one may want to frequency chirp the optical pulses.

In M.J. Soileau's review paper a very useful formula was brought forth for approximating damage threshold over a wide range of parameters. Over a wide range the damage threshold within an order of magnitude is essentially equal to 1 gigawatt per square centimeter per nanosecond, with the pulse width being scaled as the half power.

### 3. Acknowledgments

The editors would like to acknowledge the invaluable assistance of Mr. Aaron A. Sanders and the other involved staff members of the National Institute of Standards and Technology in Boulder, Colorado, for their interest, support, and untiring efforts in the professional operation of the symposium. Particular thanks to Ms. Susie Rivera of NIST for her lead in the preparation and publication of the proceedings as well as Ms. Edit Haakinson of NIST. Thanks also go to Ms. Pat Whited of the Air Force Weapons Laboratory and Ms. Ann Mannos of NIST for conference coordination.

#### 4. References

- [1] Glass, A.J.; Guenther, A.H., eds. Damage in Laser Glass, ASTM Spec. Tech. Pub. 469, ASTM, Philadelphia. PA; 1969.
- [2] Glass, A.J.; Guenther, A.H., eds. Damage in Laser Materials, Nat. Bur. Stand. (U.S.) Spec. Publ. 341; 1970.
- [3] Bloembergen, N. Fundamentals of Damage in Laser Glass, National Materials Advisory Board Publ. NMAB-271, National Academy of Sciences; 1970.
- [4] Glass, A.J.; Guenther, A.H., eds. Damage in Laser Materials: 1971, Nat. Bur. Stand. (U.S.) Spec. Publ. 356; 1971.
- [5] Bloembergen, N. High Power Infrared Laser Windows. National Materials Advisory Board Publ. NMAB-356; 1971.
- [6] Glass, A.J.; Guenther, A.H., eds. Laser Induced Damage in Optical Materials: 1972, Nat. Bur. Stand. (U.S.) Spec. Publ. 372; 1972.
- [7] Glass, A.J.; Guenther, A.H., eds. Laser Induced Damage in Optical Materials: 1973, Nat. Bur. Stand. (U.S.) Spec. Publ. 387; 1973.
- [8] Glass, A.J.; Guenther, A. H. Laser Induced Damage in Optical Materials: A Conference Report. Appl. Opt. 13 (1): 74-88; 1974.
- [9] Glass, A.J.; Guenther, A.H., eds. Laser Induced Damage in Optical Materials: 1974, Nat. Bur. Stand. (U.S.) Spec. Publ. 414; 1974.
- [10] Glass, A.J.; Guenther, A.H. Laser Induced Damage in Optical Materials: 6th ASTM Symposium. Appl. Opt. 14 (3): 698-715; 1975.
- [11] Glass, A.J.; Guenther, A.H., eds. Laser Induced Damage in Optical Materials: 1975, Nat. Bur. Stand. (U.S.) Spec. Publ. 435; 1975.
- [12] Glass, A.J.; Guenther, A.H. Laser Induced Damage in Optical Materials: 7th ASTM Symposium. Appl. Opt. 15 (6): 1510-1529; 1976.
- [13] Glass, A.J.; Guenther, A.H., eds. Laser Induced Damage in Optical Materials: 1976. Nat. Bur. Stand. (U.S.) Spec. Publ. 462; 1976.
- [14] Glass, A.J.; Guenther, A.H. Laser Induced Damage in Optical Materials: 8th ASTM Symposium, Appl. Opt. 16 (5): 1214-1231; 1977.

- [15]Glass, A.J.; Guenther, A.H., eds. Laser Induced Damage in Optical materials: 1977, Nat. Bur. Stand. (U.S.) Spec. Publ. 509; 1977.
- [16]Glass, A.J.; Guenther, A.H. Laser Induced Damage in Optical Materials: 9th ASTM Symposium, Appl. Opt. 17 (15): 2386-2411; 1978.
- [17]Glass, A.J.; Guenther, A.H. Laser Induced Damage in Optical Materials: 1978, Nat. Bur. Stand. (U.S.) Spec. Publ. 541; 1978.
- [18]Glass, A.J.; Guenther, A.H., eds. Laser Induced Damage in Optical Materials: 10th ASTM Symposium, Appl. Opt. 18 (13): 2212-2229; 1979.
- [19]Bennett, H.E.; Glass, A.J.; Guenther, A.H.; Newnam, B.E. Laser Induced Damage in Optical Materials: 1979, Nat. Bur. Stand. (U.S.) Spec. Publ. 568; 1979.
- [20]Bennett, H.E.; Glass, A.J.; Guenther, A.H.; Newnam, B.E. Laser Induced Damage in Optical Materials: 11th ASTM Symposium, Appl. Opt. 19 (14): 23375-2397; 1980.
- [21]Bennett, H. E.; Glass, A.J.; Guenther, A. H.; Newnam, B.E. Laser Induced Damage in Optical Materials: 1980, Nat. Bur. Stand. (U.S.) Spec. Publ. 620; 1981.
- [22]Bennett, H.E.; Glass, A.J.; Guenther, A.H.; Newnam, B.E. Laser Induced Damage in Optical Materials: 12th ASTM Symposium, Appl. Opt. 20 (17): 3003-3019; 1981.
- [23]Bennett, H.E.; Guenther, A.H.; Milam, D.; Newnam, B.E. Laser Induced Damage in Optical Materials: 1981, Nat. Bur. Stand. (U.S.) Spec. Publ. 638; 1983.
- [24]Bennett, H.E.; Guenther, A.H.; Milam, D.; Newnam, B.E. Laser Induced Damage in Optical Materials: 13th ASTM Symposium, Appl. Opt. 22 (20): 3276-3296; 1983.
- [25]Bennett, H.E.; Guenther, A.H.; Milam, D.; Newnam, B.E. Laser Induced Damage in Optical Materials: 1982, Nat. Bur. Stand. (U.S.) Spec. Publ. 669; 1984.
- [26]Bennett, H.E.; Guenther, A.H.; Milam, D.; Newnam, B.E. Laser Induced Damage in Optical Materials: 14th ASTM Symposium, Appl. Opt. 23 (21): 3782-3795; 1984.
- [27]Bennett, H.E.; Guenther, A.H.; Milam, D.; Newnam, B.E. Laser Induced Damage in Optical Materials: 1983, Nat. Bur. Stand. (U.S.) Spec. Publ. 688; 1985.
- [28]Bennett, H.E.; Guenther, A.H.; Milam, D.; Newnam, B.E. Laser Induced Damage in Optical Materials: 15th ASTM Symposium, Appl. Opt. 25 (2): 258-275; 1986.
- [29]Bennett, H.E.; Guenther, A.H.; Milam, D.; Newnam, B.E. Laser Induced Damage in Optical Materials: 1984, Nat. Bur. Stand. (U.S.) Spec. Publ. 272; 1986.



- [30]Bennett, H.E.; Guenther, A.H.; Milam, D.; Newnam, B.E. Laser Induced Damage in Optical Materials: 16th ASTM Symposium, Appl. Opt. 26 (5): 813-827; 1987.
- [31]Bennett, H.E.; Guenther, A.H.; Milam, D.; Newnam, B.E. Laser Induced Damage in Optical Materials: 1985, Nat. Bur. Stand. (U.S.) Spec. Publ. 746; 1987.
- [32]Bennett, H.E.; Guenther, A.H.; Milam, D.; Newnam, B.E. Laser Induced Damage in Optical Materials: 1986, NIST (U.S.) Spec. Publ. 752; 1987.

## Multiple Shot Intrinsic Bulk Damage in KBr at 532 nm

R. Thomas Casper, Scott C. Jones and Peter Braunlich  
Department of Physics  
Washington State University  
Pullman, WA 99164-2814

Evidence is presented in support of a cumulative damage mechanism for multiple shot intrinsic bulk laser damage in KBr at 532 nm. The major feature of the model, suggested by Manenkov *et al.*, is the build-up of internal stresses in the interaction volume. These stresses most likely result from an accumulation of photochemically produced stable point defects, such as F-centers, and then serve to increase the rate of further accumulation. It is also found that thermal stress due to the temperature rise during the laser pulse must be considered. This plays a particularly important role at low temperatures where, otherwise, the efficiency of F-center production is very small. This model exhibits the observed temperature and flux dependences for multiple shot damage and is compared with experimental data for temperatures from 50 to 300 K.

Key Words: alkali-halide; defect accumulation; expansion; F-center; 532 nm; internal stress; KBr; multiple shot damage; thermal stress; yield stress.

### 1. Introduction

It is of great practical importance to understand the response of optical materials exposed to repetitive laser pulses. At power levels far below that required for single pulse intrinsic damage these materials experience irreversible modifications when subjected to a series of laser pulses [1-6]. The aim of this research is to answer some of the questions concerning this phenomenon.

Recent work on NaCl [7-9], KBr [10-13] and KI [14,15] lends strong support to the theory that single shot damage in these materials at 532 nm results from the production of free electrons by a multiphoton absorption process (four photons for NaCl and KBr and three photons for KI) followed by heating as the free electrons absorb additional energy from the laser pulse. These experiments showed that peak temperatures approaching the melting point can be reached with no indication of damage. This suggests that melting is the mode of failure under these conditions. Shen, *et al.* [16] have since been able to provide additional evidence for the free electron heating mechanism.

In contrast to the temperature increases of several hundred degrees in the experiments just mentioned, at the photon fluxes used in the current multiple shot experiments the peak temperature rise is less than ten degrees. It is clear that two different modes of failure are responsible for the behavior observed in the single and multiple shot experiments. This investigation pursues the idea that the failure of alkali halides due to multiple laser pulses results from the accumulation of microscopic structural changes in the crystal lattice. Perhaps the most easily produced stable primary defect is the F-H pair, or Frenkel defect. It is suggested here that these F-H pairs play a major role in the cumulative effects leading to catastrophic optical failure in alkali halides.

## 2. Theory

It has been shown in alkali halides that when a crystal is radiatively colored it undergoes an expansion [17-21]. That is, there is an increase in volume due to the production of Frenkel defects. These defects are produced in alkali-halides as a result of band gap excitations. In this study the band gap excitation is a result of the absorption of four photons from the incident laser pulse. Under normal conditions a small fraction of the electron-hole pairs generated give rise to F-H pairs which remain stable against recombination for long periods of time [22]. In such a case the H-center moves sufficiently far from the F-center to inhibit their recombination. As the F-H pairs accumulate in the focal volume local stresses will develop since this region is prevented from expanding by the surrounding uncolored crystal. If this stress reaches a sufficient level it is expected that the material will experience crack or slip plane formation resulting in a nonuniformity in the crystal which acts as a scattering center. It is this scattering which is detected and interpreted as damage.

The model presented here assumes that failure occurs when the local stress,  $\sigma$ , exceeds the yield stress,  $\sigma_y$ . The yield stress, however, is not independent of defect concentration. When alkali halide crystals are subjected to radiative coloring there is an increase in the yield stress [23-25], and it is not certain whether the failure occurs in the colored region or in the surrounding virgin material. Nadeau *et al.* [25] found the increase in yield stress to be proportional to the square root of the F-center concentration,  $n_F$ , or

$$\sigma_y = A + B\sqrt{n_F}, \quad (1)$$

with

$$A = 6.47 \times 10^6 \text{ dyne cm}^{-2} \quad \text{and} \quad B = 65.4 \text{ dyne cm}^{-1/2}$$

for KBr.

Calculation of the local induced stress,  $\sigma$ , is a complicated problem, and certain simplifications must be made in order to obtain a reasonable estimate of its magnitude. The induced stress consists of two components of different origin. The first is due to the lattice expansion in the focal volume caused by the production of F-H pairs. The volume increase due to the creation of an F-center,  $v$ , can be determined by measuring the linear expansion of a crystal as a function of F-center concentration. If we consider a cube of side  $l$  in which we produce a uniform density of F-centers,  $n_F$ , we have

$$\Delta V = 3l^2 \Delta l, \quad (2)$$

where we have neglected terms of order  $(\Delta l)^2$  and higher. This volume increase can also be expressed as

$$\Delta V = n_F V v, \quad (3)$$

where  $V$  is the volume of the cube. This gives

$$v = \frac{3\Delta l}{n_F l}. \quad (4)$$

Lin's results for NaCl [19] give a value of  $v = 4.6 \times 10^{-23} \text{ cm}^3$ . This is one fourth of the unit cell volume,  $a^3$ , in the original lattice, with  $a = 5.6 \times 10^{-8} \text{ cm}$  for NaCl [26]. In comparison, using the results of Rabin [21] we obtain  $v = 1.3 \times 10^{-23} \text{ cm}^3$  ( $0.074a^3$ ). For KBr Fuchs and Wiegand [28] also find  $v = 0.074a^3$ , where  $a = 6.6 \times 10^{-8} \text{ cm}$  [26]. For the purposes of our calculation we take, in the case of KBr, the increase in volume due to the production of one F-H pair to be on the order of one tenth of the unit cell volume.

We use this information to estimate the stress due to the accumulation of F-centers in a small region of the crystal. If the interaction volume were not prevented from expanding the increase in volume would also be given by eq.(3) with  $V$  now referring to the focal volume. If we assume hydrostatic conditions the pressure

required to compress such an expanded crystal into its original volume would be equal to the stress induced in the neighborhood of the focal volume when the expansion is not permitted. To first order the stress resulting from the accumulation of F-centers is given by

$$\sigma_F = \frac{K \Delta V}{V},$$

or

$$\sigma_F = K n_F v. \quad (5)$$

$K$  is the bulk modulus of the crystal.

In calculating the thermal stress,  $\sigma_T$ , we are able to make use of the single shot results of Shen *et al.* [13]. Their modelling showed that the peak temperature increase, during the laser pulse, is very nearly proportional to the fourth power of the photon flux at 532 nm in KBr. Therefore, the thermal stress is

$$\sigma_T = C \alpha K F_0^4 \quad (6)$$

$\alpha$  is the coefficient of thermal expansion,  $C$  is a constant of proportionality and  $F_0$  is the peak photon flux. The total stress is then the sum of these two components

$$\sigma = \sigma_F + \sigma_T. \quad (7)$$

Finally, it remains to obtain an expression for the density of F-centers. Manenkov *et al.* [1] suggested that multiple shot damage might be explained by a process whose rate is of the form  $\exp\{-(U_0 - \gamma\sigma)/k_B T\}$ , where  $U_0$  is the activation energy for the process in question,  $T$  is the temperature, and  $k_B$  is Boltzmann's constant.  $\gamma$  is a structure dependent factor to be determined experimentally. This implies that when the material is stressed there is an effective lowering of the activation energy and the process becomes more efficient. Indeed, there have been studies where an increase in F-center production with applied stress was observed [28-31].

The number of F-centers produced during any one laser pulse is proportional the the number of electron-hole pairs produced. For KBr at 532 nm this is in turn proportional to the fourth power of the peak photon flux [13]. Thus, for any one laser pulse

$$\Delta n_F = D F_0^4 \exp\{-(U_0 - \gamma\sigma)/k_B T\}, \quad (8)$$

with  $D$  being a constant of proportionality. An iterative procedure is now used to follow the build up of F-centers and stress from one shot to the next, since  $n_F$  and thus  $\sigma$  increase with the number of shots, until the condition for failure is met. The temperature increase is included in the denominator of the exponential, however, this additional term causes no significant change in the model behavior.

The behavior of the model is highly nonlinear, and it produces an F-center density profile which is sharply peaked at the center of the beam. Figure 1 shows the development of this profile at various points during a series of 362 laser pulses. The parameters used in the calculation are those determined from our experiments with KBr, and the temperature was taken to be  $T = 300$  K. The rate of F-center accumulation increases with the existing concentration as indicated by eqs.(5-8) until, in the last few shots, there is a dramatic increase in defect production. On the final shot the damage condition ( $\sigma > \sigma_y$ ) was satisfied, and the peak F-center density reached a value of  $10^{18} \text{ cm}^{-3}$ .

There are effectively three free parameters ( $\gamma$ ,  $C$ , and  $D$ ) in the current form of this model. They are determined by fitting the model predictions of the flux and temperature dependences with the experimental data. It is hoped that as this investigation proceeds these values can be determined independently.

### 3. Experimental Procedure

The laser pulses used in this experiment were produced by a Q-switched and mode-locked Quantronix model 116 Nd:YAG laser system. A single mode-locked pulse is switched into a double pass Nd:YAG amplifier, and the second harmonic used in the experiments is produced in a KDP crystal. The spatial profile is checked at the entrance plane of the focusing lens using a scanning slit technique. The focal spot size is then calculated using diffraction limited Gaussian optics. The temporal profile is measured by a zero background second harmonic generation autocorrelation procedure. The spot size is typically 8-10  $\mu\text{m}$ , and the pulse width is 72 ps. These values refer to the half-width at 1/e of the peak photon flux.

The experimental procedure is to expose the sample to a series of laser pulses of uniform peak power at a repetition frequency of about one Hertz. The sample is mounted on the cold finger of a closed cycle optical cryostat which is fitted with a resistive heating element. This arrangement allowed the temperature to be varied from about 50 K to room temperature. The condition of the crystal is monitored by observing the scattering of the laser light perpendicular to the beam axis. The scattered light is picked up by an optical fiber and guided to a photomultiplier tube which served as the detector. Figure 2 illustrates the geometry of the crystal, fiber and the incident laser pulse. Damage is assumed to have occurred when a sudden increase in light scattering is observed. The increased scattering is also observed to correlate with a deformation of the far field beam profile.

The model developed above is deterministic. As such, it is important to differentiate between data which represent the intrinsic behavior of the material and those which are extrinsic. The intrinsic behavior represents a fundamental limit of the crystal, whereas the extrinsic behavior can be caused by any number of defects or impurities initially present in the crystal. The results of one of these experiments performed at room temperature are shown in fig. 3. Although for any given photon flux there may be a large variation in the number of shots withstood by different sites in the sample, all data points are seen to lie within a distinct envelope. Rather than performing a statistical analysis of the variations we feel that, given a sufficient number of points, the intrinsic behavior of the crystal becomes evident. Since we can expect absorbing defects and impurities to always increase the susceptibility to damage, we take a curve drawn through the uppermost points to be indicative of the fundamental multiple shot limits of the crystal.

### 4. Results

In figure 4 we show data representing the intrinsic limit discussed above for four different temperatures in KBr. The solid lines are the model predictions for these temperatures. All four curves were obtained using the same values for the adjustable parameters. The model matches the the observed temperature and flux dependences fairly well.

The question arises as to whether the thermal stress, due to a temperature rise of less than ten degrees, plays a significant role in the process of multiple shot laser damage. Figure 5 shows the behavior predicted if the thermal stress term is omitted from eq.(8). In this case the flux dependence predicted is far too weak, and it becomes impossible to obtain a reasonable fit between the theory and experiment. This fact is not difficult to appreciate. If we again assume that the interaction volume does not change and treat the problem hydrostatically, we have

$$\begin{aligned} d\sigma_T &= \left( \frac{\partial \sigma_T}{\partial T} \right)_V dT \\ &= \alpha K dT. \end{aligned} \tag{9}$$

Using values for the coefficient of thermal expansion of  $\alpha = 2.25 \times 10^{-6} \text{ K}^{-1}$ , and for the bulk modulus of  $K = 1.5 \times 10^{11} \text{ dyne cm}^{-2}$  [26] a temperature increase of  $\Delta T = 10 \text{ K}$  gives rise to a thermal stress of  $\sigma_T \approx 3 \times 10^6 \text{ dyne cm}^{-2}$ . This is to be compared with a yield stress of  $\sigma_y = 6.5 \times 10^6 \text{ dyne cm}^{-2}$  (see eq.(1)). At low temperatures, where the efficiency of F-center production is very small, the thermal stress



is particularly important. In this case the thermal stress must reach a sufficient level to boost the F-center formation efficiency to start the accumulation process, and we see a distinct threshold-like behavior. At higher temperatures the F-center formation rate is large enough (without being enhanced by the thermal stress) so that there is a much weaker flux dependence.

## 5. Conclusion

It is evident that single and multiple shot damage at 532 nm in KBr results from two different mechanisms. Whereas single shot damage appears to be the result of lattice heating, multiple shot damage is likely governed by the accumulation of microscopic structural changes (such as the creation of Frenkel defects) in the crystal lattice.

We have developed a model for the behavior of KBr exposed to multiple laser pulses at 532 nm. It applies to the intrinsic behavior of the crystal in that it does not appeal to a probabilistic mechanism or to the inclusion of absorbing impurities or defects. Instead, it attempts to incorporate known responses of the crystal to the laser pulses, temperature and stress. The model at this stage in its development shows the correct dependence of multishot laser damage on temperature and photon flux. It remains to test the model on other materials and to experimentally confirm the accumulation of F-centers and stress by other means such as Raman spectroscopy.

This work was supported by the Air Force Office of Scientific Research under grant number AFOSR-87-0081.

## 6. References

1. A. A. Manenkov, G. A. Matyushin, V. S. Nechitailo, A. M. Prokhorov and, A. S. Tsaprilov, Nat. Bur. Stand. (US) Spec. Publ. 669, 1982, 436-447.
2. E. K. Maldutis, S. K. Balickas, and R. K. Kraujalis, Nat. Bur. Stand. (US) Spec. Publ. 638, 1983, 96-102. B. G. Gorshkov, Yu. K. Danileldo, V. N. Nikolaev, and A. V. Sidorin, Sov. J. Quantum Electron. **13**, 388 (1983).
3. Larry D. Merkle, Michael Bass, and Randall T. Swimm, Nat. Bur. Stand. (US) Spec. Publ. 669, 1984, 50-59.
4. L. D. Merkle, N. Koumvakalis, and M. Bass, Nat. Bur. Stand. (US) Spec. Publ. 688, 1985, 128-134.
5. Pradip K. Bandyopadhyay and Larry D. Merkle, J. Appl. Phys. **63**, 1392 (1988).
6. Larry D. Merkle and Dimitrios Kitriotis, Phys. Rev. B **38**, 1473 (1988).
7. Scott C. Jones, X. A. Shen, P. F. Braunlich, Paul Kelly and A. S. Epifanov, Phys. Rev. B **35**, 894 (1987).
8. Scott C. Jones, Alfred H. Fischer, Peter Braunlich and Paul Kelly, Phys. Rev. B **37**, 755 (1988).
9. S. C. Jones, X. A. Shen, P. F. Braunlich, Paul Kelly and A. S. Epifanov, Nat. Inst. Stand. Tech. (US) Spec. Publ. 752, 1988, 621-633.
10. X. A. Shen, Scott C. Jones, Peter Braunlich and Paul Kelly, Phys. Rev. B **36**, 2831 (1987).
11. X. A. Shen, Peter Braunlich, Scott C. Jones and Paul Kelly, Phys. Rev. Lett. **59**, 1605 (1987).

12. X. A. Shen, Peter Braunlich, Scott C. Jones and Paul Kelly, Proceedings of the 19th Boulder Damage Symposium (1987), to be published.
13. X. A. Shen, Peter Braunlich, Scott C. Jones, and Paul Kelly, Phys. Rev. B **38**, 3494 (1988).
14. G. Brost, P. Braunlich and P. Kelly, Phys. Rev. B **30**, 4675 (1984).
15. Lin Simpson, S. A. Shen, Scott C. Jones, Peter Braunlich and Paul Kelly, Proceedings of the 20th Boulder Damage Symposium (1988), to be published.
16. X. A. Shen, Scott C. Jones and Peter Braunlich, Proceedings of the 20th Boulder Damage Symposium (1988), to be published.
17. I. Estermann, W. J. Leivo, and O. Stern, Phys. Rev. **75**, 627 (1949).
18. W. Primak, C. J. Delbecq, and P. H. Yuster, Phys. Rev. **98**, 1708 (1955).
19. Lan-Ying Lin, Phys. Rev. **102**, 968 (1956).
20. D. A. Wiegand and R. Smoluchowski, Phys. Rev. **116**, 1069 (1959).
21. Herbert Rabin, Phys. Rev. **116**, 1381 (1959).
22. R. Thomas Casper, M.S. project report, unpublished.
23. John S. Nadeau, J. Appl. Phys. **34**, 2248 (1963).
24. W. A. Sibley and E. Sonder, J. Appl. Phys. **34**, 2366 (1963).
25. John S. Nadeau, J. Appl. Phys. **35**, 1248 (1964).
26. Neil W. Ashcroft and N. David Mermin, *Solid State Physics* (Saunders College, Philadelphia, 1976).
27. W. Fuchs and D. A. Wiegand, J. Phys. Chem. Solids **36**, 17 (1975).
28. P. V. Mitchell, D. A. Wiegand, and R. Smoluchowski, Phys. Rev. **121**, 484 (1961).
29. P. W. Levy, P. L. Mattern, K. Lengweiler, and M. Goldberg, Solid State Commun. **9**, 1907 (1971).
30. P. W. Levy, K. J. Swyler, and R. W. Klaffky, J. Phys. Colloq. **41**, C6-344 (1980).
31. T. S. Orlova and B. I. Smirnov, Sov. Phys. Solid State **28**, 866 (1986).

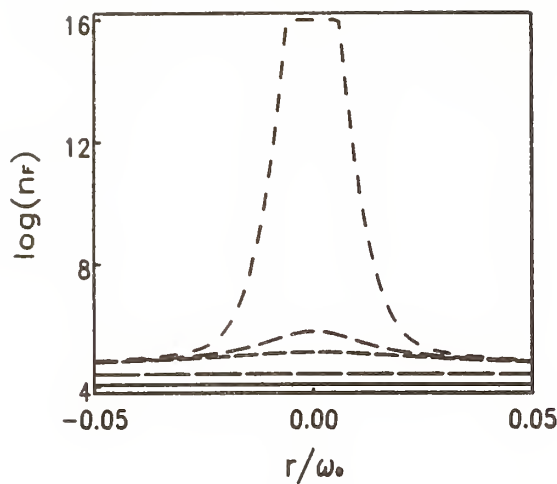


Figure 1. The calculated F-center density profile is shown for several shots in a series of 362. The profiles, progressing from the bottom curve upward, are for shots numbered 200, 300, 360, 361, and 362.  $\omega_0$  is the beam waist of the laser pulse, and  $r$  is the radius from the beam axis. For the last shot (362) the peak F-center concentration reached  $10^{18} \text{ cm}^{-3}$ . The peak of this curve (top curve) has been cut off to show some detail of the earlier shots.

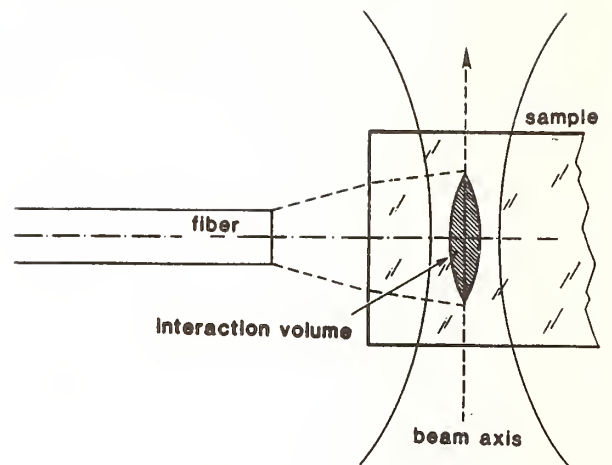


Figure 2. The position of the sample, laser beam, and optical fiber are shown here. the fiber is used to transmit the scattered laser light into a photomultiplier tube. A sudden increase in scattered light is the indication of damage.

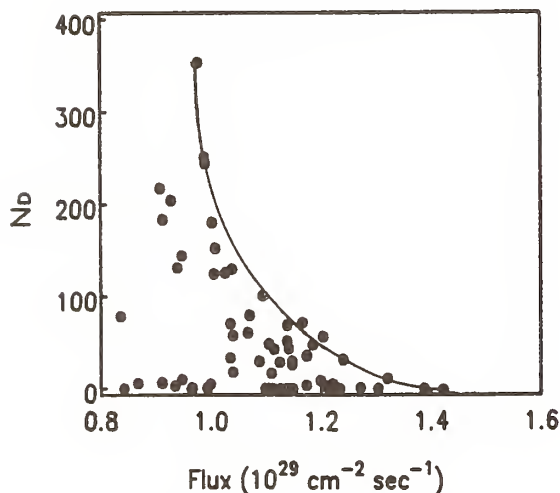


Figure 3. The number of laser pulses required to observe damage is plotted as a function of the peak photon flux at room temperature. The circles are the experimental data, and the line marks the upper bound to the envelope of data points. Points falling below this bound are attributed to extrinsic damage processes.

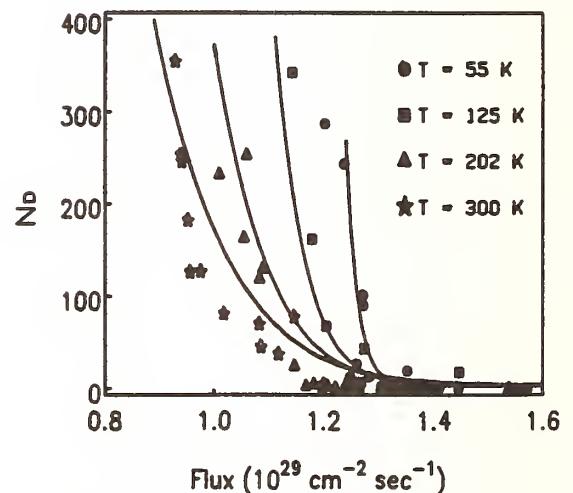


Figure 4. The results from experiments at four different temperatures are shown together with the predictions for these temperatures. The model demonstrates the correct temperature and flux dependences for multiple shot damage in KBr at 532 nm.

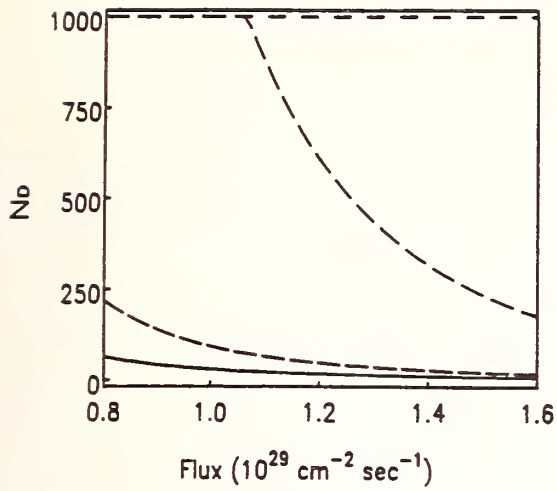


Figure 5. The temperature and flux dependence of the model when thermal stress effects are neglected is shown here. Without the thermal stress the flux dependence is too weak. In particular there is no sharp threshold behavior for low temperatures. The temperatures represented here, beginning with the top curve, are 55, 125, 200 and 300 K.

#### COMMENTS

Question: Did you speculate as to the lifetime of the F centers?

Answer: These are fairly stable F centers. If we can color the crystal using for example a UV pulse so that the F centers are visible to the eye, they will persist for days. We are only concerned with the F centers which are long lived. Some of them, in fact, most likely the majority of them, do recombine relatively quickly, but there will be some where the displaced atom is removed far enough away from the vacancy that they will persist in the crystal.

Question: I'd like to ask a question about those points you threw away. Were there any that you threw away at 55° K?

Answer: There were. There was almost a vertical transition in the data at 55° K. At a certain peak flux I never saw any sites which survived more than 2 to 3 shots. Below that flux I could get sites that would survive a couple of thousand shots. However, there were some below that flux which would succumb at a lower number of shots. They are probably due to some sort of a defect.

Question: In your final plot, where you showed a plot of the number of pulses to damage versus the incident flux, was there, on your theoretical curve, an adjustable fit parameter?

Answer: There are 2 parameters which can be adjusted, I don't have any limits on at the moment as to their values. One is in material dependent parameter, the gamma that was shown in the expression. There is a little leeway on the relative contributions between the F center induced stress and thermal stress. They are certainly not exactly accurate and I believe that there is going to be some problem with that number. As a result there is a little bit of leeway in the coefficient of that variable.

Question: I would like to ask you a question on your experimental setup. What fiber diameter did you use, what is the numerical aperture or acceptance angle and what is the length of the fiber?

Answer: The fiber diameter was 1 mm and the numerical aperture 0.2.

Question: In your last slide you indicated that you might want to use Raman scattering to look at stress. Could you tell us a little bit about how you want to do that?

Answer: The idea is to use a second dialyzer beam. At various points in the experiment we would actually interrupt the firing and use a dialyzer tuned to achieve a resonant Raman scattering.

Question: This is a cubic crystal. Would you expect Raman scattering in KBR?

Answer: Once you produce the F centers you will have first order Raman scattering. The interaction volumes are fairly small, and so the total number of them is not that great, so it may involve integrating. We don't know how long we'll have to integrate the signal and how difficult it will actually be to detect, but that's our hope.

Question: I just want to comment that there's an increasing body of knowledge that indicates that the F center generation is intimately connected with the dislocation content and I would like to see you make some effort to include that into your mechanism.

Answer: I am aware of this. At this point, it is not in there, but I hope to look into that, I have not done it at this point.



Question: Is there a temperature at which you would expect the healing to offset the temperature dependence you've seen in the generation? Would you get the threshold starting to go up with temperature?

Answer: I am not certain. We have tried some experiments at temperatures above room temperature, but we have the problem that with increased temperature the material actually comes off the crystal itself, so our optics have been impaired when we tried the experiment. It is conceivable that at a high enough temperature the mobility of the interstitials would increase, but then they would be likely to move away from the vacancies, so I don't know that you would get a complete healing.

## Laser Heating of Free Electrons and the Mechanism of Intrinsic Laser Breakdown in Wide-Gap Optical Materials at 1064 nm

X. A. Shen, Scott C. Jones, and Peter Braunlich  
Department of Physics  
Washington State University  
Pullman, WA 99164-2814

Free electron absorption of 1064 nm photons is measured photoacoustically in NaCl and SiO<sub>2</sub>. The electrons are generated with a 266 nm pump pulse by two- or three-photon transitions from the valence band. For a given pump pulse energy which is chosen sufficiently low to avoid heating of the interaction volume by itself, the dependence of the photoacoustic signal and temperature rise are observed as a function of the energy of the 1064 nm pulse and found to be in agreement with the theory of free carrier heating by Epifanov et al. Temperatures approaching the melting point are produced in the materials under prebreakdown conditions. This work provides direct experimental proof that free electron absorption is the primary mechanism for heating wide-gap optical materials by intense laser pulses in the visible and near infrared, confirming the indirect measurements reported earlier by Shen et al. No evidence of electron impact ionization and ensuing avalanche formation is found up to the intrinsic damage threshold, throwing doubt onto the commonly held belief that it is responsible for free electron generation and eventual breakdown at 1064 nm.

Keywords: Avalanche ionization; free electron absorption; fused silica; NaCl

### 1. Introduction

Generation of free electrons and subsequent lattice heating via electron-photon-phonon interactions are the two major processes leading to laser-induced intrinsic damage in transparent optical materials.<sup>1-4</sup> We have shown recently that in KBr and NaCl, exposed to intense laser pulses at 532 nm, these two processes are free electron formation by four-photon transitions across the band gap and free-electron photon absorption,<sup>5,6</sup> resulting in a significant rise of lattice temperature. Damage occurs when the peak temperature in the interaction volume approaches the melting point. The experiments provide conclusive proof that under these conditions impact ionization does not measurably contribute to free carrier formation.

In previous investigations of laser damage, a single wavelength is used to achieve the above two processes. Each pulse serves two purposes: (a) generating free-electrons and (b) subsequently heating them via free-electron-photon-phonon interactions. But these studies can easily be carried further by employing simultaneously two laser pulses of different wavelengths. One can efficiently generate free electrons with a short wavelength and heat them with a longer one, thus separating processes (a) and (b) for independent study. The wavelengths for the two pulses have to be chosen so that the free carrier generating pump pulse does not contribute significantly to lattice heating, while the heating pulse does not create a significant number of carriers via multiphoton absorption. By keeping the energy of the pump pulse, and, thus, the total number of free electrons constant and varying that of the heating pulse, we can then measure with a photoacoustic method the total energy absorbed by the lattice as a function of the laser flux and determine its power dependence.

The materials chosen in our investigation are NaCl and SiO<sub>2</sub> (fused silica). As pump pulses, we use the fourth harmonic (266 nm) of a Nd:YAG laser and its fundamental wavelength (1064 nm) to heat the electrons. The carrier generation process here is two- or three-photon absorption and its efficiency does not require pulses of very high flux to generate a sufficient density ( $\approx 10^{16} \text{ cm}^{-3}$ ) of electron-hole pairs for the measurement of free electron heating. Furthermore, photon absorption by free electrons is less efficient at 266 nm than it is at 1064 nm (approximately by a factor of 8, e.g., in KBr).<sup>7</sup> Thus, we can neglect the contribution from the pump pulse to lattice heating. Similarly, we do not have to consider carrier generation by 1064 nm pulses because it would require valence electrons to absorb at least seven photons simultaneously to cross the band gap. The experiments were also performed with the intention to verify the validity of so-called multiphoton-assisted avalanche mechanism of laser

damage.<sup>4</sup> In a low-order multiphoton process (here two- and three-photon absorption), a large free electron density can be generated which would represent the starting density for avalanche formation during the interaction with a 1064 nm pulse.

To assure that indeed intrinsic effects are studied and not energy absorption due to material imperfections, it is essential to measure the energy deposited by the two laser pulses in the prebreakdown regime rather than monitoring only damage thresholds.<sup>6,8,9</sup> By direct photoacoustic measurement of the energy deposited in the interaction volume as a result of the free electron-phonon-photon interaction at 1064 nm, we show below that in NaCl and SiO<sub>2</sub>:

1. for constant pump pulse energy, the photoacoustic signal (deposited energy),  $S$ , depends on the energy,  $E$ , of the 1064 nm pulse according to the free-electron heating theory developed by Epifanov et al.<sup>7</sup>:  $S \propto aE^{3/2} + bE^3$ ,
2. significant increases in peak temperature can be observed under pre-breakdown conditions and intrinsic damage occurs close to the melting point of the materials investigated,
3. electron impact ionization and avalanche formation, which would manifest themselves as a sudden explosive increase in absorbed energy above a certain power density of the heating pulse, are conspicuously absent up to the intrinsic damage threshold.

In the following we review briefly the free-electron-heating theory by Epifanov et al.<sup>7</sup> and derive an expression which relates the photoacoustic signal generated in a two-wavelength experiment to the energy of the laser pulse. Section III provides the details of the experiment and measurements. In Sec. IV we present a discussion of the results and show that they are indeed due to laser heating of free electrons. The last section contains the summary and conclusions.

## 2. Free Electron Heating in Wide-Gap Solids

The free electron heating theory predicts that, when free electrons in a wide-gap solid (generated via either multiphoton absorption or electron avalanche formation) interact with external photon fields, the rate of increase of lattice temperature follows the equation<sup>7</sup>

$$c\rho \frac{dT(r,t)}{dt} = AT^{1/2}(r,t)n_c(r,t)F^{3/2}(r,t), \quad (1)$$

where  $c$  is the specific heat,  $\rho$  the mass density, and  $F$  the photon flux,  $n_c$  the density of conduction electrons and

$$A = \frac{1.09}{l_{ac}v_s} \left( \frac{m^*k}{2\pi} \right)^{1/2} \left( \frac{e}{m^*\omega} \right)^3 \left( \frac{240\pi\hbar\omega}{n} \right)^{3/2}.$$

Here  $l_{ac}$  is the mean free path of conduction electrons with regard to electron-phonon collisions,  $v_s$  the longitudinal sound velocity,  $m^*$  the band mass of electrons,  $\omega$  the laser frequency,  $n$  the index of refraction,  $e$  the electron charge, and  $k$  the Boltzmann constant.

To relate Eq. (1) to the total energy absorbed by the lattice in a two-wavelength experiment, let us rewrite  $n_c(r,t)$  and  $F(r,t)$  as  $n_c(r,t) = n_c(r)f_1(t)$  and  $F(r,t) = F(r)g_1(t)$ , where  $f_1$  and  $g_1$  are the temporal distributions of the variables. For well-characterized laser pulses,  $g_1(t)$  does not change with the pulse energy, while  $f_1(t)$  does because the rate of recombination of electron-hole pairs varies with their density: the higher the density, the faster the recombination.<sup>10</sup> However, if the experiment is carried out under the condition of constant pump energy,  $f_1$  will remain unchanged. For NaCl and SiO<sub>2</sub> the specific heat,  $c$ , and mass density,  $\rho$ , do not vary significantly above room temperature where the measurements are performed. Therefore, we can consider them constants and integrate Eq. (1) over time to obtain the temperature rise resulting from the laser-solid interaction, i.e.,

$$2c\rho \left( T^{1/2}(r,\infty) - T_0^{1/2} \right) = ABn_c(r)F^{3/2}(r), \quad (2)$$

where

$$B = \int_{-\infty}^{+\infty} f_1(t) g_1^{3/2}(t) dt,$$

is a constant. This yields

$$T^{1/2}(r, \infty) = T_0^{1/2} + \frac{AB}{2cp} n_c(r) F^{3/2}(r). \quad (3)$$

Defining a constant  $D = AB/2cp$  and taking the square of Eq. (3), we obtain the temperature rise as a function of photon flux and free electron density:

$$\Delta T(r) = T(r, \infty) - T_0 = 2T_0^{1/2} D n_c(r) F^{3/2}(r) + D^2 n_c^2(r) F^3(r). \quad (4)$$

The total energy absorbed by the lattice from the free-electron-photon interaction is then given by

$$U = \int_V cp \Delta T(r) dV. \quad (5)$$

The integral is taken over the interaction volume,  $V$ .

In general,  $n_c(r)$  and  $F(r)$  can be expressed as  $n_c(r) = n_0 f(r)$  and  $F(r) = F_0 g(r)$ , where  $n_0$  is the peak density,  $F_0$  the peak flux, and  $f(r)$  and  $g(r)$  are the spatial distributions of free electrons and flux, respectively. Thus, the total energy can be expressed as

$$U = cp \left( 2T_0^{1/2} D n_0 F_0^{3/2} \int_V f(r) g^{3/2}(r) dV + D^2 n_0^2 F_0^3 \int_V f^2(r) g^3(r) dV \right), \quad (6)$$

or

$$U = cp \left( 2T_0^{1/2} V_1 D n_0 F_0^{3/2} + V_2 D^2 n_0^2 F_0^3 \right), \quad (7)$$

with

$$V_1 = \int_V f(r) g^{3/2}(r) dV,$$

and

$$V_2 = \int_V f^2(r) g^3(r) dV.$$

Knowing  $f(r)$  and  $g(r)$ , one can calculate  $V_1$  and  $V_2$  (see Appendix) and obtain the total absorbed energy  $U$ .

In a two-wavelength experiment, the measured photoacoustic signal is comprised of two parts: (a) the normally very small energy,  $U_0$ , deposited via multiphoton carrier generation and (b) the energy,  $U$ , due to electron heating. The signal is proportional to the sum of the two parts, i.e.,  $S = A(U_0 + U)$ . Substituting  $U$  with Eq. (7) and redefining the constants, we obtain

$$S = A_1 + A_2 \left( 2T_0^{1/2} V_1 D n_0 F_0^{3/2} + V_2 D^2 n_0^2 F_0^3 \right). \quad (8)$$

There are unknown constants  $A_1$ ,  $A_2$ , and  $D$  in Eq. (8) which can be determined, in principle, from the measurements of  $S$  as a function of  $F_0$ .



Experimentally, one measures the pulse energy  $E$  instead of  $F_0$ , and it is usually not calibrated, i.e.,  $F_0 = QE$  with  $Q$  an unknown. Therefore, Eq. (8) becomes

$$S = A_1 + A_2 \left( 2T_0^{1/2} V_1 Dn_0 Q^{3/2} E^{3/2} + V_2 D^2 n_0^2 Q^3 E^3 \right). \quad (9)$$

Redefining  $P = 2A_2 T_0^{1/2} V_1 Dn_0 Q^{3/2}$  and  $R = A_2 V_2 D^2 n_0^2 Q^3$ , one has

$$Dn_0 = 2T_0^{1/2} \left( \frac{V_1}{V_2} \right) \left( \frac{R}{P} \right) Q^{-3/2} \quad (10)$$

The peak temperature rise in the interaction volume as a function of the heating pulse energy,  $E$ , can now be expressed in terms of  $R/P$  and  $E$  from Eq. (4):

$$\Delta T(r=0) = 4T_0 \left( \left( \frac{V_1}{V_2} \right) \left( \frac{R}{P} \right) E^{3/2} + \left( \frac{V_1}{V_2} \right)^2 \left( \frac{R}{P} \right)^2 E^3 \right). \quad (11)$$

The derivation here does not require the knowledge of the temporal dependences of free electron density and photon flux as long as the energy of the pump pulses stays constant. This simplifies considerably our investigation because the temporal distribution of free electrons is usually not known. The peak temperature can be determined without an absolute calibration of the pulse energy and photoacoustic signal, provided that the measured photoacoustic signal follows the energy dependence in Eq. (9). Of course, absolute calibration of both variables poses no principle problem.<sup>6</sup>

### 3. Experimental Details

#### A. Apparatus

A schematic of the experimental arrangement is given in Fig. 1. The laser system is a Quantronix model 116 Q-switched and mode-locked Nd:YAG laser with a double-pass amplifier. A single mode-locked pulse of approximately 100 ps is selected and subsequently converted to 532 nm by a second harmonic generator with an efficiency of 60%. A harmonic beam splitter separates the 532 nm output from the residual fundamental pulse. The 532 nm pulse is then converted to 266 nm by a fourth harmonic generator. The two pulses, at 266 nm and 1064 nm, are recombined in front of the focusing lens with the aid of another harmonic beam splitter. A variable attenuator is used for each wavelength so that their pulse energies can be varied independently. In order to overlap the focal planes of each wavelength with a single focusing lens, we place a variable beam compressor consisting of a positive and a negative lens in the infrared-beam path to control the effective focal length for 1064 nm independently. A movable prism is installed to vary the path length of the 1064 nm pulse for temporal overlap with the 266 nm pulse.

The detection system consists of a resonant PZT transducer and a fused silica rod of approximately 5 inches in length. The transducer is glued onto one end of the rod, while the sample is attached to the other. This separation of the sample from the transducer allows us to discriminate, by a time-of-flight method, light scattered onto the transducer from the acoustic signal generated by the laser-solid interaction. The transducer is coupled to a pulse amplifier, whose output is fed to a Data Precision 6000 transient digitizer for analysis. The photoacoustic signal obtained on the digitizer is a modulated sine wave; its peak-to-peak amplitude is used as measure for the absorbed energy. The NaCl crystals are obtained from the University of Utah, while the SiO<sub>2</sub> is purchased from Wale Apparatus Co.

#### B. Experimental Procedure

As stated earlier, the two-beam approach to the study of free electron heating in wide-gap solids requires precise spatio-temporal alignment of the laser pulses, which includes overlapping their focal planes. The latter is very crucial to the measurement. If the focal waists of the two pulses do not coincide, the location of highest heating flux does not overlap a sufficient number of free electrons for the interaction to generate a measurable signal. As a result, one observes either no heating effect or extrinsic damage by the 1064 nm laser pulse. This alignment turns



out to be the major difficulty in the experiment because the laser pulses are tightly focused with a typical focal waist of only 5  $\mu\text{m}$ . We employ the following approach to the problem.

We use a third harmonic cross-correlation method to first obtain the temporal overlap of the two pulses. After having the two beams approximately aligned at the focal point, we replace the 266/1064 nm beam splitter located between the focusing lens and the infrared attenuator by a harmonic beam splitter that transmits the residual green from the fourth harmonic generator and reflects the 1064 nm incident pulse. Now the laser pulses travel in the direction perpendicular to the ones before the replacement of the 266/1064 nm beam splitter. We then place a third harmonic generator (THG) in front of the new beam splitter and detect its output at 355 nm. By moving the prism (see Fig. 1) and maximizing the output from the THG, we can overlap the two beams accurately in time. Since the 266 nm pulse and that of the residual green share the same path, it also ensures the temporal overlap of the 266 and 1064 nm pulses.

After the two laser pulses temporally overlapped, we can now proceed to precisely position their focal planes. In the preceding section we have shown theoretically that the interaction of free electrons with photons under the two-pulse condition will result in the generation of a photoacoustic signal in addition to that induced by the pump pulse. This increase of the signal depends on the local electron density and flux. The higher the density or flux, the stronger the signal. This property can now be employed to overlap the two focal planes. By changing the distance between the two lenses in the beam compressor and monitoring the photoacoustic signal generated in the sample, we can detect the relative motion of the two focal planes. If the focal point of the pump pulse coincides with that of the heating pulse, we will observe a maximum in the photoacoustic signal. However, the energy of the 1064 nm pulse required to provide a detectable acoustic signal is usually very high and close to the damage thresholds of our samples. This makes the alignment difficult to achieve. Most of the time we observe either no increase or extrinsic damage.

### C. Results

Before measuring the total energy absorbed by the lattice as a function of the pulse energy at 1064 nm under the condition of constant pump energy, it is necessary to verify how the free carriers are generated in the samples by the 266 nm laser pulses. This is accomplished by blocking the heating pulse and measuring the acoustic signal generated by the pump pulse and its dependence on the pulse energy. The results are shown in Fig. 2. The upper and the lower curves are the measurements from NaCl and SiO<sub>2</sub>, respectively, plotted on a log-log scale. They show a slope of approximately 2 for NaCl and nearly 3 for SiO<sub>2</sub>, indicating that the primary free carrier generation processes are two- and three-photon absorption, respectively.

Having identified the processes for the generation of free electrons in NaCl and SiO<sub>2</sub>, we can now proceed to study the free-electron-photon interaction with two laser pulses. Figures 3 and 4 show the results obtained in NaCl and SiO<sub>2</sub> under the condition of constant pump energy. In both materials, the photoacoustic signal increases nonlinearly with the energy of the heating pulse. When the 1064 nm pulse is blocked, we observe only a very weak signal resulting from free-carrier recombination. The data are obtained before any indication of damage and, therefore, are considered to be prebreakdown results. It should be mentioned that if we instead block the pump pulse in the experiment and let the samples be exposed to 1064 nm pulses only, we detect no photoacoustic signal. The signal can only be obtained by exposure of the samples to both laser pulses simultaneously, which implies that the signal must result from the interaction of the 1064 nm laser pulse with two- or three-photon generated electron states, i.e., free electrons.

The solid lines in Figs. 3 and 4 are the fits to the experimental results using the theory of free electron heating, i.e., Eq. (9). They show a very good agreement with experiment, indicating that the energy deposition observed here is very likely due to laser heating of free electrons at 1064 nm. However, in order to draw this conclusion we have to carefully consider other possibilities, such as photon absorption by laser-generated primary defects or interband transitions by valence electrons absorbing simultaneously one 266 nm photon and several 1064 nm photons. The latter can also have a nonlinear dependence on the energy of the heating pulse.

### 4. Discussion

The comparison of our experimental results with the free-electron-heating theory in the preceding section shows that there is a nonlinear component in the relation of the acoustic signal,  $S$ , versus pulse energy,  $E$  (see Figs. 3 and 4), that depends on  $E^3$ , because the equation to which our results are fitted has a term proportional to  $E^3$  [see Eq. (9)]. This suggests another rate possibility: we may have observed, instead of free electron heating, a multiphoton process in which a valence electron absorbs simultaneously four photons, one 266 nm and three 1064 nm. However, these two effects can be differentiated by examining the dependence of the acoustic signal on the polarization of the heating pulses. According to the theory of free electron heating, interaction of free electrons with photons does not depend on the polarization of the photon fields, while multiphoton absorption does.<sup>11</sup> The latter will have a maximum value when the pump and heating pulses have the same polarization.

However, we detect no significant dependence on the laser polarization which excludes the possibility of four-photon absorption discussed above. Figure 5 shows the results for SiO<sub>2</sub>, where we measure the photoacoustic signal induced by both 266 and 1064 nm laser pulses as a function of the polarization of the heating pulse under the condition of constant pulse energies. The absence of four-photon absorption is further supported by the fact that both materials, NaCl and SiO<sub>2</sub>, exhibit identical dependence on the 1064 nm pulse energy. If such multiphoton processes were present, one would expect them to be for SiO<sub>2</sub> of higher order than those for NaCl because the former has a much wider band-gap and requires absorbing more photons to cross it.

Another possibility of inducing a photoacoustic signal with a 1064 nm laser pulse in the two-wavelength experiment may be photon absorption by multiphoton generated primary defects. It is possible that primary defects<sup>12</sup> created by the pump pulse absorb photons at 1064 nm. However, it is very unlikely because two different materials, NaCl and SiO<sub>2</sub>, exhibit identical response to the absorption. Furthermore, defect absorption is usually linear and it will easily saturate as one increases the intensity of the laser light. Both phenomena were not observed in our experiment.

A further experiment ensures that photon absorption by primary defects does not play an important role in our measurement. We repeat the two-wavelength experiment with constant pump and heating pulses and measure the acoustic signal as a function of the delay of the latter with respect to the pump pulse. If the signal is indeed due to free electron heating, one expects it occurs only for very short delay times after the pump pulse, e.g., on the order of our pulse length (approximately 100 ps). Because the lifetimes of primary defects are usually much longer, typically on the order of nanoseconds or longer, heating by primary defect absorption should be possible for delays on that order. Our results (Fig. 6) show that the absorption occurs immediately after the pump pulse lasting only about 150 ps.

The shape of the curve in Fig. 6 depends mainly on the lifetime of the free electrons. This parameter is, however, not known because it varies with the electron density as discussed in Sec. II. We expect that its width should be at least on the order of our pulse lengths, which agrees with the measurement here. The fact that the peak of the absorption curve in Fig. 6 does not coincide with that of the pump pulse is expected. The reason for this is that the free electron density peaks when the rate of recombination of electron-hole pairs equals that of free electron generation, which implies that the peak must appear when the pump rate is decreasing, i.e., after the peak of the pulse.

With this we conclude that the nonlinear energy deposition from 1064 nm photon fields into NaCl and SiO<sub>2</sub> observed in the two-wavelength experiment is indeed due to heating of free electrons. It should be pointed out that we have not considered here the polaron heating mechanism.<sup>4</sup> The reason is very simple. Polaron heating has a linear dependence on laser pulse energy, in disagreement with our experimental results. Furthermore, it has been already shown to be too inefficient compared to free electron heating.<sup>9</sup>

Having identified the mechanism for the energy absorption, we can now estimate the peak temperature rise in the interaction volume as a result of free electron heating at 1064 nm using Eq. (11). Theoretically, this can be easily accomplished by fitting our data to the equation to obtain the parameters  $R$  and  $P$  as discussed in Sec. II. However, experimentally it is very difficult to acquire an accurate value for these parameters, especially,  $P$ , which depends strongly on the choice of the pump energy. If this energy is overestimated, one will detect, at low heating fluxes, mainly the contribution from the pump pulse, i.e., the first term in Eq. (9) and can not resolve the second term containing  $P$ . Consequently, one will obtain an inaccurate value for  $P$ .

In our measurement, the pump energy required to obtain a detectable photoacoustic signal is slightly too high, resulting in underestimation of  $P$ . This could be improved in future experiments by appropriately choosing the photon energy of our pump pulses such that they do not provide significant excess energy to the conduction electrons via multiphoton absorption. Despite the complexity of the experiment, our estimation, using Eq. (11), show that the highest temperatures reached at the center of the interaction volume are above 1000 K in SiO<sub>2</sub> and well over 500 K in NaCl.

## 5. Summary and Conclusions

We have demonstrated, using two laser pulses of different wavelength, that the interaction of free electrons with photon fields in NaCl and SiO<sub>2</sub> at 1064 nm is governed by the free-electron-heating mechanism proposed by Epifanov et al.<sup>7</sup> The interaction leads to photon absorption by the free electrons, which in turn introduces a significant increase of temperature in the interaction volume. The estimated highest temperature reached in our experiment is close to the melting point of the materials, confirming the earlier measurement in KBr by Shen et al.<sup>5,9</sup> We have further demonstrated that up to the intrinsic damage threshold avalanche formation by electron impact ionization at 1064 nm is insignificant or absent even under the condition of a large density of starting electrons. These results throw doubt on the prevailing opinion that avalanche formation is the mechanism of intrinsic damage in wide-gap materials at near-infrared wavelengths.

The two-wavelength approach reported here also provides a new tool for the investigation of the fundamental processes involved in laser-induced intrinsic damage of optical materials. It removes some of the difficulties associated with the previous single-wavelength approach.<sup>5,6,9</sup> Further application of this technique will permit the study of lattice heating as a function wavelength.

We would like to thank Mr. R. Thomas Casper for his valuable assistance. This work was supported by the U.S. Air Force Office of Scientific Research under Grant No. AFOSR-87-0081.

## 6. References

1. W. L. Smith, Opt. Eng. **17**, 489 (1978).
2. N. Bloembergen, IEEE J. Quantum Electron. **QE-10**, 375 (1974).
3. B. G. Gorshkov, A. S. Epifanov, and A. A. Manenkov, Zh. Eksp. Teor. Fiz. **76**, 617 (1979) [Sov. Phys. JETP **49**, 309 (1979)].
4. A. Schmid, P. Kelly, and P. Braunlich, Phys. Rev. B **16**, 4569 (1977).
5. X. A. Shen, P. Braunlich, Scott C. Jones, and P. Kelly, Phys. Rev. Lett. **59**, 1605 (1987).
6. Scott C. Jones, A. H. Fischer, Peter Braunlich, and Paul Kelly, Phys. Rev. B **37**, 755 (1988).
7. A. S. Epifanov, Zh. Eksp. Teor. Fiz. **67**, 1805 (1974) [Sov. Phys. JETP **40**, 897 (1975)].
8. P. Braunlich, Scott C. Jones, X. A. Shen, R. Thomas Casper, and P. Kelly, Proceedings of the 19th Boulder Laser Damage Symposium, October 26-28, 1987, Boulder, CO.
9. X. A. Shen, P. Braunlich, Scott C. Jones, and P. Kelly, Phys. Rev. B **38**, 3494 (1988).
10. R. T. Williams, J. N. Bradford, and W. L. Faust, Phys. Rev. B **18**, 7038 (1978).
11. See, for example, Y. R. Shen, *The Principles of Nonlinear Optics* (Wiley, New York, 1984).
12. M. N. Kabler, in *Point Defects in Solids*, Vol. 1, edited by J. H. Crawford, Jr. and L. M. Slifkin (Plenum, New York, 1972).



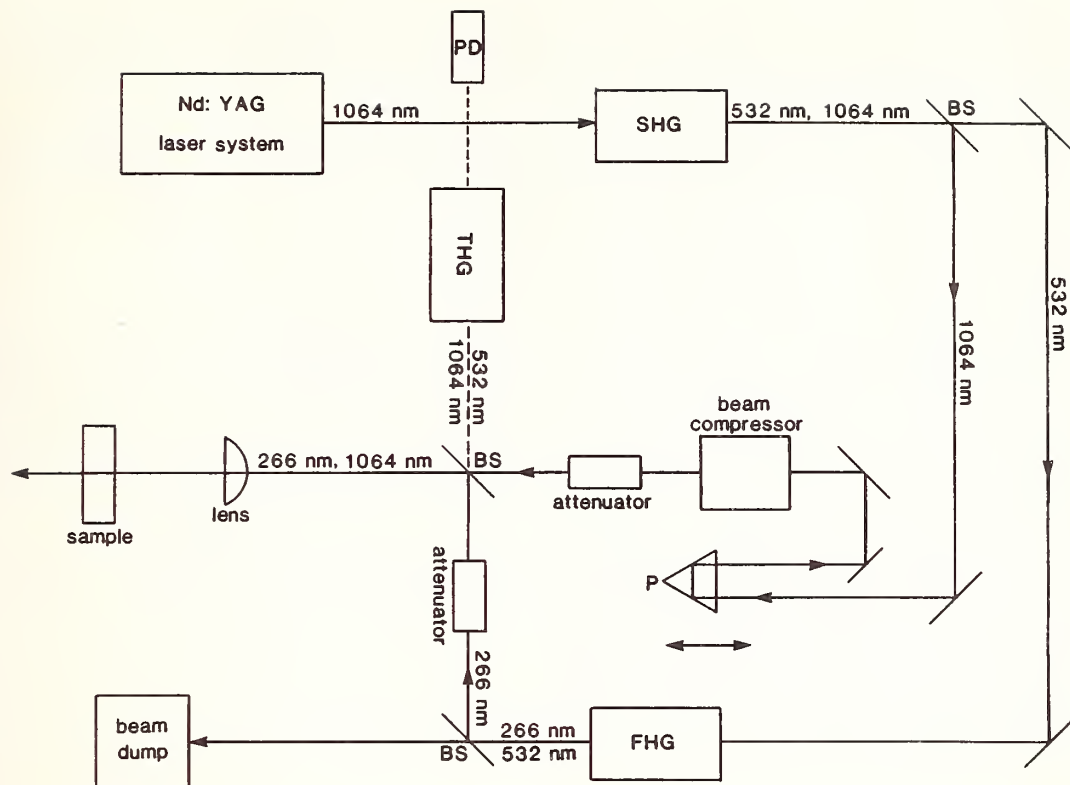


Figure 1. Schematic of the experimental arrangement for the measurements of free electron heating in NaCl and SiO<sub>2</sub>. The output from the Nd:YAG laser is a single mode-locked pulse whose wavelength is 1064 nm, with a halfwidth of approximately 100 ps. The laser pulse is passed through a second harmonic generator (SHG), which converts part of the pulse to 532 nm. A harmonic beam splitter (BS) separates the two wavelengths emerging from the SHG, and the 532 nm pulse is further converted to 266 nm by a fourth harmonic generator (FHG). A movable prism (P) is installed in the path of the 1064 nm laser pulse to vary its path length. The two pulses, 266 and 1064 nm, then reunite in front of the focusing lens with the aid of another BS, and are focused subsequently into a sample. A beam compressor is used to change the effective focal length for the infrared pulse to ensure the overlap of the 266 and 1064 nm focal waists. Two attenuators are installed to vary the energy of the two pulses incident on the sample. By replacing the BS in front of the infrared attenuator by a 532/1064 nm beam splitter (see discussion in text), we can convert the residual green from the FHG and 1064 nm pulse to 355 nm with the aid of a third harmonic generator (THG). This setup allows one to overlap the pulses from the two different paths in time as discussed in Sec. III.

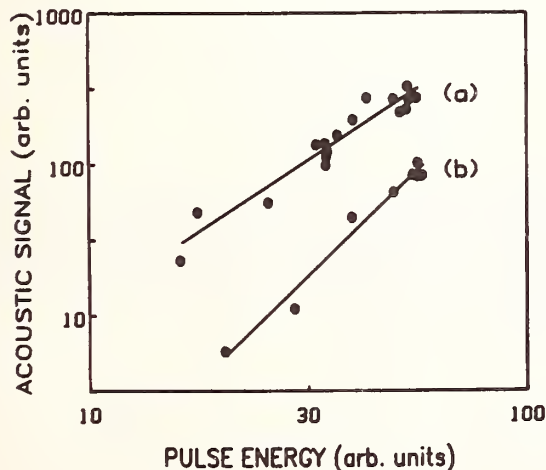


Figure 2. Photoacoustic signal as a function of the energy of a 266 nm laser pulse in (a) NaCl and (b) SiO<sub>2</sub>, plotted on a log-log scale. The slopes are approximately 2 for NaCl and nearly 3 for SiO<sub>2</sub>, indicating that the primary free carrier generation processes here are two- and three-photon absorption.

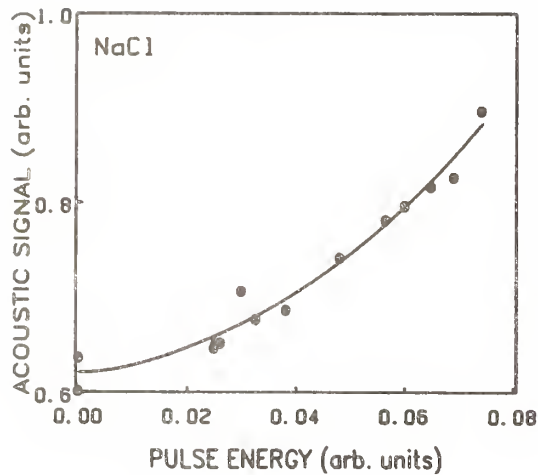


Figure 3. Measured photoacoustic signal as a function of energy of the 1064 nm pulse, obtained in NaCl under the constant pump condition. It clearly shows a nonlinear dependence on the energy of the heating pulse. The solid line is the fit to the experimental results using Eq. (9), showing good agreement between theory and measurement.

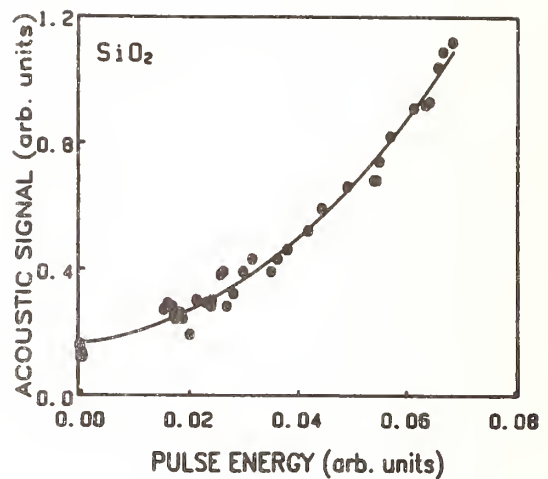


Figure 4. Same as Fig. 3 but in SiO<sub>2</sub>.

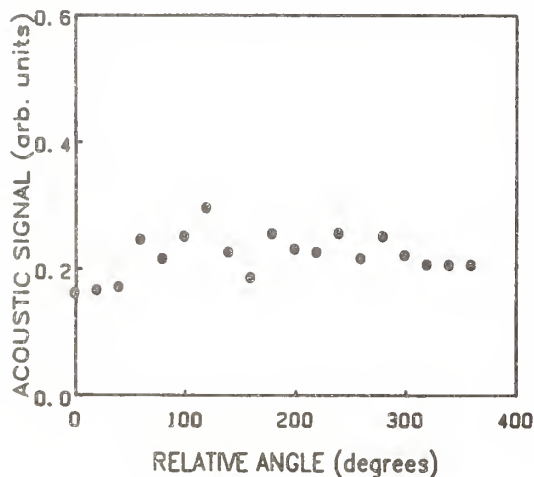


Figure 5. Dependence of the two-pulse generated photoacoustic signal on the polarization of the heating pulse. The results here do not show any periodic structure as, otherwise, expected for multiphoton absorption, which excludes the possibility of four-photon absorption discussed in the text.

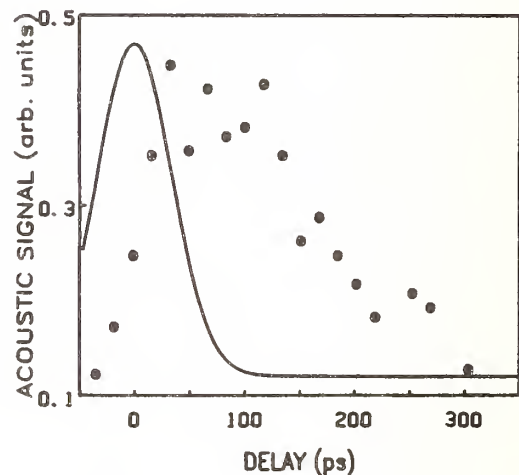


Figure 6. Photoacoustic signal as a function of delay of the heating pulse. The solid line represents the temporal profile of the pump pulse. The width of the absorption curve is approximately 150 ps and its peak occurs after that of the pump pulse as expected (see discussion in the text).



## APPENDIX: CALCULATIONS OF $V_1$ AND $V_2$

Since the free electrons here are generated by  $m$ -photon absorption from a  $\text{TEM}_{00}$  mode laser pulse, the spatial distribution  $f(\mathbf{r})$  of the free electron density has the form

$$f(\mathbf{r}) = \frac{w_{01}^{2m}}{w_1^{2m}(z)} \exp\left(-\frac{mr^2}{w_1^2(z)}\right),$$

where  $w_{01}$  is the Gaussian waist of the pulse which creates the electrons. The spatial distribution of the laser pulse that interacts with free electrons,  $g(\mathbf{r})$ , also has a Gaussian profile

$$g(\mathbf{r}) = \frac{w_0^2}{w^2(z)} \exp\left(-\frac{r^2}{w^2(z)}\right).$$

Therefore,

$$\begin{aligned} V_1 &= \int_V f(\mathbf{r}) g^{\frac{3}{2}}(\mathbf{r}) dV \\ &= \int_V \frac{w_{01}^{2m} w_0^3}{w_1^{2m}(z) w^3(z)} \exp\left(-\frac{mr^2}{w_1^2(z)} - \frac{3r^2}{2w^2(z)}\right) dV \\ &= 2\pi \int_0^\infty \int_{-d/2}^{+d/2} \frac{w_{01}^{2m} w_0^3}{w_1^{2m}(z) w^3(z)} \exp\left(-\frac{(2mw^2 + 3w_1^2)r^2}{2w_1^2(z)w^2(z)}\right) r dr dz \\ &= 2\pi \int_0^{+d/2} \frac{w_{01}^{2m} w_0^3}{w_1^{2m}(z) w^3(z)} \frac{2w_1^2(z)w^2(z)}{(2mw^2 + 3w_1^2)} dz \\ &= 4\pi w_{01}^2 \int_0^{+d/2} \frac{1}{\left(\frac{w_1}{w_{01}}\right)^{2m-2} \left(\frac{w}{w_0}\right)^2 2m \left(\frac{w}{w_0}\right)^2 + 3 \left(\frac{w_1}{w_0}\right)^2} dz, \end{aligned}$$

where  $d$  is the thickness of the sample.

Similarly,

$$\begin{aligned} V_2 &= \int_V f^2(\mathbf{r}) g^3(\mathbf{r}) dV \\ &= \int_V \frac{w_{01}^{4m} w_0^6}{w_1^{4m}(z) w^6(z)} \exp\left(-\frac{2mr^2}{w_1^2(z)} - \frac{3r^2}{w^2(z)}\right) dV \\ &= 2\pi \int_0^\infty \int_{-d/2}^{+d/2} \frac{w_{01}^{4m} w_0^6}{w_1^{4m}(z) w^6(z)} \exp\left(-\frac{(2mw^2 + 3w_1^2)r^2}{w_1^2(z)w^2(z)}\right) r dr dz \\ &= 2\pi \int_0^{+d/2} \frac{w_{01}^{4m} w_0^6}{w_1^{4m}(z) w^6(z)} \frac{w_1^2(z)w^2(z)}{(2mw^2 + 3w_1^2)} dz \end{aligned}$$

$$= 2\pi w_{01}^2 \int_0^{+d/2} \frac{1}{\left(\frac{w_1}{w_{01}}\right)^{4m-2} \left(\frac{w}{w_0}\right)^4} \frac{dz}{2m \left(\frac{w}{w_0}\right)^2 + 3 \left(\frac{w_1}{w_0}\right)^2}.$$

If we define  $R_1 = w_1^2/w_{01}^2 = 1 + z^2/z_{01}^2$ ,  $R_2 = w^2/w_0^2 = 1 + z^2/z_0^2$ , and  $R_3 = w_1^2/w_0^2 = (w_{01}/w_0)^2(1 + z^2/z_0^2)$ , we can rewrite the above two integrals as

$$V_1 = 4\pi w_{01}^2 \int_0^{+d/2} \frac{1}{R_1^{m-1} R_2^{\frac{1}{2}}} \frac{dz}{2m R_1 + 3 R_3},$$

and

$$V_2 = 2\pi w_{01}^2 \int_0^{+d/2} \frac{1}{R_1^{2m-1} R_2^2} \frac{dz}{2m R_1 + 3 R_3}.$$

These two parameters can be calculated numerically if one knows  $w_{01}$  and  $w_0$ . A typical value for  $V_1/V_2$  is around 2.0.

## COMMENTS

- Question: Were these photoacoustic measurements all done on the same site?
- Answer: Yes. Okay, you did not see any conditioning effect with a reduction of the acoustic signal as you proceeded on a particular site under the same conditions? No. This effect has been observed on wide gap materials recently at short wavelengths. Not in this case. Thank you.
- Question: Did you do the measurement where you turned off the probe pulse and just measured the acoustic signal through the pump alone?
- Answer: Yes we did. It shows that with sodium chloride the slope is two and with silicon dioxide it is three, so we conclude that in sodium chloride you have basically two photon absorption and in silicon dioxide you have three photon absorption.
- Question: I guess what I would have liked to have seen is a curve like shown with a photo acoustic signal, but just with the probe. I mean just with the pump.
- Answer: When we do an experiment we turn the pump in the pulse down to the minimum. You cannot see a signal on the display. Then we increase the heating pulse on so that we see a signal. The experiment is done under the condition of very weak pump - signal due to pump pulse.
- Question: How is the temperature calculated?
- Answer: The temperature is based on equating the increase in lattice temperature to the free electron heating mechanism. It is related to the ratio of R to P, which is obtained by fitting the data. This is the equation we used to calculate temperature and you see that for arbitrary e, you can calculate any temperature at any photon energy.
- Question: How do you expect the heating results to scale with the wavelength of the heating pulse? You used only a 1.06 micron laser to heat the sample. What if you varied that wavelength, how would you expect the results to vary?
- Answer: If the heat free electron heating theory is correct, then you would expect that the wavelength dependence would be very similar to the energy dependence, except that you replace e by the reciprocal of the frequency. Here is one of the immediate applications that you can make. Change the wavelengths, see if it still works.
- Question: You have a problem with multiphoton generation, because in order to see the heating effect, you have to increase the photon energy to something like a flux of  $10^{26}$ . You could easily see multiphotons at that flux. How do you separate the free electron heating process from multiphoton heating?
- Answer: I would be very surprised if you saw multiphoton effects in  $\text{SiO}_2$  at a wavelength of half a micron, of the experiment to try inserting the second harmonic of YAG and see what one gets.

Optical Measurements  
At PMS Electro-Optics

Ramin Lalezari and Scott Knollenberg

PMS Electro-Optics, Inc.  
1855 South 57th Court  
Boulder, Colorado 80301

Rapid and accurate measurements of scatter and absorption losses of optical elements provide essential feedback required for the development and production of low loss elements. Two techniques for the measurement of total loss and total integrated scatter are discussed. The total loss is determined using measurements of the resonant power in a two-mirror versus three-mirror active laser cavity. The difference in the power between a two- and three-mirror cavity can be directly related to the added third (test) element's loss. This simple apparatus will be described. The details of the measurement and some data on very low loss Ion Beam Sputtered mirrors will be presented. An apparatus developed for the measurement of total integrated scattered light from low-loss mirrors will be described. The instrument, which was designed to measure TIS levels of 1 to  $10^{-5}$ , consists of two coaxial parabolic mirrors with the sample located at the focal point of one mirror and a detector at the focal point of the second mirror. A chopped laser source and a filtered amplifier allow for the accurate measurement of a few ppm of scatter. Calibration is straight forward using a "white" diffuse scattering test specimen.

Key Words: cavity loss; loss measurement; low-loss optics; mirrors; scatter measurement; total integrated scatter.

## 1. Introduction

Loss measurements on optical elements provide the feedback required for the development of critical optical elements and intercavity components specifically. Measurements of three of the following four quantities are helpful in characterization of the losses of a component (1-R for mirrors and 2-R for windows): total loss, absorption, scatter, and transmission (reflection for windows). Direct measurement of absorption is difficult and requires significant instrumentation. It is also greatly dependent on the thermal characteristics of the film and the substrate and its size and shape. Absorption is therefore only deduced from other loss measurements and not measured directly. Total loss, scatter, and transmission measurements can be made with relatively simple instrumentation and accuracy adequate for the testing of a large group of components, including low-loss mirrors for Ring Laser Gyroscopes.

## 2. Total Loss Measurement

Total loss measurements can be made most accurately using resonant cavities. In 1984, Anderson et.al. described a mirror reflectometer based on optical cavity decay time. [ 1 ] This measurement technique is extremely sensitive to optical losses and is widely used to determine the losses of a variety of low-loss elements including RLG mirrors. This measurement requires relatively fast electronics (10 nsec response time) and great care in mode matching of the source laser beam to the test cavity. Another commonly used technique for measurement of losses

of a mirror is to construct a scanning Fabry Perot interferometer from the mirrors and measure its finesse and throughput. This technique is also very sensitive to the mode matching of the source beam to the cavity and to the mechanical stability of the cavity. For extremely high finesse cases ( $10^{-5}$ ), it becomes difficult to measure the finesse of throughput. The measurement technique developed at PMS utilizes the power buildup in a saturated helium neon tube to determine the "Q" of the resonant cavity, which is inversely proportional to the cavity losses. This measurement is done at 632.8nm. The major assumption in the measurement is that the gain of the laser tube is constant over the range of measurement. The total cavity loss is measured for a two mirror high finesse cavity, including loss of the laser medium, Brewster's window, and capillary diffraction losses. The cavity is then folded by inserting the flat test mirror inside the cavity as indicated in the diagram (b). The drop in the resonant power is proportional to the increase in total losses which, is exactly twice the reflectance loss of the inserted mirror. The following steps are involved in the calibration and the measurement.

### 3. Reference Cavity Calibration

$$M1_0 = \text{Mirrors with } 10^{-3} < T < 10^{-2} \text{ and } 1 - R - T \ll 10^{-3}$$

$$L_{\text{cavity}} = L_{M1_0} + L_{\text{tube}} \approx T_{M1_0} + L_{\text{tube}}$$

$$Q_0 = \frac{\text{Energy Stored}}{\frac{\text{Energy Lost}}{\text{Pass}}} = \frac{1}{T_{M1_0} + L_{\text{tube}}}$$

$$P_0 = K \cdot Q_0$$

Where  $P_0$  is measured power and  $K$  is the constant for the tube,  $K = P_s \cdot g_0$ .

$M1_0$  is replaced by a low loss reference mirror  $M1_1$ .

$$Q_1 = \frac{Q_0 P_1}{P_0} = \frac{1}{L_1}$$

$$\frac{1}{L_1} = \frac{1}{T_{M1_0} + L_{\text{tube}}} \cdot \frac{P_1}{P_0}; \quad L_{\text{tube}} = L_1 - T_{M1_1}$$

$$L_1 = \frac{(T_{M1_0} - T_{M1_1}) P_0}{P_1 - P_0}$$

Where  $L_1$  is loss of the reference cavity.

The data is produced using the following reference cavity. See diagram (a).



$$T_{M1_0} = 5.9 \times 10^{-3}$$

$$T_{M1_1} = 10^{-5}$$

$$P_0 = 12 \cdot 6 \times 10^{-6} \text{ W}$$

$$P_1 = 240 \times 10^{-6} \text{ W}$$

$$L_1 = 326 \times 10^{-6} \text{ Loss of reference cavity}$$

#### 4. Loss Measurement

Test mirror M2 is inserted in the cavity as shown in diagram (b).

$$Q_2 = \frac{Q_1 P_2}{P_1}$$

$$L_2 = \frac{L_1 P_1}{P_2} = L_1 + (2 \cdot L_{\text{test mirror}})$$

$$L_{\text{test mirror}} = \frac{1}{2}(L_2 - L_1)$$

$$= \frac{1}{2} L_1 \left( \frac{P_1}{P_2} - 1 \right)$$

Note that for a given test set up,  $P_1$  and  $Q_1$  are constants and different elements can be measured by aligning the cavity and measuring  $P_2$ . A similar calculation can be used to measure insertion loss of an AR coated window or Brewster's angle window from the reduction in  $Q$  of the reference cavity.

#### 5. Error

There is some predictable uncertainty due to the nonlinearity of the power produced in the tube as a function of cavity  $Q$ . This error can be understood by considering the following equation: [ 2 ]

Where  $P_r$  is resonant power.

$$P_r = P_s \left( \frac{g_0}{L} - 1 \right)$$

$P_s$  is resonant power for threshold of lasing.

$g_0$  is saturated gain.

$L$  is total losses.

An estimated value of 0.04 for  $g_0$  and 0.0061 for L of the reference cavity will cause that cavity's losses to be 15% higher than the linear case where it is assumed that  $P_r = P_s g_0/L$ .

$\pm 1\%$  uncertainty in the measurement of the power and laser noise due to mode sweeping creates a 2% uncertainty in the Q measurement and respectively a 2% uncertainty in the total cavity loss.

There is also some error due to variations in gain with the mode structure conforming to defect patterns on the test element. This effect is generally not present except on elements with large defects. These errors can be avoided by monitoring the beam profile.

## 6. Scatter Measurement

A simple scatterometer is constructed for rapid measurement of scattered light from highly reflective dielectric mirrors. The scatter measurement is only approximate since the near angle (0.2 steradians) scatter is not collected on the detector. Even though the instruments' measurements should not be compared to other instruments with different geometrical configuration, it has provided an extremely rapid and reproducible measurement for process development and quality control purposes. See diagram (c).

The scatterometer utilizes two coaxial 4" diameter parabolic mirrors with a spider web fixture in the center which holds the sample and the detector in the focal points of the two mirrors. A diaphragm and a flat black aperture provide a coarse but effective way of blocking the undesirable near angle scatter content of the illuminating beam. The laser beam is modulated with a 1KHz liquid crystal switch, and the detector amplifier has a 1KHz band pass filter. A lock-in amplifier would enhance the signal-to-noise ratio of the instrument. However, the improvements are not significant for an added cost of about 200%.

The 1KHz signal from the detector is recorded on a digital oscilloscope and signal averaging is used in the case of low scatter mirrors, (less than 10ppm) to reduce noise. The system is calibrated using a  $MgO_2$  coated element which is assumed to have 100% scatter. A five decade, two stage amplifier is used to provide necessary gain for the measurement.

## 7. Data

The following table presents some loss and scatter data from a variety of mirrors.

Table 1. Test Results

Mirror Type	Total Loss (+17%, -3%)	Transmission ( $\pm 2$ ppm)	Scatter ( $\pm 10$ ppm)	Absorption + Scatter ppm
E-Beam				
TiO <sub>2</sub> /SiO <sub>2</sub> @ 280° C	438	69	74	374-364
TiO <sub>2</sub> /SiO <sub>2</sub> @ 200° C	345	10	68	340-330
Ta <sub>2</sub> O <sub>5</sub> /SiO <sub>2</sub> @ 280° C	90	41	70	54- 44
-----				
Ion Beam H.R.'s				
#102 Dense Point Defects				
Spot #1	89	9	57	85- 75
Spot #2	126	9	57	122-112

Table 1. Test Results

Mirror Type	Total Loss (+17%, -3%)	Transmission (±2ppm)	Scatter (±10ppm)	Absorption + Scatter ppm
Ion Beam H.R.'s				
#103 Point Defects				
Spot #1	37	15	28	27- 17
Spot #2	67	15	47	57- 47
# 83 Clean Coatings <sup>(a)</sup>	13	9	5	0- 9
# 84 Clean Coatings	9	12	10	0- 2
#124 Clean Coatings	15	10	8	0- 10

(a) Samples from run #83 were measured by three additional laboratories. The results are as follows.

Table 2. Additional Test Results

Lab	Total Mirror Loss	Technique
Lab #1	8ppm	Ring Down
Northrop Precision Products Norwood, MA (J. Segre)	16ppm	Ring Down
N.I.S.T. Boulder, CO (J. Birquist)	52ppm	Cavity Finesse & Throughput

Note: All samples are deposited on super polished F.S. substrates with RMS roughness <0.75Å and no visible defects in central aperture.

## 8. Conclusion

Measurements of total loss and scatter are difficult at few ppm levels. The dependence of the measurement depends on the condition of the components and on the spot size. These can cause great discrepancies in the measurements, making it difficult to make conclusions on the reliability of each measurement. However, the measurements presented in this report were found valuable in development of very low-loss mirror coatings. The measurements are done at the 632.8nm wavelength and are limited to parts with less than  $5 \times 10^{-3}$  total loss. In the case of the loss measurements, the greatest virtue of the two instruments is the simplicity of the actual measurement and the very low cost of assembling the two measurement setups.

## 9. References

- [1] Anderson, D.Z.; Frisch, J.C.; Masser, C.S. Mirror reflectometer based on optical cavity decay time. Applied Optics. Vol. 13, p. 1238; 1984
- [2] Yariv, A. Introduction to Optical Electronics. Holt Reinhart Winston. p.p. 98-140; 1971

# REFERENCE CAVITY

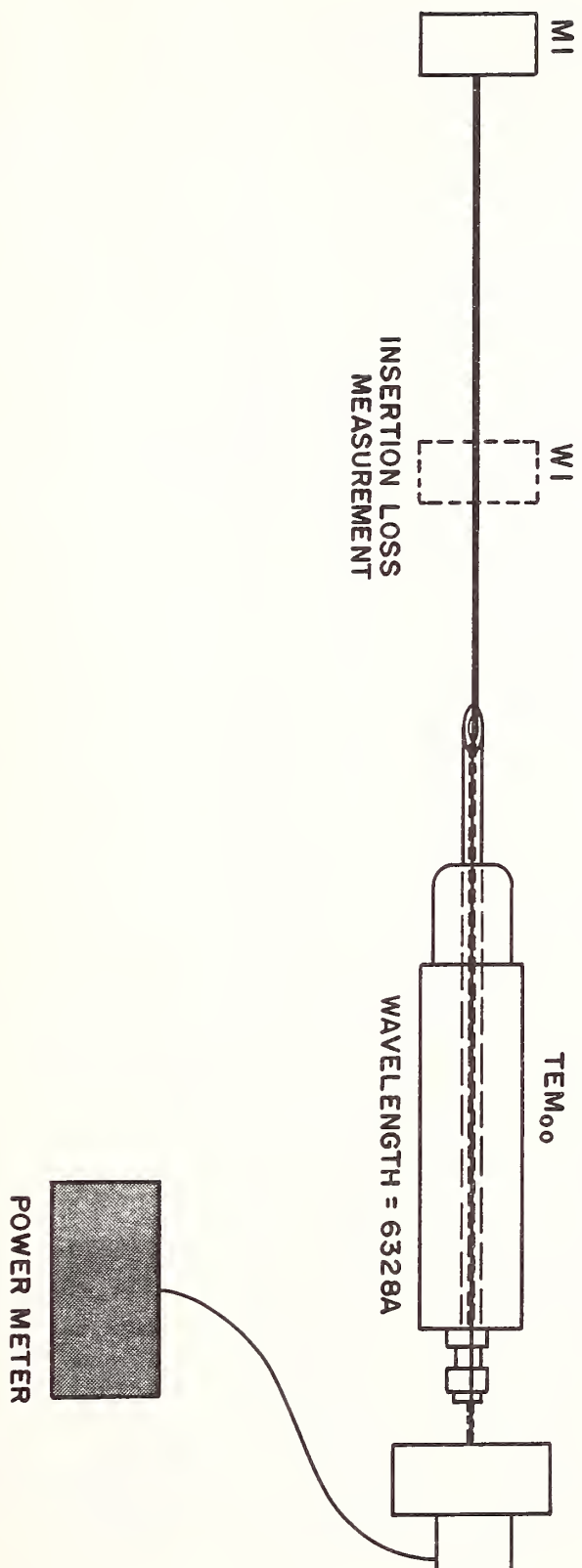


DIAGRAM A

# TEST CAVITY

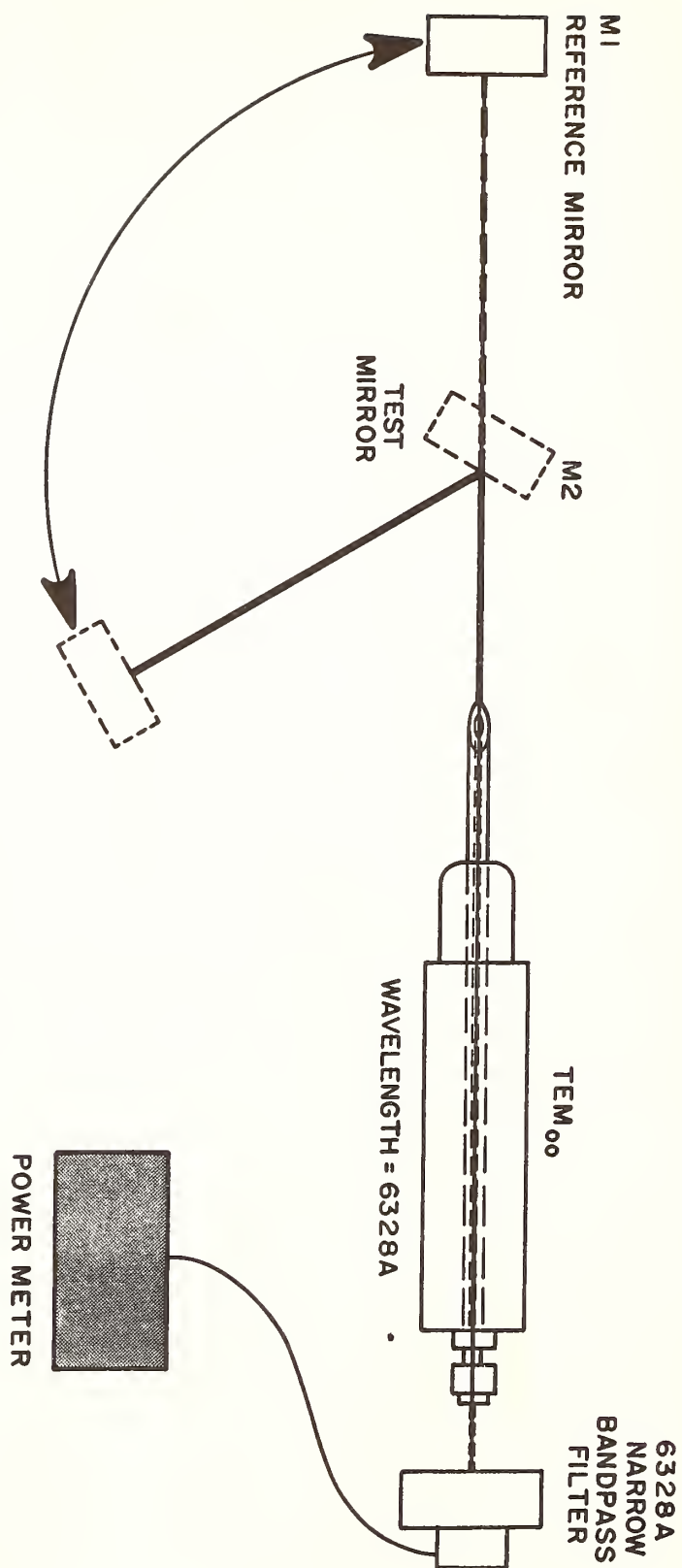
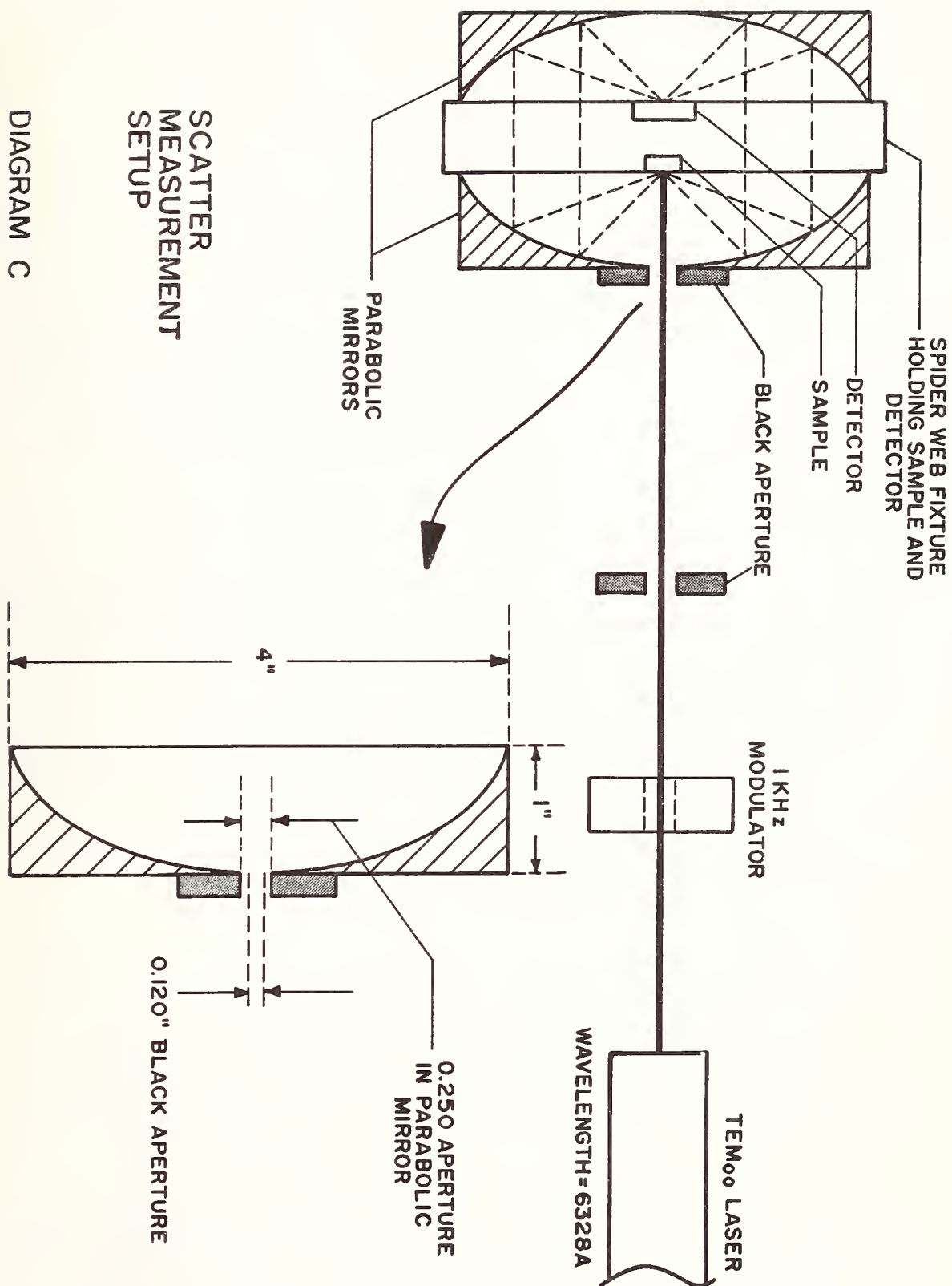


DIAGRAM B





## The Art of Optical Scatter Measurement

Thomas A. Leonard

Ball Systems Engineering Division  
2875 Presidential Dr.  
Fairborn, OH 45324 (513)429-5005

A BRDF round robin was recently conducted in the United States with 18 participants from government, university and industry scatter laboratories. The spreads in reported BRDF levels from the set of four master samples were quite large. They clearly show the need for more rigorous measurement procedures within the scatter community. Suggestions are made for optimizing measurements and minimizing errors, based on information gathered during the round robin. A "BRDF standard test method" being considered in ASTM subcommittee E12.09 is discussed.

KEY WORDS: BRDF; Round Robin; Scatter

### 1. Introduction

Optical scatter measurements are subject to all the subtle inaccuracies and complications that plague any radiometric measurement. A recent nationwide BRDF round robin confirmed that the scatter community is not immune to these problems. Large differences in reported BRDF levels from a set of four master samples clearly show the need for more rigorous measurement procedures and the utility of physical reference standards.

The author was present for all but one of the 18 measurement sets in the round robin. A good deal of information was accumulated on instrumentation, procedures and capabilities which should benefit the entire scatter community. Standardized measurement procedures and data formats would be very helpful for data intercomparisons, and to that end we are pursuing a standard test procedure through ASTM.

Possible continuation of the round robin measurements and promulgation of a standard test procedure will hopefully bring the scatter community closer to the accuracy levels needed for critical design of space-based optical surveillance systems.

### 2. Round Robin Results

The master sample set for the round robin consisted of four, two-inch diameter samples. In order of decreasing BRDF:

- W - Aluminum disk coated with Desothane Aliphatic untinted white Polyurethane enamel for a diffuse white surface with a flat BRDF of about 0.27/sr at 633 nm.
- B - Aluminum disk coated with gunship black Polyurethane enamel for a diffuse black surface with a BRDF of about 0.01/sr at 633 nm.
- M - Industrial grade, bare Molybdenum mirror with a surface roughness of about 45 Å rms (40-1000/mm).
- A - Aluminized SiO coated glass mirror with a surface roughness of about 7 Å rms (40-1000/mm).

In-plane scatter at 0.6328  $\mu\text{m}$  and 10° angle-of-incidence was measured from these samples at 18 optical scatter facilities in the United States. They included government laboratories, universities and industry. A detailed report on the round robin was presented at SPIE Conference 967, "Stray Light and Contamination in Optical Systems", San Diego, August, 1988. Figures 1 and 2 show the BRDF results for the W and A samples. The reported curves from this diffuse and specular sample are sufficient to demonstrate the problem areas in BRDF measurements. In an effort to quantitize the variations, a statistical analysis was made of the 18 measurement sets for each sample over the range of

scatter angles,  $\theta$ . The fractional deviation,  $\sigma/\mu$ , is the standard deviation of the 18 measurements divided by the mean, for a particular sample and  $\theta$ . Figure 3 shows  $\sigma/\mu$  for the 4 samples as  $\theta$  varies from 15° (5° from specular) to 70°. Figure 4 shows  $\sigma/\mu$  as a function of  $\mu$ , the mean BRDF level. Each of these curves has a message about measurement accuracy.

### 3. Suggestions For Improved Accuracy

Sources of error in this round robin cover the full spectrum of difficulties encountered with radiometric measurements. Nearly all facilities had problems. There was no correlation found between the "quality" of the equipment and the "correctness" of the results. The "correct" BRDF curves for the samples are, of course, still an unknown. Whom shall we believe? Lacking an absolute answer, we will use  $\mu$  as a reasonable reference. Each of the identifiable error sources which contributed to  $\sigma/\mu$  will be discussed, along with suggestions for improvement.

#### Sample Variations

A fundamental question in any round robin is the expected variation due to sample aging, cleanliness and positioning. Similar measurements before, during and after the round robin confirmed that there was no significant aging of the samples. None would be expected except for scratches from the cleaning procedure. The samples were cleaned before each measurement set by blowing with dry gas and dragging with methanol or acetone wetted lense tissue parallel to the plane of incidence.

Measurement position or spot size could certainly affect the scatter levels, so BRDF in the central 1 cm of each sample was mapped with 0.25 mm resolution. The results show that for the average facility spot size of 0.6 cm<sup>2</sup>, we could expect  $\sigma/\mu \leq 0.01$  for W and B and  $\sigma/\mu \leq 0.1$  for M and A. This certainly contributes to the error budget but it is not a significant factor. If this round robin has the desired effect of drawing the scatter community together in their measurement results, the next round robin will have to play close attention to sample variations and spot size. In this test series those potential effects were overshadowed by other errors.

#### Optical Filter Attenuation

Several facilities used an optical filter to measure the source beam power. This is a reasonable approach to an absolute calibration if you correctly calibrate the filter. It must be inserted in the optical train at the same position and angle each time. Multiple reflections are best avoided by tilting off axis. If more than one filter is used, they should be tilted in opposite directions or calibrated as a single unit.

#### Electronic Gain Settings

Some facilities used electronic gain reduction to measure the source beam. They were at the mercy of their gain calibration, which is more straight forward than an optical calibration, but subject to drift and nonlinear effects in the preamplifier section.

#### Solid Angle Error

Surprisingly, several facilities had a poorly defined collection aperture, but they reported BRDF based on an absolute (incident power) calibration. You must know the actual collection aperture size to calculate radiance/irradiance.

Any of these first four error sources will lead to an "offset" in the reported BRDF level as clearly shown by some curves in figures 1 and 2. An excellent method of avoiding these errors is to use a reference standard for calibration. If the BRDF level of the reference is near the unknown, you avoid optical/electronic gain errors and nonlinear effects. You also do not have to know the detector collection aperture; however it is not wise to leave it poorly defined.

Did some one say there are no good reference standards? A piece of plain white bond paper (flat BRDF of about 0.27/sr) would suffice to bring the W results to a  $\sigma/\mu \leq 0.05$ . Commercial diffuse white samples for the visible are now available, and there should soon be whites and blacks for the IR. The strongest recommendation from this round robin is to monitor a reference sample on a daily basis, even if it does not have a separately calibrated BRDF level. In fact, several samples are desirable for different signal level regimes. They will confirm instrument repeatability and help avoid the major errors.

### Inappropriate Detector Aperture

The "noisy" behavior of most W curves in figure 1 is a result of speckle interference from the rough surface. Diffuse samples always have a rough surface with respect to the wavelength, so the operator should routinely choose a larger collection aperture for obviously diffuse samples. In fact, it would probably be good operating practice to always view a sample visually before making a BRDF run. This can reveal interesting artifacts that have a large effect on BRDF such as glints from uncleaned dust, diffraction spikes that may be out of plane or speckle from a rough surface.

### Source Power Variations

All facilities monitor their laser power to ratio with the scatter level and avoid errors due to laser power drift. Unfortunately, most measure at the laser output port and are insensitive to sample irradiance changes due to angular drift accentuated by a spacial filter pinhole. Ideally, the reference detector should view the incident power downstream from any apertures or spacial filters.

### Vignetting

As the detector is moved in  $\theta$ , it is essential that the detector FOV includes all of the illuminated spot on the sample. The detector FOV should be as small as possible to reduce stray light background, so detector/sample alignment can be critical. This problem is most easily seen by measuring a diffuse sample with a flat BRDF. Vignetting is shown by gradual "fall-off" in BRDF at larger angles. There are several examples of this effect in figure 1.

### Nonlinear Detector/Preamp

BRDF measurements can cover a dynamic range of 12 decades or more from the incident power to large angle scatter from smooth samples. This dynamic range is typically covered by a combination of optical filters, electronic gain and aperture changes. Luckily for 0.6328  $\mu\text{m}$  measurements, silicon photodiodes are very linear over 7 decades. Unfortunately, preamplifiers tend to be less linear and must be carefully calibrated. There are simple "bootstrap" methods using a filter or aperture change that permit checking linear response over the full dynamic range. Many facilities have ignored this fundamental calibration technique and continue to naively accept manufacturers' gain settings or attenuation factors.

### Stray Light

The instrument signature or noise level, which is typically measured in the straight-through, no-sample configuration, is a fundamental measure of instrument performance. In the small angle regime, the noise limit results from source beam diffraction (usually only  $< 0.1^\circ$  from specular) or scatter from the final focusing element and apertures. At larger angles, electronic noise is usually the limiting factor. Of course, the electronic noise equivalent BRDF can be made as small as desired by increasing the detector aperture.

Amazingly, many facilities did not have a BRDF equivalent instrument signature available. For the specular samples (M & A), they were typically noise limited at small angles and large angles due to stray light. This is shown clearly in figure 3 where M & A exhibit minimum  $\sigma/\mu$  in the mid-angle regime. Unfortunately, many facilities did not realize they were in the noise and they reported results as sample BRDF.

It is usually quite important to "dump" the reflected beam from a specular sample so that it does not contribute to stray light spikes at larger angles. These spikes are not seen on a signature run, since the straight-through beam goes in a different direction. Ideally, the signature should be run from a low-scatter, specular sample, with a beam dump to intercept the reflected beam.

### Electronic Noise

The electronic noise floor is usually evidenced by a "leveling off" of BRDF at large angles. Several curves in figure 2 show this effect. Figure 4 clearly shows the increased  $\sigma/\mu$  due to ignoring electronic noise and stray light as we move to lower BRDF levels.

### Reporting Procedures

The definition of BRDF was not consistent among participants in this study. The most common confusion resulted from the angle reference. Is it the classical scatter angle from the sample normal, the angle from specular, the angle from the incident beam or some



combination? Some facilities referenced BRDF to reflected power instead of incident irradiance. Others did not know if the  $\text{COS}\theta$  term was in the denominator of their BRDF calculation to obtain true radiance. There was also confusion over which angle to use for  $\text{COS}\theta$ .

#### 4. Standard Test Procedures

All of the problem areas discussed in section 3 point toward the need for a standard test procedure document. The Air Force has an immediate need for this document to provide a common ground for procurement discussions with contractors. We have chosen ASTM as the most appropriate voluntary consensus standards group to promulgate this document. A new ASTM subcommittee, E12.09, "Scattering" has been formed to pursue this and other optical scatter standards.

There are many established conventions and documents which relate to BRDF measurements. In addition, all members of the scatter community have specific thoughts about the best way to take data and display the results. Our hope is to blend existing documentation and community consensus together to obtain a working document (BRDF standard test method) along with supporting text that will provide a common ground for discussion and exchange of data. This will alleviate confusion in procurements and interlaboratory exchanges and also provide the format for a national data base. Some of the many considerations which must go into this type of effort are listed in table 1.

Table 1. Considerations to include in a  
voluntary consensus, BRDF standard test method.

---

##### Definitions:

Defined parameters must conform with established convention and NBS monograph 160

##### Instrumentation:

Angular resolution, spot size, source beam conditioning, final focusing mirror, detector FOV, power monitor

##### Measurement limitations:

Single wavelength, in-plane scatter, spacial resolution, sample contamination

##### Measurement procedures:

Incident power, acceptance aperture, angle coverage, signature scan, power monitor ratio

##### Data format:

Raw data, calculated data (BRDF in  $\beta$ - $\beta_0$ , log-log format), digital files (ASCII format)

##### Surface model extrapolations:

Power spectrum, total scatter, surface roughness, linear shift invariance

##### Reference standards:

Types available, wavelength dependence, accuracy, NBS involvement

##### Common Errors:

Sample Variations, Optical Filter Attenuation, Electronic Gain Settings, Solid Angle Error, Inappropriate Detector Aperture, Source Power Variations, Vignetting, Nonlinear Detector/Preamplifier, Stray Light, Electronic Noise, Reporting Procedures

---

#### 5. Acknowledgments

This work was supported by the U.S. Air Force, Rome Air Development Center, under program manager Mike Pantoliano, Contract F30602-85-C-0294. Cooperation of the BRDF scatter facilities was essential to the study, and their participation is greatly appreciated.



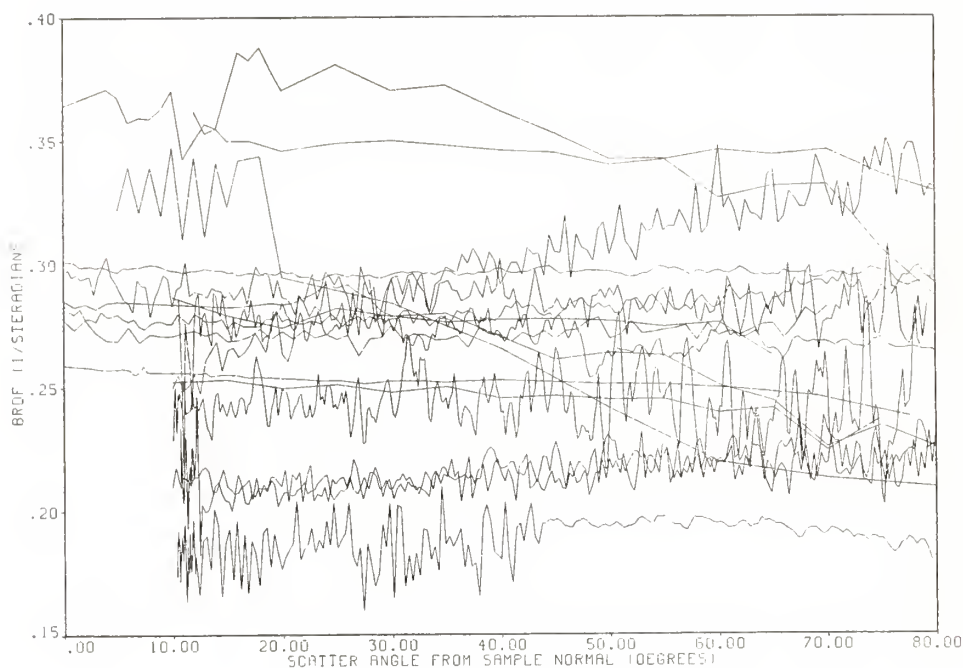


Figure 1. BRDF curves for the W. sample. The specular beam would be at  $10^\circ$ ; however, this sample has a flat BRDF.

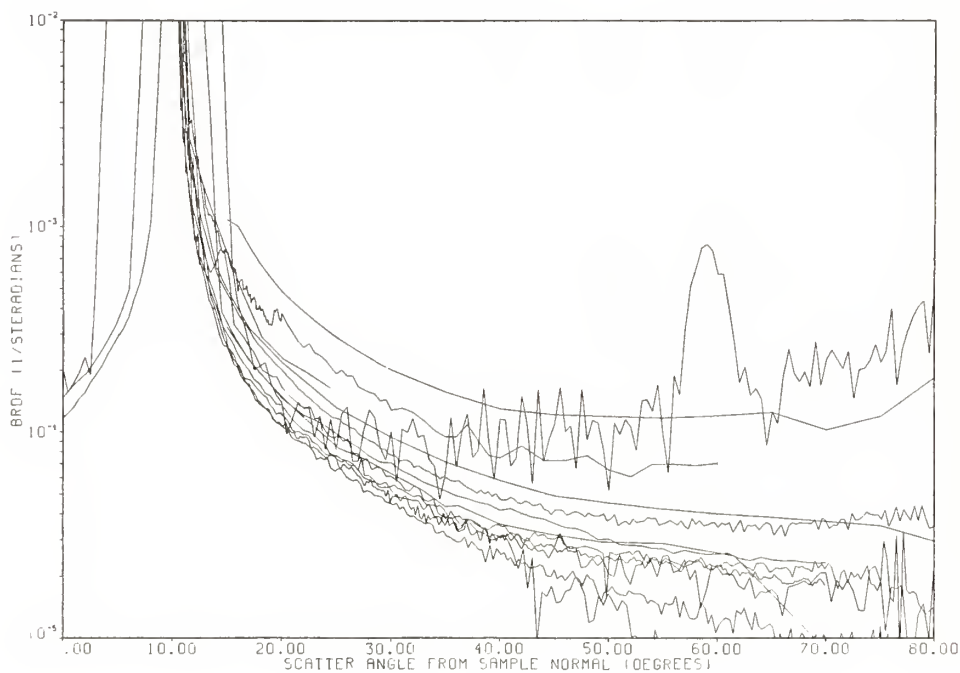


Figure 2. BRDF curves for the A sample. The peak at  $59^\circ$  is a typical wall reflection and was recognized as such by the facility. The curves which flatten at large angles are typical of electronic noise limits.

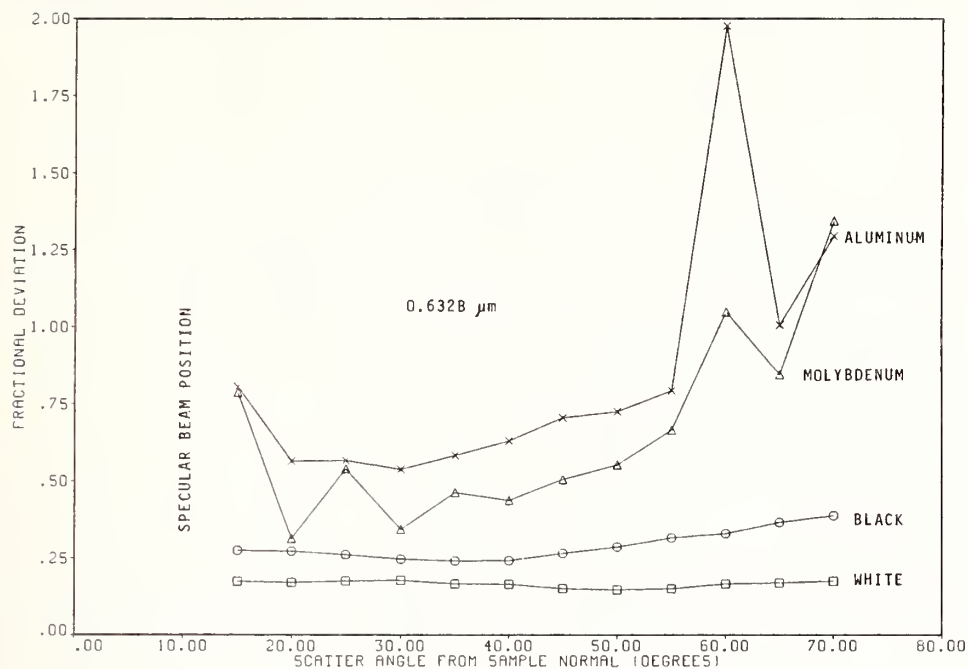


Figure 3. Fractional deviations in the BRDF measurements from 18 facilities for the four samples as a function of scatter angle. The midangle region has a lower chance of error.

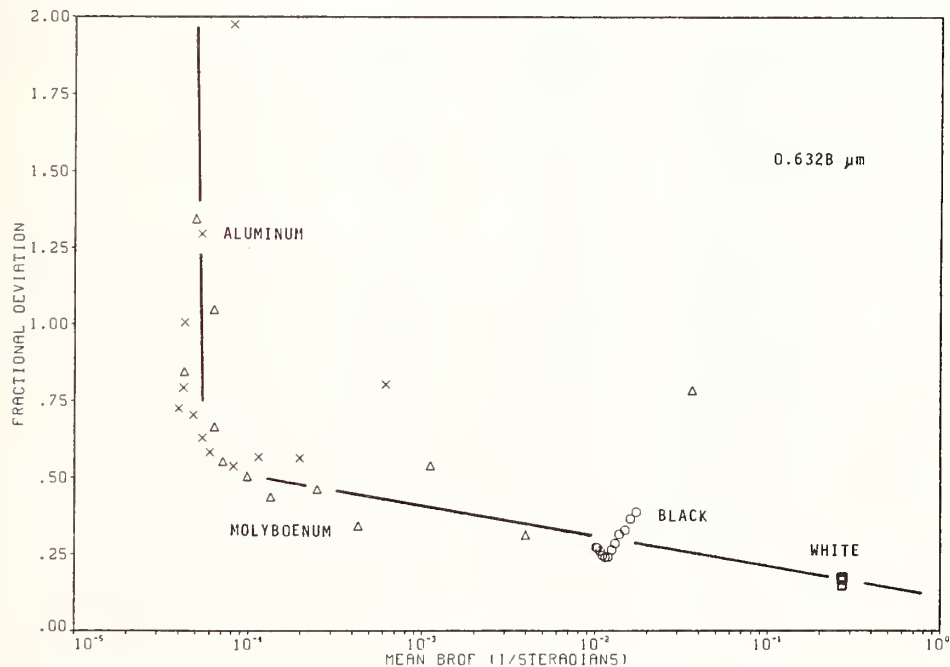


Figure 4. Fractional deviations in the BRDF measurements from 18 facilities for the four samples and 12 scatter angles as a function of the mean BRDF level. Lower BRDF levels have the potential for greater errors.

MANUSCRIPT NOT RECEIVED

=====

ARE 1 METER SQUARE CALCIUM FLUORIDE LASER WINDOWS POSSIBLE?

C. William King  
Ontario H. Nestor

Harshaw Crystals & Electronics  
6801 Cochran Road  
Solon, Ohio 44139

ABSTRACT

Calcium Fluoride ( $\text{CaF}_2$ ) crystals are grown in a vacuum at approximately 1400 Deg C via a Bridgman-Stockbarger method. This process traditionally has limitations in the size of the single crystals that can be produced. Another limitation, in current practice, is the randomness of the crystallographic orientation of the crystals. A new process for producing large, single, crystallographically oriented crystals of calcium fluoride that overcomes these limitations is described. This process has been reduced to practice to produce single oriented crystals  $17.5 \times 17.5 \times 5 \text{ cm}^3$ . Currently under construction is a system for producing  $35 \times 35 \times 7.3 \text{ cm}^3$  crystals. This process is considered scalable to 1 meter square. The concept employed in the growth process plus seeding the crystal growth provides sufficient control over the entire process to produce a single oriented crystal. This crystal growing process makes possible the fabrication of very large  $\text{CaF}_2$  windows suitable for high power lasers.

Radiation Damage in Barium Fluoride Detector Materials\*

P. W. Levy, J. A. Kierstead and G. L. Woody

Brookhaven National Laboratory  
Upton, NY 11973

To develop radiation hard detectors, particularly for high energy physics studies, radiation damage is being studied in  $\text{BaF}_2$ , both undoped and doped with La, Ce, Nd, Eu, Gd and Tm. Some dopants reduce radiation damage. In La doped  $\text{BaF}_2$  they reduce the unwanted long lifetime luminescence which interferes with the short-lived fluorescence used to detect particles. Radiation induced coloring is being studied with facilities for making optical measurements before, during and after irradiation with  $^{60}\text{Co}$  gamma rays. Doses of  $10^6$  rad, or less, create only ionization induced charge transfer effects since lattice atom displacement damage is negligible at these doses. All crystals studied exhibit color center formation, between approximately 200 and 800 nm, during irradiation and color center decay after irradiation. Thus only measurements made during irradiation show the total absorption present in a radiation field. Both undoped and La doped  $\text{BaF}_2$  develop damage at minimum detectable levels in the UV--which is important for particle detectors. For particle detector applications these studies must be extended to high dose irradiations with particles energetic enough to cause lattice atom displacement damage. In principle, the reduction in damage provided by dopants could apply to other applications requiring radiation damage resistant materials.

Key Words: radiation damage; radiation damage "protection;" barium fluoride; doped barium fluoride; particle detectors.

## 1. Introduction

In recent years, a number of programs, e. g. SDI, have needed optical materials that are resistant to radiation damage, particularly materials that are resistant to the radiation induced coloring that reduces light transmission. Most recently, the advent of colliding beam facilities for high energy physics research has created a new need for radiation resistant optical materials, particularly for luminescent light emitting particle detectors. In these particle detectors it is necessary to preserve certain luminescent features, such as the fast fluorescent lifetimes and to minimize other features, such as long-lived phosphorescence, in addition to preserving light transmission. To develop a luminescent particle detector that is resistant to radiation damage, and to obtain improved understanding of the mechanisms involved in reducing radiation induced coloring by the addition of impurities, radiation induced coloring is being studied in barium fluoride ( $\text{BaF}_2$ ) crystals, both pure and doped with La, Ce, Nd, Eu, Gd and Tm rare earth elements. Pure  $\text{BaF}_2$  is currently used as a high energy detector. Recently it was shown that lanthanum doping of  $\text{BaF}_2$  reduces the ratio of the long-lived, or slow, component to the short-lifetime, or fast, luminescent emission without causing any additional coloring [1].

\*Research supported in part by the US Department of Energy, Contract DE-AC02-CH7600016, and in part by a grant from the Government of Japan.

## 2. Radiation Damage in Nonmetals

### 2.1 Basic Mechanisms

The qualitative features of radiation induced coloring in glasses and most transparent crystals is reasonably well understood [2]. However, there is very little information on the processes that occur to reduce the luminescent light emission when scintillators are exposed to radiation other than the reduction in light intensity that can be attributed to absorption by radiation induced coloring. For exposures to purely ionizing radiation, gamma rays and/or fast electrons, the radiation induced coloring is, with only a few exceptions, due to the formation of color centers by the trapping of (ionization) electrons and holes on the defects and impurities in the material. The number of defects produced by doses of  $10^6$  rad ( $10^4$  Gray) or less is negligible when compared with those originally present before irradiation, except in a few materials, such as the alkali halides. Thus, for doses less than  $10^6$  rad, curves of radiation induced coloring against dose usually increase, with continuously decreasing slope, to a saturation level. For larger doses the coloring curves often contain a saturating component superimposed on a slowly increasing component. The latter component is due to the trapping of charges --to form color centers-- on the defects introduced by radiation damage processes.

It is well known that the luminescence emitted by a scintillator, when traversed by ionization producing radiation, usually contains both fluorescent and phosphorescent components. The fluorescence is emitted by a center, usually a defect or an impurity, that is, with few exceptions, excited directly by the incident particle produced ionization event (electron and/or holes). More specifically, the normal fluorescence process probably does not include a charge migration step. If the emission center excited state lifetime is sufficiently short the center decays by the emission of short lifetime fluorescence. This fast emission is an essential characteristic of high energy particle detectors. If the light emission process includes a charge migration step, such as the migration of an electron to a trapped hole, the emission is comparably long-lived and is called phosphorescence. Both of these mechanisms are affected by radiation, i.e. they show radiation damage effects. However, phosphorescence processes are almost always altered more rapidly by radiation damage than the fluorescence processes.

Both of the luminescence processes mentioned above appear to be occurring in pure barium fluoride crystal high energy particle detectors [1]. A comparably long-lived phosphorescent emission is seen with an emission band that peaks at roughly 320 nm and with a lifetime of approximately 625 nanoseconds (ns). Also occurring is a short-lived emission that has peaks at roughly 195 and 220 nm and has a life time of approximately 0.6 ns, which appears to be a fluorescent process. This fast, or short-lived, emission is used for particle detection. The long-lived emission gives rise to an unwanted background and the usefulness of BaF<sub>2</sub> particle detectors would be greatly improved if it could be eliminated.

### 2.2 The Mafia Principle -- Pay Now For Protection Later

Many articles contain statements like, "the addition of cerium prevents glass from being colored by radiation," or, "protection against radiation damage is provided by adding cerium." Such statements are usually gross oversimplifications or incorrect. The addition of cerium to the typical hot-cell window lead glass creates absorption bands in the UV and upon exposure to radiation additional UV bands form and continue to grow as long as the radiation continues. In the visible absorption bands appear as soon as radiation commences and continue to increase throughout irradiation. However, the bands in the visible grow much more slowly than bands in similar lead glass without cerium. Consequently, the cerium does provide "protection" against coloring in the visible --actually it slows down the coloring rate in the visible-- but at the expense of increasing the coloring rate in the UV. The cerium appears to do two things to provide "protection." First, it provides traps, which trap ionization electrons and holes to form color centers in the UV, that have much larger trapping cross-sections than the traps that produce color centers in the visible. This process diverts the ionization produced charges from creating color centers in the visible to the creation of color centers in the UV. Second, the cerium functions as a large cross section electron-hole recombination center. The recombination process "uses-up" ionization pairs and slows down the conversion of traps to color centers.



An example of cerium provided protection occurs in lead glass Cerenkov counters, for high energy particle detection [3]. New cerium protected Cerenkov counters emit less light than similar counters without cerium. However, the emission efficiency is quite sufficient for normal use. As the counters are used, in radiation fields strong enough to induce non-negligible coloring, the Cerenkov emission continuously decreases. Most importantly, however, at doses that would render the cerium free counters completely useless the protected counters would still be useful. Thus cerium provides useful protection but "at a price" -- in this case reduced light output -- like the Mafia.

### 3. Present objectives

In terms explained in the previous section, the goals of this study can be described succinctly. Namely, find a dopant, such as cerium, that can be incorporated into  $\text{BaF}_2$  to accomplish the following:

- 1) Reduce or eliminate the radiation induced coloring or cause the coloring to occur in a wavelength region(s) that will not interfere with the fast emission.
- 2) Reduce or eliminate the slow emission component, most likely by providing large cross section nonradiative recombination centers that "out compete" the slow emission luminescent centers for ionization electrons and holes.

### 4. Experimental details

#### 4.1 Samples

All of the  $\text{BaF}_2$  samples were purchased from the Optovac. When given, the dopant concentrations are in molar percent of the material added to the melt, not a measurement of the dopant incorporated into the crystal.

#### 4.2 Fast to slow luminescence emission ratio measurements

Because they differ in lifetime, the ratio of the two emission components can be measured by counting pulses, produced by irradiating with a  $^{137}\text{Cs}$  gamma-ray source, with a gated detector. Details are given elsewhere [4].

#### 4.3 Apparatus used for optical absorption measurements

Optical absorption measurements were made before and/or after irradiation, but not during irradiation, with a Cary spectrophotometer. Optical absorption measurements were made in a facility for making optical -- and other -- measurements before, during and after irradiation with Co-60 gamma rays. This facility has been described elsewhere [5] and numerous studies made with it are included in reference 2.

### 5. Measurements

#### 5.1 Absorption spectra of doped $\text{BaF}_2$ crystals before irradiation

The absorption spectra of both undoped and rare earth doped  $\text{BaF}_2$  crystals shown in figure 1 were recorded with a Cary spectrophotometer. These spectra show the sharp lines and occasional broad absorption bands expected for rare earth impurities in crystals like  $\text{BaF}_2$ .

#### 5.2 Measurements on the ratio of the fast to slow luminescent intensities

As mentioned above, the fast luminescent emission is used for high energy particle detectors and it is important to maximize the fast to slow intensity ratio. Table 1 shows the ratios measured with  $\text{BaF}_2$  containing the specified rare earth impurities. None of the samples used for table 1 were irradiated.

Table 1 -- Fast To Slow Luminescent Emission Ratios  
(detector photoelectrons per MeV)

Percent Impurity	Normal phototube total/MeV	fast/slow	Solar blind phototube total/MeV	fast/slow
"pure"	1324	.16	226	.79
0.2 La	829	.26	195	.89
1.0 "	420	.50	186	1.21
0.2 Tm	623	.38	183	1.12
1.0 "	400	.55	128	1.37
1.0 Nd	341	.42	91	1.07
5.0 "	106	.47	30	---
0.2 Gd	698	.30	177	1.01
1.0 "	420	.37	177	1.10
5.0 "	141	---	---	---
0.2 Eu	106	---	---	---
1.0 "	---	---	---	---
5.0 "	---	---	---	---
1.0 Ce	888	---	---	---

"---", signal too small to measure

### 5.3 Radiation induced absorption spectra recorded during irradiation

The radiation induced absorption spectra of undoped  $\text{BaF}_2$  and  $\text{BaF}_2$  doped with various rare earth impurities, shown in figures 2 through 11 were recorded with the apparatus for making optical measurements during irradiation. However, not all of these absorption spectra were recorded during irradiation. Some were recorded, during a long sequence of irradiations, immediately after a number of interruptions of irradiation. This rarely used procedure was employed since some samples emit very strong luminescence and the spectrophotometer could not be operated reliably in the far UV below approximately 300 nm. Consequently, the irradiation had to be interrupted to obtain meaningful absorption measurements. (With this apparatus reliable absorption measurements can be made in the far UV during irradiation at dose rate levels that produce even stronger luminescence. However, this requires additional equipment that, unfortunately, was not installed when these measurements were made.) These spectra show the expected characteristics. Information on each of these figures is given below.

It should be mentioned that similar spectra were also recorded for additional  $\text{BaF}_2$  samples containing other dopants. Samples with these other dopants developed more radiation induced absorption than the pure and La doped samples and, at least at this time, they do not appear to provide useful radiation damage protection for high energy particle detectors.

The figures included below were chosen to illustrate two, somewhat disparate, objectives: First, features of the data that are important for high energy particle detector applications. And second, features that have general applicability to radiation damage in optical materials, particularly those that are best detected by making measurements during irradiation.

#### 5.3.1 Undoped $\text{BaF}_2$

Absorption spectra of "pure" or undoped  $\text{BaF}_2$ , measured during irradiation with  $^{60}\text{Co}$  gamma rays at a dose rate of  $6.9 \times 10^3$  rad/hour, is shown in figure 2. This figure does not show data below 300 nm since the luminescence was so intense reliable absorption measurements could not be made in this region. The curves correspond to measurements at total doses of 0 (i. e. before irradiation),  $5 \times 10^4$ ,  $10^5$  and  $10^6$  rad. The breaks in the curves occur in the region of the overlap of the separate monochrometers used for the UV and visible regions.

The absorption spectra, from the same sample and measurement, but recorded immediately after interruptions of radiation is shown in figure 3. The curves correspond to total doses of 0,  $10^3$ ,  $10^4$ , and  $10^6$  rad. These spectra are quite similar to those recorded during irradiation and indicate that the radiation induced absorption does not change, i. e, does not increase or decrease, in the 10-20 minute interval between the interruption of radiation and the recording of the spectra. In terms of the coloring usually observed in optical materials exposed to similar doses, this sample shows very little radiation induced coloring, i.e. it is damage resistant or "hard". Consequently,  $\text{BaF}_2$  should be very useful for both particle detectors and other applications involving high radiation levels.

#### 5.3.2 $\text{BaF}_2$ doped with 1.0 percent Lanthanum (La)

Absorption spectra, recorded shortly after an interruption of irradiation, for a  $\text{BaF}_2$  crystal doped with 1 percent La is shown in figure 4 for total doses of 0,  $10^3$ ,  $5 \times 10^3$ ,  $2 \times 10^4$ ,  $10^5$  and  $10^6$  rad. In comparison with the undoped  $\text{BaF}_2$ , this sample shows the same or slightly higher overall induced absorption in the ultraviolet as well as a pronounced broad absorption that peaks at approximately 490 nm. As described below this band is unstable. Also, and most importantly, this strong band lies outside of the wavelength range of the luminescence emission band that is important for particle detection.

#### 5.3.3 $\text{BaF}_2$ doped with 1.0 percent Thulium (Tm)

The absorption spectra of  $\text{BaF}_2$  doped with 1.0 percent Tm recorded immediately after interruptions of irradiation for total doses of 0,  $10^3$ ,  $10^4$ ,  $10^5$ ,  $2 \times 10^5$ ,  $5 \times 10^5$  and  $10^6$  rad is shown in figure 5. A number of interesting features are illustrated by this plot. First, the radiation induced absorption is much more similar to that typically observed when optical materials are exposed to radiation than is shown by any of the preceding figures. At least eight different radiation induced absorption bands are observed. The magnitude of the induced absorption is roughly that induced in most optical materials and the height of the observed bands is highest at the short wavelength end of the spectrum and irregularly decreases in intensity toward longer wavelengths. Also, as indicated by table 1, the 1 percent Tm doping reduces the fast to slow luminescent emission ratio at least as much as 1 percent La doping. However, figure 5 clearly shows that the absorption in the region of the fast emission is so high it is quite unlikely the Tm doped  $\text{BaF}_2$  would be a useful particle detector.

#### 5.3.4 $\text{BaF}_2$ doped with 1.0 percent Neodymium (Nd)

The radiation induced absorption spectra of  $\text{BaF}_2$  containing 1.0 percent Nd is included here because it demonstrates a feature that is observed in only a small percentage of optical samples. Absorption spectra of this material, in the restricted wavelength range from 250 to 350 nm, is shown in figure 6 for total doses --from bottom to top --extending from 0 (before irradiation) to  $1.25 \times 10^6$  rad. The zero and low dose spectra contain an easily seen absorption band at approximately 290 nm. However, as the dose increases the optical

absorption throughout this region steadily increases and, in comparison with the generally increasing absorption, the band at 290 becomes less and less obvious. There is a possibility that the radiation induced bands in this region grow in a way that obscures the band at 290 nm without it actually disappearing. However, it is much more likely that this is a case where the band is observable before irradiation but gradually disappears as the radiation increases. Most often this situation occurs when an impurity is incorporated into a crystal in a valence state that gives rise to the optical absorption transition producing the observed band and as the dose increases the valence state is changed by electron or hole capture and the new state does not give rise to a band at the same wavelength.

#### 5.4 Optical absorption changes occurring after irradiation

As mentioned above, one of the principal reasons for making optical absorption (radiation damage) measurements during irradiation is to determine the total absorption (damage) induced in contrast to that observed after irradiation. Clearly if the absorption (damage) changes appreciably after the irradiation is terminated a belated measurement can indicate quite misleading information on the damage levels present during irradiation. In high energy particle detectors it is particularly important to know the absorption present during irradiation. Described below are changes occurring after irradiation in pure and doped  $\text{BaF}_2$ . They illustrate the changes usually observed in optical materials.

##### 5.4.1 Undoped $\text{BaF}_2$

The changes occurring after irradiation in the radiation induced absorption spectrum, from 400 to 800 nm, observed in "pure" or undoped  $\text{BaF}_2$  is shown in figure 7. From top to bottom, the curves shown were measured 7, 13, 25 and 46 hours after the sample had received a total dose of  $1.25 \times 10^6$  rad. While the total coloring induced in this sample is very much less than that usually observed in typical optical materials, the coloring decay is unusually large. In a sense, this accounts, at least in part, for the low coloring induced. A large fraction of the color centers formed during irradiation also decay during irradiation.

##### 5.4.2 Barium Fluoride doped with 1 percent Lanthanum

The measurements made on  $\text{BaF}_2$  doped with 1 percent La provide a very good example of the changes that occur after irradiation in many optical materials. Also, it illustrates one feature of the radiation induced coloring that often is observed in materials showing large changes after irradiation. Figure 8 shows the last two measurements made on  $\text{BaF}_2$ : 1.0 percent La before the irradiation was terminated and the measurements made 7, 13, 25 and 46 hours after irradiation. There is very little change in the measurements made during irradiation. This indicates that the color-center peak at approximately 475 nm has reached a fairly steady equilibrium level. Once the irradiation is terminated the coloring decays comparatively rapidly. Although the data for the peak at roughly 680 nm is too close to the noise to be considered reliable, the data indicates that this peak increases after irradiation. Peaks that increase after irradiation have been observed before, particularly in sodium chloride crystals.

Additional decay data from this same crystal is shown in figure 9 which shows the optical density at the peak of the 475 nm band measured during irradiation, during interruptions of irradiation and after the irradiation was terminated. During each interruption the absorption decreases and as soon as the irradiation is resumed the color center density returns, actually quite rapidly, to the equilibrium color center level. It is likely, but not certain at this time, that the equilibrium level is fixed by the competition between coloring and decay processes. The decay occurring after the last termination of irradiation is often seen in optical materials. A cursory "semi-log" plot of the final decay data indicates that it contains two exponential decay components with half-lives of approximately 2.0 and 20.5 hours. Thus these components will have decayed to negligible levels in periods of roughly 10 hours and 4-5 days. These decay components are superimposed on one or more components that appear to be constant i.e. non-decaying, over the period of the measurements. It is well established that color-center decay can be resolved into 1, 2, or more exponential components [2].



#### 5.4.3 BaF<sub>2</sub> doped with 1 percent Gadolinium (Gd)

An interesting example of the behavior demonstrated in figure 9 is obtained from the data for BaF<sub>2</sub> doped with 1 percent gadolinium. Figure 10 is a plot, similar to figure 9,

showing the measured optical density at 560 nm in the Gd doped BaF<sub>2</sub> recorded both during and after interruptions of irradiation and after the irradiation is completed. This plot shows all of the features in figure 9 but they occur on a larger scale. Both the decay occurring after interruptions of irradiation and the rate that coloring is restored after the irradiation is resumed is larger.

#### 5.4.4 Induced absorption not decaying after irradiation

Inasmuch as a number of examples have been given that illustrate change occurring after irradiation, it is essential to counteract the impression that this occurs in almost all of the cases studied. Measurements made after irradiation on BaF<sub>2</sub> doped with 0.2 percent Thulium (Tm) are shown in figure 11. The last two spectra recorded during irradiation and spectra recorded 7, 13, 25 and 46 hours after irradiation all show a pronounced broad band peaking at approximately 555 nm. The intensity of this band remains quite constant during the entire data recording period. From such data one can conclude that the coloring induced into this sample is constant for time periods comparable to the measurement time. However the coloring may not be stable over periods much longer than those used in the measurement.

### 6.0 Summary and conclusions

1) Radiation damage has been studied in BaF<sub>2</sub>, both undoped and doped with various rare earth elements, using apparatus for making optical absorption and other measurements before, during and after irradiation with <sup>60</sup>Co gamma rays.

2) Undoped BaF<sub>2</sub> does not develop appreciable radiation induced coloring when exposed to <sup>60</sup>Co gamma-ray irradiation. However, the luminescence, used for high energy particle detection, contains both a useful short lifetime fast component and troublesome long lifetime slow component. The slow component limits the useful range for particle detection to comparatively low counting rates.

3) BaF<sub>2</sub> doped with Lanthanum is quite similar to undoped BaF<sub>2</sub> with regard to radiation induced coloring in the light transmission regions, near 200 nm, important for particle detection applications. However, and most importantly for particle detection, as reported previously [1] the La doping reduces both the total fast and slow luminescent emission in a way that causes the ratio of the fast to slow components to increase. Thus the La doped BaF<sub>2</sub> is more useful at higher counting rates than the undoped material.

4) The result described in 3) is an example of the "Mafia principle -- pay now for protection now and/or later", i.e., the purposeful reduction of one or more desirable characteristics to improve other characteristics. In this case, a reduction in total luminescent light output to obtain an improved fast to slow ratio with equal resistance to radiation induced coloring.

5) The radiation induced coloring in BaF<sub>2</sub> doped with some rare earths, e.g. Tm, Nd, Gd and Ce, actually increases the radiation induced coloring or radiation damage. This is a case where the addition of a dopant has increased the concentration of defects and/or lattice atoms that are converted to color centers by charge transfer during irradiation.

6) A number of the samples studied, e.g. La and Gd, contained color-center bands that exhibited maximum intensity during irradiation and subsequently decreased or decayed after irradiation. In one typical case, BaF<sub>2</sub> doped with 1 percent La, a band is observed at 475 nm during irradiation that has decreased appreciably 46 hours later. The decay of this band contains two principal components. One, which accounts for roughly half of its total intensity has a half-life of close to 2.0 hours and totally disappears in approximately 10 hours. The other decay component half-life is roughly 20.5 hours and this component will decay to negligible intensity in 4 or 5 days. This is a good example of the type of information that can be obtained with equipment for making measure before, during and after irradiation. Rapid decay processes can be detected only by making measurements during irradiation.



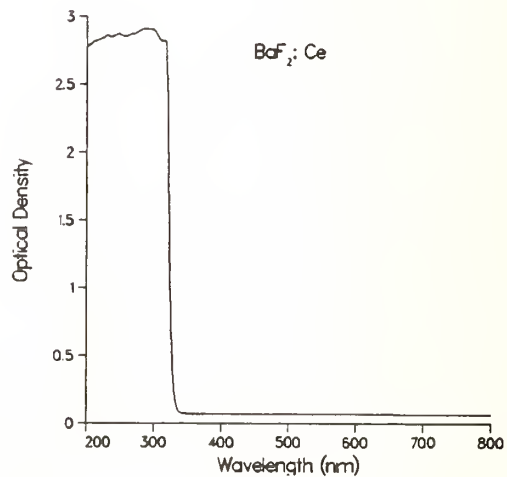
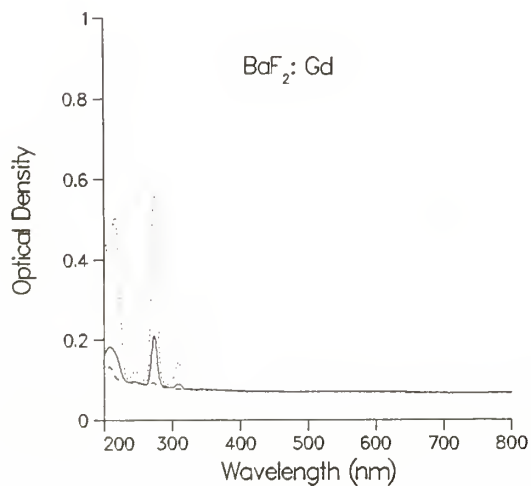
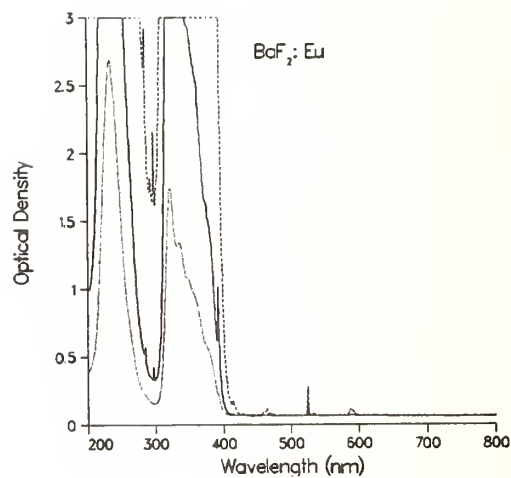
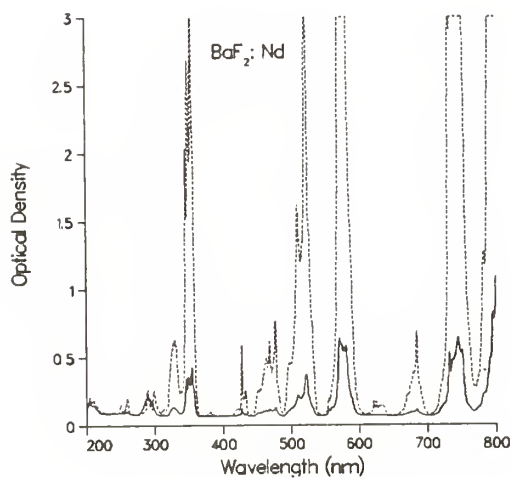
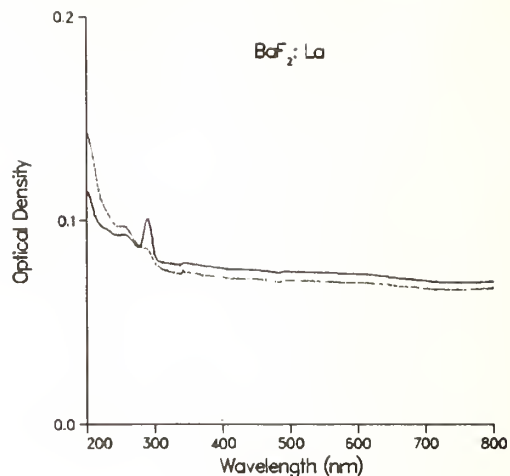
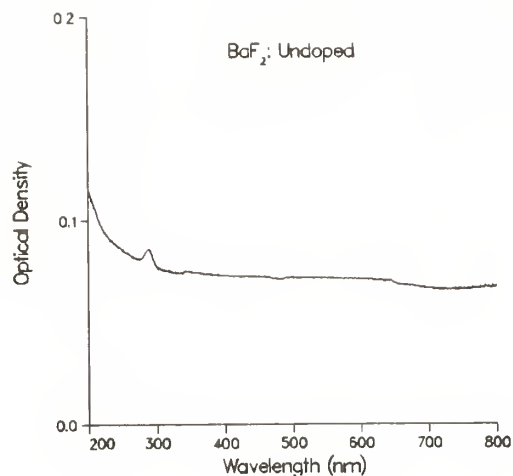


Figure 1. Typical absorption spectra, recorded with a Cary spectrophotometer, of  $\text{BaF}_2$  doped with rare earths. The sharp lines occasionally superimposed on broad bands are a characteristic of rare earth impurities.

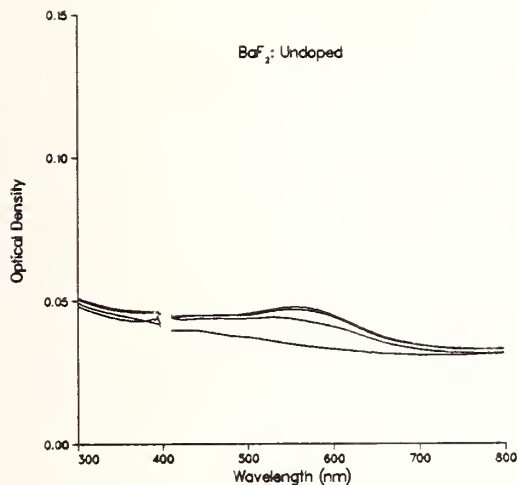


Figure 2. Optical absorption of undoped  $\text{BaF}_2$  measured during irradiation at total doses of 0,  $5 \times 10^4$ ,  $10^5$  and  $10^6$  rad.

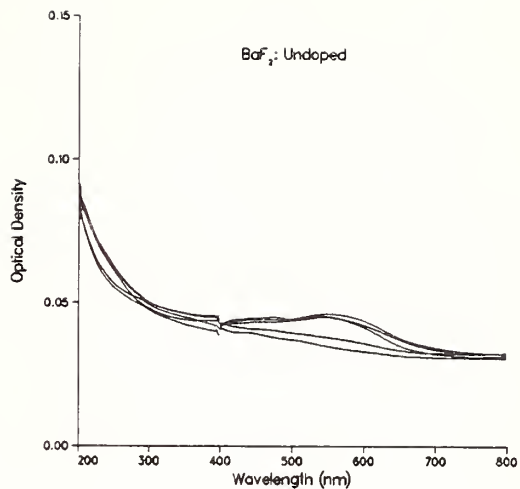


Figure 3. Absorption of undoped  $\text{BaF}_2$  measured shortly after interruption of irradiation for total doses of 0,  $10^3$ ,  $10^4$ ,  $10^5$  and  $10^6$  rad. The similarity to figure 2 indicates that the coloring does not decay rapidly.

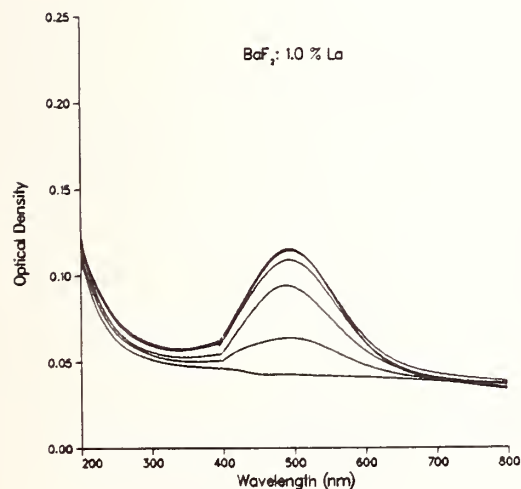


Figure 4. Absorption of  $\text{BaF}_2$  doped with 1 percent La measured shortly after interruption of irradiation for total doses of 0,  $10^3$ ,  $10^4$ ,  $2 \times 10^4$ ,  $10^5$  and  $10^6$  rad.

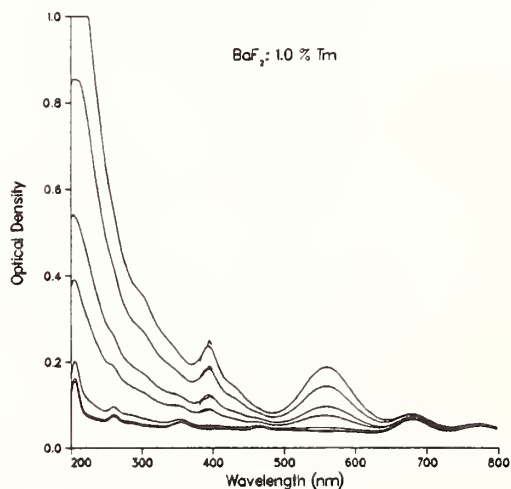


Figure 5. Absorption of  $\text{BaF}_2$  doped with 1.0 percent Tm measured after interruption of irradiation for total doses of 0,  $10^3$ ,  $10^4$ ,  $10^5$ ,  $2 \times 10^5$ ,  $5 \times 10^5$  and  $10^6$  rad. The coloring shown by this sample is typical of most optical materials.

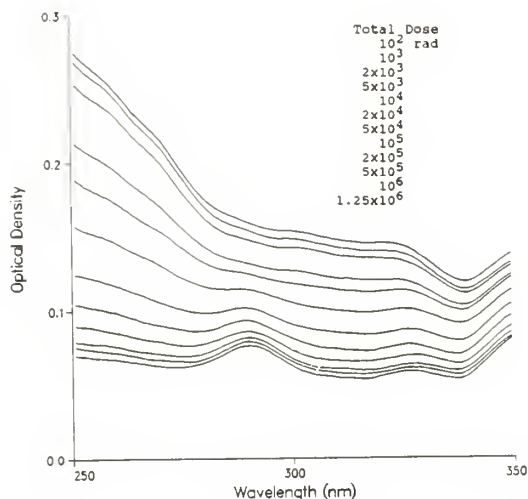


Figure 6. Absorption of  $\text{BaF}_2$  doped with 1 percent Nd measured before and during irradiation at the specified doses. The absorption band at approximately 290 nm is of a type observed rarely. It is present before irradiation and gradually decreases as the dose increases.

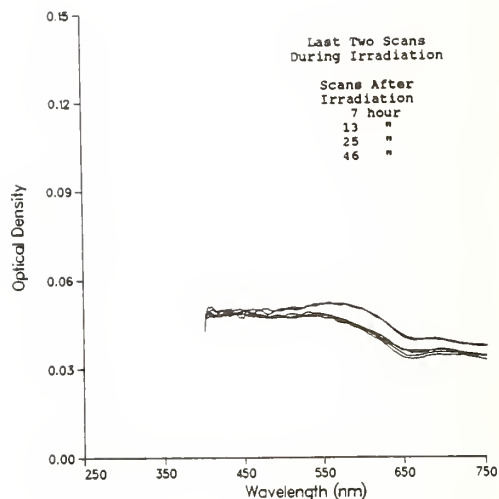


Figure 7. Decay of the radiation induced coloring in undoped  $\text{BaF}_2$  after a total dose of  $1.25 \times 10^6$  rad. Shown are the last two scans during irradiation and scans 7, 13, 25 and 46 hours after irradiation.

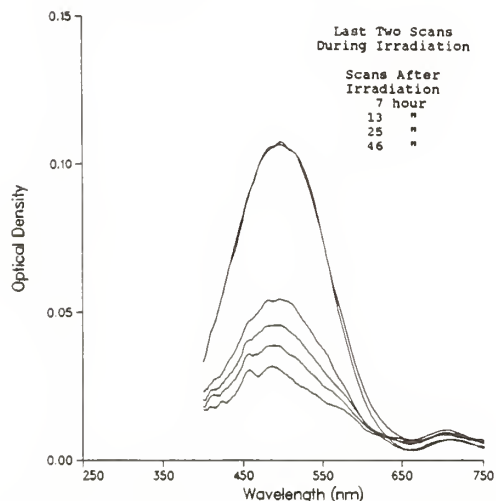


Figure 8. The absorption of  $\text{BaF}_2$  doped with 1.0 percent La. Shown are the last two scans measured during irradiation, to a total dose of  $1.25 \times 10^6$  rad, and scans measured 7, 13, 25 and 46 hours after irradiation.

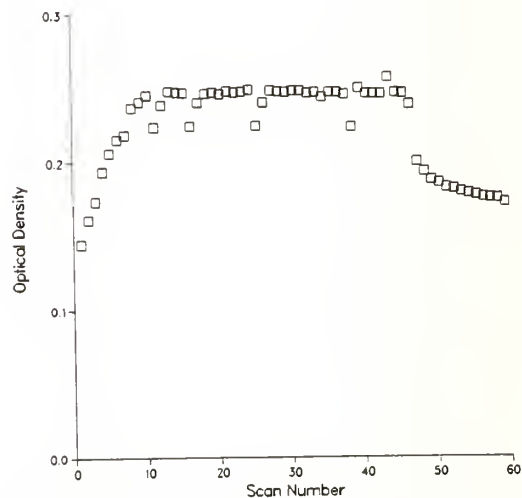


Figure 9. Absorption, at roughly 475 nm, of  $\text{BaF}_2$  doped with 1.0 percent La measured during irradiation and during interruptions of irradiation. Each interruption causes the band to decay and when irradiation is resumed the decrease is rapidly restored.

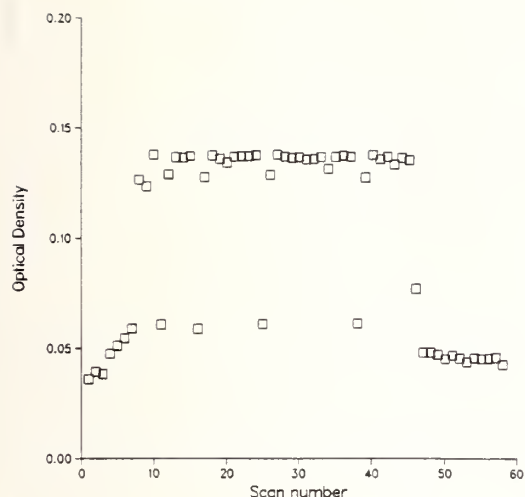


Figure 10. The absorption, at roughly 560 nm, of BaF<sub>2</sub> doped with 1.0 percent Gd, measured during irradiation and during interruptions of radiation. This shows the same behavior demonstrated by Figure 9. However, the rapid decay is comparatively much larger.

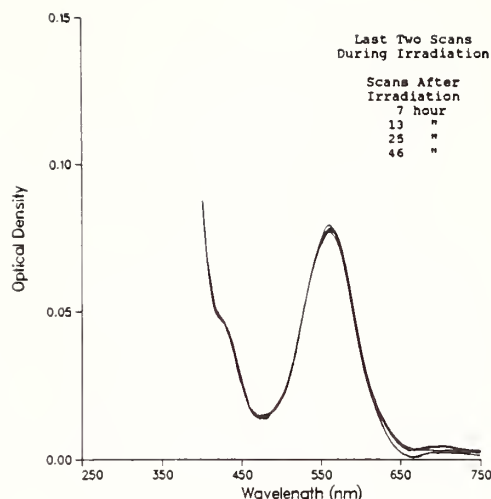


Figure 11. Absorption of BaF<sub>2</sub> with 0.2 percent Tm measured before and after receiving a total dose of  $1.25 \times 10^6$  rad. Shown are the last two measurements during irradiation and measurements 7, 13, 25, and 46 hours after irradiation. This is an example of a crystal showing little or no change immediately after irradiation.

## 7. References

- [1] Schotanus, P., van Eijk, C. W. E., Hollander, R. W and Pijpelink, J. Development Study of a New Gamma Camera. IEEE Trans. Nuc. Sci. NS-34(1):272-276; 1987, February 1.
- [2] Levy, P. W., "Overview of Nuclear Radiation Damage Processes: Phenomenological Features of Radiation Damage in Crystals and Glasses," in Radiation Effects in Optical Materials, SPIE 541, Levy, P. W., ed. Bellingham, WA: SPIE, 1985. 2-24.
- [3] Adams, M. R., Englemann, R., Grannis, P. D., Horstkotte, J., Godfrey, L., Linn, S. L., Marx, M. D., Timms, J., Tuts, P. M., Willins, J., Ahrens, L., Aronson, S., Levy, P. W., Yamin, P., Franzini, P., Youssef, S., Cutts, D. and Callas, J. Radiation Damage Studies of Cerium-Doped Radiation Resistant Lead Glass Detectors. Nuc. Inst. and Tech in Phys. Res., A238: 333-340; 1985.
- [4] Woody, C. L., Levy, P. W. and Kierstead, J. A. Slow Component Suppression and Radiation Damage in Doped BaF<sub>2</sub> Crystals. To be published in IEEE Trans Nuc. Sci. NS-36; 1989, February 1.
- [5] Levy, P. W. Facilities for Studying Radiation Damage in Nonmetals During Irradiation. Society for the Advancement of Material and Process Engineering (SAMPE) Journal. 21(2): 35-40; 1985, March 1.

#### COMMENTS

Question: We have found that radiation induced absorption in quartz is a function of the total history of the dose applied. The dose rate and also the temperature plays a very important role. Did you control the temperature in your experiments?

Answer: The coloring of samples and the luminescence efficiency of practically anything depends on the temperature. It's a universal property of this type of solvent.

Question: I have a comment about your Mafia principle. In case of glass when you add Cerium, it attaches to the open oxygen. Oxygen forms the color of the centers so Cerium boxes the oxygen and it does not form the color center. I'd like to ask you a question. What's the origin of Mafia principle?

Answer: It originated approximately 30 years ago when people were forced to develop windows for hot cells and at that time a large amount of work was done, just empirical work, to try to find some way of impeding the coloring. What the Cerium actually does in most glasses is at least two things. First of all, it introduces potential centers which have much higher cross sections for capturing the electrons and-or holes than the defects or impurities which color the glass in the visible; most of these new centers are in the ultraviolet. So, in that case, you give away coloring in the ultraviolet to gain transmission in the visible. The other thing that Cerium does is to act as a large recombination cross section material, in other words, it has a large recombination cross section. It traps holes, they then immediately trap electrons and so you short circuit the passage of these electrons and holes to the defects which produce color centers.



MANUSCRIPT NOT RECEIVED

=====

OPTICAL DAMAGE IN GLASS FROM FOCUSED NANOSECOND RADIATION

Evaldas K. Maldutis, Stanislovas K. Balickas, Silvinas V. Sakalauska  
Institute of Physics, Academy of Sciences  
Lithuanian SSR, Vilnius

ABSTRACT

In this report the results of complex investigations and the understanding of glass optical damage by interaction with intense laser radiation is presented. The mechanism of glass damage threshold decrease is discussed. Under repeated nanosecond laser radiation when the quantum energy is less than a half of glass matrix ionization energy the changes in SBS intensity, the light absorption and refractive index have been detected. On this account, the main cause of damage accumulation is assumed to be color centers generation in glass resulting in thermal change of the refractive index and a following radiation intensity increase in the successive pulse focal region. The pulse duration, focal region size, radiation wavelength dependence of damage threshold, the accumulation effect and other calculations have considerably proved the presented glass damage model.

## The Non-Destructive Prediction of Laser Damage

S.E.Clark and D.C.Emmony

Department of Physics  
Loughborough University of Technology  
Loughborough  
Leics.  
LE11 3TU  
United Kingdom

We have developed a simple practical technique for the non-destructive prediction of potential damage sites. Excellent correlation is found between the predicted sites and the areas that damage first. The technique is based on using a short pulse dye laser and high resolution video framestore based Schlieren imaging system to record the transient i.e. non-destructive heating of a test surface by an excimer laser. The fluence of the excimer laser is then increased until the damage threshold is reached, whereupon the surface is re-imaged. Computer aided analysis of the transient image allows the areas of anomalous absorption to be found, which are then compared to the locations of areas that actually damaged. On all types of sample tested (metal, semiconductor and dielectric) and for both single and multiple pulse experiments excellent agreement is found between predicted and observed damage sites.

Keywords: non-destructive; prediction; laser damage; Schlieren imaging  
transient heating; anomalous absorption

### 1. Introduction

The non-destructive prediction of laser induced damage is a process whereby some form of 'transient' non-damaging effect associated with the interaction of the laser beam and the component in question is 'monitored' so that predictions as to where the component will damage can be made. In an ideal world the surface of a component would be completely uniform and would thus damage uniformly over the beam surface interaction area[1,2,3]. In reality, where optical quality surfaces are used, residual mechanical stress, strain and surface scratches together with contamination from polishing material and the general surroundings ensures that the samples do not have uniform surfaces. Consequently damage tends to occur in spatially isolated places corresponding to these defects with a factor of 2 or more in damage threshold between areas on the same sample not being uncommon.

### 2. Review

It is generally accepted that for real surfaces, laser induced damage (LID) for large area beams, i.e. larger than a few tens of square microns and pulses longer than a nanosecond, can be attributed to the presence of surface defects which absorb sufficient incident radiation to cause the surface temperature to rise excessively leading to damage via melting, vaporization or mechanical failure of the surface.

As the failure mechanism is thermal in nature most workers have attempted to perform the prediction of LID by means of thermal probes[4,5,6,7] involving photacoustic or photothermal effects either by scanning[5,6] or directly detecting[4]/imaging[7] the surface. All of these previous approaches had significant drawbacks such as not being able to provide spatial information about the defects[4], requiring many hours to collect the data in scanning systems or using direct optical detection[7] to detect defects which suffers from the possibility that areas that are optically good can contain thermal flaws which result in low damage thresholds.

The technique that we have developed obtains in a single non-damaging laser pulse spatial information about the surface defects both optical and/or thermal in nature in the form of a direct image of the surface. The process uses the same laser for both non-damaging and damaging pulses to avoid any possible problems relating to different pulse lengths or beam profiles and is built around a computer controlled high resolution video framestore based Schlieren imaging system.

### 3. The Loughborough Damage Facility

The damage facility at Loughborough is based on a Lambda Physik KrF excimer laser working at 249 nm and producing nominal 1 J pulses of 20 ns duration. Control of the on-target excimer energy is achieved by means of a liquid dye cell attenuator, whilst energy measurement is by use of a Laser Instrumentation calorimeter. To reach the required fluences a quartz lens was used to focus the beam, with spatial beam profiling being performed by means of a computer controlled video framestore[8] system that images the fluorescence produced by absorbing the excimer laser radiation on a suitable glass fluorecser. Using this system it is possible and is our standard practice to quote the peak fluence on the target. Damage detection at Loughborough has been developed to a point where it is routinely performed by use of high resolution Schlieren imaging (i.e. imaging with a suitable stop/filter in the focal plane of the imaging lens) linked to a computer controlled video framestore[9] to enable fast, accurate and reliable processing of the images.

### 4. The Technique

The technique that we have developed works on the basis that defects in a test surface will absorb anomalous amounts of the incident light and therefore cause a larger deflection of a probe beam in these areas than in surrounding areas. These absorbing areas then show up as anomalously bright or dark areas in the Schlieren image. The technique uses a short (<1ns) pulse dye laser as a probe beam to obtain 4 distinct images of the same area of the surface under test. These are subsequently processed and compared. The 4 images are

- Image a) The initial undamaged surface
- Image b) The surface showing transient non-damaging heating
- Image c) The surface after all transient effects have decayed
- Image d) The surface after damage has occurred.

Computer processing (including subsequent comparison) of images a and c was used to indicate if any permanent change had occurred due to the 'non-damaging' excimer pulse having been incident on the surface, whilst a and b when processed revealed the transient heating effect. Processing of a and d revealed the areas that actually damaged. Comparison of the latter two processed images would allow correlation between areas of transient and permanent change to be made.

### 5. Experimental Arrangement/Considerations

Figure 1 shows schematically the experiment arrangement that was used. The excimer laser was used for both the non-damaging pulse and the subsequent damaging pulse(s). The probe beam was provided by a short pulse PRA model LN103 nitrogen pumped dye laser operating at a wavelength of 514 nm. The video framestore used, an Eltime ImageIII with 256 by 256 pixel

resolution and 64 greylevels was controlled by a Sperry PC/IT computer so that processing operations[9] such as storage on and retrieval of images from hard disc, image subtraction, image enhancement etc. could be performed. A purpose built electronic trigger box[9] was used to provide the correct relative delay in triggering the framestore, excimer and dye lasers, and to synchronize their triggering to the output of the video camera connected to the framestore.

Imaging was performed via 2 CCD video cameras connected to a compound microscope arrangement in which a knife edge was placed in the focal plane of the first lens so as to form a Schlieren imaging system. One video camera was connected to the video framestore and used to record the dye laser images of the surface whilst the other monitored the surface in real time using a small cw HeNe laser.

In order to reduce the variation across a given sample of the damage threshold, and prior to obtaining image a, all samples were subjected to 5 very low fluence ( $\approx 10\%$  of the single shot damage threshold) excimer pulses. Image b was obtained by firing the dye laser 375 ns after the excimer pulse so that the transient i.e. non-damaging heating of the sample could be recorded. Image c was obtained approximately 80 ms after image b at which time all the transient effects had decayed and was used as a check to ensure that the excimer pulse in b had caused no permanent damage to the test surface. Image d was obtained after the surface had been damaged.

Initial experiments showed that the output energy of the dye laser varied enormously and that some form of energy correction between individual shots would be required if accurate processing was to be achieved. This was performed by using a fast photodiode connected directly i.e. unterminated to an oscilloscope. In this mode of operation, measurement of the output voltage at any time yields a value proportional to the number of incident photons and hence incident energy. By means of a suitable oscilloscope the output voltage of the photodiode as a function of time for each dye pulse was obtained. Comparison of the traces at a common time yielded the relative pulse energies.

In view of its effect on the interpretation of results, the spatial profile of both the excimer and dye beams must be carefully analysed. By use of our beam profiling system the dye laser beam was found to be Gaussian with a  $1/e^2$  diameter of approximately 2mm. The excimer laser was roughly Gaussian with  $1/e^2$  diameters of 2mm horizontally and 0.5 mm vertically. By varying the focal length of the lens attached to the video cameras two magnifications (as viewed on the video monitor) of times 680 (high magnification) and times 260 (low magnification) were used. The area actually imaged was 1.08 mm by 0.81 mm in the low magnification setup and 0.41mm by 0.31 mm in the high magnification setup. Treating the beams as Gaussian it can be readily shown[9] that in the high magnification setup, the spatial variation in the dye beam can be ignored whilst that of the excimer can only be ignored along the horizontal axis. In the low magnification setup the spatial variation in the dye beam is small but that of the excimer beam is enormous particularly in the vertical direction. Hence in the recorded images the heating and damaging fluences are essentially uniform in the horizontal direction but vary vertically across the image such that if the surface was completely uniform the damage would occur first along a horizontal axis in the centre of the image due to the higher intensity there. If however damage is found to first occur away from the centre vertically where the excimer fluence is lower, then it must be due to the presence of weak spots i.e. defects in the surface and as such is a good indication of their presence.

Computer processing routines[9] were used to perform a number of tasks such as storing images onto disc, subtracting images and enhancing the contrast of a given image. The subtraction routines made allowance for the pulse to pulse variation in dye laser energy on the basis that the energy in images b, c and d is expressed as a fraction of that in image a.

Three sets of samples were used 1) Commercially pure/polished Al 2) Laser quality (for CO<sub>2</sub> use) polished to  $\lambda/10$  polycrystalline Ge and 3) Multi layer (quarter wave) dielectric stacks on fused silica substrates designed to be high reflectors at a wavelength of 249 nm.



Two sets of experiments were performed 1) To investigate the correlation between areas of anomalous absorption as revealed by the transient signal and the areas that first damage on a single shot damage basis 2) As in 1 but on a multiple shot basis.

The fluence used to record the transient image was that found by experiment to be the lowest fluence i.e. furthest below the single shot damage threshold that would give a readily detectable signal. For the metallic samples this was about  $1/3$  to  $1/4$  of the single shot threshold level whilst being slightly higher at about  $1/2$  the single shot level for the dielectric samples. The limit as to how far below threshold the system would work is controlled by 2 parameters 1) the sensitivity of the camera and 2) the output energy of the dye laser. The output energy of the dye laser was such that in operation, the camera was typically operating in the lower half of its dynamic range. A doubling of dye laser energy would have been ideal.

## 6. Results

Figures 2a-e show a sequence of images recorded using the high magnification setup of an Al sample where the transient effects were obtained using an excimer fluence of  $0.18 \text{ J cm}^{-2}$  and the damage caused by a single excimer pulse of fluence  $0.56 \text{ J cm}^{-2}$ . Figures 2a-c show respectively the image of the surface after the cleaning pulses, the image of the transient heating and the damaged surface after one damaging excimer pulse. Processing of figures 2a and b gives the net transient signal (fig. 2d) where it can be seen that there are several areas of anomalous absorption which show up as a decrease in the processed signal i.e. the area becomes darker. Processing of figures 2a and c gives the net damage (fig. 2e) and reveals the areas that have actually damaged. Comparison of figures 2d and e shows that there is excellent agreement between not only the areas of large anomalous absorption and the more heavily damaged areas but between the general location of the damage sites and the somewhat less black areas of the transient image. The fact that damage occurs over areas that are well separated from each other particularly in the vertical direction over which the excimer intensity varied significantly indicates that the damage has been caused by the presence of localised defects on the surface rather than by thermal induced changes on a uniform surface.

The excimer fluence was gradually reduced until it was equal to the fluence used to record the transient image ( $0.18 \text{ J cm}^{-2}$ ) at which point approximately 50 pulses were required to cause damage on the Al samples. Figures 3a-d recorded in the low magnification setup show the development of the damage as the number of incident pulses increases. The sequence shows the gradual development of the damage site from a few isolated areas in the centre to a heavily damaged area with dimensions corresponding to that of the transient effect. It can be seen (fig. 3b) that the first stages of damage occur in the centre areas that according to the transient effect (fig. 3a) show the greatest heating effect and that the damage as it propagates across the field of view generally first occurs in those places that on the transient image are darkest.

Figures 4a-e show a sequence of images recorded using the high magnification setup of a Ge sample where the transient effects were obtained using an excimer fluence of  $0.06 \text{ J cm}^{-2}$  and the damage caused by a single excimer pulse of fluence  $0.18 \text{ J cm}^{-2}$ . After processing to give the net transient signal (fig. 4d) and the actual damage (fig. 4e) excellent agreement is seen between the areas of anomalous absorption in the transient and those areas that actually damaged. The fact that the damage is essentially in isolated areas particularly well spread out in the vertical direction in which the excimer fluence varies by about a factor of 2.5 over the field of view shows that defects are again the prime cause of damage.

Although the dielectric sample used was a high reflector at  $249\text{nm}$  it was transparent at visible wavelengths. It was therefore necessary for the system to be rearranged to work with dye laser light that is transmitted through the sample. Initial work by us had shown that these samples had a single shot threshold of around  $3.5 \text{ J cm}^{-2}$ , so initially the fluence for transient recording was set to  $\approx 1 \text{ J cm}^{-2}$  but this proved insufficient to produce a detectable transient effect. The fluence was gradually increased to a value of  $1.7 \text{ J cm}^{-2}$  at which point there was a detectable transient signal.



Figures 5a-e show a sequence of images recorded using the high magnification setup of a dielectric sample where the transient effects were obtained using an excimer fluence of  $1.7 \text{ J cm}^{-2}$  and the damage caused by a single excimer pulse of fluence  $3.5 \text{ J cm}^{-2}$ . After processing to give the net transient signal (fig. 5d) and the actual damage (fig. 5e) initial comparison reveals excellent agreement between the area (marked as 1 in fig. 5d) of anomalous absorption in the transient and the area of main damage (marked as 1 in fig. 5e). A more detailed study of 5d and e reveals that there is an anomalous transient signal at each of 3 secondary areas of damage (labelled 2-4). The nature of the damage on this sample, i.e. very isolated areas of point damage, strongly indicates that thermal failure through the presence of surface defects such as scratches, voids, inclusions etc is the main cause of damage on these samples.

## 7. Conclusions

A simple, fast and accurate technique has been developed for the non-destructive prediction of LID which gives excellent correlation between predicted and actual damage locations. An increase in the dye laser energy or using more sensitive cameras would improve both the sensitivity and the usefulness of the system as it would enable detection of the transient effects to be made at a smaller fraction of the single shot damage threshold.

-----

Grants from USAF/ONR and the Science and Engineering Research Council are gratefully acknowledged.

## References

- [1] Fountain, C. W.; Porteus, J. O.; Soileau, M. J. Slip banding in Al single crystals produced by  $10.6 \text{ } \mu\text{m}$  laser pulses. Appl. Phys. Lett. 29: 156-158; 1976
- [2] Fountain, C. W.; Jernigan, J. L.; Porteus, J. O. Multi-threshold damage to highly reflecting metals by a  $10.6 \text{ } \mu\text{m}$  pulsed laser in High energy laser mirrors and windows, NWC TP 5988 Annual report no.9: 1977 145 p.
- [3] Loh Jr., E.; Sparks, M. Temperature dependence of absorptance in laser damage of metallic mirrors: I. Melting. J. Opt. Soc. Am. 69: 847-858; 1979
- [4] Green, J. M.; Jeen, A. M. Two techniques for early detection of pulsed laser induced damage in optical materials. J. Phys. E: Sci Instrum. 17: 191-193; 1984
- [5] Freese, R. P.; Teegarden, K. J. Pre-pulse identification of localised laser damage sites in thin films using photoacoustic spectroscopy. Nat. Bur. Stand. (U.S.) Spec. Publ. 568; 1979 313 p
- [6] Abate, J.A.; Roides, R. Spatially resolved absorption and detection of microscopic impurities in optical thin films by photothermal detection, J. Phys. Colloq. (France) C-6: 497-502; 1983
- [7] Marrs, C. D.; Palmer, J. R.; Porteus, J. O. Non-destructive defect detection in laser optical coatings, J. Appl. Phys. 57: 1719-1722; 1985

- [8] Clark, S. E.; Emmony, D. C.; Laidler, I.; Omar, B. A.; Shaw, M. J. Laser beam diagnostics using a computer controlled video frame store system, Nat. Bur. Stand. (U.S.) Spec. Publ. 746; 35 p
- [9] Clark, S. E. Excimer laser induced modifications of optical surfaces, Ph.D. Thesis Loughborough University of Technology 1988

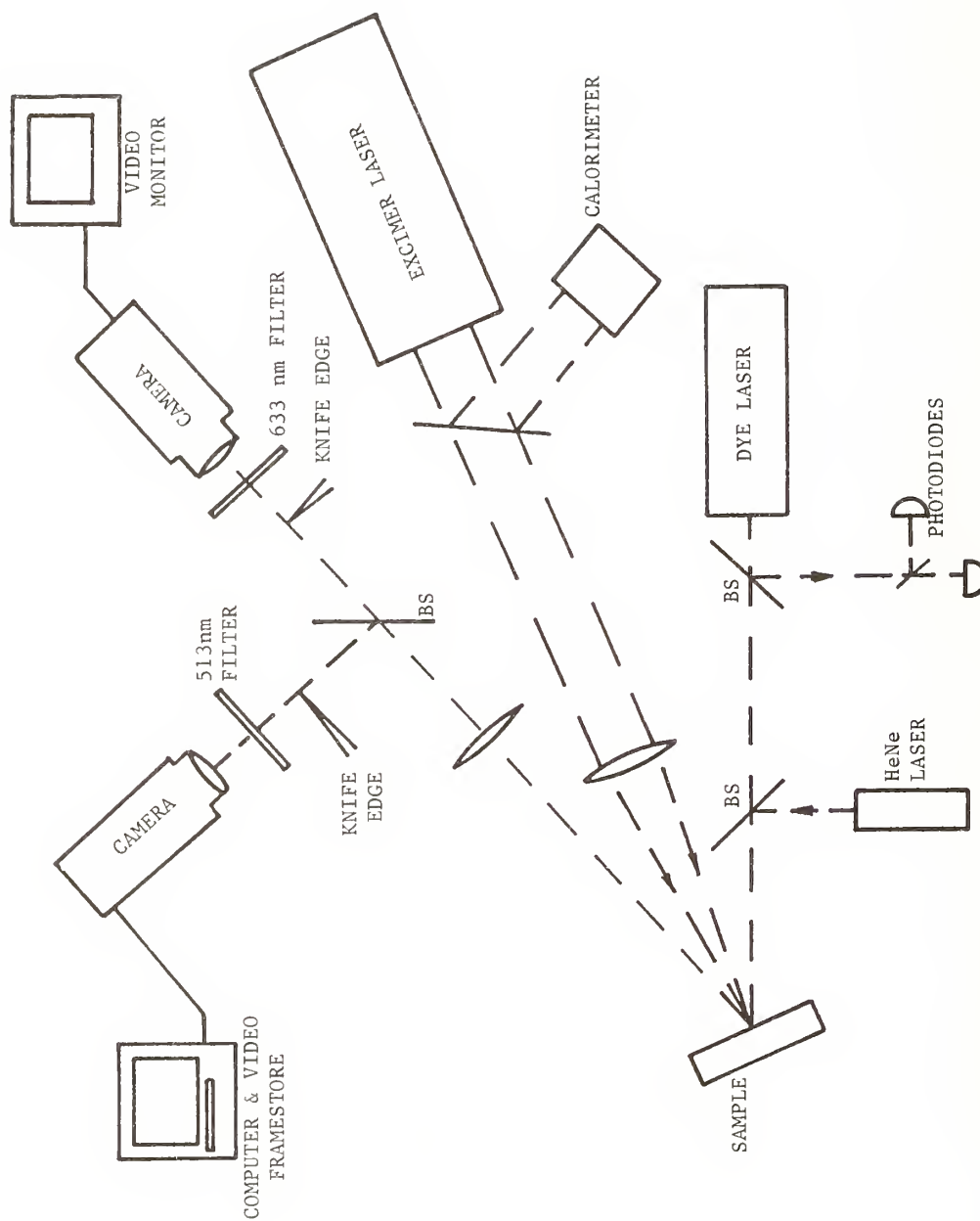
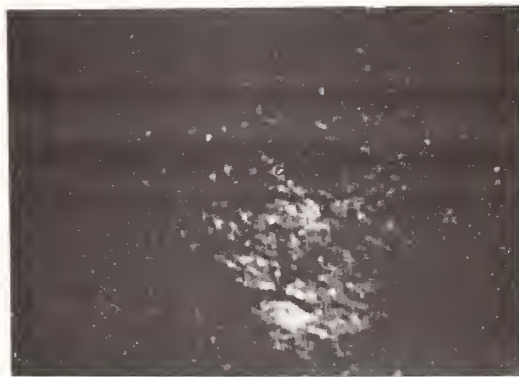


Figure 1. Experimental Arrangement



(a) Initial undamaged surface.



(b) Transient image  $0.18 \text{ Jcm}^{-2}$   
375 ns delay.



(c) Permanent damage  $0.56 \text{ Jcm}^{-2}$ .



(d) Computer processed transient.



(e) Permanent damage.

Figure 2. Aluminium single shot damage.



(a) Transient.



(b) Damage 50 shots.



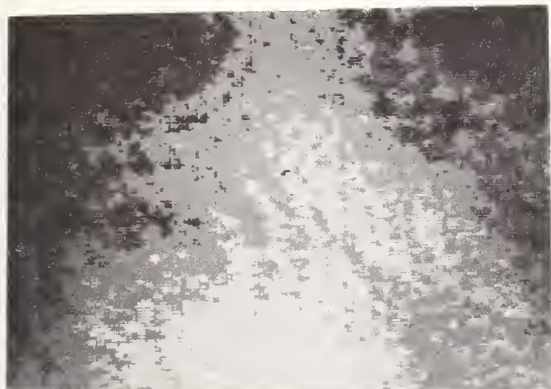
(c) Damage 200 shots.



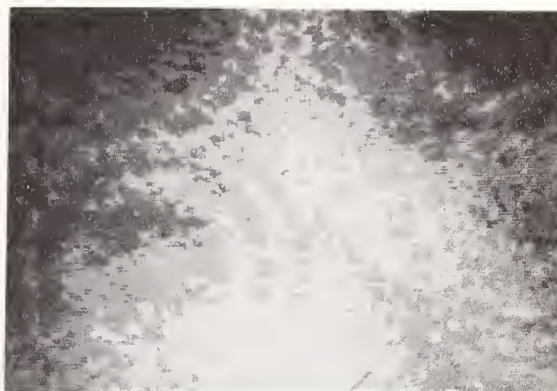
(d) Damage 400 shots.

Figure 3. Aluminium multiple shot damage.





(a) Initial undamaged surface.



(b) Transient image  $0.06 \text{ Jcm}^{-2}$   
375 ns delay.



(c) Permanent damage  $0.18 \text{ Jcm}^{-2}$ .

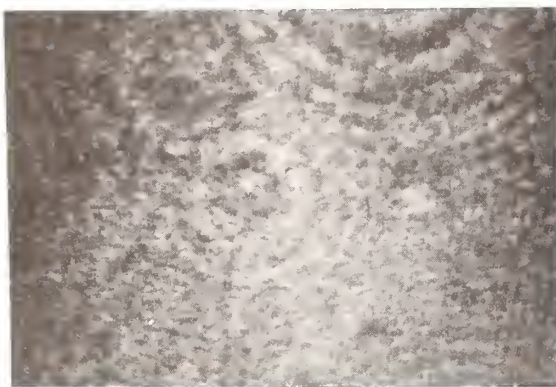


(d) Computer processed transient.

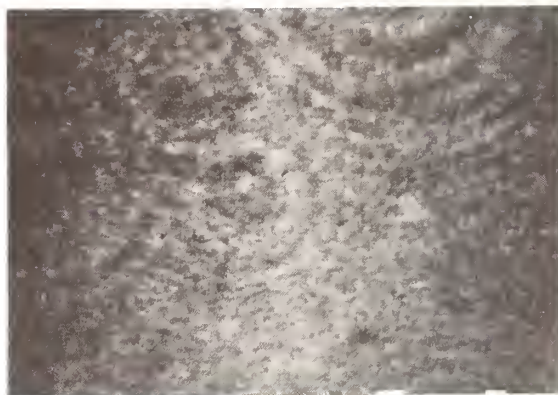


(e) Permanent damage.

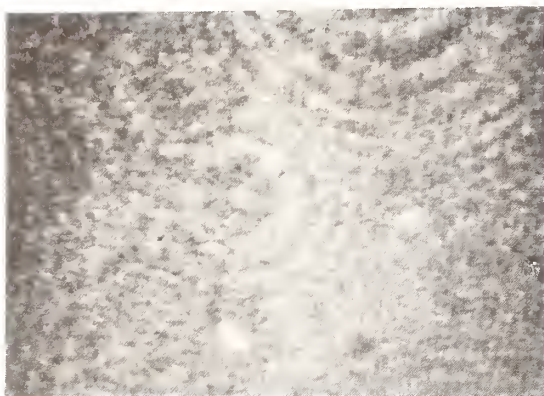
Figure 4. Germanium single shot damage.



(a) Initial undamaged surface.



(b) Transient image  $1.75 \text{ Jcm}^{-2}$   
375 ns delay.



(c) Permanent damage  $3.50 \text{ Jcm}^{-2}$ .



(d) Computer processed transient.



(e) Permanent damage.

Figure 5. Dielectric reflector (max. at 249 nm) single shot.

MANUSCRIPT NOT RECEIVED  
=====

REPETITIVELY PULSED BEAM DIAGNOSTICS  
FOR LARGE LASER OPTICS DAMAGE\*

D.B. Nichols, D.J. Morris, and W.B. Shepherd  
Boeing Aerospace  
Seattle, WA 98124

T.M. Donovan, J.L. Stanford, and C.D. Marrs  
Naval Weapons Center  
China Lake, CA 93555

and

C.F. Zahnow  
Maxwell Laboratories Inc.  
San Diego, CA 92123

ABSTRACT

Increasingly detailed information about the progression of damage to optical surfaces during repetitively-pulsed irradiation has accentuated the need for corresponding detailed information about the incident beam profiles. The invariance of spatial profile from pulse to pulse typical of small lasers cannot be invoked in many larger lasers. The product of amplitude resolution times spatial resolution times pulse rate produces high data rate requirements during repetitively-pulsed testing. This paper describes the utilization of one pulse-laser beam profiling system<sup>1</sup> in optics tests at four laboratories, to illustrate single-pulsed DF, repped DF, single-pulsed XeF, and repped XeF, laser beam diagnostics.

\* This work was supported by SPAWARS SYSCOM PMW-145, through the Naval Weapons Center, China Lake, CA.

<sup>1</sup> D.B. Nichols, P.D. Teixeira, and T.M. Donovan, "High-Energy Pulsed Laser Beam Profiling System," Eighteenth Annual Symposium on Optical Materials for High Power Lasers, Boulder, Colorado, 3-5 November, 1986.



MANUSCRIPT NOT RECEIVED

=====

EMERGENCE OF "CONSENSUS STANDARDS" IN LASER DAMAGE ACCEPTANCE  
TESTING OF PRODUCTION Nd:YAG LASER OPTICS

S.C. Seitel and E.A. Teppo  
Montana Laser Optics\*, Inc.  
Bozeman, Montana 59715

J.W. Arenberg  
Santa Monica, California 90403

ABSTRACT

Many government-sponsored Nd:YAG laser system programs now require comprehensive laser-damage testing for optics vendor qualification and parts acceptance. The most visible artifacts of these test programs are the test specifications. Initially idiosyncratic and often incomplete, recent examples of production test specifications show remarkable similarity of nomenclature, test parameter set, exposure procedure, calibration verification, "damage" definition and pass/fail criteria. For one segment of the industry, at least, reasonable order appears to be emerging from chaos.

We review the emergence and refinement of these apparent "consensus standards". Specific examples of incomplete and ambiguous early specifications are given with discussion of how the loopholes allow bad parts to reach hardware. We show that careful consideration of key issues helps make the specification (and test program) consistent, complete, and system-relevant; and we present a "generic" specification which results from this process. Not by coincidence, our format embodies the important features of many recently issued Nd:YAG production test specifications.

Finally, we ask whether the success of the "white-label" Nd:YAG specification might serve as a model for other segments of the industry, and offer it as our contribution toward one original and often-restated goal of this Symposium: standardization of test methods for better interchange of information between laboratories.

MANUSCRIPT NOT RECEIVED

=====

OPTICAL BREAKDOWN IN PARTICLE SUSPENSION

Kamjou Mansour, M.J. Soileau, and E.W. Van Stryland  
Center for Research in Electro-Optics and Lasers  
University of Central Florida  
Orlando, Florida 32816

ABSTRACT

Recently there has been a growing interest in the use of particle suspensions as nonlinear media for use in optical limiters for sensor protection. Using a tight focusing geometry we have observed the onset of limiting at input powers of as low as  $\approx 20$  W using nanosecond  $0.53 \mu\text{m}$  input pulses. We present evidence that is consistent with scattering from rapidly expanding microplasmas initiated by thermionic emission from the carbon particles that are heated by linear absorption of the input light. A simple calculation of the temperature of the  $\approx 50$  nm diameter carbon particles gives sufficient to produce significant thermionic emission to initiate avalanche ionization monitored transmission, absorption (using photoacoustic detection) and scattering (looking at side scattered light), we find that nonlinear scattering is the dominant mechanism limiting the transmission.



## Colloidal Materials as Optical Filtering Media

K. J. Kogler, R. G. Pastor, R. L. Burton, R. A. Spence, and N. P. Murarka

IIT Research Institute  
Chicago, Illinois 60616-3799

Particles 1  $\mu\text{m}$  or less in diameter are said to be colloidal sized particles. When the colloids are metals dispersed in a dielectric matrix, the transmittance of the system may possess an absorption band. The shape, depth, and resonant wavelength of the stop band are determined by the size of the metal particles, the volume fraction of the metal particles in the dielectric, and the complex index of refraction of both the metal colloids and the dielectric matrix. The purpose of our experimental work was to produce colloids of vanadium dioxide embedded in a dielectric matrix and to study its optical properties. During this investigation, we also produced colloidal size particles of silver and gold and studied their optical properties.

**Key words:** metal colloids; optical filters; plasmon resonances; sphere masks; switchable filters;  $\text{VO}_2$  colloids.

### 1. Introduction

The motivation for the optical materials development discussed herein is the demonstration of a switchable blocking filter based on the plasmon resonant absorption phenomenon exhibited by small metallic particles (on the order of hundreds of nanometers). The concept pursued is the substitution of  $\text{VO}_2$  particles of similar dimensions for the metal with expectation of achieving an absorption resonance that would be switched by the phase transition of  $\text{VO}_2$  to a metal-like state when heated. This approach improves upon a continuous thin film of  $\text{VO}_2$  by providing rejection of a narrow band of wavelengths only and offers potential for improving dynamic range (ratio of switching threshold to damage threshold). Furthermore, plasmon resonance of metallic particles occurs at visible wavelengths suggesting the applicability of  $\text{VO}_2$  to that part of the spectrum.

### 2. Theory and Approach

The observation of the resonant absorption phenomenon in noble metal island films is well documented in the literature [1,2].\* Several theories have been developed to explain the absorption phenomenon with none providing good quantitative agreement. Many of them stem from the basic theory of Garnett [3] which at least qualitatively predicts the presence or absence of absorption maxima and their shift with wavelength in terms of the observed structure of the films and the bulk optical properties of the metal. The simplicity of the theory and its utility in predicting absorption maxima and their spectral location made this an attractive tool for validating the  $\text{VO}_2$  colloidal concept.

Relationships derived by Garnett to determine an effective index of a composite consisting of dispersed metal particles of bulk index and extinction coefficients  $n$  and  $k$  are given by eq (1) and (2).

---

\*Numbers in brackets indicate the literature references at the end of this paper.

$$n'k' = \frac{3Qb}{(1 - Qa)^2 + 4Q^2b^2} \quad (1)$$

$$k'^2 - n'^2 = 2 \frac{3(1 - Qa)}{(1 - Qa)^2 + 4Q^2b^2} \quad (2)$$

where  $Q$  is the volume of metal per unit volume of medium and necessarily  $0 < Q < 1$ , and

$$a = \frac{(k^2 - n^2 + 1)(k^2 - n^2 - 2) + 4n^2k^2}{(k^2 - n^2 - 2)^2 + 4n^2k^2} \quad (3)$$

$$b = \frac{3nk}{(k^2 - n^2 - 2)^2 + 4n^2k^2} \quad (4)$$

These equations were applied to qualitatively predict resonance absorption in  $VO_2$  particles by collecting optical constant dispersion data from spectral measurements on  $VO_2$  thin films above and below the phase transition temperature. The values of transmittance and reflectance for light passed in both directions through the film were used to determine the reflectance of the films on an infinitely thick substrate (with no back surface reflectance). From these data and dispersion data for the substrate, it was possible to obtain a good fit for a multi-parameter model. For room-temperature measurements ( $VO_2$ -transmitting state) good fits were obtained by modeling the dispersion with five Lorentzian oscillators. The high-temperature data ( $VO_2$ -blocking state) was well fitted with a model that incorporated one free carrier oscillator and four Lorentzian oscillators. The best fit parameters were then used to generate the dispersion curves for the index and extinction coefficient. The fitting procedure described above was repeated for three  $VO_2$  films. The data generated for all three films were quite similar. The data for the three were averaged to improve accuracy.

### 3. Results

Figures 1 and 2 show some typical results of the fitting procedure, in the case of the 137 nm thick film. Figure 1 shows the reflectance data and the best fit results at room temperature. Figure 2 is a similar plot for high temperature. At room temperature the film is transmitting over most of the data range. Therefore, the reflectance shown in figure 1 is due to the combined effects of dispersion from multiple oscillators and interference phenomena. By comparison, the reflectance in figure 2 is very close to the bulk reflectance of  $VO_2$  at 90°C since the transmittance over most of the data range is less than one percent.

The results of the analysis of the room-temperature data are presented in figures 3 and 4. Figure 3 shows the refractive index as a function of wavelength for the average of three films. The three low-temperature data sets do not match exactly but are all within  $\pm 0.04$  of their average value. The extinction coefficient results are shown in figure 4. The low-temperature data, in this case, were all very close together and demonstrate that absorption decreases with increasing wavelength for  $VO_2$  at low temperature. This is the opposite of the high-temperature case.

For the high-temperature data, both  $n$  and  $k$  exhibit a large spread between the three samples. This may be due to the dominant effect of the free carrier oscillator on the reflectance, since the free carrier optical properties are highly dependent on electrical conductivity, which may vary from film to film due to differences in film quality. The extinction coefficient in the high-temperature regime is found to increase with increasing wavelength, as expected.

The product  $n'k'$  gives a measure of the absorption of the film, the relationship derived by Goos [4] being:

$$n'k' = (\lambda/4\pi t)n_2(A/T) \quad (5)$$

where  $t$  is the thickness of the film,  $n_2$  is the refractive index of the substrate,  $\lambda$  is the wavelength,  $T$  is the transmission of the film, and  $A$  its absorption. This parameter is shown as a function of wavelength in figure 5 at low and high temperatures. Clearly, a switchable absorption band is evident at a wavelength slightly above 1000 nm for a volume fraction of 0.20. The sensitivity of the absorption maximum wavelength and spectral bandwidth to changes in the volume fraction is shown in figure 6.

To ascertain the effects of varying particle sizes, which would create a nonconstant volume density, a normally distributed volume density was considered. The effect of normal distributions having variances ranging from 0 to 0.3 on the absorption spectrum is shown in figure 7. As the variance increases, the absorption maximum diminishes and broadens to a continuum for variances exceeding 0.3.

With the theoretical validation of an absorption band resonance, interest was directed toward synthesis of  $VO_2$  colloidal particles. Based upon the work performed by Kaiser and Logothetis [2], RF sputtering was selected as a synthesis approach. The approach devised for synthesizing small particles in a dielectric matrix was to sputter the particulate material from one target and the dielectric from another target. The RF sputtering system used (R. D. Mathis Model No. RFG1250) allowed locating the targets above and below the substrate. By dividing the power between the two targets, sputtering occurs continuously from both. The substrate, midway between the two targets, is shielded so that it receives a deposit only from the target that it faces. The small particle/dielectric composite is grown by rotating the substrate between the two targets. The thickness of the composite is determined by the amount of time that the substrate faces a given target, and the power applied to the target.

Initial composites were made from silver particles in a silicon dioxide matrix. Figure 8 shows the spectral transmittance for one of the better silver-silicon dioxide composites made by the above RF sputtering technique. The substrate temperature during the deposition averaged 163°C. Films deposited by this technique at lower temperatures and different rates and deposition times showed no improvement in optical density or bandwidth. The results achieved by RF sputtering, as illustrated by figure 8, were found to produce absorption bands of smaller attenuation and broader bandwidth than those formerly achieved by thermal evaporation of thin island-like silver films [1].

To investigate the potential of thermal evaporation as an approach to synthesizing composites, very thin films of silver were deposited on glass substrates. The spectral transmittance of a 15 Å silver film deposited at 0.15 Å/s onto a room-temperature glass substrate is shown in figure 9. Typically, as demonstrated by figure 9, the rejection band produced by thermal evaporation has both a greater attenuation and a narrower bandwidth than that produced by RF sputtering in spite of the fact that the thickness of the sputter-deposited silver film is greater than the thermally evaporated film. In addition, the rejection wavelengths of the thermally evaporated films are at a shorter wavelength than the RF sputtered films.

We believe that the longer rejection wavelength of the RF sputtered films is caused by the particle size of the films being much greater than the particle size of the thermally evaporated films. Figure 10 is an SEM micrograph of the RF sputter-deposited silver particles. These particles range in size from less than 500 Å to 2000 Å in diameter. In contrast, the particles grown by thermal evaporation were too small to be seen using the scanning electron microscope. The data indicate that the silver particles produced by RF sputtering have a larger size distribution than the silver particles produced by thermal evaporation. If the particle size distribution is greater for the RF deposited films, the bandwidth should be larger for RF sputtered films and it is. The smaller attenuation of the RF sputtered films can also be attributed to their greater size distribution because few particles will be absorbing energy at a given wavelength.



Since the RF sputtering approach to synthesizing Ag colloidal composites did not achieve a high attenuation narrow absorption band due to the large distribution in particle size, an approach was sought to achieve a more uniform distribution for synthesis of  $\text{VO}_2$  particles. Buncick et al. [5] have demonstrated that polystyrene spheres several hundred nanometers in diameter could, in principle, be used as a mask through which thin films could be deposited. By removing the spheres, small islands would remain. By achieving a uniform close-packed distribution of the spheres on the substrate, a uniform distribution of thin film islands should remain after dissolving the spheres in a solvent. Subsequently, the optical density of the absorption band should increase and the bandwidth should decrease.

Buncick et al. distributed the spheres on the glass surface by spin coating water/sphere solutions onto the glass substrate. In following this procedure, we found that only small sections of the substrate were covered with a monolayer of spheres having a high packing density; large areas on the substrate had no spheres. Clearly, it was necessary to improve the coverage to achieve the desired results. It was hypothesized that the poor overall sphere coverage was caused by the inability of the water/sphere solution to wet the glass substrates. In an attempt to achieve better wetting of the glass, an alcohol/water/sphere solution was used. After trying a number of alcohols it was found that an ethanol/water/sphere solution worked the best. Performing experiments with various mixtures indicated that 53.4 vol% ethanol, 44.7 vol% water, and 1.9 vol% spheres produced the most uniform sphere coverage. With this solution and a spin speed of 2000 rpm, a monolayer sphere coverage of over 92% on a 0.5 in. diameter area was achieved on a 1.0 in. diameter substrate. Figure 11 is an SEM micrograph showing a representative portion of the uniformly covered area.

The low softening temperature of polystyrene precluded the reactive sputtering of  $\text{VO}_2$  through the sphere mask. Since the formation of  $\text{VO}_2$  at the substrate requires a temperature on the order of  $500^\circ\text{C}$ , it was found necessary to deposit VO, which forms at a lower temperature, and to further oxidize the film to the desired stoichiometry ( $\text{VO}_2$ ) by a high-temperature anneal after removal of the spheres.

The annealing was achieved in an oxygen atmosphere, and the  $\text{VO}_2$  phase was kinetically trapped as the VO oxidized. Films of VO 800 Å thick were deposited onto glass substrates and annealed in air at  $480^\circ\text{C}$ . A sequence of films was annealed for different times to establish the time required to produce  $\text{VO}_2$  films before the equilibrium phase ( $\text{V}_2\text{O}_5$ ) is formed at that temperature and oxygen partial pressure. Figure 12 shows spectral transmittance curves for a sample annealed for 2.0 min. The evidence of  $\text{VO}_2$  formation is the change in transmission from 61.2% to 21.2% when the film is heated to the phase transmission temperature ( $67^\circ\text{C}$ ).

Figure 13 is an SEM micrograph of a VO film after the polystyrene spheres were dissolved away. However, with a sphere coverage of approximately 90%, missing spheres in the mask create large islands destroying the uniform size distribution. The effect of the nonuniform distribution is illustrated in figure 14, showing spectral transmittance through a VO film (525 Å thick) annealed at  $475^\circ\text{C}$  for 3 min in air after dissolving the sphere mask. Although this film switched, there is no indication of an absorption band. The lack of an absorption band is most likely related to the large distribution in the size of the  $\text{VO}_2$  particles. If the quality of the monolayer sphere coverage can be improved, a smaller size distribution would result and an absorption band would be produced. Work is continuing to achieve this objective.

#### 4. References

- [1] Sennett, R. S., and Scott, G. D. J. Opt. Soc. Am. 40: 4; 1950.
- [2] Kaiser, W. J., and Logothetis, E. M. Solid State Commun. 57: 1; 1986.
- [3] Garnett, J.C.M. Trans. Roy. Soc. (London) 203A: 385; 1904.
- [4] Goos, F. Z. Phys. 100: 95; 1936.
- [5] Buncick, M. C., Warmack, R. J., and Ferrell, S. L. J. Opt. Soc. Am. (B) 4: 6; 1987.

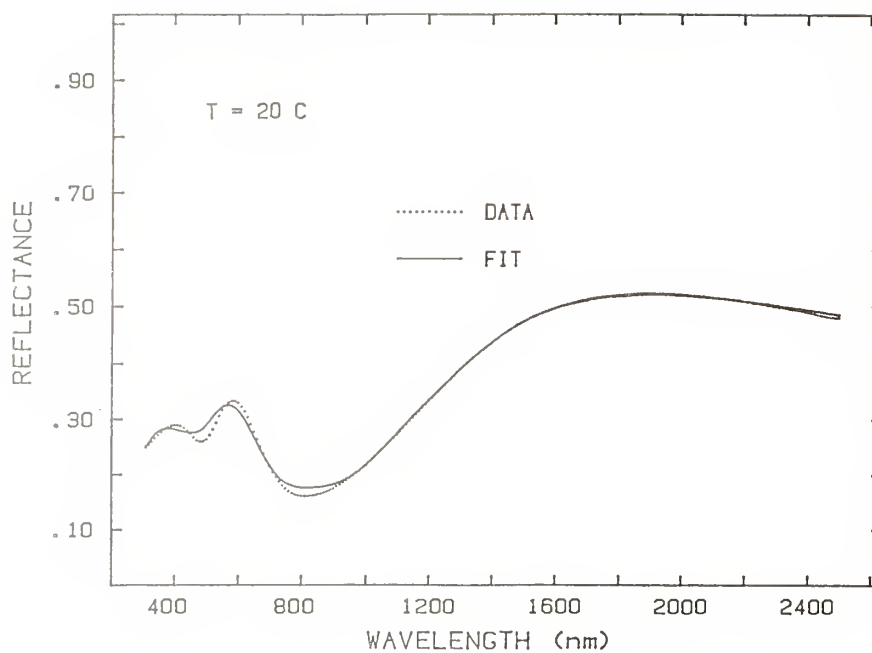


Figure 1. Reflectance data and best fit results for a 137 nm thick  $\text{VO}_2$  film ( $T = 20^\circ\text{C}$ ).

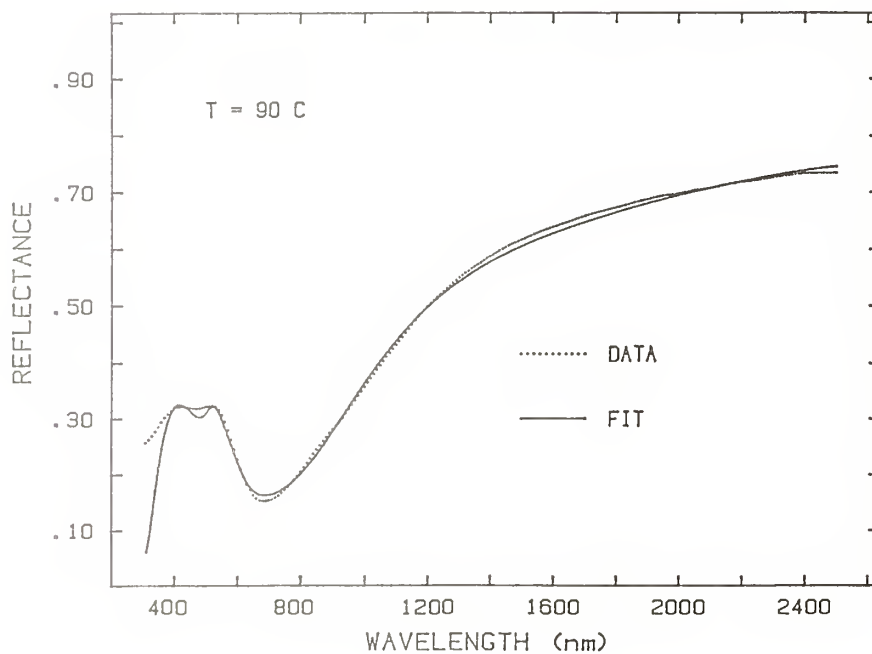


Figure 2. Reflectance data and best fit results for a 137 nm thick  $\text{VO}_2$  film ( $T = 90^\circ\text{C}$ ).



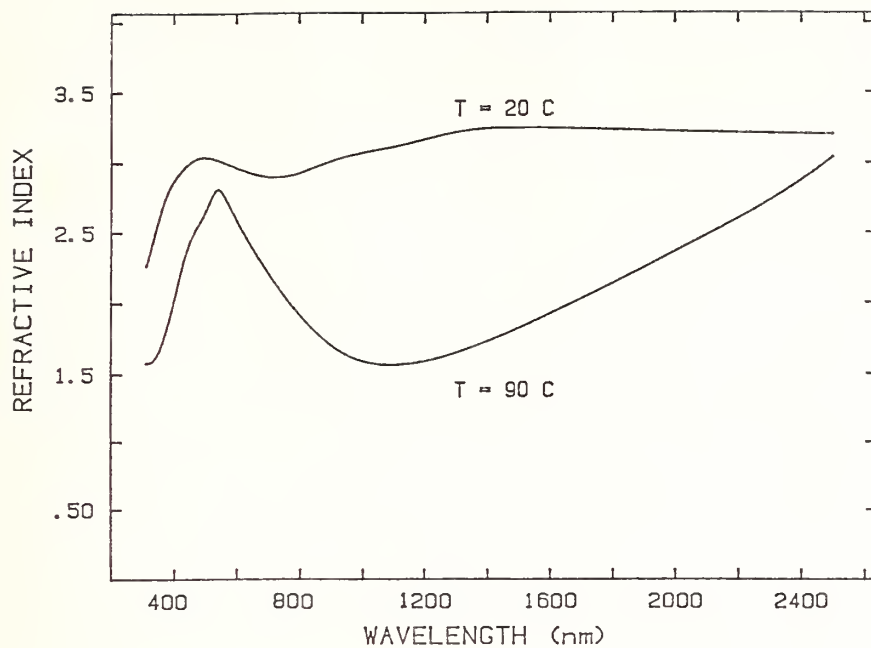


Figure 3. Low and high temperature refractive indices for  $\text{VO}_2$  films.

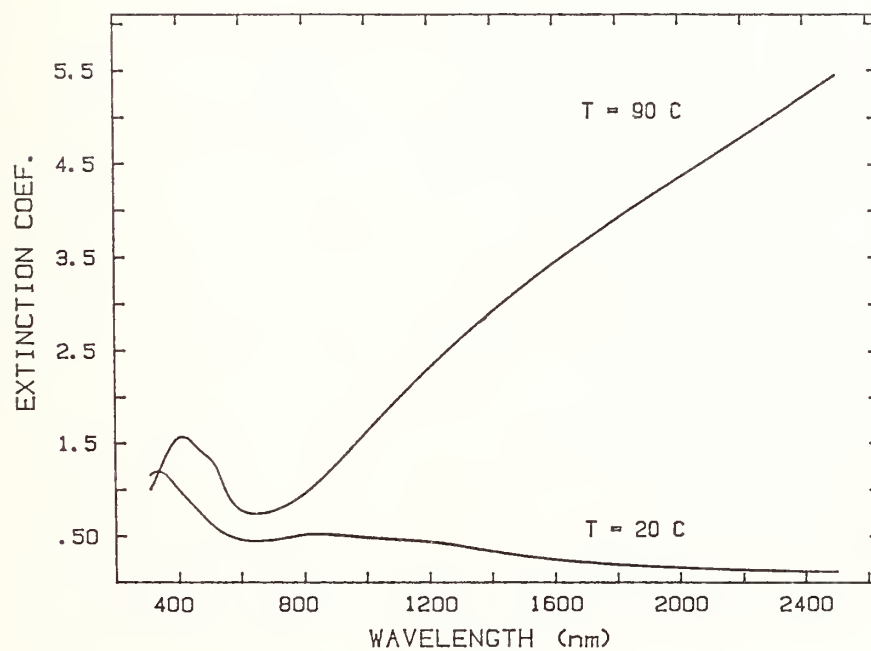


Figure 4. Low and high temperature extinction coefficients for  $\text{VO}_2$  films.

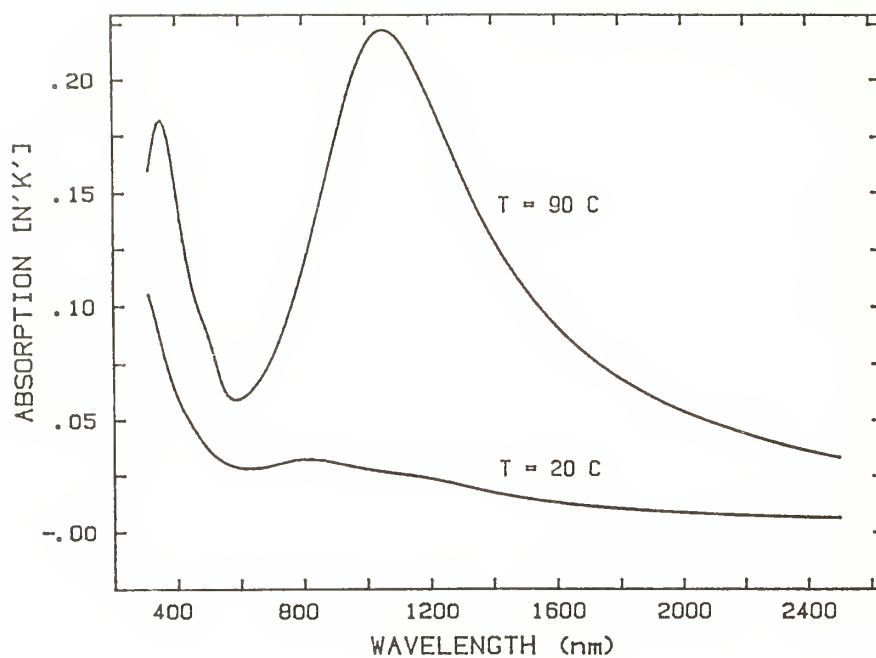


Figure 5. Absorption calculations based on  $\text{VO}_2$  properties for low and high temperatures ( $Q = 0.20$ ).

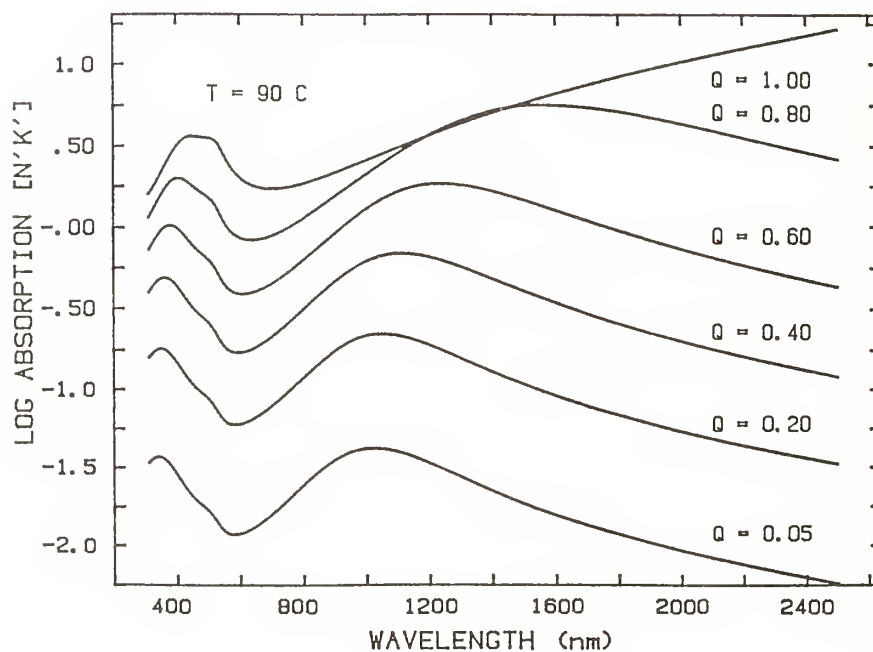


Figure 6. Absorption calculations based on  $\text{VO}_2$  properties for various  $Q$ s.

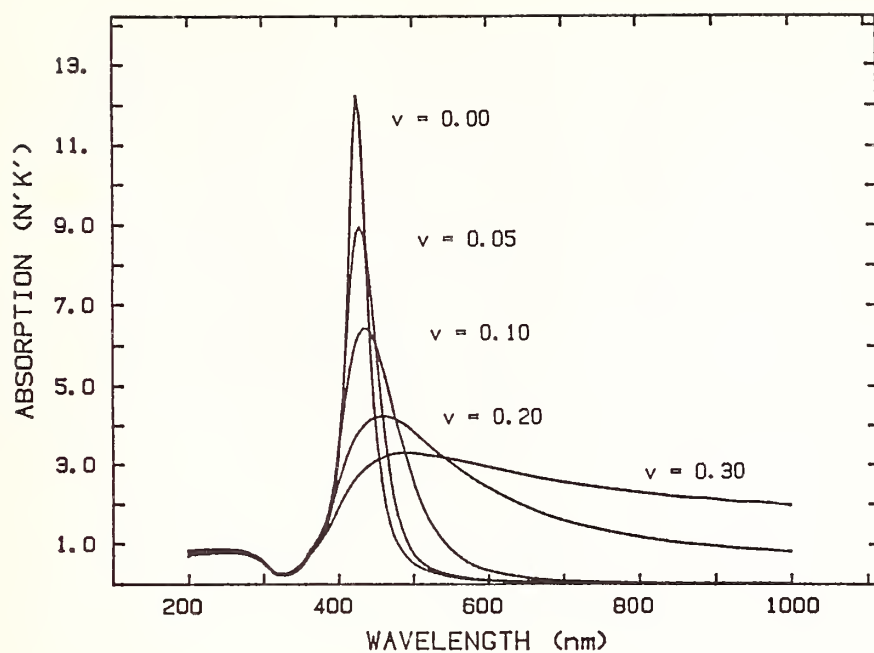


Figure 7. Absorption results for different Q distributions.

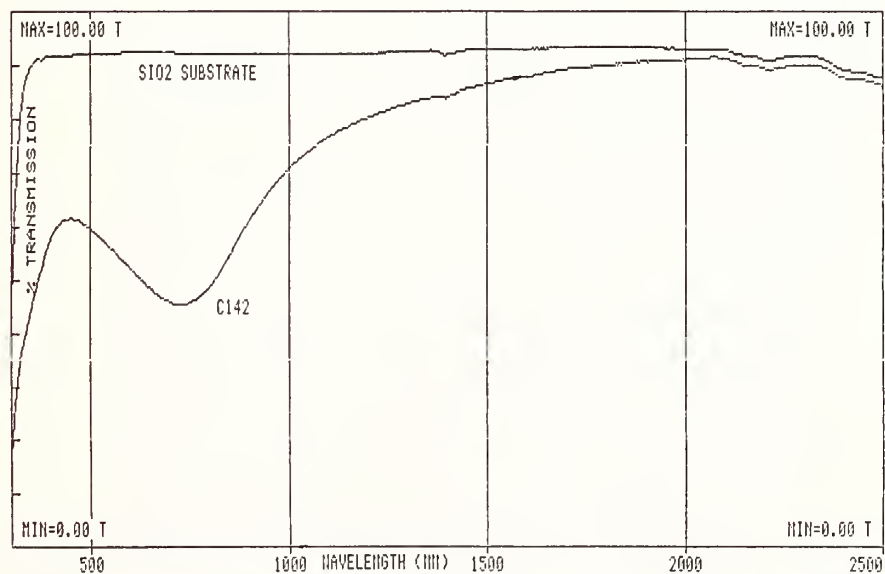


Figure 8. Transmittance curve for RF sputter-deposited silver on a glass substrate.

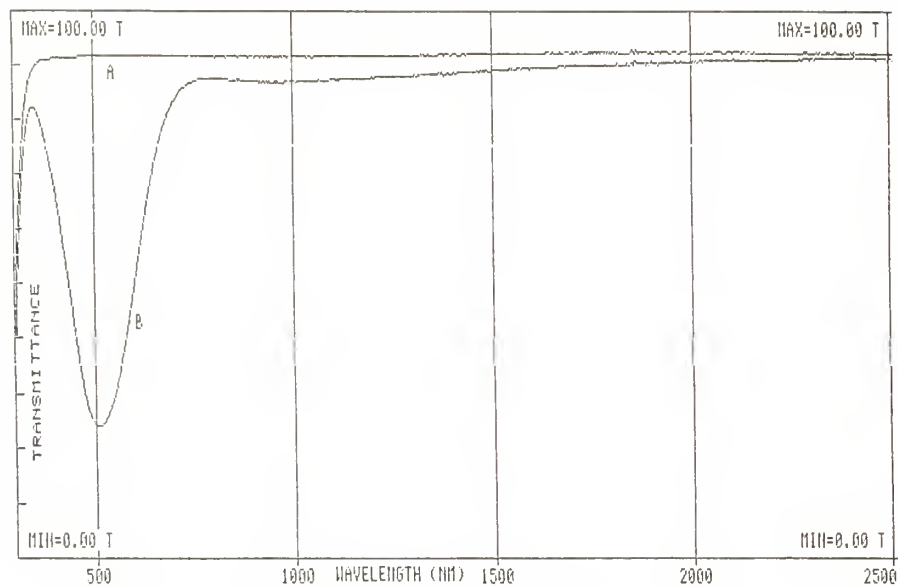


Figure 9. Transmittance curves for (a) a glass substrate, (b) 15 Å film of thermally evaporated silver on a glass substrate.

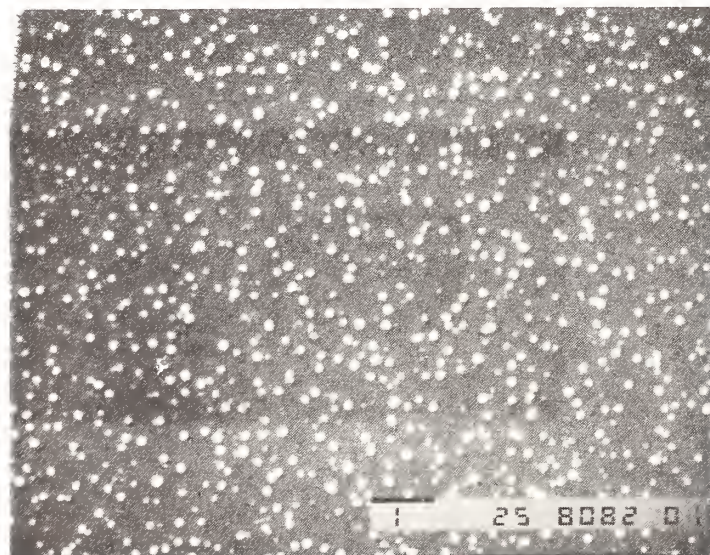


Figure 10. SEM micrograph of an RF sputter-deposited silver film.

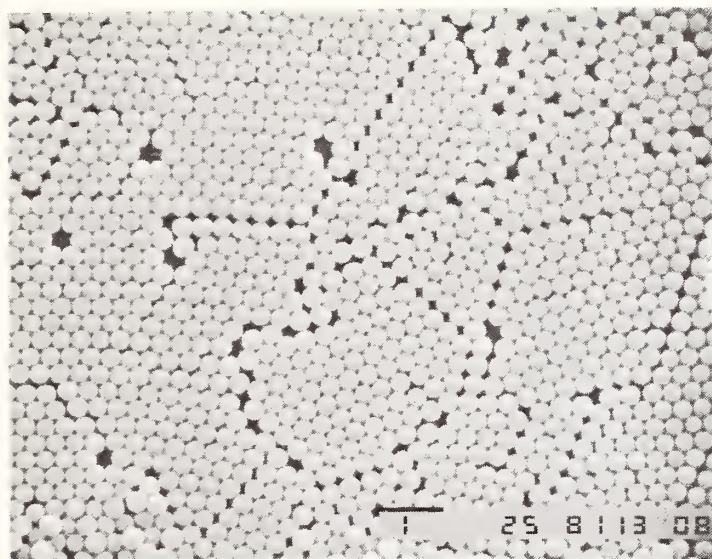


Figure 11. SEM micrograph showing the type of coverage that can be obtained by spin coating  $0.3\ \mu\text{m}$  diameter polystyrene spheres onto a glass substrate. The monolayer sphere coverage is 94%.

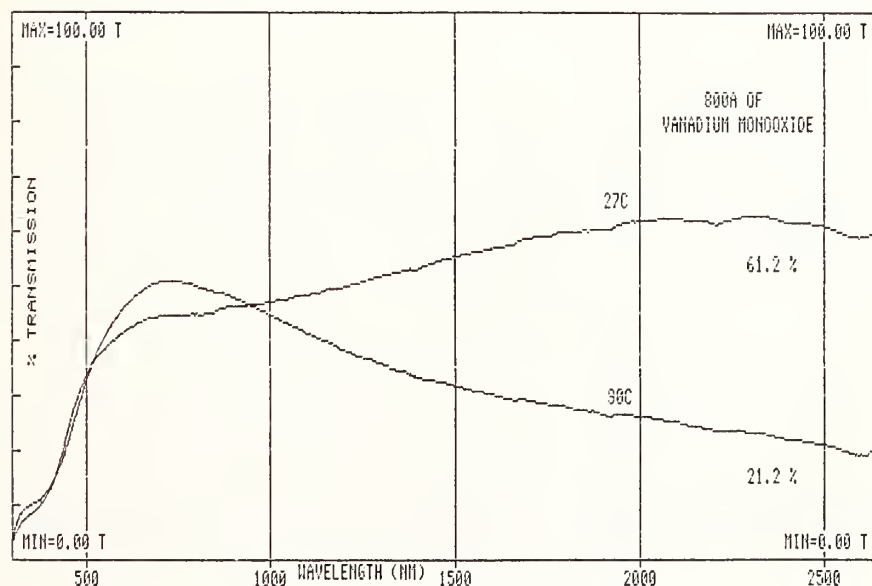


Figure 12. Transmittance curves for a continuous VO film annealed in air for 2.0 min at  $480^{\circ}\text{C}$ .





Figure 13. SEM micrograph of an annealed  $\text{VO}_2$  film after the polystyrene spheres were lifted off and the VO film was annealed in air.

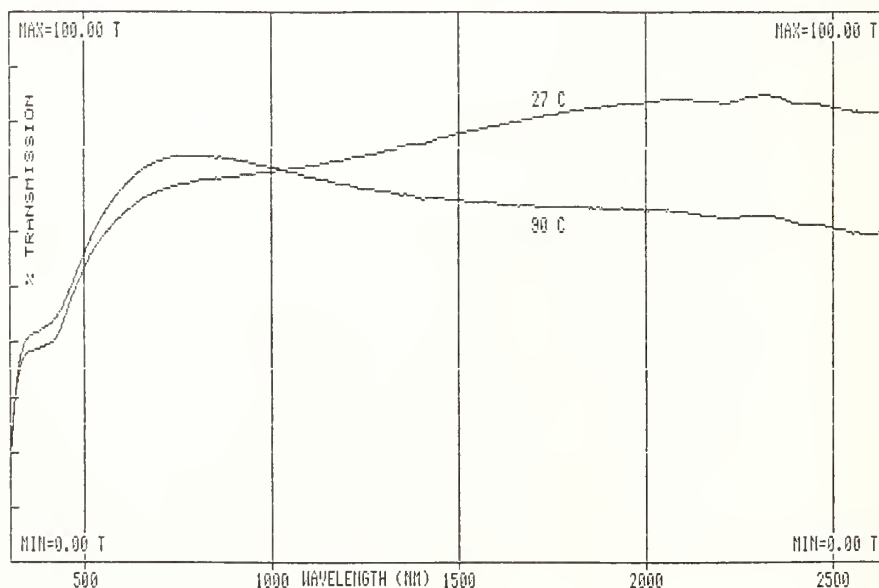


Figure 14. Transmittance spectra for island-type structures of  $\text{VO}_2$  on a glass substrate. These structures were produced by depositing VO on a polystyrene/glass substrate, lifting off the polystyrene spheres, and annealing the VO in air to form  $\text{VO}_2$ .

## Structural Damage and Analysis of the Nova Final Focusing Lenses

John H. Pitts

Lawrence Livermore National Laboratory  
P. O. Box 5508, L-481  
Livermore, California 94550-0618

Two types of damage (cracking and pitting) have been observed on the Nova fused-silica-glass final focusing lenses. Cracking occurred in the center of the vacuum (tension) face of one lens. We believe the cracking was a result of acoustic waves focusing radially on the axis of the lens, producing tensile stresses that exceeded the strength of the glass. This type of damage can result in catastrophic failure and in extensive damage to expensive equipment. This lens was removed immediately and pressure tested to failure. Failure occurred when a pressure difference of 150 kPa was placed across the lens—which is only 50% higher than the pressure difference at normal operating conditions.

Pitting occurs because laser light is diffracted and scattered around an apodized groove, concentrating in an annular region on the vacuum face. It also occurs at random locations when contaminants, adhering to the lens vacuum face, absorb laser light. In both cases, thermal stresses produce pitting; however, this pitting is not of structural concern because any flaws exceeding the fracture toughness of the glass propagate toward the vacuum face where the highest tensile stresses in the lenses exist.

Key Words: cracking; fracture toughness; laser damage; lenses; Nova; pitting; thermal stress

### 1. Introduction

The final focusing lenses of the Nova laser concentrate up to 100 kJ of energy on fusion targets placed at the center of a target chamber (see fig. 1). Because the target chamber is evacuated, these lenses also function as a vacuum barrier. Under normal laser operation, a pressure difference of 100 kPa exists across these lenses; this pressure difference produces tensile stresses in the lenses. We routinely inspect these lenses because the glass is brittle and these tensile stresses could cause lens failure. If failure occurred, it could result in extensive damage to expensive equipment. During these routine inspections, we noted two forms of damage on the vacuum (tension) face of the lenses.

First, we found a 30-mm-long crack at the center of the vacuum face of one lens. This damage occurred during a high-yield shot. We removed this lens immediately and pressure tested it to destruction [1]. Failure occurred when a 150-kPa pressure difference was placed across the lens for 100 minutes, which is only 1.5 times the magnitude of the pressure difference under normal operating conditions. We then made and tested four chevron-notched fracture toughness specimens from one of the remaining pieces of glass, and we found that the minimum fracture toughness [2] was 770 kPa  $\sqrt{\text{m}}$  with an average of 820 kPa  $\sqrt{\text{m}}$ . We also performed one flexure test and found the tensile strength to be 39 MPa. These results compare favorably with published values [3,4] of 750 kPa  $\sqrt{\text{m}}$  and 49 MPa, respectively.

We originally thought that the lens cracked because the back reflection of laser light from a calorimeter concentrated laser energy at the damaged location. However, Smith et.al. [5] later showed that the damage was caused by acoustic waves that were generated when stimulated Brillouin scattering was produced in the lens. The wave began as a compression wave and then propagated to the periphery of the lens where it reflected back as a tension wave. The magnitude of the tension wave increased as the wave focused on the lens axis, where it produced stress levels that were high enough to crack the glass.

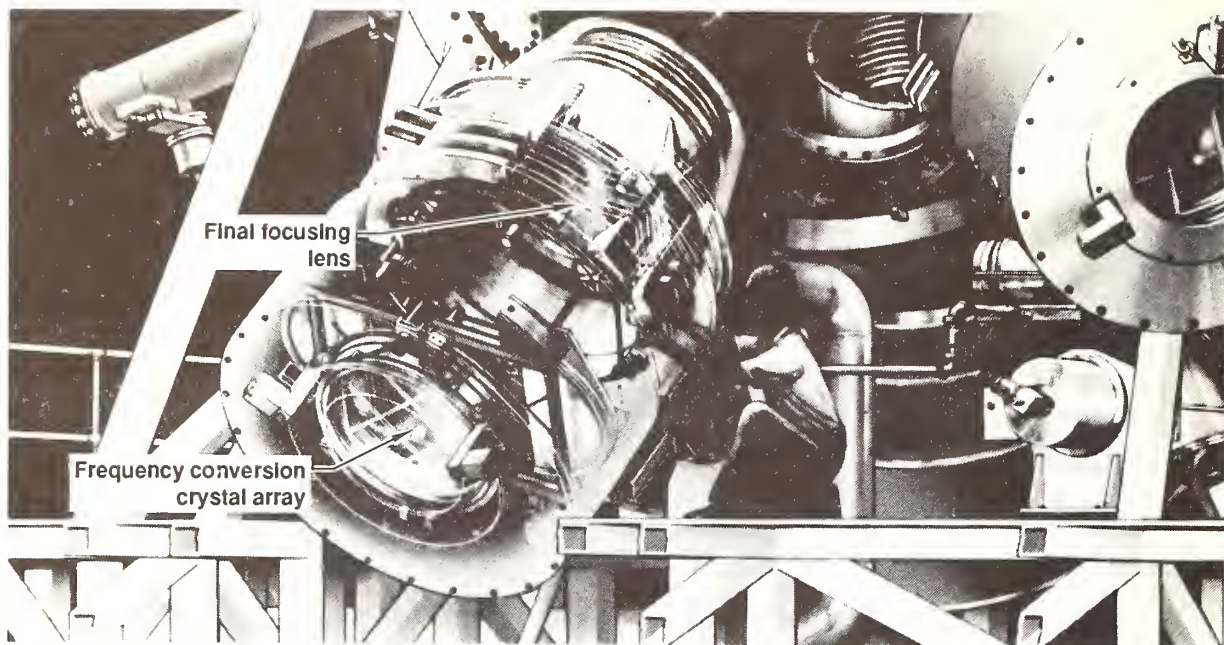


Figure 1. Cutaway view of a spool containing the final focusing lens and frequency-conversion crystal array for one of the 10 arms of the Nova laser. The final focusing lenses are made of silica glass and are 800 mm in diameter. These lenses form part of the vacuum barrier for the 2.2-m-radius aluminum target chamber.

Second, we observed pitting on the vacuum faces of all of Nova's final focusing lenses. This pitting covered a large area located opposite a groove that was first machined into the pressure (compression) face and then was apodized by bead blasting (see fig. 2). The pitting had an annular form with a diameter slightly larger than the edge of the apodizer. The pitting increased in width and depth with laser operation. Carbon contamination caused a substantial increase in the damage rate, but we found that this rate could be slowed by frequent cleaning [6]. A typical profile through the damaged area is shown in the detail drawing in figure 2(b). In this type of lens damage, the light passes through the lens near the edge of the apodizer, which diffracts and scatters it, concentrating it in one area. This concentrated light heats the glass and any contaminants present on the glass, producing thermal stress that damages the lens by chipping off shards. Once damaged, the lens becomes partially opaque and absorbs more light during the each successive laser shot, which produces additional thermal stress and chips off more shards.

We were initially concerned that stress concentrations coupled with flaws located at the sharp corners of the damaged area could result in catastrophic crack propagation. However, after using more refined inspection techniques, we found that thousands of small shards of glass were being chipped away during laser operation. In all cases, this cracking, which produced the shards, propagated to the vacuum surface of the lens without causing catastrophic failure.

Randomly spaced pitting was also observed on the vacuum face of all lenses [figure 2(a)]. This type of pitting results when opaque contaminants, particularly carbon, adhere to a sol-gel coating on the lens' vacuum face. Absorbed laser light heats the contaminants which in turn causes thermal stress in the lens. Shards of glass then chip off (in a fashion similar to that described above) at locations on the lens' vacuum face where the laser beam intensity is high.



## 2. Lens Stresses and Safety Factors

Williams [7,8] used a finite element stress analysis code to predict the stress state throughout a final focusing lens with and without an annular apodized groove on the compression (pressure) side. Nova's final focusing lenses have a diameter of 800 mm and are made of Corning 7940 silica glass. Williams found that the peak tensile stress with a 100-kPa pressure difference across a final focusing lens was 3.5 MPa and occurred at the center of the vacuum face. The stress on the vacuum face is nearly constant near the center of the lens and reduces to 2.3 MPa near the edge. Williams found that the tensile stress on the vacuum face was about the same with a groove as without one. A peak compressive stress of 9 MPa occurred at the bottom of the apodized groove; however, compressive stresses are not of concern because fracturing starts only where tension exists.

Hauber [9] designed Lawrence Livermore National Laboratory equipment (other than laser glass) that contained brittle, fused silica and other glasses. He incorporated a safety factor of 8 based on a brittle material's ultimate strength in these designs. Comparing Williams' predicted peak tensile stress of 3.5 MPa with our experimental ultimate tensile strength of 39 MPa shows that we have a safety factor of 11—which is 1.4 times higher than that used by Hauber. However, fracture mechanics is a more common method for predicting failure in brittle

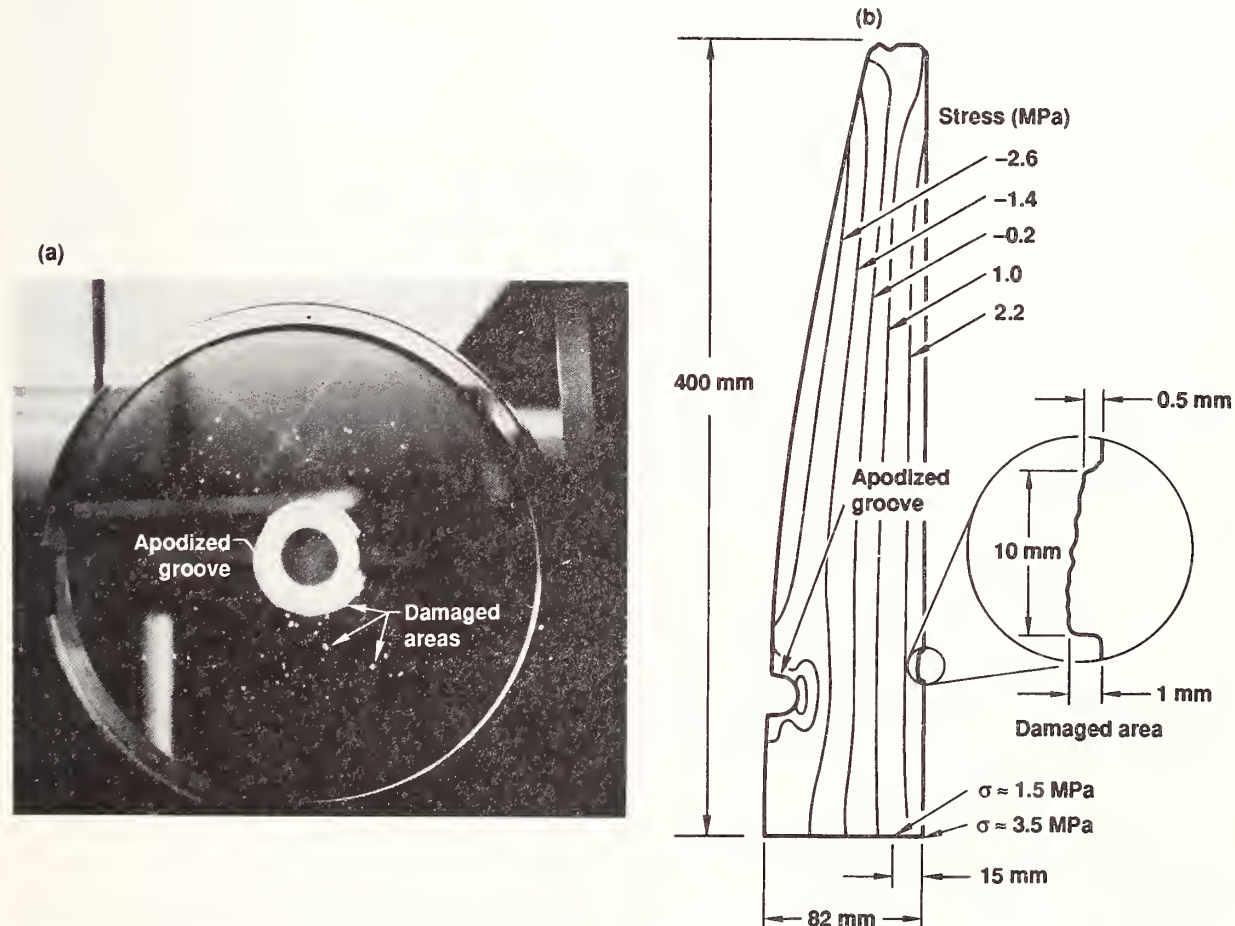


Figure 2. (a) Photograph of a damaged Nova final-focusing lens, and (b) a diagram of calculated stresses. (Negative values of stress denote compression; positive values denote tension.) The annular damaged area [shown in the detailed drawing of (b)] results from small shards of glass chipping off as diffracted and scattered laser light concentrates in the area. The randomly spaced damage shown in (a) is caused by opaque contaminants that adhere to the lens vacuum face and are heated as the contaminants absorb laser light. This results in thermal stress and pitting of the lens. The types of damage shown here are of little structural consequence.

materials. A critical crack radius,  $a$ , necessary to cause failure under our conditions of peak tensile stress,  $\sigma = 3.5$  MPa, and of fracture toughness,  $K_{Ic} = 750$  kPa  $\sqrt{\text{m}}$ , is

$$a > \left( \frac{K_{Ic}}{\sigma} \right)^2 / \pi = 15 \text{ mm.} \quad (1)$$

This calculated flaw size that will cause failure is large when compared with our experimental evidence, which suggests that Hauber's criterion is reasonable.

We applied fracture mechanics to calculate  $K_{Ic}$  in the lens that we pressure tested to failure. Visual inspection showed that the initial crack depth was about 15 mm, but the magnitude was difficult to accurately ascertain. The fracture toughness so calculated was 1.2 MPa  $\sqrt{\text{m}}$ , which is 50% higher than the value obtained from the fracture toughness specimens. This suggests that the actual crack depth was less than our visual estimate. Using this higher value of  $K_{Ic}$  gives an even longer calculated critical crack radius, which results in an even higher factor of safety.

Finally, we addressed the concern that stress concentrations at the corners of the pitted damage area in figure 2 could result in catastrophic failure. The highest tensile stresses occur at the vacuum face of the lens and decrease with depth into the lens. If a small flaw were present in the glass at the corner of the damage area and if a crack started to propagate from this flaw, the crack would tend to curve toward the vacuum face where the highest tensile stress is located. Further, a flaw tends to propagate more easily when it is oriented parallel to the lens face or when the tip of the flaw is closer to the lens face because in these cases the tip region where fracture occurs is located in a field of high tensile stress.

Conversely, if a flaw were oriented with the tip located further into the lens and, therefore, in a lower tensile stress field, then propagation is less likely. It is this type of crack orientation that could cause catastrophic failure because the crack would probably not reverse its direction before propagating through the thickness of the lens. Consider this example: a damaged area 1 mm deep and a flaw oriented into the lens with the tip located 15 mm away from the lens face. For crack lengths greater than about one-tenth the depth of the damaged area, Dowling [10] suggests that the critical crack radius,  $a$ , in eq. (1) can be equated to the sum of the depth of the damaged area plus the length of the crack without considering the stress concentration factor. In this example, the length of the crack would be 14 times the depth of the damaged area—well beyond the region where stress concentration factors need to be considered. To propagate, the flaw in this example must be located in a tensile stress field of ~3.5 MPa. The nominal tensile stress field calculated by Williams [7,8] at a depth 15 mm away from the lens vacuum face is about 1.5 MPa, which leads us to conclude that no crack propagation will occur. Our experimental evidence verifies this conclusion.

### 3. Summary and Conclusions

Nova's final focusing lenses are inspected routinely because catastrophic failure can cause extensive damage to expensive equipment. Two types of damage have been observed: cracking and pitting. A 30-mm-long crack appeared at the center of the vacuum face on one lens during a high yield shot. We removed the lens immediately, tested the lens to failure, and determined the structural properties of the lens glass. We believe that this type of failure occurred because an acoustic wave focused on the axis of the lens.

The second type of damage occurs continuously during laser operation and consists of pitting on the vacuum face opposite the apodizing groove. Damage results because diffracted and scattered light is concentrated in the area. Small shards of glass are chipped off, but analysis and experimental evidence show that this type of damage should not result in catastrophic failure. Randomly positioned pitting is also present and is caused by opaque contaminants adhering to a sol-gel coating on the lens vacuum face. The contaminants are heated as laser light energy is absorbed—causing thermal stress and pitting in lenses at locations where the laser beam intensity is high.



#### 4. Acknowledgments

The culmination of this work was possible only because of the efforts of many colleagues. All but two of these colleagues are referenced. D. Kyrakis offered direction and critique, and H. Patton worked hand in hand with us to resolve the issues documented herein. We extend our appreciation to all of these colleagues.

This work was performed under the auspices of the U. S. Department of Energy by the Lawrence Livermore National Laboratory under contract number W-7405-Eng-48.

#### 5. References

- [1] Engle, R. B., and Brown, A. E., "Acoustic Emission Monitoring of Pressure Tests on Primary Focus Lens 12," Lawrence Livermore National Laboratory, Livermore, Calif., internal memorandum to D. Kyrakis, July 31, 1987.
- [2] Riddle, R., and Freeman, D., "Fracture Toughness Tests on Nova Laser Glass," Lawrence Livermore National Laboratory, Livermore, Calif., internal memorandum MTE87-184 to D. Kyrakis and J. Pitts, September 11, 1987.
- [3] Marion, J., private communication, Lawrence Livermore National Laboratory, Livermore, Calif., 1987.
- [4] Mazurin, O. V., Streltsina, M. V., and Shvaiko-Shvaikozskaya, T. F., Handbook of Glass Data, Elsevier Press, Amsterdam, Part A, 1983, p. 123.
- [5] Smith, J. R., et. al., "Acoustic Damage to Large-Aperture Optics," Lawrence Livermore National Laboratory, Livermore, Calif., UCRL-99316, Rev. 1, 1988.
- [6] Wegner, P., Hatcher, C. W., and Price, C. W., "Damage to Target Chamber Optics," Lawrence Livermore National Laboratory, Livermore, Calif., UCRL-50021-87, in press.
- [7] Williams, J., "Stress Analysis of Annular Groove on Nova f4.3 Focus Lens," Lawrence Livermore National Laboratory, Livermore, Calif., internal memorandum Nova TGT 83-16 to L. Seppala, March 1, 1983.
- [8] Williams, J., "Stress Analysis of Annular Groove on Nova f4.3 Focus Lens," Lawrence Livermore National Laboratory, Livermore, Calif., internal memorandum Nova TGT 83-72 to W. Simmons, December 2, 1983.
- [9] Hauber, J., private communication, Lawrence Livermore National Laboratory, Livermore, Calif., 1987.
- [10] Dowling, N. E., "Fatigue at Notches and the Local Strain and Fracture Mechanics Approaches," in Fracture Mechanics, ASTM STP-677, C. W. Smith, ed., American Society of Testing Materials, Philadelphia, 1979, pp. 247-273, with particular attention to pp. 253-255.

## Photoconductivity Study of Charge-Producing Defects in $\text{CaF}_2$ \*

Robert M. O'Connell  
Electrical and Computer Engineering Department  
University of Missouri, Columbia, Missouri 65201

C. Denton Marrs  
Physics Division, Research Department  
Naval Weapons Center, China Lake, California 93555-6001

A study of linear and nonlinear photoconductivity (PC) in  $\text{CaF}_2$  is reported. Linear spectral scans from 800 (1.55) to 200 nm (6.20 eV) revealed PC peaks at 280 and 306 nm, which varied in strength with certain trivalent trace-element impurities. To explain these results, a defect model based on charge-compensating interstitial fluorine is proposed. The behavior of the peak photocurrents produced with variable energy pulses from a 496.5-nm laser was highly nonlinear, indicating the occurrences of multiphoton absorption and electron avalanche. The data asymptotically approached the material laser damage threshold of approximately 27 GW/cm<sup>2</sup>. Time-domain measurements showed that the pulse-induced photocurrent tracks the laser during charge generation and recombines with a lifetime of 0.5 ms.

Key words:  $\text{CaF}_2$ ; coloration threshold; electron avalanche; interstitial fluorine; multiphoton absorption; photoconductivity; recombination lifetime; trivalent impurities.

### 1. Introduction

Calcium fluoride ( $\text{CaF}_2$ ) is a popular wide-band-gap window material for high-power laser systems. As is true of all optical materials, it can be damaged by a sufficiently intense optical beam, even if the photon energy in the beam is much smaller than the band gap. Charge-producing crystalline defects, which may be present in only very low concentrations, are suspected of causing this damage by participating in nonlinear processes that lead to electron avalanche.

In order to investigate the role of charge-producing defects in laser damage to  $\text{CaF}_2$ , a photoconductivity (PC) study of the material was performed. The PC technique was used because it is a nondestructive and highly sensitive method for probing low-density charge-producing defects. This paper presents and discusses the results of that study.

Descriptions of the  $\text{CaF}_2$  samples studied and the PC facility used to perform the measurements are followed by the results of linear PC spectral scans from 800 (1.55) to 200 nm (6.20 eV). A specific defect model to explain the features of the linear data is proposed. Next, the results of nonlinear PC measurements made with 496.5-nm, 950-ns laser pulses are presented and interpreted in terms of multiphoton absorption, electron avalanche, and the onset of coloration of the material. Finally, the measured temporal behavior of the laser-pulse-induced photocurrent is discussed.

---

\*This work was supported by Navy Independent Research funds.

## 2. CaF<sub>2</sub> Samples

Six CaF<sub>2</sub> samples from three manufacturers were used in the PC study. Information about the composition of each sample and the specific measurements in which it was used are summarized in table 1. The four samples from BDH Ltd. listed in the table contained different proportions of Optipur (a high-purity synthetic CaF<sub>2</sub>) and a naturally occurring Mexican-grade CaF<sub>2</sub> (containing significant amounts of yttrium, lanthanum, and several other rare earth metals). The most significant of these and their concentrations in parts per million (ppm) (determined by mass spectroscopy [1]<sup>1</sup>) in the Optipur and Mexican grades of CaF<sub>2</sub> are given in table 2 along with their trivalent ionic radii. These data will be used to interpret the results of the PC measurements in Section 4.

Table 1. Composition information and measurement summary for the six CaF<sub>2</sub> samples used in the investigation. LS = linear spectral scan; NL = pulsed nonlinear PC measurement; TD = pulsed-mode time-domain measurement.

Sample	Composition information	PC measurements
Optovac	none available	LS, NL
Harshaw	none available	LS
BDH:A <sup>a</sup>	100% Optipur	LS, NL, TD
BDH:C	50% Optipur, 50% Mexican	LS, NL
BDH:E	100% Mexican	LS
BDF:F	100% Optipur with cerium contamination	LS

<sup>a</sup>The four BDH samples were provided by Professor D. Emmony, University of Technology, Loughborough, U.K.

Table 2. Concentrations (ppm) and trivalent ionic radii of the most significant trace-element impurities in the Optipur and Mexican grades of CaF<sub>2</sub> used in the four BDH samples listed in table 1.

Impurity element	ppm in Optipur	ppm in natural Mexican	Trivalent ionic radius (Å)
Yttrium (Y)	< 0.1	30	0.89
Lanthanum (La)	< 0.1	10	1.02
Cerium (Ce)	< 0.13	3	1.03
Praseodymium (Pr)	< 0.1	3	1.01
Neodymium (Nd)	< 0.4	3	1.00
Samarium (Sm)	< 0.4	< 0.6	0.96
Europium (Eu)	< 0.2	0.6	0.95
Gadolinium (Gd)	< 0.3	2.0	0.94
Terbium (Tb)	< 0.1	0.3	0.92
Dysprosium (Dy)	< 0.1	1.0	0.91
Holmium (Ho)	< 0.1	0.3	0.89
Erbium (Er)	< 0.3	1.0	0.88
Ytterbium (Yb)	< 0.3	< 0.6	0.86

<sup>1</sup>Numbers in brackets indicate the literature references at the end of the paper.

### 3. Experimental Details

The experimental arrangement used in the PC measurements is illustrated in figure 1. A DC circuit is designed to measure photocurrents produced when photons are absorbed by crystalline defects and produce free charge carriers in the conduction band. The wide band gap of the crystal ensures that the electrodes are nonohmic, i.e., blocking electrodes. Thus, the photocurrent is a displacement current associated with the motion of the photo-generated charge in the electric field produced by the bias voltage ( $V_{DC}$ ). The magnitude of  $V_{DC}$  varied from -1000 to -3000 V in the measurements.

The sample under test was mounted in an aluminum vacuum chamber that was typically evacuated to  $10^{-5}$  torr to prevent electrode-to-electrode breakdown along the edges of the sample. The electrode arrangement was the same as that used by Lee *et al.* [2]. The ground electrode was constructed from brass; the front or bias electrode was constructed from 28-mesh etched nickel screen supported by an aluminum ring. The nickel mesh was used to optimize the uniformity of the electric field in the sample. Together, the sample holder and aluminum vacuum chamber constituted a guard ring to minimize the effects of ground loops.

For the linear PC measurements, light from a 450-W UV-enhanced xenon arc lamp was dispersed with a 2.6-nm bandpass McPherson 218 scanning monochromator before entering the vacuum chamber through a fused-silica window. Because the monochromator uses a grating to disperse the light, optical cutoff filters were used to prevent false PC readings resulting in higher order wavelength effects. As illustrated in figure 1, the light from the arc lamp then illuminated the  $\text{CaF}_2$  test sample from the front, i.e., through the nickel mesh electrode. By arranging the polarity of  $V_{DC}$  as shown in figure 1 (i.e., with a large negative potential on the nickel electrode), any photoelectrons generated there would be rejected, thereby eliminating interference in detecting small internally generated photocurrents. Those currents were measured with a Keithley 640 vibrating reed electrometer. By interfacing the spectral position of the monochromator to the x-axis of an X-Y recorder (through a potentiometer) and using the electrometer current to drive the y-axis of the recorder, the spectral scans presented and discussed in Section 4 were produced.

Nonlinear PC measurements were made by illuminating the  $\text{CaF}_2$  samples from the side (see figure 1) through a fused-silica window with 950-ns-wide pulses from a 496.5-nm-wavelength dye laser. Neutral density filters were used to vary the laser pulse energy, which was monitored with a Gentek pyroelectric energy meter. Considering the inherent accuracy of the energy meter ( $\pm 2\%$ ) and the pulse-pulse stability of the laser ( $\pm 5\%$ ), the laser pulse energies were probably accurate to within  $\pm 7\%$ . By varying the laser pulse energy in this manner and recording the resulting peak photocurrent with the X-Y recorder, the peak-photocurrent-versus-laser-pulse-energy data were generated.

To measure the temporal behavior of pulse-induced photocarriers, the electrometer was replaced with a 216-M $\Omega$  resistor, as illustrated in figure 1. The sample was then illuminated with a laser pulse of known energy, as in the nonlinear PC measurement, and the voltage across the 216-M $\Omega$  resistor was recorded with an oscilloscope. This procedure led to the photographs presented and discussed in Section 6.



## 4. Linear PC Spectral Scans

### 4.1 Data

Although the spectral scans covered the wavelength range from 800 to 200 nm, significant photocurrents were observed only in the lower half of that range. The appropriate data for the Optovac and BDH samples are shown in figures 2 through 6. The PC spectrum from the Harshaw sample was similar to that from the Optovac sample and is not shown. The error bars on the PC spectra represent the peak-to-peak variation in the background noise.

Note that the PC spectra shown in figures 2 through 6 have not been normalized to a constant photon flux, i.e., scaled appropriately to account for the relative spectral output of the arc lamp. However, since the output spectra of typical UV-enhanced xenon lamps are known to roll off relatively slowly with decreasing wavelength, normalization will not significantly affect the data.

There are several noteworthy features in the spectra of figures 2 through 6. First, they all have a high-energy peak in the neighborhood of 280 nm. Because of the relatively wide bandwidth of the data, the peak wavelengths at 282 and 285 nm in the BDH sample data are not considered significantly different from the 275-nm peak in the Optovac sample data. Thus, it is assumed that these peaks all represent the same charge-producing defect. The second noteworthy feature of the data is that only three of the four BDH samples had a lower energy peak at approximately 306 nm. Finally, note that the spectra of the BDH samples have broad low-energy tails that taper off very slowly. This is most evident in figure 4, where the strongest photocurrent was measured. Thus, there is some finite, albeit weak, photoconductivity at 496.5 nm. This result is important for understanding the results of the nonlinear PC measurements discussed in Section 5.

### 4.2 A Tentative Defect Model

In order to develop a physical explanation for the peak wavelengths (at approximately 280 and 306 nm) observed in figures 2 through 6, let it be understood that they are not among those associated with the well-known color centers in  $\text{CaF}_2$ . Thus, it appears reasonable to rule out excess  $\text{Ca}^{+2}$ , which is responsible for absorption bands at 375 and 525 nm, and  $\text{Y}^{+2}$ , which is produced by either e-beam or x-ray irradiation of the impurity yttrium and is responsible for absorption bands at 225, 335, 400, and 580 nm [3-5]. Furthermore, BDH sample A produced the weakest photocurrent ( $2 \times 10^{-14}$  amps) of the six samples studied. Since sample A was composed of 100% Optipur material and thus had the smallest trace-element impurity content (see table 2), it is reasonable to assume that the observed PC signals are related in some way to the impurities listed in table 2.

Assuming that the impurities in table 2 played a causative role in the observed PC, note that the preferred valence of each of the impurities is 3, i.e., they are trivalent. Substantial research has been conducted on trivalent impurities in  $\text{CaF}_2$  and other alkaline-earth fluorides, some of which can be applied to our problem.

It is well established that trivalent impurities in  $\text{CaF}_2$  replace  $\text{Ca}^{+2}$  ions substitutionally and are charge compensated by fluorine ions ( $\text{F}^-$ ) that occupy either nearest-neighbor (nn) or next-nearest-neighbor (nnn) interstitial positions [6-10]. These points are clarified in figure 7, which illustrates the unit cell of  $\text{CaF}_2$ . The cell can be thought of as consisting of eight cubes with  $\text{F}^-$  ions on all the corners and four  $\text{Ca}^{+2}$  ions in the centers of alternating cubes. When one of the  $\text{Ca}^{+2}$  ions is replaced with a trivalent impurity, the charge-compensating  $\text{F}^-$  ion occupies the center of either an adjacent cube (the nn interstitial



position half a lattice constant away) or a next nearest empty cube (the nnn interstitial position  $a\sqrt{3}/2$  away). For reasons of symmetry, these nn and nnn pairs are called tetragonal and trigonal dipolar defect complexes, respectively.

The relative amounts of nn and nnn complexes in  $\text{CaF}_2$  appears to depend in some way on the impurity. For example, nn and nnn complexes of  $\text{Y}^{+3}-\text{F}^-$  have been shown to be present in the ratio 1.53 to 1 [9]. Similarly, defect complexes formed with  $\text{Gd}^{+3}$ ,  $\text{Er}^{+3}$ , and  $\text{Yb}^{+3}$  also have been shown to be predominantly tetragonal [11]. However, predominantly trigonal complexes are evidently possible also. It has been shown [12], for example, that in  $\text{SrF}_2$  the relatively small ions  $\text{Yb}^{+3}$  and  $\text{Lu}^{+3}$  form trigonal defect complexes and the relatively large ions  $\text{La}^{+3}$ ,  $\text{Ce}^{+3}$ , and  $\text{Pr}^{+3}$  form tetragonal complexes. Thus, there may be a correlation between the relative sizes of the impurity and displaced host ion and the type of defect complex formed.

The Coulombic association energies of tetragonal and trigonal complexes of  $\text{Y}^{+3}-\text{F}^-$  have been studied previously. It is determined that they are approximately 0.48 and 0.28 eV, respectively [11]. This means simply that the nn  $\text{Y}^{+3}-\text{F}^-$  ion pair is more tightly bound than the more widely separated nnn pair.

In consideration of these results, the following explanation for the peak wavelengths in the PC spectra is proposed. First, the PC peaks at 280 and 306 nm are due to nn and nnn defect complexes, respectively. This is consistent with a higher association energy for the nn complexes [11]. Furthermore, the energy separation of the two peak PC signals is approximately 0.38 eV. This agrees well with the 0.2-eV difference in the association energies of nn and nnn  $\text{Y}^{+3}-\text{F}^-$  defect complexes [11], considering the approximate nature of the association energy calculation [11] and the fact that the PC spectra have not been normalized to the xenon lamp spectrum.

Next, the two peaks in the PC spectra can be associated with the ionic radii of the impurities.  $\text{Y}^{+3}$ ,  $\text{Gd}^{+3}$ ,  $\text{Er}^{+3}$ , and  $\text{Yb}^{+3}$  are known to form predominantly nn complexes [9,11]. As shown in table 2, their ionic radii are all smaller than that of the  $\text{Ca}^{+2}$  ion that they replace (0.99 Å). If, as suggested by den Hartog [12], an ionic radius association with defect type is valid, it is likely that the other impurities in table 2 with ionic radii smaller than 0.99 Å (i.e.,  $\text{Sm}^{+3}$ ,  $\text{Eu}^{+3}$ ,  $\text{Tb}^{+3}$ ,  $\text{Dy}^{+3}$ , and  $\text{Ho}^{+3}$ ) also form predominantly nn complexes. As stated above, these nn defects would be associated with the high-energy peak in the PC spectra. Those ions in table 2 with radii larger than 0.99 Å (i.e.,  $\text{La}^{+3}$ ,  $\text{Ce}^{+3}$ ,  $\text{Pr}^{+3}$ , and  $\text{Nd}^{+3}$ ) would, in this model, form nnn defect complexes and be associated with the low-energy peak in the PC spectra.

The proposed model now can be used to explain the origin of the PC peaks in figures 3 through 6. Since no impurity information on the Optovac and Harshaw samples exists, they will not be included in the discussion. The impurity data in table 2 show that the Optipur material used in making the BDH samples contained at least three times as many small radius ionic impurities as large radius impurities. Thus, nn defect complexes should predominate in Optipur  $\text{CaF}_2$ ; since BDH sample A was composed of 100% Optipur material, it should show evidence of this predominance. As figure 3 shows, the PC spectrum from this sample has only a high-energy peak, suggesting the presence of mainly nn defects, in agreement with our model. The spectra from the other three BDH samples have a low-energy peak in addition to the high-energy peak. Thus, their impurity contents should show a much larger proportion of nnn defects (i.e., large-radius ions), and they do. For example, BDH sample F was different from sample A only in that it was contaminated with cerium. The low-energy PC peak shown in figure 6 can have been caused only by the cerium, which (consistent with our model) has a large ionic radius and should therefore form the nnn defects associated with the low-energy PC signal. Note that the cerium probably forms a

substantial number of nn defects, too, because the strength of the high-energy PC peak increases from figure 3 to figure 6. Similar arguments can be made about BDH samples C and E (figures 4 and 5, respectively), which contained 50 and 100% natural Mexican  $\text{CaF}_2$ , respectively (i.e., larger proportions of the large-radius ions characteristic of the low-energy peaks in their PC spectra).

Having proposed that the PC signals in figures 2 through 6 are the result of nn and nnn complexes formed by trivalent substitutional impurities and interstitial fluorine ions, it should be possible to explain how these defects contribute charge to the measured photocurrent. It should be possible also to associate the actual absorbed energy (from the PC spectra) with a calculated estimate of the energy needed to release charge from the defect complex into the crystal. It is proposed that PC occurs when the extra electron associated with the  $\text{F}^-$  ion in the defect complex absorbs a photon of either 4.43 eV (the high-energy case associated with nn complexes) or 4.05 eV (the low-energy case associated with nnn complexes) and is raised to an excited state from which it is released thermally into the conduction band. This mechanism is suggested; it is not a direct transition to the conduction band since the PC spectra have peaks at certain photon energies rather than a monotonically increasing behavior.

The energy  $E_B$  needed to remove the extra electron from a  $\text{F}^-$  ion in the proposed defect complex can be estimated in terms of the electron affinity  $E_A$  of the free ion and the energy  $E_L$  due to the influence of the crystal lattice on the electron [13], i.e.,

$$E_B = E_A + E_L \quad , \quad (1)$$

where  $E_L$  can be found using a Born model calculation [14,15], i.e.,

$$E_L = E_M - E_R + E_V - E_Z \quad . \quad (2)$$

In equation (2),  $E_M$ ,  $E_R$ ,  $E_V$ , and  $E_Z$  represent the energies associated with Coulombic point charge (Madelung) effects, repulsion due to core electrons of surrounding ions, van der Waals forces, and the zero point (Uncertainty Principle), respectively. Generally,  $E_V$  and  $E_Z$  are much smaller than  $E_M$  or  $E_R$  [13] and will be neglected here. Combining equations (1) and (2), we have

$$E_B = E_A + E_M - E_R \quad . \quad (3)$$

Electron affinities of various ions are available to evaluate equation (3) [16], i.e., for  $\text{F}^-$ ,  $E_A = 3.45$  eV; however, the Madelung and repulsive energies must be calculated.  $E_M$  is found by evaluating the expression [13,15]

$$E_M = \frac{1}{4\pi\epsilon_0} \frac{\alpha_x}{x} \quad , \quad (4)$$

where  $\epsilon_0$  is the permittivity of free space ( $8.854 \times 10^{-12}$  F/m), and  $\alpha_x$  is the Madelung constant [15,17] at a given position in the crystal in terms of some reference length  $x$ , such as the lattice constant  $a$ . Various methods have been developed for evaluating Madelung constants [15], and results applicable to our problem are available [18]. For example, at the site of a lattice  $\text{F}^-$  ion,  $\alpha_a = 4.071$  [18], where the lattice-constant  $a = 5.463$  Å. For comparison, this Madelung constant will be used in equation (3) to estimate the binding energy of the electron on a lattice  $\text{F}^-$  ion. It should resemble the band-gap energy of the material. At an interstitial position, where our  $\text{F}^-$  defect ion would be located,  $\alpha_a = -0.5756$  [18]. This value can be easily corrected for the presence of a trivalent ion rather than a  $\text{Ca}^{+2}$

ion in an nn site, giving  $\alpha_a = 1.424$ . Repulsive energies are determined with a procedure detailed in reference 15 and applied to  $\text{CaF}_2$  in reference 13. The result for a lattice  $\text{F}^-$  ion is  $E_R = 2.76$  eV. When the same equations are applied to the case of an interstitial  $\text{F}^-$  ion,  $E_R = 2.84$  eV.

The numbers just determined are listed in table 3, along with the values of  $E_B$  found by using them in equation (3). Note that the binding energy of a lattice ion ( $\text{F}_s^-$ ) calculated this way (11.42 eV) agrees quite well with the band-gap energy of  $\text{CaF}_2$  (12.2 eV [18]). This is as expected and lends credibility to the use of equation (3). Note also that the calculated binding energy of the  $\text{F}_i^-$  ion in an nn defect complex (4.37 eV) compares very well with the photon energy of the high-energy peak in the PC data (4.43 eV), which is proposed to be associated with nn defect complexes.

Table 3. Quantities calculated for use in evaluating the binding energy  $E_B$  of the extra electron on a lattice fluorine ion ( $\text{F}_s^-$ ) and on a fluorine ion in an nn defect complex ( $\text{F}_i^-$ ).

	$E_A$ (eV)	$a$ (Å)	$\alpha_a$	$E_M$ (eV)	$E_R$ (eV)	$E_B$ (eV)
$\text{F}_s^-$	3.45	5.463	4.071	10.73	2.76	11.42
$\text{F}_i^-$	3.45	5.463	1.424	3.76	2.84	4.37

Although the calculated values of  $E_B$  for the  $\text{F}_s^-$  and nn  $\text{F}_i^-$  ions agree well with the expected values, there remain some points that do not agree as well. For example, when the calculation is repeated for the nnn  $\text{F}_i^-$  ion, equation (3) yields  $E_B = 2.13$  eV, which is significantly less than the photon energy of the low-energy peak in the PC data (4.05 eV).

## 5. Nonlinear PC Results

Nonlinear PC data measured as described in Section 3 (950-ns-wide laser pulses at 496.5 nm) were obtained from the Optovac sample and BDH samples A and C. The results are shown in figures 8 through 11. Note that the laser was focused inside the Optovac and BDH:A samples (figures 8 and 9) and both inside and outside the BDH:C sample (figures 10 and 11, respectively).

Examination of the data in figures 8 through 11 reveals several interesting features. First, at low laser pulse energies, the slopes of all four plots are between 1 and 2, indicating the presence of charge-producing defects that absorb at 496.5 nm. This verifies the statement made in Section 4.1 that there was some very small but finite linear PC at 496.5 nm.

A second interesting feature of the data is the nonlinear increase of photocurrent with increasing laser pulse energy in figures 9 through 11. Figure 8 shows no such behavior in the Optovac sample, probably because the pulse energies were simply not high enough to see the nonlinear effects. The nonlinear behavior seen in figures 9 through 11 suggests the onset of multiple-photon-induced PC, which adds to the one-photon linear effect at 496.5 nm. Note that two-photon PC would occur at 248.3 nm, a wavelength at which the linear PC spectra of figures 2 through 6 show significant photoresponse. Three-photon effects at 165.5 nm are also possible; however, since the linear PC was not measured at this wavelength, only speculation to that possibility is suggested.



The effects of focusing the laser inside or outside the  $\text{CaF}_2$  sample are compared in figures 10 and 11. The illuminated volume was much smaller when the laser was focused inside the sample; the photon density was much greater than when the laser was focused outside the sample. Thus, the photocurrent saturation apparent in figure 10 (laser focused outside) is probably due to space charge effects in the larger illuminated volume. No such saturation is apparent in figure 11 (laser focused inside), probably because the photo-induced charge could easily diffuse away from the smaller illuminated volume. Note also that at any given laser pulse energy below the onset of space charge effects, the photo-response was greater in figure 10 (laser focused outside) than in figure 11 (laser focused inside). The difference can be explained as a greater number of charge carriers generated by the unfocused beam. It is likely that the photon density in the focused beam was great enough to sufficiently deplete the low charge-producing defect population so that many photons were not absorbed. In the unfocused-beam situation with the same number of photons spread over a larger volume, less if any of this bleaching occurred, resulting in more absorbed photons and more photocurrent.

Finally, note that the near-vertical slopes of the focused-laser data in figures 9 and 11 at laser pulse energies above 300 mJ suggest the onset of electron avalanche. The samples (BDH:A and C) were slightly colored (blue) at these pulse energies, but not catastrophically damaged, suggesting that nonlinear PC measurements may constitute a nondestructive method of estimating the laser damage threshold of an optical material. In figures 9 and 11, the vertical line represents the asymptote to the experimental data. This asymptote would be the laser damage threshold, i.e., catastrophic failure, of the material. The laser damage threshold is approximately 500 mJ for these  $\text{CaF}_2$  samples. When the pulse width (950 ns) and spot size (estimated to be approximately 50  $\mu\text{m}$  in diameter) of the laser beam are taken into account, the laser damage threshold is estimated to be approximately 27  $\text{GW}/\text{cm}^2$ .

## 6. Temporal Behavior of Pulse-Induced Photocarriers

Figure 12 shows an oscilloscope trace of the voltage induced across the 216-M $\Omega$  resistor in figure 1 during illumination of BDH sample A by a 400-mJ pulse from the 496.5-nm laser. From the photo, it is evident that the signal decayed with an  $e^{-1}$  time constant  $T_M$  of approximately 440  $\mu\text{s}$ . The leading edge of the signal in figure 12 is shown on a wider time base in the upper trace of figure 13, along with the response of a fast PIN diode to the laser pulse. The two signals were measured simultaneously, so the photo shows their true temporal relationship. Notice that the photocurrent signal begins simultaneously with the laser pulse and continues to rise until the laser pulse has fallen back to zero. This shows that the laser-induced photocurrent tracks the laser pulse and has a rise time of approximately 1  $\mu\text{s}$ .

The 440- $\mu\text{s}$  decay time  $T_M$  associated with the falling edge of the signal in figure 12 can be used to infer the recombination lifetime  $T_R$  of the laser-induced photocarriers. Note that the  $\text{CaF}_2$  crystal and holder electrodes in figure 1 constitute a capacitor. Thus, the photocurrent can either decay through the 216-M $\Omega$  resistor or recombine in the crystal. Actually, both avenues are used, so that the net rate of decay is the sum of the rates associated with both processes. Thus, we can write

$$\frac{1}{T_M} = \frac{1}{T_{RC}} + \frac{1}{T_R}, \quad (5)$$

where  $T_M$ ,  $T_{RC}$ , and  $T_R$  represent the measured decay time (440  $\mu\text{s}$ ), the RC time constant of the 216-M $\Omega$  crystal capacitance combination, and the actual recombination lifetime of the photocarriers, respectively. A careful measurement of the crystal capacitance, including

everything between the input and the output of the vacuum chamber in figure 1, showed its value to be 16.7 pF. Thus,  $T_{RC} = 3.6$  ms and  $T_R = 0.5$  ms. Although it has not been done at this point, it should be possible to associate this recombination lifetime with a specific type of defect and thereby gain additional information that would tend to support or dispute the proposed model.

## 7. Summary and Conclusions

Linear photoconductivity (PC) measurements in  $\text{CaF}_2$  produced significant photocurrents in the spectral range from 275 to 350 nm. The linear PC results varied with the concentrations of certain trace element impurities and are thought to be due to charge-producing defects that involve those impurities.

A tentative model of the charge-producing defect is proposed. It involves electron removal from interstitial fluorine ions that enter to charge-compensate the trace-element impurities. A Born-model estimate of the electron binding energy of the proposed defect agrees well with the photon energy of the peak PC signal.

Nonlinear PC measurements at 496.5 nm revealed a steady transition with increasing laser pulse energy from one- to two-photon absorption to the possible onset of electron avalanche. The onset of coloration—not catastrophic damage—at the higher laser pulse energies suggests that nonlinear PC can be used as a nondestructive estimator of the laser damage threshold.

Measurement of the temporal decay of the photocurrent induced by 400-mJ laser pulses and consideration of the crystal capacitance showed the recombination lifetime of the photocarriers to be 0.5 ms.

## 8. References

- [1] Emmony, D. C. Private communication.
- [2] Lee, R. S.; Merklin, J. F.; Marrs, C. D.; Richter, M. H. "Impurity photoconductivity of  $\gamma$ -irradiated LiF," *Phys. Status Solidi (b)* 103; 605; 1981.
- [3] Messner, D.; Smakula, A. "Color centers in alkaline-earth fluorides," *Phys. Rev.* 120; 1162; 1960.
- [4] Scouler, W. J.; Smakula, A. "Coloration of pure and doped calcium fluoride crystals at 20°C and -190°C," *Phys. Rev.* 120; 1154; 1960.
- [5] O'Connor, J. R.; Chen, J. H. "Color centers in alkaline earth fluorides," *Phys. Rev.* 130; 1790; 1963.
- [6] Zintl, E.; Udgard, A. *Z. Anorg. u. allgem. Chem.* 240; 150; 1939.
- [7] Southgate, P. D. "Anelastic and dielectric loss in yttrium-doped calcium fluoride," *J. Phys. Chem. Solids* 27; 1623; 1966.
- [8] Short, J.; Roy, R. "Confirmation of defect character in calcium fluoride-yttrium fluoride crystalline solutions," *J. Chem. Phys.* 67; 1860; 1963.



- [9] Stott, J. P.; Crawford, J. H. "Dipolar complexes in calcium fluoride doped with erbium," *Phys. Rev. Lett.* 26; 384; 1971.
- [10] Ure, R. W. *J. Chem Phys.* 26; 1363; 1957.
- [11] Heist, R. H.; Fong, F. K. "Maxwell-Boltzman distribution of  $M^{+3}$ -  $F^-$  interstitial pairs in fluoride-type lattices," *Phys. Rev. B* 1; 2970; 1970.
- [12] den Hartog, H. W. "Defect structure and defect-defect interactions in solid solutions of  $AlF_2$  and  $RbF_3$  doped with  $Gd^{3+}$  probes," *Phys. Rev. B.* 27; 20; 1983.
- [13] Poole, R. T.; Szajman, J.; Leckey, R.G.C.; Jenkin, J. G.; Liesegang, J. "Electronic structure of the alkaline-earth fluorides studied by photoelectron spectroscopy," *Phys. Rev. B* 12; 5872; 1975.
- [14] Born, M.; Meyer, J. E. *Z. Phys.* 75; 1; 1932.
- [15] Tosi, M. P. "Cohesion of ionic solids in the Born model," in *Solid state physics*, Vol. 16, F. Seitz and D. Turnbull, eds. New York; Academic Press; 1964.
- [16] *Handbook of chemistry and physics*. CRC; Cleveland, OH; 1972.
- [17] Kittel, C. *Introduction to solid state physics*, 4th ed. New York; Wiley; 1971. P. 111.
- [18] Hayes, W., ed. *Crystals with the fluorite structure*. London; Oxford University Press; 1974. P. 13.

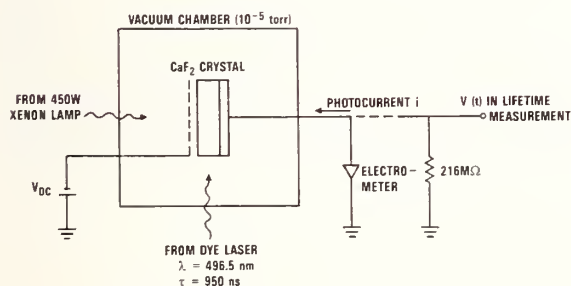


Figure 1. Experimental arrangement used in the photoconductivity measurements.

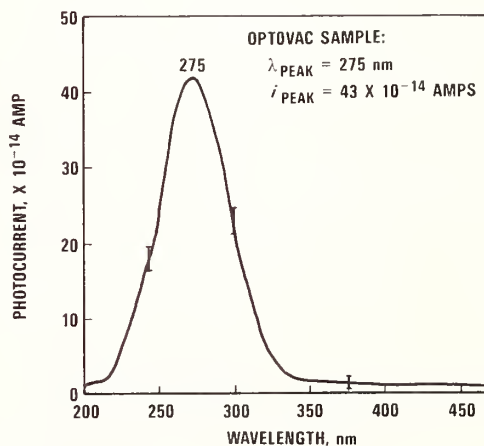


Figure 2. The short wavelength portion of a typical linear PC spectrum from the Optovac sample.

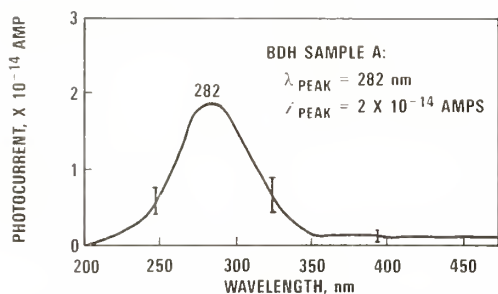


Figure 3. The short wavelength portion of a typical linear PC spectrum from the 100% Optipur BDH sample.

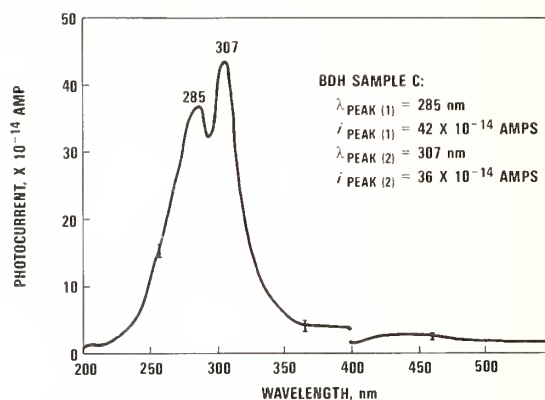


Figure 4. The short wavelength portion of a typical linear PC spectrum from the 50% Optipur, 50% natural Mexican BDH sample.

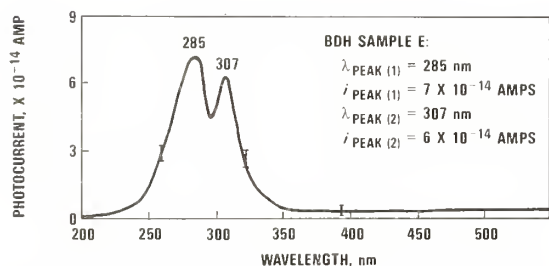


Figure 5. The short wavelength portion of a typical linear PC spectrum from the 100% natural Mexican BDH sample.

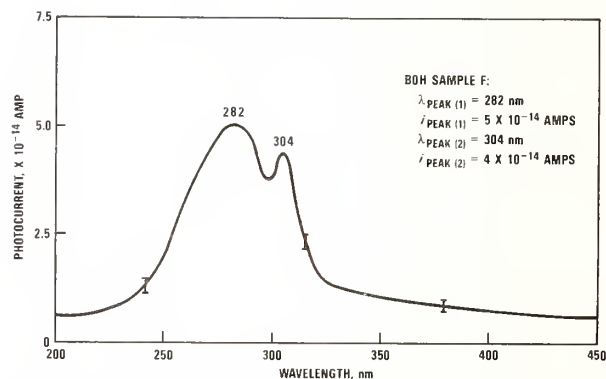


Figure 6. The short wavelength portion of a typical linear PC spectrum from the cerium-contaminated 100% Optipur BDH sample.

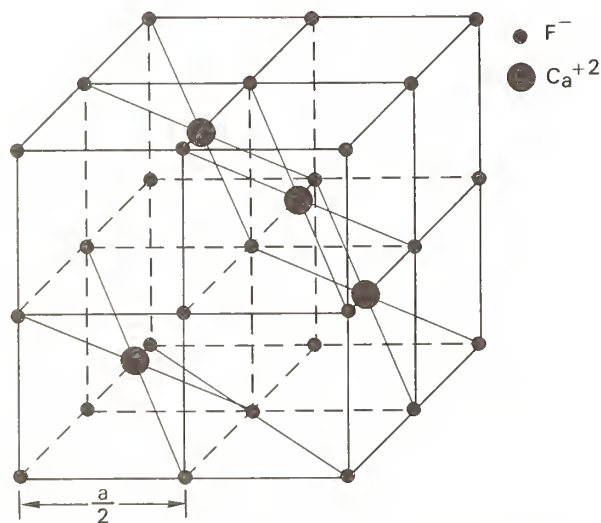


Figure 7. The unit cell of  $\text{CaF}_2$ , consisting of eight cubes with  $\text{F}^-$  ions on all the corners and  $\text{Ca}^{+2}$  ions in the body centers of alternating cubes.

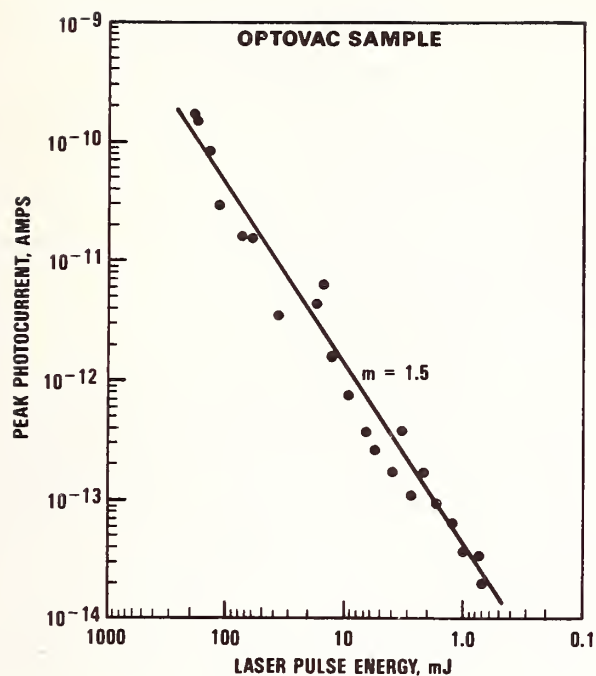


Figure 8. Nonlinear PC data from the Optovac sample obtained with the laser focused inside the sample.

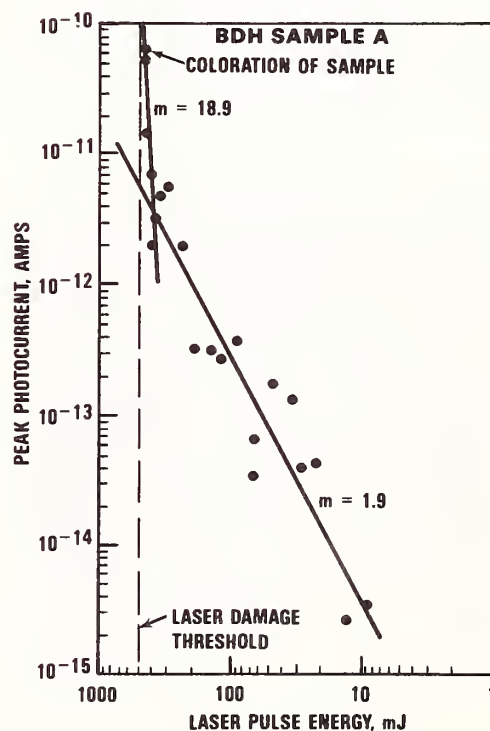


Figure 9. Nonlinear PC data from the BDH:A sample obtained with the laser focused inside the sample.

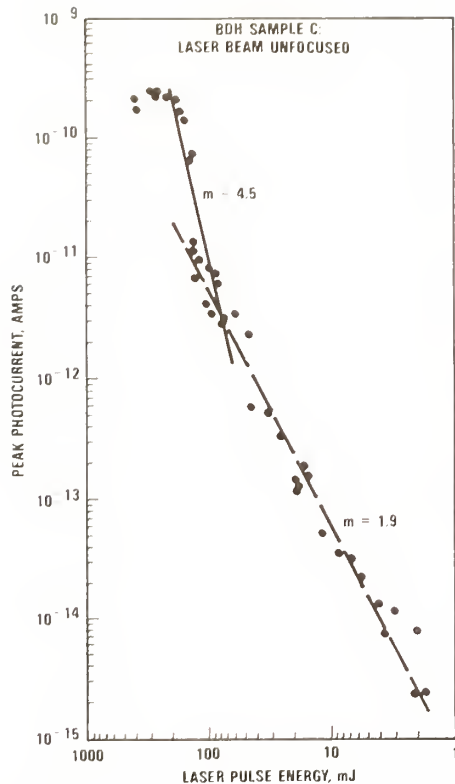


Figure 10. Nonlinear PC data from the BDH:C sample obtained with the laser unfocused inside the sample.

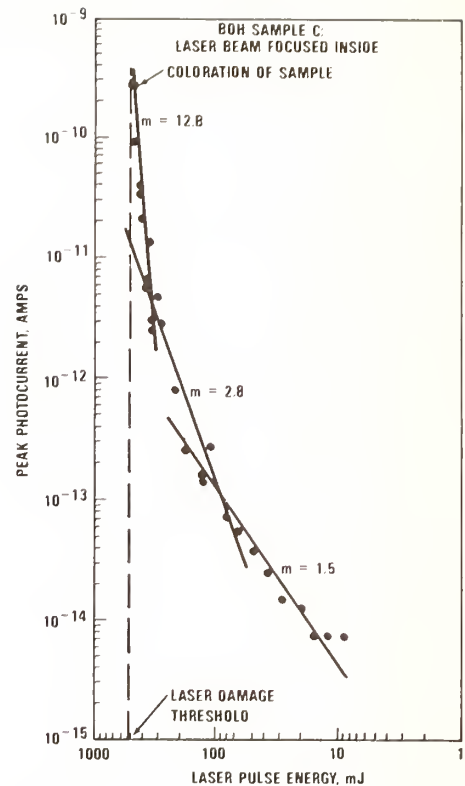


Figure 11. Nonlinear PC data from the BDH:C sample obtained with the laser focused inside the sample.

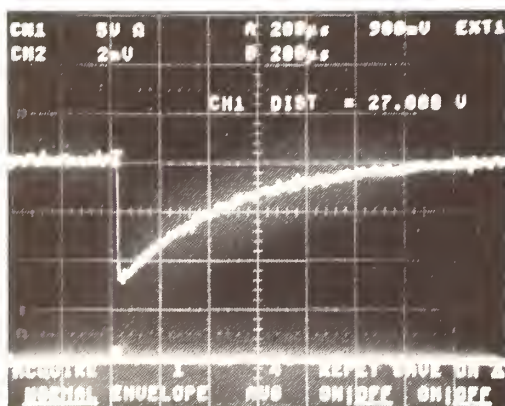


Figure 12. Oscilloscope trace of the pulse-induced voltage across the 216-M $\Omega$  resistor in figure 1. Time base = 200  $\mu$ s per division.

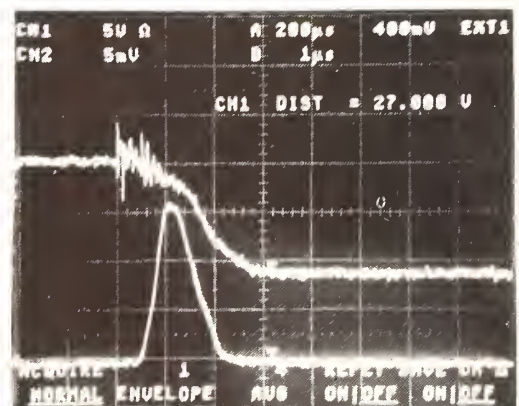


Figure 13. Oscilloscope traces of the leading edge of the signal in figure 12 on a wider time base (upper trace) and the simultaneous response of a 2-ns rise time PIN diode to a pulse from the laser (lower trace). Time base = 1  $\mu$ s per division.



## Laser-Induced Changes in the Electrical Performance of Silicon MOS Device Structures

Chen-Zhi Zhang, Steve E. Watkins, Rodger M. Walser and Michael F. Becker  
Center for Material Science and Engineering and  
Department of Electrical and Computer Engineering  
The University of Texas at Austin  
Austin, TX 78712

Laser-induced morphological damage and electrical changes in the basic silicon MOS structure have been investigated using Q-switched Nd:YAG laser irradiation at 1064 nm. The threshold values for the onset of morphological damage to poly-silicon and Al layers have been obtained. It was found that the two poly-silicon films have different laser-induced damage thresholds. Both 1-on-1 and N-on-1 electrical damage behavior were studied for sheet resistors and MOS capacitors fabricated from the poly-silicon films. Severe electrical parameter changes were observed at fluences below the onset of visible morphological damage. Poly-silicon gate MOSFETs have been characterized in terms of leakage current, transconductance change, and threshold voltage shift. The experiments indicated that changes in these parameters after laser irradiation at low fluence were probably due to changes in poly-silicon gate morphology. Drain/source edge junctions which were not covered by the gate were also very sensitive to the effects of transient laser heating. Laser-induced defects are thought to be introduced into this region.

Key words: laser damage, MOS structure, electrical degradation, morphological damage.

### 1. Introduction

It is well known that the silicon MOS structure is a basic unit in MOS integrated circuits and CCD arrays, which are widely used to perform logic, memory, and imaging functions [1]. Many special applications such as communication, military and space systems require these devices to be operated in laser environments, where it becomes important to understand their laser damage processes [2]. A series of tests have been conducted to investigate both the morphological and electrical effects of pulsed laser irradiation on poly-silicon, aluminum film, and MOS structures. We have also correlated surface damage behavior with the electrical degradation of MOS devices at different laser fluence levels.

The test samples were poly-silicon gate, n-channel and buried-channel MOSFETs, as shown in figure 1. For imaging use, poly-silicon is chosen as the material for the gate of most devices since it is semi-transparent for visible light. The samples were irradiated with 1064 nm, 10 ns pulsed laser radiation from a Nd:YAG laser. The low frequency performance of MOSFETs for both analog and digital applications is characterized in terms of leakage current, transconductance, and threshold voltage both before and after laser irradiation.

In this paper, we first describe the devices under test and the Nd:YAG laser system in some detail, then report the results of experiments on laser-induced morphological changes to poly-silicon and Al films. Next we describe experiments on laser-induced changes to the electrical properties of poly-silicon sheet resistors and of MOSFETs which have various ratios of channel length to width. The experimental relation of morphological damage to electrical degradation at various laser fluences is given. Finally, a concluding summary of laser damage to MOS structures is given.

### 2. Experiments

The samples had been fabricated on 100 mm diameter Si wafers by standard MOS-LSI process which include LOCOS (Local Oxidation of Silicon) field oxidation, poly-silicon deposition and Al lines for electrical connection. The devices were buried-channel and n-channel TDI CCD arrays of 2048x96 elements. Each wafer contained additional test and characterization devices including:

- (1) resistor bars of poly-silicon,  $960 \times 60 \mu\text{m}^2$  and  $960 \times 10 \mu\text{m}^2$  in size,
- (2) serpentine of poly-silicon and  $n^+$  wells which have square resistance of 70 ohm/sq (10 mm width),
- (3) poly-silicon capacitors,  $350 \times 350 \mu\text{m}^2$  and  $500 \times 620 \mu\text{m}^2$  in size, and
- (4) n-channel and buried-channel MOSFETs which have varying ratios of channel width to length, i.e.,  $W/L = 54...3/6$ ,  $W/L = 36/36...3$  (see fig. 2). Some of the MOSFETs were shielded by Al and polyimide layers.

Figure 3 shows the laser test system. The laser source for these experiment was a Q-switched Nd:YAG laser operating at 1064 nm with 10 ns pulses (FWHM) and with a 10 Hz repetition rate. The incident energy on the samples was controlled by an attenuator consisting of a rotating half-wave plate followed by a fixed, thin-film polarizer and

monitored by a reference energy meter. The standard deviation of the pulse-to-pulse energies was two percent or less. The spatial profile of the Gaussian beam was measured by the scanning slit method and the FWHM was determined. The  $1/e^2$  beam-spot radius  $w_0$  was obtained using the equation  $2w_0 = \text{FWHM} (\ln 2/2)^{1/2}$ . The beam was focused to an approximately 300  $\mu\text{m}$  spot radius. The peak-on-axis irradiation fluences were calculated using  $F = 2E/\pi w_0^2$ , where  $E$  is the pulse energy. The reference energy meter was calibrated and the spot size was determined during each test session.

In the damage testing process, the samples were positioned using a He-Ne beam and a 20X alignment microscope. The computer recorded the energy of each incident pulse, controlled the shutter which blocked the beam after the desired number of pulses, and calculated the peak-on-axis fluence. The alignment microscope was used to check for gross surface damage. Details of the morphological damage were observed subsequently with a Nomarski microscope and a SEM. Morphological damage is defined as any visible change induced by laser irradiation using the 50 - 500X Nomarski optical microscope.

Before irradiation and at each of the intermediate levels of fluence, the following measurements were performed on the MOSFET samples using an HP4145B Semiconductor Parameter Analyzer:

- (1) Breakdown voltage of the source and drain well junctions at various values of  $V_g$ .
- (2) Output characteristics, i.e.,  $I_d$  vs.  $V_d$  curves for various values of  $V_g$ .
- (3) Transfer curves,  $I_d$  vs.  $V_g$  at several values of  $V_{\text{sub}}$ .
- (4) Transconductance curves,  $G_m$  vs.  $V_g$  at several values of  $V_{\text{sub}}$ .

### 3. Results and Discussion

The results showing the onset of laser-induced morphological damage at several major stages of successive laser damage to the poly-silicon and aluminum resistor and capacitor patterns are listed in tables I and II. Laser damage threshold values are defined as the fluence at which a color change (surface height change) can be detected by Nomarski microscopy for poly-silicon films and at which surface roughness occurs for Al films. A few general observations can be made. First, poly-1 (poly-silicon layer 1) films had a lower damage threshold than poly-2 films for all geometries. Second, the damage threshold for aluminum lines and plates fell generally close to that for poly-1. Third, the  $N=10$  pulse thresholds are all about 20-40% lower than the corresponding one shot thresholds for the same test structure. Finally, all of the capacitor plate structures had higher damage thresholds than the line (or serpentine) structures. The latter is presumably due to the more effective thermal diffusion in the 2-D plates as compared to the 1-D linear structures, thus allowing the linear structures to reach melting temperature with less fluence. Figures 4 (a) - (d) display typical near-threshold damage morphologies for the poly-silicon capacitor plates.

Another planar structure tested was shielding layers of aluminum and polyimide. In some cases, active devices were covered by this optical shielding layer pair. In other cases, three layer pair structures were damage tested with multiple laser pulses. We found that the aluminum-polyimide layer-pairs made good ablating shields for high fluence pulses. Each layer pair provided good shielding for 1 shot, up to fluences of about 5  $\text{J}/\text{cm}^2$ . MOSFET devices showed no significant change in static electrical performance even after the top shielding layer had been stripped away by laser irradiation. Multiple layer pairs gave corresponding protection from multiple pulses. Only one layer pair was removed per pulse so that the three layer-pair structures gave effective protection from three relatively high fluence pulses. The related damage morphologies are shown in figures 4 (e) and (f). The aluminum is just beginning to melt in figure 4 (e) while the layer pair has been stripped from above a set of interconnect lines in figure 4 (f).

Laser-induced electrical parameter changes were examined for both the linear resistor structures described above and for MOSFET devices. Changes in sheet resistance were measured as a function of laser fluence for the poly-silicon films and the  $n^+$  well resistors, and the results are shown in figures 5 (a) and (b). For poly-silicon, the sheet resistance decreased slightly at very low fluences, starting at about 0.2  $\text{J}/\text{cm}^2$ , and then decreased significantly at about 0.4  $\text{J}/\text{cm}^2$ . All of these changes occurred below the visible damage onset fluence at around 1.0  $\text{J}/\text{cm}^2$ . This decrease may be due to grain growth by fast laser heating or due to the creation of electrically active impurities or defects. Successive laser pulses continued this trend, as shown in figure 5 (c). The sheet resistance for the  $n^+$  wells only decreased by about 0.2%, and this small change may not be experimentally significant. The relatively small resistivity changes observed in the poly-silicon as well as the  $n^+$  wells would have a negligible effect on the electrical performance of a MOSFET if this were the only change taking place. In experiments on MOSFETs, other changes appear to take place at fluences above 0.2  $\text{J}/\text{cm}^2$ , and they are described in the next section.

Electrical measurements on MOSFETs included leakage current (both source/drain to substrate and source to drain), transconductance, and threshold voltage. Leakage current as a function of laser fluence is shown in figure 6. Leakage from the drain/source wells to the substrate seems to dominate drain to source leakage, as shown in figure 6 (a). The intersection of the surface and the edge of the source or drain depletion region is both sensitive to defects and exposed to the full laser fluence. Laser induced defects at this point can significantly increase the surface leakage current. Close inspection of the data reveals a slight improvement in the leakage current at fluences around 0.4  $\text{J}/\text{cm}^2$ , well below the morphological damage threshold. This leakage reduction may be related to modification of the  $\text{SiO}_2/\text{Si}$



interface states at the junction intersection with the surface. The subsequent rapid increase in the substrate leakage with increasing fluence could easily result in device failure. This surface-junction intersection can be protected by a poly-silicon layer, as in the CCD active area or for a closed gate design FET.

The onset fluence for drain to source leakage was about  $0.4 \text{ J/cm}^2$  as shown in figure 6 (b). This leakage appeared to be insensitive to the gate width or length as all samples showed similar behavior. The threshold fluence for changes in electrical properties was always much lower than the onset fluence for morphological damage to the same device. Leakage current was observed to increase as fluence increased until the poly-silicon gate was open circuited. During this process, the poly-silicon gates were observed to successively suffer color change (poly-1 only), edge erosion, melting or shrinkage, and breaking, as summarized in tables I and II. The edge erosion can be observed in figure 2 in the entire top row of MOSFETs. In addition, this figure shows that the shortest gate device (uppermost right) has punctured the cap oxide over the gate, presumably by melting and boiling of the poly-silicon below.

Degradation of the transconductance and threshold voltage shifts were observed at generally the same fluence levels as laser-induced leakage, as shown in figures 7 and 8. The measured changes in these parameters were greater for larger ratios of  $W/L$ , that is, for shorter channel lengths. The larger area gates suffered less laser-induced change in transconductance and threshold voltage. In addition, the polarity of  $\Delta V_{th}$  behaved irregularly. In some samples it was positive, but for others it was negative. We deduce that the laser pulses have the less effect on the interface states behind the gate area, due to strong optical absorption in the poly-silicon gate, than they would in an uncovered region. That leaves changes in the poly-silicon gates as being largely responsible for the transconductance reduction and change in threshold voltage in MOSFETs. In practice, a reduction in  $G_m$  causes more serious degradation in analog electrical performance than in digital performance. The laser-induced changes in  $I_{ds}$  and  $V_{th}$  below the onset for visible damage may well be considered as acceptable for digital applications such as CCD arrays and their associated logic circuitry.

#### 4. Conclusions

Experiments have been conducted to investigate both the morphological and electrical effects of pulsed laser irradiation on poly-silicon films and interconnects, aluminum films, and MOS transistors. In most cases, as the laser fluence increased from around  $0.7 \text{ J/cm}^2$  to  $1.1 \text{ J/cm}^2$ , morphological damage appeared in the form of color change (thickness change), gate edge erosion or damage pits, melting or shrinkage, and breaking of the poly-silicon gates and aluminum lines. For shorter gates and other narrow structures, laser damage thresholds at the lower end of this range were observed. Also the poly-2 layer had a significantly higher damage threshold than either the poly-1 or the aluminum interconnects. This is attributed to processing differences which also resulted in poly-2 having a 40% higher sheet resistance than poly-1. The sheet resistance of the poly-silicon layers was found to decrease at fluences below the onset of visible damage. For poly-silicon interconnects, the sheet resistance decreased significantly above  $0.4 \text{ J/cm}^2$  up to the melting and open circuiting of the interconnect at  $1.1$  to  $1.3 \text{ J/cm}^2$ . No corresponding change was observed in the  $n^+$  well resistors fabricated in the base wafer material. Grain growth and defect activation are the suggested mechanisms for this resistivity decrease.

Changes in several electrical parameters of MOSFETs were detected at fluences below the onset of visible morphological damage. The drain/source edge junction regions not covered by the gate, the laser induced leakage current to the substrate increased rapidly above  $0.4 \text{ J/cm}^2$ . The surface termination of these p-n junctions was particularly vulnerable to laser-induced damage resulting from surface defects produced during the laser heating transient. Degradation of the electrical performance of MOSFETs also became significant at  $0.4 \text{ J/cm}^2$ . Increased leakage,  $I_{ds}$ , decreased transconductance,  $G_m$ , and threshold voltage shifts,  $\Delta V_{th}$ , were all observed at fluences below the onset of visible damage. Electrical degradation increased as the poly-silicon melted, and eventually, the poly-silicon connections were open circuited rendering the device non-functioning. At fluences below those that caused catastrophic failure, the electrical parameter changes are probably not severe enough to render the MOS device useless except in critical applications.

---

This work was supported in part by Acurex Corporation /Aerotherm Division.

#### 5. References

- [1] S. M. Sze, *Physics of Semiconductor Devices*, 2nd Ed., 1981.
- [2] M.F. Becker, C.-Z. Zhang, S.E. Watkins, R.M. Walser: "Laser-Induced Damage to Silicon CCD Imaging Sensors", *Proceedings of SPIE* **1105**, (1989).
- [3] H.-Y. Tsoi, J.P. Ellul, M.I. King, J.J. White, and W.C. Bradley, "A Deep-Depletion CCD Imager for Soft X-Ray, Visible, and Near-infrared Sensing," *IEEE Trans. on Elect. Dev.* **ED-32**, 1525 (1985).
- [4] J.P. Ellul, H.-Y. Tsoi, J.J. White, and W.C. Bradley, "State-of-the Art Imaging Arrays and Their Applications," *Proceedings of SPIE* **501**, 117 (1984).

**Table I. Damage threshold values for bar patterns\***

Units are  $\text{J}/\text{cm}^2$ \*\*

Material	Color change (height change)	Melting or shrinkage	Breaking
Poly-Si 1	0.7 (0.5)	0.9 (0.6)	1.1 (0.7)
Poly-Si 2	N.A.	1.1 (0.9)	1.3 (1.2)
Aluminum	N.A.	0.9 (0.6)	1.0 (0.8)

\* These are obtained from the average values of four specimens.

\*\* The values are for  $N=1$  shot ( and for  $N=10$  shots in parenthesis).

**Table II. Damage threshold values for capacitor structures\***

Units are  $\text{J}/\text{cm}^2$ \*\*

Material	Color change (height change)	Pits	Melting	Balling-up
Poly-Si 1	0.8 (0.5)	0.9 (0.6)	1.0 (0.8)	1.1 (0.8)
Poly-Si 2	1.6 (1.1)	1.5 (1.1)	1.6 (1.3)	1.7 (1.3)
Aluminum	N.A.	0.9 (0.7)	1.0 (0.7)	1.2 (0.8)

\* These are obtained from the average values of six specimens.

\*\* The values are for  $N=1$  shot ( and for  $N=10$  shots in parenthesis).

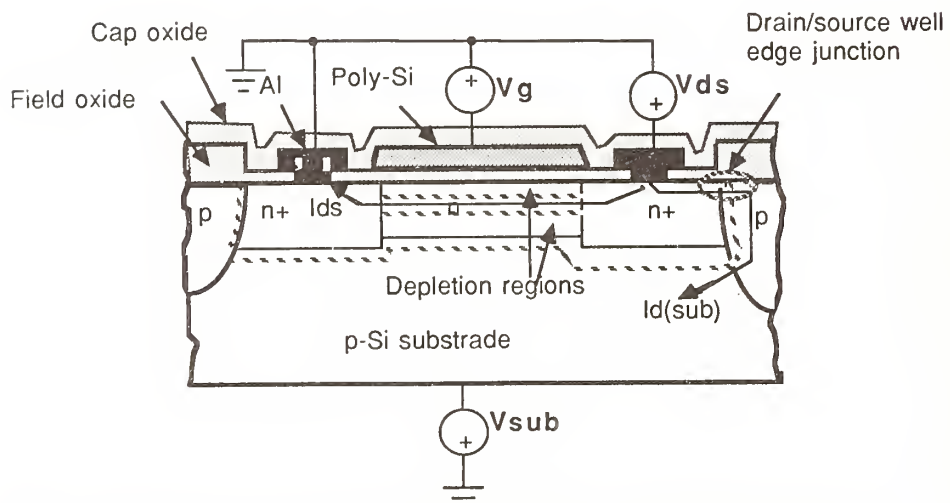


Figure 1. Schematic cross-sectional view of the buried-channel MOSFET sample and the bias circuit used for measuring the static electrical parameters before and after pulsed laser irradiation.



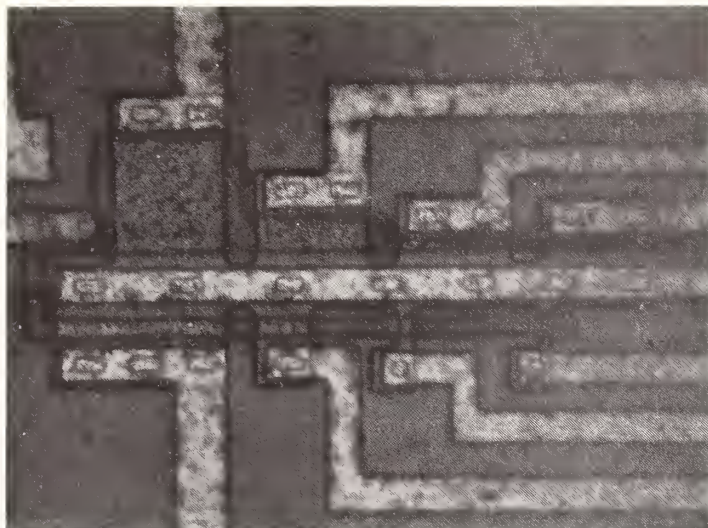


Figure 2. Nomarski optical micrograph (500x) of MOSFETs with Poly-Si 1 gate after laser irradiation at  $F = 1.0 \text{ J/cm}^2$ , where  $W/L = 36/36...3 \text{ micron}$  (top row), and  $W/L = 54...3/6 \text{ micron}$ .

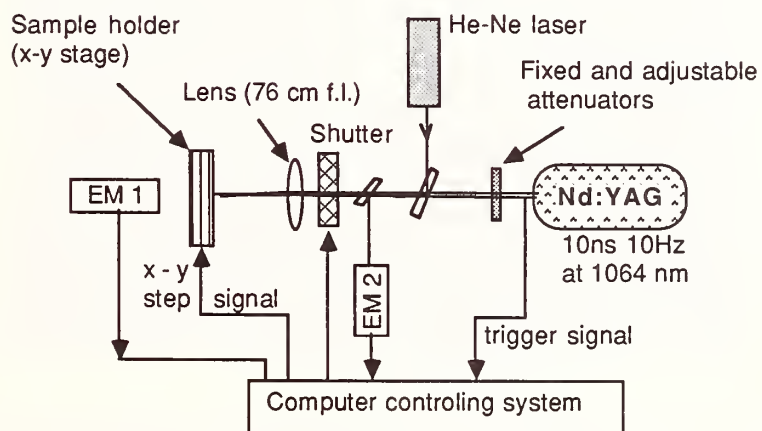
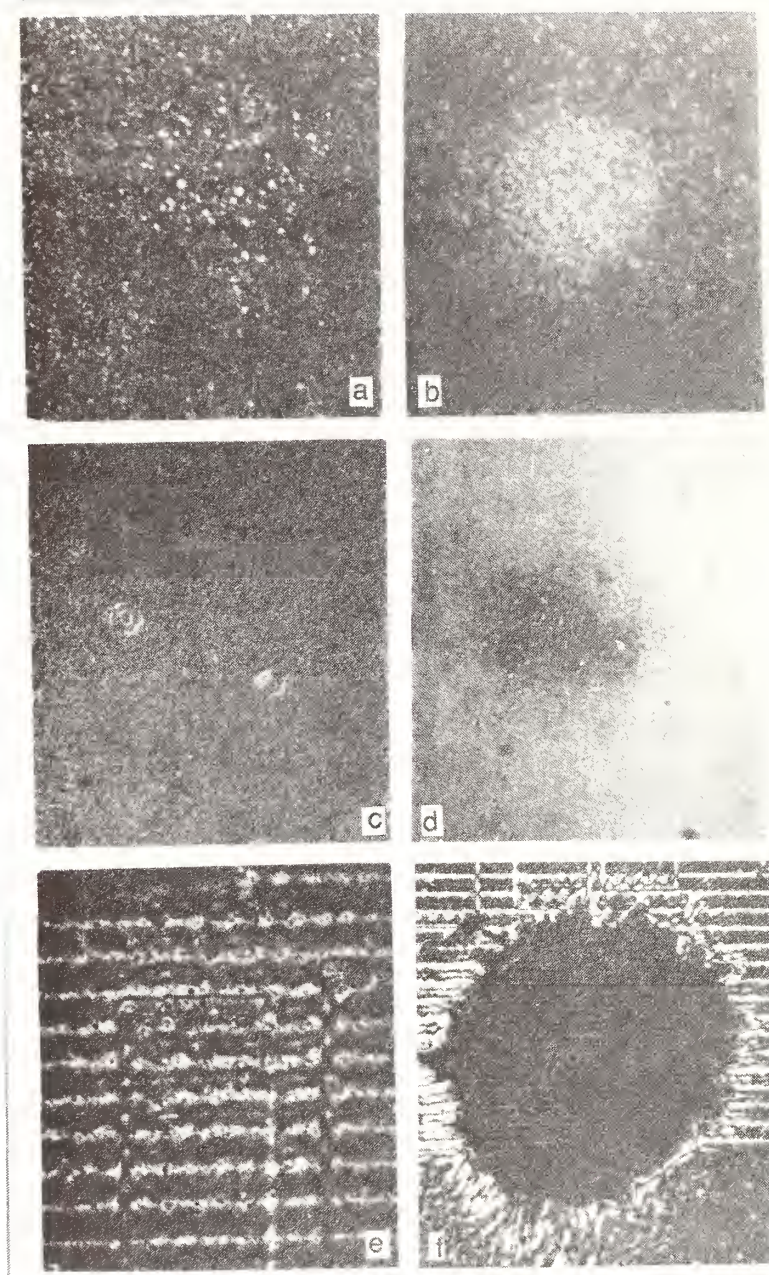


Figure 3. Block diagram of the experimental system used for laser irradiation.



**Figure 4.** Nomarski micrographs showing damage morphologies of Poly-Si and Al films.  
 (a) and (b) for Poly-Si 1 (500x):  $0.9 \text{ J/cm}^2$  and  $1.1 \text{ J/cm}^2$ , respectively;  
 (c) and (d) for Poly-Si 2:  $1.6 \text{ J/cm}^2$  (500x) and  $1.7 \text{ J/cm}^2$  (60x), respectively;  
 (e) and (f) for Al - Polymer layers:  $1.0 \text{ J/cm}^2$  (240x) and  $1.3 \text{ J/cm}^2$  (120x) respectively.

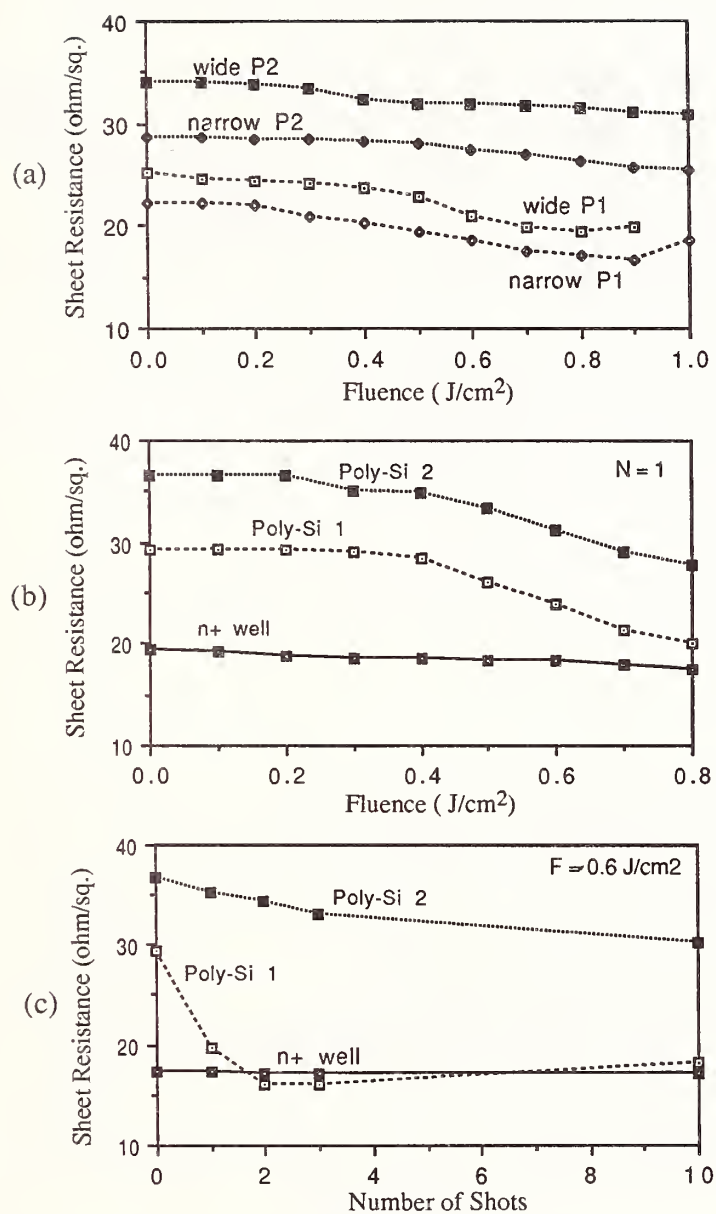


Figure 5. Sheet resistance of poly-silicon 2 and  $n^+$  well resistors vs. laser irradiation: (a) for the bar pattern; (b) and (c) for the serpentine pattern.

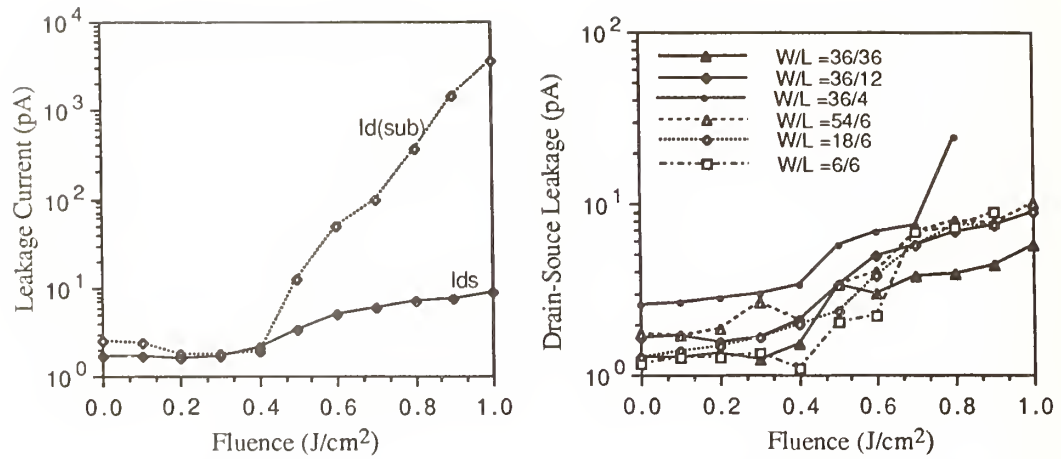


Figure 6. Leakage current of MOSFETs in the Off-state vs. laser fluence for  $N = 1$ , where the gates are poly-2,  $V_g = -0.8$  V, and  $V_{sub} = -3$  V:  
 (a)  $W/L = 36/12$ ; (b) various  $W/L$  ( $I_{ds}$  only).

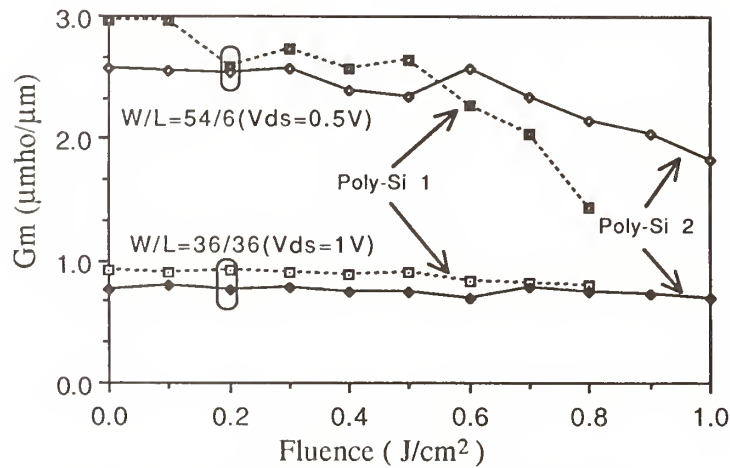


Figure 7. Transconductance of MOSFETs vs. laser fluence.



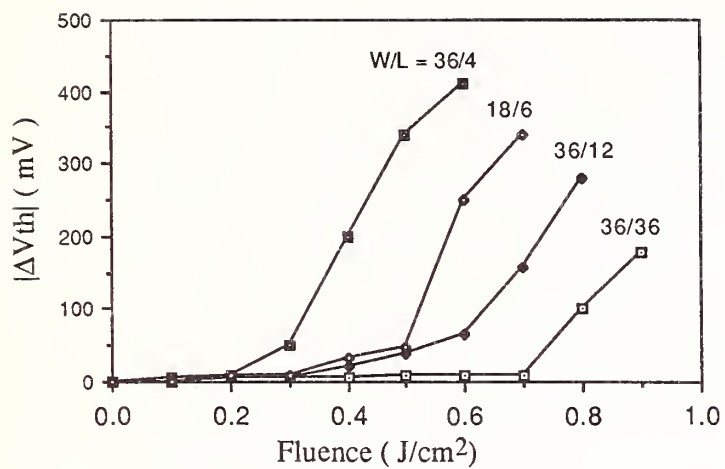


Figure 8. Magnitude of threshold voltage shift vs. fluence for various ratios of channel width to length, where the gates are poly-2,  $I_{ds} = 0.1 \mu A$ , and  $V_{ds} = 1 V$ .

Marion L. Scott

Materials Science & Technology Division  
Los Alamos National Laboratory  
Los Alamos, NM 87545

We have investigated a new concept in retro-reflectors for use in the extreme ultraviolet, namely, UHV aluminum coated, multi-facet, grazing-incidence mirrors. Our results indicate that this type of mirror, which utilizes total-external-reflectance, works very well in the wavelength range from 35 nm to 100 nm ( $89 \pm 3\%$  measured retroreflectance at 58.4 nm for a 9-facet mirror). However, the coated mirror surfaces must not be allowed to oxidize after deposition, which implies that the retro-reflector must be coated and used in situ or the oxide layer must be removed in an ultra-high vacuum (UHV) system.

Key Words: XUV; extreme ultraviolet; aluminum; reflector; multi-facet.

## INTRODUCTION

The search for good reflectors in the extreme ultraviolet (XUV) spectrum has gone on for many years. Some samples of silicon carbide and diamond have been shown to exceed 40% normal incidence reflectance at wavelengths greater than 60 nm. The silicon carbide results have not proven to be easily reproduced with thin film depositions. Diamond film technology has greatly improved in recent years, however, XUV reflectance measurements on these thin films have not yet come up to bulk values. Near-normal incidence reflectance measurements on multilayer coatings have reached 60% at 17 nm [1] but reproducibility has been a problem and multilayers at longer wavelengths have not been very successful. Also, multilayer reflectors will only reflect over a narrow spectral band.

Our present work on multi-facet reflectors was motivated by the resonator mirror requirements of an XUV free-electron-laser to be constructed at Los Alamos National Laboratory [2]. The resonator mirrors are required to equal or exceed 40% retroreflectance over the wavelength range from 10 nm to 100 nm. It is possible to construct the XUV FEL in segments so that one resonator does not have to span the entire wavelength range, however, the wavelength tunability of the FEL necessitates that the resonator mirrors be as broad-band as possible. The total-external-reflectance of UHV aluminum at 58.4 nm measured in our previous work ( $98.66\% \pm 2\%$  for a single bounce at 80 degrees) indicated that a 9-facet reflector with this coating would yield a retro-reflectance between 74% and 100% at this wavelength [3].

## MULTI-FACET MIRROR

A 9-facet mirror structure was designed on the Los Alamos computer-assisted-design system and fabricated with the aid of a numerically-controlled mill (see Fig. 1). The nine silicon mirror substrates were fabricated by Laser Optics to a figure accuracy of  $1/20$  wave in the visible and 0.5 nm rms surface roughness. The assembled 9-facet mirror aligned with a visible HeNe laser is shown in Fig. 2. Note that the visible beam accurately strikes the center of each of the nine facets before exiting the array parallel to the input beam. This 9-facet structure is supported in our UHV deposition and analysis system by UHV alignment manipulators attached to each side of the three strut frame.

## UHV DEPOSITION SYSTEM

Our UHV deposition system (illustrated in Fig. 3) has been previously described and only a cursory description will be given here. The UHV chamber has a base pressure of  $5 \times 10^{-10}$  Torr and is pumped with hydrocarbon free pumps to avoid carbon contamination of the coated reflector. A water-cooled e-gun source located in the lower part of the deposition chamber is shielded with a cylinder to avoid wide angle coating in the chamber. Some additional shielding inside the 9-facet array requires lateral movement of the array between the position for deposition and the position used in later reflectance measurements. The deposited coating thickness is monitored with a quartz crystal monitor connected to an IC 6000 rate controller.

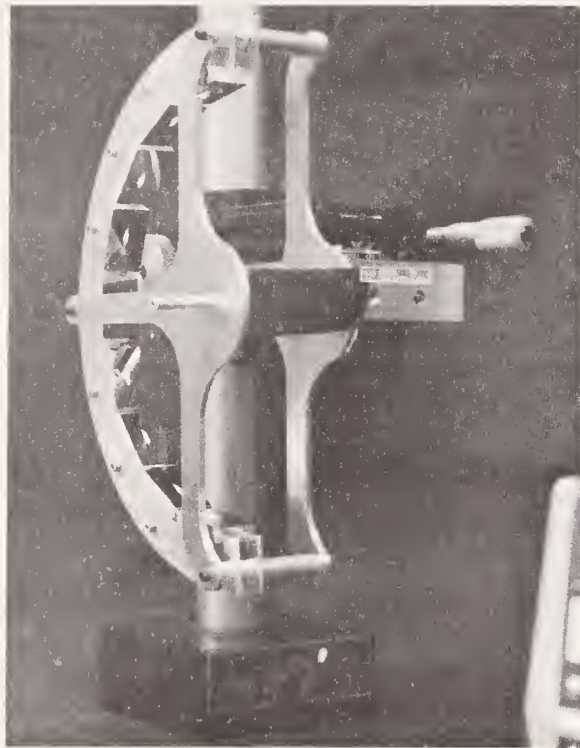


Figure 1. The 9-facet XUV mirror structure fabricated and measured at Los Alamos.

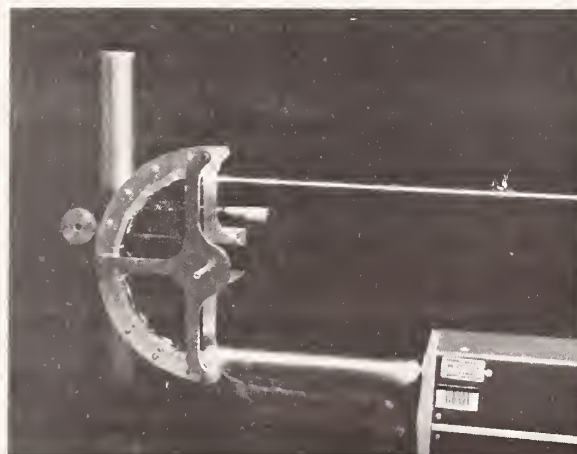


Figure 2. The 9-facet XUV mirror shown with a retroreflected HeNe alignment laser.



Figure 3. UHV deposition and analysis system utilized in demonstrating the 9-facet XUV reflector.

#### UHV ALUMINUM DEPOSITION

A thin film (70 nm) of high purity aluminum is deposited through appropriate masking onto three of the nine silicon mirror substrates simultaneously, before rotating the structure to coat the remaining substrates in groups of three. We have achieved good results with a deposition rate of approximately 0.1 nm/sec although we have not performed measurements to determine whether this rate is optimum. After coating deposition on all nine mirror substrates, the mirror assembly is moved into position and aligned to make the XUV reflectance measurement at 58.4 nm.

#### IN SITU XUV REFLECTANCE MEASUREMENT

Many modifications were made to our UHV system to adapt the in situ XUV reflectometer (previously used to measure single-surface reflectance) to measure the reflectance of a 9-facet retroreflector. The XUV beam entrance to the UHV chamber had to be lowered and the sample holder had to be raised. The detector was mounted on a linear feedthrough in the top of the chamber and is capable of rotation about the axis of this magnetically coupled feedthrough. The high voltage and signal leads to the imaging microchannel plate detector are also in the top of the chamber for easy removal. The mirror array can be accurately aligned for reflectance measurement by use of the Huntington x,y,z rotatable feedthroughs on either side of the array.

The measurement of the reflectance of this 9-facet mirror at 58.4 nm was accomplished by first positioning the imaging detector in front of the XUV beam entrance to the UHV chamber and carefully noting the x,y position of the beam on the detector and recording the count rate of the source. Secondly, the detector is raised and rotated to intercept the XUV beam exiting the properly aligned, 9-facet mirror. The detector is positioned to place the beam image at the same spot on the detector as in the previous measurement and the count rate in this detector position is recorded.



A correction must be made to the raw count rates recorded in this manner because the detector responds to counts that are outside of the well defined beam image seen on the oscilloscope. These out-of-beam counts arise from scattering in the system, as well as dark counts from the detector. This correction is determined for each detector position by electronically gating out those counts which are outside the beam image to determine the ratio of beam to scattered counts. The reflectance of the 9-facet array is then computed from the ratio of the corrected counts recorded from the beam exiting the array to those entering the array.

The result of averaging several such measurements on the 9-facet mirror array was  $89 \pm 3\%$ . This value is within the uncertainty of our previous single surface reflectance measurement on UHV aluminum at 80 degrees incidence angle raised to the ninth power (74% to 100%).

## CONCLUSIONS

We conclude that an unoxidized, UHV aluminum, 9-facet reflector is an excellent XUV retroreflector at 58.4 nm. We also conclude that an XUV mirror constructed in this fashion will provide an adequate reflectance over a significant portion of the XUV spectrum (35-100 nm) to operate an XUV free-electron laser resonator.

## ACKNOWLEDGEMENTS

The author would like to acknowledge the support of this work by the DOE Office of Basic Energy Sciences, Advanced Energy Projects Division.

## REFERENCES

1. T. W. Barbee, Jr., S. Mrowka, and M. Hettrick, "Molybdenum Silicon Multilayer Mirrors for the Extreme Ultraviolet," *Appl. Opt.*, **24**, 883-886 (1985).
2. B. E. Newnam, "Multifacet, Metal Mirror Design for Extreme Ultraviolet and Soft X-Ray Free-Electron Laser Resonators," *Proceedings of Laser Induced Damage in Optical Materials: 1985*, NBS Spec. Pub. 746, 261-269 (1988).
3. M. L. Scott, P. N. Arendt, B. J. Cameron, J. M. Saber, and B. E. Newnam, "Extreme Ultraviolet Reflectance Degradation of Aluminum and Silicon From Surface Oxidation," *Appl. Opt.*, **27**, 1503-1507 (1988).

Measurement of the Three Photon Absorption Cross Section and  
Intrinsic Optical Breakdown of KI at 532 nm

Lin Simpson, X. A. Shen, Scott C. Jones and Peter Braunlich

Department of Physics  
Washington State University  
Pullman, WA 99164-2814

and

Paul Kelly  
National Research Council, Ottawa, K1A 0R6, Canada

The self trapped exciton recombination luminescence (STERL) technique is used to measure the three photon absorption cross section in KI at 532 nm. STERL is used as a thermometric property to obtain the laser induced temperature increase, up to values near the melting point, before sample damage occurs. Computer modelling of the results indicates that the intrinsic damage process is absorption of light by three photon generated free carriers, according to the mechanism reported for KBr by Shen *et al.*[1].

Key Words: alkali halides; bulk damage mechanism; exciton recombination luminescence; 532 nm laser; free electron heating; potassium iodide; self-trapped exciton; three photon absorption cross section.

## 1. Introduction

The self-trapped exciton recombination luminescence (STERL) technique of measuring multiphoton absorption and the resulting laser induced temperature increase was devised by Shen *et al.*[1-3] to study intrinsic bulk laser damage in KBr at 532 nm. Using this method it was shown that bulk damage to high purity samples is a result of secondary energy absorption by four-photon generated free electrons, causing lattice melting. The purpose of this work is to validate the earlier results by repeating the experiments and calculations described in references [1-3] in a different material; potassium iodide.

Potassium iodide exhibits the self-trapped exciton (STE) phenomena in common with all alkali halides, in particular the two-band emission spectrum and temperature dependent luminous efficiency. However, KI presents a three-photon band gap at 532 nm, thus the free electron generation will be of third order.

In order to perform the computational analysis, the three-photon absorption cross-section is required. This information is obtained by the methods described in ref.[4] except the system is calibrated using the third harmonic of Nd:YAG, 355 nm (two 355 nm and three 532 nm photons have equal total energy). The result is  $\sigma^{(3)} = (6 \pm 2.8) \times 10^{-81} \text{ cm}^6 \text{ sec}^2$ , where  $\sigma^{(3)}$  is defined in the equation

$$\frac{dn_c}{dt} = N\sigma^{(3)}F^3. \quad (1)$$

Here  $n_c$  is the free electron density,  $F$  is the photon flux ( $\text{photons cm}^{-2} \text{ sec}^{-1}$ ), and  $N$  is the valence electron density.

## 2. Induced Temperature Measurements

The laser induced temperature measurements are carried out in precisely the same manner as used by Shen *et al.* described in references [1] and [3]. The description of the experimental apparatus and procedures are contained therein. First the luminous efficiency is obtained by monitoring the relative emission output following stimulation by two-photon (355 nm) absorption. The crystal temperature is altered while the stimulating beam remains at a constant low (non-heating) intensity. The results are presented in figure 1. The data fits the equation

$$\eta(T) = \frac{A}{1 + \tau\nu \exp(-E/kT)}, \quad (2)$$

where  $\eta$  is the efficiency, with  $\tau\nu = 5200$  and  $E = 0.069$  eV. Thermal quenching begins at  $T = 70$  K.

Armed with this information, the crystal is then irradiated with 532 nm photons while the cryostat maintains the initial crystal temperature at 50 K. The energy of the 100 ps pulse is increased by small increments, beginning with low intensities, which just yield measurable luminescence, up to damaging levels. One such run is shown in fig. 2. At relatively low levels of photon flux (below  $8 \times 10^{28}$  photons  $\text{cm}^{-2} \text{sec}^{-1}$  peak flux) the luminescence signal follows a third-order dependence on flux (slope of three on the double-logarithmic plot), indicating three-photon absorption as the carrier generation process. The curve begins to bend over (*i.e.*, the dependence falls below third-order) when the center of the focused Gaussian beam reaches the thermal quenching temperature,  $T = 70$  K, because the luminescence efficiency begins to decrease from a constant level. In this experiment, the center of the irradiated volume thus reaches a temperature of 70 K ( $\Delta T = 20$  K) at  $F = 8 \times 10^{28}$  photons  $\text{cm}^{-2} \text{sec}^{-1}$  (see fig. 2). This yields one calibration point for the luminescence thermometer.

Computational modelling [3,4] demonstrates that the temperature rise depends on the photon flux in the third order, and with the fixed point at  $T = 70$  K ( $\Delta T = 20$  K),  $F = 8 \times 10^{28}$  photons  $\text{cm}^{-2} \text{sec}^{-1}$ , the temperature at the center of the focal volume resulting from a given pulse can be calculated (fig. 3). This assumes no new processes become involved in the interaction, *e.g.*, avalanche ionization. Barring this, the peak lattice temperature for the most intense nondamaging pulse we observed was 890 K, 50 degrees below the melting point. This occurs at a peak flux of  $2 \times 10^{29}$  photons  $\text{cm}^{-2} \text{sec}^{-1}$  ( $\approx 75 \text{ GW/cm}^2$ ). If another carrier generation process were operative, the expectation is that the crystal would heat more rapidly than shown in figure 3, and thus damage would occur at a lower temperature than that inferred in fig. 3. Thus we conclude that no additional processes occur.

## 3. Conclusion

The experimental results given here do validate the mechanism of intrinsic damage of alkali halides by visible light discovered by Shen *et al.* Free electrons are generated according to eq. 1 with  $\sigma^{(3)} = (6 \pm 2.8) \times 10^{-81} \text{ cm}^6 \text{ sec}^2$ , and these carriers subsequently absorb light energy according to the theory of Epifanov [5] inducing lattice heating expressed by

$$\rho c \left( \frac{dT}{dt} \right) = 1.09 \left( \frac{m^* kT}{2\pi} \right)^{1/2} \frac{n_c}{l_{ac} v_s} \left( \frac{eE}{m^* \omega} \right)^3, \quad (3)$$

with small contributions ( $< 10\%$ ) by laser generated lattice defects. In the above,  $m^*$  is the electron effective mass,  $k$  Boltzmann's constant,  $l_{ac}$  and  $v_s$  are the electron mean free path and speed of sound respectively,  $e$  the electron charge,  $\omega$  the laser frequency and  $E$  the electric field amplitude. Again, we see no evidence for the existence of electron avalanche impact ionization in the damage process.

This work was supported by the U.S. Air Force Office of Scientific Research under Grant No. AFOSR-87-0081.

#### 4. References

1. X. A. Shen, Peter Braunlich, Scott C. Jones and Paul Kelly, Proceedings of the 19th Boulder Damage Symposium (1987), to be published.
2. X. A. Shen, Peter Braunlich, Scott C. Jones and Paul Kelly, Phys. Rev. Lett. **59**, 1605 (1987).
3. X. A. Shen, Peter Braunlich, Scott C. Jones and Paul Kelly, Phys. Rev. B **38**, 3494 (1988).
4. X. A. Shen, Scott C. Jones, Peter Braunlich and Paul Kelly, Phys. Rev. B **36**, 2831 (1987).
5. A. S. Epifanov, Zh. Eksp. Teor. Fiz. **67**, 1805 (1974) [Sov. Phys. JETP **40**, 897 (1975)].



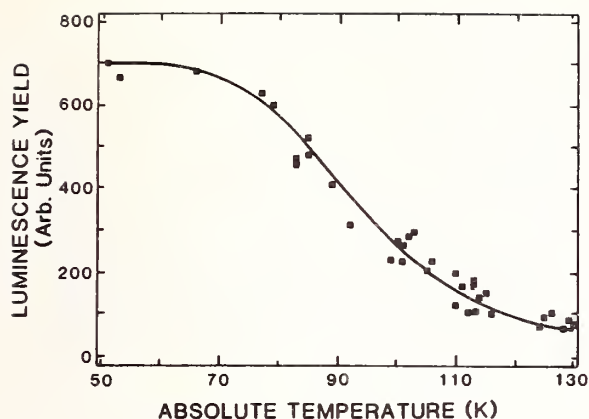


Figure 1. Luminescence efficiency ( $\eta$ ) vs temperature ( $T$ ) in KI. The curve is given by eq.(2). Thermal quenching begins to occur at  $T = 70$  K. As the temperature increases, the luminescence continues to decrease even though the laser intensity is the same for each point.

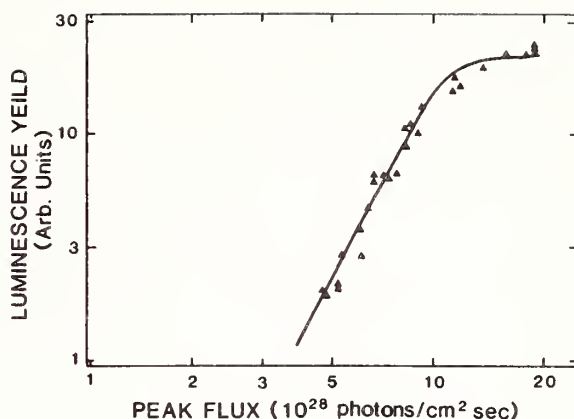


Figure 2. Experimentally determined and numerically calculated dependence of luminescence yield on incident peak photon flux. The log-log slope of three in the lower part of the curve is indicative of the three photon process we are studying here. At about  $8 \times 10^{28}$  photons  $\text{cm}^2 \text{sec}^{-1}$  incident flux we observe a deviation from the slope of three. Here the quenching temperature at the interaction volume's center has been reached and thus temperature effects become important above this flux. The curved part is due to a decrease in luminescence efficiency. The theoretical curve was generated using the Epifanov free carrier heating mechanism and the end point at the top of the curve indicates a temperature approximately 50 K lower than the KI melting temperature of 954 K.

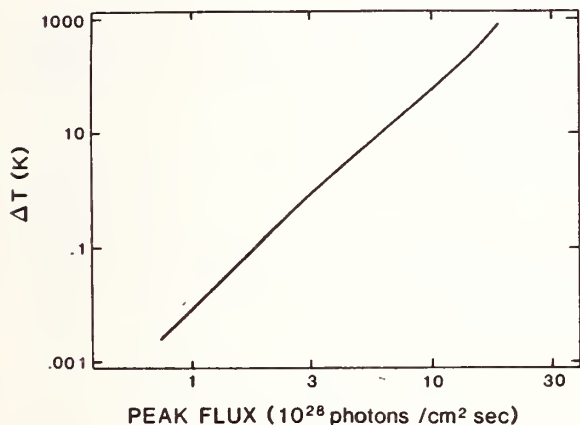


Figure 3. Theoretical temperature dependence on flux. The ending flux of  $2 \times 10^{29}$  photons  $\text{cm}^{-2} \text{sec}^{-1}$  corresponds to a temperature of approximately 890 K (approximately 50 K less than the melting temperature of 954 K, but still very close considering the nonlinearity involved in the calculations). The  $\Delta T$  scale for temperature is the difference between the actual temperature and the initial temperature at 50 K.

## DAMAGE TO SILVER COATINGS FROM HIGH AVERAGE POWER 1- $\mu$ m LASER

V. Sanders, L. Jolin, and S. Salazar  
Los Alamos National Laboratory  
Chemical and Laser Sciences Division  
P. O. Box 1663, MS J564  
Los Alamos, NM 87545

Optical coatings are being developed for use in high average power, pseudo continuous wave, 1- $\mu$ m lasers. In particular, the subject of this study is a silver coating to be applied to a cooled substrate for use in a radio frequency-free electron laser (RF-FEL). Damage threshold measurements and finite element thermal calculations were made that demonstrate the pure thermal nature of heating, and eventual damage, from this RF-FEL pulse format.

**Key Words:** silver coatings, damage thresholds, thermal damage, radio frequency-free electron laser, cooled optics.

### Introduction

The rise in temperature to eventual melt of a silver coating from exposure to a continuous wave, 1- $\mu$ m wavelength, high-average power laser is caused by pure thermal equilibrium heating from absorption of light. However, the subject silver coating in this study is being considered for use in a 1- $\mu$ m RF-FEL where the pulse format is referred to as pseudo continuous wave. The purpose of this study is to determine if the train of picosecond pulses from the RF-FEL interacts with the silver coating as if it were a true continuous wave exposure. Therefore, the experiments that were conducted and will be described were fashioned with an emphasis on demonstrating the physical nature of the minimal melt damage threshold.

### Experiments and Calculations

Three experiments were conducted each of which included a controlled variable to be compared with damage threshold measurements. These measurements were either compared with calculations or compared with each other to indicate a scaling dependence on the controlled variable to determine the physical nature of the damage.

The damage threshold experiments were conducted using a simulation of the RF-FEL pulse format. The simulator was constructed from a mode-locked Nd:YAG laser directed through a series of four amplifiers, two active pulse-shaping/slicing attenuating optical devices, and two passive Faraday rotation isolation optical devices. The goal was to create the constant amplitude pulse train indicated in figure 1. The results were: a train of 100-ps pulses at 100 MHz with approximately a constant peak-to-peak amplitude (within  $\pm 5\%$ ) on the 100-ps pulses for 100  $\mu$ s with negligible energy associated with post-pulse ringing. The beam was plane polarized to better than 300:1.

The damage threshold determined, using this pulse format, was one associated with a statistical zero probability of creating damage. Damage is indicated by any minimal microscopic visible indication of disruption of the exposed surface. For the purpose of this study we are assuming minimal surface melt, or near melt, at the surface of the coating as the physical nature of the observed disruption.

In the first of the three experiments mentioned above, the controlled variables were the substrate materials and the thickness of the silver coating. The coated substrates were Si, Mo, and SiO<sub>2</sub>. These three substrates were coated at the same time and in close proximity to each other. This ensures the same thickness and coefficient of absorption for each coating. A damage threshold was determined for each. This was done for three particular silver coating thicknesses: 0.2, 2.0, and 20  $\mu$ m. The data is graphed in figure 2 in a comparative fashion to each other and compared with a corresponding calculation. Keep in mind that the goal of this study is to determine the physical nature of damage. Therefore, we have plotted ratios of damage threshold measurements on the corresponding coatings. For example, the dot in the upper left portion of the graph indicates that the damage threshold for the 0.2- $\mu$ m-thick silver coating on Mo substrate was a ratio factor of 2.0 greater than the same coating on Si. Likewise, for this same coating, the damage threshold comparing SiO<sub>2</sub> and Si as the substrates, the damage threshold for SiO<sub>2</sub> is only 0.3 that of Si.

The corresponding calculation ratio is also shown in figure 2. The calculations were done using a one-dimensional, finite-element, pure thermal diffusion analysis. Two significant simplification assumptions for these calculations were that the irradiated spot size (0.2 mm) was much larger than the coating thickness, and that the thermal/mass properties of coating and substrates were constant over the full range from room temperature to melt. This second assumption is significant in that the thermal conductivity of Si and SiO<sub>2</sub> changes significantly over this temperature range. The values used in the calculations were those at 490°C, mid-range to silver melt temperature. The calculations generated the energy per pulse required to bring the top center of the irradiated spot on the silver coating to melt temperature in 10<sup>4</sup> pulses (10<sup>4</sup> 100-ps pulses in the 100 MHz, 100-μs pulse train shot). Figure 3 is an example plot of the calculated temperature rise as a function of exposure time. The temperature is indicated at both the top center of the coating and at the silver/substrate interface. Note that the 10-ns between 100-ps pulses is near the thermal relaxation time and the mean temperature gradually rises. Note also that for this example, thinnest coating, the temperature excursions between pulses are significantly damped at the silver/substrate interface.

The resulting comparison between pure thermal diffusion theory and experimental data is good.

The variable in the second of the three experiments was the coefficient of absorption of the silver coating. This was accomplished by varying the angle of incidence of the irradiation exposure. The absorption is enhanced by a factor of inverse cosine of the incident angle ("S" polarized only). Figure 4 graphs damage threshold data compared to an inverse cosine curve. The data was generated by measuring damage thresholds on half of a coated substrate at normal incidence and on the other half of the coating at the indicated angle of incidence. The graph indicates the ratio or enhancement factor associated with the damage threshold. The data at 80° and 84° were generated at KMS Fusion Inc. in Ann Arbor, Michigan, because the power density required to create damage was greater than could be generated by the Los Alamos RF-FEL simulator. The laser at KMS produced the same pulse format as is indicated in figure 1 but with more energy per pulse.

Again the experimental data agrees with a pure thermal assumption that the temperature rise to melt corresponds to the absorbed energy.

The results of the third experiment are shown in the table. In this experiment the variable is the pulse train length. Again damage threshold measurements were made on corresponding samples. In this experiment, and the previous one, the silver coating was 0.2 μm thick. The table indicates two pulse lengths. The 100-μs measurements were done at Los Alamos and the 3-ms measurements at KMS. Again the pulse train characteristics were the same as in figure 1 except for the pulse train length. The pure thermal theory predicts that the two damage threshold measurements should ratio as the root of the ratio of the pulse lengths, i.e., 5.5. The measured damage threshold ratios in the right column in the table are in fair agreement with theory.

## Conclusions

The results from one of these experiments alone does not generate a high confidence conclusion. However, the cumulative results from all three make a strong case that the picosecond pulses in the RF-FEL pulse train interact with the silver coating as if it were a true continuous wave 1-μm wavelength laser. Another interpretation is that minimal melt damage to this silver coating is from average power absorbed.

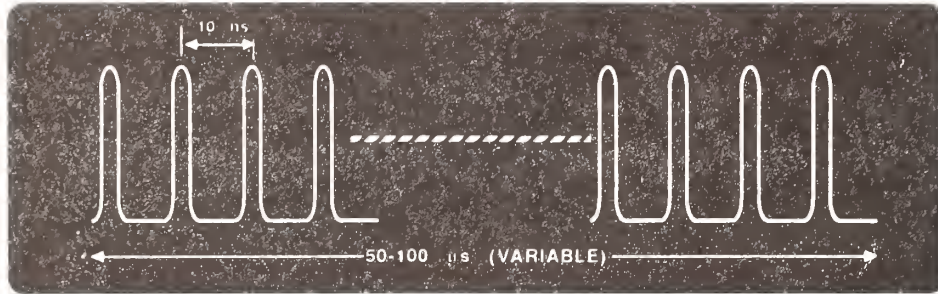
The significance of this conclusion to the FEL is that, given this RF pulse format, this silver coating used on an actively cooled substrate may be exposed continuously at power levels subject only to the rate at which heat can be removed from the cooled substrate.



# Nd: YAG MODELOCKED AND AMPLIFIED 1.06 $\mu\text{m}$

## Micro-Pulse Characteristics

TEMPORAL : 100 PS (FWHM) NEAR GAUSSIAN  
 ENERGY :  $2 \times 10^{-4}$  J  
 POWER :  $2 \times 10^6$  W



## 10 Hz Macro-Pulse Characteristics

TEMPORAL : EQUAL INTENSITY MICRO-PULSES (TOP HAT) SEPARATED BY 10 ns, VARIABLE FROM 50 TO 100  $\mu\text{s}$  (1  $\mu\text{s}$  RISE TIME, EQUAL INTENSITY TO  $\pm 5\%$ )  
 ENERGY : 1 TO 2 J ( VARIABLE WITH PULSE LENGTH)  
 POWER :  $2 \times 10^4$  W  
 SPATIAL : NEAR GAUSSIAN AT TARGET  $1/E^2$  (DIA.) 0.5 TO 0.2 MM

Figure 1. FEL simulator train.

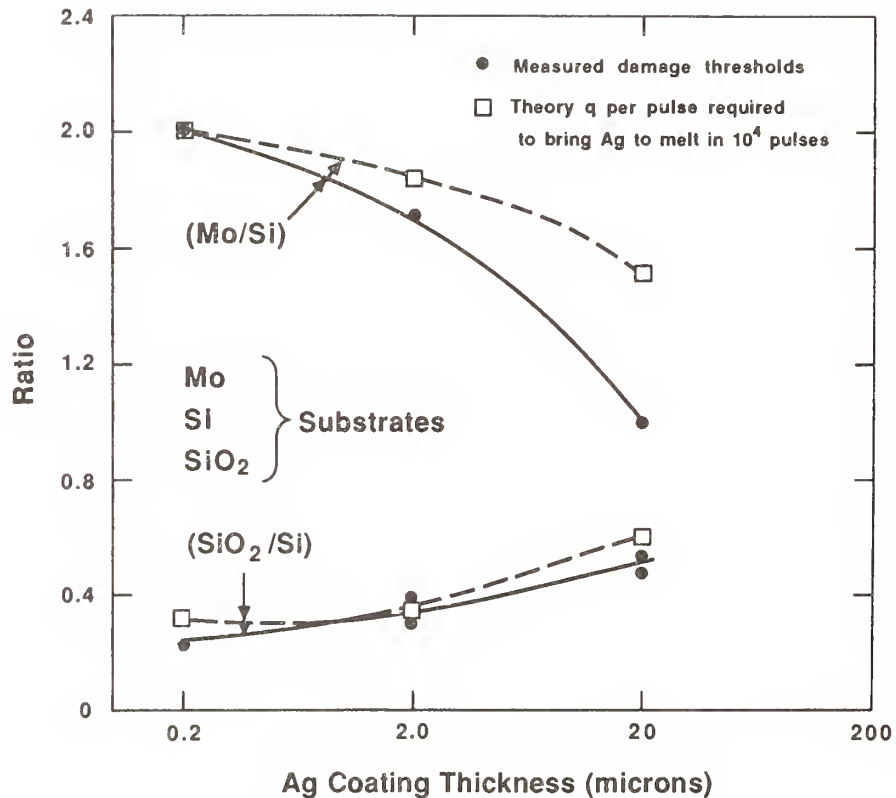


Figure 2. Thermal diffusion theory vs damage data.



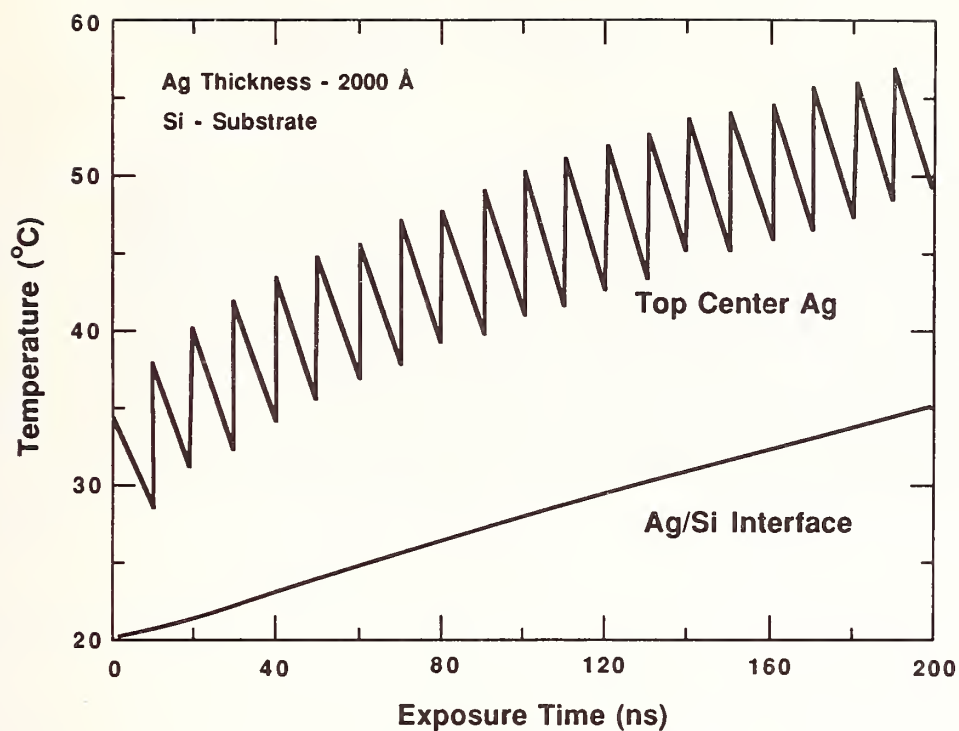


Figure 3. Finite-element thermal analysis.

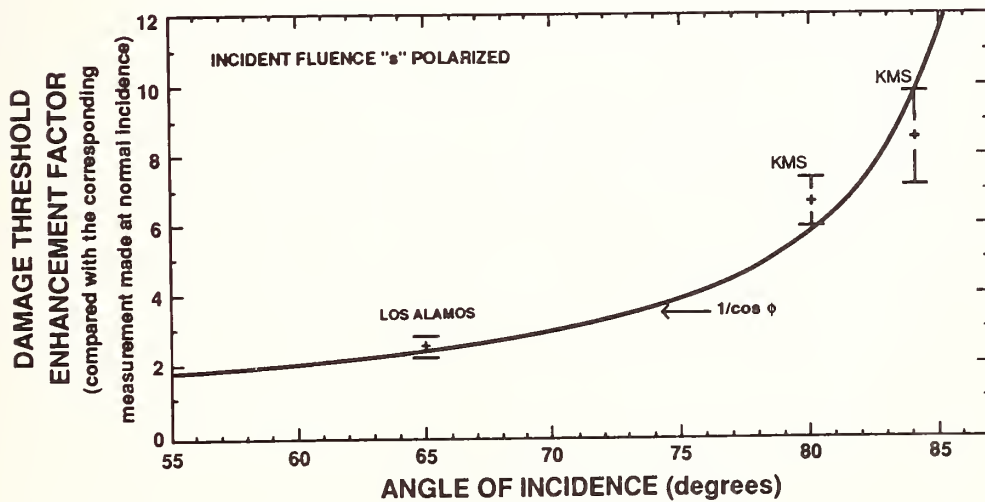


Figure 4. Damage threshold enhancement vs angle of incidence.

**TABLE**  
**RESULTS FROM PULSELENGTH SCALING AT KMS**  
**SUPPORT PURE THERMAL ASSUMPTION**

<u>Coating</u>	<u>Substrate</u>	<u>Sample Number</u>	<u>Threshold 100 ms</u>	<u>Threshold 3 ms</u>	<u>Measured Ratio</u>
Ag	SiO <sub>2</sub>	3	0.7	0.1	7.0
Ag	Si	6	4.7	0.8	5.9
Ag	Mo	5	7.9	1.6	4.9

Theory : $\sqrt{\frac{3 \text{ ms}}{100 \mu\text{s}}} = 5.5$ Ratio :
---

#### COMMENTS

Question: Two comments. One is that as I understood it, you didn't include the variation in reflectance with temperature as you used the room temperature absorption. And the second is, did you include the heat of fusion in your calculation?

Answer: To the first question, no we did not. To the second also no. This was a fairly simple but still a one dimensional finite element analysis calculation. And although it wasn't two dimensional or three dimensional and didn't include a lot of stuff, I think the business of comparing the ratios are valid. Errors caused by the loose assumptions that we have made in one coating versus another coating should cancel, so ratios give a reasonable way to compare. The results do seem to behave as expected for a pure thermal model.

Question: Do you plan to do an analysis of what sort of errors the approximate assumptions would introduce?

Answer: Well, we are going to do a more detailed calculation. Yes, and at least extend the one dimensional calculation to a two dimensional calculation. But I don't really expect to see any difference or anything new.

Question: How did you handle the effect of the temperature dependence of various thermal properties in modelling? The second question I had was how did you handle the matter of thermal contact resistance?

Answer: The coefficients were sort of chosen as an average between room temperature and melt, some reasonable average. In the calculation we have assumed that there was no chrome binder between the silver film and the substrate and that there was essentially perfect thermal contact.

Question: The third question was to ask you about the chrome binder. Does it contribute by improving the thermal bond or is it just mechanical?

Answer: It certainly improves the mechanical bond and I assume by the fact that you need it to stick the coating that it would indeed affect the thermal bond.

Question: The conclusion that because the damage threshold has a root dependence on square on pulselength and is therefore thermal and thus can be handled by cooling is one possible interpretation. However, damage due to imbedded particles could give the same dependence of the damage threshold on pulsewidth. In that case cooling of the substrate may not effect the damage threshold.

Answer: These are metal coatings and so the effect of varied inclusions is not quite the same as it is for multi-layer dielectrics.

Investigation of the Effect of Surface Finish  
on the Damage Threshold of Nd:Cr:GSGG Slabs

D.W. Mordaunt and D.E. Maguire

Hughes Aircraft Company  
Electro-Optical and Data Systems Group  
El Segundo, CA 90245-0902

This paper reports on the effect of varying surface polish and fabrication techniques on the laser damage threshold of uncoated Nd:Cr:GSGG slabs. A series of GSGG samples were prepared with a uniformly high quality surface polish. Chamfers were applied to these samples using a standard 220 grit grind, a window polish and a laser quality polish to finish the surface of the chamfer. The chamfers produced by each technique were analyzed for the degree of subsurface damage produced during fabrication. Samples of each method were damage tested in the chamfer area and on the polished surface. The test results are presented and compared to typical results for antireflection coatings on GSGG laser rods. Implications for the use of Nd:Cr:GSGG slabs in high power laser systems are presented.

Key words: laser damage; Nd:Cr:GSGG damage thresholds; chamfer damage.

## 1. Introduction

In recent years, Nd:Cr:GSGG has matured as a laser material to the point where it can be considered as a substitute for Nd:YAG in production laser systems. The higher efficiency of GSGG compared to YAG makes this material very attractive for applications where size, weight or operational lifetime are important. Hughes currently has an internal R&D program on solid state laser technology aimed at developing new materials and scaling of solid state laser technology to higher energies. During this research program, we developed a GSGG oscillator/amplifier configuration using rectangular slabs of GSGG for the amplifiers. For this configuration, the oscillator output is expanded and overfills the amplifier slabs. The oscillator beam is amplified once on the first pass, reflected and fully amplified on a second pass through the amplifier slabs. At the end of the second pass the energy in the laser beam is at a maximum and is still filling the entire aperture of the amplifier slabs.

During experiments designed to scale this configuration to energies in the 5 to 10 J range, we observed damage to the beveled edges or chamfers of the amplifier slabs. This damage occurred because the GSGG amplifier slabs have a nonuniform gain profile with the highest gain occurring at the edges of the slab closest to the flashlamps. This result was not particularly surprising when the high absorption of this material is considered. When combined with diffraction effects, this nonuniform gain causes the highest fluence in the entire laser system to occur at the edges of the amplifier slabs as the amplified beam completes its second pass through the amplifier. This high fluence resulted in damage to the chamfer, accompanied by ablation of material off of the chamfer. This ablated material can then deposit on the antireflection (AR) coated end faces of the amplifier slabs and cause catastrophic surface damage and a resulting failure of the laser system. In order to scale this configuration up to higher energies, the chamfer damage threshold needs to be increased to the point where it is at least as durable as the AR coatings on the end faces of the slabs. This paper reports on a series of damage test experiments performed in order to determine how the fabrication method and degree of surface polish applied to the chamfers affects the damage threshold.

## 2. Experimental Results

We report on two sets of experiments. The first series of tests were performed on samples provided by Litton Airtron of Morris Plains, NJ. These samples were used to provide a baseline for typical performance of coated and uncoated Nd:Cr:GSGG substrates. Two of these samples were produced with a normal ground chamfer, two with a polished chamfer and two with acid etched chamfers. Because the results of these experiments were not conclusive, an additional series of GSGG substrates were fabricated under known and well controlled conditions. These samples consisted of uncoated or AR coated substrates with chamfers which were fabricated with either a normal 220 grit grind, a low quality window polish or a high quality surface polish similar to that which would be applied to the face of a laser rod. The results of all of these experiments are presented in the remainder of this section.



A layout of the damage test facility used for these experiments is given in figure 1. The test station consists of a Nd:YAG based laser system which uses an oscillator/amplifier configuration and a phase conjugate mirror to produce a high quality output at a wavelength of  $1.06\text{ }\mu\text{m}$ . The beam quality is quite good and consists of a 9 mm diameter circular beam with approximately 250  $\mu\text{rad}$  beam divergence. All of our damage test measurements were performed using a  $1.06\text{ }\mu\text{m}$  beam and typical test conditions consisted of a 15 nsec pulsewidth (FWHM), a pulse repetition rate of 1 Hz and a 1 mm diameter spot size in the target plane. All tests were performed as unconditioned tests in which each test site on the surface is exposed to a single fluence level. Each site was exposed to at least 20 shots and damage was defined as any permanent change in surface scatter when the test site is illuminated by a He-Ne laser and viewed online under 20X magnification.

Preliminary testing was performed on samples provided by Litton Airtron of Morris Plains, NJ. Two coated samples with different coating designs were provided as well as two uncoated GSGG pieces which had the chamfers fabricated by three different techniques. The damage test results are presented in table 1 and are summarized here. The coated samples and the polished surfaces of the uncoated pieces had damage thresholds in the  $20\text{ J/cm}^2$  range. The chamfers of the two uncoated pieces were fabricated using three different manufacturing techniques: a 220 grit grind, a polished chamfer and a polished chamfer which was then acid etched. The chamfer test results were not conclusive and showed little difference between the chamfer damage thresholds for the three different fabrication techniques. All of the chamfers had damage thresholds between 5 and  $8\text{ J/cm}^2$ , although one might expect that the polished chamfers would exhibit behavior similar to the polished faces of the samples. Two main factors tend to cast some doubt on these test results. First, we did not have any control and were not able to adequately specify the surface finish of the chamfers and the possibility is quite strong that they were not polished to the same degree as the faces of the GSGG pieces. Although they were not characterized quantitatively, we feel that the surface quality of the polished chamfers was not up to the quality of the polished faces, which had a typical laser rod type finish applied to them. Second, the chamfers were quite small in size with a diameter of only about 0.15 to 0.20 mm while the laser damage test beam had a diameter of approximately 1 mm. As a result, the laser test beam overlapped the chamfer on the polished surface and also on the outside edges of the chamfers.

Because the first round of testing did not produce conclusive results, a more carefully controlled series of experiments was designed. For these tests, GSGG substrates were supplied to Lightning Optical Corp. of Tarpon Springs, FL, where they were polished and coated in a prescribed and well controlled manner. Two coated samples were provided with normal ground chamfers and a  $1.06\text{ }\mu\text{m}$  AR coating on one face. In addition, nine uncoated pieces were provided with polished faces and three different chamfer fabrication techniques. For these nine samples, a large chamfer with a width of approximately 2.5 mm was applied to provide a chamfer which was wider than the laser spot size used for the test. This allowed reliable positioning of the beam on the chamfer without overlapping either edge. Three samples were provided with a normal 220 grit ground chamfer, three with a low quality "window polish" and three with a high quality surface polish similar to that which would normally be applied to the polished end face of a laser rod.

The results of the second round of damage testing are presented in table 2. This data follows much more of an intuitive trend than the previously tested samples. The coated parts were consistent with the previous test samples and had damage thresholds around  $20\text{ J/cm}^2$ . The uncoated polished faces of the samples were consistently around  $17\text{ J/cm}^2$ . The chamfers fabricated with a 220 grit grind were also consistent with previous results and averaged around  $5\text{ J/cm}^2$ . With these samples a large improvement in the chamfer damage threshold was obtained by polishing the chamfer. Both the window polish and the high quality laser rod type polish showed substantial increases in the damage threshold, with the good polish exhibiting the largest increase. The window polished chamfers averaged around  $14\text{ J/cm}^2$  while the highly polished chamfers averaged around  $16\text{ J/cm}^2$ , which is essentially equivalent to the values measured for the polished faces of the GSGG samples.

The lower thresholds measured for the window polished chamfers were due to a large amount of small surface scratches and subsurface damage which were not removed during the polishing process. Both the window polish and the highly polished chamfers looked very clean when observed visually under a bright light without magnification. In both cases no visible scratches or pits were observed. However, a large difference between the two fabrication methods was observed under 100X magnification using a Nomarski phase contrast microscope. The difference between the two surfaces is presented in figure 2. Under these observation conditions, the highly polished chamfers still appeared virtually featureless while the window polish showed a grid of fine scratches which had not been fully polished out. We believe that these scratches were the reason for the lower damage threshold for the window polished chamfers. A similar phenomenon may have caused the inconclusive results for the samples tested during the first round. The polished

chamfers from these parts were also examined at 100X under the Nomarski microscope and showed a grid of very fine scratches similar to that observed in figure 2b.

### 3. Conclusions

In conclusion, we have shown that the damage threshold observed for the chamfers of polished GSGG substrates is dependent on the fabrication conditions. In the context of addressing an engineering problem in the development of a medium energy Nd:Cr:GSGG laser source, we encountered severe problems with damage to the GSGG amplifier slabs. By controlling the chamfer fabrication conditions and applying a high quality laser rod type finish to the chamfers, we were able to increase their damage thresholds by greater than a factor of 3. The polished chamfers exhibited damage thresholds equivalent to the uncoated polished faces of the GSGG pieces at a level of about 17 J/cm<sup>2</sup>. These results provide a means of controlling the chamfer damage in real laser hardware systems and show the importance of carefully controlling the fabrication conditions of laser materials when laser induced damage is a critical issue.

Table 1. Results of the preliminary damage testing on the samples provided by Litton Airtron.

Sample ID #	Surface Tested	Coating	Threshold (J/cm <sup>2</sup> )
8Z	Polished Face	1.06 $\mu$ m AR	20
9A	Polished Face	1.06 $\mu$ m 45%R	37
8T	Polished Face	None	21
8U	Polished Face	None	16
8T	Polished Chamfer	None	8
8T	Ground Chamfer	None	7
8U	Etched Chamfer	None	5
8U	Ground Chamfer	None	6.5

Table 2. Results of the damage testing on the samples provided by Lightning Optical under controlled fabrication conditions.

Sample ID #	Surface Tested	Coating	Threshold J/cm <sup>2</sup>
9B	Polished Face	AR @ 1.06 $\mu$ m	21
9C	Polished Face	AR @ 1.06 $\mu$ m	19
9D-9L	Polished Face	None	17 (Avg.)
9D-9F	Ground Chamfer	None	5.3 (Avg.)
9G-9I	Window Polished Chamfer	None	14 (Avg.)
9J-9L	Polished Chamfer	None	16 (Avg.)

Figure 1. The laser damage test facility consists of a Nd:YAG oscillator/amplifier configuration. The abbreviations are defined as follows: OSC = oscillator; AMP = amplifier; EXP = beam expanding telescope; TFP = thin film polarizer;  $\lambda/4$  = quarter wave plate;  $\lambda/2$  = half wave plate; and DET = energy detector.

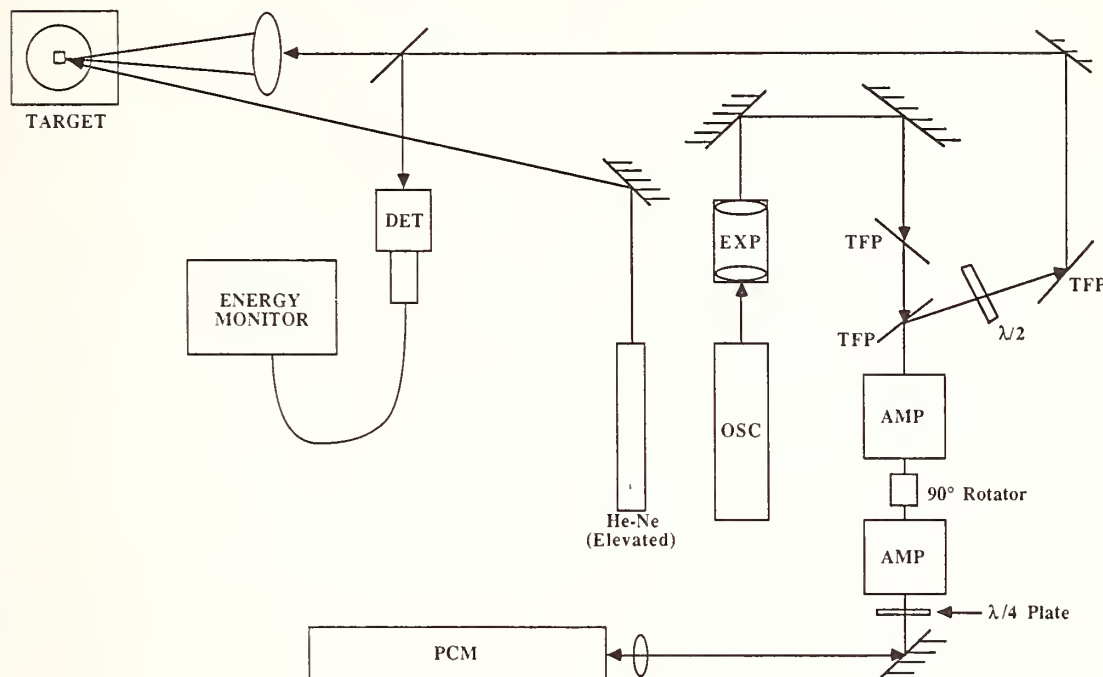
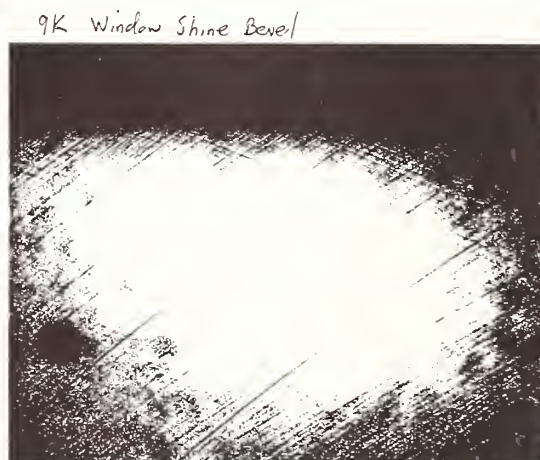
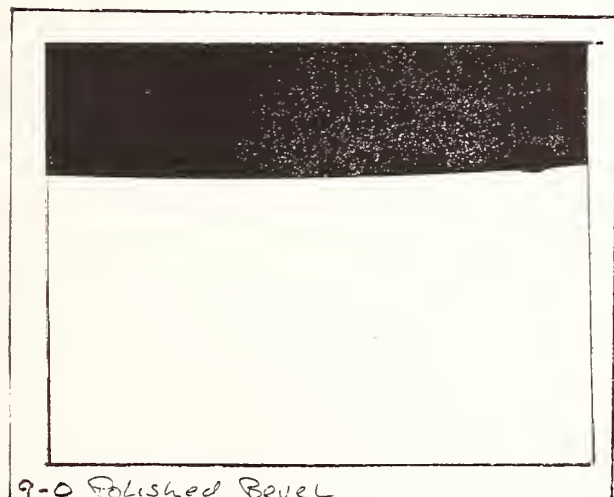


Figure 2. The two photomicrographs shown below compare the surface quality of the (a) highly polished chamfers and (b) the chamfers with the window polish. Both pictures were taken at 100X magnification using a Nomarski phase contrast microscope.

(a) Photomicrograph of the highly polished chamfers.

(b) Photomicrograph of the chamfers with the window polish



## COMMENTS

- Question: Did you try to characterize the sub-surface damage and if so, how did you do it?
- Answer: We haven't done that yet. We're contemplating trying to do an acid etch to remove some of the surface layers and see what the sub-surface damage looks like. Other than that, I don't have diagnostics that would do that.
- Question: What's the difference between the damage threshold of the polished area and of the chamfer in terms of a fraction?
- Answer: On the coated surfaces, we cut some pieces off the undamaged areas and the coatings actually tested around 40 joules per sq. centimeter. We didn't test the chamfers on those, and I don't know the exact fluence that the system was running at so I can't really tell you how that compares with the damage threshold.
- Question: You still have a line of intersection between the chamfer and the face, what about damage there?
- Answer: The damage was pretty much catastrophic on the chamfer, typically what we saw on the slabs that damage during use is that it overlapped from the chamfer onto the face. I haven't tried to do a calculation of electric field or anything on that corner to see what it does.
- Question: What I was referring to was if you solved the problem of damage on the chamfer and you have no damage on the face, you still have an edge that's essentially not as high quality and I'm wondering whether fixing chamfer problem really solves the damage problem.
- Answer: I would say it's got to be an improvement, I don't know if it's going to solve all of our problems.



Surface Damage Thresholds of Fluorite Crystals:  
Dependence on Surface Quality and Irradiation Mode

S. Petzoldt, A.P. Elg, J. Reif, and E. Matthias

Fachbereich Physik, Freie Universität Berlin,  
D-1000 Berlin 33, FRG

The intensity dependence of photoacoustic beam deflection was employed to investigate for fluorite crystals the influence of surface quality on the laser surface damage threshold. It is demonstrated that the damage mechanism can be changed from avalanche breakdown to multiphoton ionization by increasing the density of defect states on the surface.

Key words: damage threshold; avalanche breakdown, multiphoton absorption, acoustic probe beam deflection

In a contribution to the 1987 Boulder Damage Symposium [1] we have shown that the acoustic beam deflection technique [2] can be successfully used to measure surface damage thresholds. This method is based on the fact that pulse laser damage is inherently connected with shock wave generation [3], and the associated gradient in refractive index in turn deflects a perpendicularly oriented probe laser beam. By varying the pump laser intensity over a large range, the onset of damage can be recorded. The measured quantity is the energy of the acoustic pulse emitted from the interaction region, which can be derived directly from the deflection signal. It was shown [4] that this acoustic energy is correlated to the volume of the material removed from the surface. The details of the technique have been described elsewhere [1,4].

The data for polished surfaces of LiF, BaF<sub>2</sub>, CaF<sub>2</sub>, MgF<sub>2</sub> and quartz reported in Ref. [1] clearly indicate the existence of two classes of materials. One class owns "inert" surfaces with a high damage threshold, like CaF<sub>2</sub>, MgF<sub>2</sub> and quartz. The damage mechanism for these materials is avalanche breakdown, as evidenced by the very steep rise of the energy of the acoustic pulse emitted from the interaction region. The other class, represented by LiF and BaF<sub>2</sub>, is characterized by a considerably lower damage threshold and a much smaller slope of the acoustic energy immediately above threshold. The observed slope is reminiscent of the number of photons which are needed for multiphoton ionization from the valence band. Furthermore, the slope can be manipulated by changing the defect density on the surface. Therefore we believe that the mechanism leading to damage for this second class of materials is multiphoton ionization, resonantly enhanced by defect states in the band gap and subsequent ablation by Coulomb forces.

The distinction between two different photon absorption mechanisms close above threshold is sketched in Fig. 1. According to our observation, which for a typical multishot (N-on-1) experiment on BaF<sub>2</sub> is displayed in Fig. 2, one has to distinguish between three intensity ranges for defect-rich surfaces, and between two for inert surfaces. At high intensities above the breakdown point there is no longer any difference between the two: a dense plasma is formed which absorbs the laser light and decouples it from the surface. At low intensities only desorption of individual particles takes place and there is no difference either. In this regime no shock wave is generated and no probe beam deflection is detectable. For inert surfaces the desorption range extends up to the breakdown point (cf. Fig. 1). The different nature of the damage mechanism for the two classes of materials shows up only in a limited intensity interval immediately above threshold for defect-rich surfaces, as sketched in Fig. 1. The data in Fig. 2 are a typical example for such characteristic. They represent a defect-rich surface because the spot advance was about 1/100 of the spot diameter and therefore each laser shot hit a damaged roughed-up surface.

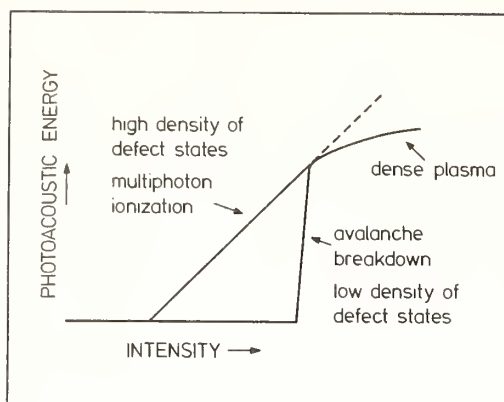


Fig. 1: Schematization of the change of damage threshold and damage mechanism when altering the surface quality. The photoacoustic energy is a measure of the amount of material removed from the surface [4]. The intersection of the sloping line with the background (horizontal line) is defined to be the damage threshold.

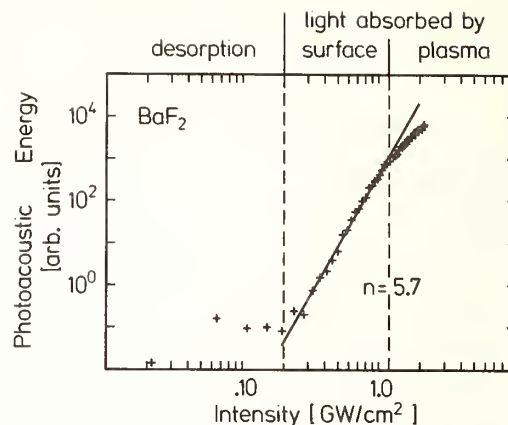
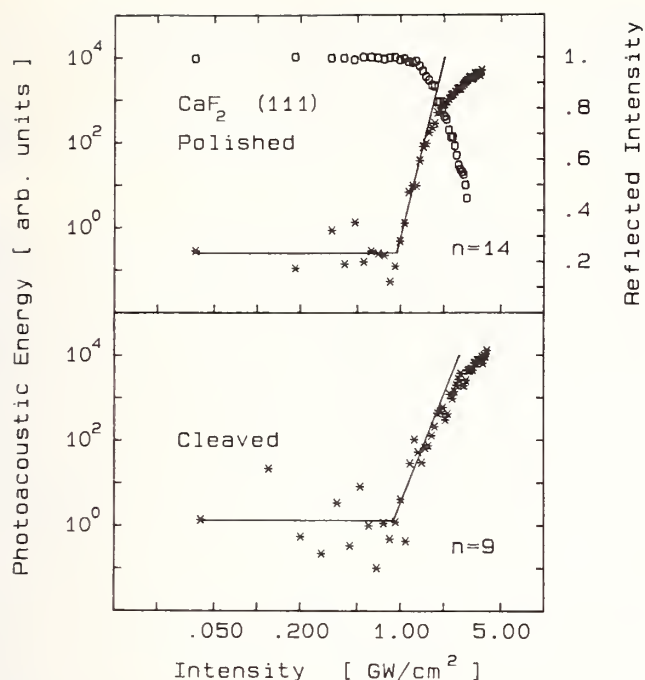


Fig. 2: Intensity dependence of the acoustic energy measured with 530 nm, 3 ns laser pulses in a multi-shot mode (spot advance small compared to spot diameter) on a cleaved surface of  $\text{BaF}_2$  in air. Dashed lines mark the intensity range for which the data yield the fit represented by the solid line. The dashed line to the left represents the damage threshold, i.e., the transition from the desorption range to the one of macroscopic damage. The dashed line to the right indicates the formation of a dense plasma.

Inert surfaces represent the expected behavior for clean polished surfaces of transparent single crystals: The cross section for multiphoton ionization from the valence band is so small that the breakdown threshold is reached before multiphoton absorption takes place. It is expected, however, that the situation reverses as soon as the multiphoton absorption is assisted by intermediate states. In fact the cross section of a five-photon process which is resonant in all intermediate steps is about  $10^{10}$  times larger compared to the non-resonant process [5]. Therefore it is conceivable that in those cases where there exists a large density of states in the band gap, the damage threshold falls below the intensity limit for avalanche breakdown. The nature of those defect states for  $\text{LiF}$  and  $\text{BaF}_2$  [1] is unknown at present. We do suspect, however, that adsorbed water may be one reason. The solubility of  $\text{LiF}$  and  $\text{BaF}_2$  in water is two orders of magnitude larger compared to the one for  $\text{CaF}_2$  and  $\text{MgF}_2$ . Nonstoichiometry might be another cause, but there is no obvious reason why the fluorides should differ in that respect. Another point is the driving mechanism for the material removal in this range where multiphoton absorption takes place. There is no confirmed knowledge available either, although models suggested by Casper et al. [6] (when extended to the surface), Rothenberg and Kelly [7], Itoh et al. [8], and others may apply. In general, however, we expect that Coulomb repulsion and thermal stress are the main causes for surface erosion in this multiphoton range.

A high density of states in the band gap can be mimicked easily by generating gross structural defects at the surface, and this can lend at least qualitative support to the model sketched in Fig. 1. It is the purpose of the present contribution to show results about the variation of the damage threshold with surface quality for  $\text{CaF}_2$  crystals. The quality of the surface was either changed by crude mechanical means like cleaving or roughening, or else by damaging it with the laser or by altering it with a preceding laser shot at an intensity below the damage threshold (incubation). All data were measured using laser pulses of 3 ns width and a wavelength of 530 nm (2.34 eV), with the crystal surfaces exposed to air.

In Fig. 3 an example is shown of single shot (1-on-1) damage threshold and slope above threshold for a polished and a cleaved surface of  $\text{CaF}_2$  (111). In the following the horizontal line always indicates the average background where no acoustic signal can be detected. Its intersection with the sloping line is taken to represent the damage threshold. The slope itself is obtained by a fit to the data in the relevant interval above threshold where they still follow a straight line. For the polished and cleaved surfaces in Fig. 3 there is no difference in damage



**Fig. 3:**  
The upper part shows the damage behavior of a polished  $\text{CaF}_2$  (111) surface in air, irradiated by 530 nm, 3 ns pulses in single shot mode (1-on-1). The damage threshold is 1  $\text{GW}/\text{cm}^2$ , with a steep rise of the acoustic energy indicating avalanche breakdown. The lower part of the figure shows data taken under the same conditions but with a cleaved  $\text{CaF}_2$  (111) surface. In the upper half stars denote acoustic beam deflection results and circles represent reflectivity data for comparison [4].

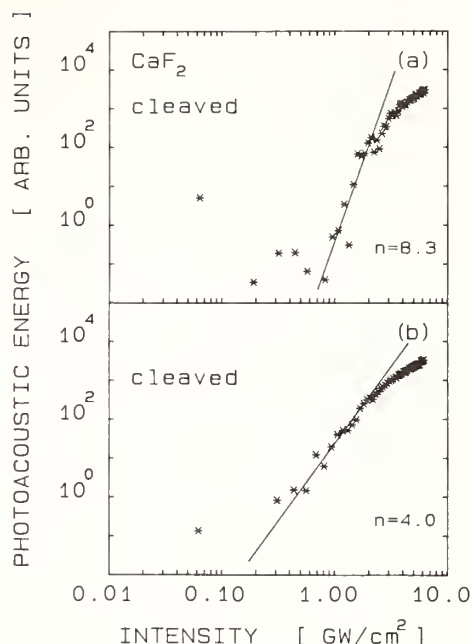
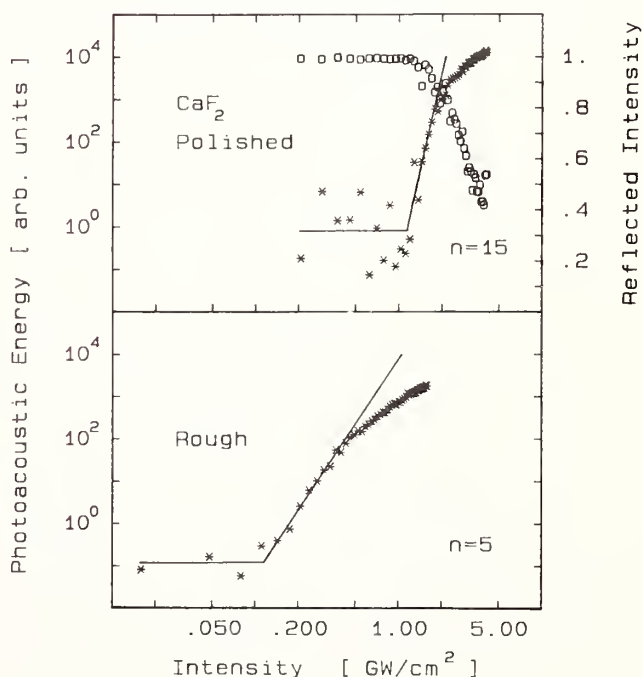


**Fig. 4:**  
Comparison of the damage behavior of two cleaved  $\text{CaF}_2$  (111) surfaces, measured under identical conditions as described in Fig. 3. The irreproducibility of the damage threshold for cleaved surfaces is apparent.

**Fig. 5:**  
The acoustic energy as a function of laser intensity in a 1-on-1 mode on a polished surface reveals avalanche breakdown in the upper part of the figure, while the lower part of the figure shows multiphoton absorption for a grounded defect-rich surface. The polished surface was cut 90° to the (111) plane, for which data are shown in the upper half of Fig. 3. Again, stars and circles indicate photoacoustic and reflectivity data, respectively.





threshold, however, the slope is significantly smaller for the latter. Unfortunately this result is rather fortuitous. It is important to recognize that cleaved surfaces do not yield reproducible results, since one can never predict whether the laser shot hits a perfect plateau or an area full of imperfections. This arbitrariness is demonstrated in Fig. 4, where single-shot measurements on two cleaved  $\text{CaF}_2$  (111) surfaces are compared. Microscopic inspection of the surface showed that the data in the lower part of Fig. 4 originated from an area with a high density of steps, while the data in the upper part came from a surface part with considerably less imperfections.

Another example is a mechanically roughened (grounded) surface displayed in the lower part of Fig. 5. This time it is compared to a polished surface (upper part) cut perpendicular to the (111) plane. First of all, the influence of a very high defect density on both threshold and slope is evident. The grounded surface layer absorbs light easily which leads to a rather low damage threshold. Surprisingly, above threshold a slope of  $n=5$  is found, which indicates that, even in case of a poor surface quality, 5-photon absorption is still the dominant energy intake within a certain intensity interval. The total energy of 5 photons (11.7 eV) compares well with a band gap of 12.1 eV for  $\text{CaF}_2$  [9]. A roughened surface probably comes close to the extreme case where the multiphoton absorption from the valence band is resonant in each intermediate step, and it is justified to talk about cascade or multiple photon excitation. A second fact can be learned from comparison of the data in the upper part of Figs. 3 and 5: there is no difference in the damage threshold for the two polished surfaces cut perpendicular to each other. Hence we conclude that only the surface quality but not its orientation determines the damage threshold.

We turn now to surfaces beforehand damaged by laser shots. Irradiation in multishot mode belongs to this category. In Fig. 6 the single shot data already shown in the upper part of Fig. 3 are compared with results obtained for a small spot advance. To be specific, the focal diameter was in both cases  $160\text{ }\mu\text{m}$ , and the spot advance for the data in the upper part of Fig. 6 was  $250\text{ }\mu\text{m}$ , while for the data in the lower part it was only  $12.5\text{ }\mu\text{m}$ . For the latter, on average 13 laser shots were at least partly hitting the crater dug up by the first one. Although the reduction of both damage threshold and slope is obvious, it is by no means as dramatic as for the grounded surface in Fig. 5.

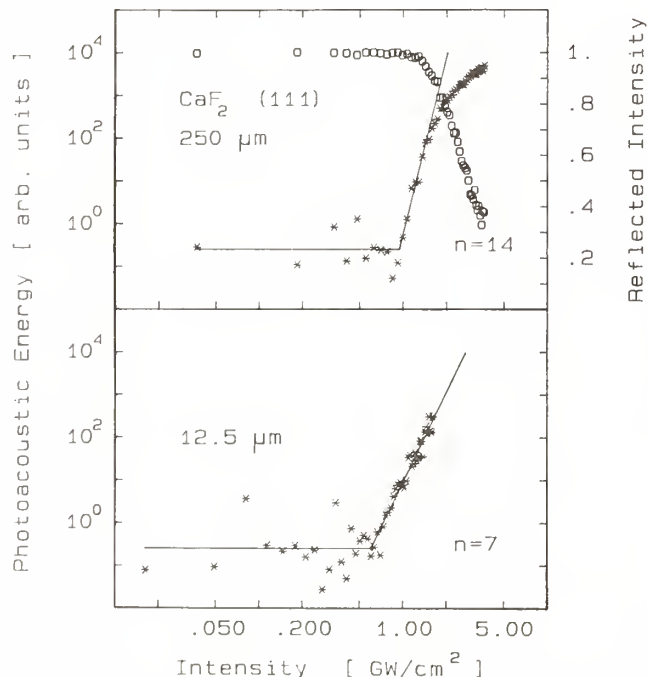


Fig. 6:  
Measurements on a polished and oriented surface of  $\text{CaF}_2$  with different irradiation modes. The spot diameter was  $160\text{ }\mu\text{m}$ . The acoustic data in the upper half of the figure (denoted by stars) were recorded with a spot advance of  $250\text{ }\mu\text{m}$ , i.e., in single-shot mode. The data in the lower part were taken with a spot advance small compared to the spot diameter, equivalent to multishot mode.

Finally in Fig. 7 the effect of a preceding laser shot of an intensity below the damage threshold (no acoustic signal) is illustrated. Again the damage threshold is considerably reduced and the slope is consistent with the band gap. This reveals that even in an intensity range where no macroscopic damage occurs, the desorption of individual particles leads to a sufficient degree of microscopic defects such that the damage threshold for each consecutive shot is effectively reduced. Those defects may be missing fluorine atoms leaving behind F-centers at the surface, or other defects near the surface, including local stress [6]. In this connection it would be of great interest to study the variation of damage threshold and slope with the



intensity of the preceding laser shot. The data in the upper part of Fig. 7 were measured with a polished surface oriented at  $45^\circ$  to the (111) plane. The damage threshold is identical to the one for the (111) plane (cf. upper part of Figs. 3 and 6) and for the surface cut perpendicular to the (111) plane (upper part of Fig. 5). Again this testifies that the damage threshold does not depend on the crystal orientation.

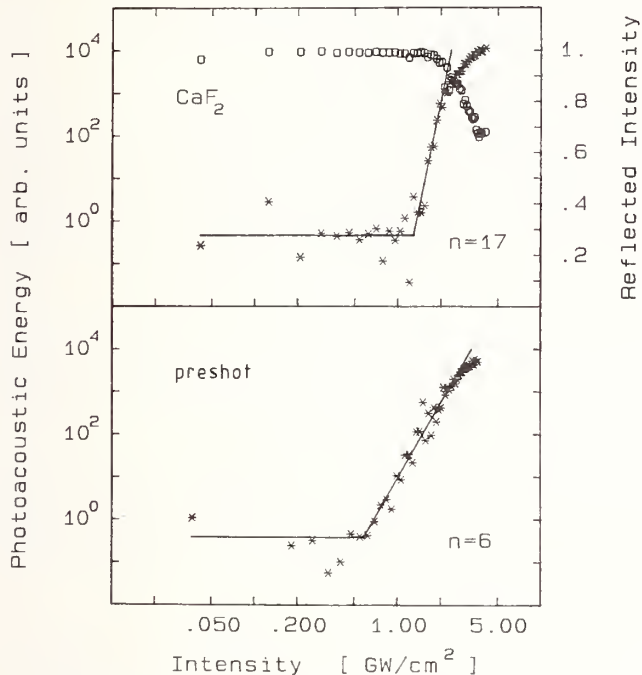


Fig. 7:

The influence of a preceding laser shot at an intensity below the damage threshold is shown (lower half) compared to the 1-on-1 damage behavior for a polished crystal. In this case the polished surface was cut at  $45^\circ$  with respect to the (111) plane. Stars represent acoustic deflection data and circles reflectivity measurements.

In conclusion, by manipulating the defect density at the surface we have substantiated the notion presented in Fig. 1. The close correlation between damage thresholds and density of surface states was experimentally confirmed. Polished crystals of  $\text{CaF}_2$  are inert and dielectric breakdown is the cause of damage. No dependence of the damage threshold on surface orientation was found. For a higher density of structural imperfections, generated by roughening the surface either mechanically or by preceding laser irradiation, damage thresholds are substantially lowered. In these cases the rise of the energy of the acoustic pulse indicated that multiphoton absorption across the band gap is the damage initiating mechanism.

This work was supported by the Deutsche Forschungsgemeinschaft, Sfb 337. We thank Dr. P. Greve, Carl Zeiss, Oberkochen, for providing the sample crystals.

#### REFERENCES

- [1] Matthias, E., Petzoldt, S., Elg, A.P., West, P.J., and Reif, J.; Proc. 1987 Boulder Damage Symposium (NIST Special Publication, to be published).
- [2] Boccara, A.C., Fournier, D., Jackson, W., and Amer, N.M.; Optics Lett. **5**: 377-379; 1980.
- [3] Belikova, T.P., Savchenko, A.N., and Sviridenkov, E.A.; Sov. Phys. JETP **27**: 19-23; 1968.
- [4] Petzoldt, S., Elg, A.P., Reichling, M., Reif, J., and Matthias, E.; Appl. Phys. Lett. **53**: 2005-2007; 1988.
- [5] Bepp, H.B. and Gold, A.; Phys. Rev. **143**: 1-24; 1966.
- [6] Casper, R.T., Jones, S.C., and Braunlich, P.; Proc. 1988 Boulder Damage Symposium.
- [7] Rothenberg, J.E., and Kelly, R.; Nucl. Instr. Meth. **B1**: 291-300; 1984.
- [8] Itoh, N., Nakayama, T., and Tombrello, T.A.; Phys. Lett. **108A**: 480-484; 1985.
- [9] Rubloff, G.W.; Phys. Rev. **B5**: 662-684; 1972.

## COMMENTS

Question: You show damage of polycrystalline calcium fluoride, mag fluoride, and lithium fluoride. It's hard to get smooth ten angstrom type surfaces of crystal and lithium fluoride. You also stated that high defect densities on lithium fluoride and barium fluoride led to multi-photon processes rather than an avalanche. Do you know what the surface quality, in terms of roughness was of the lithium fluoride as compared to the calcium and barium fluoride?

Answer: These are commercially optically high grade pieces. More, I don't know. But, I would like to make the point that the barium fluoride and the lithium fluoride have  $10^2$  more solubility in water compared to magnesium fluoride and calcium fluoride. This fact is what made me suggest doing the talk that we believe that lithium fluoride and barium fluoride have a large number of defect states on which water can adsorb. However, I am aware of the fact that polished lithium fluoride has a lot of defects introduced by the polishing process.

Question: I still am not sure that I understand completely this idea that you need a large density of defect states to get multi-photon absorption across the gap. Quantitatively, how do you justify that? It seems that one photon transitions from those states or involving those states would predominate.

Answer: Yes, but you have to take into account the high density, you see. The electrons are predominantly in a given spin. And even if you have defect states, they are comparatively very low concentration compared to the density of states in the given spin. So once you have some states available that can promote the multi-photon process, the high density of electrons in the given spin state would favor that process. Am I making myself clear?

Question: We'll talk about it some more later. Because if you have occupied defect states on the surface, their density will be in any case very much lower than those electrons in the given spin state. I also have difficulty of being convinced of multi-photon process here in lithium fluoride. A number of years ago, we measured the damage threshold of bulk lithium fluoride and found out that it was loaded with bulk defects which we concluded were non-stoichiometric sites. I would assume that those sites would exist on the surface as well, and that they have their own absorption spectrum and one photon could easily cause damage. And so, if you have those, you don't have to invoke multi-photon absorption to damage non-stoichiometric material.

Answer: The point is that if you are talking only about 1-photon process, you are most likely only making heat. Now I did not show those morphology pictures, but from those, it's clear that there's no melting or so going on. We surely will have some heat generated, but we think it's a small amount that goes into that channel compared to the other one. Now you questioned the multi-photon process as well. There are several indications here, for example, when you measure by the fluorescent light from these breakdowns, it's a 5-photon dependence. When we measure the desorption, it's a 5-photon dependence. And of course, the first idea here was not to see the multi-photon process, in fact, we were surprised to see slopes like 5, which would sort of bridge the band gap, but I don't see any other interpretation and what we will be following now is this transition from multi-photon to the low defect dielectric breakdown. All I can say is, come up with another interpretation about the slope, and we can discuss it.

Question: First I want to compliment you on having the foresight to look at cleave surfaces in comparison with polished surfaces. But, I'd like to comment that I know from lots of work, that if you look at the dislocation content of crystals, particularly lithium fluoride, and you can do this easily by making etch pits

counts, you find that the cleave surfaces have very few dislocations. The polished surfaces have a large variation in dislocation density, depending on the person and the technique used to polish them and that the roughness crystals such as you would get by using sand paper have extremely high surface dislocations. Have you looked at this, and if you have, what do you make of this dislocation possibility?

Answer: We have not looked at that yet in the systematic manner and I'd like to emphasize again that these are qualitative data. I'm very much aware of the fact that we have to quantify the number of defects on the surface in order to make this case a little bit better. But, give us a year or two and we might be able to do this. What we have done up to now is only a qualitative measurement. But, I thank you for the suggestion.

Laser-Induced Surface Ablation and Optical Damage of ZnS Crystals  
Caused by Single- and Multiple-Pulse Laser Irradiation\*

H. F. Arlinghaus,\*\* W. F. Calaway, D. M. Gruen

Materials Science, Chemistry, and Chemical Technology Divisions  
Argonne National Laboratory  
Argonne, IL 60439

L. L. Chase

Lawrence Livermore National Laboratory  
University of California  
P.O. Box 5508  
Livermore, CA 94550

Velocity distributions and yields of neutral Zn atoms emitted from laser-irradiated ZnS crystals at power densities far below the single-pulse damage threshold have been analyzed by high-resolution two-photon laser-induced fluorescence spectroscopy and also by electron impact ionization mass spectrometry. Large differences in the measured kinetic temperatures have been found between the single- and multiple-pulse laser irradiation experiments. The high-kinetic temperatures, obtained in multiple-pulse experiments, may be caused by cumulative surface modification, such as thermally-induced cracking, leading to a reduction of the thermal conductivity compared to the bulk value. Optical damage was related to the interaction of a plasma formed at a critical combination of particle density and laser intensity, with the surface.

Key words: Laser damage, laser fluorescence spectroscopy, particle emission; temperature, threshold, time-of-flight, vaporization, zinc sulfide.

## 1. Introduction

The ability to produce optical materials that can transmit or reflect intense laser radiation without suffering surface damage requires the identification of the initial mechanism for deposition of laser energy at the surface and an understanding of the resulting physical processes that precipitate catastrophic material failure. Despite its importance, the nature of this damage is still not well understood. In transparent optical materials, for example, there are several possible interaction mechanisms that could cause absorption of laser energy at the surface. The problem of detecting these surface absorption processes is formidable because they may be very localized and cause small unobservable changes in the transmitted or reflected laser intensities and average surface temperatures [1]. To get more information about the interaction phenomenology, the effects of laser radiation on materials, and the processes that cause laser damage, we investigated sputtered particles originating from laser-irradiated surfaces with fluences far below the accepted damage threshold. These particles are characterized by their yield, kinetic energy and angular distributions,

---

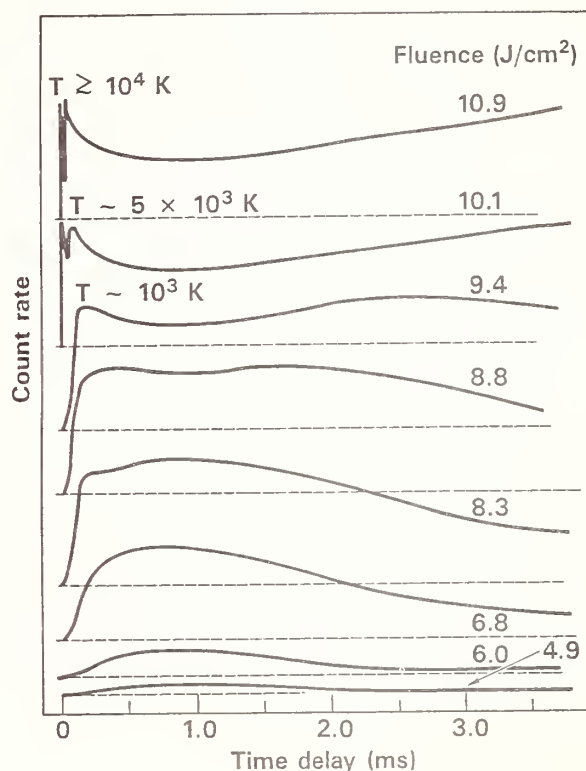
\* Work performed under the auspices of the U.S. Department of Energy, BES-Materials Sciences, under Contract W-31-109-ENG-38 (ANL) and Contract W-7405-ENG-48 (LLNL).

\*\* Present address: Atom Sciences, Inc., 114 Ridgeway Center, Oak Ridge, TN 37830



relative abundance, and spatial origin. Chase and Smith, and Arlinghaus et al. [1-6] have found that, in general, most of the particles sputtered at laser fluences far below the damage threshold are neutral atoms or molecules, and have shown that this particle emission is a precursor to observable damage.

Figure 1. TOF data for Zn emission from ZnS following a series of 1.06  $\mu\text{m}$ , 8 ns long laser pulses with the indicated fluences. Labelled temperatures are estimates based on the time delay,  $t_d$ , of the peak of the "Maxwellian" emission component. (from Ref. 1).



Last year at this conference Chase and Smith presented time of flight (TOF) data on the emission of Zn from single-pulse irradiated ZnS single crystals using an electron impact ionization mass spectrometer (MS) as a detection system [1]. As shown in figure 1, they observed Zn emission occurring for a time interval of several hundred microseconds. At fluences above 8  $\text{mJ}/\text{cm}^2$ , a peak develops at a delay time of about 250  $\mu\text{s}$ , which is attributed to promptly emitted Zn particles with a kinetic temperature of less than 1000 K. As the damage threshold is approached; however, the characteristic temperature increased to several thousand Kelvin. Similar data has been obtained at 532 nm, 355 nm, and 266 nm and for the emission of S and S<sub>2</sub> [1]. With decreasing wavelength, the general characteristics of the TOF distributions are unchanged, which suggests that the same processes are involved in the emission at all four laser wavelengths.

In this work, we used 308 nm laser irradiation deposited on ZnS to study the above described phenomena in more detail. This photon energy lies between the third and fourth harmonic of the Nd:YAG; thus, direct comparison to the above described single-pulse experiments should be possible. An experimental technique, which has proven to be more sensitive than electron impact ionization MS and is particularly useful in measuring velocity distributions and particle densities of ejected neutral particles, is laser-induced fluorescence spectroscopy (LFS). To determine the velocity distribution for laser-ablated particles from nanosecond laser pulses, TOF measurements have been performed. This is accomplished by detecting the ejected particles at a known distance from the target at various times after the ablating laser strikes the target. The capabilities of this type of experiment have been expanded in our apparatus by incorporating a high-resolution (single-mode) tunable laser into the LFS system in order to obtain Doppler-shifted velocity profiles of ablated

atoms as a function of TOF. Using the velocity determined from the Doppler shift and the measured TOF, the time at which an atom was ejected from the surface can be calculated. Thus, it is possible to separate prompt from delayed emission of ablated atoms, as well as to probe possible molecular or cluster fragmentation. This approach of determining velocity distributions, both from Doppler shift and TOF, was thought to be required to investigate delayed emission of atoms as seen for the single-pulse experiments described above.

To estimate the amount of material removed with each laser shot and the number of shots needed to remove one monolayer, the absolute yield of Zn atoms was determined by comparison with LFS measurements of Zn atoms sputtered from pure metal targets by  $\text{Ar}^+$  ions.

An important problem in laser-induced optical damage is the dependence of the damage threshold on the number of laser shots striking the surface. Significant reduction in the damage threshold over the single-pulse value appears to occur as a result of multiple-pulse operation [7,8]. This problem was examined by measuring the velocity distribution and the neutral yield from ablated particles as a function of the number of laser shots.

## 2. Experimental Technique

The experimental arrangement is shown in figure 2. It consists of an ion gun, an ablating laser, an LFS detection system, an ultrahigh vacuum (UHV) chamber (typical base pressure  $3 \times 10^{-8}$  Pa), and computer-controlled electronics. The experimental apparatus was recently described in detail [4,5] so only certain key features will be discussed in this account. The interaction of the ablation laser with the sample causes atoms to be ejected from the surface. After a specific delay time, a narrow-band probe laser (85 MHz bandwidth, 1.3 mJ/pulse, 15 ns pulse) is triggered. Its wavelength is set to twice the wavelength of the Zn transition,  $4s^2 \ ^1S_0 - 4d \ ^1D_2$  (160 nm). The induced fluorescence is detected at 636 nm ( $4d \ ^1D_2 - 4p \ ^1P^0_1$ ) by light collection optics that image the fluorescence from the probed volume, a known distance from the sample through a narrow bandpass interference filter onto a photomultiplier. The frequency of zero velocity for Zn was determined by a two-photon Doppler-free experiment [9].

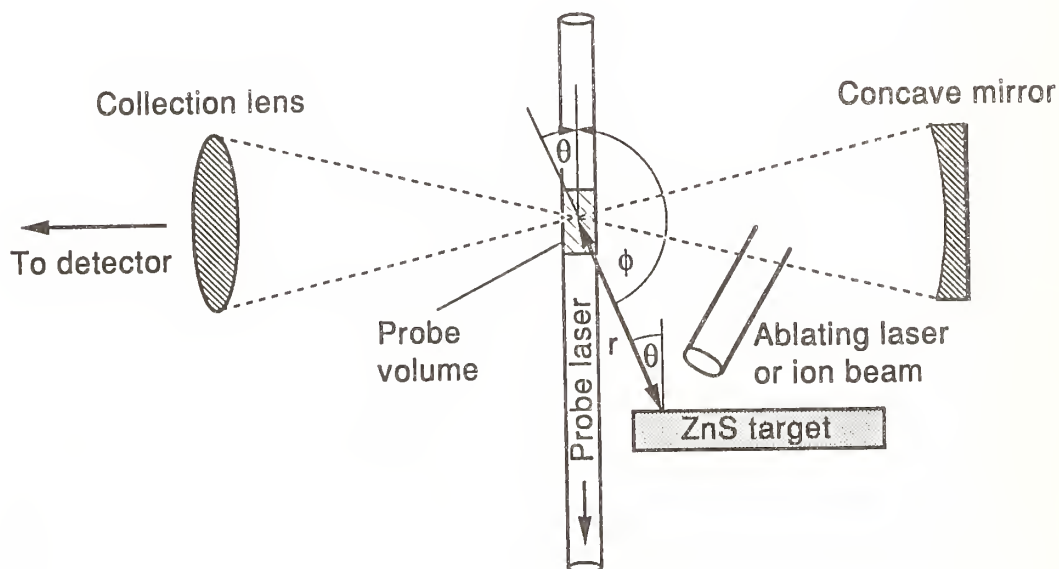


Figure 2. LFS TOF experimental arrangement.

An excimer laser operated with XeCl to produce an output wavelength of 308 nm with a pulse width of 30 ns was used to irradiate the targets. The output of the ablating laser (typically 350 mJ) is attenuated with filters to produce fluences in the range 10 to 80 mJ/cm<sup>2</sup> (spot size ~ 3 mm<sup>2</sup>), which is well below the single-pulse damage threshold of ZnS (>1 J/cm<sup>2</sup> in the UV) [1,10].

In Doppler-shifted experiments, the frequency,  $\nu$ , at which a particular atom absorbs radiation, depends on the velocity,  $v$ , of that atom as given by the equation:

$$\nu = \nu_0 \left(1 + \frac{v \cos \phi}{c}\right) = \nu_0 \left(1 - \frac{v \cos \theta}{c}\right) \quad (1)$$

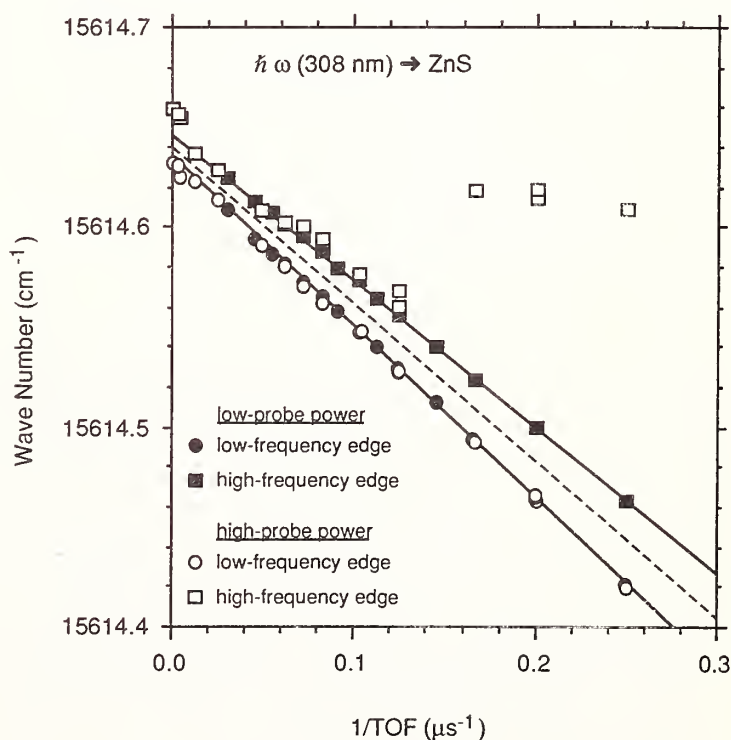
where  $\nu_0$  is the frequency of the atom at rest,  $c$  is the speed of light, and  $\phi$  is the angle between the direction of propagation of the laser and the velocity vector of the sputtered atom being probed. (In this experimental arrangement, the sputtered atoms and the laser are counter propagating and thus  $\cos \phi = -\cos \theta$  as shown in figure 2).

In Doppler-shifted LFS TOF experiments, the velocity,  $v$ , of the particles is derived from the distance,  $r$ , between the target and the location where the particle is detected, and the delay time,  $t$ , between when the ablating laser strikes the surface and when the probe laser is directed through the imaged volume. Since the size of the probed volume is not negligibly small, the expected width of the Doppler profile for a fixed delay time is given by:

$$\Delta \nu = \nu_0 \frac{\Delta r \cos \theta}{c t} \quad (2)$$

where  $\Delta r = r_{\max} - r_{\min}$  is the difference between the maximum and the minimum distance a particle can travel and still remain in the probed volume. For comparison with laboratory data, the Doppler width must be convoluted with the laser bandwidth. Equations (1) and (2) show that both frequency shift and spectral width of the fluorescence signal are inversely proportional to the delay time (TOF). For short delay times, this results in both a shift of the fluorescence signal to lower probe laser frequency and a broadening of the atomic transition.

Figure 3. Doppler shifts of Zn atoms for a probe laser power of 12 kW and 1.7 MW as a function of inverse time of flight. The circles and squares represent data obtained from the low- and high-frequency edge of the Doppler profile, respectively. The solid lines are least-squares fits to the data. The dashed line shows the peak of the Doppler-shifted profile assuming a Gaussian shape.





### 3. Results and Discussion

The unique combination of LFS and TOF permits unambiguous detection of prompt and delayed emission of ablated atoms, as well as probing possible molecular or cluster fragmentation. In figure 3 the measured minimum and maximum wave numbers of the Doppler profiles, defined at FWHM of the signal, have been plotted versus  $1/t$  for two laser probe powers. The solid lines are least-squares fits to the data where the UV probe laser power was 12 kW. They fit the data points very well and are in good agreement with eq. (2). The dashed line is the expected Doppler-shifted frequency [eq. (1)] which was calculated from the two solid lines assuming a Gaussian distribution for the Doppler-shifted signal. Here, the low-frequency edge data show no deviation from the expected theoretical straight line suggesting that we are not detecting any delayed emission of Zn atoms. This is contrary to the results obtained for single-pulse laser ablation data from ZnS (fig. 1), where delayed emission in the millisecond range has been observed. One possible explanation of the discordant results is that different ejection mechanisms are at work for single-pulse versus multiple-pulse laser ablation. It is possible that with multiple-pulse experiments cleaning effects such as ejection of loose-bond materials, removal of dislocations, and so forth, occur in the first laser shots. These effects are not detectable when thousands of laser shots are required to measure a velocity distribution and could explain the observed differences between single-pulse and multiple-pulse experiments.

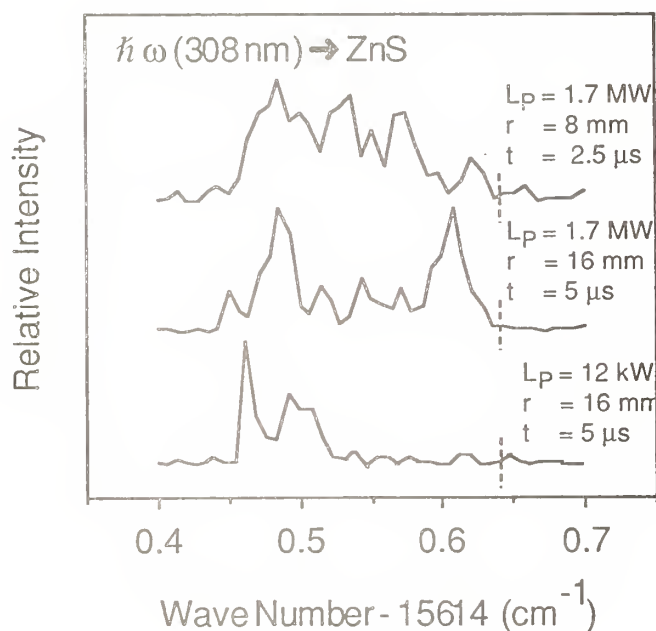


Figure 4. Three spectra that show the Doppler-broadening obtained from a laser-ablated ZnS crystal using two different probe laser power ( $L_p$ ), TOF ( $t$ ), and distances ( $r$ ) between the target and the probed volume while preserving the ejection angle  $\theta = 22^\circ$  (see fig. 2). The vertical dashed lines represent the frequency of Zn atoms with zero velocity.

Analysis of similar data, obtained at higher UV probe power (1.7 MW), shows substantial deviations from a straight line on the high-frequency side for short delay times. Deviation toward higher frequencies, i.e., slower velocity, would indicate that there are particles in the probed volume with velocities too slow to have travelled from the sample to that volume at constant velocity in time,  $t$ . This phenomenon was analyzed more thoroughly by varying the UV probe laser power, TOF, and distance between the target and the probed volume while preserving the angle  $\theta$  (see fig. 2). Figure 4 shows three spectra for short delay times each having a mean velocity of 3200 m/s. The bottom spectrum, obtained with low probe laser power, shows a Doppler broadening as expected from eq. (2). Increasing the probe power results in a broadening only towards higher frequencies, as can be seen in the middle and top spectra. By doubling the distance,  $r$ , and the delay time,  $t$ , without changing the angle,  $\theta$ , (see fig. 2), the velocity resolution can be increased (eq. 2), thus resolving the broad peak (top spectrum) into two Doppler-shifted peaks (middle spectrum). The velocity of Zn atoms as determined by TOF indicates that the Doppler-shifted absorption for Zn promptly ejected from the sample should be positioned at the low frequency peak. The high frequency peak appears to be Zn atoms with a perpendicular velocity vector some 2400 m/s too slow. A likely explanation for



this is that the probe laser causes fragmentation of fast ZnS molecules or clusters, thus producing Zn atoms with slower velocity components than the directly ejected particles interrogated at the same delay time. An interesting point which supports this hypothesis is that the kinetic energy partitioned to Zn from a two photons ( $\lambda = 320$  nm) dissociation of ZnS ( $D_0 = 2$  eV [11]) will be  $\approx 1.9$  eV which corresponds to a velocity of 2400 m/s. Since the broadening was observed only in the direction towards higher frequencies, instead of to both sides, and did not shift very much as a function of time of flight, the above explanation would require an assumption that the molecules are oriented or that the fragmentation is directional. This behavior will be analyzed in more detail in future experiments using resonance and nonresonance ionization mass spectrometry for identification of the fast molecules or clusters.

It should be noted that broadening occurred only in the high-velocity tail of the particle energy distribution, and this represents only about 5 - 10% of the total particle density. Therefore, the anomalous excess density was not included in the velocity distributions presented below. Other techniques for detecting neutrals, such as broadband probe lasers or electron impact ionization, cannot discriminate between these alternatives and may, therefore, overestimate the velocity distribution in the higher velocity tails. The high energy molecules or clusters were observed only at higher ablation power ( $80 \text{ mJ/cm}^2$ ) and presumably were the result of cracking or cleaving of the crystal. This means that some degree of damage occurs on each laser shot. At these higher fluences, high energy Zn neutral emission has also been observed by Chase and Smith (see fig. 1) in single-pulse experiments. It is possible that this observation was also the result of fragmentation of molecules or clusters due to electron impact ionization, and thus, is in agreement with our results.

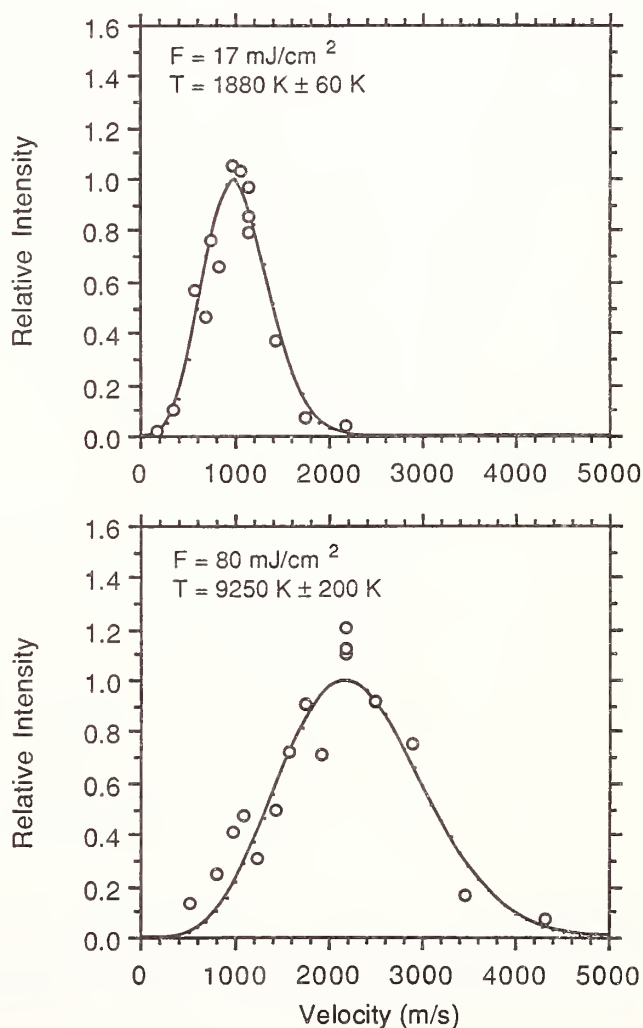


Figure 5. Velocity distributions of Zn atoms ablated from a ZnS surface for two different ablation fluences. The solid lines are Maxwell-Boltzmann fits to the measured data (circles) at the temperature indicated. The shown standard deviations were calculated from the least-squares fits.

The absolute yield of Zn atoms produced by laser irradiation was ascertained by comparison of its velocity distribution with that of Zn atoms ejected from an ion-bombarded metallic Zn target. The two distributions were measured for the same angle and at the same distance to the probed volume. Cosine distributions have been assumed for both cases. The absolute Zn yield from ZnS, due to 0.9 mJ irradiation at 308 nm on a 3 mm<sup>2</sup> (30 mJ/cm<sup>2</sup>) area, was determined to be 10<sup>9</sup> atoms/pulse, corresponding to »10<sup>-6</sup> atoms/photon [4]. For an area of 3 mm<sup>2</sup>, it was estimated, assuming stoichiometric ablation, that 4x10<sup>-4</sup> of a monolayer is removed per laser pulse. This corresponds to 2500 shots/monolayer.

As explained above, the velocity distribution can be obtained by measuring the fluorescence signal at the appropriate frequency for each delay time (i.e., a single velocity component out of the velocity integral) and plotting those numbers against the velocity determined from that delay time. If the experimental velocity distribution corresponds to a thermal equilibrium distribution, then the data should follow a Maxwell-Boltzmann distribution. In this case, the number density of atoms in the probed volume  $N(u) \propto u^4 \exp(-u)^2$ , where  $u$  is the reduced velocity which is related to the velocity by  $u = v/v^*$  with  $v^* = \sqrt{2 k T/M}$ .

Figure 5 shows velocity distributions for different ablation laser fluences. In order to obtain the velocity distributions as shown in figure 5 between 2,000 and 15,000 laser shots were necessary for fluences between 80 and 17 mJ/cm<sup>2</sup>, respectively. The solid lines are Maxwell-Boltzmann velocity distributions that have been fitted using the Levenberg-Marquardt nonlinear least-squares method [12]. The Maxwell-Boltzmann distributions fit the data for both fluences quite well. The scatter in the data, particularly at higher ablation laser fluence, is believed to be caused by a combination of shot-to-shot fluctuations in laser intensities, changes in the substrate properties with consecutive laser shots, and variable contributions such as fragmenting molecules and clusters.

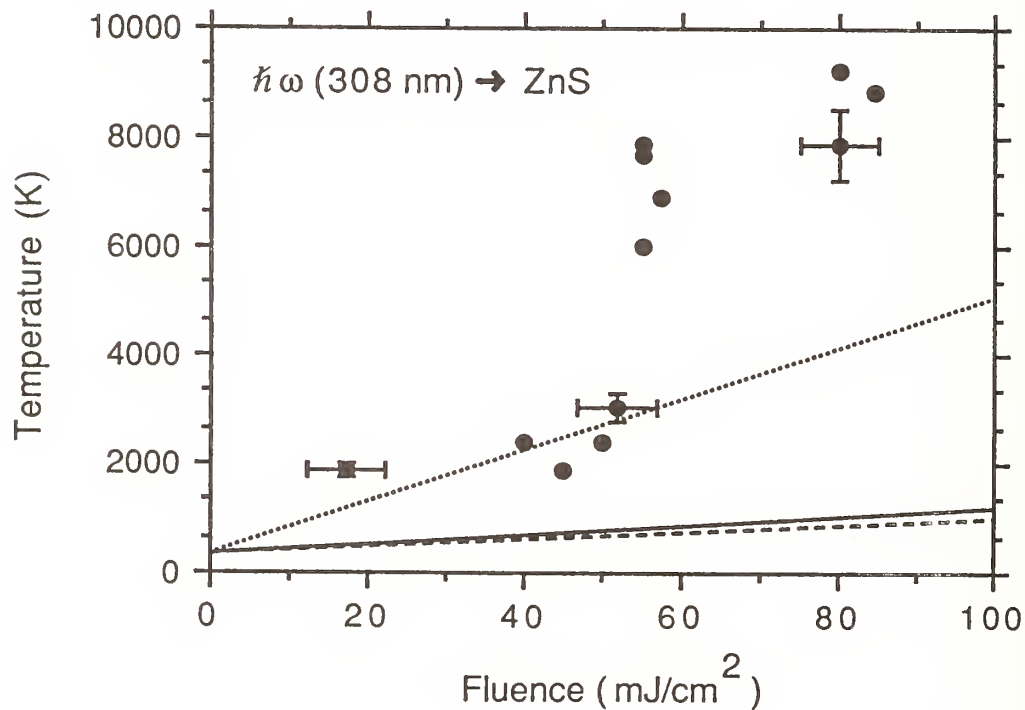


Figure 6. Increase of the kinetic temperatures as a function of ablation fluence. The lines represent calculated surface temperatures using different heat models. Solid line = surface heating;  $\alpha \rightarrow \infty$ ,  $K = 0.2 \text{ W/(cm K)}$ ; dashed line = volume heating;  $\alpha = 10^5$ ,  $K = 0.2 \text{ W/(cm K)}$ ; dotted line = volume heating, taking into account only the heat capacity,  $C$ , and a depth of 100 nm for the ablated area.

The experimentally determined kinetic temperatures as a function of ablation laser fluence are depicted in figure 6. The temperature increases slowly with increasing fluence until  $\sim 55 \text{ mJ/cm}^2$  where the temperature rises suddenly from 3000 to  $\sim 7000 \text{ K}$ . After the sharp rise, the temperature slowly increases further with increasing fluence. It should be noted that for each temperature measurement a new ablating area was used on the target. Visible damage was only observed for the three measurements made at an ablation fluence of  $\sim 80 \text{ mJ/cm}^2$ . The solid line and the dashed line in figure 6 are modelled surface and bulk temperatures due to laser illumination at 308 nm. For modelling, we used solutions of the heat-flow equation from Bechtel [13] for two cases: the volume generation of heat, which includes the presence of bulk heating, and the surface generation of heat, where the absorption coefficient  $\alpha \rightarrow \infty$ , thus giving an upper limit for the surface temperature of a flat surface. We assumed a rectangular temporal shape for the beam intensity, a flat surface, and instantaneous conversion of the total optical energy into heat at the point at which the light was absorbed. We are in the regime such that lateral diffusion of heat is small compared to characteristic radial dimensions, the thermal diffusion length,  $\sqrt{4 \kappa t}$ , being  $1.1 \mu\text{m}$  in our case. In all of the calculations presented here, it is assumed that the absorptivity, reflectivity, thermal conductivity, and thermal diffusivity are independent of temperature and have used their values at 300 K [14,15].

As seen in figure 6, the measured temperatures are much higher than the calculated maximum expected surface temperature. One possibility for these high temperatures is that the thermal conductivity is much lower than the bulk value. This can happen when cracks are generated by thermal stress due to multiple laser shots. For example, the dotted line in figure 6 is a plot of temperature versus fluence for an isolated slice of ZnS with a thickness of 100 nm. This line appears to fit the low fluences data. Single-pulse experiments show an increase of only  $\sim 500 \text{ K}$  at low ablation fluences. This again demonstrates the substantial differences that exist between single- and multiple-pulse experiments, and show unambiguously that cumulative surface modification will occur with multiple pulse laser irradiation. At  $60 \text{ mJ/cm}^2$ , the temperature rises suddenly from 3000 to  $\sim 7000 \text{ K}$ . This step may indicate that a critical particle density for formation of a plasma has been reached. The laser pulse absorption in the plasma causes direct heating of the ablated particles. A plasma can bombard the surface and lead to damage of the surface similar to that observed during the measurements of the three velocity distributions taken at  $80 \text{ mJ/cm}^2$ .

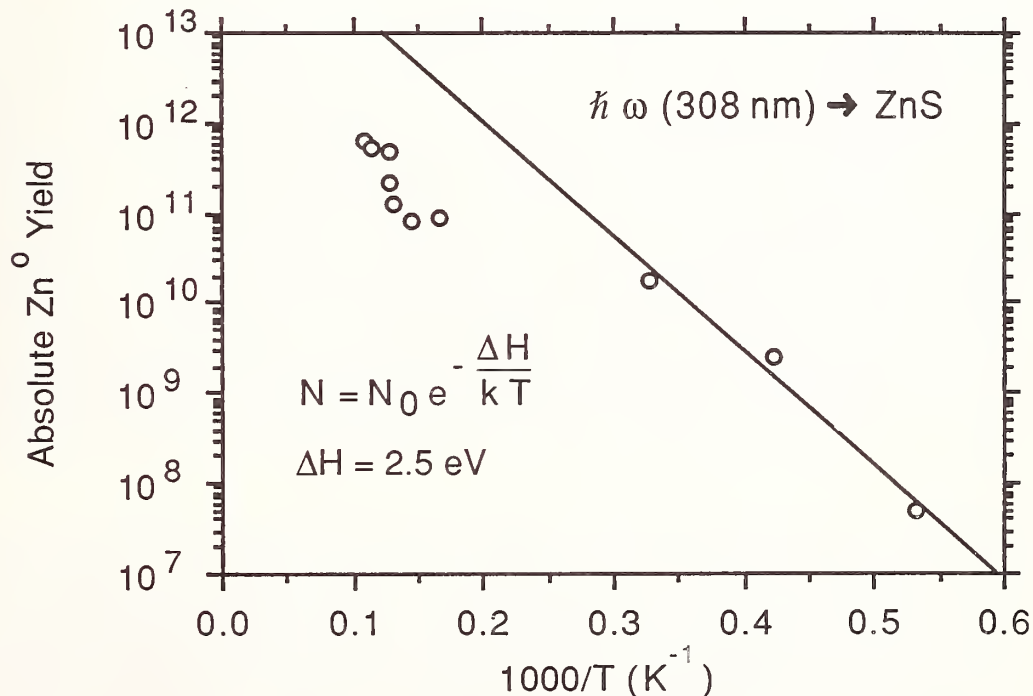


Figure 7. Arrhenius plot of the absolute neutral Zn yield as a function of the inverse temperature. The solid line is a least-squares fit to the three data points obtained at low ablation fluences. The slope of the solid line yields an activation energy of 2.5 eV.



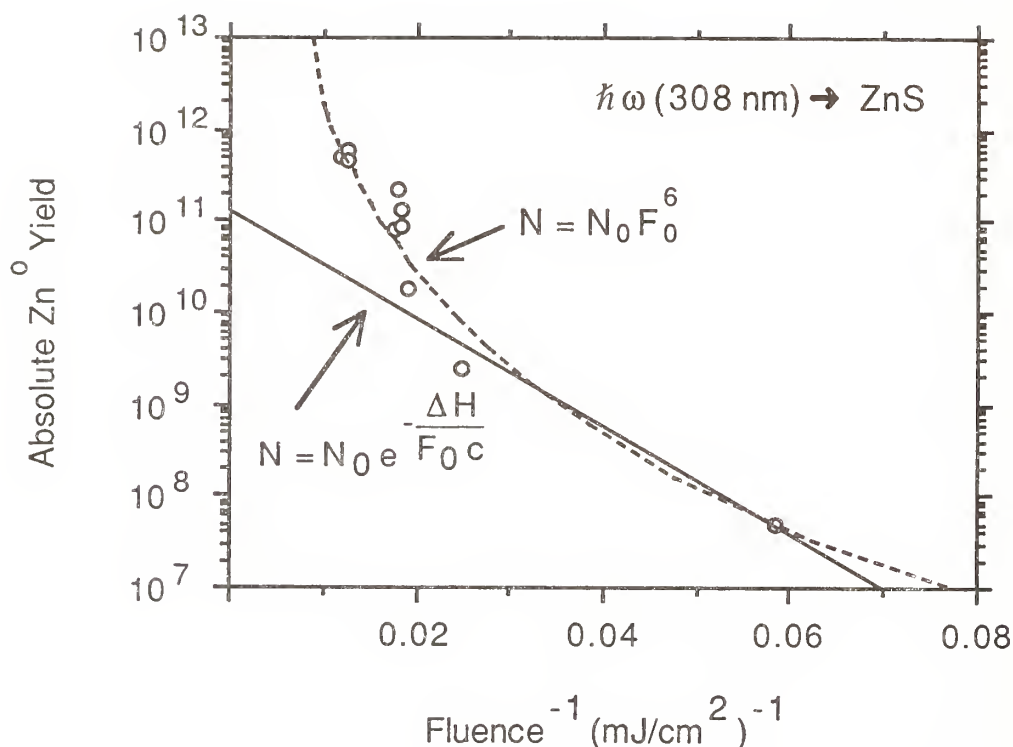


Figure 8. Change of the absolute neutral Zn yield as a function of the inverse of fluence. The solid line is a least-squares fit of an Arrhenius expression to the three data points obtained at low ablation fluences. The dashed line is a least-squares fit to the power law using all data.

In figure 7, the increase of the absolute neutral Zn yield is depicted as a function of the inverse temperature. The Zn yield follows an Arrhenius relation for fluences between 20 and 60 mJ/cm<sup>2</sup> with an activation energy of 2.5 eV. This is approximately the heat of vaporization of ZnS which indicates that a thermal process, such as sublimation, may account for the emission [14]. At higher fluences, the measured temperatures deviate significantly from the straight line. This deviation also occurs as an abrupt step, similar to figure 6, indicating that a second process has started. Figure 8 shows the absolute neutral Zn yield as a function of the inverse fluence. Since for thermal evaporation at low fluences  $1/F \propto 1/T$ , a straight line should be expected. For fluences higher than 60 mJ/cm<sup>2</sup>, the yield shown in figure 8 deviates from the straight line. This change accompanies the jump in temperature in figure 7. This behavior suggests that the plasma interacts with the surface leading to a rise of the yield. Since we are only detecting neutral Zn particles once a plasma is formed, the total particle density may be significantly higher than the measured value. The relationship,  $N \propto F_0^6$ , appears to fit the data very well. Such power laws are often used to explain multiphoton processes [16-18]. In this case, however, the ablation laser wavelength was in the region of interband absorption; thus, there is no obvious physical meaning to this power law dependence in our experiment.

Figure 9 shows the Zn yield, the kinetic temperature derived from the velocity distribution, and the first occurrence of visible damage for a multipulsed experiment on a single spot at a fixed fluence of 45 mJ/cm<sup>2</sup>. It can be seen that after 30,000 shots the particle density increases nearly exponentially with consecutive laser shots. The kinetic temperature was about 1900 K and did not change very much during the entire experiment. After 150,000 shots (corresponding approximately to a removal of 60 monolayers), the first visible damage occurred. The observed increase in particle emission with consecutive laser shots could be attributed to a change in the surface morphology, which in turn could lead to better coupling between the laser light and the surface as well as to changes in the surface stoichiometry. Clearly, figure 9 shows unambiguously that microscopic damage increases with the number of laser shots and, consequently, leads to catastrophic failure at lower laser fluence than the single-pulse damage threshold.



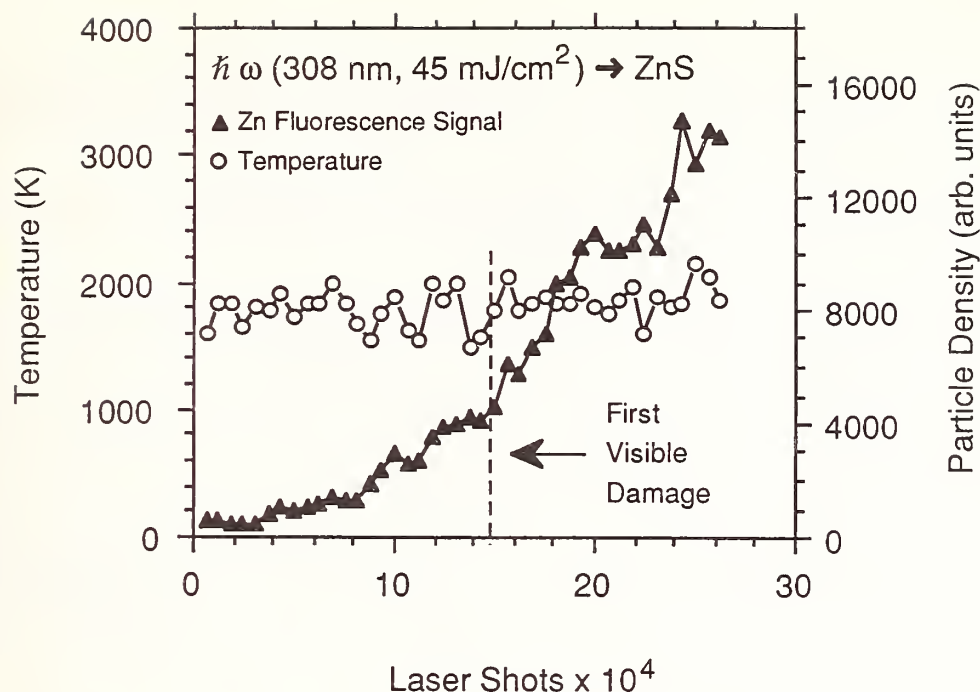


Figure 9. Plot of the kinetic temperature and particle density as a function of the number of laser shots striking one site.

The results reported in this paper can be rationalized on the basis of the following model. The high kinetic temperatures obtained for low laser ablation fluences are due to reduced thermal contact of the surface region with the bulk. This can result from cracks in the crystal produced by repetitive laser pulses heating the surface, thus causing localized stresses due to differential thermal expansion [19]. This effect may also explain the large differences in kinetic temperatures of the ejected atoms obtained in single-pulse [1] compared to multiple-pulse experiments. The sudden rise in temperature at a particular fluence indicates that a critical combination of particle density and laser intensity leads to formation of a plasma. The plasma thus formed interacts with the surface and leads to catastrophic failure. The very small size of the observed damage spots ( $\mu\text{m}$ ) in comparison to the irradiated area (mm) suggests the possibility that local breakdown between the plasma and the surface may be leading to damage. In both single-pulse and multiple-pulse experiments, high-energetic neutral particles were observed at fluences near the visible damage threshold. Combined LFS TOF measurements indicate that these neutrals are products from molecule or cluster fragmentations caused by the excitation laser. Presumably, electron impact ionization could also fragment such species. The emission of these fast molecules or clusters are believed to be the result of cleaving or cracking of the surface. Clearly, additional measurements are necessary to verify this damage model and to gain more detailed information on the mechanism for atomic and cluster emission during laser irradiation.

#### 4. Conclusions

It can be concluded that the LFS TOF technique is a very sensitive and effective method for detecting ejected neutral particles from laser-irradiated surfaces for a variety of elements and transitions as well as their characterization by yields and velocity distributions. Neutral particle emission was identified as a precursor of observable damage. The unique combination of Doppler-shifted LFS and TOF techniques is a useful tool for separating prompt from delayed emission of particles ejected from laser-irradiated surfaces as well as for probing possible molecular or cluster fragmentation. To get more detailed information about the physical processes involved in particle ejection and optical damage, measuring of the spatial dependence of the emission and quantitative relative yields of various surface constituents have to be included in future investigations.

## 5. References

- [1] Chase, L.L.; Smith L.K. Laser Induced Surface Emission of Neutral Species and Its Relationship to Optical Surface Damage Processes, in the Proceedings of Laser Induced Damage in Optical Materials (NIST Special Publication 756, (1987), in press.
- [2] Chase, L.L.; Lee, H.W.H. Accumulated Surface Damage on ZnS Crystals Produced by Closely Spaced Pairs of Picosecond Pulses, to be published in the Proceedings of the 20th Symposium on Optical Materials for High Power Lasers, (1988).
- [3] Arlinghaus, H. F.; Calaway, W. F.; Young, C. E.; Pellin, M. J.; Gruen, D. M.; Chase, L. L. Laser Fluorescence Spectroscopy of Zinc Neutrals Originating from Laser-Irradiated and Ion-Bombarded Zinc Sulfide and Zinc Surfaces, in the Proceedings of Laser Induced Damage in Optical Materials (NIST Special Publication 756, (1987), in press.
- [4] Arlinghaus, H. F.; Calaway, W. F.; Young, C. E.; Pellin, M. J.; Gruen, D. M.; Chase, L. L. High-Resolution Multiphoton Laser-Induced Fluorescence Spectroscopy of Zinc Atoms Ejected from Laser-Irradiated ZnS Crystals, *J. Appl. Phys* 15 (1988).
- [5] Arlinghaus, H. F.; Calaway, W. F.; Young, C. E.; Pellin, M. J.; Gruen, D. M.; Chase, L. L. Analysis of Ion-Bombarded and Laser-Irradiated ZnS and Zn Surfaces via High-Resolution Multiphoton Laser-Induced Fluorescence Spectroscopy, *J. Vac. Sci. Technol. May/June A* (1989), in press.
- [6] Arlinghaus, H. F.; Calaway, W. F.; Young, C. E.; Pellin, M. J.; Gruen, D. M.; Chase, L. L. Laser Damage Studies of ZnS via Neutral Zn Particle Emission, in the Proceedings of the 4th International Laser Science Conference (1988), in press.
- [7] See, for example, Lee, C. S.; Koumvakalis, N; Bass, M. A. Theoretical Model for Multiple-Pulse Laser-Induced Damage to Metal Mirrors, *J. Appl. Phys.* 54, 5727 (1983).
- [8] See, for example, Jee, Y.; Becker, M. F.; Walser, R. M. Laser-Induced Damage on Single-Crystal Metal Surfaces, *J. Opt. Soc. Am. B5*, 648 (1988).
- [9] Arlinghaus, H. F.; Calaway, W. F.; Young, C. E.; Pellin, M. J.; Gruen, D. M.; Chase, L. L. Isotope-Shifts of Zn Neutral Atoms Measured by Two-Photon Doppler-Free Laser-Induced Fluorescence Spectroscopy, submitted to *Opt. Lett.*
- [10] Wood, R. M. Laser damage in optical materials. Bristol: Adam Hilger; 1986.
- [11] De Maria, G; Goldfinger, P; Malaspina, L.; Piacente, V. Mass-Spectrometric Study of Gaseous Molecules, *Trans. Faraday Soc.* 61, 2146 (1965).
- [12] W. H. Press, W. H.; Flannery, B. P.; Teukolsky, S. A.; Vetterling, W. T. in *Numerical Recipes: The Art of Scientific Computing*, Cambridge University Press, Cambridge (1986).
- [13] Bechtel, J. H. Heating of Solid Targets with Laser Pulses, *J. Appl. Phys.* 46, 1585 (1975).
- [14] Landolt Börnstein, N.S., Vol. 17b, Springer-Verlag, Berlin (1982), pp. 110-114.
- [15] Touloukian, Y. S.; DeWitt, D. P. Thermophysical Properties of Matter, IFI/Plenum, New York (1972), Vol 8., p. 1217.
- [16] Bräunlich, P.; Schmid, A.; Kelly, P. Contributions of Multiphoton Absorption to Laser-Induced Intrinsic Damage in NaCl, *Appl. Phys. Lett.* 26, 150 (1975).
- [17] Matthias, E.; Nielsen, H. B.; Reif, J. Multiphoton-Induced Desorption of Positive Ions from Barium Fluoride, *J. Vac. Sci. Technol. B5*, 1415 (1987).
- [18] Petzoldt, S.; Elg, A.P.; Reif, J.; Matthias, E. Surface Damage Thresholds of Fluoride Crystals: Dependence on Surface Quality and Irradiation Mode, to be published in the Proceedings of the 20th Symposium on Optical Materials for High Power Lasers, (1988).
- [19] Krutyakova V.P.; Smirnov, V. N. Electron Emission from Alkali Halide Crystals Irradiated by a Pulsed CO<sub>2</sub> Laser, *Sov. Phys. Tech. Phys.* 24, 1085 (1979).

Comments -

Question: And what is the initial process responsible for damage?

Answer: We could talk a whole day about it, and there's a lot of Russian literature on that. In fact, they have done most of it in this. Let me just say the following: where the curves bend often we have a dense plus when there's no question that the shock wave comes from the plasma expansion. I think that's beyond any discussion. In that part, where we think we have this multi-photon process, but where surely the laser talks directly to the surface, we can either think about a thick plasma, which does not absorb the laser radiation and that might create some shock wave, but I personally believe more it's the piston effect which has been also discussed in the literature. There they talk more about the material taking off and sort of generating by high speed velocity. But if you want to involve the piston effect, you have to make clear what is the force that drives off the whole layer. Now we believe that this whole business actually starts with multi-photon ionization and you get holes and you get then cooling propulsion and when you have a sufficiently large number of holes, then they might eject the material at a velocity where the shock wave is generated. I should also say, below the threshold, we have been doing some evaluating -- the data aren't good enough to present it to you. But, we have an indication that even below the threshold, when you integrate long enough, that there is slight signal.



## Substrate Cleaning in Vacuum by Laser Irradiation

Tilak Raj, D. E. McCready and C. K. Carniglia

Martin Marietta Astronautics Group, Laser Systems Technology  
P.O. Box 9316, International Airport, Albuquerque, NM 87119

The cleaning of a substrate prior to the deposition of a coating on its surface is an important factor influencing the quality of the coating. In most cases, the cleaning of the surface takes place before the substrate is placed in the coating chamber. This paper presents the results of an investigation of the effects of the irradiation of the surfaces of fused silica substrates in a UHV chamber using a CW CO<sub>2</sub> laser. The laser beam was rastered over the substrate surface, and desorbed gases were detected using a residual gas analyzer. Water was desorbed from the surface upon irradiation with a low-power beam, while hydrocarbons required higher laser power for removal. It was determined that a single irradiation of a substrate was effective in removing organic contamination and water from its surface. The laser power required to remove the majority of the contamination was lower than the power which resulted in damage to the surface as observed using an interferometer and a polariscope. With the part maintained in a UHV environment, the surface remained uncontaminated for several hours. A series of surfaces was cleaned with various solvents. Residual gas analysis indicated that the solvents had not been removed completely during a high-temperature vacuum bake of the system. Laser cleaning of optical surfaces immediately prior to coating deposition is expected to improve adhesion and to affect the nucleation, growth and other characteristics of the deposited coating.

Key Words: CW CO<sub>2</sub> laser; fused silica; substrate; laser irradiation scan; mass spectrometer; residual gas analysis; substrate cleaning

### 1. Introduction

The cleaning of a substrate before the deposition of a coating on its surface is an important factor influencing the quality of the coating. In most cases, the cleaning of the surface is performed before the substrate is placed in the coating chamber. However, cleaning of a substrate in vacuum before coating deposition would be more desirable, but is not always practical. Some of the techniques which could be used for precleaning in vacuum are glow discharge, sputter ion etching and laser irradiation. Since a glow discharge cleaning [1] is not confined to the substrates, particulates are removed from substrates, fixtures and surrounding chamber walls. The resulting redeposition of the contaminants onto the substrates is a serious drawback of this technique. Sputter ion etching with a noble gas like argon has been employed successfully for precleaning elemental substrates. But, in the case of a dielectric substrate, preferential sputtering [2] and damage to the substrate surface occur.

This paper describes a successful application of CO<sub>2</sub> laser irradiation in removing organics and water from the surface of fused silica substrates placed in an ultrahigh vacuum (UHV) chamber. It was determined that a single irradiation with a scanned high-power laser beam was most effective in removing the volatile contaminants. The highest laser power which can be used is limited by the surface damage. A redeposition of contaminants on the substrates in the UHV chamber did not occur for several hours.

It should be noted that laser irradiation of optical components has been used in other contexts. For example, laser irradiation was suggested to remove ice from the surface of metal mirrors used at cryogenic temperatures [3]. As another example, a study of C and H<sub>2</sub>O removal from optical coatings by laser irradiation was reported recently [4].

### 2. Experimental

An x-y scanned CO<sub>2</sub> laser beam was directed at the substrate placed in a UHV chamber. The gaseous components released from the substrate surface were detected by a mass spectrometer. The experimental details are described below.



## 2.1. CO<sub>2</sub> Laser Optical Train

A schematic top view of the CO<sub>2</sub> laser optical train is shown in figure 1. The principal components of the train included a 200-W CW CO<sub>2</sub> laser (Coherent Model 41), a HeNe alignment laser (NRC Model 1103P), an aluminum alignment mirror, a zinc selenide beamsplitter, and two 3.8-cm-dia molybdenum scanning mirrors mounted on automated motorized stages (Aerotech Model ATS-302M). The translation stages were controlled by a motorized stage controller (Aerotech Unidex II) interfaced with a microcomputer (Hewlett-Packard 9836).

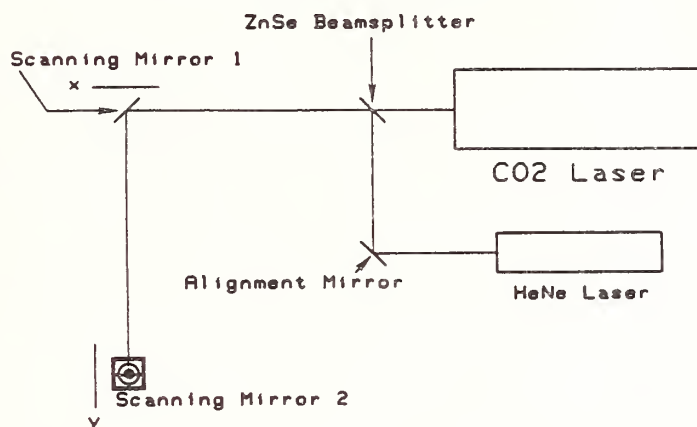


Figure 1. Schematic of optical train used for laser irradiation experiments.

The apparatus shown in figure 1 provided a two-dimensional x-y scan of both the CO<sub>2</sub> and HeNe laser beams. The optical surface of scanning mirror 1 was perpendicular to the plane of the figure; its motion provided the x-dimension of the scan pattern. The optical surface of scanning mirror 2 was at a 45-deg angle to the plane of the figure; its motion provided the y-dimension of the scan and directed the laser beams upward, perpendicular to the plane of the figure. The mirrors could be moved independently at speeds ranging from 0.1 to 4.0 mm/sec, in 0.1-mm/sec increments. The maximum range of mirror translation in either the x- or y-direction was 50 mm.

An adjustable, three-axis, 7.5-cm-dia, copper steering mirror (not shown in fig. 1) was mounted on a post directly above steering mirror 2. The copper mirror was used to direct the CO<sub>2</sub> and HeNe laser beams and the scan pattern to the surface under investigation.

The laser beam intensity profile varied with output power. It was nearly circular with a diameter of approximately 7 mm. A 100-W beam had an average area of 0.34 cm<sup>2</sup>, which corresponded to a power of density of 300 W/cm<sup>2</sup>. For the data reported in this paper, the beam was scanned in a pattern of three parallel lines with a spacing of 3.75 mm, as shown in figure 2. The scan speed was 4 mm/sec. It was determined that this scan pattern and speed did not produce detectable damage to fused silica parts when 100 W of laser power were used.

## 2.2. UHV System

A schematic top view of the UHV chamber used for the laser irradiation experiments appears in figure 3. The vacuum chamber was a metal-sealed UHV chamber with a 10-in (25-cm) Conflat main flange and several smaller diameter, Conflat-flanged accessory ports.

The system was equipped with a sorption pump (Varian Model 941-6501 Vacsorb) and an ion pump (60 l/s Varian Model 911-5034). The lowest pressure achieved after a standard bakeout was  $2 \times 10^{-9}$  torr. The absence of a sublimation pump prevented the ultimate pressure from being lowered to the  $10^{-10}$  torr range. The chamber pressure was monitored with a Bayard-Alpert type nude gauge (Varian).

For each pumpdown, four substrates were loaded on a carousel attached to a three-axis-plus-rotational-motion manipulator (Huntington). The samples were 5.0-cm diameter, 1.3-cm thick fused silica (ESCO UV grade) substrates. The substrates were cleaned with trichloroethane, 2-propanol, CaCO<sub>3</sub>/deionized water, Orvus paste/deionized water, 2-propanol followed by drying in a Genesolv system. As described later, some of the parts were wiped with various solvents before transferring into the vacuum chamber.

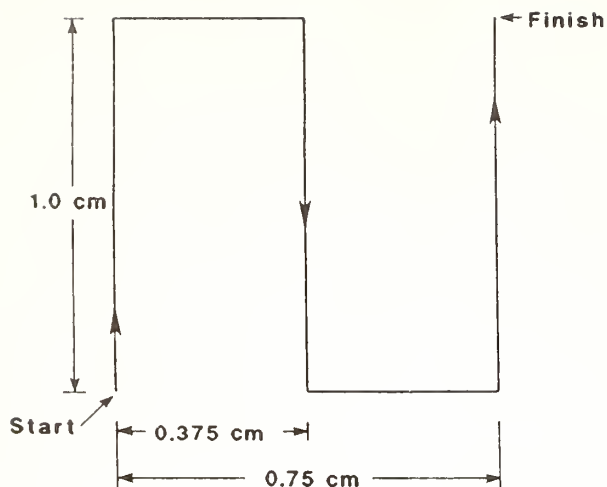


Figure 2. Three-line scan pattern used for laser irradiation.

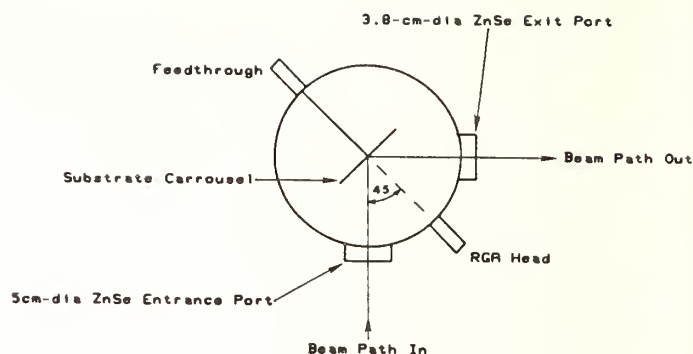


Figure 3. Schematic of the UHV chamber.

### 2.3. Mass Spectrometer

The mass spectrometer was a residual gas analyzer (RGA) (Inficon Model Quadrex 100) with a mass range of 0 to 100 atomic mass units (amu). The minimum detectable partial pressure of this instrument was in the low  $10^{-10}$  torr range, and the mass resolution ( $M/\Delta M$ ) of this instrument was  $\geq 2M$ , where  $M$  was the mass of the peak in amu.

As is shown in figure 2, the RGA sensor head was mounted on a port with a direct line-of-sight to the substrate carousel. Since the RGA sensor utilized a beryllium-copper electron multiplier detector, which must be isolated from the atmosphere during loading and unloading of the chamber, a straight-through valve (Huntington Model MS150) was placed between the vacuum chamber and the RGA sensor. The sensor was about 30 cm from the sample surface. However, the sensitivity of the RGA appeared to be adequate to detect desorbed species at this separation distance.

It was found that the sensor head became contaminated with the background gases from the vacuum chamber. Some cleaning was performed by the usual bakeout, with a degassing of the filament several times at the end of the bakeout. In addition, the filament was degassed, and an RGA spectrum was taken approximately an hour before the start of each irradiation experiment. The procedure of degassing of the filament, followed by RGA monitoring, was repeated until a reproducible mass spectrum was obtained.

Several video output modes were available for the data display. These included single-peak amplitude as a function of time, 0-100 amu digital display (amplitude of integer mass peaks displayed) and bar-subtract display. In the bar-subtract mode, a reference spectrum was taken as in the 0-100 amu digital mode and stored in the controller memory. Any new spectrum taken was displayed after subtracting the contribution of the reference spectrum from the measured spectrum. In other words, the display represented only the changes. This subtract mode was deemed the best suited for the present degas study.

A fresh reference spectrum was taken 1-2 minutes before a laser irradiation scan. Thus, the displayed data taken during the scan originated only from the laser irradiation of the substrate surface. It should be noted that the amplitude could be displayed only linearly (compared to a log display), which limited the dynamic range (the ratio of the largest to the smallest resolvable amplitude). In other words, to accommodate the display of the largest peak, the signal gain had to be lowered, thereby reducing the detectability of peaks of low amplitude. It should also be noted that the instrument could be used only in the RGA mode; i.e., a thermionic filament had to be functioning before the detector (electron multiplier) could be turned on. The consequence of this limitation was that molecular fragments were detected and not larger molecular species, as with a conventional mass spectrometer.

## 2.4. Irradiation Experiments In Vacuum

A typical irradiation experiment in vacuum consisted of the following steps:

- Step 1. Bring chamber pressure to  $2 \times 10^{-9}$  torr.
- Step 2. Check colinear alignment of CO<sub>2</sub> and HeNe laser beams.
- Step 3. Calibrate laser power by measuring the beam current versus laser power with a power meter (Coherent Inc.).
- Step 4. Align substrate for irradiation.
- Step 5. Clean RGA sensor head and collect a reference (background) spectrum.
- Step 6. Irradiate the part with a scanned CO<sub>2</sub> laser beam of measured power. Take an RGA spectrum concurrently with the laser scan.
- Step 7. Make additional CO<sub>2</sub> laser scans and record RGA spectra. Typically 8 to 15 scans were performed on each part.
- Step 8. Repeat Steps 4-7 for each substrate to be irradiated.
- Step 9. Calibrate the laser power at the end of the experiments.

## 3. Data and Discussion

Over 400 RGA spectra were collected from more than 30 substrates in this study. The data selected for this publication were collected in the bar-subtract mode.

After the laser irradiation experiments, the substrates were checked visually for any cracks or other damage. This was followed by examination under a polariscope (Wale Apparatus Co.). It was determined that a three-line scan of a 100-W laser beam did not cause any detectable damage to fused silica parts.

### 3.1. Chemical Identification of Detected Mass Peaks

Molecular fragments detected by a mass analyzer (RGA in this study) vary with the chamber environment, so assigning chemical formulas to various detected peaks requires some knowledge of the vacuum system. For example, a peak of mass 17 is assigned to NH<sub>3</sub> in a N<sub>2</sub> plasma system and to OH in an ordinary vacuum chamber. Table 1 lists the chemical assignments to peaks detected in the present study. However, the list is not exhaustive, as other chemical possibilities might exist.

Table 1. Possible Chemical Identification of Detected Mass Peaks

Mass*	Chemical Identification	Mass*	Chemical Identification
1	H	27	C <sub>2</sub> H <sub>3</sub> , CH•CH <sub>2</sub> , CH <sub>3</sub> •C
2	H <sub>2</sub>	28	CO, CH <sub>2</sub> •CH <sub>2</sub> , N <sub>2</sub>
12	C	29	CH <sub>3</sub> •CH <sub>2</sub> , CHO
13	CH	30	CH <sub>2</sub> O
14	CH <sub>2</sub> , CO <sup>+</sup> , N	31	CH <sub>3</sub> O
15	CH <sub>3</sub>	32	O <sub>2</sub>
16	O, CH <sub>4</sub> ,	39	CH <sub>3</sub> •C•C
17	OH,	41	CH•CO, CH•CH <sub>2</sub> •CH <sub>2</sub>
18	H <sub>2</sub> O	42	CH <sub>2</sub> •CO, CH <sub>2</sub> •CH <sub>2</sub> •CH <sub>2</sub>
24	C•C	43	CH <sub>3</sub> •CH <sub>2</sub> •CH <sub>2</sub> , CH <sub>3</sub> •CO
25	CH•C	44	CO, CH <sub>3</sub> •CH <sub>2</sub> •CH <sub>3</sub>
26	CH•CH	45	CH <sub>3</sub> •CH <sub>2</sub> O

\* Mass in atomic mass units.  
+ Doubly ionized (i.e., detected at half the mass of ordinary species).

### 3.2. Hydrogen Peaks

All UHV systems show hydrogen (masses 2, 1) as the largest peaks. Several processes produce  $H_2$  in the UHV environment; e.g., the decomposition of water, the reaction with stainless steel walls when oxygen is adsorbed, or the action of titanium gettering. With these contributing factors, it is complicated to ascertain the effects of external processes (e.g., laser irradiation) on the production of  $H_2$ . Therefore, hydrogen peaks have not been taken into account in this study.

### 3.3. Detected Peaks

Ignoring hydrogen peaks, all RGA data collected in this study were combined into three groups of peaks; these being the following:

- 12-18 group: water (18, 17, 16)  
methane (15, 14, 13)  
carbon (12)
- 28 group: peaks 25-31
- 44 group: peaks 39-45

It should be noted that the highest mass detected in this study was 45, independent of the laser power and the organic solvent used in the substrate cleaning.

An overall view of the experiments performed for the selected fused silica parts can be obtained from table 2. The sample number and the laser beam power (watts) are listed in the first two columns. The next group of columns gives the scan number for the three-line pattern and the elapsed time since the previous scan. Typically, the repetitive scans were 2-4 minutes apart. The chamber pressure, listed next, was recorded on the nude gauge at various phases of the experiments: at the beginning of the irradiation scan, at the highest pressure reached during the scan and at the steady level noted at the end of the scan. The next column shows the peak amplitude data listed in order of descending amplitude. The final column contains miscellaneous comments including the remarks on damage observed on certain parts. Horizontal lines separate the data collected for each part.

Table 2. RGA data of selected irradiation experiments

Part No.	Laser Beam Power (W)	Irradiation Scans		Total Chamber Press (x10 <sup>-9</sup> torr)			Peaks Detected	Comments <sup>b</sup>
		No.	Time <sup>a</sup> (h:min)	Start	Max	Final		
45	88	1		2.3	11.0	2.6	18,17,28,16	Std clean
		2	0:04	2.3	5.0	2.5	18,17	
		3	0:03	2.3	4.9	2.4	18,17	
		4		2.3	4.9	2.4	18,17	
46	106	1		2.2	14.0	3.1	18,17,16,15,28	Std clean
		2	0:03	2.3	7.2	2.6	18,17	
		3	0:03	2.3	7.3	2.8	18,17,16	
		4	0:03	2.4	7.3	2.8	18,17,44	
47	120	1		2.2	17.0	3.4	18,17,16,28,15	Std clean
		2	0:03	2.4	8.9	3.0	18,17,16	
		3	0:03	2.4	8.2	3.0	18,17,16	
		4	0:03	2.5	7.5	3.0	18,17	
		5	0:03	2.5	7.9	3.2	18,17	
		6	0:02½	2.6	8.3	3.4	18,17	
								Damage detected with polariscope



Table 2. RGA data of selected irradiation experiments (continued)

Part No.	Laser Beam Power (W)	Irradiation Scans		Total Chamber Press ( $\times 10^{-9}$ torr)			Peaks Detected	Comments <sup>b</sup>
		No.	Time <sup>a</sup> (h:min)	Start	Max	Final		
48	130	1		2.4	17.0	3.4	18,17,16,15,28,14, 44,12	Std clean     Damage detected with polariscope
		2	0:02½	2.6	9.9	3.2	18,17,16	
		3	0:03	2.6	9.6	3.2	18,17,16	
		4	0:03	2.7	9.3	3.5	18,17	
		5	0:02½	2.7	9.2	3.4	18,17	
		6	0:02	2.7	9.4	3.4	18,17	
49	102	1		2.5	28.0	3.6	16,15,18,28,12,14, 17,13,44,41	Std clean & TCE drag wipe
		2	0:02½	2.7	9.1	3.3	18,17,16,15	
		3	0:03	2.7	8.2	2.8	18,15,16,17,14,13	
		4	0:02	2.7	8.5	2.8	18,15,16,17,14,13, 28	
		5	0:02½	2.8	8.0	3.0	18,16,17,15	
		6	0:04½	2.7	6.6	2.9	18,17,16,15	
		7	0:02	2.7	7.2	3.1	18,17,16,15	
		8	0:02½	2.8	7.1	3.1	18,17,16,15	
50	102	1		2.7	18.0	3.5	18,16,28,17,15,14, 26,44,12	Std clean & acetone drag wipe
		2	0:02½	2.9	8.0	3.1	18,17,16,28,15	
		3	0:02	2.9	8.5	3.2	18,17	
		4	0:02	2.9	7.9	3.2	18,17	
		5	0:02½	2.8	8.3	3.1	18,17,28,16	
		6	0:02½	2.8	7.4	3.0	18,17,16,15	
		7	0:02½	3.0	7.7	3.2	18,17,16	
		8	0:02	3.0	7.7	3.4	18,17	
51	102	1		3.0	21.0	3.6	18,28,15,16,17,14, 26,44,41,42,12,13, 29,32,39,31,33	Std clean & 2-propanol drag wipe - Data invalid, not recorded           - Very little redeposition after 16:33 elapsed time
		2	0:05	3.0	8.7	3.1		
		3	0:04	2.9	8.3	3.4	18,17,28,16	
		4	0:03	2.9	8.8	3.4	18,17,28,16	
		5	0:02	3.0	9.1	3.4	18,17,28,16,15	
		6	0:02	3.1	8.7	3.5	18,17,28,16	
		7	0:02	3.1	9.1	3.6	18,17	
		8	0:02	3.1	8.1	3.5	18,17,16	
		9	0:02	3.1	8.6	3.6	--	
		10	0:03	3.1	8.6	3.6	--	
		11	0:33	2.8	6.1	3.1	18,17,16,12	
		12	1:03	2.7	6.2	3.1	18,17,15,16	
		13	16:33	3.0	5.3	3.0	17,18,16,15	
52	102	1		2.8	23.0	3.4	18,28,17,16,15,44, 41,26,39,12,14,13, 40,38	Std clean & Genesolv DS drag wipe
		2	0:04	2.8	7.8	3.0		

Table 2. RGA data of selected irradiation experiments (continued)

Part No.	Laser Beam Power (W)	Irradiation Scans		Total Chamber Press (x10 <sup>-9</sup> torr)			Peaks Detected	Comments <sup>b</sup>
		No.	Time <sup>a</sup> (h:min)	Start	Max	Final		
52 (cont)		3	0:02½	2.9	8.5	3.2	18,17,28,16	
		4	0:02½	2.9	8.0	3.4	18,17,28,16	
		5	0:02	2.9	8.4	3.4	18,17,28,16,15	
		6	0:02½	3.0	8.4	3.5	18,17,28,16	
		7	0:02½	3.0	8.1	3.5	18,17	
		8	0:02	3.0	8.2	3.6	18,17,16	
57	102	1		2.3	23.0	2.9	16,[18,15],28,44 17,26,14,12,13	Std clean & xylene drag wipe
		2	0:03	2.4	9.0	2.7	18,16,17,15,28	
		3	0:02½	2.5	7.7	2.8	18,17,16,15,28	- Amplitudes lower than scan 6
		4	0:02	2.6	8.8	2.8	18,16,17,15,12	
		5	0:02	2.6	8.2	2.9	18,[17,15],16,28,12	
		6	0:02½	2.6	8.1	2.9	18,17,16,28	
		7	0:02½	2.6	7.8	3.0	18,17,16,15	
		8	0:02	2.7	8.0	3.0	18,17,16,15,28,12	
		9	0:03	2.7	7.8	3.0	--	
		10	0:03	2.6	7.1	3.0	--	
		11	0:28	2.5	5.4	2.6	18,17	
		12	1:10	2.5	5.5	2.6	18,17,15	
		13	1:50	2.6	5.2	2.7	18,17,16	
58	104	1		2.5	110.0	5.5	28,18,44,29,16,15, 26,32,31,14,30,43 42,12,13,46,39	Std clean & MEK drag wipe
		2	0:04½	3.2	12.0	3.4	18,17,28,12,16	
		3	0:02½	3.1	15.0	3.5	18,17,28,16,44,12	
		4	0:02½	3.0	16.0	3.6		
		5	0:04	3.0	14.0	3.4	18,17,16,28,12	
		6	0:02½	3.0	15.0	3.5	18,17,28	
59	104	1		2.9	130.0	5.5	[18,28,44],29,16, [15,17],26,14,12, 30,43,41,42,39,13	Std clean & dichloromethane drag wipe
		2	0:03	3.7	23.0	4.3	18,17,28,44	
		3	0:02½	3.5	27.0	4.1	18,28,17,44,16,15	
		4	0:02	3.5	29.0	4.1	18,44,28,17,16,15	
		5	0:02½	3.5	23.0	4.1	18,17,44,28,16,15	
		6	0:02	3.5	22.0	4.2	18,[28,44,17],16	
60	104	1		3.4	51.0	4.7	18,16,15,28,17,14, 26,44,13,12,29	Std clean & n-butyl acetate drag wipe.
		2	0:02½	3.6	14.0	4.1	18,17,28,16	
		3	0:02½	3.4	12.0	4.1	18,17,28,16,15	
		4	0:02½	3.5	14.0	4.1	18,17,16,15,28,14	
		5	0:02	3.4	9.5	4.1	18,17,28,16	
		6	0:02½	3.4	9.1	4.1	18,17,28,16,15	

a. Elapsed time between consecutive scans.

b. - indicates comment refers to that scan only.

### 3.4. First Irradiation Scan

RGA data taken with the first laser irradiation scan of beam power 88 and 130 W on parts number 45 and 48, respectively, are shown in figures 4(a) and (b). The peaks detected at 88 W [fig. 4(a)] were in order of decreasing intensity, 18, 17, 16, 15, and 28. The peaks detected at 130 W [fig. 4(b)] were 18, 17, 16, 15, 14, 12, and 28.

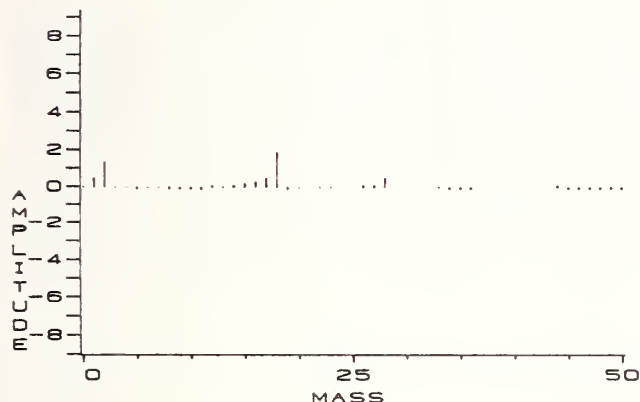


Figure 4(a). RGA spectrum (subtract mode) for irradiation scan 1, part 45 (88 W).

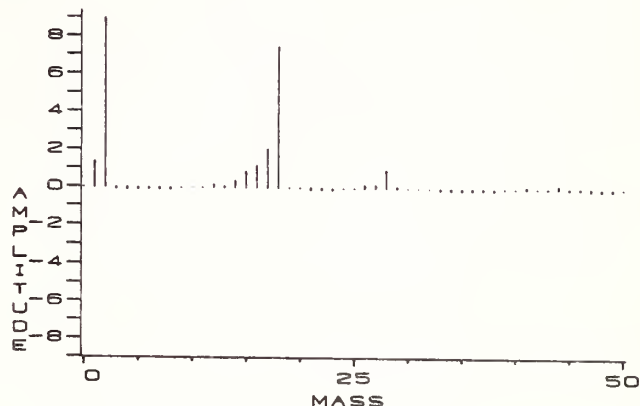


Figure 4(b). RGA spectrum (subtract mode) for irradiation scan 1, part 48 (130 W).

The following observations can be made from this figure. (1) The number of detected peaks increased as the radiation power was increased. This implies that a higher surface temperature caused by a higher laser power irradiation removed more strongly bound species. It was observed that hydrocarbons of mass range 12-15 amu required more power for removal than did water vapor. (2) As the irradiation power was increased, the amplitudes of the detected peaks increased.

The second observation is further confirmed by figure 5, which shows the peak amplitude of water (mass 18) and the chamber pressure observed from the first irradiation scans versus the laser power. There was a monotonic increase in the amount of water removed and also the chamber pressure with an increase in the irradiation power. This increase in desorbed vapors with increased laser power could be attributed to two factors: (1) the removal of adsorbed material directly from the irradiated area, and (2) the enhanced removal of material from the surrounding (non-irradiated) area due to elevated surface temperatures during irradiation.

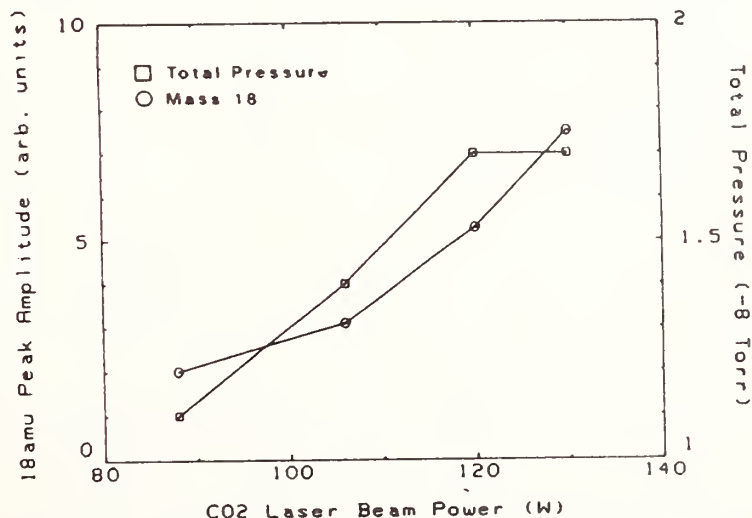


Figure 5. Peak amplitudes for water and total chamber pressure as a function of laser beam power, parts 45-48.

It should be noted that the above substrates were cleaned with the best available procedure before introducing them into the UHV chamber. The chamber was subjected to the standard bakeout, producing a pressure of  $2 \times 10^{-9}$  torr. Even for these clean parts placed in a clean chamber, the first irradiation scan of the laser beam produced an RGA spectrum showing water and hydrocarbon species. This indicated that the cleaning of substrates outside a vacuum chamber was not a complete process. Only an in-situ cleaning process (in vacuum) could remove the surface contaminants.

### 3.5. Second and Successive Irradiations

Figures 6(a) and (b) show RGA spectra obtained with the second irradiation scan for part numbers 45 and 48 (same parts as in figure 4). The only peaks detected were of the water group (peaks 18, 17). The amplitudes of water peaks were slightly higher for the part number 48 irradiated with the higher power (130 W) than for part number 45 irradiated with the lower power (88 W). Similar data (not shown) were obtained for successive scans.

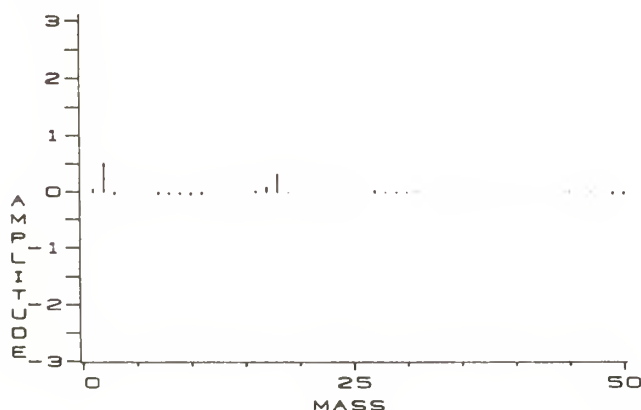


Figure 6(a). RGA spectrum for irradiation scan 2, part 45.

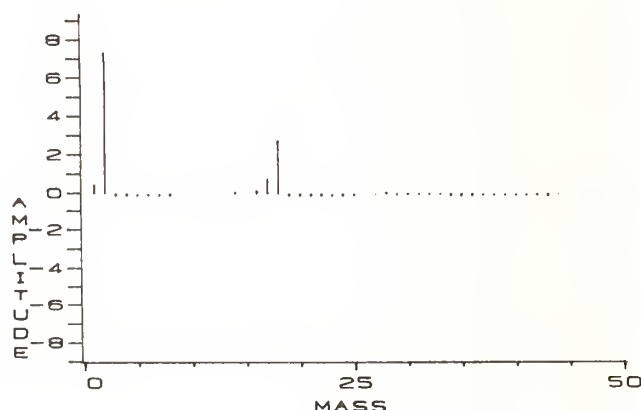


Figure 6(b). RGA spectrum for irradiation scan 2, part 48.

Figures 7 (a) and (b) show the RGA peak amplitudes of peaks 18, 17 and 28, together with the chamber pressure as a function of the number of irradiations for the same parts, numbers 45 and 48. For both laser power levels (80 and 130 W), there was almost no change in peak amplitudes or the chamber pressure beyond scan number 2. This implies that most of degassing of the substrate surface took place with the first laser irradiation scan.

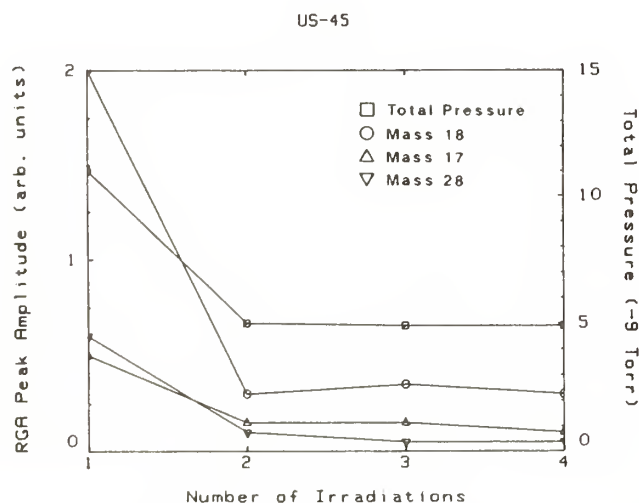


Figure 7(a). Peak amplitudes and total chamber pressure as a function of irradiation scan number, part 45.

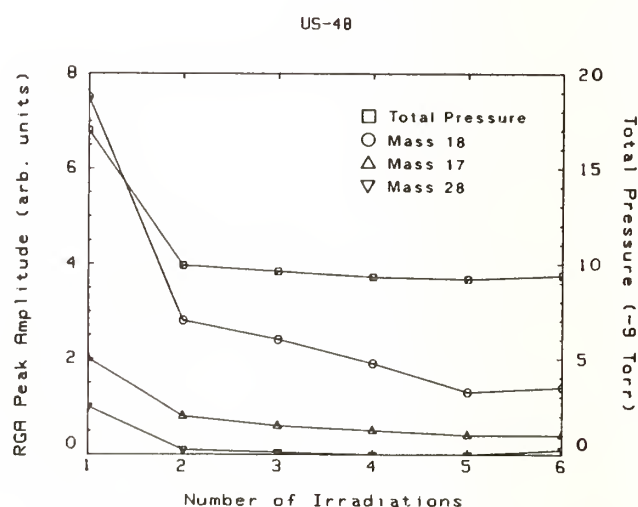


Figure 7(b). Peak amplitudes and total chamber pressure as a function of irradiation scan number, part 48.



All of the fused silica substrates (up to part number 48) were examined visually and with the polariscope after irradiation experiments. It was observed that detectable damage was produced on the surface of the parts at power levels of 110 W or greater. The laser power was lowered to 100-105 W for the remainder of the study.

### 3.6. Solvent Residues

After having shown that one scan of laser irradiation of sufficient power can remove most of the organic residue left from a cleaning operation, the next step was to study the effectiveness of laser irradiation in removing the residue from an applied solvent. Towards this end, a set of four substrates (numbers 49-52) were cleaned with the standard cleaning procedure, followed by a drag wipe with one of the following reagent-grade solvents: trichloroethane (TCE,  $\text{Cl}_3\text{C}\cdot\text{CH}_3$ ), acetone ( $\text{CH}_3\cdot\text{CO}\cdot\text{CH}_3$ ), 2-propanol ( $[\text{CH}_3]_2\text{COH}$ ) and Genesolv (95%  $\text{Cl}_3\cdot\text{CF}_3$ , 5%  $[\text{CH}_3]_2\text{COH}$ , water-free). Once again it was determined that most of the degassing took place in the first scan. Figure 8(a) and (b) illustrate the RGA data from the first and second irradiation scans for part number 49 drag wiped with TCE. Note the peak pattern in the 12-18 mass group for the first scan. Peaks of masses 16 ( $\text{CH}_4\text{O}$ ) and 15 ( $\text{CH}_3$ ) were the predominant peaks in contrast to the water (18) peak for the clean parts. The second scan [fig. 8(b)] produced peak 18 and small amounts of 17, 16, 15. Figure 9 shows the RGA peak amplitudes for 18 and 15, and the chamber pressure as a function of number of irradiations for part 49. No significant change was observed in the data beyond the second scan.

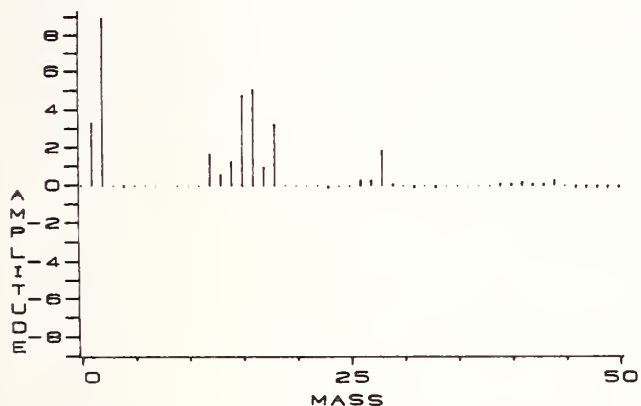


Figure 8(a). RGA spectrum (subtract mode) for irradiation scan 1, part 49 (102 W). The part was drag wiped with reagent-grade TCE after standard cleaning.

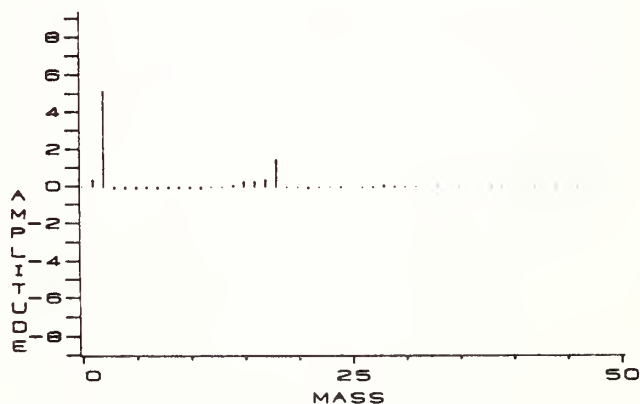


Figure 8(b). RGA spectrum (subtract mode) for irradiation scan 2, part 49 (102 W).

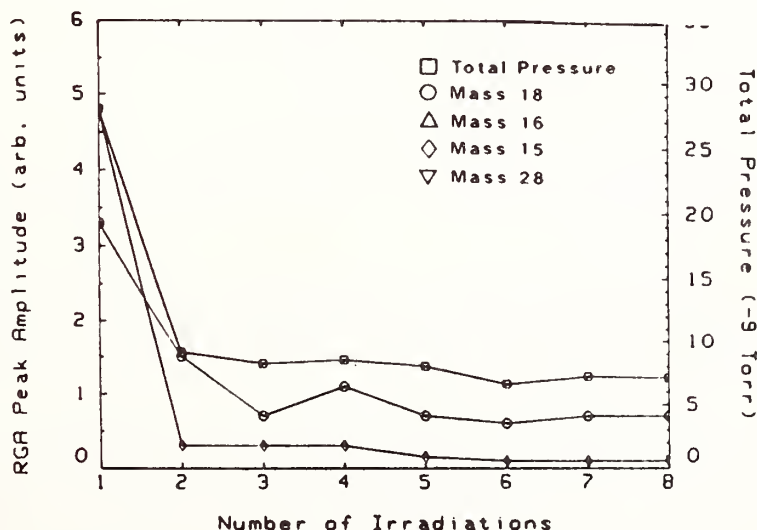


Figure 9. RGA peak amplitudes and total chamber pressure as a function of irradiation scan number, part 49.

An examination of chamber pressure data in table 2 shows that the increase in the chamber pressure during the first scan was much higher for the part number 49 subjected to a TCE drag wipe than the parts (numbers 45-48) cleaned by the standard cleaning procedure. This information along with the data in figures 4 and 8 implies that the organic residue left on a substrate after a proper cleaning procedure was much lower than the residue left after a drag wipe with TCE.

Another observation from table 2 and figures 6 and 9 is that the chamber pressure and the amplitudes of the detected peaks beyond scan number 2 remained the same (or even became slightly higher) regardless of the number of times the parts were irradiated. The vapor desorbed from scan number 2 onwards could be coming either from the directly irradiated area, implying that the first scan had not removed all the vapor, or from the surrounding area, which was not directly irradiated but which was heated increasingly by the repetitive irradiations. To separate the contributions of the irradiated and non-irradiated areas to the RGA spectrum, several parts (one cleaned with standard procedure and the others with drag-wipe of solvents) were irradiated using longer time intervals between irradiations, ranging from one-half to greater than 12 hours.

Figure 10 shows the RGA amplitude of peaks 18 and 15, and the chamber pressure for the successive scans, performed 2-5 minutes apart for part number 51 (also see table 2). There was no significant change in peak amplitudes and the chamber pressure beyond scan number 2. The chamber pressure was in the range of  $(8.3-9.1) \times 10^{-9}$  torr for scan numbers 2 to 10. However, for scan number 11, performed 33 minutes after scan number 10, the chamber pressure dropped to  $6.1 \times 10^{-9}$  torr and the amplitudes of the peaks detected were significantly lower than those from scans repeated after shorter time intervals. This implies that heat conducted to areas surrounding the directly irradiated area was responsible for some desorption. Furthermore, since the peak amplitudes decreased in about 30 minutes time, it was concluded that no redeposition took place on the substrate during this time. It should be pointed out that even an elaborate detection system will not be able to separate unambiguously the contribution to the desorption of the directly irradiated area from the surrounding areas.

The RGA spectrum (fig. 11) taken for scan number 13 taken 16:33 hours after scan number 12 shows only a very small redeposition of  $\text{CH}_4$  and  $\text{CH}_3$  species.

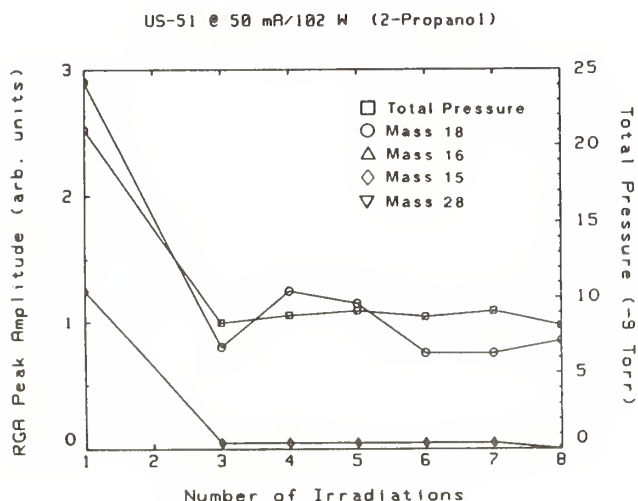


Figure 10. RGA peak amplitudes and total chamber pressure as a function of irradiation scan number, part 51. The part was drag wiped with reagent grade 2-propanol.

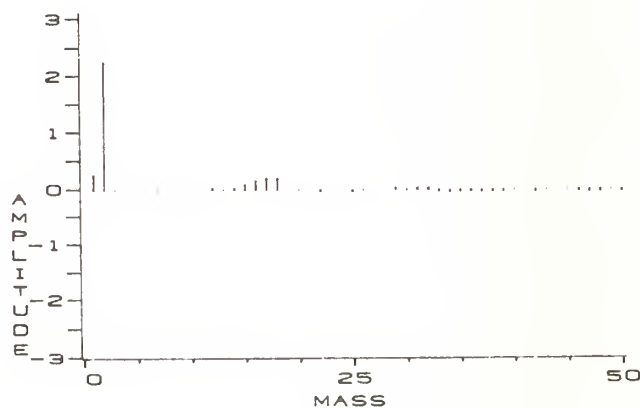


Figure 11. RGA spectrum for scan 13, taken 16.5 h after scan 12 (part 51, 102 W). Note the small amplitude of the peaks.

Finally, to test the effectiveness of laser irradiation in removing other volatile organic reagents from a substrate surface, four organic solvents were chosen, each with different characteristics. These were xylene ( $\text{C}_6\text{H}_4 \cdot [\text{CH}_3]_2$ ), methylethylketone (MEK,  $\text{CH}_3 \cdot \text{CO} \cdot \text{CH}_2 \cdot \text{CH}_3$ ), dichloromethane ( $\text{Cl}_2\text{CH}_2$ ), and n-butyl acetate ( $\text{CH}_3 \cdot \text{CH}_2 \cdot \text{CH}_2 \cdot \text{CH}_2\text{OOC} \cdot \text{CH}_3$ ). The MEK and dichloromethane used were of industrial or technical grade; thus the impurity concentration of the solvents was unknown. Xylene is a nonpolar aromatic compound and is immiscible with water. Methylethylketone is a heavier ketone than the commonly used acetone ( $\text{CH}_3 \cdot \text{CO} \cdot \text{CH}_3$ ) and is miscible

with water. Dichloromethane is a chlorohydrocarbon and is immiscible with water. N-butyl acetate is a long-chain aliphatic solvent having good miscibility with water.

A set of four substrates (numbers 57-60) were cleaned with the standard cleaning procedure followed by a drag wipe with one of these organic solvents.

The first laser irradiation scan produced a very high chamber pressure (see part numbers 57 through 60 in table 2) and all three groups of peaks with large amplitudes. For example, figure 12 shows the RGA spectrum for the first scan from part number 59 wiped with dichloromethane. Three groups of peaks were present:

1. 12-18 group: 18, 16, 17, 15, 14, 12, 13
2. 28 group: 28, 29, 27, 26, 30, 31, 32
3. 44 group: 44, 43, 42, 41, 40, 39

No Cl-containing group was detected -- an indication that the dichloromethane was removed completely from the substrate surface during bakeout.

Note the very large amplitude of peaks 18 ( $\text{H}_2\text{O}$ ), 28 ( $\text{CO}$ ,  $\text{CH}_2\cdot\text{CH}_2$ ,  $\text{N}_2$ ), and 44 ( $\text{CO}_2$ ,  $\text{CH}_3\cdot\text{CH}_2\cdot\text{CH}_3$ ). The residue, which was most likely left by the impure solvent, was desorbed by the first irradiation scan.

Figure 13 shows the RGA spectrum for the first scan on part number 60 wiped with n-butyl acetate. Once again, three group of peaks were detected, but with a different peak structure than obtained from dichloromethane (fig. 12). Similar observations were noted for the first irradiation of parts wiped with xylene or MEK. The second and subsequent scans produced small water peaks (18, 17) and very small peaks like 15, 28, etc. This implies that one irradiation of sufficient laser power was able to remove most of the volatile organic residue and water from fused silica substrates, regardless of the nature of the organic contamination.

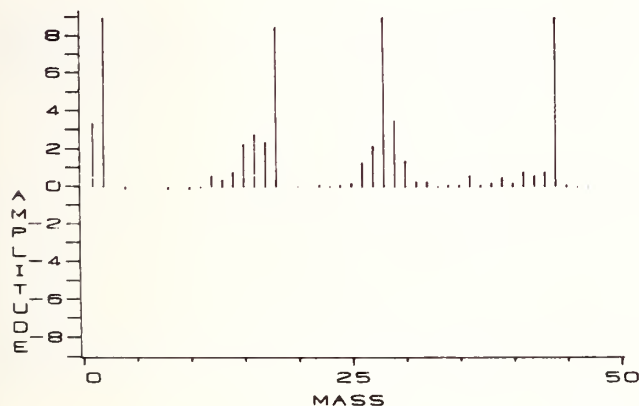


Figure 12. RGA spectrum for irradiation scan 1, part 59 (104 W). Part was drag wiped with dichloromethane after standard cleaning.

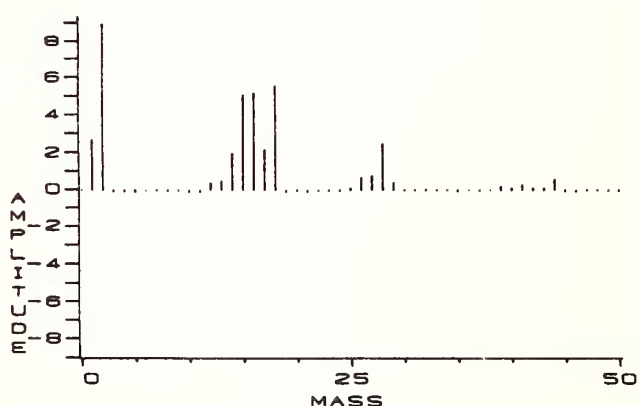


Figure 13. RGA spectrum for irradiation scan 1, part 60 (104 W). Part was drag wiped with n-butyl acetate after standard cleaning.

It should be noted that the cracking patterns caused by the solvents employed in the laser irradiation experiments were totally different than those obtained by conventional gas analysis with a RGA spectrometer. In the irradiation experiments, small hydrocarbons or water components were detected, regardless of the complexity of the organic molecule present at the substrate surface. For example, the largest peak obtained from an RGA spectrum of a substrate with MEK should be 43, but laser irradiation produced 16 and 15 as the predominant peaks. This might be due to fragmentation of the surface molecules caused by the high surface temperature ( $>1000^\circ\text{C}$ ) created by repetitive laser irradiation. It should be noted that the highest mass detected in this study was 45, independent of the laser power and the organic solvent used in the substrate cleaning.

#### 4. Summary

Cleaning of substrates outside the vacuum chamber was not a complete process. Only an in-situ cleaning process in vacuum could remove the residual surface contaminants.

A single irradiation scan of sufficient laser power can remove the volatile organic residue and water vapor from the substrate surface, independent of the nature of the solvent present on the substrate.

The water and other peaks detected after repetitive laser irradiation scans originated from the areas adjacent to the directly irradiated area and not from the irradiated area itself.

There was very little redeposition of organic contamination on the substrate 12-16 hours after the laser irradiation.

Only small hydrocarbons or water components were detected regardless of the complexity of the organic molecule at the substrate surface. This might be due to the molecules at the surface breaking due to the high surface temperature caused by the laser irradiation.

The rise in chamber pressure during irradiation corresponded to the rise in amplitude of peaks detected by the mass spectrometer. Thus, the effect of laser irradiation could be monitored by noting the total chamber pressure. As soon as the maximum chamber pressure from one irradiation no longer differs from that of the previous irradiation, a complete degassing has taken place. From a practical application, laser degassing or cleaning can be monitored in such a manner by a simple pressure gauge rather than with a mass spectrometer.

---

The authors wish to acknowledge the help of Jerry Kienle and Art Westerfeld for fabricating the UHV fixtures required to perform the experiments.

This effort was sponsored by the Air Force Weapons Laboratory, Air Force Systems Command, United States Air Force, Kirtland AFB, New Mexico 87117 and was funded by the Air Force Office of Scientific Research.

#### 5. References

- [1] Dylla, H.F. Glow discharge techniques for conditioning high-vacuum systems. J. Vac. Sci Technol. A6 (3): 1276-1278; 1988.
- [2] Holloway, P.H. and Nelson, G.C. Preferential sputtering of Ta<sub>2</sub>O<sub>5</sub> by argon ions. J. Vac. Sci Technol. 16: 793; 1979.
- [3] Piper, L.G.; Spencer, M.N.; Woodward, A.M.; Green, B.D. Optical System Contamination: Effects, Measurements, Control. SPIE Proc. 777; 1987. 320-332.
- [4] Domann, F.E. and Stewart, A.F. Laser induced particle emission as a precursor to laser damage. Presented at 1987 meeting of the Boulder Damage Symposium, to be published in Nat. Inst. Stand. Tech. (U.S.) Spec. Publ.



#### COMMENTS

Question: Did you ever see any evidence of coating material in the RGA or in the substrate material?

Answer: I don't think we had any solute remover.

Question: Have you tried to correlate your results with the study that Allen and Porteus did 4 or 5 years ago on laser desorption of water?

Answer: Our goal was slightly different so we really did not try to do that.

Question: That was partially my question. Are you aware of any work on the correlation of surface cleanliness measured by this technique with subsequent film quality?

Answer: I think some work probably is going on and we plan to pursue the question.

Question: And the other question was, have you used this to quantify how effective low discharge is for surface planning?

Answer: No, I have my personal opinion on low discharge. It is a dirtying process, not a cleaning process. There is some work that has recently been done giving a correlation between the absorption of film surfaces and the damage thresholds after having been cleaned by lasers. There is a direct correlation and I can give you that reference if you want it.

Question: Did you try dielectrics, metals, different things?

Answer: No, we tried a few silica. We believe there should be two or more dielectrics investigated.

Question: And the second question is did you ever observe onset of damage after repetitive shocks, did you look for it and was there a damage onset after a number of shots?

Answer: No, no, we have here a pretty low power and we did not see any damage. But, of course, it was the sort of damage, but we tried looking, but there was no residual damage.

Question: Did you see any indication at all, either through your mass spectrographic analysis or even just a visual inspection, whether there was ablation of the fused silica?

Answer: I don't think the powers were high enough to do that and you know from the mask data that we did not see any.

Question: I think if you try and calculate what that temperature would be at the surface and under those conditions, I think you can reach a temperature high enough to begin vaporizing the surface.

Answer: Yes, that is true.

Question: I was wondering if you have any reason to expect that laser radiation is better than baking the substrates.

Answer: This is a surface phenomena and temperatures are high. Baking will not do.

## Cavity Ringdown Measurements of High-Reflection Mirrors at 1.06 $\mu\text{m}$

L. John Jolin, Virgil R. Sanders, Thomas P. Turner  
Chemical and Laser Sciences Division  
Los Alamos National Laboratory  
Los Alamos, NM 87545

A 1064-nm-cavity-ringdown reflectometer was used to study reflectances of a variety of high reflectance dielectric coatings and silver mirrors. Reflectances of the dielectric coatings were measured at near-normal angle of incidence. The multilayer dielectric high reflectors included  $\text{ZrO}_2$ ,  $\text{HfO}_2$ ,  $\text{SiN}_4$ ,  $\text{TiO}_2$ , and  $\text{Al}_2\text{O}_3$ , which were used in combination with  $\text{SiO}_2$  in conventional quarter-wave designs. Reflectors from more than a dozen vendors were surveyed in this effort. Metallic reflectors investigated were silver and silver protected with a thin (10 Å) alumina overcoat. These reflectors were tested at both normal incidence and at high (grazing) angles.

The results of these studies show that, although high reflectances ( $R > 0.9990$ ) can be achieved for 1064-nm-multilayer dielectrics, the majority are not of this caliber. Reflectances for dielectric designs ranged from 0.96 to  $>0.9990$ . The silver mirrors exhibited predictable behavior with reflectances of 0.992 at near-normal angle.

Key words: multilayer dielectrics; Nd:YAG; high reflector; reflectance; reflectometer; silver coatings; 1064 nm.

### 1. Introduction

Reflectance is a key parameter in understanding fundamental relationships between mirror characteristics and laser damage susceptibility. An accurate, high precision reflectance measurement capable of measuring reflectances that are near unity is essential. A cavity-ringdown reflectometer utilizing a 1.06- $\mu\text{m}$  laser source has been developed for this purpose. Adapted for our use is the ringdown device thoroughly described by Anderson et al. [1] in 1984.

### 2. Experimental

The source for this reflectometer is a repetitively pulsed Nd:YAG laser operating at the fundamental wavelength of 1.06  $\mu\text{m}$ . The repetition rate is variable but is set at 3,000 pps for these measurements to allow for long decay times. The laser temporal profile is near Gaussian with a time duration of 150 ns (FWHM). The average power is approximately 7 W (2.3 mJ per pulse).

Dielectric-thin-film polarizers are used, external to the laser cavity, to produce highly planar polarized light. At the test specimen the ratio of S-polarized light (E vector perpendicular to incident plane) to P-polarized light (E vector parallel to the incident plane) is greater than 300 to 1.

The reflectometer cavity is a folded configuration consisting of three mirrors – two end mirrors and the test sample (figure 1). The end mirrors are multilayer-dielectric coatings deposited on the concave side of a plano/concave fused silica substrate with a radius of 4.5 m. The test sample is flat. The cavity is folded about the test specimen at an angle of 2 degrees. Both end mirrors are equidistant from the test specimen creating a round-trip cavity length of 11.47 m. To accommodate insertion of the laser beam into the ringdown cavity the entrance end mirror has slightly lower reflectance than the second end mirror. Because the entrance mirror is a high reflector, a little less than 1% of the available laser light is actually coupled into the cavity. The remainder is reflected, dispersed and absorbed in a beam dump. In order to minimize atmospheric effects the entire reflectometer is encased in a Plexiglas housing. Figure 2 is a photograph of the ringdown device and laser source.

The cavity-intensity decay (ringdown) is monitored by measuring the leakage through the second end mirror. A commercially available InGaAs detector having a 2-mm diameter is used. A short focal length lens, in close proximity to the exit mirror, focuses the light to a small spot size on the detector. This conveniently corrects for minor cavity misalignments by resteeering the misdirected light back to the detector. Accurate alignment is quite easily accomplished because misalignments are recognized by simple sinusoidal oscillations superimposed on the decaying signal as the light scans on and off the detector during subsequent bounces.

A low-power beam expander is used between the laser and the ringdown cavity to increase the laser-beam spot size on the test sample. The spot size on the test sample is approximately 3-mm diameter for near-normal angle testing.

Non-normal angle testing is accomplished by unfolding the cavity and increasing the size of the test specimen to 4-in. diameter to accommodate the elongated spot. As mentioned previously, the laser light at the test sample is S polarized. A shorter cavity is used for these measurements but is accounted for in the calculations.

Figure 3 shows the digital-storage oscilloscope display of a cavity-intensity decay. The quality of the ringdown and the decay constant is determined manually by using the inherent capabilities of the oscilloscope.

As described by Anderson, et al., the reflectance product of a ringdown cavity is,

$$R_p = \left( 1 - \frac{1}{2 \frac{C}{L} \tau_c} \right)^2 \quad (1)$$

where  $\tau_c$  is the cavity-intensity-decay time constant,  $L$  is the cavity round-trip optical path length, and  $C$  is the speed of light. For the folded ringdown cavity represented schematically in figure 1 the reflectance product is,

$$R_p = R_1 R_u^2 R_3 \quad (2)$$

Thus,

$$R_u = (R_p/R_1 R_3)^{1/2} \quad (3)$$

where  $R_1$  is the reflectance of one end mirror,  $R_3$  is the reflectance of the second end mirror, and  $R_u$  is the reflectance of the unknown. Note that in a folded cavity there are two bounces on  $R_u$  for each round trip, accounting for  $R^2$  in eq (2).

### 3. Calibration

The reflectance values for the two end mirrors are determined by using a two-mirror ringdown cavity. First the two end mirrors are used as the cavity mirrors. Next, each of the two curved mirrors is used in a cavity with a high-reflector flat as the second mirror. A reflectance product is measured for each of the three configurations. Given these values, the reflectance of any or all of the reflectors can be calculated. Finally, all three mirrors are placed in the folded cavity to measure the combined reflectance product. This confirms the earlier two-mirror cavity results. The flat mirror used in this set of experiments is used from that point on as the calibration mirror. When used as the third mirror of the reflectometer, a repeatable decay constant is expected. Shorter decays usually indicate cleaning is necessary, however, they (decays) could also indicate an increase in airborne particulates, moisture, scratched cavity mirrors, etc.

### 4. Test Samples

Multilayer-dielectric high reflectors for this effort were secured from more than a dozen vendors. In most cases the vendor was allowed to select coating materials and design, however, in a few cases the material was specified. In all cases the minimum reflectance specification was greater than or equal to 0.9970 at 1.06  $\mu\text{m}$ . As a control, all of the substrates were supplied by Los Alamos. All of the silver and protected silver reflectors, including one 4-in.-diameter specimen used for the high-angle testing, were manufactured at Los Alamos National Laboratory. These coatings are 2,000 Å of silver deposited on a silicon substrate with a 40-Å-thick chromium binder layer. They are overcoated with a 10-Å-thick layer of alumina to prevent degradation. An NBS gold standard is available and was measured for comparison at the lower reflectance end of the measurement range.

### 5. Results and Discussion

The reflectometer has a demonstrated precision of  $\pm 50$  ppm and, when  $R_u$  approaches unity, the absolute accuracy also approaches this value. Table 1 is a summary of reflectors measured at near-normal (1 degree) angle of incidence. The quantity in run refers to the number of samples measured from a given run, and the mean reflectance shown is for measured samples from that run. For the most part, as indicated by the standard deviations, there is considerable variation in reflectors coated in the same run. However, although not reported here in any quantitative fashion, these same variations are generally observed on the individual specimens as well.



The  $\text{TiO}_2 / \text{SiO}_2 / \text{ZrO}_2$  has results similar to the  $\text{TiO}_2 / \text{SiO}_2 / \text{HfO}_2$  except that one of the reflectors is 0.005 below the mean of the corresponding three samples. However, all four samples are included here, which substantially decreases the mean.

Two pristine, bare silver reflectors from each of three runs were measured. The mean reflectance of all six samples is  $0.992 \pm 0.001$ . As seen in the table, silver coatings with an alumina overcoat demonstrate the same reflectance values as for the bare silver.

For rough comparison near the lower end of the reflectometer range, an NBS gold standard was measured. NBS reported  $R = 0.977$ ; we report  $R = 0.97679$ . Only one site on the specimen was measured.

Figure 4 shows the increase in measured reflectance of the alumina-overcoated sample as the incident angle is increased. Although the coating process is theoretically the same, the reflectance for this sample, at near-normal angle, is slightly lower than for all other similar runs. Due to space limitations at the time, angles between 10 and 80 degrees were not possible to attain.

## 6. Conclusions

A 1064-nm ringdown reflectometer has been developed and is being used to measure the reflectance of high-reflection, multilayer dielectric reflectors and silver mirrors at that wavelength. The reflectometer has a demonstrated precision of 50 ppm when the reflectance is near unity.

We have seen that although multilayer dielectric reflectors of  $R > 0.9990$  are available, a fair number of samples do not meet the minimum requirement of 0.997. We have also seen that some runs exhibit large intrarun reflectance variation, up to 9,000 ppm. Finally, silver reflectors with an alumina overcoat demonstrate a reflectance of 0.9916, which is quite near the value observed for similar mirrors without the overcoat.

## 7. References

[1] Anderson, Dana C.; Frisch, Joseph C.; Masser, Carl S. Mirror Reflectometer Based on Optical Cavity Decay Time, *Appl. Opt.* Vol. 23, No. 8, 1984.

Table 1. Measured reflectance values for a variety of reflector designs.

Coating Mat'l.	Mean Reflectance	± One Std. Dev.	Quantity In Run	Comments
ZrO <sub>2</sub> /SiO <sub>2</sub>	0.988	0.003	6	IBS
	0.996	0.002	6	
	0.998	0.002	3	IBS
	0.9959	0.0004	6	EBD, Si sub
	0.9962	0.0004	6	EBD, Si sub
	0.9971	0.0004	3	EBD
	0.9975	0.0002	6	EBD, Si sub
	0.99896	0.00003	3	IBS
HfO <sub>2</sub> /SiO <sub>2</sub>	0.990	0.009	7	EBD
	0.9977	0.0004	3	EBD
	0.9984	0.0004	3	PIP
	0.9989	0.0004	5	IBS
	0.9992	0.0003	3	EBD
	0.9964	0.0002	2	IAD
TiO <sub>2</sub> /SiO <sub>2</sub>	0.994	0.002	3	EBD
	0.9977	0.0004	5	IBS
	0.9997	0.0001	4	IBS
Al <sub>2</sub> O <sub>3</sub> /SiO <sub>2</sub>	0.9984	0.0001	5	EBD
SiN <sub>4</sub> /SiO <sub>2</sub>	0.9987	0.0002	4	IBS
TiO <sub>2</sub> /SiO <sub>2</sub> /ZrO <sub>2</sub>	0.998	0.002	4	EBD
TiO <sub>2</sub> /SiO <sub>2</sub> /HfO <sub>2</sub>	0.9992	0.0003	3	EBD
HfO <sub>2</sub> /SiO <sub>2</sub> /ZrO <sub>2</sub>	0.9966	0.0003	5	EBD
Ag/Al <sub>2</sub> O <sub>3</sub>	0.9916	0.0008	4	EBD, Si sub
Au	0.97679	---	1	NBS std. (0.977)

-----  
All substrates are C7940 unless otherwise noted

PIP = plasma ion plated

IBS = ion beam sputtered

IAD = ion assisted deposition

EBD = electron beam deposited

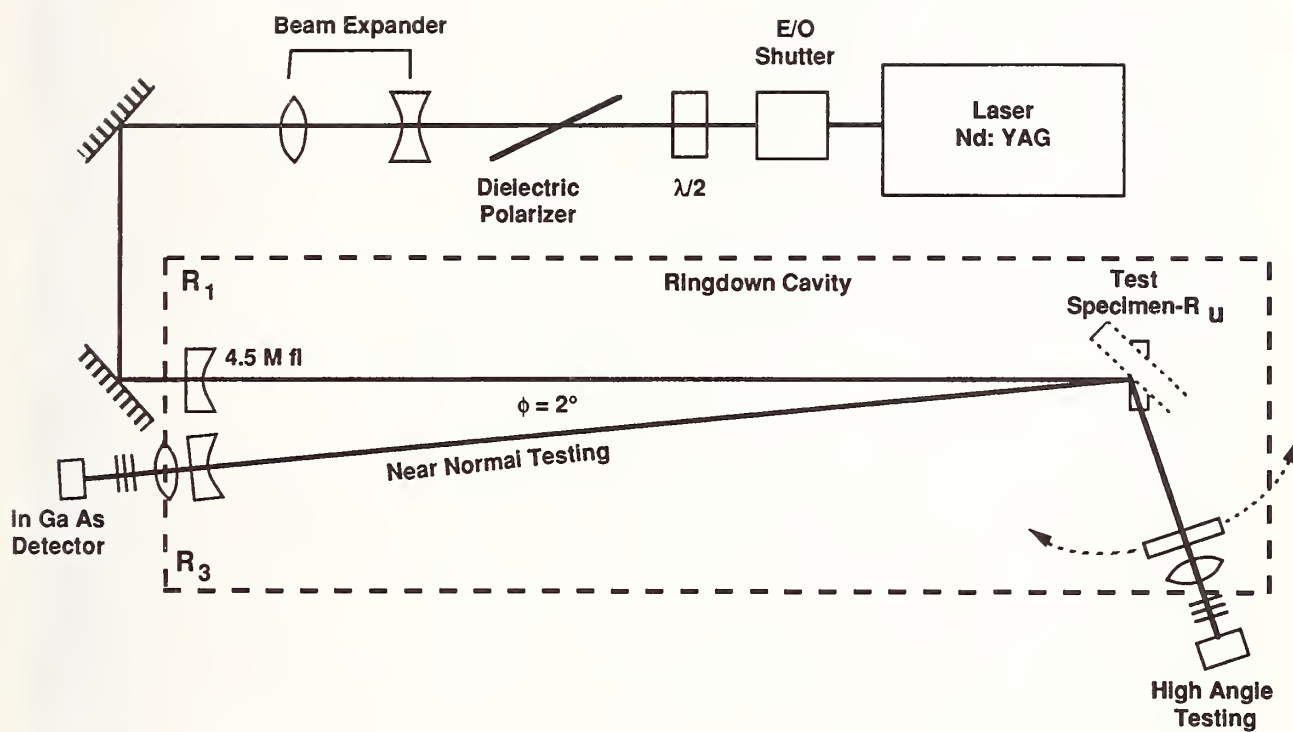


Figure 1. Schematic of the ringdown reflectometer system.



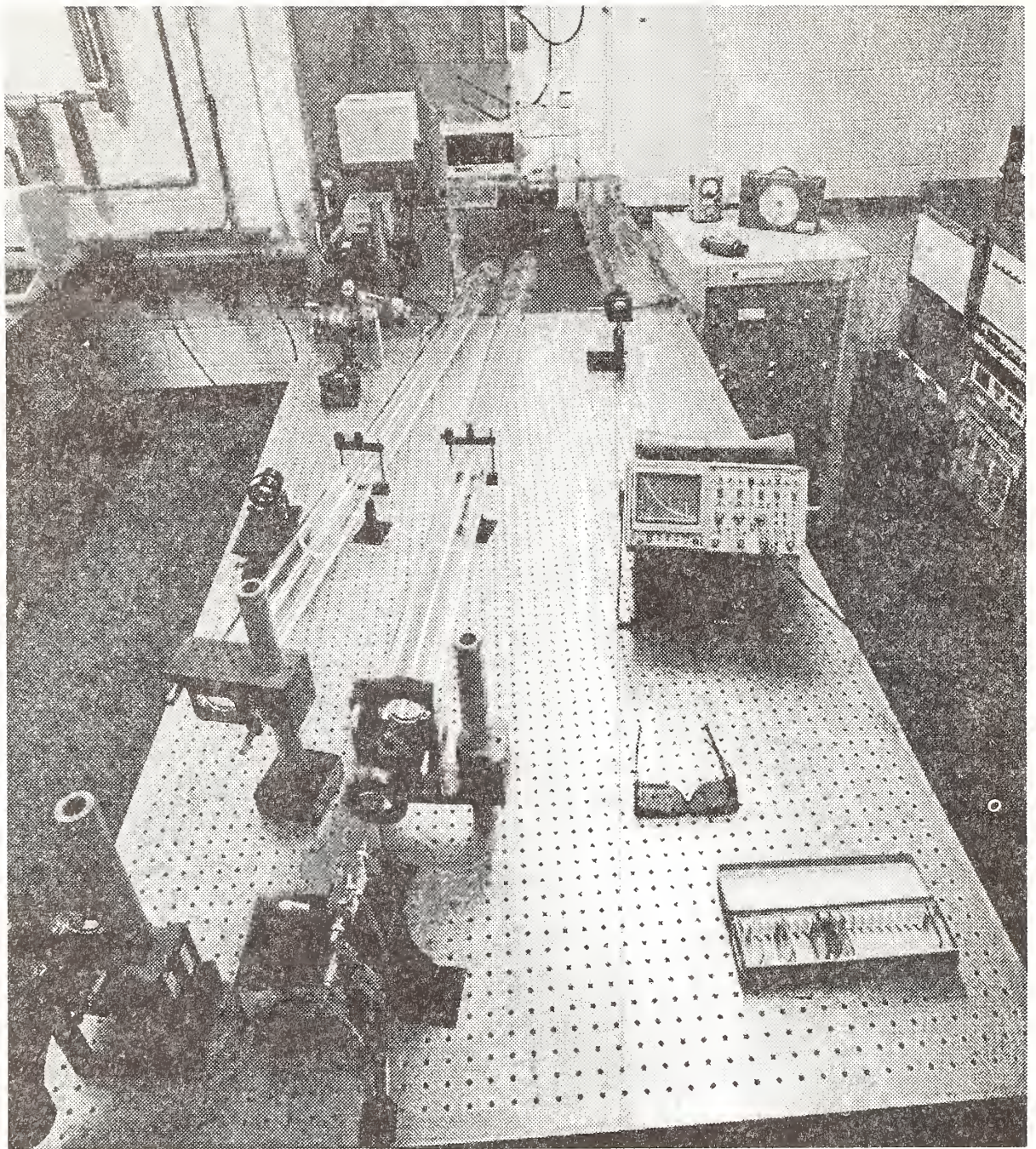


Figure 2. Ringdown reflectometer photo.



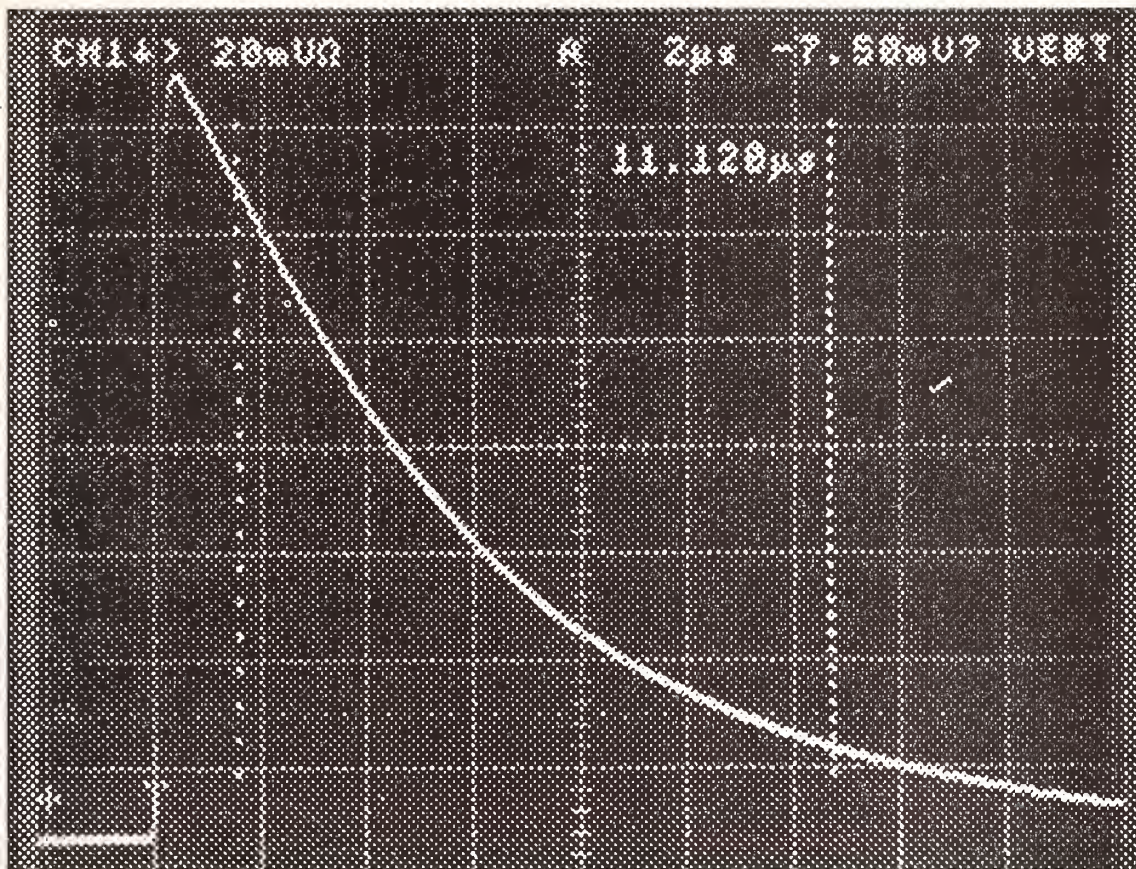


Figure 3. Oscilloscope output showing cavity decay time ( $11.120 \mu\text{s} = 2\tau_C$ ).

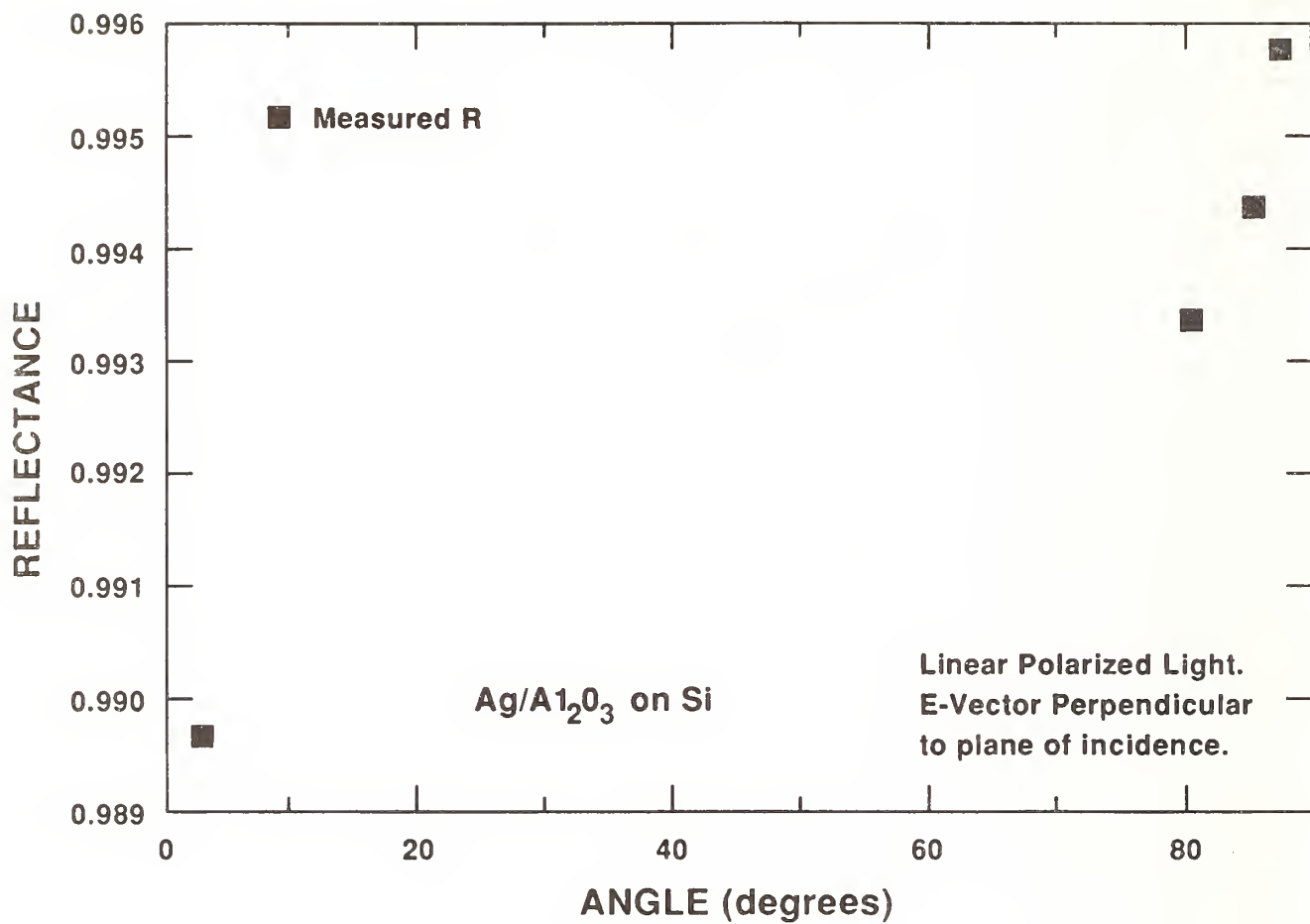


Figure 4. Measured reflectance of a protected silver reflector at various angles.

MANUSCRIPT NOT RECEIVED

RADIATION EFFECTS IN MIRROR SUBSTRATE MATERIALS

E.J. Friebele, J.A. Ruller, and P.L. Higby  
Optical Sciences Division  
Naval Research Laboratory  
Washington, DC 20375

ABSTRACT

Large mirror substrates in surveillance and directed energy applications will be exposed to nuclear radiation from the natural space environment and hostile activity. Ionizing radiation is known to alter the physical properties of ceramics. For example, changes in the density and/or coefficient of thermal expansion result in surface deformation and a resultant loss of optical figure.

In contrast to the radiation-induced compaction measured in silica and Zerodur at high dose ( $>10^6$  rads), there has been a recent report of expansion in silica exposed at lower doses. We report here the effects of radiation on the density of various silicas, SiC, ULE, and Zerodur over a wide range of dose ( $10^4$  -  $10^9$  rads). The changes in density have been correlated with the concentration of electronic defect centers such as the oxygen vacancy E' center and the non-bridging oxygen hole center, leading to the development of structural models for the densification process. In addition, the changes in the thermal expansion behavior of these materials have been measured with a high-resolution Michelson interferometer. Results of the study indicate the possibility of significant surface deformation and loss of optical figure.

## Laser Polished Fused Silica Surfaces: Absorption Data

Alan F. Stewart and Arthur H. Guenther\*

Air Force Weapons Laboratory  
Kirtland AFB, NM 87117

Simultaneous laser polishing of both faces of fused silica windows has produced exceptionally uniform high quality surfaces. Thin wafers of fused silica were laser polished and the absorption measured at 351 nm using a laser calorimeter. The data shows virtually no change in the measured absorption even with the highest power levels used in the polishing process. This data can be related to the conventional polishing process used to prepare these samples before laser polishing.

Key words: absorption; contamination; fused silica; laser polishing

### 1. Introduction

The process of laser polishing has been proposed as an effective method for finishing of fused silica surfaces.[1-5] Several authors have reported that laser polished surfaces exhibit higher laser damage thresholds.[1-3] It has also been determined that these surfaces can exhibit extremely low scatter levels comparable to those produced by the most advanced superpolishing techniques.[5] In an earlier study, we have observed high residual stresses in laser polished surfaces and unusual chemical bonding of the silica which have been modelled by others.[4,5] These changes have been related to the extremely high temperatures of the surface during the polishing process. It is widely assumed that the intense heating heals or fuses microcracks in the surface and/or simply burns off residual contamination which control laser damage thresholds and scatter levels.

We report here the results of a test series intended to demonstrate the correlation of laser polishing with the removal of adsorbed contamination. Specifically, absorption at 351 nm was measured on a series of laser polished substrates. Our data does not show any correlation between laser polishing parameters and the measured absorption of these parts. We believe this null result is due, in part, to residual contamination from the pre-laser irradiation polishing process which is or becomes chemically bonded to the surface.

### 2. Experiment

Laser polishing of fused silica wafers was performed using a double-sided technique. Earlier data had suggested that thermal cycling of laser polished surfaces might lead to a degradation of the surface and low laser damage thresholds.[5] Simultaneous polishing of both surfaces of a substrate eliminated this effect as a possible complication.

The optical bench in the laser laboratory was set up for double sided polishing as shown in figure 1. The high power CW CO<sub>2</sub> laser used in this study, the beam diameter(6-7 cm), and beam dwell time(6.5 sec) were the same as described in reference [5]. The arrangement of optics in figure 1 split the laser output into two opposing beams of equal power which were focussed to the same diameter on the sample surfaces.

The substrates used in this study were commercially available fused silica wafers 2.54 cm in diameter and 0.025 cm thick. These substrates were the standards used for laser calorimetry where low mass is of extreme importance. Each substrate was held in a split

\* Current addresses are:

(A.F.S.) Battelle Pacific Northwest Laboratories, P.O. Box 999, Richland, WA 99352  
(A.H.G.) Los Alamos National Laboratory, MS A110, Los Alamos, NM 87545



copper ring which loosely contacted the part on the faces near the rim. Because of the temperatures involved in the laser polishing process, the substrate needed room for expansion and thus was not constrained.

Laser polishing of the parts proceeded at power levels ranging from 0 to 40 Watts per square centimeter. As in the earlier studies, an infrared camera system was used to monitor the surface temperature of the parts during the polishing process. Peak temperatures recorded varied in a nearly linear fashion to 2900 degrees Centigrade at 40 W/cm<sup>2</sup>. These values were considerably higher than the linear dynamic range (1500 degrees) of the camera system. As such, incident power levels were recorded as they were considered to be more reliable and reproducible.

Following irradiation, the polished substrates were measured for total absorption at 351 nm using a laser calorimeter. The instrument, which has been described extensively in reference [6], has a baseline resolution of approximately 10 ppm. No additional cleaning process was performed prior to measurement.

### 3. Analysis

Laser calorimetry data of absorption for the laser polished fused silica at 351 nm is shown in fig. 2. Given the resolution of the instrument, this data indicated there was essentially no change in the absorption of the parts with laser power employed in the polishing.

These results were quite surprising because residual hydrocarbon contamination was suspected to be a major component of surface absorption at 351 nm. The intense surface temperatures generated in the laser polishing process should have desorbed or oxidized all surface contamination. Laser polished surfaces should be among the cleanest of optical surfaces. This surface would definitely remain clean if the ion polishing were performed under UHV conditions as in reference [7]. Based on scattering data, we expected that fractures in the surface left from the conventional polishing process would have "healed" driving out impurities and reducing the number of dangling surface bonds. With no change in absorption observed, either hydrocarbon or other contamination managed to reestablish themselves as resident on the surface between polishing and measurement, or some other agent - extrinsic or intrinsic - was active.

In fig. 3, contamination data on a zirconia film deposited on a fused silica wafer from the same manufacturer. This data was obtained using a quantitative technique called Secondary Neutral Mass Spectroscopy (SNMS) [8]. An anomaly appears in this data as well that we believe correlates with our data from the laser polishing experiments. As the SNMS instrument sputtered through the film after 2300 seconds, peaks for aluminum and titanium rose to nearly the 1% level of total counts. These contaminants could not be traced to any aspect of the coating process such as the crucible material used or previously deposited species in the chamber or the cleaning process used prior to coating.

Tracking backwards to locate the source of this contamination, the manufacturer provided us with a sample of their grinding compound used to fabricate the fused silica substrates. As shown in fig. 4, an energy dispersive x ray scan shows that the compound is 95% alumina with approximately 5% titania. Clearly from fig. 3, conventional cleaning could not remove this contamination layer. As alumina and titania are refractory materials, they would not decompose during laser polishing. It is suspected that this layer is chemically bonded to the surface and could not be removed except by an ion or chemical etching process.

The presence of a bonded contamination layer of refractory materials would reduce the utility of laser polishing as an effective surface cleaning process. No measurable changes in absorption would be expected either. Further studies will be required to isolate this variable in the fabrication, cleaning, and polishing process.

### 4. Conclusion

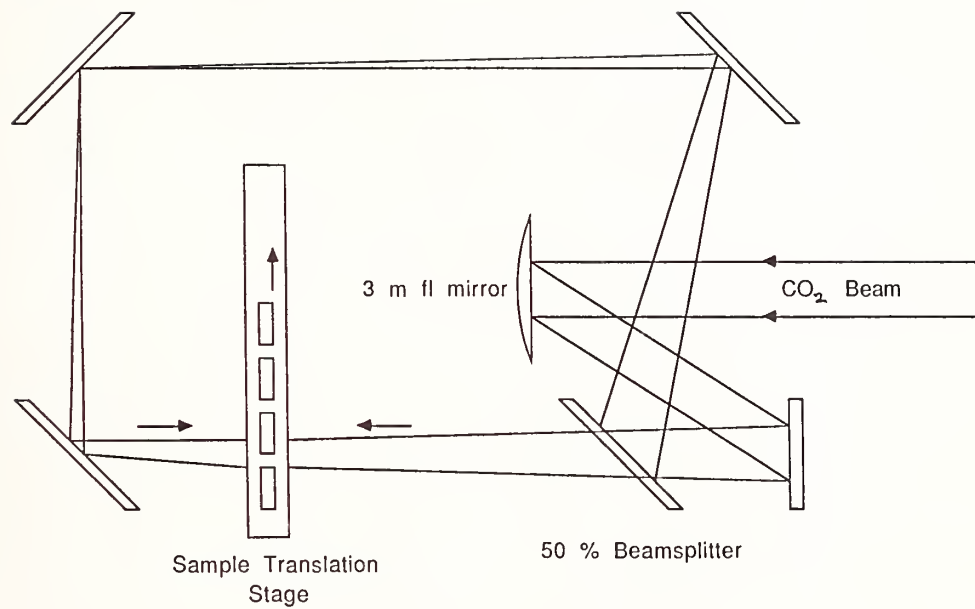
Double sided laser polishing of fused silica windows has been performed. In absorption measurements performed on windows polished at different incident power levels, no significant changes were observed. Contamination data obtained on identical substrates

appears to provide the key to explaining this observation. Absorbing refractory materials chemically bonded to the substrate surface could not be removed by the laser polishing process. Laserpolishing may actually promote bonding of species such as titania which are physisorbed or chemisorbed onto the surface during conventional polishing. It is perhaps ironic that the substrates laser polished in this study and in use almost continuously on the laser calorimetry system were selected because of exceptional quality control and uniformity in fabrication. The discovery of a highly absorbing contamination layer on the surface in this study should promote a careful preselection process before the next "standard" substrate is adopted.

Future work in the study of surface contamination and polishing will hopefully benefit from the results of this effort. A characteristic of titania and alumina is that they can be easily identified with a technique such as SNMS. Accurate depth profiling of concentrations at the ppm level with 3 nm resolution has been demonstrated using SNMS. As we have discovered, the use of alumina or titania effectively tags the surface contamination layers for further study. On the other hand, further studies of laser polishing on substrates which have been fabricated under more controlled conditions may help identify other more subtle sources of contamination.

## 5. References

- [1] P.A. Temple, D. Milam, and W.H. Lowdermilk, Nat. Bur. Stand. (US) Spec. Publ. 568, 1980, pp 229-236.
- [2] P.A. Temple and M.J. Soileau, Nat. Bur. Stand. (US) Spec. Publ. 620, 1981, pp. 180-188.
- [3] P.A. Temple, W.H. Lowdermilk and D. Milam, Appl. Opt. 21, 1982, pp. 3249-3255.
- [4] Y.M. Xiao and Michael Bass, Appl. Opt. 22, 1983, pp.2922-2936.
- [5] Annetta J. Weber, Alan F. Stewart, Gregory J. Exarhos and W. Kent Stowell, Nat. Bur. Stand. (US) Spec. Publ. #752, 1986, pp 542-556.
- [6] A.F. Stewart and D.J. Gallant, "Ultraviolet Thin Film Coating Characterization", Nat. Bur. Stand.(US) Spec. Publ. #727, 1984, pp. 272-284.
- [7] R. Wolf, B. Steiger, G. Zscherpe and D. Schafer, "Absorption and Laser Damage Resistance of TiO<sub>2</sub> Thin Films Deposited on Laser Irradiated Substrates," Thin Solid Films, 162 (1988) 217-221.
- [8] Alan F. Stewart, Arthur H. Guenther, Tilak Raj and Hans Oechsner, "Quantitative Chemical Analysis of Optical Coatings by Secondary Neutral Mass Spectroscopy," to be published in Thin Solid Films or Surface and Coatings Technology, November 1988.



Experiment layout for double sided laser polishing

Fig. 1

OPTICAL ABSORPTION OF LASER POLISHED SILICA WAFERS  
(351 nm)

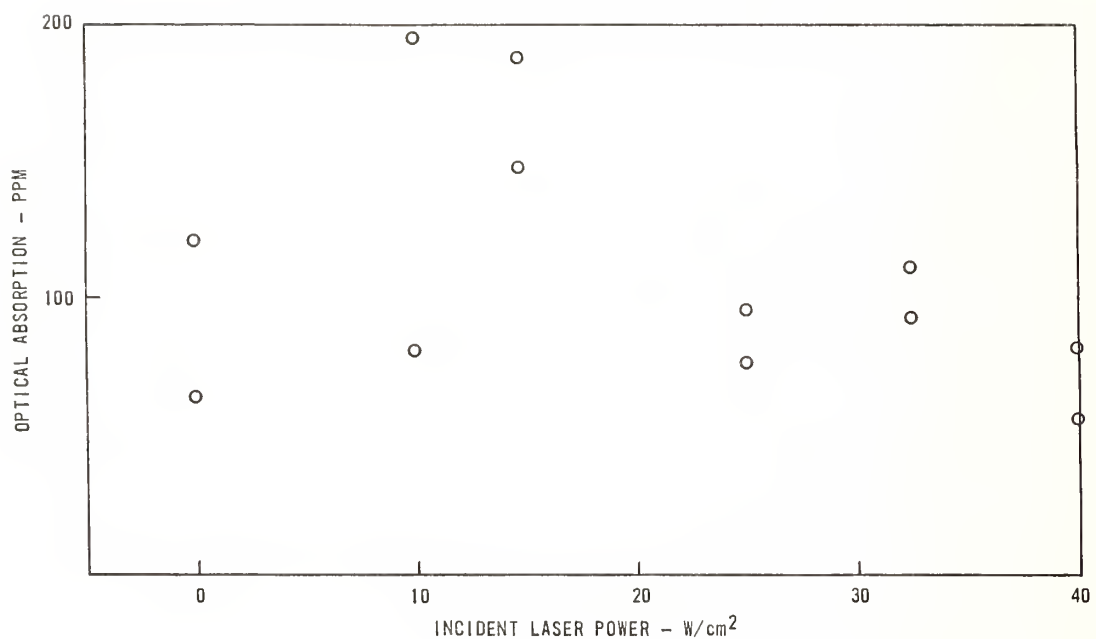


Fig. 2

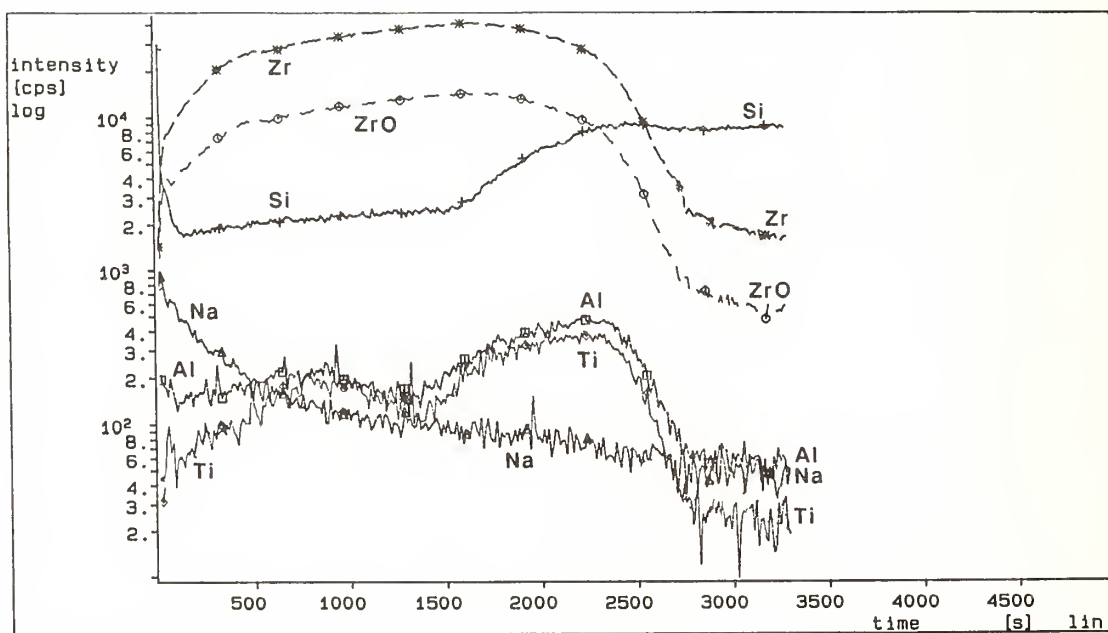


Fig. 3



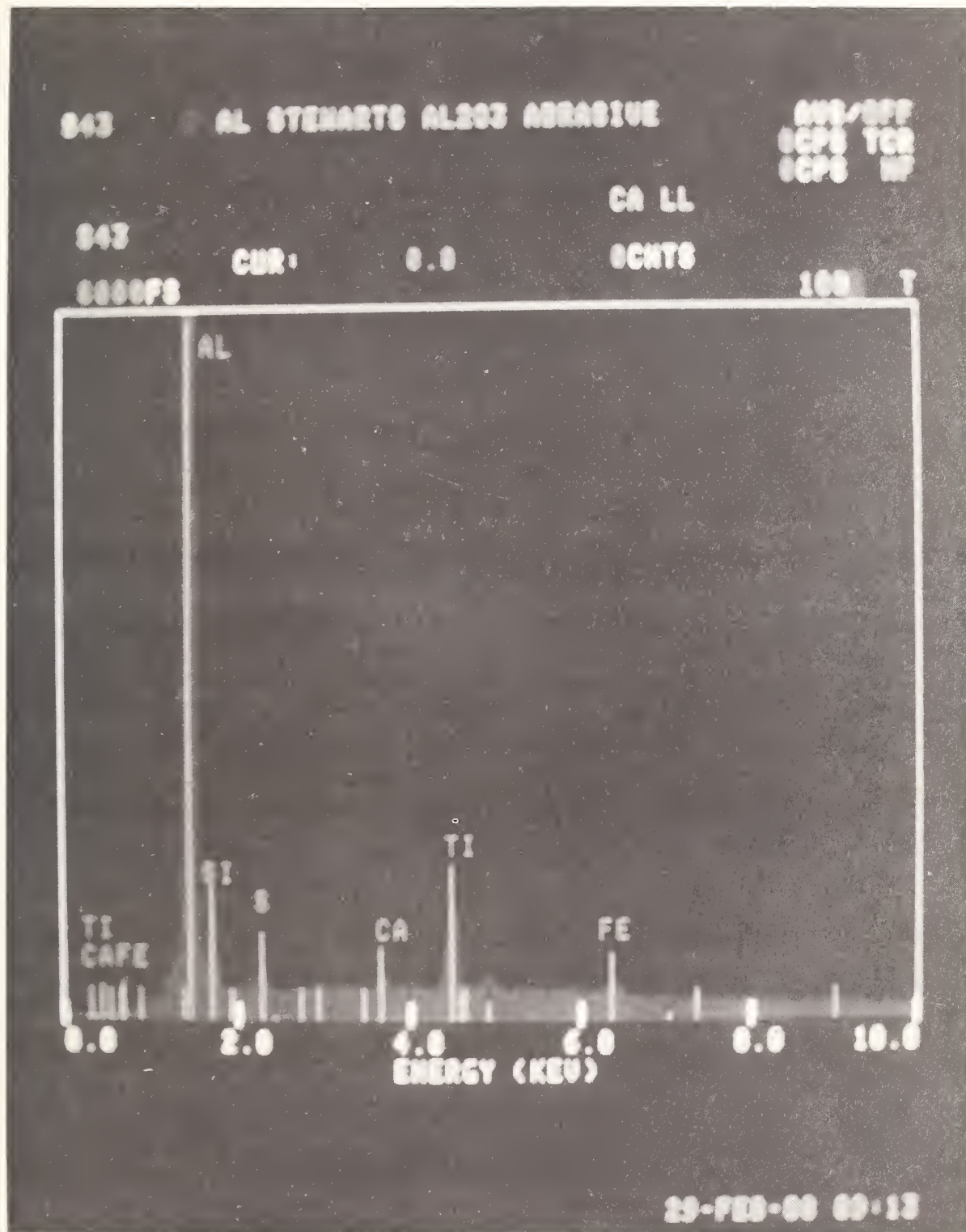


Fig. 4

## 6. List of Figures

1. Experimental layout for double sided laser polishing of fused silica. A high power CW CO<sub>2</sub> laser system is split into two beams of equal power which are focussed to the same diameter on the sample surfaces.
2. Optical absorption of laser polished fused silica wafers measured using laser calorimetry at 351 nm. Virtually no change in absorption is measured for wafers processed at 40 W/cm<sup>2</sup>. The resolution of the calorimeter is 10 ppm with a measurement precision of 10%.
3. Secondary Neutral Mass Spectroscopy (SNMS) data obtained on a zirconia film deposited on a fused silica wafer identical to that used in the laser polishing study. Titania and alumina peaks appear as the instrument sputters through the film and begins to sputter into the substrate surface.
4. Energy dispersive x-ray data on grinding compound used by vendor supplying fused silica wafers. The material is a 9 micron powder and is approximately 95% alumina with 5% titania.

## The Detection, Removal and Effect on Damage Thresholds of Cerium Impurities on Fused Silica

R. C. Estler,\* N. S. Nogar, and R. A. Schmell  
Chemical and Laser Sciences Division  
Los Alamos National Laboratory  
Los Alamos, New Mexico 87545

We describe the detection, by resonance ionization mass spectrometry (RIMS), of cerium impurities on fused silica optical substrates. The impurity is desorbed into the gas phase by an infrared laser ( $1.06\text{ }\mu\text{m}$ ), and detected, as both free cerium atoms and cerium oxide, by RIMS. In addition, we describe an acid wash procedure that both improves the damage threshold, and reduces significantly the measured levels of near-surface cerium.

Key words: cerium; cleaning; damage; fused silica; impurities; lasers; mass spectrometry.

### Introduction

Low-optical-absorption fused silica is a commonly used substrate material for ultraviolet optics. It has good optical properties, and is resistant to both chemical and physical abuse. The measured damage thresholds for this material are widely scattered, and usually lie significantly below the intrinsic damage threshold. This, and other evidence, implies that the dominant damage mechanism in fused silica is dielectric breakdown initiated by absorption at impurity sites [1-2]. Further, recent evidence [1] indicates that absorption in fused silica is not due to bulk impurities such as Al or OH. This suggests that damage may be initiated by the presence of inhomogeneously distributed absorbing impurities or inclusions. Small levels of chemical impurities including residual polishing compound and absorbing inclusions, or physical imperfections, such as grain boundaries or misoriented microcrystals, are among the candidates for initiation sites. These impurities can be detected with a high degree of sensitivity using resonance ionization mass spectrometry (RIMS) [3].

Fused silica is routinely polished with cerium oxide [4], a compound known to absorb at ultraviolet wavelengths. It has been speculated that reduced optical damage thresholds may result from cerium contamination left as polishing artifacts in surface dislocations. We have recently examined the effect of various surface treatment processes on both damage thresholds and the concentration of detectable cerium on the optic surface.

### Experimental

Two-inch-diameter by 3/8-inch-thick Corning 7940 fused silica windows from a commercial vendor were prepared using standard optical fabrication techniques.

Cerium was detected as both free Ce atoms and CeO by resonant, or quasi-resonant ionization processes. The apparatus has been described previously [5]. Briefly, desorption was initiated by  $\approx 10$ -nsec pulses from a Q-switched Nd<sup>3+</sup>-YAG laser (Quanta Ray DCR-2). Fundamental or frequency multiplied pulses from this laser were focused to a fluence of  $\approx 5$ -20 J/cm<sup>2</sup> at the surface of the optical substrate. At a variable time delay, typically 10-15  $\mu\text{sec}$ , an excimer-pumped dye laser was triggered. Pulses from this laser (15 nsec, 1-3 mJ,  $\lambda=435\text{ nm}$ ,  $\Delta\nu=0.3\text{ cm}^{-1}$ ) passed through the ionization region of the time-of-flight mass spectrometer parallel to, and  $\approx 1\text{ cm}$  from, the substrate surface. Photoions were repelled down the flight tube at right angles to both incident lasers. Ions were identified by both optical and mass spectra.

\*Permanent address: Department of Chemistry, Fort Lewis College, Durango, Colorado 81301.

The mass spectrometer has a 0.4-m flight tube, and was maintained at a vacuum better than  $10^{-7}$  by a liquid-nitrogen trapped oil diffusion pump. Ions were detected by a channel electron multiplier, and the signals processed by a series of amplifiers and either a transient recorder or a boxcar averager.

Surface roughness was measured using a heterodyne surface profilometer. The average surface roughness before cleaning was 3.7 Å RMS, with a peak-to-valley maximum of 21 Å. Photos of the surface were taken before and after cleaning treatments, and before and after laser irradiation, with a Nomarski microscope. The parts were checked before and after cleaning for cerium by RIMS, and also with the KrF optical damage test stand [6].

The cleaning procedure used consisted of an acid wash in 1:2 mixture (volume) of aqueous  $\text{HNO}_3$  in  $\text{H}_2\text{SO}_4$  at 90°C for 12 hours. The samples were then rinsed with distilled water and re-cleaned with acetone. The samples were then rechecked on the profilometer. The average surface roughness increased 1 Å rms.

## Results and Discussion

Figure 1 shows a schematic energy level diagram for Ce and CeO in the energy (wavelength) region of interest, while figure 2 displays the experimental spectra in that region for masses 140 and 156. It should be noted that Ce has  $\geq 12$  states lying below 3500  $\text{cm}^{-1}$ , all of which may have substantial population following laser desorption [8]. In addition, the density of even levels near the one-photon resonance is  $\approx 0.1/\text{cm}^{-1}$ . The net effect is the very congested, nondescript spectrum observed in figure 2a, exacerbated by power broadening at the intensities ( $10 \text{ MW}/\text{cm}^2$ ) required for efficient ionization and detection. In addition, some of the signal detected at mass 140 may be due to simultaneous dissociation/ionization [8] of a  $\text{CeO}_x$  precursor. Similarly, the CeO ground state is split into at least four levels [9,10] (probably  $^3\phi_2$ ,  $^3\phi_3$ ,  $^3\phi_4$  and  $^1\phi_3$ ), of generally unknown splitting, the chief exception being a well-defined  $2060 \text{ cm}^{-1}$  splitting for  $^3\phi_3$ - $^1\phi_3$ . The resonance state is an ill-defined level of B symmetry. In all cases, the vibrational constant is  $\approx 600$ - $800 \text{ cm}^{-1}$ , and the rotational constant is  $\approx 0.35 \text{ cm}^{-1}$ . The result is another very congested spectrum, as shown in figure 2b. Although the optical spectra cannot be used by itself to "fingerprint" the species, the combination of optical and mass spectra can be used to positively identify the desorbates, as shown in figure 3.

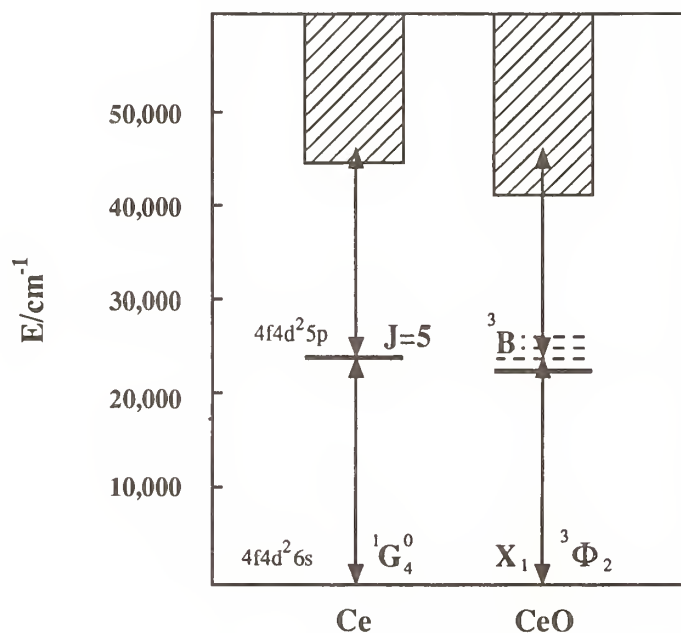


Figure 1. Schematic energy level diagrams for Ce and CeO, showing potential resonant levels. The cross-hatched area indicates the ionization continuum.



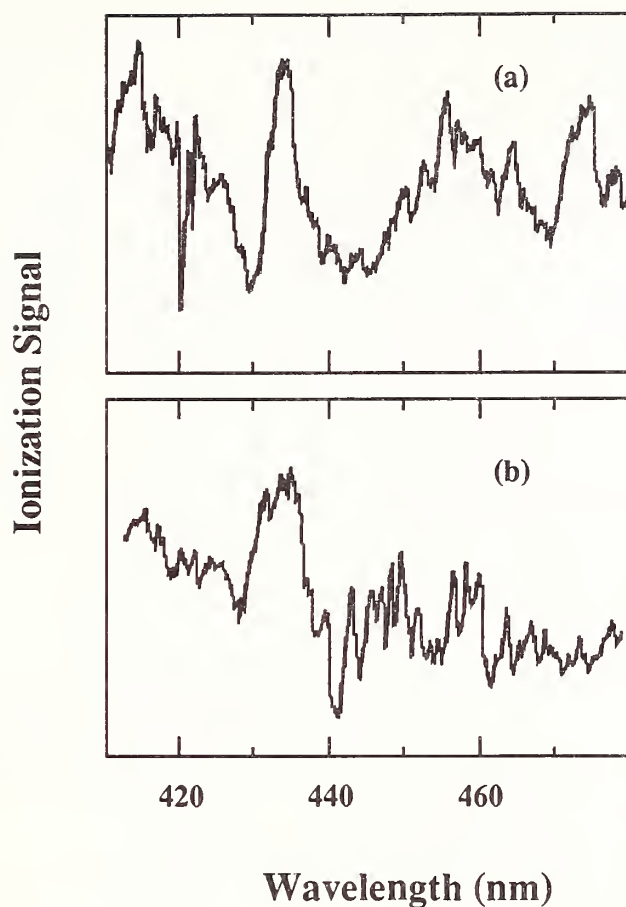


Figure 2. Ionization spectra, obtained at intensity of  $10 \text{ MW/cm}^2$ , for laser-desorbed neutrals from a ceria slurry:  
 a) mass 156 ( $\text{CeO}^+$ ) and b) for mass 140 ( $\text{Ce}^+$ ).

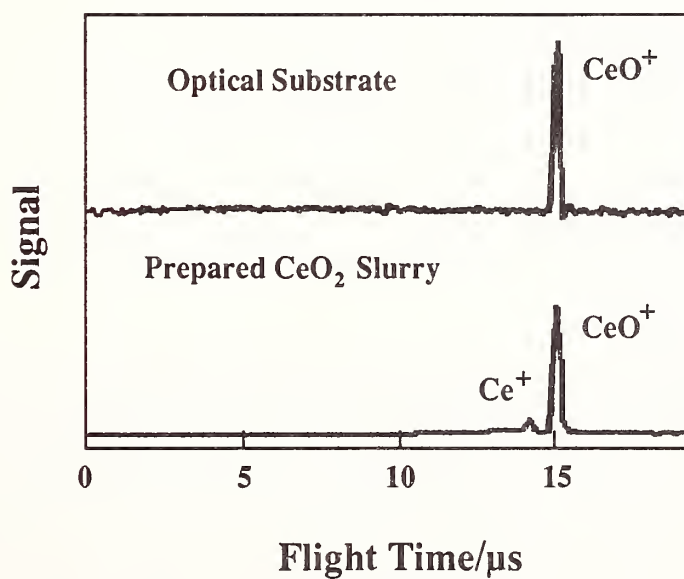


Figure 3. The top trace shows the single-shot time-of-flight RIMS spectrum obtained from material laser desorbed from a fused silica optic, while the lower trace shows a calibration mass spectrum from a ceria slurry.

In figure 3a, obtained by laser desorption/RIMS from a prepared ceria slurry deposited on glass, both mass 140 (Ce) and 156 (CeO) are easily identified in the time-of-flight spectrum. In figure 3b, obtained from the ceria-polished fused silica substrate, only CeO is observed.

For materials desorbed from the optical surface, ion signals were typically processed in a pulse-counting mode, sent to either a transient recorder, as in figure 3, or to a gated integrator set to accept signals from CeO, and displayed on an X-Y recorder. Single ion signals were easily observed above the a.c. noise level, as seen in figure 4. The relative concentration of cerium impurity was determined from the number of single ion spikes observed as the sample was rotated to sweep the laser across a predetermined arc of the optic.

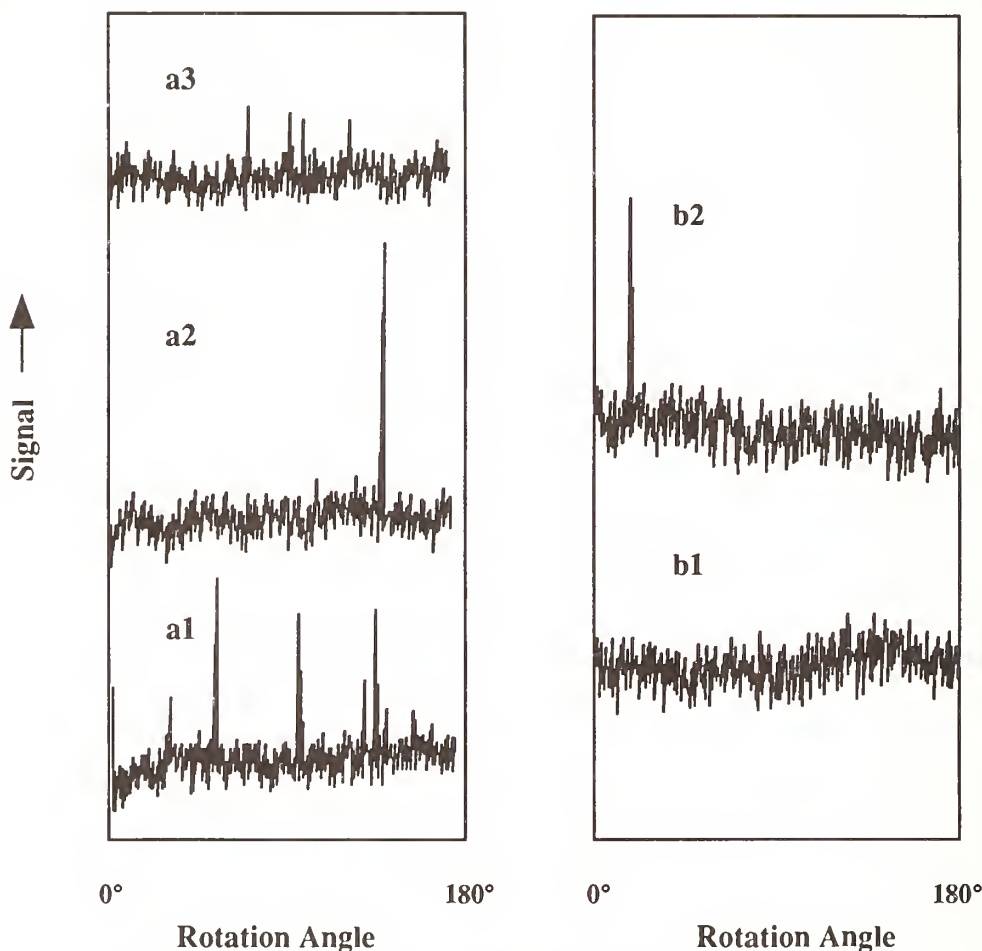


Figure 4. Laser-desorbed CeO signal a) for untreated sample and b) for acid washed samples. Fluence levels were 1) 6 J/cm<sup>2</sup>, 2) 12 J/cm<sup>2</sup>, and 3) 19 J/cm<sup>2</sup>.

Figure 4a shows the cerium/cerium oxide signal obtained by sweeping the laser beam across  $\approx 180^\circ$  ( $\approx 0.5$ -in. radius) on an untreated SiO<sub>2</sub> optic, for several incident 1.06- $\mu$ m laser intensities. Figure 4b shows a similar trace for an optic subjected to the acid wash procedure described previously. For the untreated optic, 11 CeO ions were detected (the third, fourth, and sixth peaks correspond to two ions), while for the acid-washed samples, no ions were detected at 6 J/cm<sup>2</sup>. At 12 J/cm<sup>2</sup>, two ions were detected in each case, so that the overall ratio of detected cerium is 12:1 for these two samples. These results are typical of those obtained for six pairs (treated and untreated) of samples, where the average ratio was  $11 \pm 1.2:1$  ( $\sigma_{n-1}$ ). It should also be noted that the number of CeO ions observed increased with the maximum fluence to which the sample was exposed. This result is consistent with models [11,12] of damage based on a distributed, or nondegenerate defect ensemble. Low fluence irradiation removes surface or near-surface contaminants with minimal damage [3], while higher-fluence irradiation may remove more deeply embedded, or lower susceptibility, contaminants, with concomitant removal of surrounding coating material.

Based on previous results with this apparatus[5,13] and the magnitude of the observed ceria signals, the number of *cerium oxide fragments* removed from the sample lies in the range  $10^7$ -  $10^8$  for *each detected CeO ion*. This estimate assumes that the distribution is spatially isotropic and kinetically thermal (2000 K), and that the fraction of molecular quantum states addressed by

the laser of  $10^{-3}$ (partition function). It should be noted that this does not place an upper limit on the *total* amount of material removed in the desorption process. Cerium clusters, oxides, and other impurities may also be desorbed.

The results of damage threshold measurements are displayed in figure 5 for both untreated and acid washed samples. The difference in measured damage threshold indicated in this figure is representative of the difference in four pairs of samples:  $7.57 \pm 1.77 \text{ J/cm}^2$  ( $\sigma_{n-1}$ ) for untreated samples, and  $9.72 \pm 1.09 \text{ J/cm}^2$  for the acid-washed samples.

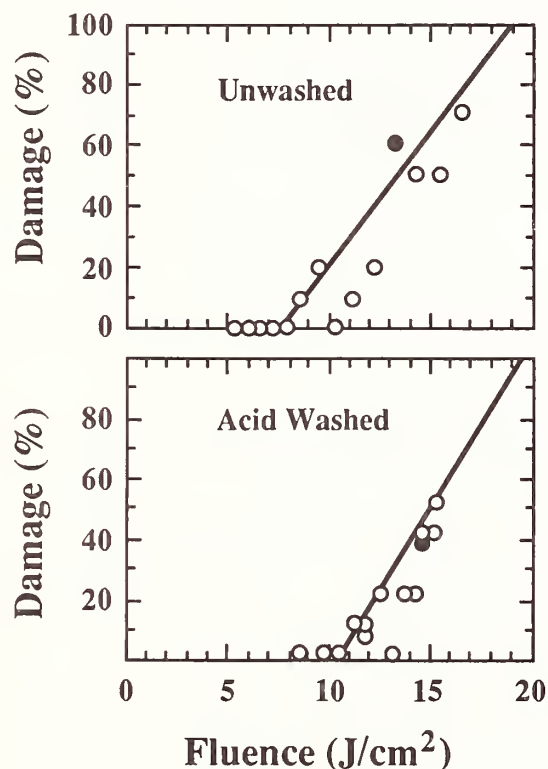


Figure 5. Threshold damage measurements for unwashed (upper) and acid washed (lower) fused silica samples. Solid circles indicate macroscopic damage, while the open circles indicate microscopic damage.

## Conclusions

We have demonstrated a correlation between an acid wash procedure, and the reduction of measured cerium impurities on polished fused silica optical flats. At the same time, the acid wash procedure affects a substantial,  $\approx 30\%$ , improvement in the measured damage threshold at 248 nm. It is tempting to speculate that damage was initiated in unwashed samples by absorption at inhomogeneously distributed cerium inclusions introduced by the polishing procedure.

A choice must then be made concerning the general utilization of ceria as a polishing substance. A substantial body of evidence now suggests that ceria inclusions generally tend to render optics more susceptible to damage, particularly at UV wavelengths. Should one then give up the convenience, speed and finish available from ceria polishing in return for increased damage thresholds? Should this, or some other cleaning procedure [14] be used routinely with ceria-polished optical components? These choices must be made by the individual user or user-group, in recognition of the particular application intended, and lifetime needed.

## References

1. Bandyopadhyay, P. K.; Merkle, L. D. "Laser-Induced Damage in Quartz: A Study of the Influence of Impurities and Defects," J. Appl. Phys. 63, 1392-1398; 1988.
2. a) Soileau, M. J.; Williams, W. E.; Van Stryland, E. W.; Goffess, T. F.; Smirl, A. L. "Picosecond Damage Studies at 0.5 and 1.0  $\mu\text{m}$ ", Opt. Engin. 22, 424-430; 1983. b) Soileau, M. J.; Mansour, N.; Canto, E.; Griscom, D. L. "Effects of Radiation Induced Defects on Laser-Induced Breakdown in  $\text{SiO}_2$ ", Nat'l. Bur. Stds. (U.S.) Spec. Pub. 746; 486-496 (1988).
3. Estler, R. C.; Nogar, N. S. "Chemical Precursor to Optical Damage Detected by Laser Ionization Mass Spectrometry", Appl. Phys. Lett., 52, 2205-2507; 1988.
4. a) Harada, S.; Izumitani, T.; "Polishing mechanism of optical glass" Yogyo Kyokai Shi, 78(899), 229-36; (1970); b) Brown, N. J.; "Some Speculations on the Mechanisms of Abrasive Grindings and Polishing," UCLR 96159.
5. Estler, R. C.; Apel, E. C.; Nogar, N. S. "Laser Mass-Spectrometric Studies of Optical Damage in  $\text{CaF}_2$ ", J. Opt. Soc. B4, 281-286; 1987.
6. Foltyn, S. R.; "Optical Damage Research at Los Alamos", Photonics Spectra, Nov. 1986, pp 113.
7. Martin, W.C.; Zalubas, R.; Hagen, L. "Atomic Energy Levels—The Rare-Earth Elements" NSRDS-NBS-60 (1978).
8. Downey, S. W.; Nogar, N. S.; Miller, C. M. "Resonance Ionization Mass Spectrometry of Technetium," Int. J. Mass Spec. Ion Proc. 61, 337-; 1984.
9. Huber, K. P.; Herzberg, G. Molecular Spectra and Molecular Structure IV. Constants of Diatomic Molecules, Van Nostrand, New York, 1979.
10. Barrow, R. F.; Clements, R. M.; Harris, S. M.; Jenson, P. P. "The Electronic Spectrum of Gaseous  $\text{CeO}$ ," Astrophys. J., 229, 439-447; 1979.
11. Porteus, J. O.; Seitel, S. C. "Absolute Onset of Optical Surface Damage Using Distributed Defect Ensemnbles," Appl. Opt., 23, 3796-3805; 1984.
12. Danileiko, Y. K.; Manaev, Y. P.; Nikolaev, V. N.; Sidorin, A. V. "Determination of the Characteristics of Microdefects from Statistical Relationships Governing Laser Damage to Solid Transparent Materials," Sov. J. Quant. Elec., 11, 1445-1449; 1981.
13. Nogar, N. S.; Estler, R. C.; Miller, C. M. "Pulsed Laser Desorption for Resonance Ionization Mass Spectroscopy," Anal. Chem. 57, 2441-2445; 1985.
14. Gallant, D. J.; Law, M.; Pond, B.; "Effect of Cleaning on the Optical Absorption of Calcium Fluoride and Fused Silica at 351 nm," Nat'l. Bur. Stds. (U.S.) Spec. Pub. 752; 159-167; 1988.



## Laser Damage of YAG Surfaces

Ted McMinn  
McDonnell Douglas Astronautics Co.  
Missile and Defense Electronics Div.  
St. Louis, Mo. 63166

and

Steve Seitel, Mark Babb  
Montana Laser Optics, Inc.  
Bozeman, Mt. 59772

A variety of uncoated and coated YAG substrates have been laser damaged at normal and non-normal incidence; as well as total internal reflection geometries. Testing was done at 1064 nm, with ~11 nsec pulses. Both polished and fractured uncoated surfaces were tested. Typical polished surfaces damaged in the ~10-12 J/cm<sup>2</sup> range, while the cleanest fractured surfaces survived fluences > 90 J/cm<sup>2</sup>. An assortment of different normal and non-normal incidence AR coatings was also tested. The correlation between the damage threshold and the following items is examined: high index materials in the coating design (mainly TiO<sub>2</sub>), electric field profile within the coating, and ion assisted deposition. The AR coating thresholds ranged from 1-19 J/cm<sup>2</sup>, with the better coatings being consistently over 12 J/cm<sup>2</sup>. Prism samples were fabricated to test YAG surfaces in total internal reflection.

Key words: coatings; fracture; Ion assisted deposition; Nd:YAG; total internal reflection; uncoated, YAG

## **1.0 Introduction**

YAG is one of the most important crystalline host materials used for solid state lasers. As laser diode technology has matured over the past decade, diode pumped YAG lasers have become capable of efficient, high peak power operation. In all high power laser systems laser damage is a key concern. High efficiency extraction of stored energy into the laser mode results in optical energy fluences several times the saturation fluence. Improving the damage threshold therefore can directly impact the potential efficiency of the laser system.

In addition to the standard types of normal incidence AR coatings needed on the YAG crystal, certain face pumped, total internal reflection (TIR), slab laser geometries also require special coatings. These special coatings include dual polarization AR coatings for non-normal incidence YAG surfaces, as well as AR and isolation coatings for the TIR surfaces. In this report, we give the results of laser damage testing performed on a variety of uncoated and coated YAG surfaces.

## **2.0 Samples**

Most of the substrate material was purchased from Allied Signal Corp., with a few of the samples coming from Laser Crystal Corp. The material was all undoped YAG, with the exception of a few of the uncoated and fractured samples which were Nd:YAG (~1 atomic %). Grinding and polishing was performed either at McDonnell Douglas Corp. (MDC), or by Virgo Inc. The samples were mostly disks, 25.4 mm in diameter and 2-3 mm thick. Both sides of the disks were polished to a "laser-grade" polish. The scratch/dig specification was 10/5 or better.

## **3.0 Measurements**

All laser damage threshold measurements were made by Montana Laser Optics, Inc. (MLO). The threshold measurements are considered accurate to  $\pm 20\%$ , and reproducible to  $\pm 10\%$ . Table 1 lists the test parameters which apply to any of the results in this report, except where specifically stated otherwise.

Table 1. Damage Test Parameters

wavelength:	1064 nm
pulsewidth:	11-13 nsec (FWHM)
spot size:	~1.0 mm (FW at $1/e^2$ pts), 0.15 mm in the TIR tests
repetition rate:	10 Hz
Transverse mode:	TEM <sub>00</sub>
Axial modes:	etalon in cavity, smooth pulse option
Incidence Angles:	0°, or 59.1° ( $\pm 1^\circ$ ) depending on the test
Polarization:	circular for normal incidence, linear s-pol. or p-pol. for non-normal incidence
Cleaning method:	Acetone/methanol drag-wipe
Preconditioning of sites:	none
sites/sample:	$\geq 20$
shots/site:	$\geq 100$
focal length of lens used:	1 meter for 1 mm spot, 0.25 meters for TIR tests

For this study, the term "laser damage" refers to any permanent laser-induced change to the surface. The term "threshold" refers to the least fluence which caused damage. Damage to the sample was initially detected by increased scatter by the test site from a coaxial HeNe probe beam. Damage at a site is then verified by Nomarski/darkfield microscopy at 150-300X. All the surfaces tested, except the TIR surfaces, were the entrance face of the sample with respect to the incident laser beam, see figure 1. The TIR test geometry is shown in figure 8

Some of the damage tests were conducted at 59.1° incidence. All damage fluence levels refer to the beam analysis plane which is normal to the incident laser beam, see figure 1. These fluence levels should be multiplied by the cosine of 59.1°, when comparing to normal incidence measurements.

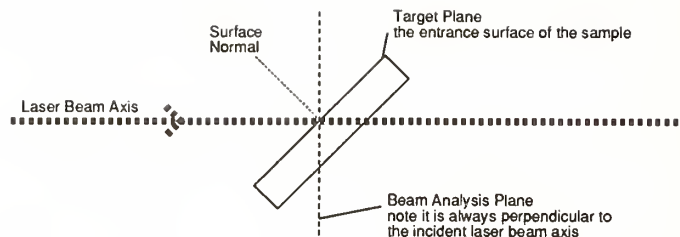


Figure 1. Flat Sample Test Geometry

The spread in the laser damage threshold values is defined in the following equation:

$$\text{Spread} = (a-b)/b$$

a= highest fluence which did not cause damage

b= lowest fluence which did cause damage  
(the damage threshold as defined by MLO)

The value of the spread is related to the spatial uniformity of a surface's damage threshold on a size scale set by the irradiated spot size.

## 4.0 Results

### 4.1 Uncoated

#### 4.1.1 Polished Surfaces

Several uncoated YAG surfaces were laser damaged to establish a baseline from which to compare coated surface results. Table 3 contains the results from 16 uncoated YAG surfaces. The average damage threshold from table 3 is  $11.1 \text{ J/cm}^2$ , with a standard deviation of  $1.7 \text{ J/cm}^2$ . In addition to the table 3 results, one uncoated YAG surface was tested at both normal and  $59^\circ$  incidence. The  $59^\circ$  threshold results were:  $26 \text{ J/cm}^2$  for s-polarization, and  $19 \text{ J/cm}^2$  for p-polarization. The normal incidence threshold was  $12 \text{ J/cm}^2$ . To compare the normal and  $59^\circ$  incidence results, one must multiply the  $59^\circ$  results by the cosine of  $59^\circ$ , or  $\sim 0.52$ . This multiplication results in  $13.5 \text{ J/cm}^2$  for s-polarization, and  $9.9 \text{ J/cm}^2$  for p-polarization. Both of the "converted" values are within two standard deviations of the average normal incidence threshold, and as such represent reasonable consistency between normal and non-normal



threshold measurements on the same surface. Yet the s and p polarization thresholds are significantly different. The reasons for this difference are not known.

The table 3 results seem to form two different groups, one group with thresholds  $\sim 9 \text{ J/cm}^2$ , and another group with thresholds  $\sim 12 \text{ J/cm}^2$ . Even though the threshold difference between these two groups is just barely significant, the groups are conspicuous on a damage histogram, and thus raise curiosity. One of the samples from the  $9 \text{ J/cm}^2$  group was known to have a poor polish and so its low result may be discounted for this reason (sample 7). Unfortunately, no other such obvious reasons exist to discount the other  $9 \text{ J/cm}^2$  results. The reasons for the two different groups are presently unknown.

Two small-scale experiments are contained within table 3. The first experiment was to see if there was a difference in the damage threshold of Nd:YAG versus YAG. Nd:YAG samples 4, 5, and 6 show no significant difference in their damage thresholds, as compared to the other YAG samples (these samples, like all the others, were tested at room temperature). The other experiment involved changing the polishing parameters, such as grit size and polish time.

Table 2. The Basic MDC YAG Grinding/Polishing Process

1	Grind:	12 micron alumina, long enough to grind entire face, and dimension sample
2	Polish:	6 micron diamond, approx. 0.5 hrs.*
3	Polish:	1 micron alumina, 3 hrs.**
4	Final Pol.:	1 micron alumina, approx. 5 hrs. was standard, see Table 3**

All alumina grits used were: Baikalo<sup>®</sup> Alumina Polishing Suspension  
agglomerate-free, with DI water, manufacturer: Baikowski  
International Corp.

\* A Hyprez<sup>®</sup> Kemet Copper lap was used, manufacturer: Engis Corp.

\*\* A Hyprez<sup>®</sup> Kemet Tin lap was used, manufacturer: Engis Corp.

Samples 8, 9 and 10 were all polished using the same procedure except for changing the grit size used for the final polishing step, see table 2. No significant damage threshold differences were observed. Samples 14 and

15 received the same polishing process until the last final polish step. Sample 14 received a 8.5 hour final polish, while sample 15 received a 24 hour final polish. The threshold difference between samples 14 and 15 is just barely significant, and in the expected direction.

Table 3.  
Damage Thresholds of Uncoated YAG Tested Normal Incidence

Sample #	Description	Threshold <sup>a</sup>	
1	MDAC	11.0	
2	MDAC	12.0	(0.13)
3	MDAC	12.0	(0.53)
4	MDAC Nd:YAG	12.0	(0.50)
5	MDAC Nd:YAG	12.0	(0.00)
6	MDAC Nd:YAG	12.0	(0.20)
7	MDAC	8.0	(0.46)
8	MDAC polish test, 0.3 micron	9.5	(0.60)
9	MDAC polish test, 0.05 micron	9.0	(0.00)
10	MDAC polish test, 1.0 micron	9.5	(0.30)
11	Virgo, Ion milled	11.0	(0.50)
12	Virgo	14.0	(1.50)
13	Virgo	9.0	(0.16)
14	MDAC polish test, 1 micron, 24 hrs.	13.0	(0.69)
15	MDAC polish test, 1 micron, 8.5 hrs.	11.0	(0.82)
16	Virgo	13.2	

a in units of Joules/cm<sup>2</sup>, values in parenthesis are the spread in threshold

At the beginning of this activity, it was expected that well-polished uncoated YAG surfaces would damage in the 20-30 J/cm<sup>2</sup> range (the spread values in table 3 indicate that some samples had sites which did not damage even at the ~30 J/cm<sup>2</sup> level). The polish quality of the YAG surfaces was called into question by the table 3 results which were typically 1/2 the expected value. To put some perspective on the results, other damage threshold measurements on YAG were sought. Montana Laser Optics, Inc. has tested eight other Nd:YAG samples, not from MDAC, under the same conditions as those in table 3. These 8 samples were AR coated. The average threshold for these samples was 13.9 J/cm<sup>2</sup>, with a standard

deviation of  $2.1 \text{ J/cm}^2$  [1]. Even though these samples were coated, the threshold agreement is fair, see section 4.2.1.

#### 4.1.2 Fractured Surfaces

After a few simple polish parameter tests were run, it was decided to damage test some fractured YAG surfaces. It was hoped that these fractured surfaces would completely skirt the messy polish parameter testing and show us the true potential damage threshold of the YAG material.

The fractured surfaces consisted of 6 pieces of YAG which had been fractured several weeks prior to the damage test, and a few fresh fractures which were made immediately before the damage test. The samples were fractured by striking them sharply, a process which was always accompanied by the generation of a certain amount of "fine sand". The spot size of the beam was reduced from  $\sim 1 \text{ mm}$  dia. to  $0.5 \text{ mm}$  dia. to allow for more test sites on the relatively small fractured surfaces. The six "old" fractured surfaces damaged in a range of  $\sim 3\text{-}20 \text{ J/cm}^2$ , with the median value being  $\sim 10 \text{ J/cm}^2$ . Small particulate contaminants (which appear as scatter sites in the HeNe probe) were identified as the damage initiation sites for all the "old" surfaces. Several different cleaning techniques were attempted to eliminate these particulates, but none were successful. The origins of at least some of these particulates is thought to be from the fracturing process. Fracturing the YAG thermally, may reduce or eliminate this problem.

When the damage tests were begun on the freshly fractured surfaces, an attempt was made to find sites which showed no particulate contamination (no scatter of the HeNe probe). These very clean sites were found to survive fluences of  $90 \text{ J/cm}^2$ . These sites finally damaged at fluences of  $\sim 110 \text{ J/cm}^2$ . Sites on the same surface that did have the particulate contamination had thresholds in the  $10\text{-}30 \text{ J/cm}^2$  range. Attempts at further cleaning of the already clean sites resulted in a lowering of their damage threshold to pedestrian levels of  $\sim 20 \text{ J/cm}^2$ . This was due to the cleaning technique dragging particulates onto the clean site.

In addition to different damage thresholds of the clean and contaminated sites, a difference in the damage morphology was also observed with a microscope. Damage observed on the contaminated sites is typically seen as the formation and growth of a small pit, accompanied by visible flash and ejecta. On the clean sites, the damage was the formation of a plasma arc, which left the surface of the sample eroded over a large area (flash halo). Very tiny pits are seen in the center of this halo. These pits are surrounded by a ring or rings, where the surface appears to have melted. The damage morphology of the clean sites is similar to that seen on superpolished, uncoated glassy substrates such as, BK7 or fused silica.

The clean sites on the freshly fractured surfaces are considered as indications of the ultimate potential damage threshold for the YAG we have been testing, ( $\sim 100 \text{ J/cm}^2$ ). In comparison, the median threshold of  $\sim 11 \text{ J/cm}^2$  for polished surfaces indicates that there is plenty of room for improvement of the YAG polishing process.

## **4.2 AR Coatings**

Table 4 contains the laser damage threshold results for 19 normal incidence AR coatings. Table 5 has the same data as table 4, only for non-normal incidence AR coatings. Both tables 4 and 5 contain a variety of different coating materials, designs, and process parameters. Several parameter tests are encompassed by this variety; some of which are discussed in the following sections.

### **4.2.1 Coated versus Uncoated YAG Surfaces**

When this YAG damage study began, it was expected that the coated surfaces would have lower damage thresholds than the uncoated surfaces. In figure 2 we compare the damage threshold of the better performing coatings from table 4 (those with thresholds  $> 10 \text{ J/cm}^2$ ), with the uncoated results in table 3. The outcome is that the average coated surface outperforms, if only slightly, the average uncoated surface. This result is the opposite of that observed on coated and uncoated fused silica and glass surfaces; but is similar to that observed on coated and uncoated lithium niobate surfaces [2,3].



Table 4.  
Damage Thresholds of AR Coatings Tested at Normal Incidence

Sample #	Coating Description	Threshold <sup>a</sup>	
1	MgF <sub>2</sub> single layer; 350° C	5.1 <sup>b</sup>	(0.11)
2	MgF <sub>2</sub> single layer; 350° C	18.4	(0.04)
3	MgF <sub>2</sub> single layer	12.4	(0.21)
4	MgF <sub>2</sub> single layer; 250° C	11.4	(-.08)
5	Virgo SHAR	13.3	(0.86)
6	Virgo SHAR	11.4	(1.00)
7	SiO <sub>2</sub> /TiO <sub>2</sub> /MgF <sub>2</sub> three layer; 250° C	2.0	(0.37)
8	TiO <sub>2</sub> /MgF <sub>2</sub> two layer	2.2	(0.43)
9	Al <sub>2</sub> O <sub>3</sub> /MgF <sub>2</sub> two layer	16.0	(0.25)
10	SiO <sub>2</sub> /Al <sub>2</sub> O <sub>3</sub> three layer	6.6	(0.41)
11	ZnSe/PrF <sub>3</sub> three layer	1.6	
12	ZnSe/PrF <sub>3</sub> three layer	1.6	
13	TiO <sub>2</sub> /SiO <sub>2</sub> two layer	1.4	(1.00)
14	TiO <sub>2</sub> /SiO <sub>2</sub> two layer	6.1	(0.08)
15	Al <sub>2</sub> O <sub>3</sub> /SiO <sub>2</sub> two layer	16.5	(0.14)
16	MgF <sub>2</sub> single layer; IPC + IAD	18.8	(0.38)
17	MgF <sub>2</sub> single layer; 300° C	18.8	(0.00)
18	Al <sub>2</sub> O <sub>3</sub> /MgF <sub>2</sub> two layer; IPC+IAD	18.8	(0.50)
19	Al <sub>2</sub> O <sub>3</sub> /MgF <sub>2</sub> two layer	14.5	(0.50)

a: in units of Joules/cm<sup>2</sup>, values in parenthesis are the spread in threshold

b: this sample damaged at this low level due to an exit face damage mechanism caused by an HR coating on the sample's backside.

Note: All coatings in the above table were deposited at 200° C unless otherwise noted

IPC stands for Ion PreCleaning

IAD stands for Ion Assisted Deposition

Table 5.  
Damage Thresholds of AR Coatings Tested at 59° Incidence

Sample #	Coating Description	Damage Threshold	
		S-pol	P-pol
1	Nb <sub>2</sub> O <sub>5</sub> /SiO <sub>2</sub> two layer	4.8	4.5
2	SiO <sub>2</sub> /Al <sub>2</sub> O <sub>3</sub> three layer	-	11.0
3	TiO <sub>2</sub> /SiO <sub>2</sub> multi-layer	3.5	6.8
4	TiO <sub>2</sub> /SiO <sub>2</sub> multi-layer	4.4	5.0
5	TiO <sub>2</sub> /SiO <sub>2</sub> multi-layer	6.5	5.9
6	SiO <sub>2</sub> /Al <sub>2</sub> O <sub>3</sub> three layer	17.0	13.0
7	SiO <sub>2</sub> /Al <sub>2</sub> O <sub>3</sub> three layer	12.0	11.0
8	TiO <sub>2</sub> /SiO <sub>2</sub> two layer	4.3	3.4
9	TiO <sub>2</sub> /SiO <sub>2</sub> two layer	4.0	2.5
10	SiO <sub>2</sub> /Al <sub>2</sub> O <sub>3</sub> three layer	15.0	12.0
11	SiO <sub>2</sub> /Al <sub>2</sub> O <sub>3</sub> three layer; IPC & IAD	57.0	50.0
12	Al <sub>2</sub> O <sub>3</sub> /MgF <sub>2</sub> /ZnSe multi-layer	3.8	3.1
13	Al <sub>2</sub> O <sub>3</sub> /MgF <sub>2</sub> /ZnSe multi-layer	3.1	3.5
14	SiO <sub>2</sub> /Al <sub>2</sub> O <sub>3</sub> three layer; IPC & IAD	8.5	13.5
15	SiO <sub>2</sub> /Al <sub>2</sub> O <sub>3</sub> three layer	18.0	19.1
16	SiO <sub>2</sub> /Al <sub>2</sub> O <sub>3</sub> three layer; IPC & IAD	16.9	29.3
17	SiO <sub>2</sub> /Al <sub>2</sub> O <sub>3</sub> three layer; IPC & IAD	11.3	11.8

Notes from Table 4 apply

In addition to the above expectation that the coatings would lower the surface damage threshold, and prior to any measurements, the expected threshold for uncoated and polished YAG was in the 20-30 J/cm<sup>2</sup> range. Had we not damaged any uncoated and polished YAG, then the combination of these expectations could have led to an incorrect conclusion that the coatings were lowering the YAG damage threshold. But the figure 2 comparison shows that it is the substrate polish which is limiting the damage thresholds and not the coatings. There is presently a plan to investigate ways to improve the polish quality on the YAG. It would be interesting to see the effects of the coatings on the surface damage threshold if the uncoated surfaces were stronger, say in the 30-

50 J/cm<sup>2</sup> range. It is felt that the uncoated surfaces tested in this study are probably indicative of what is readily available without developing special or exotic YAG polishing processes.

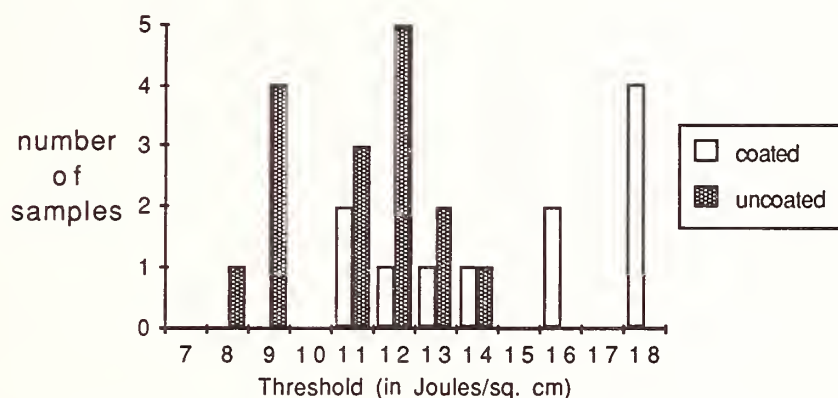


Figure 2. Coated vs. Uncoated Damage Threshold at Normal Incidence

#### 4.2.2 High Index Coating Materials

The link between lower damage threshold and high index coating materials has been observed for single layer coatings [4,5]. The same trend has even been observed with sol-gel coatings, which have demonstrated higher damage thresholds than thermally deposited coatings [6,7]. It was these earlier studies which prompted the elimination of high index materials in some of the AR coating designs tested.

The results in tables 4 and 5 can be divided into two groups, those coating designs which did and those which did not incorporate a high index material such as TiO<sub>2</sub> or ZnSe. Figures 3 and 4 show such a comparison, and clearly coatings without high index materials significantly outperform coatings with these materials. Samples #13 and #14 in table 4 had different physical thickness for the TiO<sub>2</sub> layers, but the same SiO<sub>2</sub> thickness. Sample #13 had a 290 nm thick TiO<sub>2</sub> layer and a threshold of 1.4 J/cm<sup>2</sup>, while #14 had a 40 nm thick TiO<sub>2</sub> layer and a 6.1 J/cm<sup>2</sup> threshold. When the TiO<sub>2</sub> is eliminated entirely, the threshold is typically > 10 J/cm<sup>2</sup>.

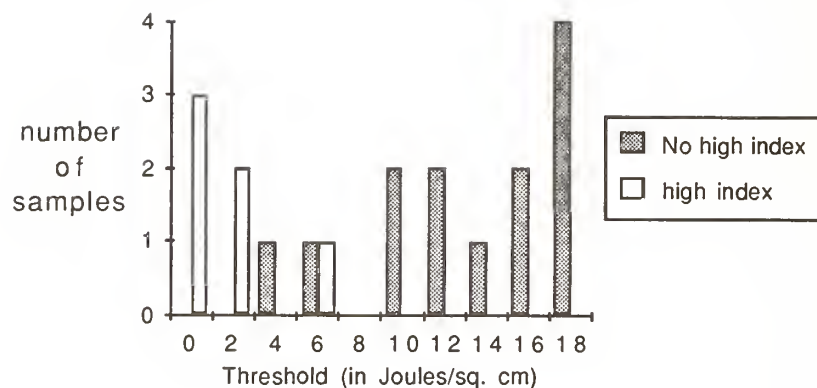


Figure 3.

The Impact of High Index Materials on the Threshold, Normal Incidence

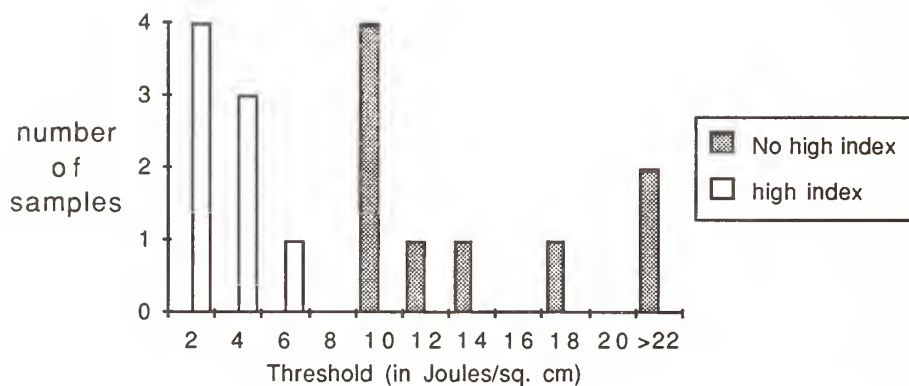


Figure 4.

The Impact of High Index Materials on the Threshold, Non-Normal Incidence

When the effects of high index materials on laser damage first became apparent over the course of testing, the initial suspicion was that the single coating laboratory that had produced the first samples was not depositing the  $\text{TiO}_2$  layers correctly. Subsequent testing on  $\text{TiO}_2$  and  $\text{ZnSe}$  coatings from two other independent coating labs (using the same substrates) led to the same conclusion. The electric field profile in the different coating designs were all checked for any bias against the  $\text{TiO}_2$  coatings. No significant differences were found between the  $\text{TiO}_2$  and



non-TiO<sub>2</sub> coatings. The evidence suggests that TiO<sub>2</sub> should be avoided, where possible, for high power AR coatings on YAG.

#### 4.2.3 Electric Field

The electric field profile throughout the incident media, coating, and substrate media has been examined by several authors for its relationship to laser damage [8,9,10,11,12]. In these references, both good and poor electric field/damage threshold correlations are reported. Several reasons for the poor correlations are discussed. These reasons included the importance of the pulsewidth, the substrate/film interface weakness, and coating defects. The most successful use of the electric field idea seems to be in the improvement of the damage threshold of HR coatings via non-quarterwave layer thicknesses. The aim of this idea is to reduce the electric field in the top few high index layers of the HR stack. This idea is in good agreement with the strong correlation seen in this study between the high index coating materials and poor laser damage.

We examined the electric field profile for all of the samples tested in Tables 3 thru 5 (in more detail the squared electric field, normalized to the incident field squared,  $|E_z|^2/|E_0|^2$ , was examined). To aid the analysis, certain features from the electric field profiles were recorded. These features were the value of the field at the substrate/film interface, the maximum field value from anywhere within the profile, and the maximum field value within any high index layer. For non-normal incidence, p-polarization, the maximum discontinuity in the field was also recorded, in addition to all the aforementioned features. The damage threshold was compared to these different measures of the electric field profile to see if any strong correlations existed. Since the coatings which contained high index materials were known to significantly affect the laser damage results, these samples were excluded from the electric field/damage threshold correlation tests.

The electric field profiles were very similar within the normal incidence coatings and non-normal incidence coatings, respectively. Figure 5 shows two of the above measures of the field profile plotted against the damage threshold. There was no dramatic correlation between any of the measures of the electric field and damage threshold.

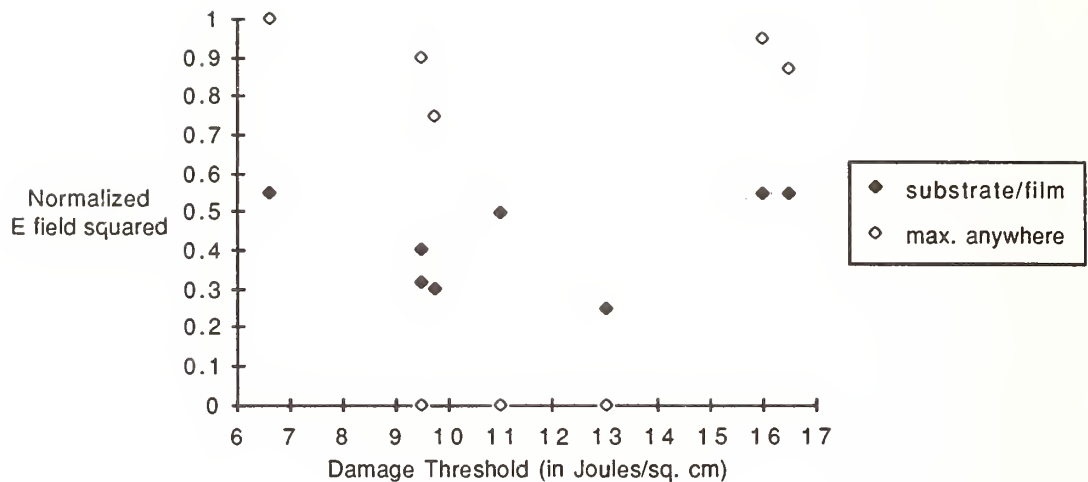


Figure 5. Electric Field/Damage Threshold Correlation

An impediment in looking for electric field/damage threshold correlations is the way in which the damage threshold was measured. The threshold measurement used for this study is determined by the weakest points on the coated surface. These weak points are probably related to imperfections resulting from the polishing and coating processes. To find a better correlation, one might want to hunt for the strongest points on the surface, rather than the weakest points. The threshold of the strongest points can be estimated from the threshold and the spread values in tables 3 and 4. Even using the estimates of the strong point thresholds did not yield a dramatic correlation between the electric field and the damage threshold. While a different damage threshold test methodology may improve the electric field/damage correlation, the present testing procedure gives the type of conservative results that are needed for engineering real systems.

#### 4.2.4 Ion Assisted Deposition

A trend observed in both the table 4 and 5 results, is the threshold improvement for IAD (ion-assisted deposition) processed coatings. Figure 6 shows 2 different examples of a coating design which was made with

and without IAD processing. One of these designs was deposited on samples 3, 4, and 16 in table 4. The IAD coating (sample 16) has a significantly higher threshold than the non-IAD coatings. It is interesting to note that if one compares the IAD coating to the same coating design made at higher substrate temperatures, but without IAD, ( $\geq 300^\circ\text{C}$ , samples 2 and 17 in table 4) then there is no difference in the damage threshold. Samples 9, 18, and 19 from table 4 are the other coating, shown in figure 6. These samples also demonstrate a small, but just significant, improvement for the IAD processed sample.

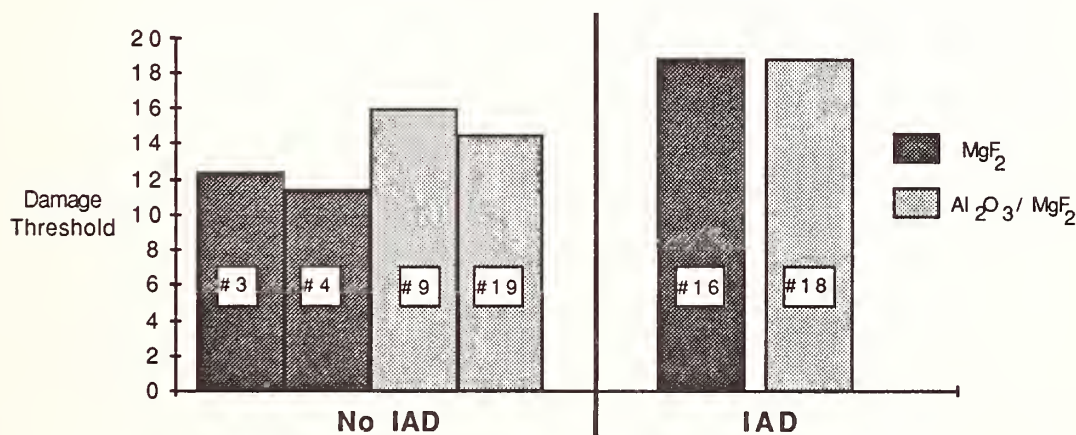


Figure 6.

Damage Threshold of Two Different Normal Incidence Coatings Made With and Without Ion Assisted Deposition

Samples 2, 6, 7, 10, 11, 14, 15, 16, and 17 in table 5 are all the same coating design except that samples 11, 14, 16, and 17 included IAD during the deposition. Figure 7 compares the damage thresholds for these samples. The results show a large range in the threshold performance of the IAD samples, in contrast to the non-IAD samples. The reasons for the large variability in the IAD samples are not presently known.

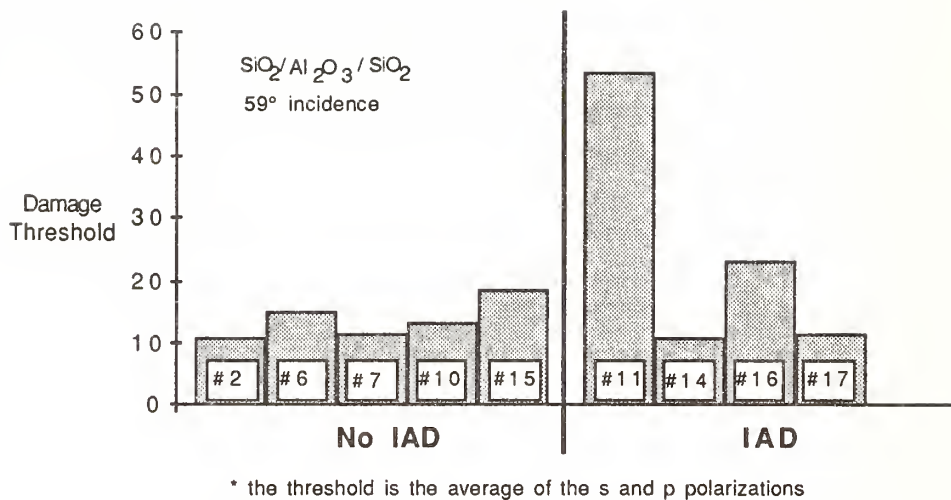


Figure 7.

Damage Threshold\* of a Single Non-Normal Incidence Coating Made With and Without Ion Assisted Deposition

There is not enough data to make any sweeping conclusions on the effects of IAD processing on laser damage. The few samples that we've tested show that the IAD processing isn't significantly degrading the damage threshold, and can potentially improve the threshold significantly. Since the IAD process has other definite benefits such as, increased coating adhesion, and environmental stability, to recommend it, the above "no-harm" conclusion is of interest.

#### 4.3 TIR Prisms

In addition to the standard types of sample geometries and coatings described in the preceding sections; 4 YAG prisms were fabricated to damage test TIR surfaces. Figure 8 depicts one of these samples. For each prism there were three different coatings placed on equal sections of one long face. The other two faces were left uncoated.



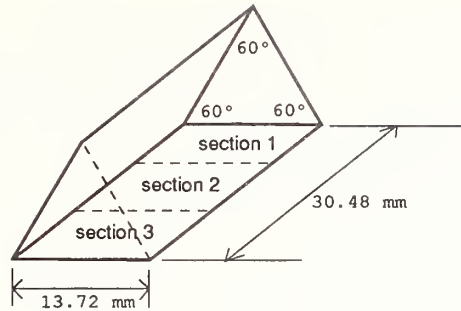


Figure 8. Prism Sample

The irradiation geometry for the prism TIR face measurements is shown in figure 9. The pulsed Nd:YAG damaging beam, incident from the left of figure 9 was focused with a lens into the prism, and onto the TIR face at  $\sim 60^\circ$  incidence. A sharply converging beam was required to suppress premature failure of the entrance face. The spot size at the waist was  $\sim 0.15$  mm (FW at  $1/e^2$ ). In placing the focal waist at the TIR face, the index of refraction of YAG was accounted for. If the entrance face damaged prior to the TIR surface, the data from this site was discarded and the sample was repositioned to a new site.

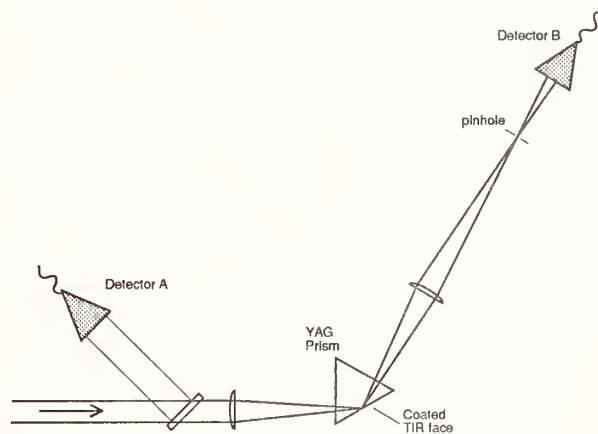


Figure 9. TIR Damage Setup

To assure that the irradiated area at the TIR face was not altered by nonlinear effects such as self focusing, the focal waist was reimaged

with a second lens onto an aperture and detector. The aperture was sized for 90% transmittance. A second detector was used to monitor the incident beam. The incident intensity was increased in small steps from a very low value up to physical damage. At each step the incident and transmitted signals were recorded.

In the absence of nonlinear effects the transmitted signal will be proportional to the incident signal. If aberrations are induced at the waist in the material (e.g. by self-focusing), the reimaging path will be altered, and the transmittance through the aperture will decrease sharply. In these experiments, the transmitted signal was proportional to the incident signal over the entire intensity range up to physical damage of the TIR face, as shown in figure 10. This indicates that self-focusing did not occur in these experiments.

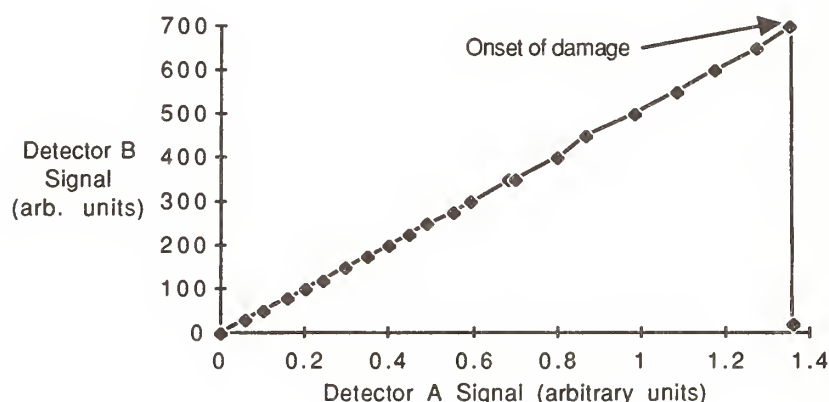


Figure 10. Test for Self-focusing with the TIR Damage Configuration

The damage threshold results for the TIR prism faces are contained in table 6. Table 6 shows that the damage threshold for most of the coatings is in the 7-10 J/cm<sup>2</sup> range. It is interesting to note that the only coating in table 6 that contained any "high" index materials was that of segment C3. This sample was the worst performing coating of all the samples in table 6, staying consistent with the previous observations regarding the effects of high index materials. But unlike the previous

non-TIR cases, the C3 coating has a significant electric field enhancement which may also have contributed to its low threshold.

Table 6. Sample Description and Results for the Prism Samples

ID	1	2	3
A	uncoated p-pol <b>7.5</b> s-pol <b>4.9</b>	uncoated* * p-pol <b>7.5</b> s-pol <b>6.5</b>	uncoated <b>13.2</b>
B	0.9 Al <sub>2</sub> O <sub>3</sub> / 2.0 SiO <sub>2</sub> p-pol <b>1.8</b> s-pol <b>1.6</b>	2.0 SiO <sub>2</sub> * p-pol <b>8.5</b> s-pol <b>9.1</b>	2.0 SiO <sub>2</sub> * p-pol <b>8.5</b> s-pol <b>9.1</b>
C	MgF <sub>2</sub> 808 nm AR p-pol <b>7.3</b> s-pol <b>7.8</b>	2.0 SiO <sub>2</sub> * p-pol <b>9.1</b> s-pol <b>8.0</b>	21 layer 808 nm HR TiO <sub>2</sub> / SiO <sub>2</sub> p-pol <b>0.4</b> s-pol <b>1.3</b>
D	MgF <sub>2</sub> / SiO <sub>2</sub> / MgF <sub>2</sub> / Al <sub>2</sub> O <sub>3</sub> p-pol <b>8.0</b> s-pol <b>7.5</b>	MgF <sub>2</sub> 808 nm AR p-pol <b>10.7</b> s-pol <b>6.9</b>	0.05 Al <sub>2</sub> O <sub>3</sub> / 2.0 SiO <sub>2</sub> * p-pol <b>9.6</b> s-pol <b>8.0</b>

Note: All values in bold lettering are in units of Joules/sq. cm

Note: All samples tested at 60 degrees incidence, except A3 which was tested at normal incidence, circular polarization.

Note: Numbers in front of chemical formulas are physical thickness in microns.

\* Ion PreCleaning (IPC) and Ion Assited Deposition (IAD) used

\* \* Ion PreCleaning used

The electric field profile was the motivation behind some of the different coatings in table 6. The examination of the electric field data is facilitated by capsulizing the data, as in table 7. There is no overwhelming quantitative or qualitative correlation between the electric fields in table 7 and the resulting damage threshold. For example; the two prism segments that had the worst damage performance, B1 and C3, do have the highest fields in either the peak or difference categories. But if one examines the magnitude of the ratio of the B1 or C3 fields compared to some of the other segments, there is not good quantitative agreement. An analysis of just the field data would indicate that the uncoated prisms, A1 and A2, should have had some of the best threshold results, yet the experimental results show they did not.

Table 7. Electric Field Profile and Damage Threshold Data

		Prism Segements						
							60°	73°
		C1,D2	A1,A2	D3	C3	B1	C2,B2,B3	B3
S-pol								
	damage thresh.	7.5	6.0	8.5	1.3	1.6	8.0	19.0
	interface <sup>1</sup>	2.2	1.4	3.2	1.2	0.0	2.8	1.1
	peak coating <sup>2</sup>	2.2	1.4	3.2	3.0	16.0	2.8	1.1
P-pol	damage thresh.	8.0	7.5	8.5	0.4	1.8	9.1	20.5
	interface <sup>1</sup>	3.0	2.6	3.2	2.2	1.0	4.2	1.1
	peak coating <sup>2</sup>	3.0	2.6	3.6	6.0	12.0	4.2	1.1
	peak diff. <sup>3</sup>	1.5	1.4	1.0	4.5	1.0	2.2	0.5

All damage thresholds in Joules/sq. cm.

- 1 Max. field value at YAG/coating interface.
- 2 The peak value of the field anywhere within the coating
- 3 The peak discontinuity anywhere within the coating.

The B3 prism segment was tested at two different angles of incidence on the TIR face as shown by the two entries in table 7. This was done to specifically test the effect the electric field would have on the damage threshold. The peak field data in table 7 indicates that the 73° test should have had ~ 3 times the threshold compared to the 60° test. In fact the ratio of the 73° to 60° thresholds is ~ 2.2-2.4. But one must also consider that the threshold values are reported in a plane perpendicular to the test beam axis. The actual fluence on a tilted surface is the reported threshold multiplied by the cosine of the angle of incidence. Thus there should be a difference in the 73° and 60° thresholds which is the ratio of the cosine of the two angles. This cosine ratio equals 1.71. Most of the observed threshold ratio of 2.2-2.4 is therefore accounted for by the cosine ratio. The extra difference that the field analysis predicts is not observed.

The TIR data supports each of the observations made with respect to the normal and non-normal incidence coatings in the preceding sections. The coated segments slightly outperformed the uncoated ones; the one segment with a high index material in the coating was the worst performer; there was little correlation between the electric field profile



and damage threshold; and the IAD processing doesn't appear to have significantly degraded the damage threshold.

## 5.0 Summary

Uncoated polished YAG surfaces have damage thresholds in the 9 -14 J/cm<sup>2</sup> range. The ultimate potential for YAG surfaces is indicated by clean sites on fractured surfaces which damaged in the 100 - 110 J/cm<sup>2</sup> range. Normal incidence AR coatings on YAG damaged in the 12-18 J/cm<sup>2</sup> range, if they avoided the use of high index materials such as TiO<sub>2</sub> and ZnSe. The non-normal incidence AR coatings, that excluded high index materials, also damaged in the 12-18 J/cm<sup>2</sup> range for both polarizations. The TIR surfaces had the following damage thresholds: 4-9 J/cm<sup>2</sup> uncoated, 7-10 J/cm<sup>2</sup> coated.

---

I wish to acknowledge and thank the following persons and groups: Alan Boxell, who fabricated most of the coatings; Art Braundmeier (of Southern Illinois University, at Edwardsville) who designed and fabricated some of the coatings; Steve Chelli and his coating group, who also designed and fabricated some of the coatings; Gordon Burkhart and the polishing group, who fabricated some of the substrates; and finally Carolyn Krebs and George Dube' for supporting this entire effort.

## References

- [1] Seitel, S. C. *Laser Damage Test Handbook and Database of Nd:YAG Laser Optics*, Montana Laser Optics, Inc., Bozeman (1988), custom report.
- [2] Lowdermilk, W.H.; Milam, D.; Rainer, F. "Damage to Coatings and Surfaces by 1.06  $\mu$ m Pulses", Natl. Bur. Stand. U.S. Spec. Publ. **568**, 391 (1981).
- [3] Seitel, S. C. *Laser Damage Test Handbook and Database of Nd:YAG Laser Optics*, Montana Laser Optics, Inc., Bozeman (1988), Tables C.14, C.15.

- [4] Bettis, J.R.; House, R.A.; Guenther, A.H. "The Importance of Refractive Index, Number Density, and Surface Roughness in the Laser-Induced Damage of Thin Films and Bare Surfaces", Natl. Bur. Stand. U.S. Spec. Publ. **435**, 289 (1975).
- [5] Turner, A.F. "Ruby Laser Damage Thresholds in Evaporated Thin Films and Multilayer Coatings", Natl. Bur. Stand. U.S. Spec. Publ. **356**, 119 (1971).
- [6] Thomas, I.; Wilder, J.; Gonzales, R.; George, D. "1064 nm and 350 nm Laser Damage Thresholds of High-Index Oxide Films Deposited from Organic Solutions and Sols", in *Proceedings, Eighteenth Annual Symposium on Optical Materials for High Power Lasers*, Boulder Colo., Nov. 1986, in process.
- [7] Thomas, I.; Wilder, J. " $\text{Al}_2\text{O}_3$ - $\text{SiO}_2$  HR Coatings Prepared from Colloidal Suspensions", in *Proceedings, Nineteenth Annual Symposium on Optical Materials for High Power Lasers*, Boulder Colo., Nov. 1987, in process.
- [8] Apfel, J.H. "Further Studies of the Role of Electric Field Strength in Laser Damage of Dielectric Layers", Natl. Bur. Stand. U.S. Spec. Publ. **509**, 251 (1977).
- [9] Apfel, J.H.; Enemark, E.A.; Milam, D.; Smith, W.L.; Weber, M.J. "The Effects of Barrier Layers and Surface Smoothness on 150-ps, 1.064- $\mu\text{m}$  Laser Damage of AR Coatings on Glass", Natl. Bur. Stand. U.S. Spec. Publ. **509**, 255 (1977).
- [10] Deaton, T.F.; Rainer, F.; Milam, D.; Smith, W.L. "Survey of Damage Thresholds at 532 nm for Production-Run Optical Components", Natl. Bur. Stand. U.S. Spec. Publ. **620**, 297 (1983).
- [11] Hart, T.T.; Lichtenstein, T.L.; Carniglia, C.K.; Rainer, F. "Effects of Undercoats and Overcoats on Damage Thresholds of 248 nm Coatings", Natl. Bur. Stand. U.S. Spec. Publ. **638**, 344 (1983).
- [12] Newnam, B.E.; Foltyn, S.R.; Jolin, L.J.; Carniglia, C.K. "Multiple-Shot Ultraviolet Laser Damage Resistance of Nonquarterwave Reflector Designs for 248 nm", Natl. Bur. Stand. U.S. Spec. Publ. **638**, 363 (1983).

MANUSCRIPT NOT RECEIVED

---

DAMAGE MECHANISM ON METAL MIRRORS INDUCED BY CO<sub>2</sub> LASER

K. Yoshida, M. Yamanaka, S. Nakai  
Institute of Laser Engineering, Osaka University  
2-6 Yamadaoka, Suita, Osaka, 565 Japan

Y. Tsunawaki  
Osaka Industrial University  
3 Naka-Caito, Daito, Osaka, 574 Japan

H. Okamoto, K. Motoba, S. Aramaki, and K. Ohta  
Central Research Laboratory, Nippon Mining Co., LTD  
3-17-35 Nizominami, Toda, Saitama, 335 Japan

ABSTRACT

It is very important to identify the mechanism of surface damage in a metal mirror, and consequently to increase the laser damage threshold.

We studied the laser damage mechanism due to impurities and grain boundaries for a molybdenum mirror. Detailed microscopic observations are made of three different damage morphologies for a diamond-turned copper mirror.

MANUSCRIPT NOT RECEIVED

=====

OPTICAL CHARACTERISTICS OF ZnSe COATED COPPER MIRROR  
FOR HIGH POWER CO<sub>2</sub> LASER

K. Yoshida, M. Yamanaka, S. Nakai  
Institute of Laser Engineering, Osaka University  
2-6 Yamadaoka, Suita, Osaka, 565 Japan

Y. Tsunawaki  
Osaka Industrial University  
3 Naka-Gaito, Daito, Osaka 574 Japan

H. Okamoto, K. Motoba, S. Aramaki, and K. Ohta  
Central Research Laboratory, Nippon Mining Co., LTD  
3-17-35 Nizominami, Toda, Saitama, 335 Japan

ABSTRACT

We have developed a ZnSe coated copper (Cu) mirror for high power CO<sub>2</sub> laser. As the Vickers hardness of ZnSe coated Cu mirror is two times harder than a normal Cu mirror, it is rather easy to clean the coated mirror surface without scratching.

For the high-power TEA CO<sub>2</sub> laser, the ZnSe coated Cu mirror has a surface damage threshold two times higher than that of Au-coated Cu mirror.



Parasitic Oscillation Suppression Coatings for Slab Lasers  
and Their Optical Damage

M.A. Acharekar and D.P. McCarthy

Litton Systems, Inc.  
Laser Systems Division  
2787 S. Orange Blossom Trail  
Orlando, FL 32703

D.A. Dobberpuhl and H.W. Willhite

Naval Weapons Center  
China Lake, CA 93555-6001

A general problem in using laser rods of solid state materials is their susceptibility to thermal distortion. With an optically pumped solid state material, heating of the host material occurs concomitant with inversion. The thermal gradients in a solid state laser arise principally from cooling, since heating associated with pumping occurs almost uniformly throughout the laser material volume. Two geometrical shapes found to reduce this thermal problem are the thin rod and thin slab. A thin slab can store more energy than a thin rod. However, the energy storage depletion due to the parasitic oscillations between the two flat and parallel total internal reflection (TIR) surfaces in the slab is a serious problem. The paper will present data obtained using Nd:YAG and Nd:Cr:GSGG slab lasers with the dielectric coating developed to suppress the parasitic oscillation between the TIR surfaces. The coated slab is immersed in the cooling fluid in the slab laser pump cavity. Therefore, the optical damage threshold data for the parasitic oscillation suppression coatings immersed in cooling fluid will be presented.

Key Words: Nd:YAG, Nd:Cr:GSGG, Slab Laser, Parasitic Oscillation,  $\text{Al}_2\text{O}_3$  Coating, TIR Surface Coating,  $\text{Al}_2\text{O}_3$  Coating Durability.

## 1. Introduction

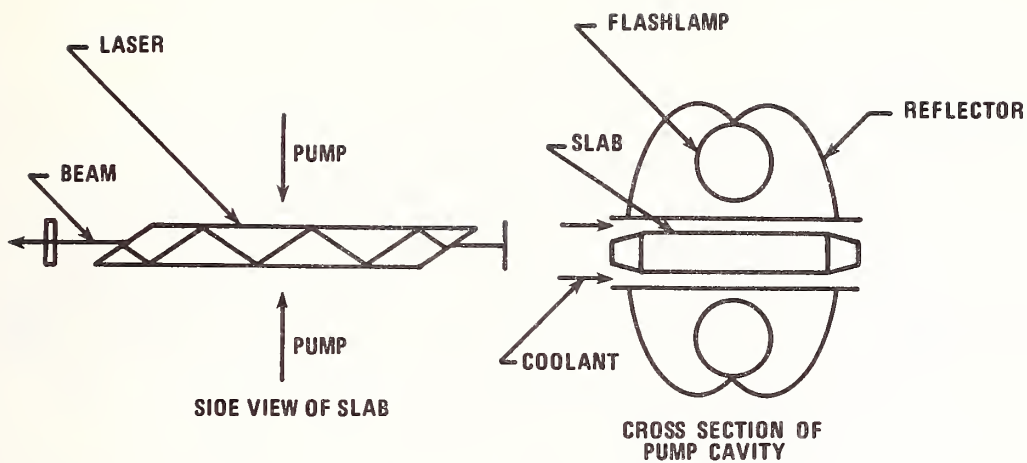
The concept of improving efficiency by co-doping a neodymium ( $\text{Nd}^{3+}$ ) laser crystal with chromium ( $\text{Cr}^{3+}$ ) ions and transferring excitation absorbed by broad  $\text{Cr}^{3+}$  absorption bands over to  $\text{Nd}^{3+}$  ions is nearly as old as the  $\text{Nd}^{3+}$  laser itself [1]. No dramatic efficiency improvement was achieved with the host yttrium aluminum garnet (YAG) crystal,

because all  $\text{Cr}^{3+}$  excitation was deposited in  ${}^2\text{E}$  level, and spin-forbidden nature of the  ${}^2\text{E} \rightarrow {}^4\text{A}_2$  transition resulted in an inefficient transfer process. However, a high transfer efficiency was demonstrated in the co-doped gadolinium scandium gallium garnet (GSGG) [2] and yttrium scandium gallium garnet (YSGG) [3]. It was reported in ref. 3 that an absolute efficiency of 3.6 percent was achieved for Nd:Cr:YSGG as compared to 2 percent efficiency observed for the Nd:Cr:GSGG crystal. Generally, the efficiency of Nd:YAG and other solid state lasers emitting single pulses does not exceed 1 percent. This efficiency data reported was for the laser crystals of cylindrical geometry; laser rods typically 5 to 7 mm in diameter and 50 to 100 mm long were used in these experiments.

A series of measurements [4] performed at Litton Laser Systems (LLS) indicated that co-doped GSGG laser rods under flashlamp pumped conditions provide efficiency approximately two times higher than the more common host, Nd:YAG. However, the data collected show that the Nd:Cr:GSGG laser rods provided higher output power at the cost of higher beam divergence when compared with Nd:YAG laser rods in the same experimental set-up. This indicates that the absorption of energy in chromium in Nd:Cr:GSGG material results in an increase in thermal distortion.

A general problem in using laser rods of solid state materials is their susceptibility to thermal distortion. With an optically pumped solid state material, heating of the host material occurs concomitant with inversion. The thermal gradients in a solid state laser arise principally from cooling, since the heating associated with pumping occurs almost uniformly throughout the laser material volume. Cooling is achieved by conduction from the material bulk to a surface. Clearly, the shorter the conducting path length from the material bulk to the cooled surface, the smaller the temperature gradient and the better the control of temperatures in the material bulk by surface cooling. Two geometrical shapes that satisfy the cooling requirement are the thin rod and thin slab. The thin rod geometry develops radial thermal gradients with surface cooling that are perpendicular to the beam direction. In addition, the variation of refractive index with temperature causes thermal lensing through the rod, and the thermal stress, which arises from the temperature gradient, causes birefringence and other distortion. The limitations of the rod geometry have led to the development of the slab geometry configurations [5] (see fig. 1) in which the effect of thermal distortion is compensated by the symmetry of thermal gradients in the laser beam path.

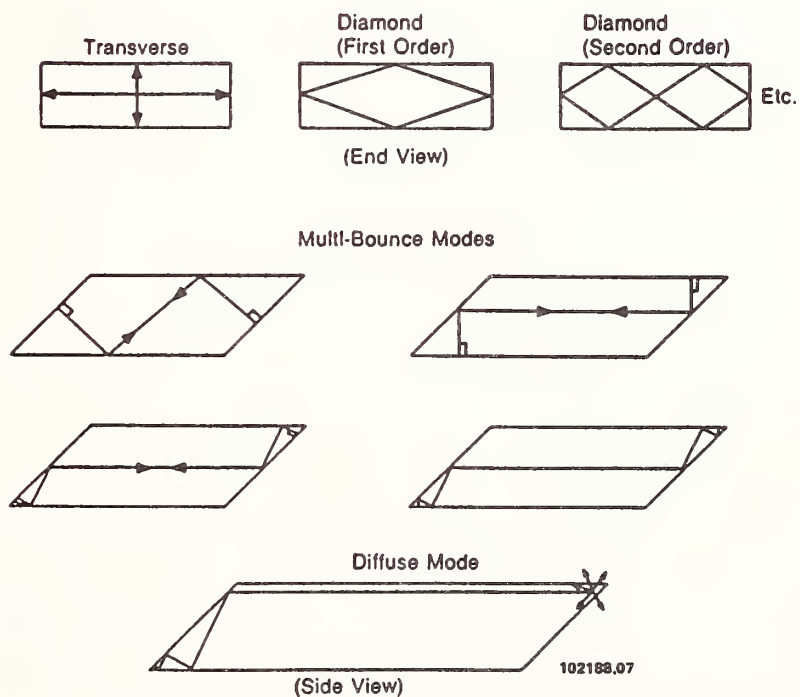
However, the energy storage depletion due to the parasitic oscillations between the two flat and parallel total internal reflection (TIR) surfaces [6] as illustrated in figure 2 is a serious problem. Secondly, the thermal conductivity of Nd:Cr:GSGG is slightly lower than Nd:YAG, resulting in material fracture when operated at high repetition rate without adequate coolant flow. In order to resolve these problems a pump cavity was designed. The slab laser pump cavity design features are provided in section 2 of this paper. The performance characteristics obtained using the pump cavity are given in section 3 of this paper. The damage of the coating used for the parasitic oscillations suppression is discussed in section 4. It may be noted that we reported the damage threshold measurements for bulk [7] and surface [8] damage for Nd:Cr:GSGG material at a



\* Ref. : W.S. Martin and J.P. Chemoch, Patent No. 3, 633, 126 (Jan 1972).

P9258

Figure 1. Schematic of a Slab Geometry\*



\* Ref. : D.C. Brown and K.K. Lee, CLEO's 1985 paper WM-37 (June 1985).

Figure 2. Parasitic Oscillations in Slab Lasers\*

previous Boulder Damage Symposium. The damage observed in the parasitic oscillation suppression coating is different in its characteristics; hence, a brief discussion of this coating is provided in section 5 of this paper.

## 2. Slab Laser Design

The implementation of slab geometry was first demonstrated at General Electric (see ref. 5), termed the total internal reflection, faced pumped laser or TIR-FPL. This somewhat cumbersome appellation describes two of the features of this slab geometry that are of basic importance in its functioning. Total internal reflection is an efficient means of guiding a laser beam through a slab in a zig-zag path that can be as long as needed for the required gain. The face pumping makes possible the uniform pumping required to avoid thermal distortion over the slab width. Not suggested in the appellation, however, is the requirement for uniform cooling through the slab faces to avoid transverse thermal gradients. Thus, the cooling temperature gradient is perpendicular to the faces and symmetrical with respect to the center plane of the slab. Compensation for distortion occurs for each traverse of a beam between the TIR surfaces, just as in the case of the single pass through a disc. Therefore, in the p-plane, compensation depends on the symmetry of the thermal gradients and thermal stress. In the s-plane there is no compensation, and the thermal gradient in this plane (and perpendicular to a ray) must be zero. The fact that the beam profiles overlap on reflection does not affect the compensation. However, thermal strains that distort the slab surface from planar have a detrimental effect, and the TIR arrangement is more sensitive to these strain effects than the single pass disc amplifier.

Therefore, during the slab design undertaken at LLS, emphasis was given to the slab cooling technique. With a uniformly pumped and cooled slab, strain effects are significant only near lateral edges of the slab, where thermal stress relief causes some surface distortion within a distance from the edges of approximately one half the slab thickness. For this reason, the full width of a slab is usually not pumped. However, with a properly cooled and pumped slab (not uniformly, but pumped and cooled to produce one dimensional thermal gradients) at LLS the entire volume of the slab material was used for lasing resulting in higher efficiency.

The Nd:YAG slab lasers that have been built to date have had a rectangular cross section with a width twice their thickness. This is necessary to avoid distortion near the slab edges that is not cancelled by simply using the slab geometry. It has been shown theoretically that this distortion can be completely eliminated if the laser polarization, the angle of propagation through the slab, and the orientation of the crystal axis are chosen correctly [9]. Initially, to develop and to perfect these techniques in the pump cavity and the resonator cavity, two identical slabs of Nd:YAG and Nd:Cr:GSGG materials were fabricated measuring 3 mm thick by 5 mm wide by 50 mm long. It was proven that the slab using Nd:Cr:GSGG material provided higher efficiency than the slab using Nd:YAG material [10]. The pump cavity design developed for the experiment is shown in figure 3. The pump cavity design included the following features:



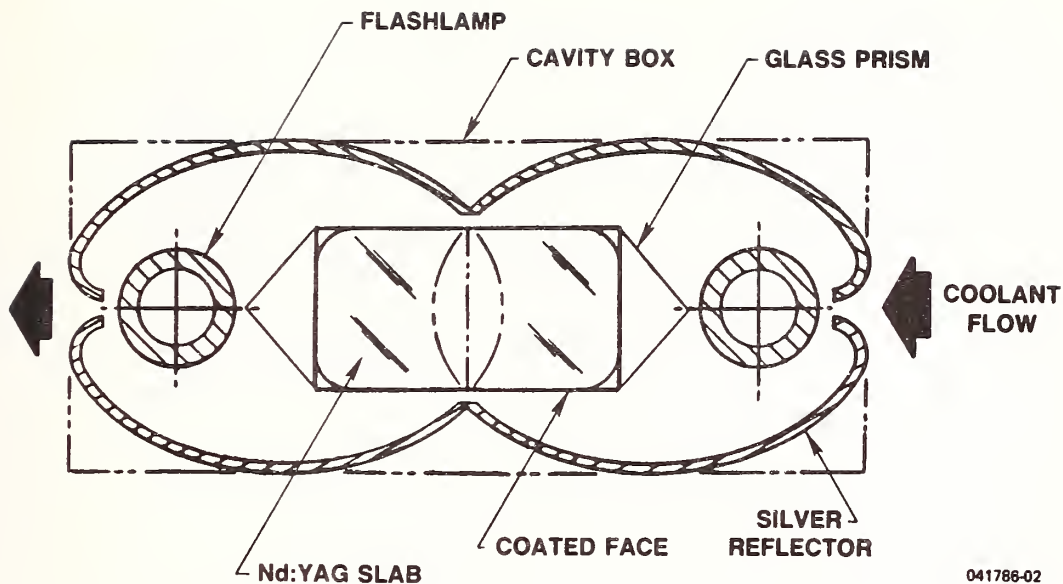


Figure 3. Pump Cavity Design

- o The TIR surfaces of the slab were coated with antireflection coating to suppress the parasitic oscillations.
- o The entire pump cavity was flooded and the direct flow of liquid coolant on the slab was allowed.
- o A clam shell double elliptical pump cavity [11] design was selected for maximum pump efficiency permitting transverse coolant flow.
- o The slab holder was designed (see fig. 4) such that the slab can be rotated inside the pump cavity for either edge or face pumping.
- o The slab holder used only a small portion of the slab for the liquid seals (O-rings), and the slab holder assemblies with either Nd:YAG or Nd:Cr:GSGG material slabs were changed in the pump cavity within minutes.

The performance characteristics were collected using the pump cavity for the slabs of Nd:YAG and Nd:Cr:GSGG materials. Based on these data, a modified pump cavity and resonator was designed using a 5 mm thick by 8 mm wide by 93 mm long slab of Nd:Cr:GSGG material. The improved slab laser utilizing the features noted above is termed the Hybrid Slab Laser (HBSL), and the summary of its performance characteristics is provided in section 3.



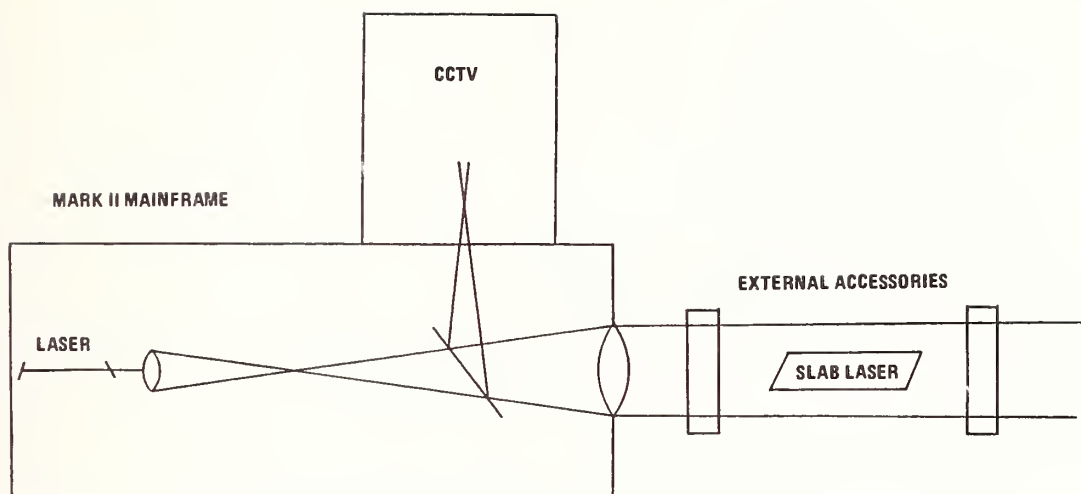
Figure 4. Photograph of the Slab Holder Assembly

### 3. Slab Laser Test Data

#### 3.1 Passive and Active Interferometry

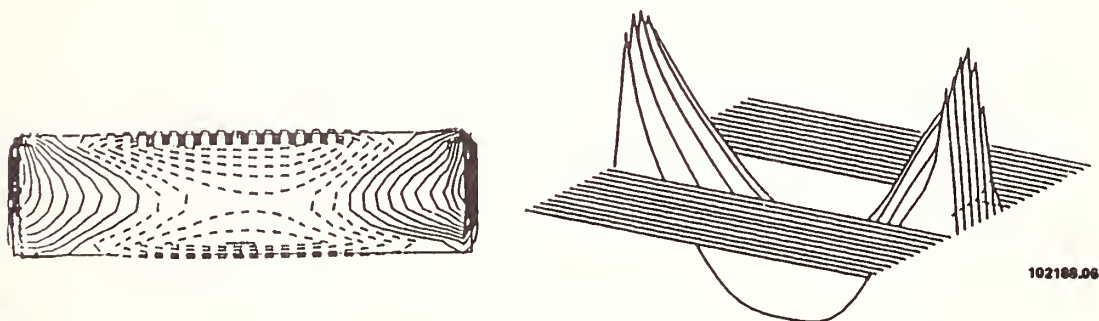
Initially, the performance of the HBSL was obtained using passive and active interferometry to show that with proper pump and cooling of the slab, a one dimensional steady thermal state is obtained. The passive (the slab not pumped or cooled) data was collected using a Zygo Mark II mainframe with a double pass interferometer (see fig. 5). Since the Nd:Cr:GSGG material was high absorption at 6328 nm, the He-Ne laser was replaced with a diode pumped Nd:YAG laser model ALC-104 manufactured by Amoco. The interferogram obtained was analyzed using a Zygo Automatic Pattern Processor (ZAPP). The identical slabs of Nd:YAG and Nd:Cr:GSGG were obtained for these experiments. The data collected for Nd:YAG material are shown in figure 6. This slab crystal quality was poor as compared to the Nd:Cr:GSGG slab.

The active interferometric data were collected using a Jamin interferometer. The experimental set-up used for the measurements is shown in figure 7. Initially, an interferogram for the empty interferometer was obtained (see fig. 8). Then, the slab pump cavity connected to the flashlamp power supply was placed in the interferometer. The slab was pumped for a given input energy at different repetition rates, and for each set, the data were recorded using a VCR and General Electric Model 2505 CID camera. Any frame in



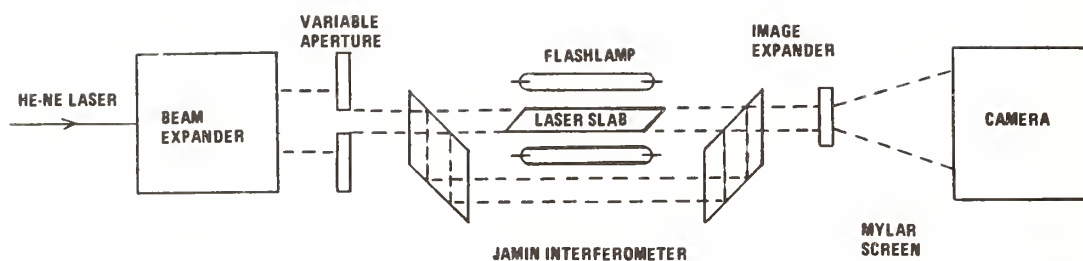
081585-07

Figure 5. Zygo Interferometer (Double Pass Fizeau) for Passive Slab Tests



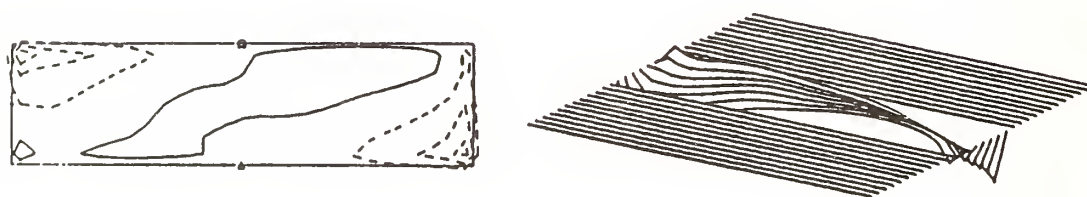
CONTOUR STEP 0.100  
 WAVEFRONT  
 PASSIVE SLAB MINUS EMPTY INTERFEROMETER  
 22-JUL-85 12:46:07 FILE: S002.DAT

Figure 6. Wavefront Distortion in Nd:YAG Slab Using Zygo Interferometer



001545-00

Figure 7. Test Layout for Thermal Gradient Induced Power in Slab Laser



102100.05

CONTOUR STEP 0.100  
 WAVEFRONT  
 EMPTY JAMIN INTERFEROMETER FOR SLAB TEST  
 22-JUL-05 12:28:24 FILE: S001.DAT

Figure 8. Jamin Interferometry



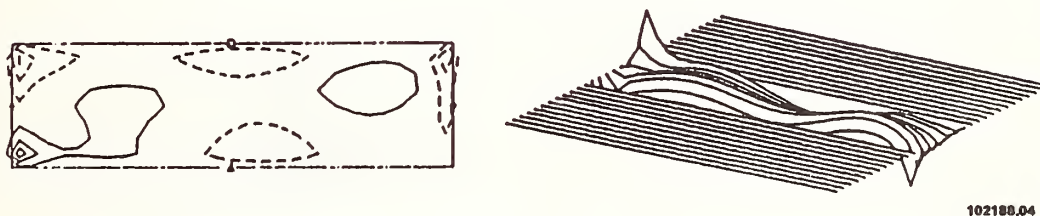
the recorded interferograms can be analyzed using the ZAPP. It may be noted that the baseline data for the empty interferometer is subtracted from the active interferogram. The result obtained for 30 joules per pulse input energy at 10 Hz repetition rate for Nd:YAG slab is shown in figure 9.

It may be noted that the interferometric data were also collected for the Nd:Cr:GSGG slab. The data show that the active interferogram depends basically on the pump cavity design and will change with pump input energy and repetition rate if the quality of crystal is within reasonable limits.

### 3.2 Normal Mode Characteristics

In this test, the 5 mm x 8 mm x 93 mm Nd:Cr:GSGG slab was operated as an oscillator. A resonator was assembled using a 10 meter radius maximum reflectivity mirror at 1.061 micron as one end, and a flat mirror coated with 50 percent reflectivity at 1.061 micron as the output coupler. The resonator mirrors were separated by 25 cm distance and the pump cavity was located approximately in the center.

In table 1, the input-output data for the slab are provided. The output energy was measured using an EG&G model 580 radiometer. As seen in table 1, the threshold input energy for the slab was measured at 1.8 joules and the data were collected at a repetition rate of 10 Hz. The input-output data are also plotted in figure 10. The input-output characteristics obtained for the slab show a net efficiency of 5.85 percent.



CONTOUR STEP 0.250  
WAVEFRONT  
ACTIVE 10PPS SLAB TEST MINUS: EMPTY INTER  
22-JUL-85 16:07:53 FILE: R008.DAT

Figure 9. Wavefront Distortion with 30 J/p at 10 Hz Pump

Table 1. Normal Mode Characteristics

Front Mirror:	50% Refl. at 1.061 micron, Flat.
Back Mirror:	Max. Refl. at 1.061 micron, 10 m Radius of Curvature
Slab:	5 mm x 8 mm x 93 mm Nd:Cr:GSGG
Power Supply:	Analog Module Inc. Model 882.
Pulse Forming Network:	Capacitor = 20 $\mu$ F, Inductor = Series Trigger Transformer.
Repetition Rate:	10 Hz.

INPUT ENERGY PER FLASHLAMP IN J/P	OUTPUT ENERGY IN mJ/P
1.8	THRESHOLD
2.0	48
3.0	185
4.0	310
5.0	450
6.0	600
7.0	730
8.0	880
9.0	995
10.0	1170

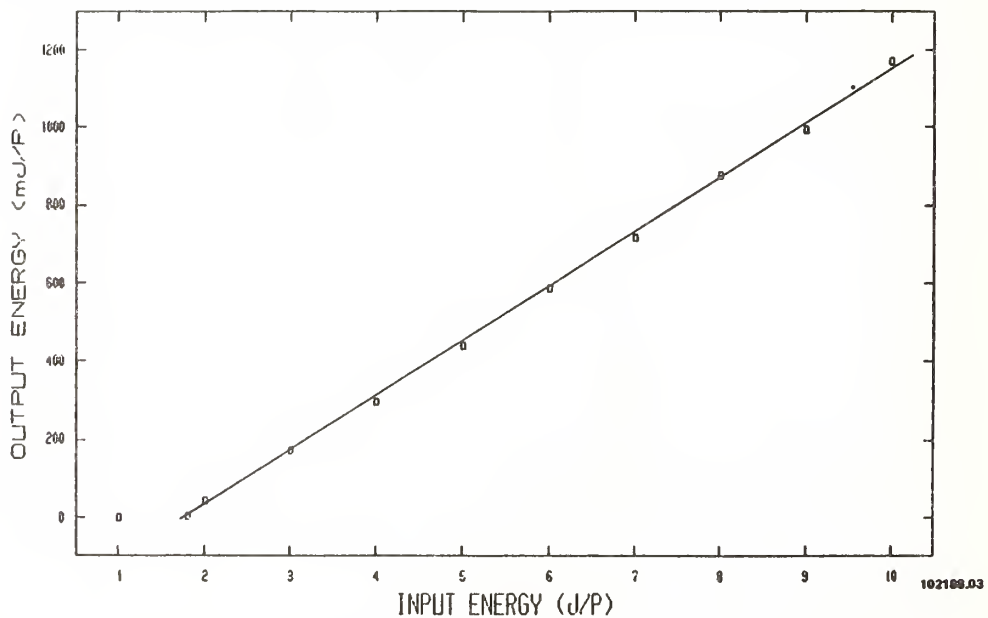


Figure 10. Input vs Output Characteristics for Slab Laser

### 3.3 Q-Switch Operation

The experimental set-up as described in paragraph 3.2 for the normal mode characteristics was used for the Q-switch operation, with the addition of a polarizer and a Pockels cell. Initially, an attempt was made to operate the slab without the polarizer since the slab ends were finished with Brewster's angle. The passive slab provided an extinction ratio of 23.6 dB, but when the slab was pumped at 10 J/p, the extinction ratio was reduced to 12.4 dB. Therefore, it was considered necessary to use the polarizer. The addition of the components in the resonator increased its length to 45 cm from 25 cm used in the normal mode set-up. Also, the output coupler reflectivity was changed to 30 percent from the 50 percent that was utilized in the normal mode experiment.

The data were collected with input energy of 5 J/p per flashlamp (total 10 J/p) for repetition rates from 10 Hz through 50 Hz (see table 2).

Table 2. Q-Switch Operation

Front Mirror:	30% Refl. at 1.061 micron, Flat.
Back Mirror:	Max. Refl. at 1.061 micron, 10 m Radius of Curvature
Polarizer:	Cube Type, 45 degree Coating.
Pockels Cell:	1/4 Wave, Lithium Niobate Crystal.
Slab:	5 mm x 8 mm x 93 mm Nd:Cr:GSGG
Input Energy:	5 J/p Input Energy per Flashlamp.

REPETITION RATE IN Hz	OUTPUT ENERGY PER PULSE IN mJ
10	120
20	130
30	133
40	157
50	142

### 3.4 Beam Characteristics

The beam characteristics were obtained using (i) beam divergence measurements and (ii) beam diagnostics data. For the beam divergence measurement a 1.575 m focal length lens was used. The beam divergence measured using the lens and burned film data is provided in table 3.

The output beam was also characterized using a beam diagnostics code developed by Big Sky Software Corp., Bozeman, Mt. The beam diagnostics code is a software package that incorporates the latest in solid state camera imaging and PC technology to provide a powerful and flexible beam diagnostics tool. The beam diagnostics software was used with a EG&G Reticon 9000 series camera and poynting products frame grabber which provides a 256 x 256 x 8 bit image of the laser beam. A Hewlett Packard series 200 scientific computer was used for data processing.

Table 3. Beam Divergence Data

Lens Focal Length:	1.575 m Focal Length.
Laser Resonator:	Front Mirror 30% Refl. at 1.061 $\mu$ , Flat. Back Mirror Max. Refl. at 1.061 $\mu$ , 10 m Radius of Curvature. Resonator Length = 45 cm.
Polarizer:	Cube Type, 45 degree Coating.
Pockels Cell:	1/4 Wave, Lithium Niobate.
Slab:	5 mm x 8 mm x 93 mm, Nd:Cr:GSGG
Input Energy:	5 J/p Input Energy per Flashlamp.

REPETITION RATE IN Hz	DIVERGENCE IN mR	
	X-AXIS	Y-AXIS
10	2.88	4.68
20	2.43	6.12
30	2.10	7.29
40	1.89	8.00
50	1.75	



The Q-switched Nd:Cr:GSGG slab material beam characteristics data were collected using the beam diagnostics code for repetition rates of 10 Hz through 50 Hz. The code provides beam divergence data for circular beams; however, for the rectangular beams software modification is required. It was not possible to modify the software at LLS due to the proprietary nature of the software.

Figure 11 shows the output of the beam diagnostics code for 10 Hz and 40 Hz repetition rate. The printout marked slab10 and slab40 are for 10 and 40 Hz repetition rates, respectively. The data obtained with the focusing lens for the divergence measurements do not appear to correlate with the beam diagnostics code. The divergence data show an increase in beam divergence with repetition rate in the non-compensated axis (Y-axis), while the beam diagnostics code does not appear to show significant increase in the divergence. A possible reason for this discrepancy may be that the faster movement of the film required at higher repetition rates stretches the burn pattern.

#### 4. Damage of the Coating for Parasitic Oscillation Suppression

The TIR surfaces of the slab were coated with an antireflection dielectric coating to suppress the parasitic oscillations. In figure 12, a sketch of the coating is shown. A single layer of aluminum oxide was coated using an E-beam process. The thickness required for the quarter wave coating was obtained using the relation [11] given below:

$$N_i t_i = \lambda/4 \quad (1)$$

It may be noted that  $N_1$  can also be fine-tuned by the percentage of glycol in water. However, a 50/50 ratio of glycol and water was selected as the coolant for the slab because of its desirable thermal properties.

The reflectivity of this thin film is calculated using relation:

$$R = \frac{r_1^2 + r_2^2 + 2 r_1 r_2 \cos X}{1 + r_1^2 r_2^2 + 2 r_1 r_2 \cos X} \quad (2)$$

$$\text{where } \cos X = \frac{4 \pi N_1 t_i \cos I_1}{\lambda} \quad (3)$$

$$\text{and } r_1 = \frac{\frac{-\sin(I_0 - I_1)}{\sin(I_0 + I_1)} + \frac{\tan(I_0 - I_1)}{\tan(I_1 + I_1)}}{2} \quad (4)$$

```

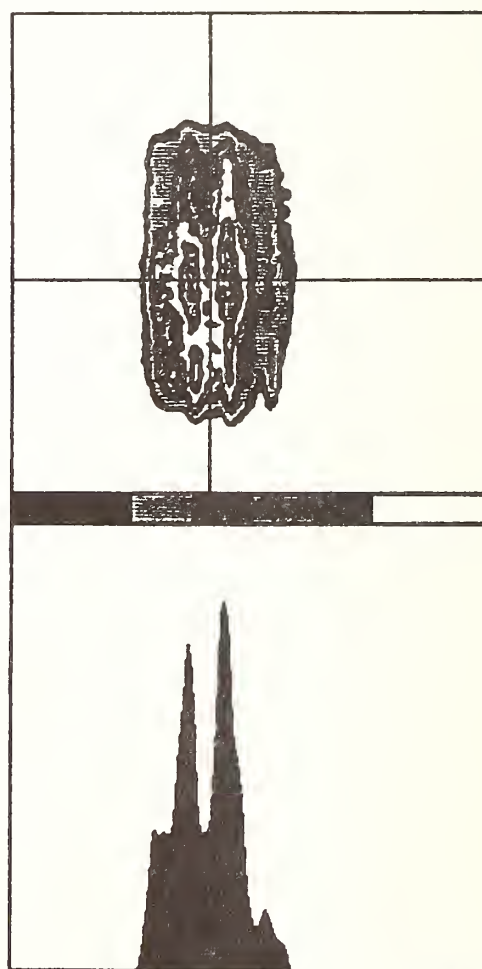
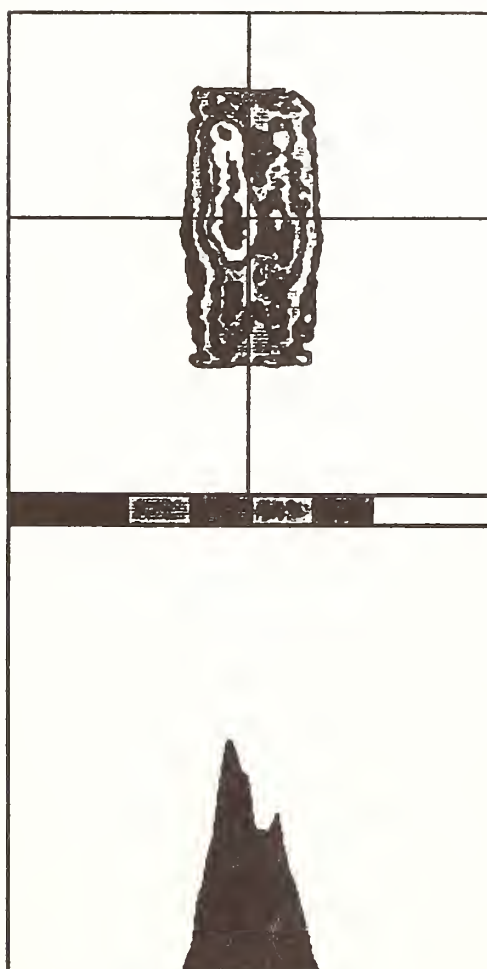
*****
DATE: Dec 31 00:54:40
*****
INPUT FILE: slab10
*****
GEOMETRIC CENTROID      = 127, 113
ENERGY CENTROID         = 126, 109
CENTROID DELTA          = 4.16
PIXEL THRESHOLD VALUE   = 20
PEAK PIXEL VALUE        = 156
AVERAGE PIXEL VALUE     = 68
RMS PIXEL VALUE         = 75
PEAK/AVERAGE RATIO     = 2.29
PEAK/RMS RATIO          = 2.08
PEAK/VALLEY RATIO       = 7.80
*****

```

```

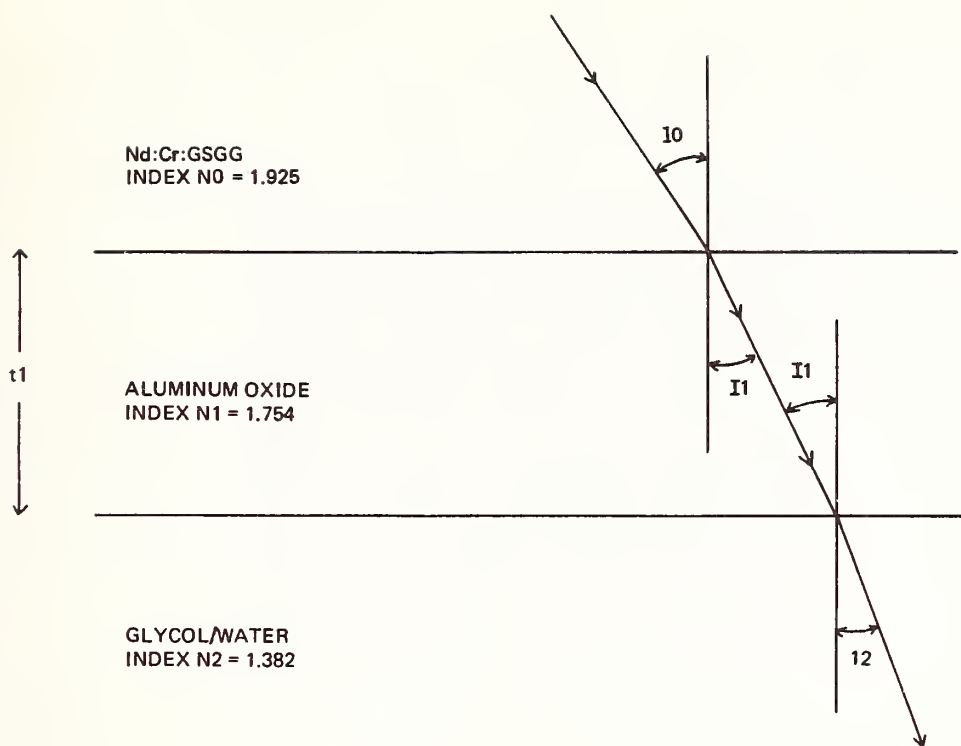
*****
DATE: Dec 31 01:25:20
*****
INPUT FILE: slab40b
*****
GEOMETRIC CENTROID      = 107, 137
ENERGY CENTROID         = 105, 142
CENTROID DELTA          = 4.88
PIXEL THRESHOLD VALUE   = 20
PEAK PIXEL VALUE        = 229
AVERAGE PIXEL VALUE     = 80
RMS PIXEL VALUE         = 91
PEAK/AVERAGE RATIO     = 2.86
PEAK/RMS RATIO          = 2.52
PEAK/VALLEY RATIO       = 11.45
*****

```



102188.02

Figure 11. Beam Quality Data for 10 Hz and 40 Hz Repetition Rate



100788.04

Figure 12. Parasitic Oscillation Suppression Coating

r2 can also be expressed as:

$$r2 = \frac{\frac{-\sin(\theta_1 - \theta_2)}{\sin(\theta_1 + \theta_2)} + \frac{\tan(\theta_1 - \theta_2)}{\tan(\theta_1 + \theta_2)}}{2} \quad (5)$$

The calculations performed show that at a 1.061 micron wavelength the coating provides excellent results. The high laser efficiency also indicates that the stored energy is not depleted due to the parasitic oscillations.

The coatings used on the first few slabs made of Nd:YAG and Nd:Cr:GSGG materials were damaged during Q-switch operation at high repetition rates (typically >50 Hz). Two types of damage were observed for the coatings. The first type can be classified as non-optical damage. The coating on the TIR surfaces of the slab, when immersed in hot glycol/water laser coolant, peeled off (fig. 13). The damage experiments were performed by preparing samples of Nd:YAG and Nd:Cr:GSGG material substrates and coating them with various materials to a thickness of a quarter wave. The samples were then immersed in a beaker containing 50/50 glycol and water mixture and boiled. The samples were examined for damage after subjecting them to boiling temperature for a minimum of two hours. The selection of aluminum oxide ( $Al_2O_3$ ) was based on the results of these experiments.



A. 75X Magnification



B. 150X Magnification

Figure 13. Photographs of a Non-Optical Damage Site



The second type of damage observed can be classified as optical damage. However, an attempt to measure the damage threshold for Nd:YAG and Nd:Cr:GSGG samples having the coated surface in contact with the laser coolant was not successful. The coating was specified to meet a general requirement of  $500 \text{ MW/cm}^2$  at 1.06 micron with pulses of 20 ns duration. However, the estimated damage threshold was observed at significantly lower power. In figure 14, photographs of an optical damage site are shown. The damage sites generally appear to be free of craters, and it appears that the coating was simply blown away by the laser pulse.

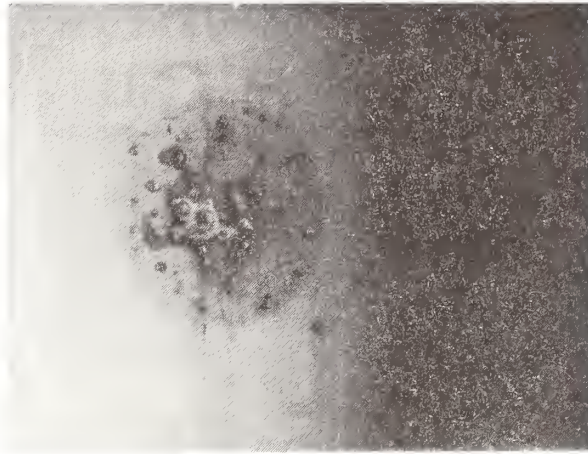
In absence of hard data for the damage threshold of the coating under its operating conditions, the damage threshold is estimated based on the laser performance. The goal of the 5 mm x 8 mm aperture laser output energy was 300 mJ, in a 20 ns pulse at 100 Hz repetition rate. The damage threshold was estimated at 190 mJ/p output energy.

The damage threshold of the single layer  $\text{Al}_2\text{O}_3$  coating was measured, using the conventional technique for 1.061 micron wavelength radiation, at 20 Hz repetition rate and was found to exceed the specification. The damage threshold measurement for an optically polished surface of Nd:YAG and Nd:Cr:GSGG material was also measured, separately, (see ref. 7) and was not the limiting factor. Thus, it was concluded that the poor damage threshold observed for the coating in its operating environment may be due to surface contaminants on the TIR surface itself. A process to clean slab surfaces before coating deposition was added. The slab coated using this process was tested recently with an output energy of more than 200 mJ/p without damage.

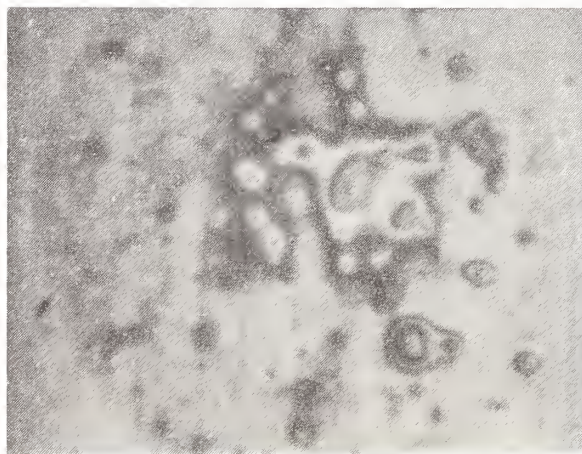
## 5. Conclusions

Based on the data collected for parasitic oscillation suppression coatings on TIR surfaces of a slab laser, the following conclusions can be drawn:

- o A slab with TIR coated surfaces can be immersed in liquid coolant for efficient cooling.
- o A 5 mm x 8 mm x 93 mm size slab of Nd:Cr:GSGG material with the parasitic suppression coating provided 5.85 percent efficiency at a high repetition rate.
- o The passive and active interferometry conducted show the pump cavity design provides a one dimensional thermal gradient in the slab, independent of the laser crystal quality.
- o The beam divergence and beam quality of the slab was measured. The data show that even at 50 Hz repetition rate the beam divergence and quality do not degrade.
- o  $\text{Al}_2\text{O}_3$  single layer coating used for parasitic suppression provides almost negligible reflectivity from the normal incidence angle to grazing incidence angle.
- o Two types of damage in the parasitic suppression coating were observed and classified as i) non-optical and ii) optical.



A. 600X Magnification



B. 1500X Magnification

Figure 14. Photographs of a Optical Damage Site

- o Non-optical damage shows that the coating peels off the surface when the coolant is boiled. This type of damage can be avoided by depositing an aluminum oxide material on the TIR surfaces with an E-beam.
- o Optical type damage of the parasitic suppression coating was not measured but was estimated. It appears that the damage threshold can be increased by processing the surfaces to be coated properly.
- o A test set-up capable of measuring the damage threshold of a sample with the coated surface in contact with the coolant will be required.

## 7. Acknowledgements

This work was conducted under contract No. N60530-86-C-0187 and No. N60530-87-M-0349 from Naval Weapons Center, China Lake, CA. The authors also acknowledge help from Jackie Gibson, Phyllis Heatley, Mark Gall and Lauryn Erndl, in preparation of the manuscript.

## References

- [1] Z.J. Kiss and R.C. Duncan, Phys. Lett. 5, 200 (1964).
- [2] D. Pruss, V.V. Laptev, et.al., Appl. Phys. B28, 355 (1982).
- [3] E.V. Zharikov, G.I. D'yakonov, et.al., Sov. J. Quantum Electron. 18, 43 (1988).
- [4] M.A. Acharekar, "Comparison of Nd:YAG and Nd:Cr:GSGG Slab Lasers," Technical Report, Contract #N60530-86-C-0187 (1986).
- [5] W.S. Martin and J.P. Chemoch, US Patent #3,633,126 (1972).
- [6] D.C. Brown and K.K. Lee, CLEO's 1985 paper WM-37 (1985).
- [7] M.A. Acharekar, D.P. McCarthy, et.al., "Laser Damage in Optical Materials: 1984," NBS Special Publication 727, 39 (1986).
- [8] M.A. Acharekar, "Laser Damage in Optical Materials: 1985," NBS Special Publication 746, 170 (1988).
- [9] R.L. Byer, "High Energy Efficient Solid State Laser," NASA Grant 1-182, G.L. Report #3634 (1983).
- [10] M.A. Acharekar, "Comparison of Face and Edge Pumped Slab Laser," Technical Report Contract #N60530-86-C-9187 (1986).
- [11] A. Vasicek, "Optics of Thin Film," North-Holland Publication Co., (1959).

MANUSCRIPT NOT RECEIVED

=====

ABSORPTION AND DAMAGE THRESHOLD OF DIELECTRIC  
REFLECTORS AT 193 nm

T. Izawa, Y. Ishiwata, I. Hashimoto, and H. Shikakura  
Showa Optical Co., Ltd.  
804 Hakusancho, Midori-ku, Yokohama, Kanagawa, 226 Japan

Y. Owadano, Y. Matsumoto, and M. Yano  
Electrotechnical Laboratory  
1-1-4 Tsukuba, Ibaraki, 305 Japan

ABSTRACT

Laser damage threshold of dielectric reflectors for UV lasers depends on absorption in the high index materials. High resistance reflector for ArF laser (193 nm) is developed by using  $\text{LaF}_3$  as high index materials.

In this paper, we present the results of damage threshold, overcoating effects, and degradation in ageing and in post-heating for  $\text{LaF}_3/\text{Na}_3\text{AlF}_6$  reflectors. Damage threshold of the reflectors was measured using 10pps 17 ns pulsewidth ArF laser. Damage threshold of the reflectors without overcoating was  $\sim 0.45 \text{ J/cm}^2$  just after the coating, and it showed the decrease of  $\sim 10\%$ , 420 days after the coating. Absorption of reflectors without overcoating was  $\sim 3.6\%$  and it increased to  $\sim 5.8\%$ , 420 days after the coating. Post-heating at  $80^\circ\text{C}$  showed the decrease of  $\sim 50\%$  in damage threshold.

$\text{Na}_3\text{AlF}_6$  overcoating on the reflector improved about twice higher damage threshold of  $\sim 0.8 \text{ J/cm}^2$ . Degradation in ageing was also improved compared with the nonovercoating reflectors. No degradation after post-heating was observed. Damage threshold of  $\text{MgF}_2$  overcoating reflectors showed worse results than that of non overcoating reflectors.

In the experiments of  $\text{LaF}_3$  single layer films, absorption of the film showed more than 10 times increase, 420 days after the coating. From this result, the cause of ageing effect is considered to be mainly due to the increase of absorption in  $\text{LaF}_3$  films.



## THE RESPONSE OF MULTILAYER DIELECTRIC COATINGS TO LOW FLUENCE UV LIGHT EXPOSURE

J. Early, V. Sanders, and W. Leamon  
Los Alamos National Laboratory  
Chemical and Laser Sciences Division  
P. O. Box 1663, MS J564  
Los Alamos, NM 87545

In support of the FEL harmonics damage program at the Los Alamos National Laboratory, an experiment was conducted to determine the damaging effects of low fluence, ultraviolet light exposure (11 to 114 mJ/cm<sup>2</sup>/pulse at a 35-Hz pulse rate) to the performance of various 1- $\mu$ m multilayer dielectric high-reflector coatings. A multiline, cw, 1.15  $\mu$ m He Ne laser was used to measure variations in coating reflectivity as damaging uv light was applied. The coated substrate under test formed one end of the He Ne laser resonator. Coating reflectivity loss was determined by relating changes in He Ne laser circulating power to changes produced by known insertion losses. Coating reflectivity degradation was measured as a function of uv exposure duration and uv fluence for uv wavelengths of 248 and 351 nm.

The reflectivity of all dielectric coatings measured was found to degrade in response to 65-min exposures to 248- or 351-nm light. Measured coating reflectivity loss varied from 0.11% for ZrO<sub>2</sub>/SiO<sub>2</sub> to 1.05% for TiO<sub>2</sub>/SiO<sub>2</sub>/HfO<sub>2</sub>. Significant reflectivity recovery after termination of 351-nm irradiation was observed, whereas reflectivity degradation induced by 248-nm irradiation was permanent.

**Key Words:** multilayer dielectric coatings; uv-induced reflectivity degradation; radio-frequency free-electron laser

### Introduction

The results presented in this paper were generated within a study to develop and evaluate multilayer dielectric coatings for application in the design of a resonator for the radio-frequency free-electron laser (RF-FEL). In addition, we have developed and will present a sensitive technique for measuring ultraviolet (uv) radiation damage to dielectric coatings. The dielectric coatings were obtained from commercial vendors and include a selection of materials and a variety of coating processes.

Multilayer dielectric-coated mirrors offer one major advantage over metal-coated mirrors in the design of an optical resonator for a high-average power near-ir laser. This advantage is the lower absorption of dielectric mirrors. At a wavelength of 1  $\mu$ m, the absorption of a silver mirror coating is about two orders of magnitude greater than that of a dielectric mirror. Hence, the amount of heat generated in a dielectric mirror is thus proportionally smaller. This is somewhat confirmed in the comparison of damage threshold results for silver coatings to those for dielectric coatings. Under identical conditions of 1- $\mu$ m laser light exposure using a simulation of a radio-frequency free-electron laser (pseudo-continuous wave), dielectric mirrors were found to fail at light fluences that were typically one to two orders of magnitude greater than fluences required to damage the silver-coated mirrors.

Despite this major advantage that multilayer dielectric coatings offer in the near infrared, incorporation of dielectric mirrors into an FEL resonator pose one serious drawback; FELs generate uv and vuv harmonics of the fundamental wavelength which tend to degrade dielectric coatings. This was observed for TiO<sub>2</sub>/SiO<sub>2</sub> mirrors located within the resonator of the Orsay FEL [1,2].

### Experimental Setup

A diagram of the apparatus developed to monitor the loss in reflectivity of various dielectric-coated substrates exposed to uv light is shown in figure 1. The apparatus consisted of a 1-m semiconfocal resonator which houses a cw multimode He Ne laser operating at a wavelength of 1.15  $\mu$ m. A dielectric mirror (radius of curvature = 1.5 m) coated for maximum reflectance at 1.15  $\mu$ m formed one end of the resonator while the test sample designated for exposure to uv light was a flat dielectric-coated substrate and

served as the other end of the resonator. A dc current-regulated supply (9 ma at 310 V) with added noise suppression filtering supplied power to the He Ne plasma tube. In order to increase thermal stability, the plasma tube was encased inside a metal tube. This reduced the relative drift in laser power to less than 0.2% per hour.

The uv light was supplied by an excimer laser where either 248- or 351-nm light was generated by forming either KrF or XeF in a flowing discharge. A set of steering mirrors directed the output beam from the excimer laser to a focusing lens, through a collimating aperture, and finally onto the dielectric-coated test mirror. The output energy of the excimer laser was monitored indirectly by placing a pellicle beam splitter directly in the path of the uv beam. The operating conditions of the excimer laser were controllable to select either 12- or 26-ns pulse widths of a 35-Hz duty cycle (see data).

The intracavity power of the He-Ne laser was determined by reflecting 1.0% of the beam off an intracavity fused quartz beam splitter oriented 45° with respect to the cavity axis. The power of the reflected beam was monitored by an InGaAs photodiode. The dc background signal was eliminated and the signal to noise was enhanced by the use of phase-sensitive detection.

Loss in reflectivity was measured using the technique developed previously by Sanders [3]. The underlying principle behind this method is that a loss induced into any given intracavity element adds to the total intracavity losses and thereby decreases the intracavity circulating power. Thus, relative changes in intracavity losses can then be measured directly by monitoring relative changes in intracavity power.

The relationship between reflectivity loss and laser-circulating power loss was established by calibrating measured power losses with known cavity-insertion losses. Our calibration procedure consisted of inserting into the cavity a pair of fused quartz plates which acts as a variable attenuator. Each plate had a thickness of 5.0 mm and was mounted on a separate precision rotary stage. The plates were initially set to Brewster's angle by a method which avoids intracavity beam walk-off. First, both plates were set to normal incidence with respect to the intracavity beam. Then, one plate was rotated clockwise to Brewster's angle while the other plate was rotated counterclockwise to Brewster's angle. Variable intracavity loss was introduced into the cavity by rotating the plates about Brewster's angle. The plates were rotated in opposite directions so as to maintain the on-axis position of the intracavity beam through the He Ne gain media and on the mirrors. Figure 2 is an example of a typical calibration curve, where the change in intracavity power is plotted vs angle of incidence.

The losses introduced by the intracavity plates were calculated by use of Fresnel's relation,

$$R(\theta_i) = \left[ \frac{\tan(\theta_i - \theta_r)}{\tan(\theta_i + \theta_r)} \right]^2 \quad (1)$$

where

$\theta_i$  is the angle of incidence

and

$\theta_r$  is the refracted angle computed from the Snell relation

$$n_i \sin \theta_i = n_r \sin \theta_r \quad (2)$$

The total single-pass loss,  $\Delta R$ , involving all four surfaces of the variable attenuator, is given by,

$$\Delta R(\theta) = [1 - (1 - R(\theta))^4] \quad (3)$$

Thus, eq. (3) directly relates relative intracavity loss to incident angle of the intracavity variable attenuator. Hence, eq. (3) allows one to transform the plot given by figure 3 to a plot which relates a change in intracavity circulating power to relative intracavity loss. The transformed plot is shown in figure 3. It is seen in the figure, that the laser has provided an increased sensitivity of approximately 6. A calibration curve is then generated by fitting the data points to a three-term polynomial where relative intracavity loss is treated as the independent variable. Once the calibration curve is obtained, the reflectivity loss of a dielectric-coated substrate exposed to uv radiation can be directly determined from the measured decrease in power of the intracavity beam. Finally, the maximum

sensitivity achieved with this technique is quite remarkable. With laser amplitude fluctuations on the order of 0.1% to 0.2%, this translates to measuring the change in reflection losses to about 100 to 200 ppm.

## Results and Discussion

Results from all coating reflectivity loss measurements at 1.15  $\mu\text{m}$  following exposure to 351- and 248-nm ultraviolet light are summarized in tables I and II and figures 4–9. In table I, for example, the tabulated results following exposure to 12- and 26-ns pulses from the 351-nm line of a XeF excimer laser are organized into five columns. The first column lists the coating materials, the second column defines the coating deposition process used, and the third column lists the mean reflective loss (%) and standard deviation involving a 65-min exposure to 351-nm light; the fourth column lists the mean reflective loss (%) and standard deviation after a 35-min. recovery interval, and the fifth column indicates the total number of measurements averaged. The abbreviations EB, IBS, or PIP appearing in column 2 of tables I and II refer, respectively, to the electron beam, ion beam sputtering, or plasma ion plating deposition methods used to fabricate the coating. For the experimental results illustrated in figures 4-9, the excimer laser was operated at a 35-Hz pulse rate with a 12-ns pulsewidth.

The results in tables I and II indicate that the coating materials selected are all susceptible to varying amounts of uv degradation. For instance, the electron beam deposited  $\text{HfO}_2/\text{SiO}_2$  (composed of multiple quarterwave pairs of hafnia and silica) suffers the least amount of uv degradation when exposed to 248-nm light, as indicated by a 0.17% loss in reflection. A  $\text{ZrO}_2/\text{SiO}_2$  coating was the most resistant to uv degradation at 351 nm with a measured 0.11% reflectivity loss.  $\text{TiO}_2/\text{SiO}_2/\text{HfO}_2$  probably ranks last in its ability to withstand uv degradation, both at 351 and 248 nm, as indicated by measured reflectivity losses of 1.05 and 0.68%, respectively. Catastrophic failure was observed for  $\text{TiO}_2/\text{SiO}_2/\text{SiO}_2$  within 60 min. of exposure to 351 nm. This may favor ranking this material below  $\text{TiO}_2/\text{SiO}_2/\text{HfO}_2$  at 351 nm. The designation  $\text{TiO}_2/\text{SiO}_2/\text{SiO}_2$ , for example, refers to a coating composed of multiple quarterwave-thick layers of titania and silica with a final coating (overcoat) of silica. Apparently the application of overcoating inhibits the uv-induced coating failure since a bare  $\text{TiO}_2/\text{SiO}_2$  coating was found to fail instantaneously upon exposure to 351-nm light at a fluence of 114  $\text{mJ}/\text{cm}^2$ .

The experimental uncertainties listed in Tables I and II also reveal an important property exhibited by the coating materials when placed under uv exposure. For some of the coating materials listed in the two tables, the relative errors are quite large, e.g.,  $\text{HfO}_2/\text{SiO}_2$  (IBS) in table I and  $\text{Al}_2\text{O}_3/\text{SiO}_2$  in table II. The large relative errors in these cases are more than likely due to inhomogeneities in the coating layers across the surface of the substrate. Conversely, the small relative errors associated with materials like  $\text{TiO}_2/\text{SiO}_2/\text{HfO}_2$  in table I and  $\text{HfO}_2/\text{SiO}_2/\text{ZrO}_2$  in table II indicate a much higher degree of uniformity in the dielectric coating.

The results described so far involved averaging the measurements over a fixed interval of time. Additional information about how the coating materials interact to exposed uv light can be obtained by determining how reflective loss depends on time and light fluence. Figures 4 and 5 illustrate the dependence of reflective loss with time and light fluence for the respective coating materials  $\text{TiO}_2/\text{SiO}_2/\text{HfO}_2$  and  $\text{HfO}_2/\text{SiO}_2$  exposed to 351-nm light. Figures 6 and 7 illustrate the same dependencies for the same materials except at a wavelength of 248 nm.

Examination of figure 4 indicates that the family of curves corresponding to fixed light fluences all share similar dependencies of reflective loss with time. The reflective loss curve starts off with an initial sharp rise for times  $<0.5$  min, followed by a much more gradual rise for times  $>0.5$  min. Such a time dependency is easily explained if one assumes first, an exponential rate of reflection loss, and second, there are two competing mechanisms at work, with two distinct rate constants. Furthermore, the curves in figure 4 would also seem to suggest that the rate constants associated with these mechanisms vary linearly with light fluence.

An even more striking feature, revealed by figure 4, is the time dependency of reflective loss when the excimer is turned off. The reflective loss in this case appears to follow simple exponential decay with time. However, closer examination of the figure 4 curves reveals an interesting correlation between the rate in which the reflective loss curve exponentially decays with time when the excimer is turned off to the rate in which the curve exponentially rises when the excimer is first turned on. In other words, fast exponential rise seems to correlate with fast exponential decay. The curves in figures 5-7 provide further evidence to support this conclusion.



In this experiment, measured reflectivity decreases are assumed to be equated with 1- $\mu\text{m}$  absorption increases within the uv irradiated coating. The two reflectivity-loss mechanisms (with fast and slow rates) indicated from the experimental results are assumed to be associated with the growth of crystal lattice defects, e.g., uv-induced F-centers. F-center formation is plausible, since the uv wavelengths of 351 and 248 nm lie near the 350- and 220-nm band-pass edges for the materials  $\text{TiO}_2$  and  $\text{HfO}_2$ , respectively [4]. Additional support for the correlation between selectivity loss and F-center growth is offered by comparison with another experiment which was conducted to measure the gamma-ray excitation of F-centers in several alkali halide materials [5,6]. Striking similarities are noted in the time dependence of the gamma-ray-induced absorption within the alkali halide material when compared to the dependence of reflectivity loss with irradiation duration as measured in this experiment. For instance, F-center absorption in gamma-ray irradiated KCl exhibits the temporal features of a fast exponential increase at the beginning of irradiation, followed by a fast exponential decay upon termination of irradiation. These features were also observed in the uv-induced reflectivity loss of dielectric coatings (see figure 4). It is also interesting to note that gamma-ray-induced F-center absorption was substantially increased in KCl by the application of strain to the crystal. This may explain why certain highly stressed coatings, such as ion beam sputtered  $\text{HfO}_2/\text{SiO}_2$ , exhibit very large variations in reflectivity loss measured from site to site on the coating.

Finally, a series of measurements were made to study the dependency of reflectivity loss with uv light fluence just prior to turning the excimer laser off after a 65-min exposure. The dependency of reflective loss with uv light fluence as a function of the two excimer laser wavelengths, 351 and 248 nm, is illustrated in figures 8 and 9 for the coating materials  $\text{TiO}_2/\text{SiO}_2/\text{HfO}_2$ , and  $\text{HfO}_2/\text{SiO}_2$ , respectively. Thus figure 8, for example, reveals that exposure to 248-nm light results in the catastrophic destruction of the  $\text{TiO}_2/\text{SiO}_2/\text{HfO}_2$  coating material at a fluence value above 45  $\text{mJ}/\text{cm}^2$ . This is in sharp contrast with the exposure of the  $\text{HfO}_2/\text{SiO}_2$  coating to 248 nm as well as the exposure of both coatings to 351 nm, where there is no indication of catastrophic destruction for fluences less than 125  $\text{mJ}/\text{cm}^2$ . Finally, it is also important to note that the reflectivity-loss curves for the  $\text{HfO}_2/\text{SiO}_2$  coating begin to saturate at fluence values approaching ~50  $\text{mJ}/\text{cm}^2$  and ~114  $\text{mJ}/\text{cm}^2$  for 248 and 351 nm, respectively. Conversely, the 351-nm  $\text{TiO}_2/\text{SiO}_2/\text{HfO}_2$  curve continues to remain unsaturated for fluences >125  $\text{mJ}/\text{cm}^2$ .

## Conclusions

The results of this experiment showed that the reflectivity of all dielectric coatings measured degraded in response to 65-min exposures of 248- or 351-nm light.  $\text{HfO}_2/\text{SiO}_2$  was found to be the most uv-resistant coating with a mean reflectivity loss of 0.21% when reflection losses for 248- and 351-nm light exposures were averaged.

Furthermore, two uv light-induced reflectivity degradation mechanisms, probably attributable to defect (F-center) formation within the coating, were indicated from the experimental results. One mechanism correlates with a fast exponential decrease in reflectivity when a coating was first exposed to uv radiation, followed by a rapid rate of coating reflectivity recovery upon termination of irradiation. This mechanism is most prominent in the response of a coating to 351-nm irradiation and is virtually absent for 248-nm coating exposures. The other mechanism is characterized by a slow exponential reflectivity decrease upon uv irradiation. Following the termination of irradiation, virtually no coating reflectivity recovery was observed from this damage mechanism.

Finally, significant differences between various coatings were revealed in the dependency of reflectivity loss with 248- and 351-nm uv light fluence. The reflectivity of a  $\text{TiO}_2/\text{SiO}_2/\text{HfO}_2$  coating was found to decrease monotonically with increasing 248- or 351-nm fluence. In fact, this coating was found to fail catastrophically at 248-nm fluences above 45  $\text{mJ}/\text{cm}^2$ . In contrast, the reflectivity loss for a  $\text{HfO}_2/\text{SiO}_2$  coating was found to saturate with increasing 248- and 351-nm fluence exposure.

## References:

- [1] Elleaume, P.; Velge, M.; Ortega, J. M. Diagnostic techniques and UV-induced degradation of mirrors used in the Orsay storage ring free-electron laser. *Appl. Opt.* 24(17): 2762-2770; 1985 September 1.
- [2] Velge, M.; Elleaume, P. FEL optics coating test device. *Nucl. Instr. and Meth. A* 259: 83-87; 1987.
- [3] Sanders, V. E. High precision reflectivity measurement technique for low-loss laser mirrors. *Appl. Opt.* 16(1): 19-20; 1977.



- [4] McLeod, H. A. Thin film optical filters, Appendix 1. New York; Macmillian Publishing Co.; 1986. 504-508.
- [5] Levy, P. W. Facilities for studying radiation damage in nonmetals during irradiation. SAMPE J. 21: 35-40; 1985.
- [6] Levy, P. W. Overview of nuclear damage processes: phenomenological features of radiation damage in crystals and glasses. Radiation effects in optical materials, Levy, P.W., ed. Proc. SPIE 541; 1985 March 2-27.

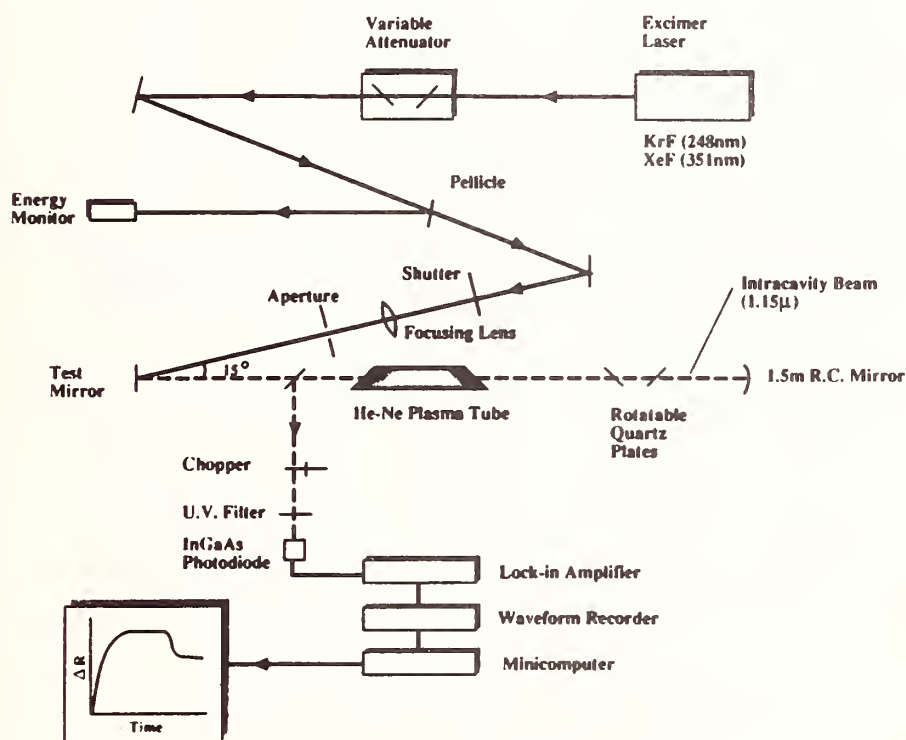


Figure 1. Experimental apparatus for the measurement of coating reflectivity loss.

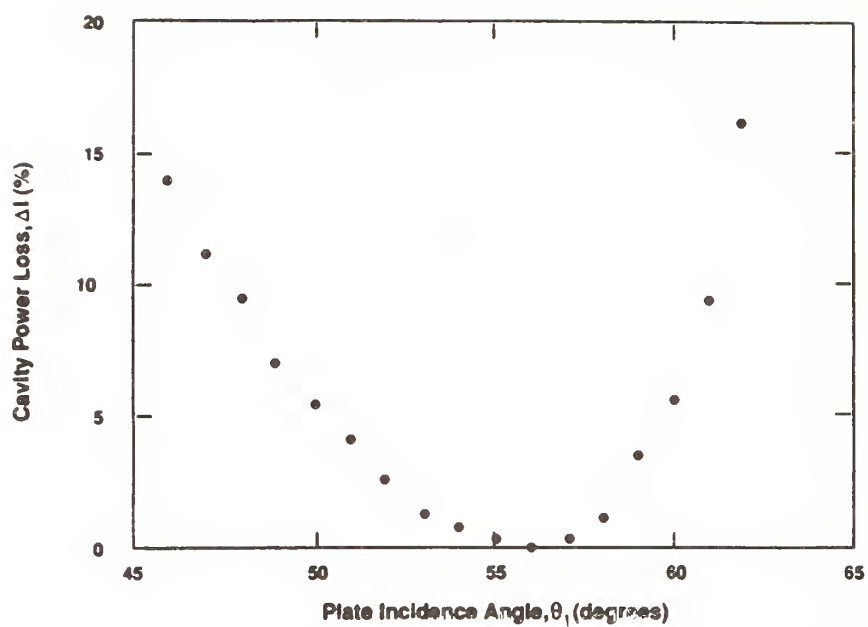


Figure 2. Calibration curve.

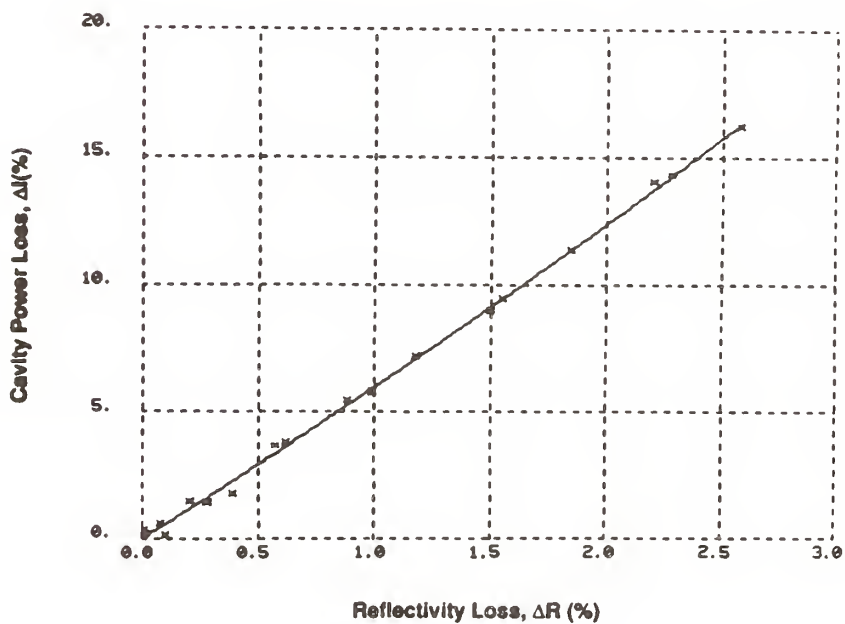


Figure 3. Dependence of the laser cavity power on reflectivity loss.

**TABLE I**  
**COATING REFLECTIVITY LOSS FOLLOWING 351nm U.V. EXPOSURE**  
**PEAK FLUENCE = 114mJ/cm<sup>2</sup>/pulse, PULSE RATE = 35 Hz**

12ns PULSE WIDTH				
Coating Material	Deposition Process	Ref. Loss (%) after 65 min U.V. Exposure	Ref. Loss (%) after 35 min Recovery period	# of Tests
TiO <sub>2</sub> /SiO <sub>2</sub> /HfO <sub>2</sub>	EB	1.05 ± 0.19	0.48 ± 0.14	14
TiO <sub>2</sub> /SiO <sub>2</sub> /SiO <sub>2</sub>	IBS	0.97 ± 0.16 <sup>(1)</sup>	0.35 ± 0.03 <sup>(2)</sup>	12
HfO <sub>2</sub> /SiO <sub>2</sub>	PIP	0.51 ± 0.16	0.17 ± 0.16	12
HfO <sub>2</sub> /SiO <sub>2</sub>	IBS	0.33 ± 0.23	0.17 ± 0.16	7
HfO <sub>2</sub> /SiO <sub>2</sub>	EB	0.26 ± 0.10	0.15 ± 0.11	19
Sc <sub>2</sub> O <sub>3</sub> /SiO <sub>2</sub>	EB	0.26 ± 0.03	0.25 ± 0.03	3
HfO <sub>2</sub> /SiO <sub>2</sub> /ZrO <sub>2</sub>	EB	0.17 ± 0.07	0.07 ± 0.04	3
ZrO <sub>2</sub> /SiO <sub>2</sub>	IBS	0.11 ± 0.07	0.07 ± 0.06	3

26ns PULSE WIDTH				
Coating Material	Deposition Process	Ref. Loss (%) after 65 min U.V. Exposure	Ref. Loss (%) after 35 min Recovery Period	# of Tests
TiO <sub>2</sub> /SiO <sub>2</sub> /SiO <sub>2</sub>	IBS	1.09 ± 0.21	0.35 ± 0.16	2
TiO <sub>2</sub> /SiO <sub>2</sub> /HfO <sub>2</sub>	EB	0.96 ± 0.35	0.58 ± 0.16	5
Ta <sub>2</sub> O <sub>5</sub> /SiO <sub>2</sub>	IBS	0.36 ± 0.17	0.32 ± 0.15	3
Al <sub>2</sub> O <sub>3</sub> /SiO <sub>2</sub>	EB	0.35 ± 0.13	0.26 ± 0.08	3

(1) Coating failed catastrophically within 25 - 60 minutes of UV exposure for 9 out 12 tests. Value is the measured loss just prior to coating failure.

(2) Evaluated for 3 coating tests which did not fail catastrophically

**TABLE II**  
**COATING REFLECTIVITY LOSS**  
**FOLLOWING 248nm U.V. EXPOSURE**

PEAK FLUENCE = 11.4 mJ/cm<sup>2</sup>/pulse, 35 Hz PULSE RATE

12 NS PULSE WIDTH				
Coating Material	Deposition Process	Ref. Loss(%) after 65 min. U.V. Exposure	Ref. Loss (%) after 35 min. Recovery Period	# of Tests
TiO <sub>2</sub> /SiO <sub>2</sub> /HfO <sub>2</sub>	EB	0.68 ± 0.20	0.64 ± 0.18	6
ZrO <sub>2</sub> /SiO <sub>2</sub>	IBS	0.60 ± 0.19	0.56 ± 0.30	3
Al <sub>2</sub> O <sub>3</sub> /SiO <sub>2</sub>	EB	0.40 ± 0.29	0.26 ± 0.31	3
Ta <sub>2</sub> O <sub>5</sub> /SiO <sub>2</sub>	IBS	0.35 ± 0.12	0.36 ± 0.25	3
HfO <sub>2</sub> /SiO <sub>2</sub> /ZrO <sub>2</sub>	EB	0.30 ± 0.09	0.27 ± 0.11	3
HfO <sub>2</sub> /SiO <sub>2</sub>	EB	0.17 ± 0.10	0.12 ± 0.06	3



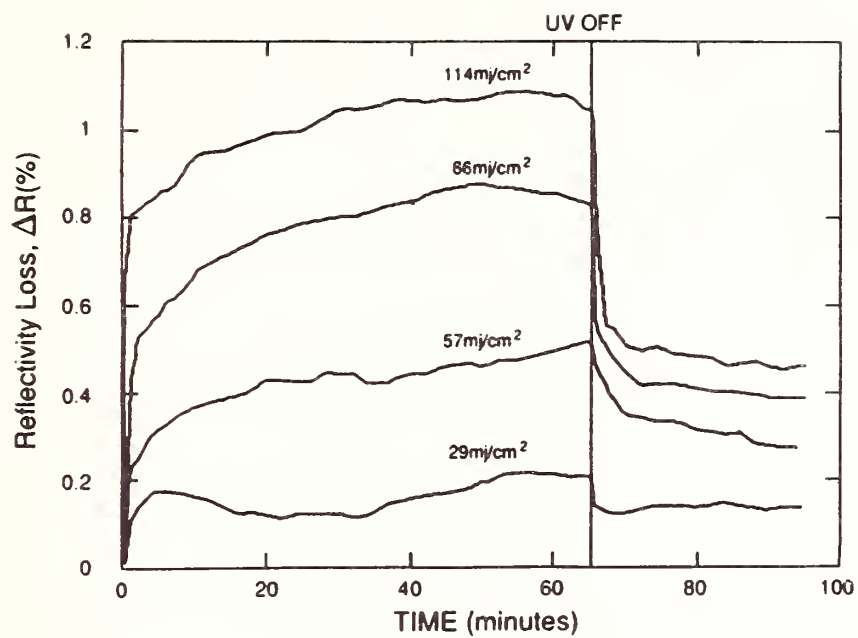


Figure 4. Response of  $\text{TiO}_2/\text{SiO}_2/\text{HfO}_2$  coating to 351-nm uv exposure.

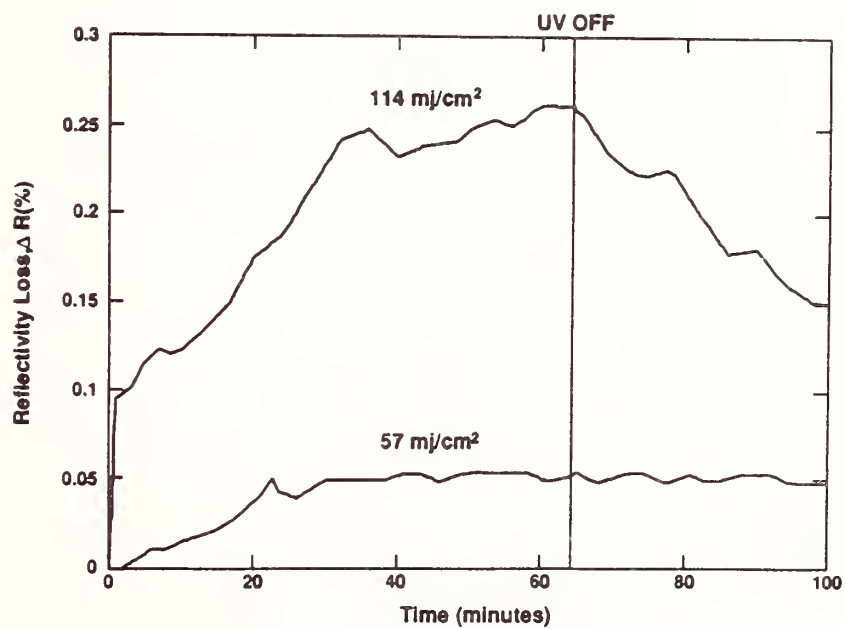


Figure 5. Response of  $\text{HfO}_2/\text{SiO}_2$  coating to 351-nm uv exposure.

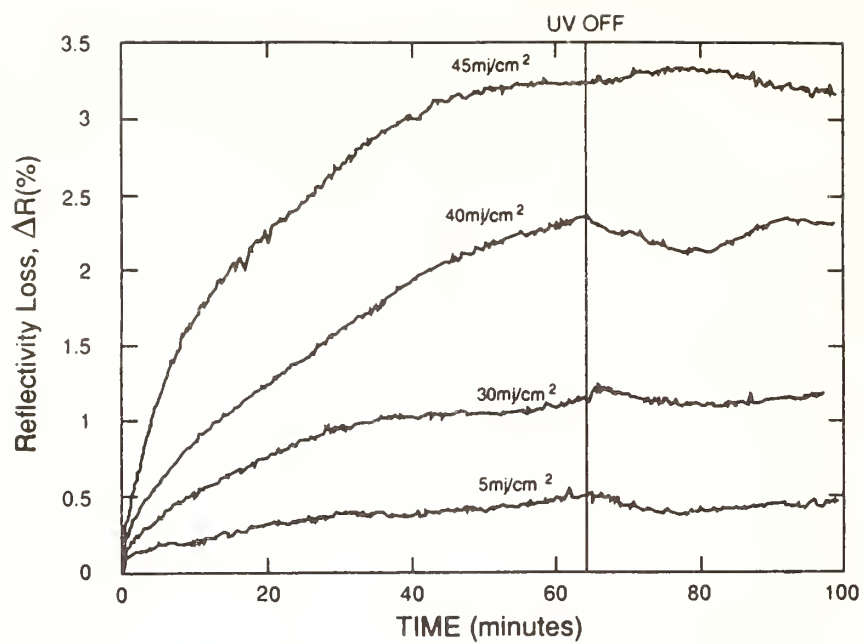


Figure 6. Response of  $\text{TiO}_2/\text{SiO}_2/\text{HfO}_2$  coating to 248-nm uv exposure.

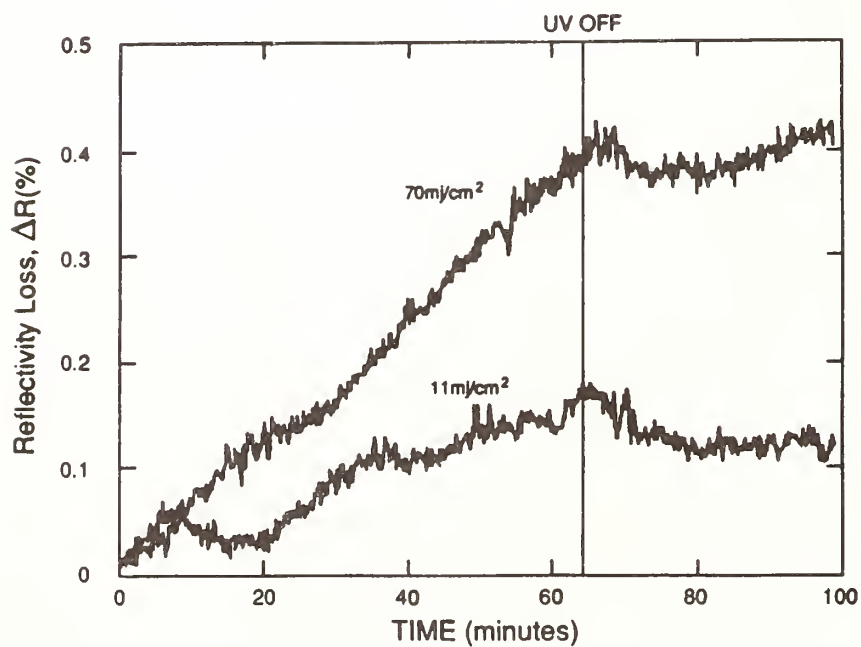


Figure 7. Response of  $\text{HfO}_2/\text{SiO}_2$  coating to 248-nm uv exposure.

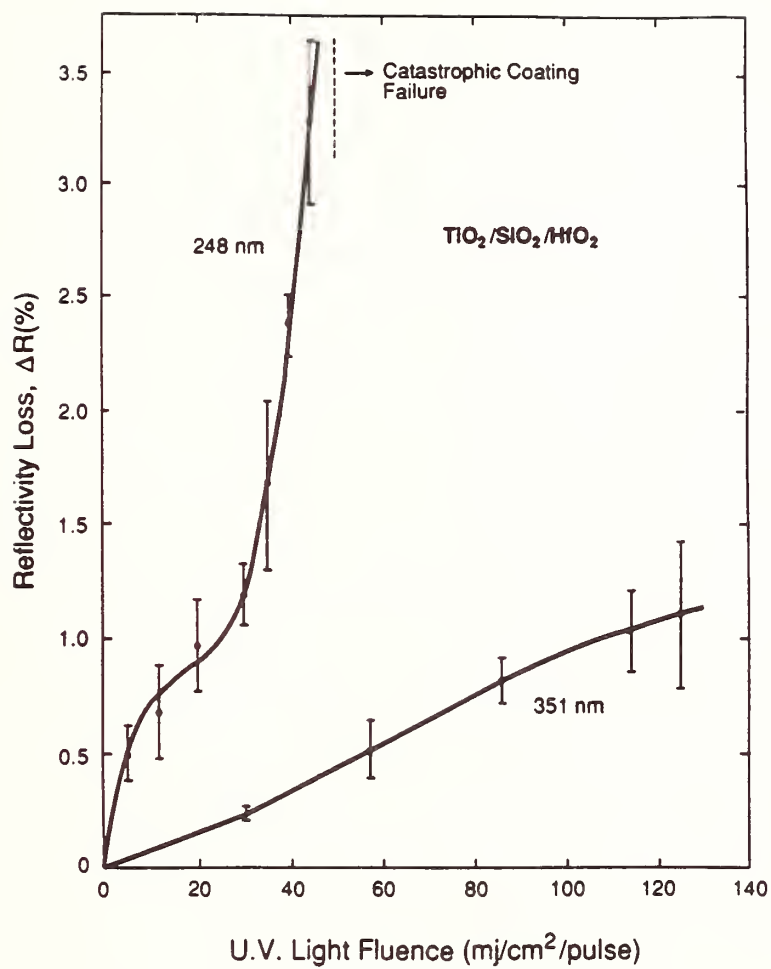


Figure 8. Reflectivity loss of a  $\text{TiO}_2/\text{SiO}_2/\text{HfO}_2$  coating as a function of 248- and 351-nm uv exposure.

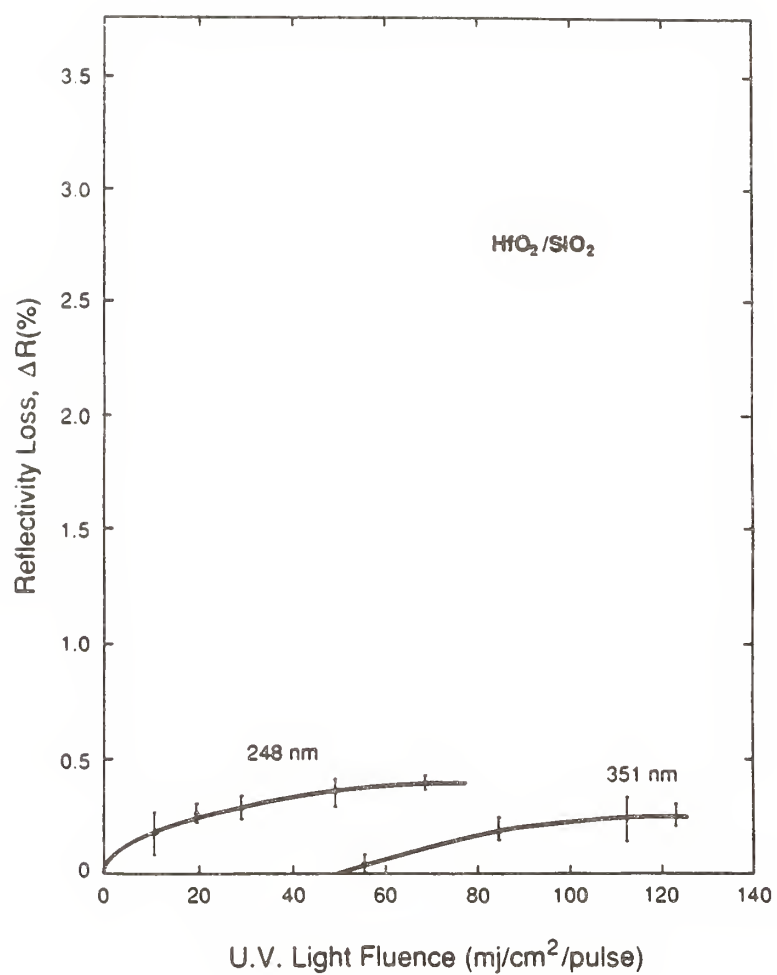


Figure 9. Reflectivity loss of a  $\text{HfO}_2/\text{SiO}_2$  coating as a function of 248- and 351-nm uv exposure.



## Thermal Imaging Studies Of Laser Irradiated Coated Optical Surfaces

Alan F. Stewart, Adam Rusek and Arthur H. Guenther\*

Air Force Weapons Laboratory  
Kirtland AFB, NM 87117

The detection of a localized temperature excursion induced by a laser beam incident on a coated optical surface has been previously employed to measure the optical absorption and the thermal properties of the coating. The application of thermal imaging to map coating absorption as a nondestructive diagnostic is reported in this study. Near angle light scatter was also used to generate maps of the same areas on these coatings. The data shows a limited correlation between coating absorption anomalies as determined with irradiation at 1064 nm and scattering defects identified at 633 nm. Calibration of absorption data obtained using thermal imaging was obtained from laser calorimetry measurements.

Key words: absorption; calorimetry; infrared imaging; scattering; thermal conductivity

### 1. Introduction

A growing awareness of the potential importance of the thermal conductivity and diffusivity in the overall performance of thin film coatings for high power, high energy applications has spurred the development of theoretical models and several new measurement techniques. That a relationship should exist between the thermal properties of a coating and the laser damage threshold under continuous power loading is intuitively clear. For pulsed laser testing, recent analysis of existing and new experimental data comparing short pulse laser damage data to thin film thermal properties has demonstrated a surprising degree of correlation.[1] Lange, McIver and Guenther assumed that thermal transport in films was equal to that of the bulk material. This has been the implicit or explicit assumption made in virtually all thin film models since only bulk material properties were available. However, experimental data on thin films provided independently by Decker, Jacobs, Swimm and Ristau appears to invalidate that assumption with indications that film thermal properties can be lower than the bulk by factors up to several hundred.[2-5] With the results of these recent investigations in mind, the development of measurement techniques which could determine the thermal properties of thin films with increasing accuracy becomes even more important.

The higher the level of absorption of light in thin films, the greater the need to transport heat efficiently to preclude or obviate damage. The laser calorimeter developed in the early 1970's provided the sensitivity required to measure the absorption of optical coatings with great precision.[6] In 1979, a new technique was developed for the measurement of optical absorption which was called infrared photothermal radiometry (IPTR)[7]. This technique relies on the detection of infrared thermal radiation emitted from a sample illuminated by a laser or other light source. Draggo et al., applied IPTR to the measurement of the absorption of coated optical surfaces using a thermal imaging system and a high average power laser.[8] The technique was simultaneously applied by Ristau et al., who demonstrated the capability to measure film absorption as well as thermal conductivity.[5]

\* Current addresses are:

(A.F.S.) Battelle Pacific Northwest Laboratories, P.O. Box 999, Richland, WA 99352.  
(A.R.) Dept. of Physics, Univ. of New Mexico, Albuquerque, NM 87131  
(A.H.G.) Los Alamos National Laboratory, MS A110, Los Alamos, NM 87545.

Using this method, they were able to show a good correlation in the data between the thermal conductivity, absorption, melting point and damage threshold. As in the earlier studies, Ristau et al., obtained values for most film thermal conductivities which were considerably lower than for the bulk material.

We report on the application of the thermal imaging technique to the determination of optical absorption in thin film coatings. Thermal imaging as used here refers to the detection of infrared radiation to measure the temperature of a surface illuminated by a laser. Our results have been directly compared to laser calorimetry data for calibration of the technique and to determine if the empirical models developed for calibration are adequate. In the course of these individual measurements, it became apparent that the local temperatures induced on these coatings varied considerably with location on the surface.

Thus, thermal imaging was used to "map" coated surfaces allowing us to study the occurrence of "thermal anomalies" or "hot spots" - regions of high absorption or low thermal conductivity. These surface "maps" from the thermal imaging data have been compared to scattered light intensities. The limited correlation between thermal anomalies and light scatter we have observed may confirm earlier work which emphasized the importance of testing coatings at the design wavelength.[9,10]

## 2. Experimental

The component layout used for thermal imaging measurements in this study is shown in figure 1. A continuous wave Nd:YAG laser system operational at either 1064 nm or 1319 nm was used to illuminate the sample.[11] The output beam was focussed onto the sample surface using a 20 cm focal length lens. The use of 2x or 4x beam expansion optics allowed us to obtain different beam diameters at the sample surface. At 1064 nm, the beam spatial profile at the sample plane was measured using a photodiode array. A series of transmission measurements through apertures of different sizes at 1064 and 1319 nm confirmed the photodiode array output. The focussed multimode beam spatial profile was circularly symmetric and nearly Gaussian. For measurements at 1319 nm, the beam FWHM with a 4x beam expander in place was 0.6 mm in diameter at the  $1/e^2$  points in the intensity. The maximum beam power level of 75 Watts at 1319 nm was used. Surface mapping experiments at 1064 nm were performed at the same beam power level but this was obtained with different resonator mirrors and at much lower cavity pump powers. At 1064 nm, no beam expander was used and the focussed beam was 1.01 mm in diameter at the  $1/e^2$  points in intensity.

The focussed laser beam was incident on the surface of the optic under test. Individual measurements at 1319 nm were carried out with incidence angles of 5 and 15 degrees. Mapping of surfaces at 1064 nm was performed with the test surface at 6 degrees elevation from the horizontal plane. A video camera and the thermal imaging camera were located in the horizontal plane as close to the sample surface as was practical. The video camera was used to monitor the progress of the mapping experiments and to determine sample registration. The thermal imaging camera had a telephoto lens with a 15 cm working distance.

The infrared camera utilized a single element cooled HgCdTe detector with front end scanners to produce standard video images.[12] An electronic zoom which reduced the field of view of the scanners was used in conjunction with the telephoto optics. The resulting field of view was 5 x 7.7 mm. The software available on the imaging system allowed image data to be averaged over a small user selectable area within the field of view. The temperature data thus recorded was the average value observed within a 0.5 mm square centered on the incident beam footprint. Sixteen video frames were averaged for each measurement.

Throughout these experiments, the infrared camera system operated reproducibly with 0.1 degree Centigrade resolution. Typical temperatures observed in the coatings testing ranged from 0.1 to 30 degrees or more above ambient. A shifting baseline in the measurements was caused by fluctuations in the room temperature. The laboratory air conditioning system was controlled with a 2 degree bandpass and these fluctuations were very clearly seen by the infrared camera system. This was of no consequence for individual measurements because the data was taken very rapidly compared to environmental fluctuations. However, mapping experiments required several hours to complete with as many as ten temperature cycles in evidence.

The most serious limitation of the thermal imaging technique for the study of coated optical surfaces is that only coatings deposited on substrates with low thermal conductivity

can be studied. For this reason, fused silica and BK-7 substrates were used exclusively throughout these experiments. The peak temperature at the center of the illuminated spot was strongly affected by heat conduction into the surrounding coating and the substrate.

### 3. Absorption Measurements at 1319 nm

Absorption measurements taken at 1319 nm required only a few minutes to complete for each sample. The ambient coating temperature was recorded with the beam blocked. A second reading was recorded with the beam illuminating the surface. Unlike calorimetry which might require several minutes for an equilibrium temperature distribution to become established in a sample, the thermal imaging technique allows the local temperature at the surface to be recorded almost instantly. The onset time for the surface temperature profile could not be resolved using this imaging system but would provide potentially useful data about thermal transport in the coating and the surface.

The absorption of high reflectance coatings designed for operation at 1319 nm was measured using the thermal imaging system. It was during the course of these measurements that it became apparent that there were regions on these coatings with anomalously high absorption or low thermal conductivity. Both average surface temperatures and peak surface temperatures were recorded. The samples used in this survey were several different types of coatings and included all-dielectric stacks and enhanced metal designs. Substrates were fused silica in three sizes - 2.54 cm diameter by 0.0254 cm thick wafers, 3.85 cm diameter by 0.95 cm thick, and 15.25 cm diameter by 2.54 cm thick. Coatings of the same type were deposited on identical substrate sets in three different runs.

Since absolute measurements of coating absorption were the objective of this test series, the emissivity of these coated samples was measured. Each sample was placed in an oven with an open port in the side for line-of-sight measurements. The measured temperature obtained from the image from the infrared camera was compared to the actual temperature to derive the emissivity. For the all dielectric reflectors, emissivities ranged from 0.83 to 0.89. For enhanced metal reflectors, emissivities ranged from 0.05 to 0.09.

Absorption in the thin coated wafers was also measured using a second independent method to assist in a calibration of the thermal imaging technique. Laser calorimetry using the system described in reference [13] was performed at 1319 nm. Measurements were performed only on the wafers due to limitations on sample mass, characteristic of the calorimetric technique.

### 4. Analysis of Measurements at 1319 nm

Data obtained in this survey of high reflectance coating designs was analyzed using the theoretical relationship derived in reference [8]:

$$\text{Absorption} = 0.045 * t^{1.11} * r^{0.83} / p^{1.05}$$

where  $t$  is the peak temperature difference in Centigrade  
 $r$  is the beam radius in cm (flat topped beam profile)  
 $p$  is laser power in Watts

Each data point appearing in figures 2-4 represents the average of measurements at three different positions on the sample surface. The measured emissivity data was used to correct the measured or apparent temperature to obtain the actual surface temperature. For the dielectric coatings tested in figure 2, the inclusion of emissivity amounts to an upward correction of 16 % in the thermal imaging data. The same correction factor exists in figure 4. In figure 3, the emissivity is very small for these enhanced metal reflectors and hence the "correction" is large - multiplication by a factor of 13 over measured temperature readings.

There are several striking features in the data in figure 2. The absorption measured using thermal imaging on parts of very different aspect ratios is practically unchanged. While the coating design is the same for all the samples tested in this figure, the deposition conditions derived for series 3 a-c were used to deposit series 4 a-c and 5 a-c. It is clear that trends in the thermal imaging data are replicated in the calorimetry data although the magnitudes differ by a factor of 2 to 4. The emissivity correction for these coatings is much smaller in comparison to these overall differences.



Similar results appear in figure 3 for a series of enhanced metal high reflectors. The thermal imaging data is virtually unchanged for the different sample aspect ratios. However, the calorimetry data is considerably higher in magnitude for these samples. The correction factor obtained from the emissivity of the samples raised the apparent absorption but not enough to bring the data into close agreement. The poor agreement with the calorimetry data suggests that the theoretical model derived in reference [8] may not accurately account for such a wide variance in sample emissivity. It is also possible that the enhanced metal reflector design may result in larger radial heat flow and hence lower peak temperatures. The work reported in reference [8] was concerned only with the response of all-dielectric coatings.

In figure 4, data obtained on a second set of dielectric reflectors is plotted and compared. Unlike the data in figure 2, for this set of samples the calorimetry data is higher than the thermal imaging data by about a factor of two. As these samples were composed of different dielectric materials from those in figures 2 and 3, it is possible that the observed variations in the thermal response of the coatings is influenced by the microstructure of the films. In these and other samples tested it became obvious upon translating the sample under the incident beam that peak absorption values may differ considerably from the average values measured. Temperatures measured at specific sites (most smaller than 0.3mm in diameter) on these samples were a factor of 2 to 10 higher than the average response of the coatings. Identification and study of these sites - whether the absorption is actually higher or the thermal conductivity is lower - provided the motivation for the mapping experiments.

## 5. Mapping Experiments

The observation of localized highly absorbing regions on thin film coatings prompted an effort to map the surface of a coating and to correlate these regions with other observables such as light scatter and visible defects. Mapping experiments were performed with a completely automated acquisition sequence. A host computer recorded the data from the infrared camera while monitoring beam power and moving the sample through its scan pattern. Sample position was controlled by servo motor driven stages with encoder readout. One centimeter square areas were mapped on the samples tested with 0.2 mm resolution. A map of each square centimeter required three hours to complete. If damage occurred at any point in the scan, the damage propagated into the substrate and along the direction of the scan destroying the sample. While higher beam powers would have resulted in greater sensitivity, the risk of damage prompted us to run at significantly lower powers for mapping experiments than we would have used for individual measurements where operator control was explicit.

The samples used in the thermal mapping experiments were commercially available high reflectors from the same coating batch. The mirror substrates were BK7 material 5.08 cm in diameter and 0.95 cm thick. Coatings were silica/zirconia quarterwave stacks. As shown in figure 5, the sample surface was divided into different areas for mapping and for pulsed laser damage testing. Up to six square centimeter areas were available for mapping experiments in the upper half of the sample but in practice only areas 1-4 were used. Damage testing was performed on the surface of the lower half of the part.

Each sample was placed in a specially designed holder which served as a kinematic mount on the thermal mapping test bench, the pulsed laser damage and light scatter mapping test bed, and the stage of a differential interference contrast (DIC) microscope. Sample registration was critical between these test beds. From comparison of identifiable sites on these surfaces, registration was accurately maintained to 0.3 mm.

After completion of the thermal mapping sequence, the parts and their kinematic holders were moved to the pulsed laser damage test bench. A near angle scatter probe used for the detection of the onset of damage in routine testing [14] was used in this investigation to map the same areas studied with the thermal imaging system. The scatter probe system operated at 633 nm with linear polarization oriented 20 degrees from the plane of incidence. Maps of scattered light were generated with the same scan pattern and resolution used in thermal imaging. The 633 nm probe beam diameter at the sample surface was 1.16 mm compared to 1.01 mm for the cw Nd:YAG beam used in the thermal mapping. It would have been preferable to map scattered light at 1064 nm simultaneously during the thermal imaging measurements. However, there was simply too much stray 1064 nm light reflected from the beam dump, etc., to perform a precision light scatter measurement.

Individual sites identified from the thermal imaging maps were photographed under the DIC microscope for possible identification and further study.



After the completion of these tests, the samples were damage tested using the pulsed Nd:YAG facility described in reference [14]. The lower half of each sample was tested. Standard single shot, pulsed test procedures were used to determine thresholds which ranged from 4 to 6.5 joules per square centimeter as listed in Table 1. No significant variations were observed in the damage threshold or the morphology and these samples were considered essentially identical for these studies.

Samples were cleaned in their holders before being tested on the thermal imaging or scattered light benches. Initial cleaning of the parts involved the application of acetone and methanol using a spin cleaner. Collodion was applied and stripped off as a final cleaning step.

## 6. Analysis - Thermal Mapping

Thermal imaging was used to map the response of high reflectance coatings at 1064 nm. Although the study began with five samples and thirty square centimeters to be mapped, the occurrence of laser damage destroyed several areas and one complete sample. As a result, nine square centimeters distributed over four parts were studied in detail as indicated in table 1.

Table 1. Sample Areas Used in Thermal Mapping Experiments

	Areas Mapped	Pulsed Laser Damage Threshold (J/cm <sup>2</sup> )
HR #1	Destroyed	--
HR #2	Area 2	--
HR #3	Areas 1 and 3	5.1
HR #4	Areas 1, 2, 3	6.6
HR #5	Areas 1, 2, 3	3.9

One or more areas on each sample sustained significant laser damage from the cw beam used to illuminate the surface for the thermal imaging experiments. The occurrence of large scale damage on the surface of the part caused the ejection of large quantities of material from the surface. Thus the data obtained from both thermal imaging and scattering must be considered suspect in the vicinity of large damage features.

A group of data recorded on sample number 4 is shown in figure 6 a-f. The horizontal bands extending across each temperature frame (6a-c) are due to changes in room temperature of a few degrees. The maps from this sample were chosen for discussion because there are features near the boundaries of the adjacent areas which demonstrate continuity in the mapping process. It is difficult to determine where the thermal anomalies are. The data has been plotted in a sixteen color format which makes it somewhat easier to discern differences between temperature levels. The color image actually reduces the amount of information available by formatting it into sixteen levels. In the thermal maps, an anomaly appears on the right hand border of area 1 and on the left side border of area 2. Similarly, two such sites rest on the right side border of frame 2 and the left side border of frame 3. Frame 1 contains two easily identifiable sites. Frame 2 contains 4 easily identifiable sites. Frame 3 contains 8 or more sites of varying temperature contrast.

Accurate identification of the thermal anomalies is difficult because of the amount of data present and our ability to discern the differences between areas. The raw temperature data from the infrared camera was normalized to a range of 0 to 255. The plot routine used separated this range into a sixteen color format to make it easier to discern differences between temperature levels. Because the data was divided into sixteen different levels, the

data was plotted with different magnifications in order to emphasize small changes in temperature. Regrettably, this data manipulation removes the absolute temperature information from the plotted data. However, as shown in frame 3, room temperature fluctuations of a few degrees are very apparent and provide a relative scale.

Comparison of the thermal imaging maps with data from the light scatter measurements (6d-f) is complicated by the appearance of large scale damage in the lower right corner of frame 2 and lower left and right quadrants of frame 3. In an attempt to verify reproducibility, two thermal imaging scans were recorded for area 3 of this sample. These massive damage features occurred during this second scanning sequence. The thermal imaging data already stored was thus unaffected while light scatter data shows the full extent of the damage. It is interesting to note, that the first laser damage within this area was initiated during the second thermal scan at a small anomaly identified in the lower right hand corner during the first scan. Ejected material caused the second area in the left hand corner to damage as the scan was completed.

Ignoring the scattered light data from area 3, comparison of the data in frames 1 and 2 shows reasonably good agreement between the major anomalies identified in the thermal scans and the light scatter data. The two anomalies identified in frame 1 are matched to features in the scatter maps. Of the four anomalies identified in frame 2, only the one on the left hand border (also appearing in frame 1) matches to a feature seen in the scatter map. The remaining anomalies are smaller in size and for the most part, they exhibited lower peak temperatures. There are no corresponding features in the light scatter data. There are, however, additional features in the light scatter data in each frame which do not correlate to thermal anomalies. These additional features may be caused by splattered material from the large scale damage which occurred. It is also probable that light scatter at 633 nm may be strongly influenced by a different set of coating defects due to the altered electric field distribution in the coating when probed at the shorter wavelength. The small line of high scatter sites across the upper left hand corner of frame 1 is a reflection from the sample mount. The remaining features in the scatter data cannot be identified.

Sites corresponding to thermal anomalies were individually photographed under a DIC microscope. Most of the larger anomalies ( $>0.4$  mm in diameter) could be correlated to identifiable features in the thin film coatings. The typical site was an isolated pit approximately 50 microns in diameter. The morphology of the identifiable sites was very consistent and quite different from native coating defects. These high reflectors were standard commercial grade optics and had what we considered to be a normal complement of cosmetic defects. Areas on the coatings that looked like stains did not correlate to thermal anomalies. These stains did not appear in the scattered light data as individual sites but may have contributed to overall higher scatter levels which swamped out the small signal caused by the individual thermal anomalies. Sites which exhibited high light scatter were not photographed individually unless they correlated to thermal anomalies.

It is possible that the thermal anomalies represent much smaller defects which damaged during the thermal imaging scan. The behavior of these sites would be reminiscent of the "microscopic" damage observed at Los Alamos National Lab which appeared after a few shots but which did not grow during continued exposure.[15] The time evolution of the temperature profile or real time scattered light measurements, in band, might be able to differentiate between a feature which has grown in size and a stationary anomaly.

The data from sample 4 is representative of what was recorded on the other samples except that the number of features observed using thermal and light scatter modes was usually higher. In contrast, data recorded on sample 2 area 2 is shown in figure 7 a, b. Again for this sample, only the largest anomaly in the thermal map correlates easily to a similar feature in the scattered light data and to a feature under the microscope. Microscopy confirms the presence of defects at the other thermal anomalies. No definite connection exists between the light scatter data and the appearance of small scale thermal anomalies. Large area thermal anomalies always seem to register using either technique. However, smaller sites which exhibit unusual thermal characteristics do not correlate with features in the light scatter data or observable defects in the coating.

## 7. Conclusions

We have demonstrated some of the potential applications of thermal imaging for the study of optical surfaces. This technique has many advantages over other methods since the measurement is virtually independent of sample size. Compared to techniques like laser

calorimetry, thermal imaging is very easy to implement. The technique provides data quickly which allowed us to design a scanning experiment which effectively mapped the response of a coated surface to a high power beam. Absolute calibration through cross comparison measurements with laser calorimetry is definitely possible but will require many more measurements on a broader range of sample types in order to develop correlation limits. The ability to measure coating absorption at many points on the surface of a coating opens up some unusual possibilities. A mapping technique such as described here may allow process engineers to modify the deposition conditions to reduce the number of defects that are most important when it comes to absorption and laser damage. We have observed an obvious and absolute one-to-one correlation between sites which damage under cw irradiation and those which exhibit high temperature responses at reduced beam power. The nature of these sites - the chemical composition and bonding as well as the microstructure - remains to be determined.

Further studies should be directed towards studying the time evolution of the thermal response of the coating and real time light scatter experiments, in band. This might determine whether the thermal imaging technique is really a destructive technique. The possible correspondence to the microscopic damage observed in reference [15] is potentially important since "damage" at these thermal anomalies does not appear to have progressed to the point of disruption of the film. Thus, it is possible that areas susceptible to microscopic damage may be localized by scanning a cw beam across the surface. Once located, these areas can be studied using a number of surface analytical techniques.

As in references [5,8], the thermal profile induced in the coating must be measured as a function of the incident beam diameter. While clearly related to the peak temperature recorded in the center of the illuminated spot, radial heat flow in the metal layer of an enhanced reflector is a useful measure of film microstructure and bonding. In dielectric films, radial heat flow is expected to be strongly influenced by the film microstructure with poor transverse conductivity in a columnar structure. Deconvolution of the radial heat flow effects and the role of emissivity is required before this technique can be generally applied to the wide range of materials and coating designs under study.

## 8. References

- [1] M.R. Lange, J.K. McIver and A.H. Guenther, "Pulsed Laser Damage in Thin Film Coatings: Fluorides and Oxides," Thin Solid Films, 125, 1985, 143-155.
- [2] D.L. Decker, L.G. Koshigoe, and E.J. Ashley, "Thermal Properties of Optical Thin Film Materials," Nat. Bur. Stand. (US) Spec. Publ. #727, 1984, pp 291-298.
- [3] S.D. Jacobs, "Thermal Conductivity in Dielectric Thin Films," LLE Review 29, October-December 1986, pp.30-38.
- [4] R.T. Swimm, "Photoacoustic Determination of Thin Film Thermal Properties," Appl. Phys. Lett. 42,11, 1983, pp.955-957.
- [5] D. Ristau and J. Ebert, "Development of a Thermographic Laser Calorimeter," Appl. Opt. 25, 1986, pp.4571-4578. S.M.J. Akhtar, D. Ristau, and J. Ebert, "Thermal Conductivity of Dielectric Films and Correlation to Damage Thresholds at 1064 nm," Nat. Bur. Stand. (US) Spec. Publ. #752, 1986, pp 345-351.
- [6] D.A. Pinnow and T.C. Rich, Appl. Opt. 12, 1973, pp. 984-988.
- [7] A.C. Tam, "Infrared Photothermal Radiometry," Invited talk, 3rd International Conf. on Infrared Physics, Zurich, Switzerland. July 1984. 965 IBM OS.
- [8] Vaughn G. Draggoo, Richard G. Morton, Richard H. Sawicki and Horst D. Bissinger, "Optical Coating Absorption Measurements for High Power Laser Systems," SPIE Proc. 622, 1986, pp 186-190.
- [9] Eastman, Jay M., "Surface Scattering in Optical Interference Coatings", PhD. Thesis, The University of Rochester, 1974.
- [10] Mark B. Moran, R.H. Kuo, and C.D. Marrs, "Scatter Intensity Mapping of Laser Illuminated Coating Defects," Appl. Opt. 27, 1988, pp.957-962.
- [11] Model 96300, Lasermetrics, 3500 Aloma Ave. Winter Park, FL 32792.
- [12] Model 600, Inframetrics Inc., 12 Oak Park Dr., Bedford, MA 01730.
- [13] A.F. Stewart and D.J. Gallant, "Ultraviolet Thin Film Coating Characterization," Nat. Bur. Stand. (US) Spec. Publ. #727, 1984, pp.272-284.
- [14] Alan F. Stewart and Arthur H. Guenther, "Scattered Light as a Laser Damage Diagnostic," Nat. Bur. Stand. (US) Spec. Publ. #756, 1987.
- [15] L. John Jolin, Virgil E. Sanders, and Steven J. Salazar, "Laser Induced Damage Measurements of Free Electron Laser Optical Components," Nat. Bur. Stand. (US) Spec. Publ. #756, 1987.



9. List of Figures

1. Experimental configuration for thermal imaging measurements of optical absorption in thin film coatings.
2. Absorption in dielectric high reflectors designed for operation at 1319 nm measured using thermal imaging and laser calorimetry. Silica substrates with three different aspect ratios were coated and measured using thermal imaging. Emissivities of these films ranged from 0.83 to 0.89.
3. Absorption measured in enhanced metal reflectors designed for operation at 1319 nm measured using thermal imaging and laser calorimetry. Emissivities of these films ranged from 0.05 to 0.09.
4. Absorption measured in dielectric high reflectors designed for operation at 1319 nm measured using thermal imaging and laser calorimetry. Peak absorption levels measured at anomalous sites exceed the average values measured by factors of 10 or more.
5. The sample test format for thermal mapping experiments. Pulsed laser damage testing was performed entirely on the lower half of the part. The upper half was divided into six square centimeter areas for mapping experiments.
6. Thermal imaging maps and scattered light data on three adjacent areas on sample number 4. Thermal anomalies near the edges of each area demonstrate the continuity in the areal maps. Scattering data recorded at 633 nm correlate well only to the large anomalies seen in the thermal imaging data.
7. Thermal imaging maps and scattered light data from area 2 on sample number 2. Many features appear in the two sets of maps but correlation is limited to the largest thermal anomaly which appears in both maps.

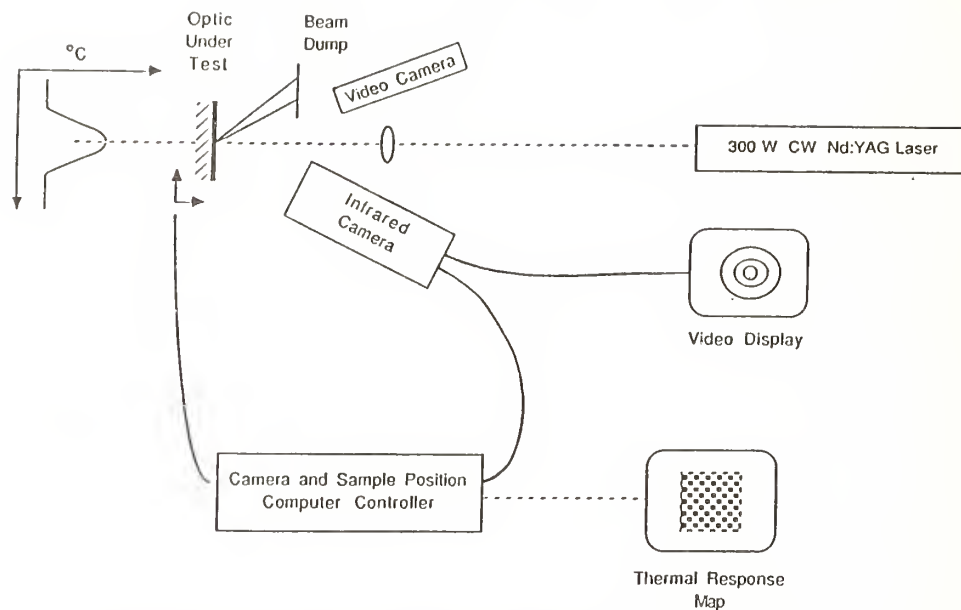


Fig. 1

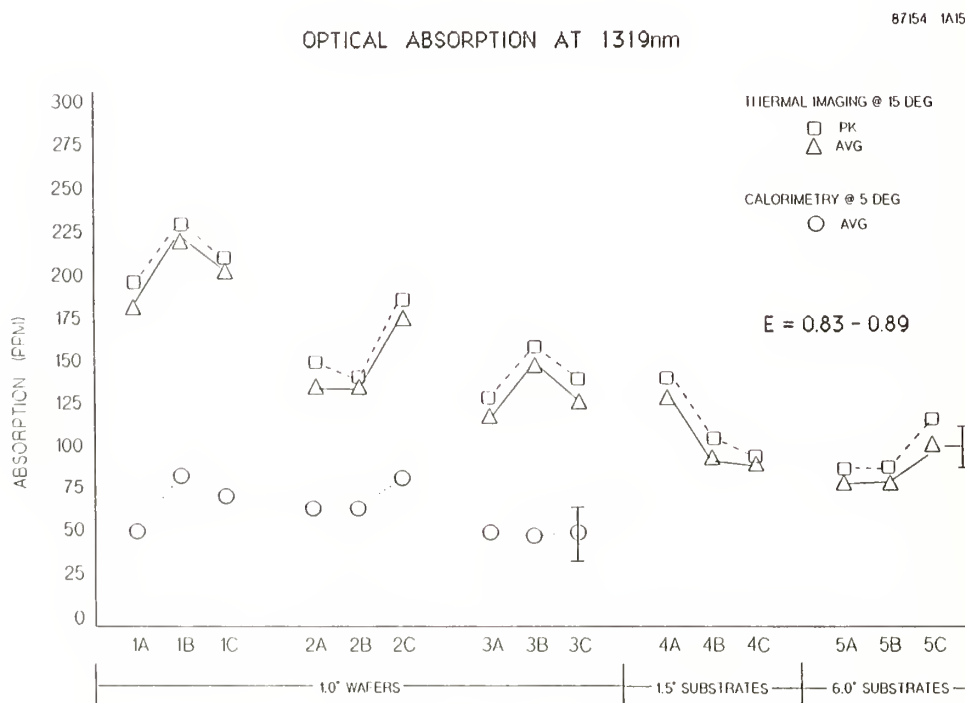


Fig. 2

# OPTICAL ABSORPTION AT 1319nm

87207 1B15

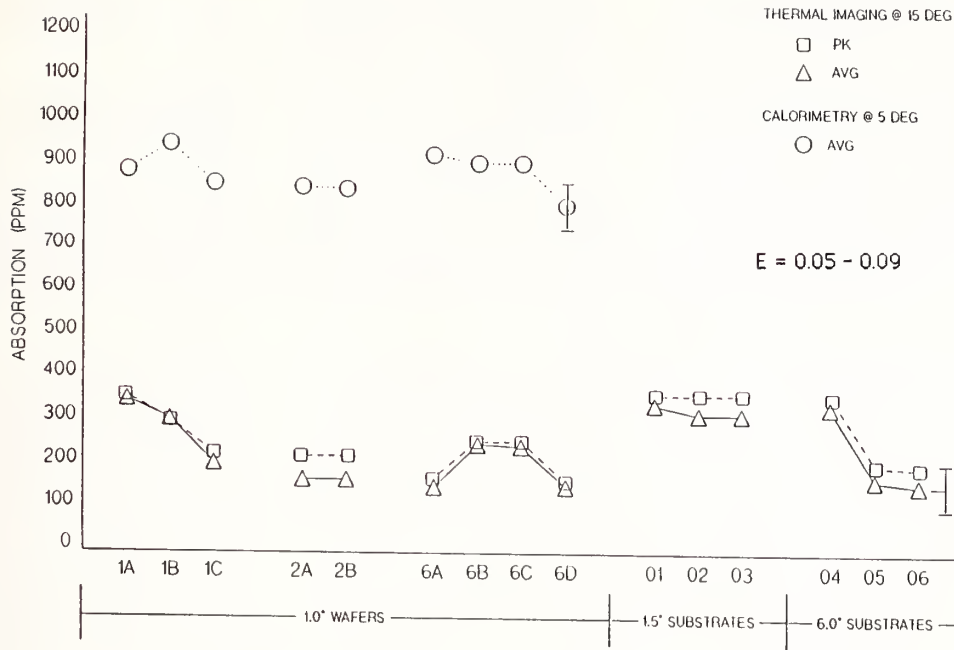


Fig. 3

# OPTICAL ABSORPTION AT 1319nm

87156 1A1R15

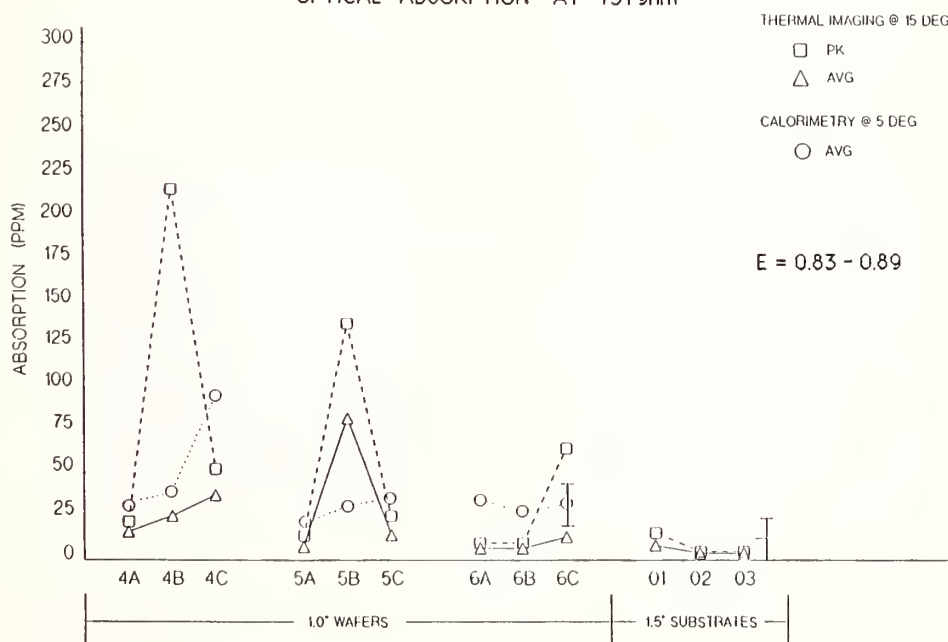
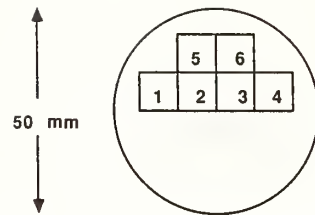


Fig. 4

### Sample Test Format for Thermal Mapping

6 cm<sup>2</sup> mapped for :



Thermal response  
Light scatter  
DIC microscopy

---

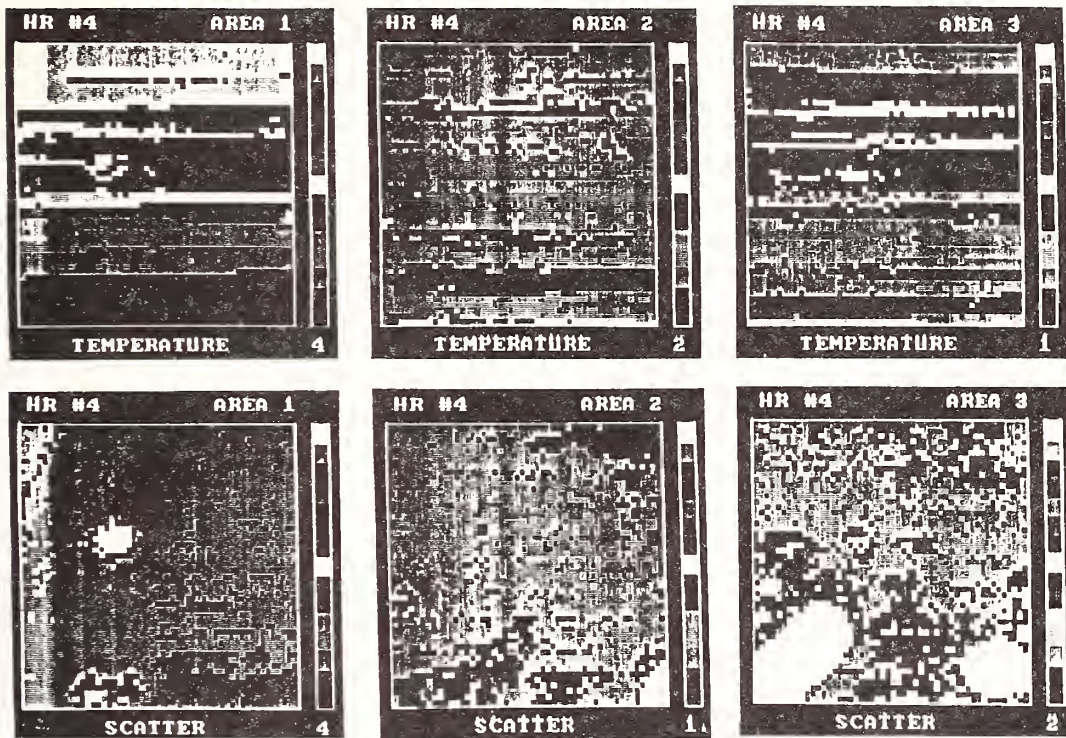
Pulsed damage testing  
1-on-1 testing, 1064 nm  
132 sites

Commercial high reflectors at 1064 nm

Silica/zirconia qw stack

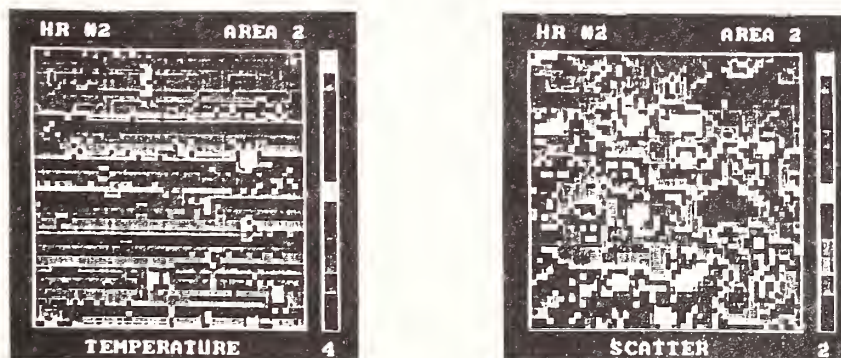
Fig. 5





Thermal response maps and scattered light data for areas 1-3 of high reflector number 4.

Fig. 6



Thermal response map and scattered light data for area 2 of high reflector number 2.

Fig. 7

## COMMENTS

Question: Can you say anything about the absorption coefficients of these hot sites that you saw?

Answer: Well, I can tell you that the thermal signatures vary by factors of 10, 20, 30 above the surrounding area. We have no way of directly measuring the response of those sites using, say calorimetry. So, when we do calorimetry, we get an average response over the whole surface of the sample and there's no way for me to give you an absolute number. But the thermal signature does vary by factors of 10, 20, 30 and that seems to be a good indication that there are substantial differences between areas on those surfaces.

Question: Did you look at the large anomalies you said were related to pits, did you look very carefully at the pits, were they contaminants or are you pretty sure of what the nature was?

Answer: I can tell you that the larger sites all had an identical appearance, they all looked like, to me, larger versions of the micropits that we see in single shot damage. In terms of going back inside and looking for specific contaminants or something like that, no we didn't do any analysis. The similarity to the microscopic pit formation was really quite remarkable and it didn't hit me until I had 60 or 70 of these things sitting on the light table that this seemed to be a very consistent morphology.

Question: How did you determine the emissivity values that you gave. Did You look those up or did you figure them out?

Answer: When you're doing thermal measurements, you have to be careful of the bandwidth of your instrument that you are using for measurements and we tried to be as self-consistent as possible. So we measured the emissivity values for these samples comparing them directly at several different temperatures to reference surface with an emissivity that we assumed to be one or very close to it. And that was how we determined those.

Question: Have you thought about the possibility that some of these small anomalies may not be absorption anomalies, but rather anomalies in the spectral emissivity of the region. Because the thermal camera can't tell the difference if there's a change in the spectral emissivity, it will represent that as a temperature change.

Answer: That is quite correct. If the coating had an emissivity of 0.8 then a higher temperature would appear if the emissivity on a localized spot were 0.1. That is not a significant change between 0.8 and 0.1 in terms of the temperatures that we would measure. It does not correlate in magnitude to the changes that we are seeing on these sites. Now for the enhanced metal reflectors, it is possible that could play a role, but again, I would expect to be able to see a difference in the emissivity just visually using the microscope and maybe that is being naive, but there is a big difference between a surface emissivity of 1 versus 0.8, at least in visual light most of the time.

Question: It would also seem that local debonding or local variation in the thermal contact resistance between the coating and substrate could give a hot spot. Do you have any way of checking for that, for example, visually to look for elimination?

Answer: Yes, I would agree entirely with that analysis, I would say that these coatings that we used for the mapping experiments were commercial reflectors and they have their fair share of cosmetic defects. Very frequently the surface of the sample was masked completely with observable cosmetic defects that look like stains in the coating or by normal pits right where we wanted to look. Within the resolution of our transport between the various systems, that is the mapping stage and the microscope and the scatter stage, there was nothing to be seen. Under a Nomarski microscope I would normally expect to be able to see a debonded area or something like that. I can't say for sure, and it is worth checking out.



## Effect of n on 1 Laser Treatment on Damage Threshold of Selected Optical Coatings

John G. Wilder and Ian M. Thomas  
University of California  
Lawrence Livermore National Laboratory  
P. O. Box 5508; L-483  
Livermore, California 94550

### Abstract

Laser damage threshold improvement was observed in selected thin film coatings that were repeatedly irradiated by 1.06  $\mu\text{m}$ , 16 nsec pulse emitted by a laser with 30 Hz repetition rate. Each sample was first irradiated for one minute at separate sites (1 on 1 testing) to determine the laser damage threshold of the thin film. A separate site was multiply irradiated (n on 1 testing) using a pulse fluence that initially was arbitrarily low, then subsequently raised in a step-wise fashion until damage occurred.

Results indicate a significant increase in laser damage threshold of some thin film coatings due to this treatment.

### Introduction

High damage threshold high reflective (HR) optical coatings for Lawrence Livermore's next generation laser is one of the research efforts being pursued by the Advanced Laser Development Group at Lawrence Livermore National Laboratory. These goals include: 99.7% minimum reflection, 40 J/cm<sup>2</sup> damage threshold at 1.06  $\mu\text{m}$  and 10 nsec, and at 20% the cost of the present HR coatings presently used in Livermore's Nova laser.

Previous studies have indicated that optical films can be altered by subthreshold laser irradiation. M.E. Frink, et al.<sup>1</sup> performed post deposition laser treatment of antireflection (AR) coatings of unknown composition. They concluded that the increased damage levels measured as a result of this treatment were temporary. J.E. Swain, et al.<sup>2</sup> studied post coating laser irradiation of neutral solution AR coatings and concluded that a damage threshold level improvement of 2.5 times that of the pretreated coating could be realized. James Rowe<sup>3</sup> reported that laser irradiation during evaporation deposition of selected coatings produced films with absorption one half that of the same coatings deposited without co-irradiation.

Alteration of bulk properties of optical materials through multiple shot irradiation has also been demonstrated. Multiple irradiation of new crystals of potassium dihydrogen phosphate (KDP) increased its bulk damage threshold by about a factor of two<sup>4</sup>. Tsutomu Shimizu, et al.<sup>5</sup> reported an innovative experiment where a disseminated absorbing species (silicon) was removed from a silica matrix via irradiation with a 308 nm and 575 nm laser.

This effort reports the results of some initial experiments of a post deposition laser treatment process on selected reflective (R) and HR coatings.

### Samples

Six R or HR coatings deposited on 5 cm diameter high purity silica substrates were tested. Two were electron beam (e-beam) dielectric HR coatings consisting of a 15 layer quarter wave design with a half wave silica overcoat. The compositions were hafnia/silica and zirconia/silica, and the primary reflection was tuned to 1.06  $\mu\text{m}$ . Four coatings, three sol-gel, and one made by evaporation, were produced by the authors. The sol-gel coatings were a single layer zirconia, a four layer alumina/silica and an eight layer alumina/silica, all having the primary reflection at 1.06  $\mu\text{m}$ . The evaporated coating was a single layer lead fluoride of undetermined thickness.

## Experiment

The 1 on 1 damage threshold of each virgin coating was first determined. One on 1 damage testing is defined as a single location being irradiated by 1.06  $\mu\text{m}$ , 16 nsec, 30 Hz repetition rate laser for one minute at a single fluence. The n on 1 threshold for each coating was then measured. N on 1 damage testing consisted of a single location being irradiated as per 1 on 1 tests; however, after a one minute exposure to sub-damage threshold intensity radiation the fluence was increased by 1-3  $\text{J}/\text{cm}^2$ , and the procedure repeated at the same location. The results are graphically illustrated (Figs. 2 thru 7). This step wise procedure was repeated with microscopic inspection between fluence increases until at least 5% of the irradiated area was damaged. Each irradiated area was visually inspected with a 100X Nomarski microscope. The area damaged was determined by measuring the size of the largest damage sites, totaling the number of sites, and reading total area percent of damage versus fluence of these samples (Fig. 1). Arrows extending above the data points in Fig. 2 thru 7 indicate catastrophic damage covering at least 50% of the irradiated area.

## Results and Discussion

On all e-beam samples, n on 1 treatment resulted in a sizable improvement in laser damage threshold. The improvement was most dramatic with the  $\text{ZrO}_2$  HR sample. The  $\text{HfO}_2$  HR sample had as high a damage threshold as the  $\text{ZrO}_2$  but the increase from 1 on 1 to n on 1 was less. In both cases, shown in Figs. 2 and 3, damage had not occurred at the laser's maximum fluence, of 50  $\text{J}/\text{cm}^2$ .

The single layer  $\text{ZrO}_2$  sol-gel was unaffected by the n on 1 treatment, and the damage thresholds were not impressive. Subsequent to these tests, it was discovered that the  $\text{ZrO}_2$  solgel precursors were contaminated with iron, which probably is the reason for the low damage threshold of this sample compared to the  $\text{ZrO}_2$  e-beam HR coatings.

The  $\text{Al}_2\text{O}_3$  sol-gel coatings were also improved by the n on 1 treatment. This improvement was not quantified because the n on 1 damage threshold was above the 50  $\text{J}/\text{cm}^2$  maximum fluence of the testing laser.

The  $\text{PbF}_2$  damage thresholds were identical and well defined. This result may indicate an absorption in  $\text{PbF}_2$  that is intrinsic.

Results of these initial experiments do not allow determination of the mechanism that caused n on 1 and 1 on 1 thresholds to differ for some, but not all, of the coatings tested. If repeated irradiation increases the threshold, the irradiation must either reduce absorption of laser light or increase the mechanical toughness of the sample. Since sol-gel samples, which are mechanically weak, have thresholds comparable to those of e-beam deposited films, it is unlikely that thresholds are strongly affected by mechanical strength. Therefore, we believe absorption was reduced.

If we assume that damage results from laser heating and rapid volatilization of isolated absorbing volumes, removal of these discrete impurities would increase the threshold. Slowly evaporating the absorbers by repeated, low level irradiation might allow their removal without the explosive evaporation that occurs when the absorbers are exposed to a single intense pulse. Coatings that were porous and contained only a few, widely separated absorbers would be most likely to exhibit threshold improvement. Dense coatings, or those with uniformly distributed absorption, would probably be severely damaged even during slow removal of absorbing material. This model would allow the improvement by laser treatment of some coatings and lack of improvement in others, in keeping with our observations.

\*Work performed under the auspices of the U. S. Department of Energy by the Lawrence Livermore National Laboratory under contract number W-7405-ENG-48.



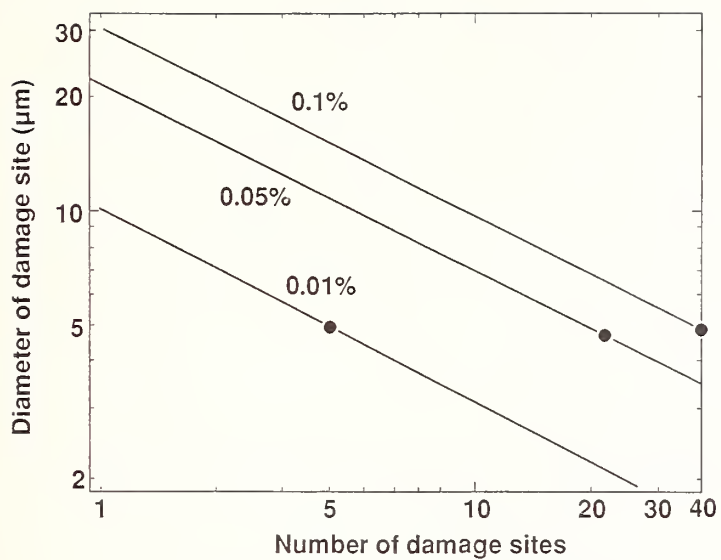


Fig. 1. Damaged area of a 1 mm beam (%)

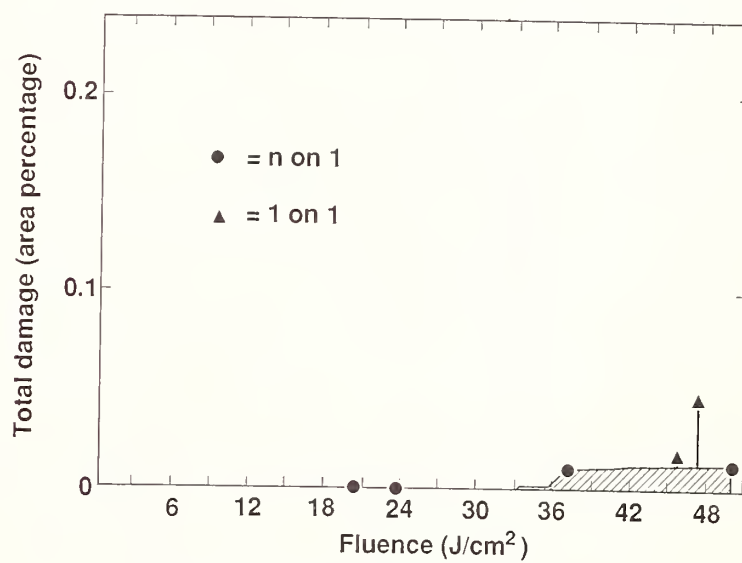


Fig. 2.  $[\text{HfO}_2\text{-SiO}_2]^8$  e-beam

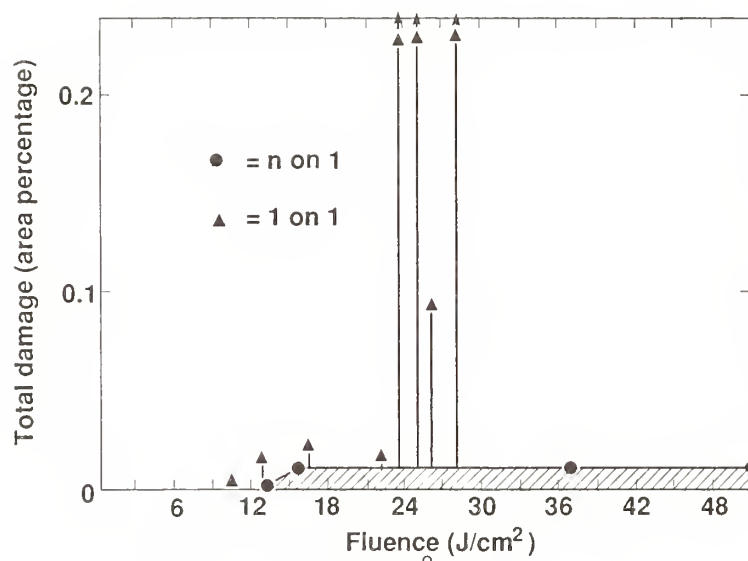


Fig. 3.  $[\text{ZrO}_2\text{-SiO}_2]^8$  e-beam

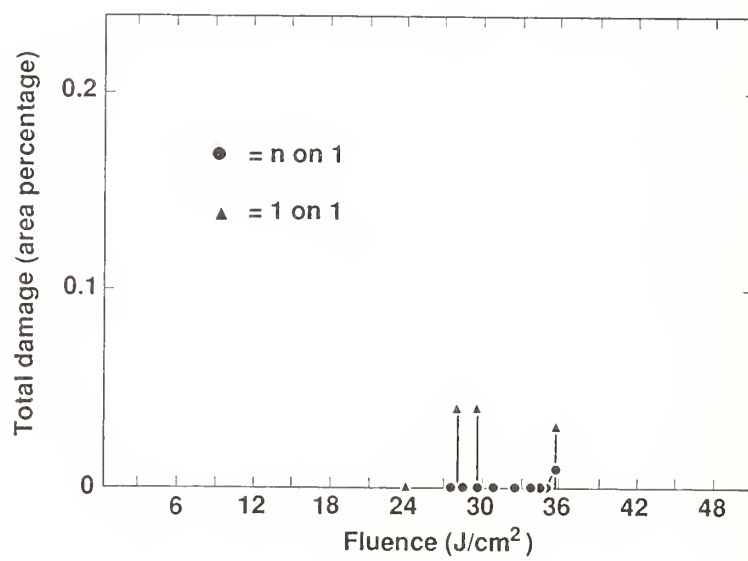


Fig. 4.  $[\text{SiO}_2\text{-Al}_2\text{O}_3]^4$  sol-gel

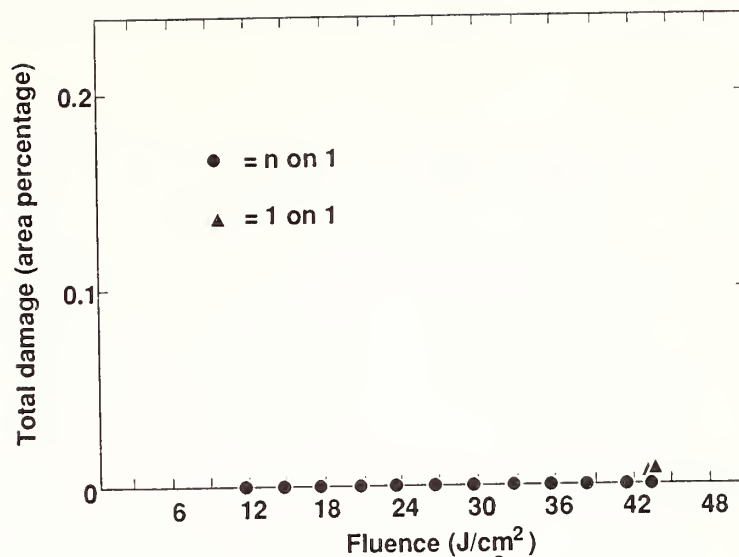


Fig. 5.  $[\text{SiO}_2\text{-Al}_2\text{O}_3]^2$  sol-gel

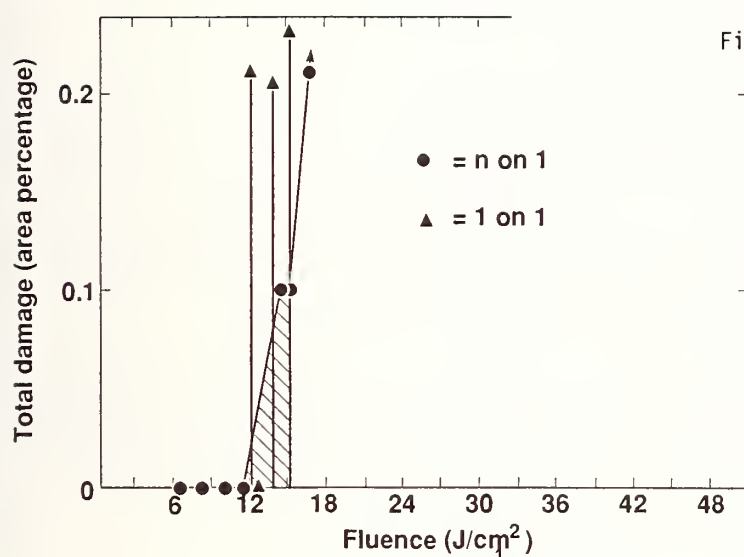


Fig. 6.  $[\text{ZrO}_2]^1$  sol-gel

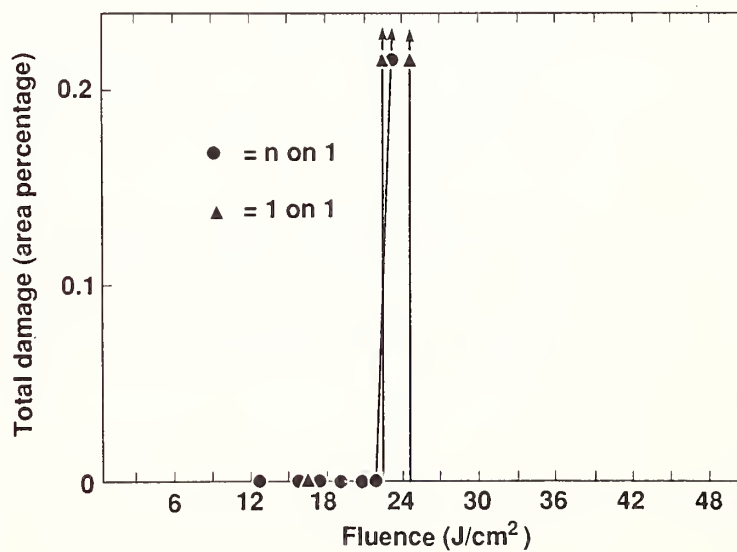


Fig. 7.  $[\text{PbF}_2]^1$  evaporated

## References

1. M. E. Frink, J. W. Arenberg, and D. W. Mordant, "Temporary Laser Damage Threshold Enhancement by Laser Conditioning of Antireflection-Coated Glass", Applied Physics Letters 51(6), (1987).
2. J. E. Swain, W. H. Lowdermilk, D. Milam, "Raising the Surface Damage Threshold of Neutral Solution Processed BK-7 by Pulse Laser Irradiation", Laser Induced Damage in Optical Materials, NBS Special Publication 669, 1982.
3. James M. Rowe, Laser-Assisted Deposition Coatings, AFWL-TR-83-34, March 1983.
4. J. Swain, S. Stokowski, D. Milam, and F. Rainer, "Improving the Bulk Laser Damage Resistance of Potassium Dihydrogen Phosphate Crystals by Pulsed Laser Irradiation", Applied Physics Letters 40(4), February 15, 1982.
5. Tsutomu Shimizu, Noriaki Itoh, Noriaki Matsumami, "Laser-induced Re-emission of Silicon Atoms Implanted into Quartz," J. Appl. Phys. 64(7), (1988).

## COMMENTS

Question: You did not mention the damage level you observed on these coatings.

Answer: Yes, they are slightly less than the damage levels that we get with our porous single layer coating. That is higher than KDP or LAP substrates and a little lower than fused silica at whatever wavelength you wish to take.

Question: Were any damage tests done on the two layer structures. What were the results?

Answer: I am sorry, perhaps you are not familiar with the damage figures that we get. At 350 nanometers, for example, at 0.6th of a nanosecond we are in this sort of 6 to 8 joules range and one is six at one nanosecond about 15, at 10 nanoseconds about 30-35.

Question: This was with a combination of zirconium oxide and silicon?

Answer: Yes, and the figures I have quoted actually were done on the sample on fused silica. As I say, on KDP substrate damage is before the coatings, so we were not able to get a figure. I am assuming that the damage thresholds that we get on silica, fused silica substrates will be the same as we get on KDP.

Question: Can you say anything about the stability of these coatings say over a day, week, month, year?

Answer: Yes, we have, as you are aware, the porosity is such that we have a high surface area and the coatings do absorb material.. We have found that the absorption when they are exposed to atmospheric type conditions is no problem, but under a vacuum they are quite severe. We solved this problem at Livermore by washing the coatings frequently with an alcohol spray. We just spray the coating down and let the liquid drain down and that in effect renews the material back to pristine conditions.



MANUSCRIPT NOT RECEIVED

=====

TWO LAYER BROADBAND AR COATING\*

Ian M. Thomas  
Lawrence Livermore National Laboratory  
University of California  
P.O. Box 5508, L-490  
Livermore, California 94550

ABSTRACT

A two layer broadband AR coating has been developed specifically for use with harmonic converter crystals where surfaces must transmit light of two different wavelengths. The coating consists of a methyl silicone or sol-siloxane layer with refractive index 1.4 overcoated with porous silica of index 1.22. Less than 0.5% reflection at 1064 nm and 532 nm or at 532 nm and 355 nm is obtained on KDP and even lower reflections with LAP.

The laser damage threshold at 1064 nm is better than that of the bare substrate surface.

\*Work performed under the auspices of the U.S. Department of Energy by Lawrence Livermore National Laboratory under Contract No. W-7405-ENG-48.

MANUSCRIPT NOT RECEIVED

SCANNING TUNNELING MICROSCOPY STUDY OF THE  
EFFECTS OF PULSED HIGH POWER LASER IRRADIATION ON CARBON,  
SILICON CARBIDE, AND GOLD SURFACES

Wigbert Siekhaus, Thomas Beebe, and Markus Schilbach  
Lawrence Livermore National Laboratory  
Livermore, CA 94550

ABSTRACT

Despite many years of study, the details of the interaction of high power laser pulses with surfaces of insulating, semiconducting and conducting materials are not understood. Though it has been shown that optically visible surface irregularities reduce the surface damage threshold, little is known about the effect of the laser beam (at or below the damage threshold) on submicroscopic irregularities.

Scanning tunneling microscopy can determine the three dimensional physical structure and the electronic structure of surfaces with atomic resolution and is, therefore, uniquely suitable to investigate the effect of irregularities in physical and electronic surface structure on damage phenomena. This paper reports our preliminary STM observations of the effect of pulsed laser irradiation of surfaces.

The scanning tunneling microscope used is a variation of Lyding's<sup>1</sup> design, in which both the tunneling needle and the target are held by tubular piezoelectric crystals, a design, which leads to very high vibrational and thermal stability, and allows reproducible movement of the target in and out of the tunneling range by purely electronic means without the use of mechanical devices. The tunneling needle is Pt/Rh.

The specimens were either cleaved in air (C) or mechanically (SiC) or electrochemically polished (au), and showed before irradiation flat areas with atomic corrugation and steps one or several atoms high. The surface disorder created by exposure to a pulsed YAG laser beam ( $\lambda = 1064$  nm, 5 ns pulse duration) will be shown.

<sup>1</sup> J.W. Lyding, S. Skala, J.S. Hubacek, R. Bockenbrough, G. Gammie, "A Variable Temperature Scanning Tunneling Microscope," APS Regional Meeting, New Orleans (1988).

## Tarnishing Measurements of $\text{Al}_2\text{O}_3$ Overcoated Silver Mirrors

W.D. Kimura

Spectra Technology, Inc.  
Bellevue, Washington 98004-1495

Q.D. Appert, P.N. Arendt, V.E. Sanders, and M.L. Scott

Los Alamos National Laboratory  
Los Alamos, New Mexico 87545

Presented are tarnishing results for silver mirrors protected using a technique, developed at Los Alamos National Laboratory, of applying a very thin overcoat (10 Å) of alumina ( $\text{Al}_2\text{O}_3$ ) on the bare silver surface. The s-polarization absorptance characteristics of the overcoated mirrors at 0.5145 and 1.06  $\mu\text{m}$  are measured as a function of incidence angle (0-88°) using a photoacoustic calorimetry technique developed at Spectra Technology, Inc. Measurements are also performed on bare silver mirrors. When untarnished, both types of mirrors give similar results. The mirrors were exposed to room air and allowed to tarnish naturally for >120 days. It is found that the bare silver mirrors suffered severe tarnishing; whereas, the overcoated silver mirrors had a significantly greater resistance to tarnishing.

Key words:  $\text{Al}_2\text{O}_3$ ; alumina; glancing incidence; photoacoustic calorimetry; silver mirrors; tarnishing

### 1. Introduction

Silver mirrors are highly reflective at visible and near infrared wavelengths, which makes them desirable for high power laser applications. Even higher reflectivity is possible by using the mirrors at glancing or grazing angles of incidence [1]. Besides the high power laser community, there is also interest in using silver mirrors for astronomical applications.

One drawback with bare silver is that once exposed to room or outside air, silver sulfide quickly forms on the mirror surface. It has been found that glancing incidence operation is particularly sensitive to this tarnishing effect [2].

Typically, dielectric overcoats on the bare silver have been used to prevent this tarnishing. This overcoat can affect the mirror reflectivity properties, especially at glancing angles of incidence [3]-[4]. Dielectric coatings are also known to have lower damage thresholds than bare metals. There have been other attempts to reduce this susceptibility to tarnishing, such as using copper underlayers [5], but this has been shown to provide insufficient protection [2].

At Los Alamos National Laboratory (LANL), two of the authors (P. Arendt and M. Scott) developed the novel idea of applying a very thin overcoat of alumina ( $\text{Al}_2\text{O}_3$ ) onto the bare silver mirror surface. Their initial tests of the tarnishing resistance of the alumina overcoated mirrors by exposing them to fuming ammonium sulfide showed that an alumina layer as thin as 10 Å appeared to still significantly retard the tarnishing process.

This paper describes tarnishing measurements performed at Spectra Technology, Inc. (STI) of alumina overcoated mirrors. The objectives of these measurements were to measure the absorptance characteristics of new bare silver and overcoated mirrors, expose the mirrors to laboratory room air (>120 days), and periodically remeasure the absorptance to detect any tarnishing.

### 2. Description of Mirrors

Two sets of bare silver and alumina overcoated mirrors were tested. The coating parameters are the same for both sets; however, one set was coated at LANL and the other set was coated at Spectra Physics Optics Division, Mountain View, CA. The 10 Å alumina (purity: 99.99%)

overcoat is evaporated onto a silver layer of thickness 1900 Å. Underneath the silver layer is a chromium underlayer of 100 Å. The mirror substrates are polished silicon [5 cm (2") diameter x 0.6 cm (0.25") or 1.3 cm (0.5") thick] with 5-10 Å rms roughness.

Bare silver mirrors with the same silver and chromium thicknesses were also coated on the silicon substrates. The mirrors were shipped to STI in special nitrogen-purged shipping containers sealed with Viton o-rings. Once at STI, the mirrors were stored in nitrogen-filled metal containers until ready for testing.

### 3. Description of Experiment

The glancing incidence absorptance properties of the mirrors are measured using a photoacoustic calorimetry system developed at STI [6]. This system is shown schematically in figure 1. The output from a cw laser (argon ion or Nd:YAG) is sent through a chopper, a collimating telescope, a half-wave plate to rotate the laser beam polarization, a "clean-up" polarizer oriented in the same direction as the half-wave plate to remove any light not rotated by the plate, and then to the mirror under test. On the back of the mirror is attached a piezoelectric transducer that detects the strain wave generated by laser energy absorbed on the surface of the mirror. Using a phase-sensitive lock-in amplifier, this system is able to detect the very small laser absorption on the mirror surface that occurs at glancing angles of incidence [1].

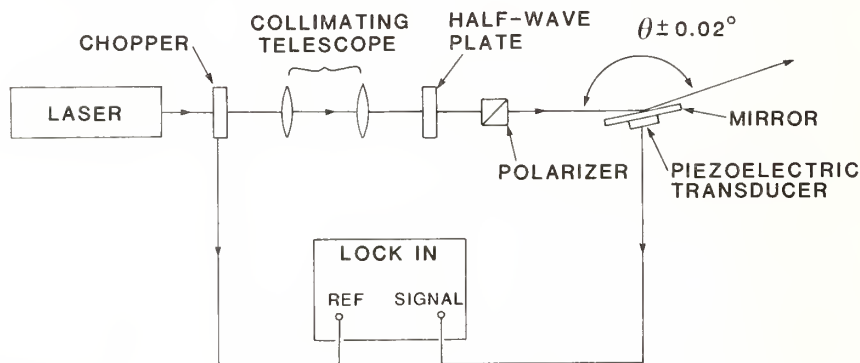


Figure 1. Schematic of glancing incidence measurement apparatus.

Although extremely sensitive and having a wide linear range, photoacoustic calorimetry is only a relative measurement. The absolute absorptance calibration of the photoacoustic calorimetry data is accomplished by using a laser energy ratiometer to measure the incident and reflected laser light at near normal incidence to the mirror. This is shown schematically in figure 2.

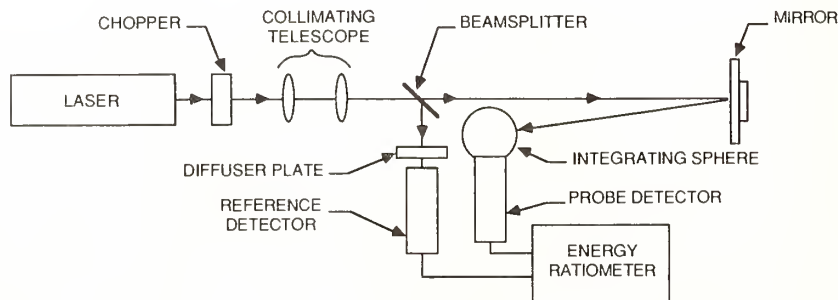


Figure 2. Schematic of absolute absorptance calibration apparatus.



A beamsplitter is inserted into the laser beam after the collimating telescope. The reflected beam off the beamsplitter is used as the reference to normalize out any power fluctuations from the laser. A second detector serves as the probe to measure the transmitted laser energy through the beamsplitter and the reflected energy off the test mirror. An integrating sphere attached to the probe detector helps reduce sensitivity to alignment position when moving the detector to measure the incident and reflected light. Typically, many chopped laser pulses are averaged at each probe detector position and an average of incident-to-reflected ratios are obtained by moving the detector back and forth several times to measure the incident and reflected laser light. Despite this care to minimize errors in the absolute absorptance calibration, the values quoted in this paper for the absolute absorptance tend to be slightly high from those measured by others [7]. This is probably due to incomplete collection by the integrating sphere of all the reflected light off the mirror (i.e. not all the scattered light is being collected). Nonetheless, the overall trends of the data given in the paper are valid, including any relative increase in absorptance observed.

The mirrors were first measured in their untarnished state at 0.5145 and 1.06  $\mu\text{m}$  for s-polarization (perpendicular to the plane of incidence). They were then exposed to the air-conditioned laboratory room air (temperature:  $21.6^\circ\text{C} \pm 0.9^\circ\text{C}$ , relative humidity:  $39.0\% \pm 4.5\%$ ). The room is a nonsmoking area and exhaust from a vacuum pump in the room is piped outside to avoid possible contamination by pump oil vapors. The mirrors are stored in an inverted position to prevent accumulation of dust and held so that nothing touches the mirror surface.

#### 4. Tarnishing Results

Figure 3 shows the tarnishing results for a bare silver mirror exposed to room air for over 40 days. The wavelength for this data is 0.5145  $\mu\text{m}$  and the angle of incidence is  $0^\circ$ . It is clear that the bare silver mirror has tarnished a great deal.

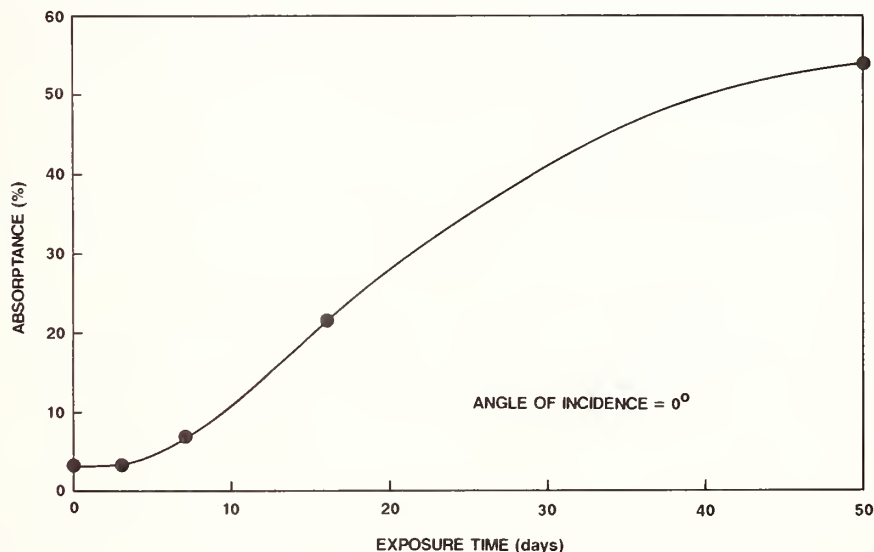


Figure 3. Absorptance of a bare silver mirror at 0.5145  $\mu\text{m}$  (s-polarization) at  $0^\circ$  angle of incidence as a function of exposure time to room air.

The results at 1.06  $\mu\text{m}$  for the LANL overcoated mirror are given in figure 4 for normal and  $88^\circ$  angle of incidence. There is little tarnishing evident after nearly 140 days of exposure. Although this is very encouraging, the affects of tarnishing tend to be more evident at shorter wavelengths.

Figure 5 shows the results for the same mirror presented in figure 4 at 0.5145  $\mu\text{m}$ . Note that little tarnishing is detected until roughly 120 days. At that point there is a definite increase in absorptance observed at both normal and  $88^\circ$  angle of incidence. Indeed, visual inspection of the LANL overcoated mirror surface using a high intensity microscope lamp revealed a faint haze starting to develop on the surface. This haze is similar to that seen on the bare silver mirror during the very early stage of its tarnishing (i.e. after only a few days of exposure).

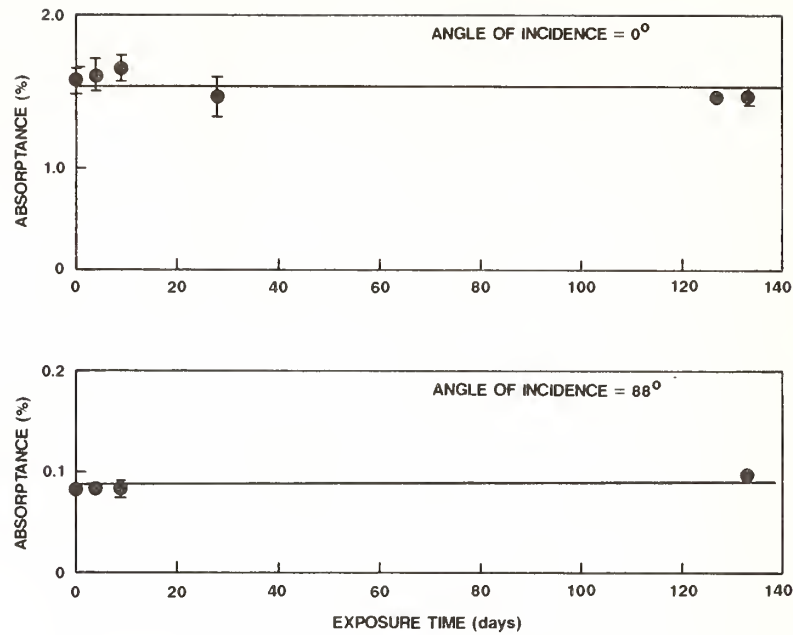


Figure 4. Absorbance of the LANL alumina overcoated silver mirror at  $1.06 \mu\text{m}$  (s-polarization) as a function of exposure time to room air. The top and bottom graphs are for  $0^\circ$  and  $88^\circ$  angle of incidence, respectively.

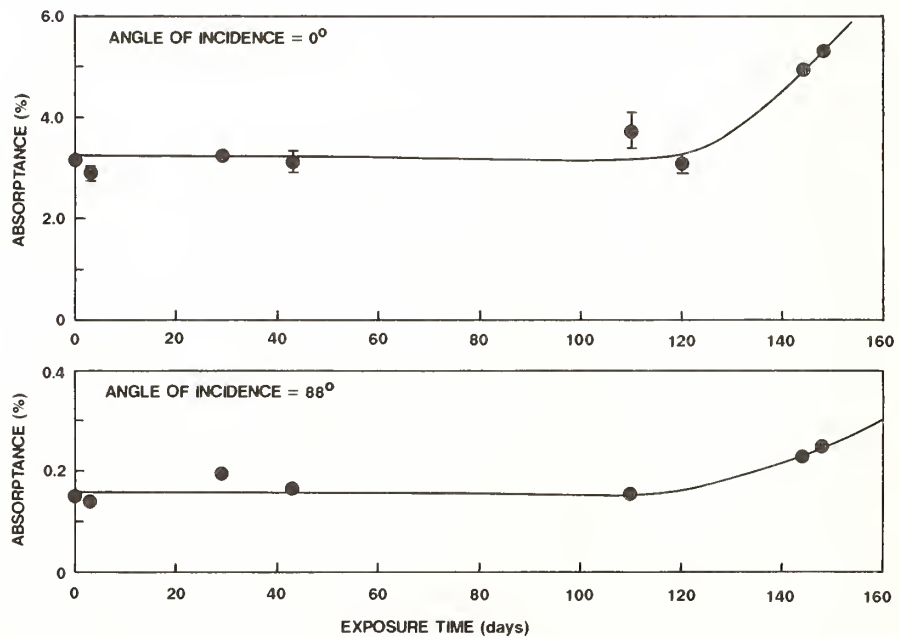


Figure 5. Absorbance of the LANL alumina overcoated silver mirror at  $0.5145 \mu\text{m}$  (s-polarization) as a function of exposure time to room air. The top and bottom graphs are for  $0^\circ$  and  $88^\circ$  angle of incidence, respectively.

An interesting contrast to this apparent slight tarnishing behavior of the LANL overcoated mirror are the results for the Spectra Physics (SP) overcoated mirror shown in figure 6. This data is also at  $0.5145\ \mu\text{m}$  and one would expect it to be similar to the results for the LANL mirror given in figure 5. However, the SP overcoated mirror results behave in an almost counter fashion to the LANL overcoated mirror. The SP mirror shows evidence of an increase in absorptance during the first 60 days of exposure, but this increase levels off thereafter and shows no further tendency to grow. Note also, that the SP mirror starts out at a lower absolute absorptance than the LANL mirror, but levels off to approximately the same absorptance value as the LANL mirror during its first 120 days.

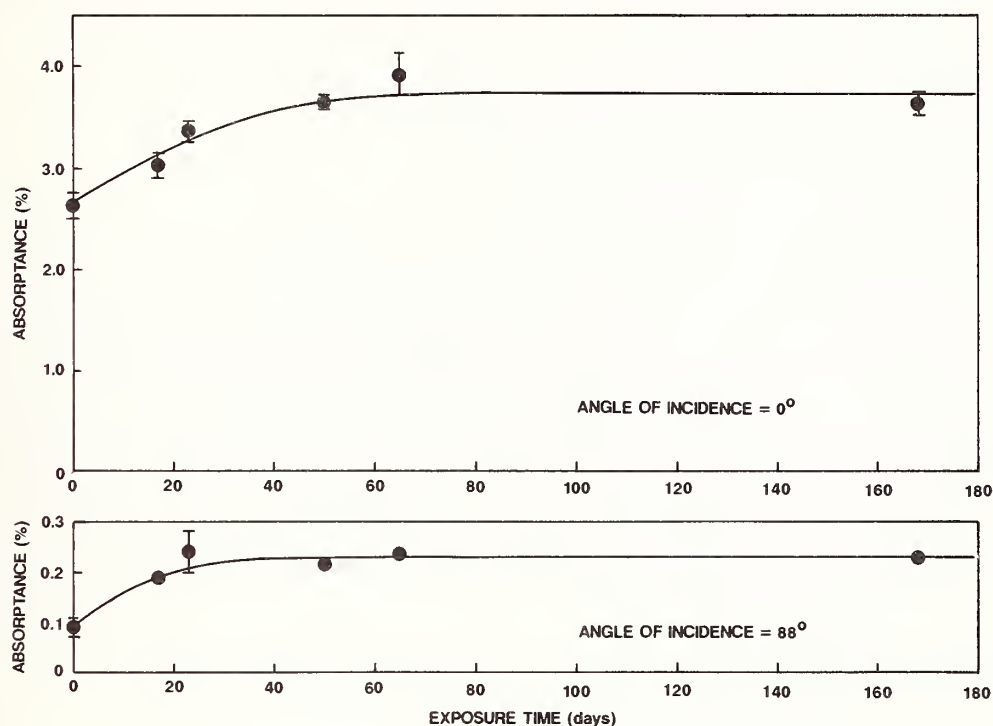


Figure 6. Absorptance of the SP alumina overcoated silver mirror at  $0.5145\ \mu\text{m}$  (s-polarization) as a function of exposure time to room air. The top and bottom graphs are for  $0^\circ$  and  $88^\circ$  angle of incidence, respectively.

## 5. Discussion

It is difficult to understand the different tarnishing behaviors of the two sets of overcoated mirrors. There are several behaviors that are puzzling. The fact that the LANL mirror clearly shows signs of tarnishing after 120 days implies that the overcoat does not permanently stop the onset of tarnishing; however, this apparent onset is rather abrupt. That is to say a more gradual increase in absorptance might be expected if the overcoat were only partially protecting the surface (cf. Ref. 2). This seems to imply that the overcoat does completely protect the surface, but that something changes after a period of time that stops this protection. What this might be is not known.

The increase in absorptance of the SP mirror during its first 60 days of exposure would seem to imply that it was tarnishing; however, it is not clear why this apparent tarnishing would stop and the absorptance level off to a constant value. If it was truly tarnishing, one might expect the absorptance to increase in a manner similar to that seen with the bare silver mirror (see figure 3).

Clearly, more work is needed to fully understand the tarnishing behaviors observed. There is also a need to understand why mirrors coated supposedly the same way by two different facilities do not have the same tarnishing protection characteristics.

## 6. Conclusion

The tarnishing resistance advantage of a thin alumina overcoat on a bare silver mirror has been demonstrated. Although aspects of the tarnishing behavior of the test mirrors are not completely understood and there may be an issue related to reliably reproducing the protection afforded by the overcoat, it is clear that the alumina overcoated silver mirrors are superior to bare silver mirrors.

Unlike silver mirrors with thick dielectric overcoats, the thin overcoat does not significantly change the reflectivity properties of the mirror, both in its absolute magnitude and its dependence on angle of incidence. Laser damage tests [8] also indicate that the damage threshold of the overcoated mirror is similar to that of the bare silver mirror.

This work was supported by Los Alamos National Laboratory, Contract No. 9-X18-8599Q-1.

## 7. References

- [1] Kimura, W.D.; Ford, D.H. Absorptance measurements of metal mirrors at glancing incidence. *Appl. Optics*. 25(20): 3740-3750; 1986.
- [2] Kimura, W.D. Absorptance characteristics of silver and silver-on-copper mirrors. *Appl. Optics*. 26(12): 2450-2455; 1987.
- [3] Kimura, W.D.; Woodberry, F.J.; DeSandre, L.F. Model Comparisons With Glancing Incidence Measurements of Overcoated Metal Mirrors. Laser Induced Damage in Optical Materials: 1986. Natl. Inst. Stand. and Tech., Spec. Publ. 752: 684-692; 1988.
- [4] Kimura, W.D. Performance of Overcoated Mirrors Designed for Glancing Incidence Operation. O-E/LASE '89, Mirrors and Windows for High Power/High Energy Laser Systems, Los Angeles, CA; 1989 Jan. 15-20.
- [5] Song, D.Y.; Sprague, R.W.; Macleod, H.A.; Jacobson, M.R. Progress in the Development of a Durable Silver-Based High Reflectance Coating for Astronomical Telescopes. *Appl. Optics* 24: 1164; 1985.
- [6] Kimura, W.D.; Ford, D.H. Photoacoustic calorimetry system for glancing incidence mirror absorptance measurements. *Rev. Sci. Instrum.* 57(11): 2754-2762; 1986.
- [7] Basegio, Larry. Spectra Physics Optics Division, private communication.
- [8] Sanders, V.; Jolin, L.; Salazar, S. Damage to Silver Coatings From High Average Power 1 Micron Laser. 20th Annual Symposium on Optical Materials for High Power Lasers. Boulder, CO. 1988 Oct. 26-28.



## The Formation of Laser-Induced Ripple Structures

N. C. Kerr, S. E. Clark and D. C. Emmony

Loughborough University of Technology,  
Department of Physics,  
Opto-electronics Laboratory,  
Loughborough,  
Leics, LE11 3TU  
United Kingdom.

We report the results of an investigation into the formation mechanism of Laser Induced Ripple Structures (LIRS) on Gallium Arsenide and Germanium. This investigation is based upon obtaining direct images of a surface whilst the transient heating induced by a low fluence excimer laser pulse is still present. To obtain the images a high resolution Schlieren imaging system based upon a computer controlled video framestore was used. The images revealed that an excimer pulse causes transient periodic heating patterns on the surface of an irradiated sample. If enough subsequent excimer pulses are incident on the surface permanent ripple structures develop. It is evident from these transient images that the surface heating is confined to the induced structures, thus strongly supporting the idea that at low fluences the ripples are formed by localised surface melting.

Key words: Laser damage; Ripple structures; Schlieren imaging; Transient heating.

### 1. Introduction

Many authors, as a result of performing investigations into the interaction of intense laser beams with solids, have noted the formation of well defined periodic damage patterns [1-8]. It is generally accepted, as first proposed by Emmony et al [2], that the cause of these structures is interference between the incident laser light and some form of induced 'surface wave'. Attempts have been made to formally model the mechanism responsible for the formation of LIRS, notably by Emel'yanov et al [7], Temple and Soileau [8], and in particular by Sipe et al [9,10,11].

Inherent in all theories of LIRS is the basic premiss that in order to form such structures there must be a periodic temperature profile induced on the surface. This study is an attempt to validate or otherwise this assumption. It is based upon using a high resolution Schlieren imaging system linked to a short pulsed dye laser to monitor the test surface, with the aim of capturing images of the surface whilst the transient heating induced by a KrF excimer laser is still present.

### 2. Experimental Technique

The damage facility at Loughborough University [5] centres around a Lambda Physik model EMG 200 excimer laser that is operated with a KrF gas mix and produces nominal 1 J pulses of 20 ns duration at 249 nm.

Our intention was to image any transient heating effects induced on the surface before the number of excimer pulses required to produce permanent ripples had been incident on the surface. Once such data had been obtained the surface would be permanently rippled by exposure to further pulses, and a comparison between the images of transient heating and permanent rippling made.

Central to the requirements to be able to perform these experiments is a high resolution Schlieren [12] imaging system. This system is based upon using a computer controlled video framestore linked to CCD type video cameras. Hardcopy was obtained by using a 3M Dry Silver Imager. Figure 1 schematically illustrates the experimental arrangement used to obtain our results. Two video cameras are used in the system, one to monitor the surface in real time, the other linked to the framestore and used to record transient events.

A 10 mW cw HeNe laser was used to monitor the surface in real time for any obvious signs of damage or LIRS. The light source for imaging the transient effects was a FL2000 dye laser synchronously pumped by the excimer beam and operated at 514 nm. Previous work [5] has shown that the heating effect at the surface was greatest immediately after the excimer pulse, and consequently by suitably reflecting the dye laser beam around the work area a 20ns delay between the arrival of the excimer and dye beams on the test surface was obtained. Narrow bandpass optical interference filters were used to ensure that each camera saw either the HeNe or dye beam but not both.

In order to separate the transient effects from dust and other scattering sites already on a surface, a sequence of 3 dye laser images was used. The first image (labelled as a) was of the unheated surface. This was obtained by having the dye beam incident upon the surface but not the excimer pulse. The second (labelled b) was an image of the surface immediately after an excimer pulse. This image was obtained by having both the excimer and then the dye beam incident upon the surface. This image shows the transient heating caused by the excimer pulse. Finally the third image (labelled as c) was taken a long time after the incident excimer pulse with just the dye laser incident on the surface. These images were then computer processed. This processing consisted of intensity normalisation followed by subtraction and enhancement. Computer processing of images a and b enabled the net transient effects to be separated from those associated with dust etc that was on the surface, whilst processing a and c enabled any permanent changes to be detected. Once the surface had been suitably permanently rippled by exposure to further excimer pulses, a dye laser image of the surface was obtained to allow comparisons of transient and permanent effects to be made.

S polarised excimer light was obtained by using the reflected light from a single quartz beam splitter orientated at Brewster's angle. Typically the excimer fluence was chosen so as to produce permanent ripples somewhere in the beam target interaction area after about 20 pulses. A sequence of transient images was recorded for each incident excimer pulse until the surface was permanently rippled over its whole area. This overall pattern developed in stages as subsequent excimer pulses were incident upon the surface.

The surfaces used were polished Ge and GaAs mirrors, which prior to irradiation with the excimer laser had no special treatment except a wipe using Methanol to remove dust etc.

### 3.Results

The excimer laser induced transient surface heating was found to be uniform until approximately five excimer pulses before the production of permanent ripples. At this point there were the first indications of periodic heating. In general, the best results were obtained in the interval between the surface being just about to permanently ripple (i.e. within 1-2 excimer pulses) and being substantially covered in them.

Figures 2a-e are results which were obtained on GaAs irradiated by S polarised excimer light incident at 60° where the ripple spacing is  $\approx 2.2 \mu\text{m}$ . Figure 2a was obtained after the

surface first showed permanent ripples with only the dye laser incident whilst figure 2b is an image of the transient surface heating induced by the next excimer pulse obtained by having the dye incident on the surface immediately after the excimer laser. Figure 2c is the surface a long time after the pulse of figure 2b with only the dye beam incident.

Inspection of figures 2a and c shows small permanent ripples on the right hand side of the image with essentially no ripples left of centre. It is just apparent from figure 2b that substantial transient periodic heating appears to the left of centre. Processing of figures 2a and c yields 2d the net permanent change whilst figures 2a and b yield 2e the net transient change. Comparison of these two images readily shows that the induced transient heating is periodic with the same spacing as the permanent ripples.

Figures 3a and 3b are processed images again for S polarised light incident at 60° on GaAs, but show transient periodic heating without any permanent ripples being initially present or formed as a result of the incident excimer pulse. The transient nature of the pattern can be clearly seen.

Figure 4 is another sequence of processed images on GaAs with S polarised light incident at 60°, and shows that initially transient heating patterns give rise to permanent ripples after sufficient incident pulses. Figure 4a is a processed image showing the permanent effect on the surface after 30 pulses have been incident and shows that no permanent rippling has occurred up to this point. Figure 4b shows the transient effect caused by the next incident excimer pulse. Figure 4c is an image of the surface after 4 more incident excimer pulses and shows that permanent ripples have formed. Close inspection of figures 4b and c reveals that the areas of transient periodic surface heating towards the right hand edge of the images have become well defined permanent ripples.

Results on Ge were very similar to the above except that the quality i.e. the definition of the ripples was less than those found on GaAs. It was noted that on Ge, the surface became mottled before even transient heating patterns were observed whereas, on GaAs it went directly from smooth to rippled. The consequence of the mottling on Ge was that it reduced the quality of the images, particularly when separating transient heating patterns from the surface mottling. Typical of the results is figure 5 which shows the transient heating pattern of spacing 6  $\mu\text{m}$  induced on Ge by S polarised light incident at 60°. The spacing of this pattern, which appears anomalously large, will be discussed in the next section.

Attempts to quantify the transient temperature profile across test surfaces by computer analysis using routines originally written for laser beam profiling were made [5]. Due to the small ripple spacing, these measurements were restricted on GaAs but indicated that any surface heating was localised to the vicinity of the ripple. As a result of the larger ripple spacing on Ge it was possible to further pursue these measurements. Figure 6b shows the temperature profile through a transient heating pattern on a surface of Ge along the vertical line in figure 6a, and it can be seen that between the ripples there is essentially no surface heating.

It was also noted that on a well rippled surface it required a fluence only a fraction e.g. 10% of that used to induce the ripples to cause further permanent changes on the surface

#### 4. Discussion

The results that we have obtained not only validate the basic assumption that the surface must have a periodic temperature profile but also, for the excimer fluences used, the idea of localised melting in the process of ripple formation.

Young et al [11] by measurement of specular reflectivity and first order transient diffraction as opposed to direct surface imaging, showed that there are 4 regimes of LIRS formation dependent upon the incident laser fluence. At low fluence the surface undergoes



localised melting i.e. melts only in the vicinity of the E field maximum such that the surface consists of a periodic array of molten strips. Under these conditions, good agreement of the ripple spacing and that predicted by the theory in reference [9] is obtained by use of optical constants characteristic of the solid state of the material. At high fluences the surface melts uniformly i.e. a continuous layer of liquid is formed with the consequence that both the morphology and spacing of the ripples is significantly different to that observed in the low fluence regime. It is worthwhile to note that in nearly all other theories of LIRS, notably that by Guosheng et al [13] and Erhlich et al [14] there is a requirement for the surface to melt uniformly before any periodic structure can develop. In the uniformly molten regime significant heating between the induced ripples would be expected as all the surface has been liquified whereas in the locally melted regime little if any heating between the ripples would be expected.

The results that we have obtained by directly imaging the surface, are consistent with the above and clearly show that at the low fluences used herein to form LIRS, the surface melts only locally as there is essentially no heating between the ripples.

Early imaging experiments showed that the dye laser had to be strongly pumped in order to produce detectable light on the cameras at the high magnification used. By using HeNe laser illumination, the incidence on a test surface of such a dye beam was found to produce no permanent effects unless the surface was already well rippled, in which case the ripples were very slightly enhanced. Unquestionably such a probe beam incident on a nominally smooth surface would cause some transient surface heating and ideally the dye beam fluence should be much less than that of the excimer to ensure that essentially all the observed effects are from the excimer and not the dye. Given that the absorbed excimer fluence was more than 10 times that of the dye, and as the dye wavelength was almost exactly double that of the excimer we feel that it is not unreasonable to conclude that as a result of the ratio of their wavelengths, the heating from the dye beam will couple directly into i.e. enhance that induced by the excimer beam rather than create its own pattern. Further more, the heating effect of the dye beam will be small compared to that of the excimer beam and will not have effected the results obtained.

The ripple spacing on Ge samples whilst anomalously large is explained on the basis of an intensity interference mechanism whereby the surface melting from 2 induced wavevectors periodically overlaps and produces the large ripple spacings. Further details of this can be found in references [5,6 and 15].

The observation that once rippled only small fluences are required to further change the surface, is indicative of a positive feedback mechanism that preferentially couples the incident light into existing ripples.

## 5. Conclusions

We have for the first time, shown directly, the requirement for a surface to have a periodic temperature profile in order to form LIRS and that at low fluences the surface melts locally i.e. forms periodic bands of molten material. We have also noted the reduced fluences required to change a surface once it has become rippled.

---

N.C.K would like to acknowledge the financial support of S.E.R.C and B.D.H Ltd of Poole, Dorset.



## References

- [1] Birnbaum M., Semiconductor surface damage produced by ruby lasers, J. Appl. Phys. vol. 36, pp. 3688-3689, 1965
- [2] Emmony D.C., Howson R.P. and Willis L.J., Laser mirror damage in germanium, Appl. Phys. Lett vol. 23, pp 598-600, 1973
- [3] Marcus G.N., Harris G.L., Lo C.A. and McFarlane R.A., On the origin of periodic surface structures of laser-annealed semiconductors, Appl. Phys. Lett. vol. 33, pp. 453-455, 1978
- [4] Mansour N., Reali G., Aiello P. and Soileau M.J., Laser generated ripple patterns on dielectrics and intermediate band gap semiconductors, National Bureau of Standards (USA) Spec.Pub. 727, 1984, pp137-146 and references therein
- [5] Clark S.E., Excimer laser induced modifications of optical surfaces, Ph.D. Thesis, 1988 Loughborough University
- [6] Clark S.E. and Emmony D.C., UV Laser Induced Periodic Surface Structures, submitted to Phys. Rev. B
- [7] Emel'yanov V.I., Zemskov E.M. and Seminogov V.N., Theory of the formation of 'normal' and 'anomalous' gratings on the surfaces of absorbing condensed media exposed to laser radiation, Sov. J. Quant Electron, vol. 14, pp. 1515-1521, 1984
- [8] Temple P.A. and Soileau M.J., Polarization charge model for laser induced ripple patterns in dielectric materials, IEEE J. Quantum. Electron, vol. QE-17, pp. 2067-2072, 1981
- [9] Sipe J.E., Young J.F., Preston J.S. and van Driel H.M., Laser induced periodic surface structures I. Theory, Phys. Rev. B, vol. 27, pp. 1141-1154, 1983
- [10] Young J.F., Preston J.S., van Driel H.M. and Sipe J.E., Laser induced periodic surface structures II. Experiments on Ge, Si, Al and brass, Phys. Rev. B, vol. 27, pp. 1155-1172, 1983
- [11] Young J.F., Sipe J.E. and van Driel H.M., Laser induced periodic surface structures III. Fluence regimes, the role of feedback and details of induced topography in germanium, Phys. Rev B, vol.30, pp. 2001-2015, 1984
- [12] Holder D.W. and North R.J., Schlieren Methods, National Physical Laboratory, England, 1963
- [13] Guosheng Z., Fauchet P.M. and Sigman A.E., Growth of spontaneous periodic surface structures on solids during laser illumination, Phys. Rev. B vol. 26, pp. 5366-5381, 1982

- [14] Ehrlich D.J., Brueck S.R.J. and Tsao J.Y., Time resolved measurements of stimulated surface polariton wave scattering and grating formation in pulsed laser annealed germanium, Appl. Phys. Lett, vol. 40, pp. 630-632, 1982
  
- [15] Clark S.E., Kerr N.C. and Emmony D.C., Anomalous laser induced ripple patterns on germanium, accepted for publication J. Phys. D.

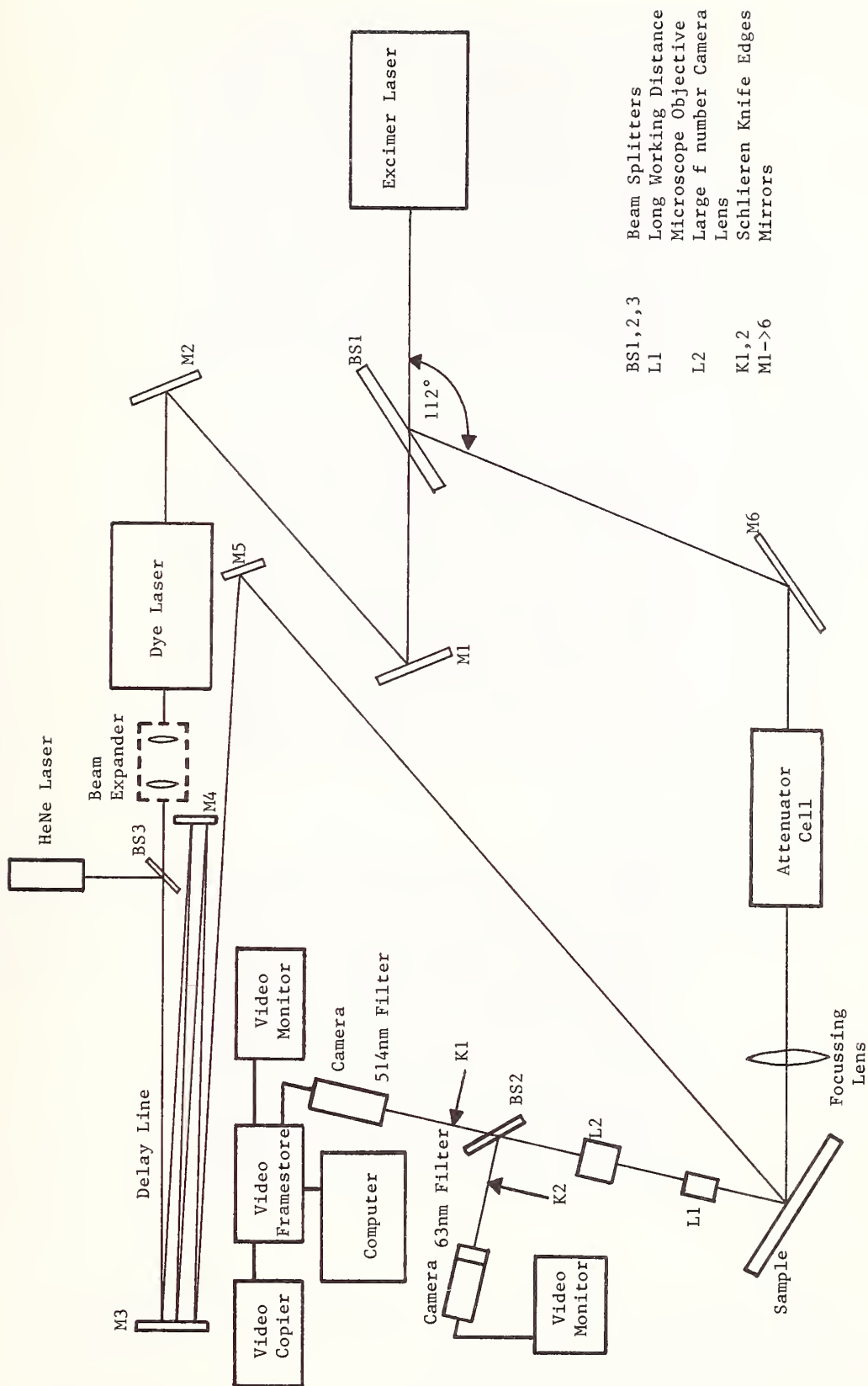
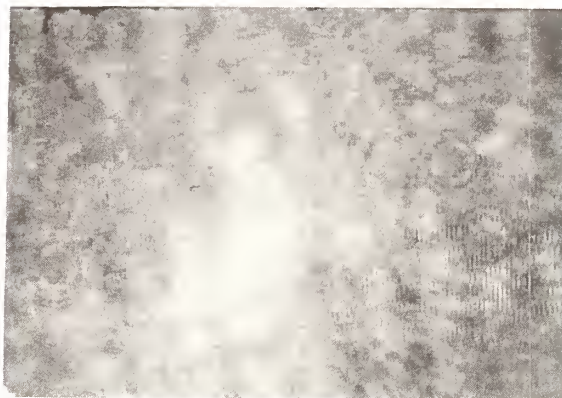


Figure 1. Schematic of Experimental Arrangement

(a)



(b)



(c)

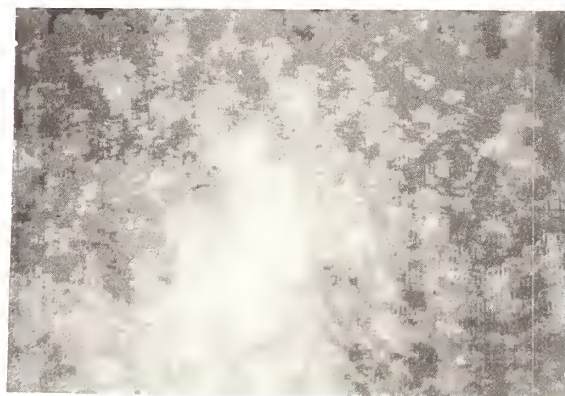
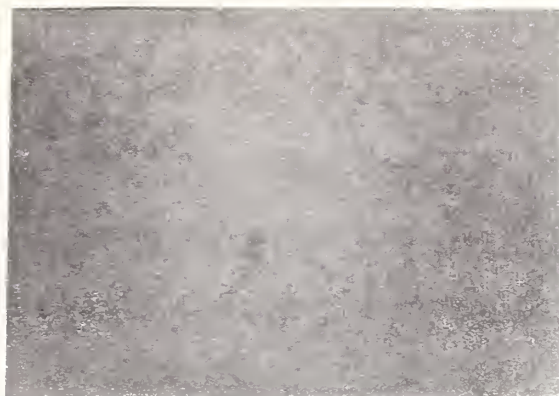


Figure 2. Transient periodic heating pattern on GaAs induced by S polarised excimer radiation incident at  $60^\circ$ .

- a) Surface after first permanent ripples have formed
- b) Transient heating on the next excimer pulse
- c) Surface a long time after the excimer pulse of 2b



(d)



(e)



Figure 2 continued.

d) Net permanent rippling

e) Net transient heating

Note that although there was a permanent change on the right handside of 2d, there was essentially no change in the middle and on the left handside where reference to 2e shows large areas of transient periodic heating.

(a)



(b)



Figure 3. a) Net permanent rippling

b) Net transient heating

Note that in this case the periodic heating pattern is purely transient and has been induced on a surface with no initial permanent rippling.

(a)



(b)



(c)

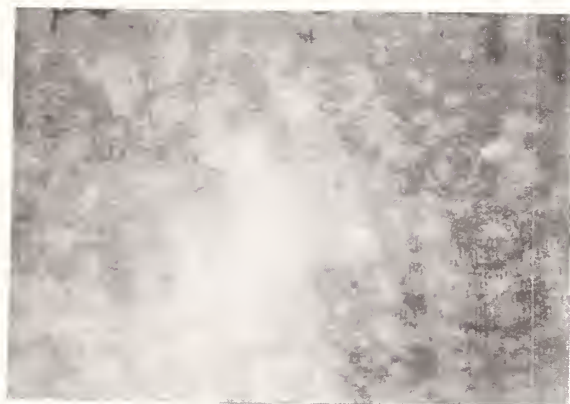


Figure 4. Transient periodic heating pattern on GaAs induced by S polarised excimer radiation incident at  $60^\circ$ . Ripple spacing is  $2.2 \mu\text{m}$ .

- a) Net permanent change in the first 30 excimer pulses
- b) Net transient heating pattern during the 31<sup>st</sup> incident excimer pulses
- c) Permanent rippling after 35 incident excimer pulses

Close inspection of b and c shows that the areas of transient periodic heating on the right hand side of 4b have become well defined permanent ripples in 4c.



(a)



(b)

Figure 5. Transient periodic heating pattern on Ge induced by S polarised light incident at  $60^\circ$ . Ripple spacing is  $6\text{ }\mu\text{m}$ .

a) Net transient heating effect

b) Net permanent rippling

It can be seen that 3 distinct transiently heated bands are induced. Figure 5b shows that this has produced no permanent rippling.

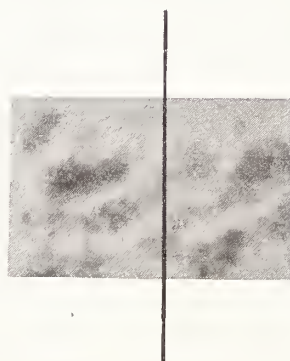


Figure 6. Profile of the transient periodic heating pattern observed in figure 5

a) Profile obtained along the vertical line shown



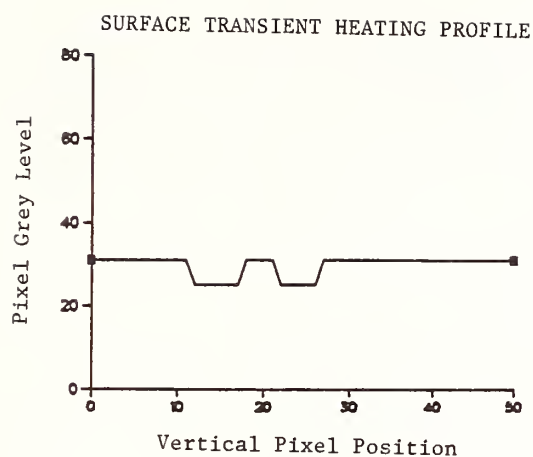


Figure 6.

b) Profile of transient heating where the vertical axis is the intensity (greylevel) of the image and the horizontal axis is position in pixels from the top.

Note that a pixel greylevel of 31 corresponds to no change between the initial and transient images that were processed to yield 6a. It is apparent that between the fringes there is no surface heating as the pixel greylevel is 31.

MANUSCRIPT NOT RECEIVED

=====

SPUTTER ETCHING OF COATING SUBSTRATES  
FOR IMPROVED LASER DAMAGE OF AR COATINGS

K. Yoshida, H. Yoshida, and S. Nakai  
Institute of Laser Engineering  
Osaka University  
Suita, Osaka, 565 Japan

and

M. Ohtani  
Physics & Chemical Technology Dept. 1  
Canon Inc.  
Ohta-ku, Tokyo 146, Japan

ABSTRACT

Glass substrates for the optical coatings have many contaminations on the surfaces which can not be removed by standard optical cleaning techniques. In this paper, the significant improvement of laser damage threshold due to sputter etching is presented.

In order to improve the damage threshold, we have prepared the BK-7 substrate sputter etched with Ar gas pressure of  $5 \times 10^{-1}$  Pa. The damage threshold of the AR coating on the etched surface showed 2 ~ 3 times improvement compared with that of un-etched surface at the laser wavelength of  $1.06 \mu\text{m}$  with a 1 ns pulse width. The roughness of the etched surface was almost the same as the polished surface ones.

MANUSCRIPT NOT RECEIVED

---

ULTRA-PRECISION GRINDING OF OPTICAL MATERIALS

Y. Namba  
Chubu University  
1200 Matsumotocho, Kasugai  
Aichi 487, Japan

ABSTRACT

The ultra-precision surface grinder has been developed to get optical surfaces with sub-micron accuracy on optical glasses. The machine has precise and rigid hydrostatic oil bearings in both spindles for a grinding wheel and table. The grinding wheel spindle is made of zero-thermal expansion glass-ceramics to prevent from thermal deformation of the spindle. The depth of cut is controlled in 0.1 micron by a numerical controller. The machine can grind optical glasses to the degree of conventionally-polished optical surfaces in figure and surface roughness.

# Laser-Induced Electrical Parameter Degradation in Silicon Photodiodes

Steve E. Watkins, Chen-Zhi Zhang, Rodger M. Walser, and Michael F. Becker

Center for Materials Science and Engineering and  
Department of Electrical and Computer Engineering  
The University of Texas at Austin  
Austin, Texas 78712

Laser-induced electrical parameter degradation and morphological damage have been observed in silicon avalanche photodiodes (APDs) and PIN photodiodes. The samples were RCA reach-through APDs in wafer form (no surface coatings) and EG&G photoconductive and photovoltaic PIN detectors (various standard coatings). The laser source was a Q-switched 1064 nm Nd:YAG laser (10 Hz, 10 ns pulses with a 300  $\mu\text{m}$  spot radius).

N-on-1 damage probability curves and morphologies were obtained for  $N=1, 30$ , and 3000. Dark current, breakdown voltage, and junction capacitance were measured for degradation. Dark current was clearly the most sensitive parameter to damage. The fluence thresholds for electrical parameter changes were significantly higher than the morphological damage thresholds. In fact, the electrical performance was insensitive to severe surface damage. The damage behavior indicated that the electrical degradation in junction photodetectors may be modeled by the introduction of defects into the depletion region by deep melting transients.

Key words: avalanche photodiodes; dark current; electrical degradation; laser damage; PIN photodiodes; silicon photodiodes.

## 1. Introduction

Laser damage to photodetectors is a growing concern. Photodetectors are particularly susceptible to damage as compared to other optical system elements since they are highly absorbing at their operating wavelengths and are often subjected to focused irradiation. Laser-induced phase changes have been modeled thermally for PbS, PbSe, and HgCdTe IR detectors[1,2]. Laser damage in silicon solar cells has caused electrical degradation without the observation of a surface phase transformation[3]. Laser-induced changes in current characteristics, breakdown voltage and light spot profiles have been observed in silicon photo-transistors and photodiodes[4,5]. Fluence thresholds for microscopic damage and loss of responsivity as a function of irradiation pulse length have been reported for silicon photodiodes[6]. The electrical damage mechanisms for high performance photodiodes irradiated by short (nanosecond) optical pulses are still largely unknown.

In this paper we examine the degradation of several electrical parameters in silicon junction photodiodes by short pulsed laser irradiation. The damage tests employed a near band gap, laser source in order to approximate typical irradiation conditions in many photodiode applications. Two types of photodiodes are considered: avalanche photodiodes and PIN photodiodes. For each type of photodiode, single-shot and multi-shot fluence thresholds are determined for surface morphological damage and for the onset of degradation in the electrical parameters. The results show that electrical device performance is insensitive to severe surface morphological damage. They also indicate that dark (reverse saturation) current is more susceptible to laser-induced change than breakdown voltage or junction capacitance. A model is proposed for the mechanisms causing the electrical-parameter degradation.

## 2. Experimental Procedures

The experimental configuration for irradiating the samples is shown in figure 1. The laser source was a 1064 nm, stable resonator Q-switched Nd:YAG laser operating at a repetition rate of 10 Hz, and with a pulse length of 10 ns (FWHM). The incident energy on the samples was controlled by an attenuator consisting of a rotating half-wave plate followed by a fixed, thin-film polarizer and monitored by a reference energy meter. The standard deviation of the pulse-to-pulse energies was two percent or less.

The spatial profile of the Gaussian beam was measured by the scanning slit method and the FWHM was determined. The  $1/e^2$  beam-spot radius  $w_0$  was obtained using the equation  $2w_0 = \text{FWHM}(\ln 2/2)^{1/2}$ . A 76 cm focusing lens was used to achieve spot radii on the samples of about 300  $\mu\text{m}$ . The peak-on-axis irradiation fluences



were calculated using  $F = 2E/\pi w_0^2$ , where  $E$  is the pulse energy. The reference energy meter was calibrated and the spotsize was determined during each test session.

In the damage testing process, the samples were positioned using a HeNe alignment laser and a 20X alignment microscope. The samples were not electrically biased during irradiation. The computer recorded the energy of each incident pulse, controlled the shutter which blocked the beam after the desired number of pulses, and calculated the peak-on-axis fluence. The alignment microscope was used to check for gross surface damage. Detailed morphological examinations and micro-photography were done subsequently with a 50-500X optical Nomarski microscope. Morphological damage was defined as any visual change in the surface observed under the Nomarski microscope. The reverse-biased IV characteristics of the irradiated APDs were measured by the manufacturer. The IV characteristics of the irradiated PIN detectors were measured with an HP 4145B semiconductor parameter analyzer.

The test samples consisted of three wafers of silicon APDs supplied by RCA and a number of silicon PIN photodiodes supplied by EG&G. The APDs were type C30817 and had the reach-through structure shown in figure 2. The surfaces of these detectors had a slightly scalloped finish resulting from a chemical etch during processing. The standard AR coating was not applied to these wafers. The active area of each device was  $0.5 \text{ mm}^2$ . The PIN photodiodes included types SGD-040, SGD-444, YAG-444, and UV-444. The guard ring structure of the SGD and YAG devices are shown in figure 3. The UV devices had a reversed structure (p-on-n) and did not have a guard ring. The SGD photodiodes had a 30 nm thick coating of thermally grown phosphorous glass. The YAG photodiodes had a 100 nm layer of evaporated  $\text{SiO}_x$  over a 30 nm layer of phosphorous glass. The UV devices had 150 nm of thermally grown  $\text{SiO}_2$ . The XXX-040 and XXX-444 devices had active areas of  $0.81 \text{ mm}^2$  and  $100 \text{ mm}^2$ , respectively.

### 3. APD Morphological Damage

The APD samples were subjected to tests of one, thirty, and three thousand laser pulses per device. For each of these N-on-1 tests, we obtained a damage probability curve which shows the probability of morphological damage versus incident fluence. A linear least squares fit was determined for the data points between the maximum non-damaging and the minimum damaging fluences. The 50% damage threshold and the damage onset (0% intercept) were obtained from the fitted curve. The probability curves are shown in figure 4 and correspond to the first observed morphological change in each series of tests.

The 1-on-1 tests were performed on wafers #1 and #3; the results are summarized in table 1. In order of increasing fluence, the observed damage morphologies were a surface depression, the formation of ripple patterns and pits, surface flow, surface flow with ripple patterns, and boiling. The probability curve for the first morphological change on wafer #1, i.e. a surface depression, is shown in figure 4.a. The 50% threshold and the onset threshold were  $0.5 \text{ J/cm}^2$  and  $0.2 \text{ J/cm}^2$ , respectively. The thresholds varied by twenty percent across wafer #1; the wafer had two regions with distinctly different thresholds. (The values given in table 1 were found using the entire data set.) The damage threshold for pits and ripple patterns (presumably the onset of surface melting) was  $1.5 \text{ J/cm}^2$  on this wafer. No surface depressions were observed on wafer #3; the first morphological change for this wafer was pit formation at  $1.3 \text{ J/cm}^2$ .

The 30-on-1 tests involved wafers #2 and #3 (see table 1). The morphologies were the same as those for the 1-on-1 tests except that no surface depressions were observed. The probability curve for pits and ripple patterns on wafer #2 is shown in figure 4.b. The thresholds for regions of this wafer differed by thirty percent.

The 3000-on-1 tests were done on wafers #1 and #3 and the results are given in table 1. The first morphological change was small localized pits. The probability curve is shown in figure 4.c. As fluence increased, the density of the pits increased and formed a single damage spot. Eventually, the underlying material was exposed ( $\sim 1.3 \text{ J/cm}^2$ ).

The various APD damage morphologies are shown in the micrographs of figures 5 and 6. Micrograph 5.a shows the morphology resulting from a single shot on wafer #1. The surface topography was measured with a Tencor surface profilometer and was found to be a bowl-shaped depression about 30 nm in depth. Surface depressions were not observed on wafers #2 and #3. Figure 5.b shows a range of 1-on-1 morphologies. Boiling is evident in the center corresponding to the spatial peak of the pulse. Away from the center, one sees surface flow with ripple patterns, surface flow alone; and, at the edge, ripple patterns alone. Also, pits (not shown) were occasionally observed at the same threshold as ripple patterns. Identical morphologies were obtained for thirty shots per site. Figures 5.c and 5.d show large boiling spots resulting from fluences far above the damage thresholds for 30-on-1 and 1-on-1 tests, respectively. The micrographs of figure 6 show the progression of damage for the 3000-on-1 tests. Scattered pits were the first observable change (fig. 6.a). At higher fluence, a single large damage spot formed as shown in figure 6.c. The underlying layers were exposed (fig. 6.d) as fluence increased still further.

Several observations can be made regarding this data. The one-shot thresholds were between 19% and 48% of the surface damage threshold of  $2.7 \text{ J/cm}^2$  for unprocessed crystalline silicon wafers as tested in our laboratory[7]. Also, considerable variation was observed in the microscopic appearance of the undamaged surfaces between wafers

and between different regions of the same wafer. Note the undamaged surfaces of wafer #1 (figs. 5.a and b) and wafer #3 (figs. 5.c and d). During device processing, the front surface of the wafers are etched to give the appropriate thickness of the high resistivity p- region before the final p+ layer is formed. Crystal quality and the etch solution mixture affect the resulting surface structure. Differences, closely corresponding to the surface structure, were found in the damage thresholds for first morphological damage, and in the types of first morphologies observed, i.e. depressions, pits, and ripple patterns. The lowest thresholds corresponding to the depression morphology occur on the highly structured surfaces (fig. 5.a), but not on the smooth surfaces (fig. 5.c). The thresholds for melting morphologies, e.g. ripple patterns, were much more consistent between wafers and regions on the wafers.

The single-shot and multi-shot thresholds show typical accumulation behavior, that is the N-shot ( $N > 1$ ) thresholds were less than the corresponding one-shot thresholds[8,9]. The thirty-shot threshold for the first morphological change on wafer #2 was greater than the one-shot threshold for the first morphological change on wafer #1, but this apparent anomaly was due to surface structure variations between the wafers and their differing damage morphologies. The thirty-shot threshold for ripple morphologies was less than the one-shot threshold for ripple morphologies as expected, that is accumulation occurs for similar morphologies.

#### 4. APD Electrical Parameter Degradation

The reverse-biased IV characteristic of the N-on-1 irradiated APDs were measured for  $N=1, 30$ , and  $3000$ . The characteristic changed as illustrated in figure 7. The undamaged device (initial curve) had an almost constant dark current as a function of voltage until breakdown abruptly occurred. Laser damage did not change the breakdown voltage, but resulted in an increase in the dark current for large bias voltages. The increase in leakage, as shown by the progression of curves #1 through #5, was more pronounced for higher laser fluences and more severe morphological damage. The increased bulk leakage current can easily dominate the noise characteristics because its noise contribution is proportional to the square of the multiplication gain times the leakage current[10]. The gain in typical applications is 100. The damaged devices with an IV characteristic similar to or worse than curve #3, figure 7, are not useful due to the noise contribution of the excess current. Even the slightly damaged detectors with characteristics like curve #1 and #2, figure 7, are not suitable for use in demanding applications because of excess noise[11].

The fluences at which electrical degradation occurred were significantly higher than the morphological damage thresholds. Hence, many devices had severe surface damage similar to the boiling spot in figure 5.d, but no change in the IV characteristic. The 50% and onset threshold fluences for this degradation are given in table 1. The single-shot values were  $9.5 \text{ J/cm}^2$  and  $5.5 \text{ J/cm}^2$ , respectively. The corresponding probability curve is figure 8.a. There was a wide range of fluences for which the probability of damage was nonzero, but not one. In this range, the degradation was typically minor, i.e. curves #1, #2, and #3 from figure 7 were observed. For fluences above about  $13 \text{ J/cm}^2$ , the degradation was severe (curve #4 or worse).

The multi-shot thresholds are also given in table 1; the probability curves are figures 8.b and c. The transition from no electrical degradation to certain change was very abrupt. Unlike the single-shot tests, the electrical degradation was always severe even in the onset region. All devices irradiated above threshold had IV characteristics worse than curve #5 in figure 7.

#### 5. PIN Morphological Damage

The PIN photodiodes were tested with one shot and three thousand shots per site. Probability curves for morphological damage were obtained as described previously. The three detector types had different surface coatings which were described in section 2, and the coating for the YAG series was an antireflector at the laser wavelength. The 50% and onset thresholds are summarized in table 2. The UV photodiode was the most resistant to damage with a 50% single-shot threshold of  $3.4 \text{ J/cm}^2$  which is higher than the threshold of  $2.7 \text{ J/cm}^2$  for unprocessed silicon[7]. The SGD and YAG detectors had thresholds below  $2.7 \text{ J/cm}^2$  with the YAG detector being the least resistant to damage. The damage probability curves are given in figure 9. The 3000-on-1 tests show a similar hierarchy of damage thresholds. However, each 3000-on-1 threshold was significantly below the corresponding 1-on-1 onset threshold, i.e. the results show accumulation. The transition from 0% to 100% multi-shot damage probability was very abrupt for all photodiodes, unlike the transition for single-shot damage.

The various morphologies differed greatly depending on the device type and the number of incident pulses. Figures 10.a-c show the progression of single-shot damage for the UV detector. The morphologies in order of increasing fluence were pitting, surface wrinkling, and boiling. The SGD damage morphologies (figs. 10.d-f) were fine surface wrinkles at threshold and surface boiling above threshold. For the YAG device, figures 10.g and h show the formation of a ridge in the coating at threshold. Above threshold, the damage (fig. 10.i) consisted of a fractured surface coating and boiling and wrinkling morphologies on the underlying silicon. Figure 11 shows the 3000-on-1 morphologies for the UV device (a and b), the SGD device (c and d), and the YAG device (e and f). Surface boiling was the dominant morphology for all three devices, although some pitting occurred for the UV and YAG devices.



## 6. PIN Electrical Parameter Degradation

Dark current, breakdown voltage, and junction capacitance were determined in the irradiated photodiodes for single and multiple shots. As for the APDs, the fluence thresholds for changes in these electrical parameters were much higher than the thresholds for surface boiling. Dark current was again the most sensitive parameter to laser irradiation. No changes were observed in the breakdown voltages. The junction capacitance was only observed to change after the dark current had increased by four orders of magnitude.

Four SDG-040 devices were tested for various combinations of pulse number and fluence. Each device had one test site. The tests and results are summarized in table 3. During each irradiation test, the dark current and the breakdown voltage were frequently measured. This current measurement was made with the guard ring open-circuited and hence included the active-area dark current and a much larger guard-ring leakage current. The increase in active-area current was not observed until it exceeded the guard-ring current of 1 to 7  $\mu\text{A}$ . (Subsequent device characterization was done with the guard ring biased, in which case only the active area leakage current was measured.) Device #1 was given 30 shots at each of three increasing fluence levels. No electrical change was seen until the last set of 30 shots. The dark current then dramatically increased as shown in figure 12. The measured values at 400 V are indicated in table 3. Device #2 was irradiated with single shots of increasing fluence. The dark current did not increase until the ninth shot (fig. 12). Device #3 was given eleven shots at about 2.7  $\text{J}/\text{cm}^2$  which has a 100% probability of 1-on-1 morphological damage. The dark current first increased at the ninth shot and continued to increase with each successive shot. As for the RCA APDs, the dark current increase was more pronounced at higher bias voltages (fig. 12). For each of these devices, the breakdown voltage was not changed. Each site showed severe morphological damage, i.e. a large boiling spot, several shots before any electrical degradation was observed. Although surface boiling and the increase in dark current are probably not directly related, the severe surface damage indicates that the device was deeply melted. The final morphologies were similar to that shown in figure 5.c.

After the damage tests, the dark current was again measured on the parameter analyzer treating the photodiodes as three terminal devices. The guard ring was maintained at the same potential as the active area and the two currents were measured separately. The resulting active-area dark currents are shown in figure 13. The corresponding measurements at 50 V are given in table 3. In typical applications, these devices are biased between 1 V and 100 V. Hence, the measured 0 V to 100 V range in figure 13 corresponds to actual bias conditions for SGD photodiodes. Device #1 showed an increase of over four orders of magnitude in dark current for this voltage range. Devices #2 and #3 were less severely damaged, but still had very large increases. Device #4 was irradiated with a single shot at 2.9  $\text{J}/\text{cm}^2$  which resulted in a boiling spot on the surface (similar to figure 11.g), but no change in the active-area dark current was observed.

Before and after irradiation, reverse-biased capacitance-versus-voltage (CV) measurements were made on the detectors. The results are summarized in table 3. No change was found in the CV characteristics of devices #2, #3, and #4, despite the large dark current increase in devices #2 and #3. The CV characteristics of device #1 are shown in figure 14. For this heavily damaged diode, the low-frequency measurements at 10 kHz were sensitive to the laser-induced damage, but the high-frequency CV measurements at 1 MHz were not. Only the low-frequency response changed which indicates that deep level defects were induced. An estimate of the defect densities can be obtained from the CV data, i.e. from the slope of  $1/C^2$  versus voltage. Defect densities in the depletion region increased by three orders of magnitude, from less than  $3 \times 10^{11} \text{ cm}^{-3}$  to over  $7 \times 10^{17} \text{ cm}^{-3}$ .

## 7. Damage Model

The data for both APD and PIN photodiodes suggests that laser-induced electrical degradation can be attributed to the introduction of deep level defects in the depletion region of the photodiode. Rapid regrowth of the crystal during deep melting transients leaves defects in this electrically sensitive region. The dark current increases when a sufficient quantity of defects are introduced. Morphological change is initially confined to the thin electrically-inactive surface layer by nonlinear limiting. The following discussion examines evidence which supports this model.

The morphological damage thresholds are more sensitive to variations in surface structure and are significantly lower than the electrical degradation thresholds. The fluence thresholds and damage morphologies for surface changes were clearly dependent on the details of the surface processing (the surface etch variations of the APDs) and the surface coatings (the layer of evaporated  $\text{SiO}_x$  for the otherwise identical surfaces of SGD and YAG photodiodes). However, the fluence thresholds for electrical degradation were not affected by such surface structure and were relatively independent of device type. For both APDs and PINs, even severe surface boiling did not cause electrical changes. Electrical-parameter degradation required high optical energies which dominated fluctuations in the surface damage thresholds and affected the silicon structure below the inactive (dead) layer at the surface.

An increase in dark current was the first electrical change observed. Junction capacitance and breakdown voltage are less sensitive to laser damage. For a large increase in dark current, the low-frequency capacitance indicates a large increase of deep level defects. Hence, the electrical degradation is associated with the introduction of these defects.

These observations, along with the high optical energies required for degradation, suggest that deep melting transients introduce defects into the electrically-sensitive depletion region. A sufficient quantity of these defects produce an observable increase in dark current.

Although the structures of the APD and the PIN diodes are quite different, the electrically-inactive surface layers of both are similar. The APD has an inverted structure with the junction at the back of the device, but in normal operation the depletion region extends through the high resistivity p- region to the p+ surface layer. The electrically-inactive layer is about 0.2 to 0.3 microns thick[11]. The junction of the PIN diode is located at the front of the device about 0.2 microns below the surface. Expectations based on the model agree with the observed thresholds in that the onset fluences for degradation in both the APD and PIN detectors should be similar since they have similar dead layer thicknesses. Thus, the location of the depletion region is critical, but the position of the junction is not significant.

Surface layers of silicon can limit the transmission of high fluences to underlying layers. For near band gap, pulsed irradiation, nonlinear optical absorption is significant as the surface approaches the melting temperature[12]. Hence, defect-inducing energies and the melted layer are initially confined to the inactive surface layers in photodiodes.

For multiple shots per site, the thresholds for electrical degradation decrease and approach the morphological damage thresholds. At or above the surface damage threshold, the structural surface damage from the initial pulses worsens with each subsequent pulse. The resulting loss of protective surface material and the repetitive melting transients lead to the introduction of higher quantities of defects at the given fluence. Therefore, the electrical degradation threshold decreases.

## 8. Summary

The APD and PIN photodiodes in this study were somewhat sensitive to morphological damage as compared to bare silicon wafers, but surprisingly resistant to electrical degradation. Almost all of the morphological damage thresholds were below the melting threshold for bare silicon. In general, device processing and surface coatings, especially antireflection coatings, lower the damage thresholds and increase their variability.

Electrical degradation occurs at substantially higher fluences than morphological damage and is relatively insensitive to fine surface structure and surface coatings. Morphological change is initially limited by nonlinear surface absorption to the electrically-inactive surface layer. Damage below this dead layer affected the dark current most strongly. Junction capacitance and breakdown voltage were not sensitive to this damage. For multiple pulses, the electrical degradation thresholds decrease and approach the morphological damage thresholds. The parameter degradation can be qualitatively modeled by the introduction of defects into the depletion region by deep melting transients.

---

This work was initiated and supported by McDonnell Douglas Astronautics Company-MDE Independent Research and Development (IRAD) funds. Further continuing support has been provided by Acurex, Inc. The APD and PIN photodiodes used in the tests were provided by RCA Inc., Electro Optics and EG&G Electro-Optics, respectively.

## 9. References

- [1] M. Kruer, L. Esterowitz, F. Bartoli, and R. Allen, "Thermal Analysis of Laser Damage in Thin-Film Photoconductors," *J. Appl. Phys.* **47**, 2867 (1976).
- [2] F. Bartoli, L. Esterowitz, R. Allen, and M. Kruer, "A Generalized Thermal Model for Laser Damage in Infrared Detectors," *J. Appl. Phys.* **47**, 2875 (1976).
- [3] Y. Matsuoka and A. Usami, "Normal Laser Damage of Silicon Solar Cells without Phase Change," *Appl. Phys. Lett.* **25**, 574 (1974).
- [4] J.F. Giuliani and C.L. Marquardt, "Electrical Effects in Laser-Damaged Phototransistors," *J. Appl. Phys.* **45**, 4993 (1974).
- [5] D.L. Parker, F. Lin, S. Zhu, D. Zhang, and W.A. Porter, "Selective Lifetime Doping in Silicon by Laser Scanning," *IEEE Trans. Electron Devices* **29**, 1718 (1982).
- [6] M. Kruer, R. Allen, L. Esterowitz, and F. Bartoli, "Laser Damage in Silicon Photodiodes," *Optical and Quantum Electronics* **8**, 453 (1976).
- [7] J. Shin, R.M. Walser, and M.F. Becker, "Relating Transient Reflectivity to Laser-Induced Damage of Silicon Surfaces," submitted for publication to *IEEE J. Quantum Electron.*



- [8] Y.K. Jhee, M.F. Becker, and R.M. Walser, "Charge Emission and Precursor Accumulation in the Multiple-Pulse Damage Regime of Silicon," J. Opt. Soc. Am. B 2, 1626 (1985).
- [9] A.A. Manenkov, G.A. Matyushin, V.S. Nechitailo, A.M. Prokhorov, and A.S. Tsaprilov, "Nature of the Cumulative Effect in Laser Damage to Optical Materials," Sov. J. Quantum Electron. 13, 1580 (1983).
- [10] R.J. McIntyre, "Multiplication Noise in Uniform Avalanche Diodes," IEEE Trans. Electron Devices 13, 164 (1966).
- [11] P. Webb, RCA Electro Optics, Personal Communication, (1988).
- [12] A.L. Smirl, T.F. Boggess, I.W. Boyd, S.C. Moss, K. Bohnert, and K. Mansour, "Application of Nonlinear Optical Properties and Melt Dynamics of Crystalline Silicon to Optical Limiting of 1 Micrometer Picosecond Radiation," Optical Engineering 25, 157 (1986).

**Table 1. Damage Test Results for RCA Avalanche Photodiodes**

Shots(N) Per Site	Wafer No.	Morphological Damage		Electrical Degradation	
		Morphology	50%(J/cm2) Onset(J/cm2)	50%(J/cm2)	Onset(J/cm2)
N=1	#1	Surface Depression	0.5	0.2	—
		Pits/Ripple Patterns	1.5		
		Boiling	2.3		
		#3 Pits	1.3	9.5	5.5
	#2&3	Pits/Ripple Patterns	0.8	2.8	2.8
		Boiling	1.7		
N=3000	#1&3	Pits	0.3	0.1	0.6
				0.6	0.4

**Table 2. Morphological Damage Results for EG&G Photodiodes**

Type of Device	Shots (N) Per Sites	Morphological Damage	
		50% (J/cm2)	Onset (J/cm2)
UV	N = 1	3.4	2.8
	N = 3000	2.4	2.4
SGD	N = 1	2.4	2.2
	N = 3000	1.5	1.5
YAG	N = 1	1.8	1.6
	N = 3000	0.7	0.7

**Table 3. Electrical Degradation of EG&G SGD-040 Photodiodes**

Device No.	Fluence x N (J/cm <sup>2</sup> )	Dark Current (50V) (400V) <sup>a</sup>		Junction Capacitance (10kHz;5V) (1MHz;5V)	
Initial	0	~2nA	~10nA	4.7pF	3.8pF
# 1	1.5 x 30		NC <sup>b</sup>		
	2.2 x 30		NC		
	3.1 x 30	55μA	>0.1mA	180pF	3.8pF
# 2	1.4 x 1		NC		
	1.7 x 1		NC		
	2.0 x 1		NC		
	2.3 x 1		NC		
	2.4 x 1		NC		
	2.7 x 1		NC		
	2.9 x 1		NC		
	2.9 x 1		NC		
	2.9 x 1	53nA	9μA	NC	NC
# 3	2.7 x 8		NC		
	2.7 x 1		11μA		
	2.8 x 1		13μA		
	2.7 x 1	1.0μA	46μA	NC	NC
# 4	2.9 x 1	NC	—	NC	NC

a. The dark current at 400 V includes both the active area current and the guard ring current.

b. NC - No Change

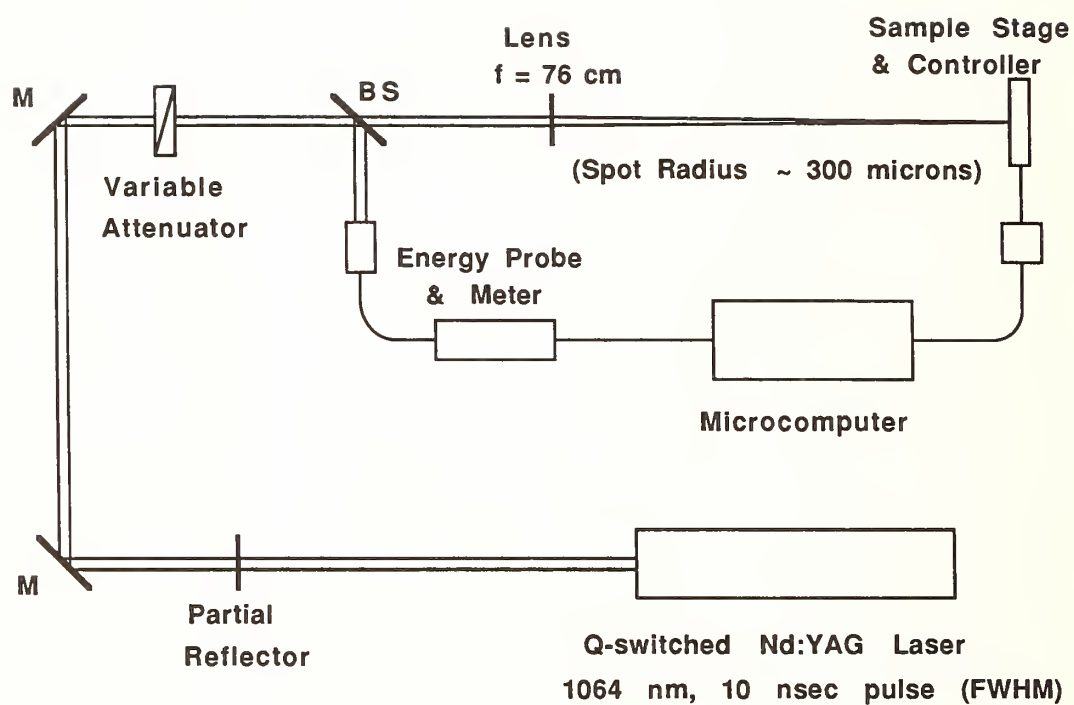


Figure 1. The experimental configuration for irradiating the photodiodes. During the damage tests, the detectors were unbiased.



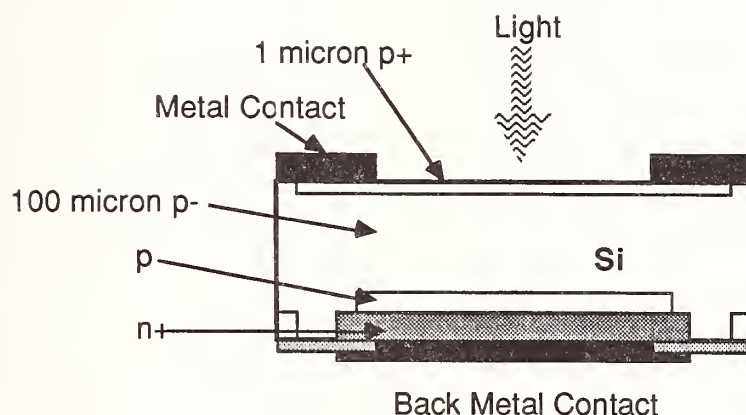


Figure 2. Cross section of the RCA avalanche photodiode type C30817 with reach-through structure. The surface was etched during processing which left a slightly scalloped finish. No AR coating was applied.

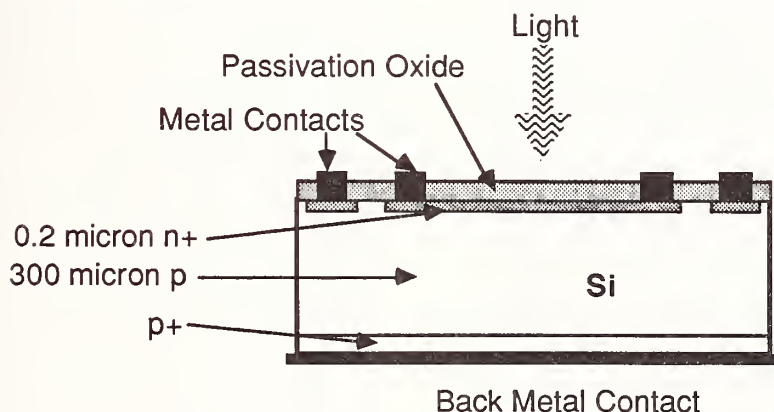


Figure 3. Cross section of the EG&G PIN photodiode with guard ring structure. The SGD device has a coating of thermally-grown phosphorous-glass; the YAG device has an identical coating of phosphorous-glass plus an overcoat of evaporated silicon oxide. The UV device has a similar cross section, but does not have a guard ring and has a reversed (p-on-n) structure. The UV device has a coating of thermally-grown silicon dioxide.

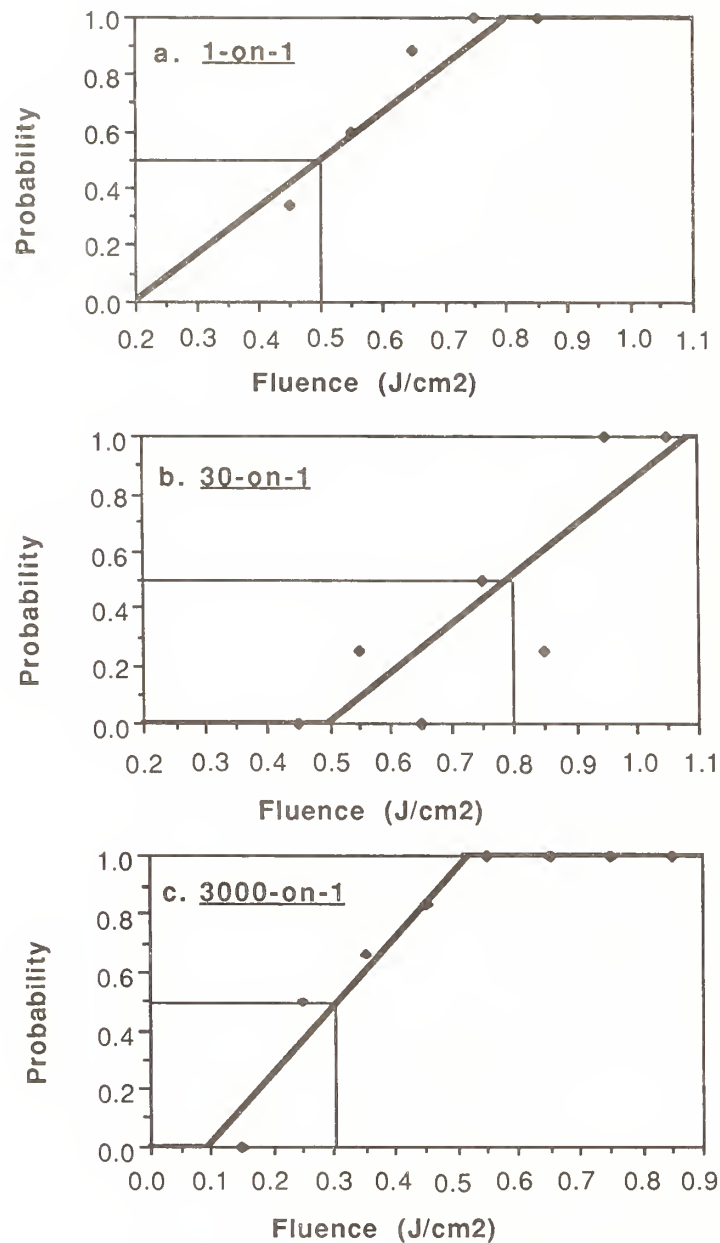


Figure 4. Morphological damage probability data for RCA APDs. Damage for curve a. (1-on-1) is surface depression; damage for curve b. (30-on-1) is the formation of pits and ripple patterns; damage for curve c. (3000-on-1) is pitting.

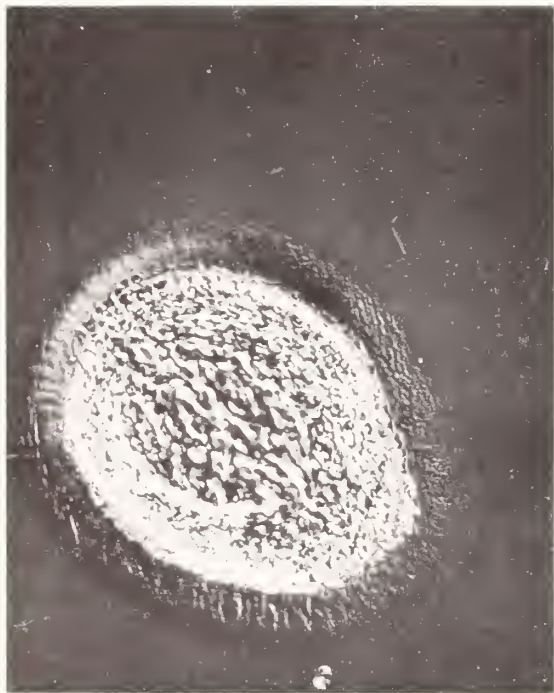
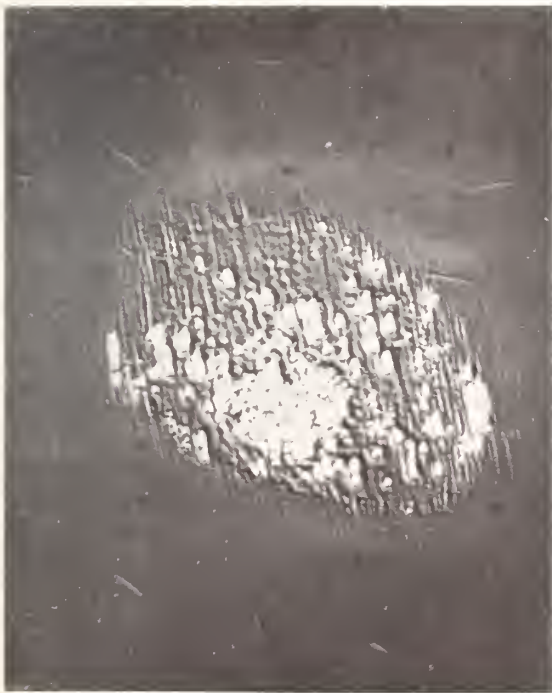


Figure 5.





Figure 6.



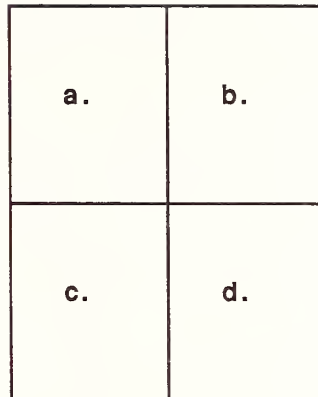


Figure 5. Damage morphology of RCA avalanche photodiodes. Micrographs a. and b. are for wafer #1; micrographs c. and d. are for wafer #3. Nomarski micrographs.

- a. 1-shot at 0.7 J/cm<sup>2</sup> (M=82X)
- b. 1-shot at 1.3 J/cm<sup>2</sup> (M=410X)
- c. 30-shots at 3.4 J/cm<sup>2</sup> (M=164X)
- d. 1-shot at 5.5 J/cm<sup>2</sup> (M=164X)

Figure 6. 3000-on-1 damage morphology of RCA avalanche photodiodes on wafer #3. Nomarski micrographs.

- a. 3000-shots at 0.3 J/cm<sup>2</sup> (M=410X)
- b. 3000-shots at 0.4 J/cm<sup>2</sup> (M=410X)
- c. 3000-shots at 0.5 J/cm<sup>2</sup> (M=410X)
- d. 3000-shots at 1.4 J/cm<sup>2</sup> (M=164X)

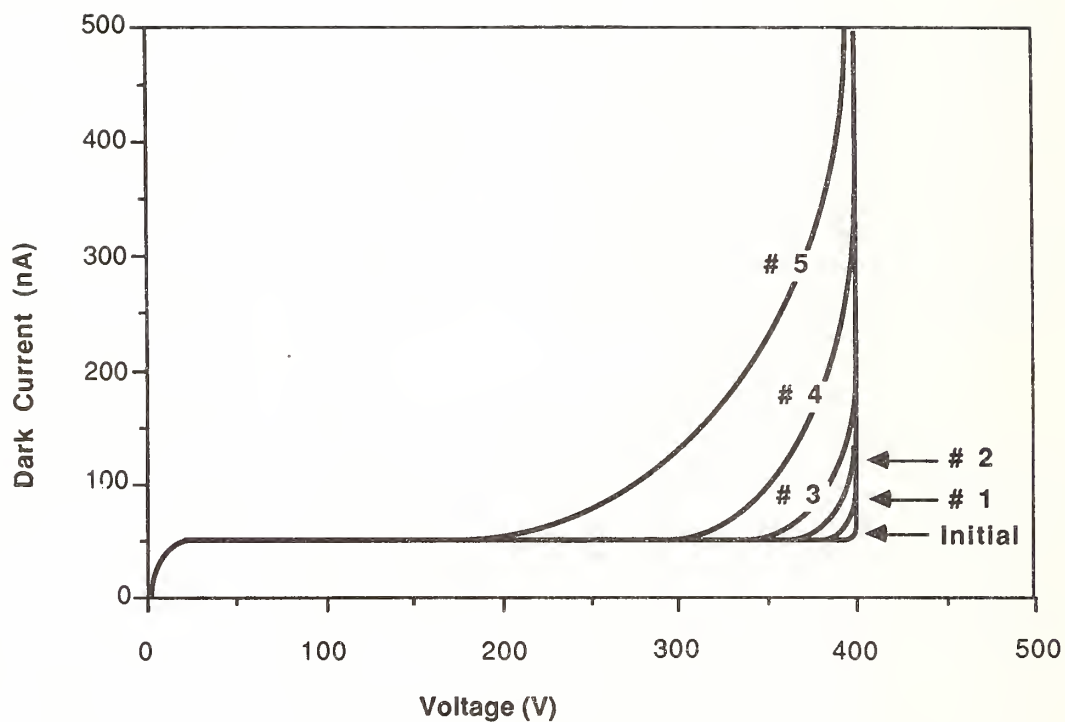


Figure 7. Reverse-biased IV characteristics of irradiated RCA APDs. The initial curve is the characteristic before degradation. Curves #1 - #5 indicate the degree of degradation for increasing fluence near threshold.

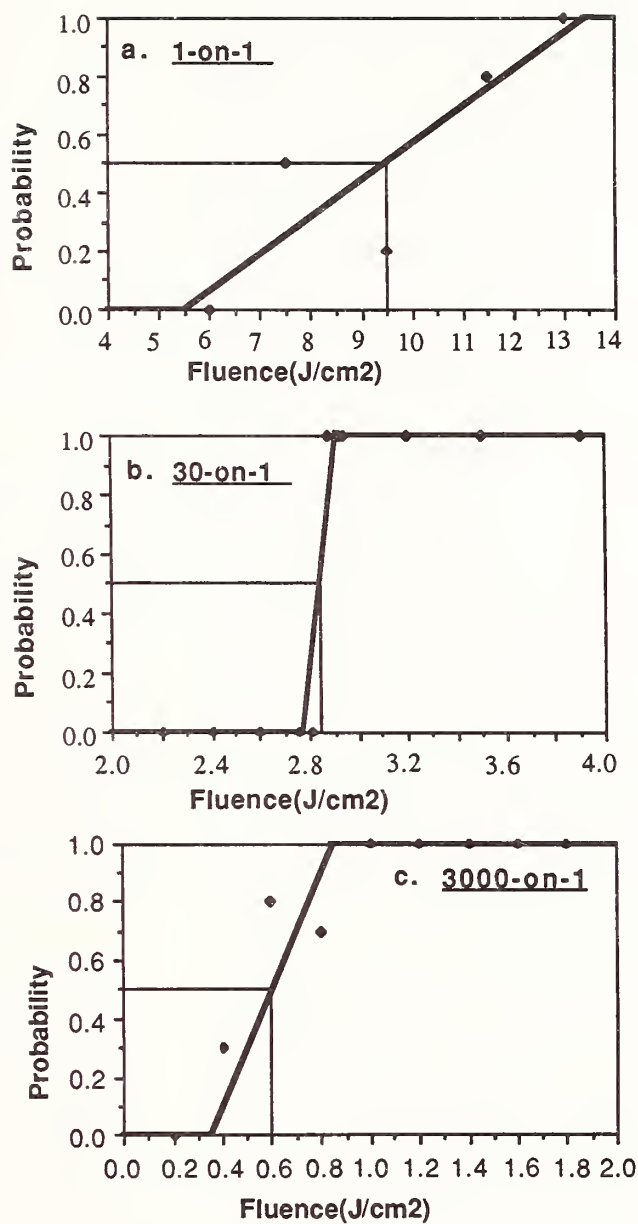


Figure 8. Electrical degradation probability data for RCA APDs. Electrical degradation for curve a. (1-on-1), curve b. (30-on-1), and curve c. (3000-on-1) is an increase in dark current.

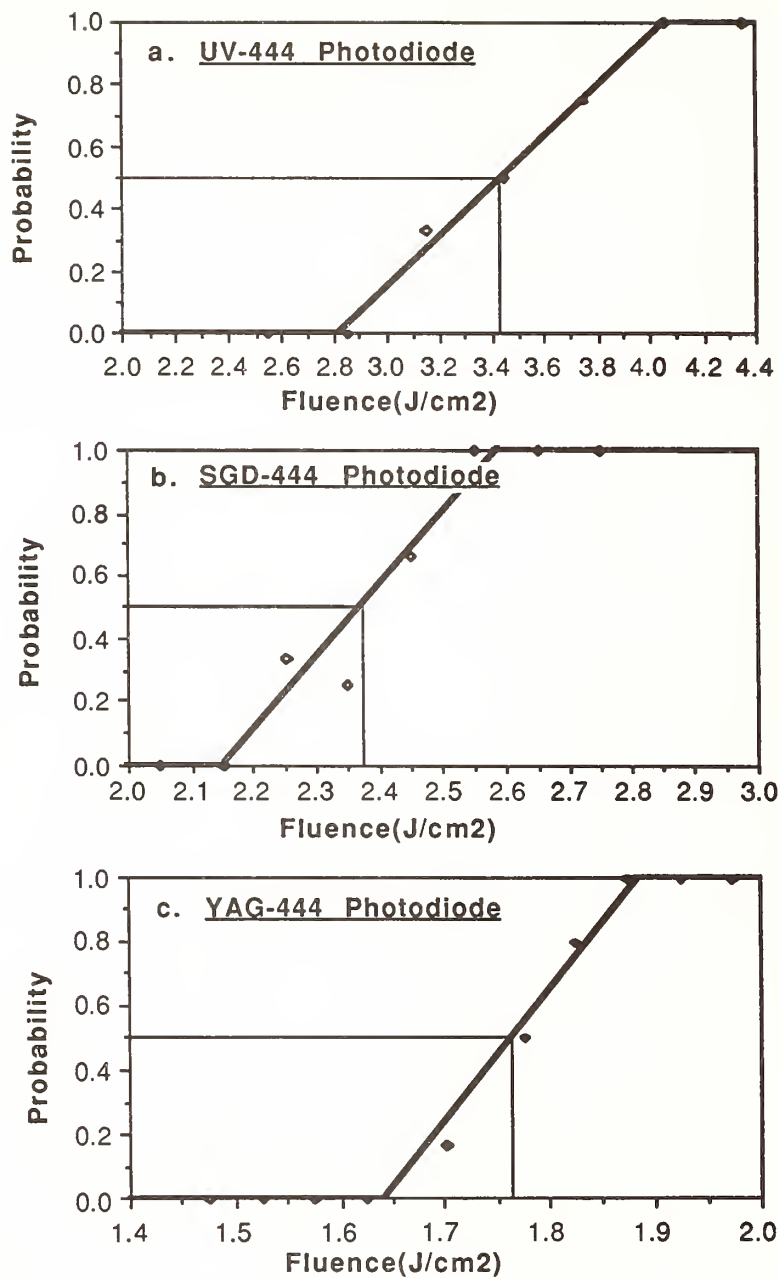


Figure 9. Single-shot damage probability data for EG&G PIN photodiodes. The curves for the UV device, the SGD device, and the YAG device are a, b, and c, respectively.



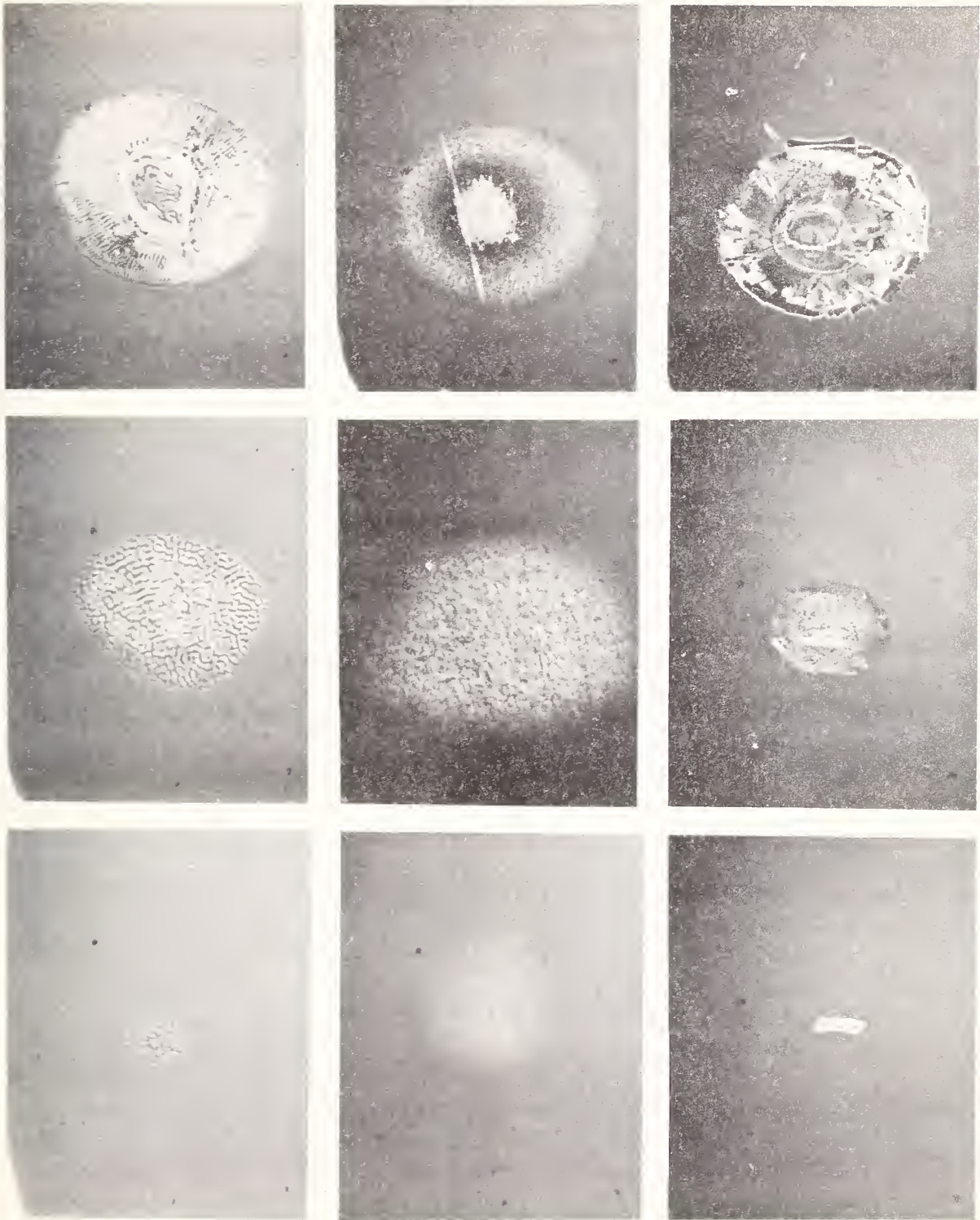


Figure 10.

a.	b.	c.
d.	e.	f.
g.	h.	i.

Figure 10. 1-on-1 damage morphology of EG&G PIN photodiodes. Micrographs a., b., and c. are for UV-444 devices; micrographs d., e., and f. are for SGD-444 devices; micrographs g., h., and i. are for YAG-444 devices. Nomarski micrographs.

- a. 1-shot for UV at 3.0 J/cm<sup>2</sup> (M=350X)
- b. 1-shot for UV at 3.5 J/cm<sup>2</sup> (M=350X)
- c. 1-shot for UV at 4.7 J/cm<sup>2</sup> (M=140X)
- d. 1-shot for SGD at 2.5 J/cm<sup>2</sup> (M=350X)
- e. 1-shot for SGD at 2.9 J/cm<sup>2</sup> (M=350X)
- f. 1-shot for SGD at 3.1 J/cm<sup>2</sup> (M=140X)
- g. 1-shot for YAG at 1.8 J/cm<sup>2</sup> (M=140X)
- h. 1-shot for YAG at 1.9 J/cm<sup>2</sup> (M=140X)
- i. 1-shot for YAG at 2.1 J/cm<sup>2</sup> (M=140X)

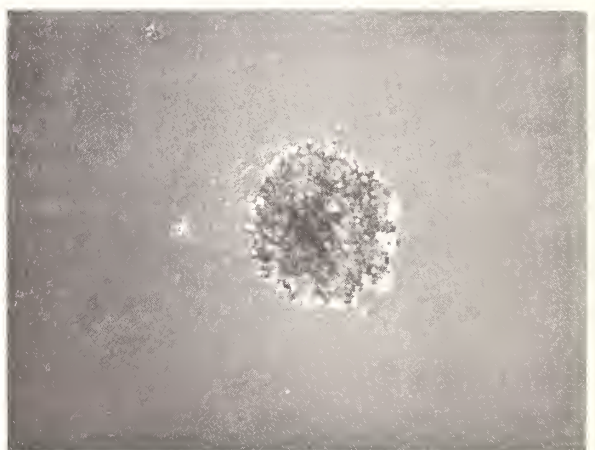
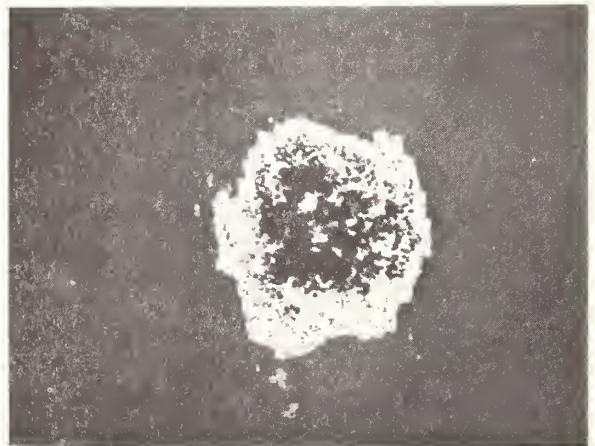


Figure 11.

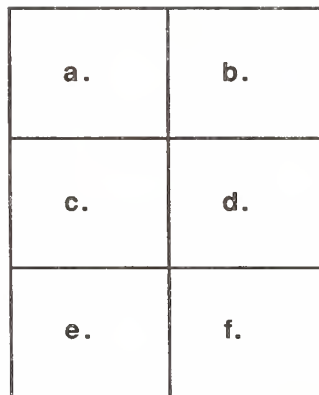


Figure 11. 3000-on-1 damage morphology of EG&G PIN photodiodes. Micrographs a. and b. are for UV-444 devices; micrographs c. and d. are for SGD-444 devices; micrographs e. and f. are for YAG-444 devices. Nomarski micrographs.

- a. 3000-shots for UV at 2.5 J/cm<sup>2</sup> (M=140X)
- b. 3000-shots for UV at 2.6 J/cm<sup>2</sup> (M=70X)
- c. 3000-shots for SGD at 1.7 J/cm<sup>2</sup> (M=140X)
- d. 3000-shots for SGD at 1.7 J/cm<sup>2</sup> (M=140X)
- e. 3000-shots for YAG at 0.7 J/cm<sup>2</sup> (M=140X)
- f. 3000-shots for YAG at 0.8 J/cm<sup>2</sup> (M=140X)



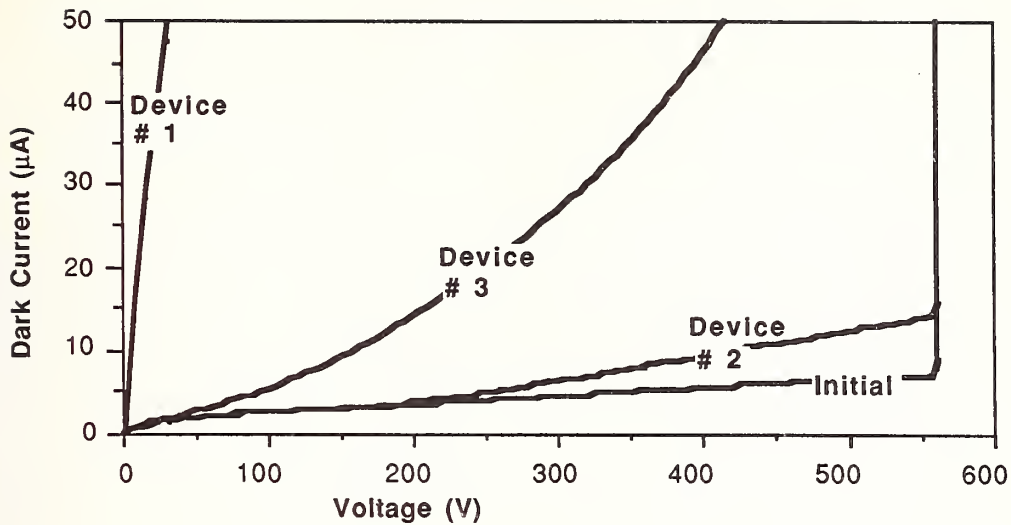


Figure 12. Reverse-biased IV characteristics of irradiated EG&G SGD-040 PIN photodiodes showing breakdown. The current is the sum of the active area dark current and the guard-ring current. The postdamage curves for device # 1, device # 2, and device # 3 and the initial predamage curve are shown.

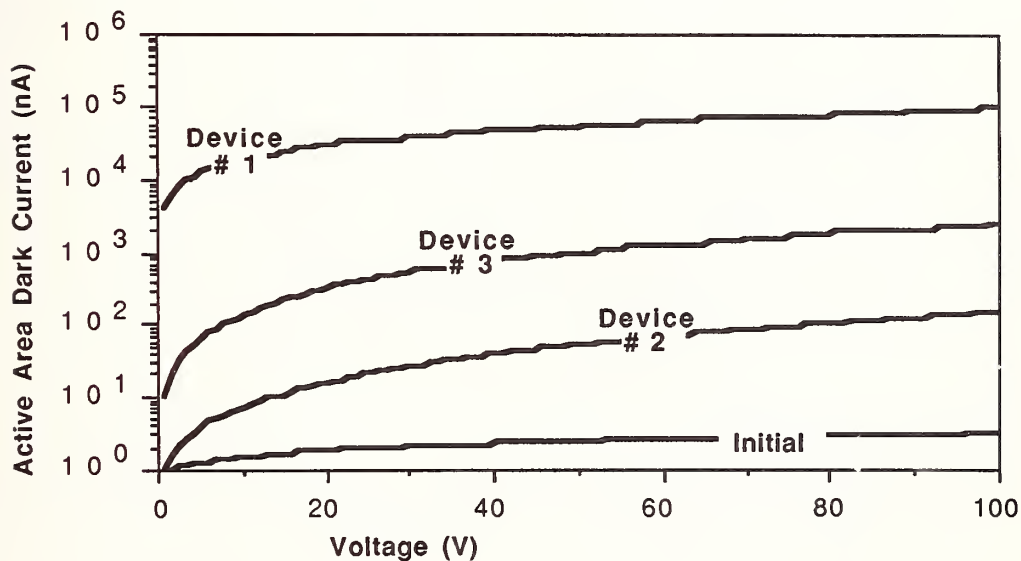


Figure 13. Reverse-biased IV characteristics of irradiated EG&G SGD-040 PIN photodiodes. The current is the active area dark current. The postdamage curves for sample # 1, sample # 2, and sample # 3 and the initial predamage curve are shown.

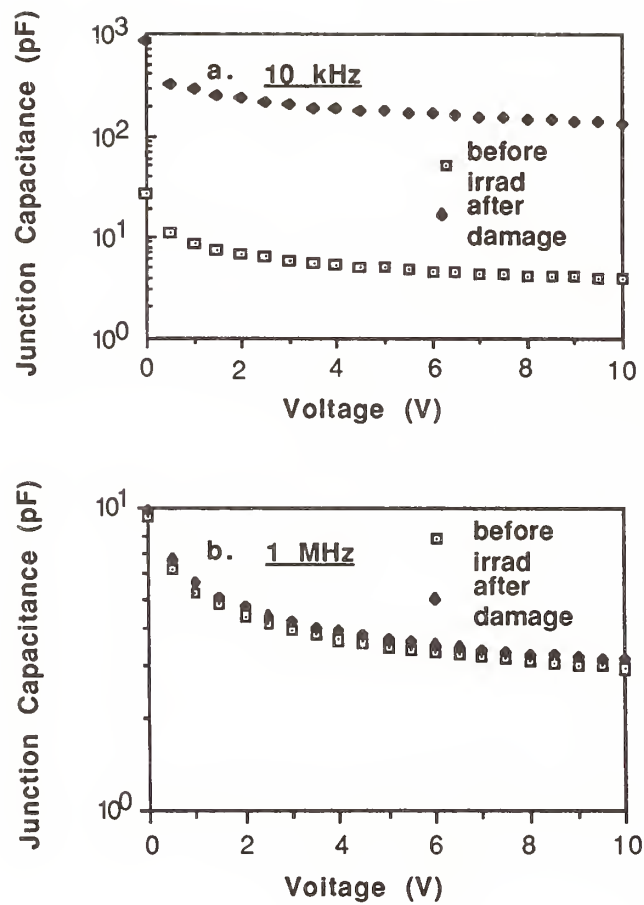


Figure 14. Reverse-biased CV characteristics of EG&G SGD-040 device #1. The CV curves for the less severely damaged devices, # 2 and # 3, were not changed by the laser irradiation.

## Stress Reduction of Ion-Beam-Sputtered Mixed-Oxide Coatings by Baking

B. J. Pond, J. I. DeBar, C.K. Carniglia and Tilak Raj

Martin Marietta Astronautics Group, Laser Systems Technology  
P.O. Box 9316, International Airport, Albuquerque, New Mexico 87119

Thin films deposited by ion-beam sputter deposition (IBSD) typically have a high compressive stress. This stress can be reduced for certain materials by cosputtering with another material [1]. The stress can be further reduced by baking the films in air after coating. Films of zirconia ( $ZrO_2$ ) and silica ( $SiO_2$ ) were prepared by IBSD from hot-pressed oxide targets using argon as the sputter gas. Films consisting of a mixture of silica and zirconia were prepared by sputtering from both targets simultaneously. Calorimetry measurements at 351 nm showed that the absorption in the mixed-oxide films was lower than the absorption in the zirconia film. A compressive stress of 219 kpsi was observed for the zirconia film and of 112 kpsi for the silica film. All of the mixed-oxide films had lower stress. Those films with silica fractions between 10% and 50% had stresses in the range of 40-50 kpsi. This stress could be reduced even further by baking the coated parts for several hours at 300°C. For mixed-oxide films with a silica fraction less than 50%, the stress of the films after baking was tensile. In particular, the film with 10% silica was changed from a compressive stress of 46 kpsi to a tensile stress of 23 kpsi by the baking process. Similar results were observed for a mixed-oxide film consisting of zirconia and alumina ( $Al_2O_3$ ). These results indicate that a stress-free multilayer coating may be achievable by IBSD.

Key words: cosputtering; ion beam; optical coatings; refractive index; silica; stress; zirconia

### 1. Introduction

Ion-beam sputter deposition (IBSD) has been shown to be a viable process for producing high-energy laser coatings [2-4]. Thin-film optical coatings made by IBSD have a higher density and lower impurity levels than conventionally evaporated films. This is due to the higher energy of the sputtered particles condensing on the substrates. The average kinetic energy of sputtered particles is approximately 5-10 electron volts, whereas the kinetic energy of conventionally evaporated species is approximately one-tenth of an electron volt [5]. These energetic particles dislodge adsorbed impurities from the substrate surface and from the coating as it is being deposited.

One limitation of coatings produced by IBSD is the high compressive stress of the films [3,6-9]. Stress can be a significant problem with thick coatings, since the mechanical forces scale with thickness. These forces can distort the substrate and cause the film to delaminate. In mirrors for optical systems, the deformed surfaces can result in considerable beam distortion.

Numerous studies have been conducted to investigate the cause of stress and to determine methods of modifying the stress in thin films. However, most of these studies have been conducted with sputtered metal films [7-16]. Recently, several studies have shown that the stress in dielectric thin films can be altered by coevaporating two materials [17-18]. One of these studies also showed a change in the grain structure of the coatings which correlated with the changes observed in the stress [17]. In the case of electron-beam (E-beam) evaporated zirconia, a change was observed in the crystalline phase, the microstructure, the grain size and the stress of the films when a glass former such as silica was added using coevaporation [18].

This paper reports on the cosputtering of zirconia ( $ZrO_2$ ) with either silica ( $SiO_2$ ) or alumina ( $Al_2O_3$ ) using IBSD. The effects of cosputtering on the stress and the optical properties of the films are presented. A total of 12 different compositions were

investigated. Eleven of the films were zirconia/silica with the silica fraction ranging from 0% to 100% in increments of approximately 10%, and one of the films was zirconia/alumina with an alumina fraction of approximately 10%. The addition of either alumina or silica to the zirconia was found to reduce the stress observed in the zirconia films.

The effect on the stress of post-deposition baking was investigated to determine whether the stress in the films could be reduced even further. The films were baked at 300°C for three hours, and a noticeable change was observed in the stress of the films.

A multilayer coating was fabricated using zirconia/silica mixed-oxide material as the high-index material and silica as the low-index material. After the coating was completed, it was baked at 300°C for several hours, and a change was observed in the stress which corresponded to the change observed in the stress of the single-layer films.

The following section discusses the experimental procedures used in depositing, analyzing, and baking the films. This is followed by a section discussing the results.

## 2. Experimental

The films were fabricated by IBSO in a cryopumped 20-inch bell jar using two Kaufman-type ion sources to sputter material simultaneously from two separate targets. The zirconia and alumina targets were in the form of hot-pressed oxide material, and the silica target was in the form of fused silica. All of the targets were 17.5-cm in diameter. The base pressure of the vacuum system was  $5 \times 10^{-7}$  torr or lower. The ion energy used with both sources was 1000 eV. The sputter gas used was argon, and a partial pressure of oxygen of  $3.0 \times 10^{-5}$  torr was supplied directly into the chamber to achieve stoichiometric films [19]. An equal pressure of argon was used in each ion source and the total chamber pressure was  $3.1 \times 10^{-4}$  torr. The substrate temperature rose above ambient during deposition due to radiant heating from the ion sources. The highest temperatures were in the range 40°–60°C. The films were deposited on substrates held in a circular rack which was rotated about its axis. The film thicknesses were monitored by an optical monitoring system using front surface reflection monitoring.

The various compositions of the single-layer films were obtained by adjusting the ion beam current incident on each target. The system was calibrated by depositing separate single-layer films of alumina, silica and zirconia using a fixed ion beam current for a fixed time. The thicknesses of these layers (denoted  $d_{\text{ao}}$ ,  $d_{\text{so}}$  and  $d_{\text{zo}}$  for the alumina, silica and zirconia films, respectively) were determined using the optical methods described below. To obtain a film with a given volume fraction  $f$  of silica, the currents  $I_{\text{s}}$  and  $I_{\text{z}}$  for the silica and zirconia ion beams are related by

$$I_{\text{s}} = I_{\text{z}} (d_{\text{zo}}/d_{\text{so}}) f/(1 - f). \quad (1)$$

For compositions with silica fractions less than 0.5,  $I_{\text{z}}$  was set to its maximum value, and eq. (1) was used to determine  $I_{\text{s}}$ . For  $f > 0.5$ ,  $I_{\text{s}}$  was set to its maximum value, and  $I_{\text{z}}$  was determined using eq. (1). A similar relation was used to obtain a film with a given volume fraction of alumina.

This deposition technique was used to give a series of single-layer coatings with approximate silica volume fractions equally spaced from 0% to 100% in 10% increments. The actual composition of each film was determined separately using analytical techniques.

Single-layer films of two different thicknesses were fabricated sequentially under identical conditions for each of the zirconia/silica compositions. The thinner films were approximately 100 nm in physical thickness, and these films were used for analysis by Rutherford back scattering (RBS) [20] to determine the actual composition of the films. The thicker films had an optical thickness of approximately 5 quarter waves at 550 nm. The thicker films were used for stress analysis, measurements of optical properties, and absorption measurements by laser calorimetry.



The deposition technique described above was also used to make a zirconia/alumina mixed-oxide coating with an approximate alumina volume fraction of 10%. Only a thick film of this composition was made, and the actual composition of this film was not determined by RBS.

The multilayer coating was a 25-layer quarter-wave-stack high reflector centered at 1.3  $\mu\text{m}$ . The high-index material was a zirconia/silica mixed-oxide film, with an approximate silica volume fraction of 10%, and the low-index material was silica. Alternate layers of the two materials were deposited in the same manner as the single-layer coatings.

The stress of the films was determined by measuring the curvature of a thin fused-silica disc coated with a single layer of the given film material [21]. The stress discs for the single-layer coatings were 2.54 cm in diameter and 0.38-mm thick, and for the multilayer film, 2.54 cm in diameter and 0.50-mm thick. The curvature was measured with a Fizeau interferometer using the 508-nm green light from a cadmium lamp. The sensitivity of the method was  $\pm 4$  kpsi. In order to reduce the data, the physical thickness of the films was needed. For the single-layer films, this thickness was calculated as part of the spectral determination of the optical constants of the films. For the multilayer coating the thickness was determined using the optical constants for each material and the theoretical optical thickness of each layer in the coating design. Thus, the determination of the stress in the single layer films is susceptible to errors in the measured refractive index of the films. In the multilayer films, it is also susceptible to errors in the optical thickness of each layer.

The envelope method [22,23] was used for determining the optical constants and the physical thicknesses of the films. This method is based on the analysis of spectral scans of transmittance and reflectance of the single-layer films. These scans were made on a Cary-2300 dual-beam spectrophotometer covering the visible, near-UV, and near-IR wavelength ranges. The envelope method of analysis allows the determination of the refractive index  $n$ , the extinction coefficient  $k$ , and the physical thickness  $d$  of the films. The method has been modified to allow for the determination of the degree of inhomogeneity  $\Delta n/n$  of slightly absorbing films [24]. This additional information provides useful insight into the structure of the films [25,26]. The precision in the determination of  $n$  was estimated to be 0.01, while the uncertainty in  $k$  varied from about 0.0015 at 1000 nm to about 0.0003 at 400 nm.

Established procedures [22] were used for making the transmittance and reflectance measurements necessary for the determination of  $n$ ,  $k$  and  $\Delta n/n$ . For these measurements, the films were deposited on UV-grade fused silica substrates with a 2.54-cm diameter and a 1-mm thickness. The transmittance measurements were made by first scanning an uncoated fused silica substrate and then scanning the coated part. The transmittance was determined by taking the ratio of the two scans. The reflectance measurements were made from the single coated surface at near-normal incidence. (The deviation from normal incidence was ignored.) The reflectance from the second surface was eliminated by using an index-matching fluid to attach a piece of fused silica to the back side of the sample being measured. The second surface of this piece of fused silica was frosted to diffuse the reflected light.

The necessary data were taken manually from the spectral scans and used to determine the optical constants and physical thicknesses of the films.

Absorption of the single-layer films at 351 nm was measured using a laser calorimeter [27,28]. The substrates used were fused-silica stress discs, 2.54 cm in diameter and 0.38-mm thick. The uncoated substrates had a absorption of 0.0150%-0.0200%. The values for the coated samples include the absorption of the substrate.

The chemical compositions of the zirconia/silica single-layer films were determined from RBS measurements conducted at Charles Evans and Associates\*. The RBS method provides a quantitative chemical analysis of most elements without any external standards. Detection sensitivity is not high for light elements like carbon and oxygen. A 2.2-MeV  $\text{He}^{++}$  ion beam was directed at the sample, and the backscattered ions were analyzed for energy and flux. The RBS results provided measured values of the relative fraction of silicon and zirconium in the films, thus allowing the atomic percentages of silica and zirconia to be determined to an accuracy of about  $\pm 1\%$ .

\* Charles Evans and Associates, 301 Chesapeake Drive, Redwood City, California, 99063.

The post-deposition baking was conducted in an air furnace. The parts were placed in the furnace, and slowly heated to 300°C. The single-layer films were baked at 300°C for three hours, and the multilayer film was baked at 300°C for eight hours. The parts were then cooled slowly to room temperature.

### 3. Results

A summary of the measured compositions and optical properties of the films is presented in table 1. The first column lists the estimated volume fraction of zirconia based on the as-deposited ion-beam currents. The second column gives the atomic percent of zirconia as measured by RBS for the zirconia/silica single layers. The following graphical presentations of the zirconia/silica results are in terms of atomic percent of zirconia as measured by RBS. The zirconia/alumina data points are included in these graphs, but this composition was only determined by the deposition parameters. The remainder of table 1 presents the optical data [ $n$ ,  $k$ ,  $(\Delta n/n)_{av}$  and layer thickness]. These data are discussed below.

Table 1. Summary of film properties for cosputtered films.

Film Composition (% zirconia)		Refractive Index	Extinction Coef. at 350 nm	Degree of Inhomogeneity <sup>a</sup> $(\Delta n/n)_{av}$	Physical Thickness
Volume %	Atomic %				
As deposited	by RBS	at 633 nm	( $\times 10^{-3}$ )	( $\times 10^{-3}$ )	(nm)
100	100	2.13	1.4	37.9	307
90	91	2.09	1.4	8.7	322
90 <sup>b</sup>	-	2.08	0.9	10.4	316
80	76	2.01	0.5	7.8	321
70	74	1.99	0.9	2.3	336
60	57	1.88	0.4	8.6	352
50	46	1.80	0.5	-4.2	353
40	34	1.70	> 0.3	-1.3	394
30	18	1.60	0.2	-1.2	412
20	15	1.56	0.1	-1.1	418
10	5	1.51	0.2	3.5	428
0	0	1.49	> 0.3	3.5	440

a Averaged from 300 nm to 900 nm.

b Zirconia/alumina film.

The measured stress values are presented as a function of measured zirconia fraction in figure 1. The stress of the zirconia/alumina film is indicated by the filled-in data point at a zirconia fraction of 90%. It can be seen that there are three distinct regions in the graph. The first region is for a zirconia film, which has a high compressive stress. The second region is for compositions with a zirconia fraction between approximately 90% and 35%. In this region, the stress values are low and relatively constant over a wide range of compositions. The third region is for a zirconia fraction less than 35%. In this region, the stress gradually increases towards the stress of the silica films.

The major observation that can be made from these results is that the high stress observed in zirconia films is reduced significantly by the addition of silica. Similar results were observed when alumina was added to the zirconia. The stress in the zirconia/alumina film was not as low as in the corresponding zirconia/silica film, although the difference was not significant. It can be seen that the addition of zirconia to silica has a different effect than the addition of silica to zirconia. The reduction in the stress of the films is believed to be caused by a modification of the structure and reduction in the grain size. However, this does not rule out other possible mechanisms of reduction in stress. In previous work it was shown that the zirconia film has a polycrystalline structure whereas the zirconia/silica mixed-oxide films have an amorphous structure [1]. The zirconia/alumina film also has an amorphous structure. The addition of either alumina or silica to the zirconia disrupts the crystalline structure and results in an amorphous film.

The measured stress values of the baked films are presented as a function of composition in figure 2. The stress of the zirconia/alumina film is indicated by the solid data point. A positive value indicates compressive stress and a negative value indicates tensile stress. The baking process modified the stress of all the films including the zirconia film and the silica film. The stress was less compressive and, in some compositions, the stress actually changed from compressive to tensile when the films were baked. The films with a zirconia fraction between 90% and 50% were tensile after baking, while films with a zirconia fraction less than 50% were compressive. It is interesting to note that the composition with a zirconia fraction of approximately 50% had the lowest stress after it was baked. The change in stress due to baking is believed to be caused by an internal rearrangement including diffusion of vacancies. The baking temperature of 300°C is lower than the annealing temperatures reported for IBSD zirconia films [29].

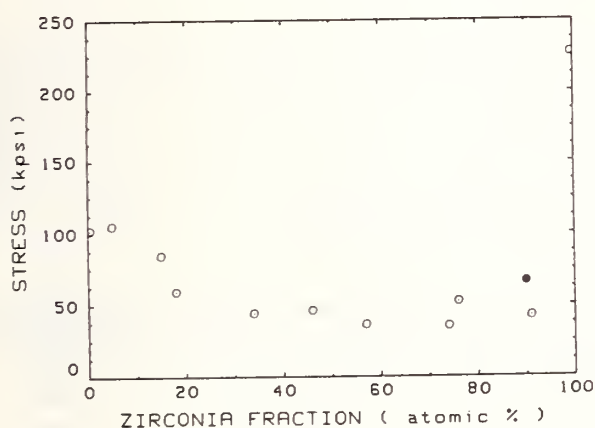


Figure 1. Stress versus film composition for cosputtered zirconia/silica films.

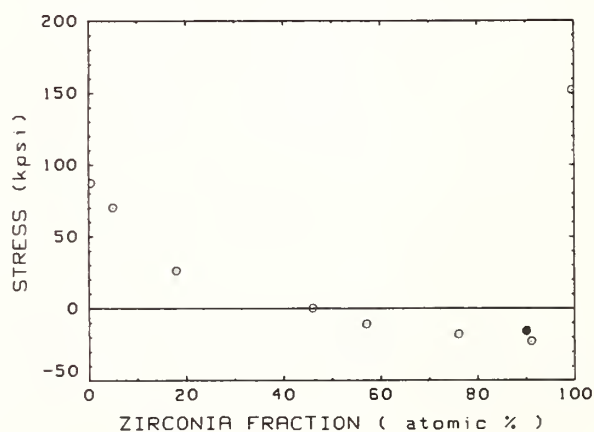


Figure 2. Stress of the baked zirconia/silica films versus film composition. Compressive stress is indicated by a positive value and tensile stress by a negative value.

The total change in stress between the unbaked films and the baked films is presented in figure 3 as a function of composition. The change in stress of the zirconia/alumina film is indicated by the solid data point. This result shows that the change in stress varies almost linearly with composition. Thus, the change in stress is proportional to the concentration of zirconia in the film.

A theoretical method was used to estimate the stress of the multilayer coating both before and after it was baked [30]. This calculation was based on the stress values determined from the single-layer coatings and the estimated thickness of the layers in the coating. The stress calculated for the multilayer coating before it was baked was 84 kpsi and the measured stress for the actual film was 98 kpsi. The calculated stress of the baked film was 39 kpsi and the measured stress for the actual film was 55 kpsi. The actual values



are slightly higher than the calculated values, but the difference between the unbaked and baked film stress is approximately the same in both cases. This result indicates that the individual layers change similarly whether they are in a multilayer coating or a single-layer coating.

The variation of refractive index at 633 nm as a function of the measured film composition is shown in figure 4. The index of the zirconia/alumina film is indicated by the solid data point at 90%. The relationship between the refractive index and the zirconia/silica film composition was modeled using several possible expressions for the refractive index of mixed-component systems. Among the models investigated were the Drude model, the Lorentz-Lorentz model, the linear model and the maximum screening form of the Bruggeman expression [31,32]. The best agreement was obtained with the Drude Model and the linear model. The curves for these two models are shown in figure 4. The upper curve represents the Drude model and the lower curve represents the linear model.

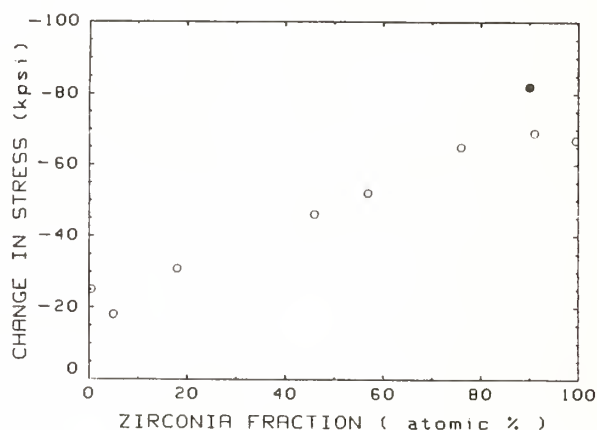


Figure 3. Change in stress between the unbaked films and the baked films versus film composition.

A linear relation between the refractive index and film composition has also been observed in films made by cosputtering other oxide materials such as  $\text{TiO}_2/\text{SiO}_2$ ,  $\text{CeO}_2/\text{SiO}_2$ , and  $\text{Ta}_2\text{O}_5/\text{SiO}_2$  [33-35]. This result is distinct from the results observed for coevaporated zirconia and silica, where the index data deviate significantly from the usual mixing models [31]. Films prepared by sputtering are not expected to follow the pattern of E-beam deposited films, since sputtered films have different optical and structural properties than E-beam films [29,36].

The measured absorption values at 351 nm for the zirconia/silica films are presented in figure 5 as a function of the measured film composition. It can be seen that the variation of absorption with composition is not the same as the linear variation observed with the refractive index. For compositions that have a zirconia fraction greater than 50%, the absorption decreases fairly abruptly, whereas in compositions with a zirconia fraction between 50% and 5%, the absorption only changes slightly. There is also a significant decrease in absorption between the composition with a zirconia fraction of 5% and the silica film. This result indicates that even small amounts of zirconia change the absorption of the film.

A summary of the average degree of inhomogeneity  $\Delta n/n$  for all of the films is presented in table 1. The measured values for the degree of inhomogeneity between 300 nm and 900 nm were averaged to obtain this value for each composition. A negative sign is used to indicate that the refractive index decreases as the film grows, and a positive sign is used to indicate the refractive index increases as the film grows. These results show that the degree of inhomogeneity in each of the mixed-oxide films and in the silica film is lower than for the zirconia film.



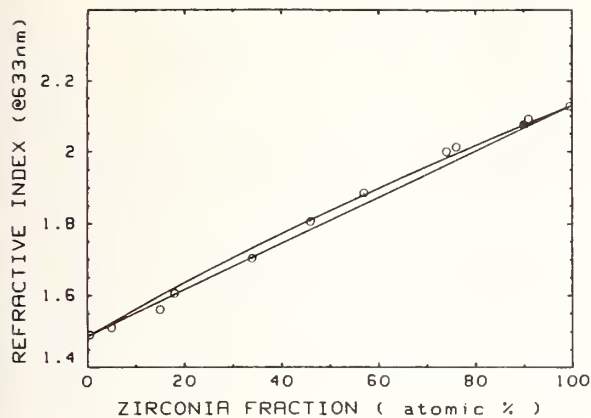


Figure 4. Refractive index at 633 nm versus film composition for cosputtered zirconia/silica films. The linear model is shown by the lower line and the Drude model is shown by the upper curve.

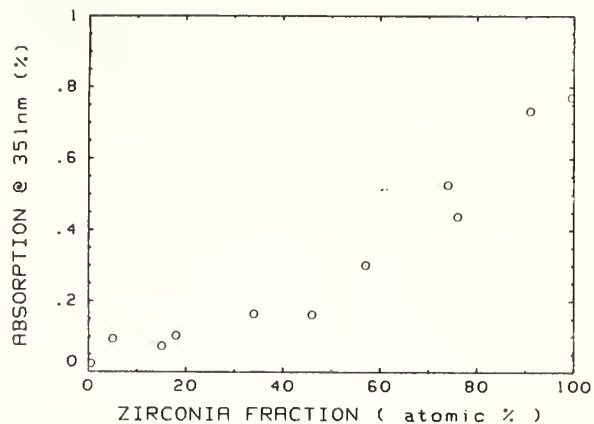


Figure 5. Absorption at 351 nm versus film composition for cosputtered zirconia/silica films.

#### 4. Conclusions

The results presented here demonstrate that the stress in zirconia films made by IBSD can be reduced significantly by mixing a relatively small amount of silica with the zirconia. This reduction in stress is believed to be caused by a change in the structure of the films from polycrystalline to amorphous. The stress was further reduced and even changed from compressive to tensile by baking the films in air. This process was used to make a low stress multilayer coating. The amount of silica required is small enough that the stress can be reduced without significantly affecting the refractive index of the film. The addition of silica to the zirconia also has the advantage of decreasing the inhomogeneity observed in the zirconia films.

The refractive index was shown to vary linearly with film composition, and a range of index values between the index of zirconia and silica can be obtained. The absorption at 351 nm varied significantly from a linear mixing model.

---

The authors acknowledge the assistance of Willy Kunzler, Wayne Wasson and Dan O'Shea of the AFWL/Technical Services Division, Metrology Laboratory, Kirtland AFB, New Mexico, in making the spectral measurements. In addition, the authors acknowledge Joe Sobczak of Martin Marietta Corporation, Laser Systems Technology, for baking the samples and making the stress measurements and Swarnalatha Mallavarapu of Air Force Weapons Laboratory, Kirtland AFB, for help with the spectral data reduction. The authors also acknowledge Jennifer Richberger of Rockwell Power Systems, Optical Coating Evaluation Laboratory, Kirtland AFB, for making the calorimetry measurements.

This effort was sponsored by the Air Force Weapons Laboratory, Air Force Systems Command, United States Air Force, Kirtland AFB, New Mexico 87117.

#### 5. References

- [1] Pond, B.J.; DeBar, J.I.; Carniglia, C.K.; Raj, T. Stress reduction in ion-beam sputter-deposited films. Appl. Opt. (submitted for publication).
- [2] Carniglia, C.K.; Pond, B. Production of resonator optics for 1315 nm oxygen iodine laser. Proceedings of the International Society of Optical Engineering Symposium on Laser and Optics; 1988 January 10-17; Los Angeles, CA. SPIE Proceedings 895; 1988. 281-287.

- [3] Sites, J.R.; Gilstrap, P.; Rujkorakarn, R. Ion beam sputter deposition of optical coatings. *Opt. Eng.* 22(4): 1983 July/August.
- [4] Varasi, M.; Misiano, C.; Lasaponara, L. Deposition of optical thin films by ion beam sputtering. *Thin Solid Films.* 117: 163-172; 1984.
- [5] Wehner, G.K.; Anderson, G.S. The nature of physical sputtering, in *Handbook of Thin Film Technology*, chapter 3, L.I. Maissel and R. Glang, eds. New York, NY: McGraw-Hill Book Co.; 1970.
- [6] Allen, T.H. Reactive ion beam sputtered optical coatings. *Proceedings of the 30th Annual Technical Conference of the Society of Vacuum Coaters.* 27-41; 1987.
- [7] Castellano, R.N. Composition and stress state of thin films deposited by ion beam sputtering. *Vacuum.* 27: 109-117; 1977.
- [8] Sey-Shing, Sun. Internal stress in ion beam sputtered molybdenum films. *J. Vac. Sci. Technol.* A4(3): 572-576; 1986.
- [9] Windischmann, H. Intrinsic stress in AlN prepared by dual-ion-beam sputtering. *Thin Solid Films.* 154: 159-170; 1987.
- [10] Hoffman, D.W. Stress and property control in sputtered metal films without substrate bias. *Thin Solid Films.* 107: 353-358; 1983.
- [11] Hoffman, D.W.; Thorton, J.A. Internal stresses in Cr, Mo, Ta, and Pt films deposited by sputtering from a planar magnetron source. *J. Vac. Sci. Technol.* 20(3): 355-358; 1982 March.
- [12] Thorton, J.A.; Hoffman, D.W. Influence of discharge current on the intrinsic stress in Mo films deposited using cylindrical and planar magnetron sputtering sources. *J. Vac. Sci. Technol.* A3(3): 576-579; 1985 May/June.
- [13] Cuomo, J.J.; et al. Modification of niobium film stress by low-energy ion bombardment during deposition. *J. Vac. Sci. Technol.* 20(3): 349-354; 1982 March.
- [14] Laugier, M. The effect of ion bombardment on stress and adhesion in thin films of silver and aluminum. *Thin Solid Films.* 81: 61-69; 1981.
- [15] Ricerby, D.S.; Eckold, G.; Scott, K.T.; Buckley-Golder; I.M. The interrelationship between internal stress, processing parameters and microstructure of physically vapor deposited and thermally sprayed coatings. *Thin Solid Films.* 154: 125-141; 1987.
- [16] Knoll, R.W.; Bradley, E.R. Correlation between the stress and microstructure in bias-sputtered  $ZrO_2$ - $Y_2O_3$  films. *Thin Solid Films.* 117: 201-210; 1984.
- [17] Sankur, H; Guning, W.J.; Denatale, J.F. Intrinsic stress and structural properties of mixed composition thin films. *Appl. Opt.* 27: 1564-1567; 1988.
- [18] Farabaugh, E.N.; Sanders, D.M. Microstructure of dielectric thin films formed by e-beam coevaporation. *J. Vac. Sci. Technol.* A1(2): 356-359; 1983.
- [19] Demiryont, H.; Sites, J.R. Effects of oxygen in ion-beam sputter deposition of titanium oxide. *J. Vac. Sci. Technol.* A2(4): 1457-1460; 1984.
- [20] Sundgren, J.E.; Rockett, A.; Greene, J.E. Microstructural and microchemical characterization of hard coatings. *J. Vac. Sci. Technol.* A4(6): 2720-2783; 1986.
- [21] Campbell, D.S. Mechanical Properties of Thin Films, in *Handbook of Thin Film Technology*, chapter 12, L.I. Maissel and R. Glang, eds. New York, NY: McGraw-Hill Book Co.; 1970.
- [22] Arndt, D.P.; et al. Multiple determination of the optical constants of thin film coating materials. *Appl. Opt.* 23: 3571-3596; 1984.

- [23] Carniglia, C.K. "Effects of dispersion on the determination of optical constants of thin films," in Thin Film Technologies II, Jacobsson, J. Roland, ed. 1986 April 15-17; Innsbruck, Austria. Proc. SPIE 652; 1986. 158-165.
- [24] Carniglia, C.K., Method for measuring the optical properties of slightly absorbing, inhomogeneous dielectric thin films. J. Opt. Soc. Am. A 3 40: 1986.
- [25] Harris, M.; Macleod, H.A.; Ogura, S. The relationship between optical inhomogeneity and film structure. Thin Solid Films, 57: 173-178; 1979.
- [26] Macleod, H.A. Structure related optical properties of thin films. J. Vac. Sci. Technol. A4 (3): 418-422; 1986.
- [27] Gallant, D.J.; Law, M.; Pond, B. Effect of cleaning on optical absorption of calcium fluoride and fused silica at 351 nm. NIST (U.S.) Spec. Publ. 752, 159-167; 1986.
- [28] Allen, T.H.; Apfel, J.P.; Carniglia, C.K. in Laser Induced Damage in Optical Materials, J.E. Bennet, A.J. Glass, A.H. Guenther and B.E. Newman, eds. Nat. Bur. Stand. (U.S.) Spec. Publ. 541; 1978. 33-36.
- [29] Ruj Korakarn, R.; Sites, J.R. Crystallization of zirconia films by thermal annealing. J. Vac. Sci. Technol. A4 (3): 568-571; 1986.
- [30] Ennos, A.E. Stresses developed in optical film coatings. Appl. Opt. 5: 51-61; 1966.
- [31] Feldman, A.; Farabaugh, E.N.; Haller, W.K. Modifying structure and properties of optical films by coevaporation. J. Vac. Sci. Technol. A4 (6): 2969-2974; 1986.
- [32] Jacobsson, R. Inhomogeneous and coevaporated homogeneous films for optical applications, in Physics of Thin Films, Vol. 8, George Hass, Maurice H. Francombe, and Richard W. Hoffman, eds. New York, NY: Academic Press; 1975. 51-98.
- [33] Motovilov, O.A.; Rudina, O.G. Optical properties of layers of oxide mixtures produced by cathode sputtering. Sov. J. Opt. Technol. 41: 327-330; 1974.
- [34] Kobayashi, Mario; Terui, Hiroshi. Refractive index and attenuation characteristics of SiO<sub>2</sub>-Ta<sub>2</sub>O<sub>5</sub> optical waveguide film. Appl. Opt. 22: 3121-3127; 1983.
- [35] Misiano, C.; Simonetti, E. Co-sputtered optical films. Vacuum. 27: 403-406; 1977.
- [36] Klinger, R.E.; Carniglia, C.K. Optical and crystalline inhomogeneity in evaporated zirconia films. Appl. Opt. 24: 3184-3187; 1985.

MANUSCRIPT NOT RECEIVED  
=====

LASER DAMAGE THRESHOLDS OF DIELECTRIC MULTILAYERS  
PRODUCED BY REACTIVE ION PLATING DEPOSITION

Karl H. Guenther, Kamjou Mansour, Paul Sachdeva, and Harald Schink\*  
Center for Research in Electro Optics & Lasers (CREOL)  
University of Central Florida  
Orlando, FL 32826

and

Francis J. Boero  
Newport Corporation  
Fountain Valley, CA 92708

ABSTRACT

Laser induced damage threshold (LIDT) tests reported last year<sup>1</sup> for TiO<sub>2</sub> single layers made by standard reactive evaporation and by reactive ion plating showed that the LIDT of the latter was higher by a consistent factor of about two. Here, we are reporting LIDT results for 1-on-1 damage tests at 532 nm and 1064 nm on dielectric multilayer coatings produced by reactive ion plating deposition. Coating materials included SiO<sub>2</sub>, TiO<sub>2</sub>, Ta<sub>2</sub>O<sub>5</sub>, and ZrO<sub>2</sub>. Initially, substrates consisted either of 50 mm square sheet glass with an average rms roughness of about 3.5 nm or of 25.4 mm diameter BK7 optical flats with a rather poor polish of 1-2 nm rms roughness. Carefully characterized laser-quality substrates polished at Newport will be used for further experiments.

For the damage testing at 532 nm wavelength, we used a Quantel laser system at CREOL consisting of a Nd:YAG laser with 600 mJ output at 1064 nm with a frequency doubler delivering 160 mJ output at 532 nm. For the actual testing, only about 20 mJ were used with single pulses of 15 ns (FWHM) and about 0.5 mm spot size (1/e<sup>2</sup>). Damage thresholds ranged from 7 Jcm<sup>-2</sup> to > 20 Jcm<sup>-2</sup>, depending on the design and the high index coating material, with a single result of > 40 Jcm<sup>-2</sup> for a particular ZrO<sub>2</sub>/SiO<sub>2</sub> coating. Damage tests at Newport with a Quanta-Ray DCR Q-switched Nd:YAG laser delivering about 75 mJ per pulse [9.8 ns (FWHM) and about 0.8 mm (1/e<sup>2</sup>) spot size] resulted in LIDT of > 28 Jcm<sup>-2</sup> on several sites of Ta<sub>2</sub>O<sub>5</sub> laser mirrors. However, damage as low as 2.8 Jcm<sup>-2</sup> was also observed on single sites on several samples. Poor polish of these early samples may have been a contributing factor in these findings.

<sup>1</sup> K.H. Guenther, Boon Loo, H.K. Pulker, A. Saxer, and S. Seitel, "Comparative Study of Reactive Ion Plated vs. Reactively Evaporated TiO<sub>2</sub> Thin Films," Paper presented at the 19th Annual Symposium on Optical Materials for High-Power Lasers, Boulder, CO, 1987.



## Damage Threshold Dependence on Film Thickness

Wu Zhouling, Fan Zhengxiu and Wang Zhijiang

Shanghai Institute of Optics and Fine Mechanics,  
Academia Sinica, P.O.Box 8211, Shanghai, PRC

This paper reports our recent results of film thickness effect on damage resistance of optical coatings. The main contents include:

(1) Damage threshold dependence on film thickness of single layers

In our experimental results with  $10^{15}$ -1.06  $\mu\text{m}$ -Nd:YAG laser,  $\text{SiO}_2$  showed essentially no film thickness dependence of damage;  $\text{TiO}_2$  and  $\text{Ta}_2\text{O}_5$  had a dependence yet this dependence disappears when the data is corrected for the internal-field strength; however,  $\text{ZnS}$ ,  $\text{ZrO}_2$  and  $\text{MgF}_2$  showed an apparent film thickness dependence of damage even after the standing-field corrections.

(2) Damage threshold dependence on film thickness of overcoats and undercoats

The damage resistance improvements of optical coatings by over and undercoats have a strong dependence on film thickness according to our recent results. For example, damage threshold of  $\text{ZrO}_2/\text{SiO}_2$  reflectors improved 80% with  $\lambda/2$  overcoat while 300% with  $3\lambda$  overcoat.

(3) Qualitative explanation of the above results with the help of absorption localization, scattering measurement, and microstructure analysis of the coatings investigated.

Key Words: film thickness; laser damage; optical coating; overcoat; undercoat.

### 1. Introduction

Damage threshold dependence on film thickness has been researched and reported by a lot of authors [1]. To understand the mechanisms behind the film thickness dependence, Newnam [2] attributed this dependence to the different field strengths in the fields and the thresholds were found to correlate with internal field strengths. However, after measurements of damage threshold dependence on film thickness of about ten different film materials and an examination of all the data concerned, Walker [3] found that there remains an additional thickness dependence of damage in many of the materials after standing-field corrections. He explained most of the results with impurity-dominated damage model [4].

In this paper, we report our recent results of film thickness effect on damage resistance of optical coatings, with qualitative explanations with the help of absorption localization [5], scattering measurement [6] and microstructure analysis [7] of the coatings investigated.

### 2. Experimental Procedure

All of the samples were produced in conventional high vacuum evaporation plants equipped with oil diffusion pumps. The deposition methods and the related characterizations of the coatings under investigation is given in table 1.

Fig.1 shows our experimental setup for damage resistance measurements. A repetitively Q-switched Nd:YAG laser at  $\lambda = 1.06 \mu\text{m}$  with a full width at half-maximum (FWHM) pulse of  $10 \text{ ns}$  was used to determine the laser damage threshold of the samples. The beam spot diameter ( $\text{TEM}_{00}$ ) taken at the  $1/e^2$  intensity points was  $44 \mu\text{m}$ . The experiment was carried out in a one-on-one format, and each single test run on a specific dielectric thin-film sample consisted of between 30 and 50 laser irradiations. The damage threshold was assigned the arithmetically averaged mean value of the highest non-damage energy density and the lowest damage energy density, corresponding to a damage probability of 50%.

### 3. Results and Discussion

#### 3.1 Single Layers

The measured results of damage threshold dependence on film thickness of single layers are given in table 2. To make the concerned trends clearer, we represent the results in a normalized form in fig.2(a). From this figure, we can clearly see: (1).  $\text{SiO}_2$  showed essentially no film thickness dependence of damage; (2).  $\text{TiO}_2$  and  $\text{Ta}_2\text{O}_5$  had a dependence yet this dependence disappears when the data is corrected for the internal-field strength; and (3).  $\text{ZnS}$ ,  $\text{ZrO}_2$  and  $\text{MgF}_2$  showed an apparent film thickness dependence of damage even after the standing-field corrections.

To understand the above experimental results, we measured the absorption losses of all the investigated samples by means of photothermal deflection technique [8], and the normalized results are shown in fig.2(b). From these results and our previous localization of absorption losses in optical coatings [5], we give our explanation of the above mentioned damage measurements as follows: (1). For  $\text{TiO}_2$ ,  $\text{Ta}_2\text{O}_5$  and  $\text{SiO}_2$  films, the film-substrate interface absorption dominates over the bulk and air-film interface absorption, being the main source of the total absorption losses and hence the direct cause of laser damage. This is why  $\text{TiO}_2$ ,  $\text{Ta}_2\text{O}_5$  and  $\text{SiO}_2$  films showed essentially no damage threshold dependence on film thickness. (2). For  $\text{ZnS}$ ,  $\text{ZrO}_2$  and  $\text{MgF}_2$  single layers, since as the film thickness increases, so do the total absorption losses and the impurity sizes, the apparent damage resistance dependence on film thickness is well correlated with the impurity-dominated thermal damage model [4].

#### 3.2 HR coating with overcoats

Table 3 and fig.3 show our measured damage threshold dependence of HR coatings on film thickness of overcoats. It is very clear from the results that the damage resistance improvements of optical coatings by overcoats have a strong dependence on the overcoat thickness. By measuring the scattering losses [6] and observing the microstructure [7] of the coatings under investigation, we believe the reported trend arises from the variation with overcoat thickness in improvement of surface morphology and interface structure. The sample with thicker overcoat has smoother surface and finer microstructure, and, therefore, higher damage threshold. Yet when the overcoats get thicker than  $(3-7/2)\lambda$ , the damage thresholds begin to decrease very sharply. Our explanation for this fact is that the surface morphology itself degraded here suddenly because of cracks induced by stresses.

#### 3.3 AR Coating with Undercoats

Table 4 and fig.4 show our measured results of AR coatings with undercoats. Here again, although relatively weaker, exists an apparent damage threshold dependence on film thickness i.e., the thicker the undercoat, the higher the damage resistance of the concerned AR coating. For this trend, we believe that the improvement of the film-substrate interface plays most important role in the whole process, though we are still lacking sufficient data to draw a sound conclusion now.

#### 4. Conclusions

For single layers, damage threshold dependence on film thickness does not always exist and this can be explained with the help of bulk/interface absorption and/or defect-dominated thermal damage model. For overcoats, the film thickness effect is always very apparent for the HR coatings investigated, and this is attributed to the variation with overcoat thickness in improvement of surface morphology and interface structure. For undercoats, we see similar, though weaker, trends to those of overcoats, and we guess that the improvement of the film-substrate interface plays most important role here, though factors like stresses may also have some effects.

---

The authors wish to acknowledge the work of Fan Ruiying and Lu Yuemei in preparing some of the samples and the work of Li Zhongya in performing some of the damage testing.

#### 5. References

- [1] Proceedings of previous Boulder Damage Symposia.
- [2] Newnam, B. E.; Gill, D. H. Influence of standing wave fields on the laser damage resistance of dielectric films. Nat. Bur. Stand. (U. S.) Spec. Publ. 435; 1976. 254p.
- [3] Walker, T. W.; Gunther, A. H.; Nielsen, P. E. Pulsed laser-induced damage to thin-film optical coatings--part 1: experimental. IEEE J. Quantum Electron. QE-17(10): 2041; 1981.
- [4] Walker, T. W.; Gunther, A. H.; Nielsen, P. E. Pulsed laser-induced damage to thin-film optical coatings--part 2: theory. IEEE J. Quantum Electron. QE-17(10): 2053; 1981.
- [5] Wu, Z. L.; Fan, Z. X. Localization of absorption losses in optical coatings. Accepted by Acta Optica Sinica.
- [6] Chen, Y. S. A method for measuring the total integrated scattering from laser mirrors. Acta Optica Sinica 4(3): 285; 1984 March.
- [7] Wu Z. L.; Fan Z. X.; Wang Z. J. Protective effects of overcoats in HR coatings. To be submitted to Appl. Opt.
- [8] Boccara, A. C.; Fournier, D.; Jackson W.; Amer N. M. Sensitive photothermal deflection techniques for measuring absorption in optically thin media. Opt. Lett. 5(9): 377; 1980.

Table 1. Absorptance, refractive index and deposition method of the coatings investigated (G, K9,  $\lambda$ , 1.06 $\mu$ m)

Material	Absorptance ( $10^{-4}$ )			Refractive Index	Deposition Method
	nd, $\lambda/2$	$\lambda$	$3\lambda/2$		
SiO <sub>2</sub>	2.1	2.3	2.0	1.46	EB evaporation T=250° C P=(2-3)×10 <sup>-3</sup> torr
TiO <sub>2</sub>	8.2	8.6	9.1	2.40	
Ta <sub>2</sub> O <sub>5</sub>	5.0	5.6	6.8	2.00	
ZrO <sub>2</sub>	4.1	6.8	9.9	1.90	
ZnS	15.2	19.8	23.1	2.30	R evaporation
MgF <sub>2</sub>	4.8	7.8	Cracked	1.38	
SiO <sub>2</sub> overcoat of ZrO <sub>2</sub> /SiO <sub>2</sub> HR	6.0	6.5	5.8	1.46	EB evaporation T=250° C P=(2-3)×10 <sup>-3</sup> torr
SiO <sub>2</sub> overcoat of TiO <sub>2</sub> /SiO <sub>2</sub> HR	7.8	7.6	8.0	1.46	
Al <sub>2</sub> O <sub>3</sub> undercoat of SiO <sub>2</sub> /TiO <sub>2</sub> AR	7.3	6.4	6.6	1.60	

EB----Electron Beam; R----Resistance; T----Substrate Temperature; P----Deposition Pressure.

Table 2. Standing-field corrected damage threshold ( $\text{Jcm}^{-2}$ ) dependence on film thickness of single layers (10ns-1.06 $\mu$ m-Nd:YAG laser with spotsize=44 $\mu$ m)

Material	nd: $\lambda/8$	$\lambda/4$	$\lambda/2$	$3\lambda/4$	$\lambda$	$5\lambda/4$	$3\lambda/2$
SiO <sub>2</sub> <sup>[a]</sup>	67.1±5.2	66.3±4.6	65.0±4.2	65.7±4.1	65.2±3.8	67.9±5.5	63.8±6.1
TiO <sub>2</sub>	18.6±6.1	19.7±6.8	17.8±3.9		18.4±3.1		16.1±3.6
Ta <sub>2</sub> O <sub>5</sub>	18.3±3.7	20.1±3.5	19.8±4.1		19.3±4.3		17.8±4.5
ZrO <sub>2</sub>	40.5±5.3	35.8±4.4	28.9±3.4		20.3±3.5		10.3±2.6
ZnS	19.8±3.8	16.2±4.1	10.9±3.2		8.4±1.2		6.3±1.0
MgF <sub>2</sub>	53.6±6.1	48.3±4.8	30.1±3.6		5.6±3.2 <sup>[a]</sup>		cracked

[a] Damage threshold data without standing-field correction.

[b] Cracks induced by stresses observable before damage testing.

Table 3. Damage threshold ( $\text{Jcm}^{-2}$ ) of HR coatings on film thickness of SiO<sub>2</sub> overcoats (10ns-1.06 $\mu$ m:YAG laser with spotsize=44 $\mu$ m)

HR material	Without overcoat	nd of overcoat, $\lambda/2$	$\lambda$	$2\lambda$	$3\lambda$	$7\lambda/2$	$4\lambda$
ZrO <sub>2</sub> /SiO <sub>2</sub>	14.1±2.8	25.8±3.2	30.5±2.9	46.3±3.8	55.2±4.0	53.8±3.6	16.3±3.1
TiO <sub>2</sub> /SiO <sub>2</sub>	12.6±3.5	22.5±2.6	28.3±3.6	37.6±4.2	42.8±4.5	26.4±4.8	9.5±3.4



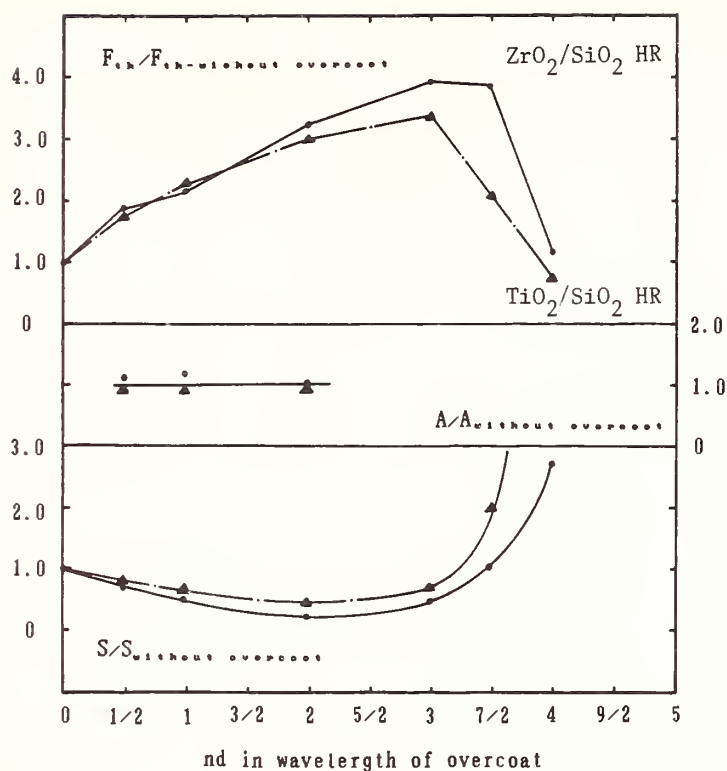


Figure 3. Normalized representation of the results in table 3 [fig.3(a)], in table 1 [fig.3(b)], and measured scattering of the related HR samples before damage testing [fig.3(c)].  
 S—Total integrated scattering.

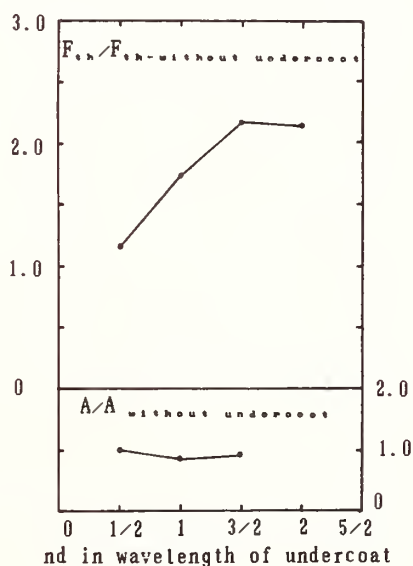


Figure 4. Normalized representation of results in table 4 [fig.4(a)] and table 1 [fig.4(b)].

Table 4. Damage threshold ( $\text{Jcm}^{-2}$ ) dependence of AR coatings on film thickness of  $\text{Al}_2\text{O}_3$  undercoats (10ns-1.06um-Nd:YAG laser with spots size=40um)

AR Materials	Without Undercoat	$nd, \lambda/2$	$\lambda$	$3\lambda/2$	$2\lambda$
$\text{SiO}_2/\text{TiO}_2$	$4.8 \pm 1.4$	$5.6 \pm 2.3$	$8.3 \pm 2.1$	$10.4 \pm 2.1$	$10.3 \pm 2.3$

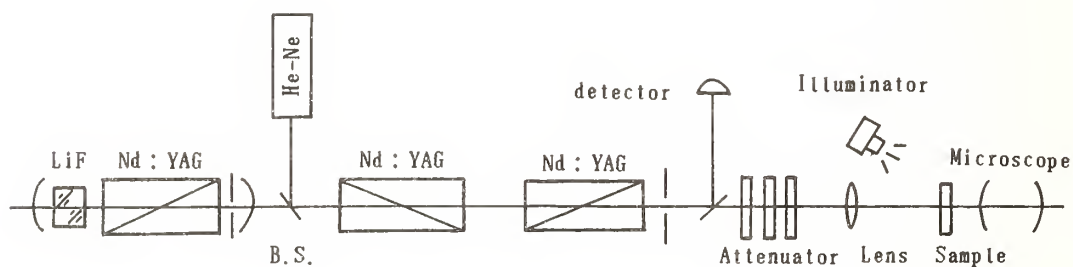


Figure 1. Experimental setup for damage testing.

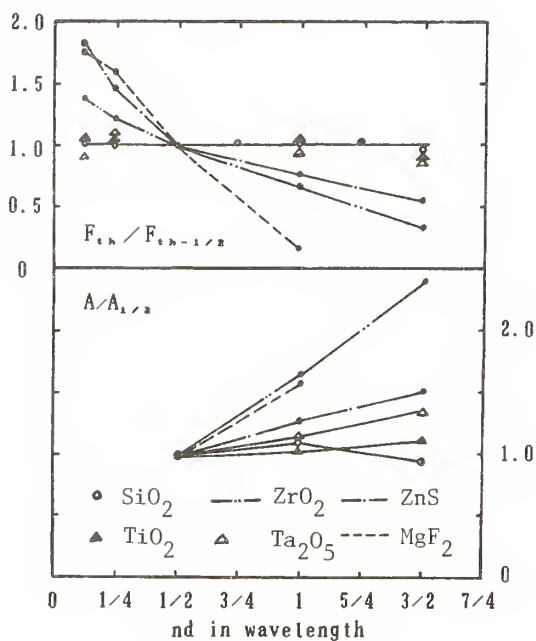


Figure 2. Normalized representation of the results in table 2 [fig.2(a)] and table 1 [fig.2(b)].

$F_{th}$  - Damage threshold ( $\text{Jcm}^{-2}$ );  $A$  - Absorbance; Index 1/2 indicates the sample with a half-wave thickness.

Table 4. Damage threrhold ( $\text{Jcm}^{-2}$ ) dependence of AR coatings on film thickness of  $\text{Al}_2\text{O}_3$  undercoats (10ns-1.06um-Nd : YAG laser with spotsize=40um)

AR Materials	Without Undercoat	nd, $\lambda/2$	$\lambda$	$3\lambda/2$	$2\lambda$
$\text{SiO}_2/\text{TiO}_2$	$4.8 \pm 1.4$	$5.6 \pm 2.3$	$8.3 \pm 2.1$	$10.4 \pm 2.1$	$10.3 \pm 2.3$

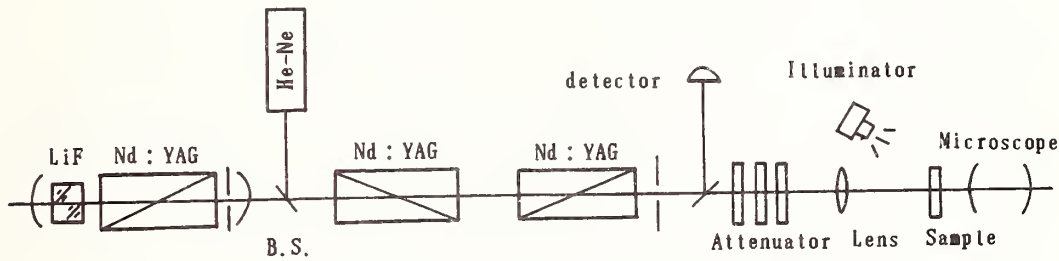


Figure 1. Experimental setup for damage testing.

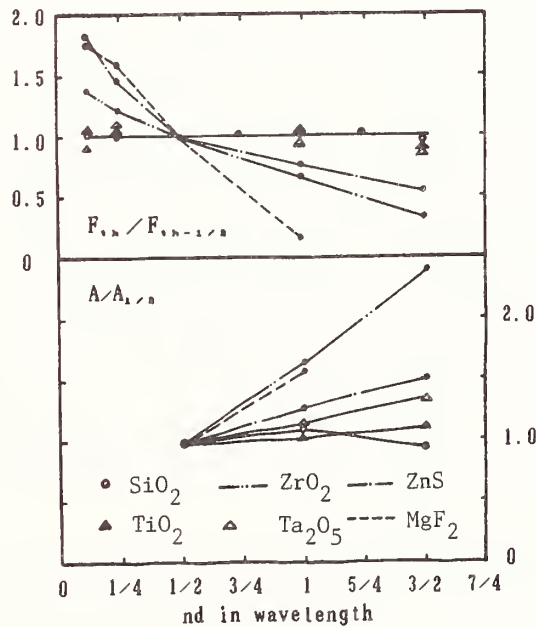


Figure 2. Normalized representation of the results in table 2 [fig.2(a)] and table 1 [fig.2(b)].

$F_{1,n}$  - Damage threshold ( $\text{Jcm}^{-2}$ ); A - Absorptance; Index 1/2 indicates the sample with a half-wave thickness.

Kim F. Ferris, Michael R. Thompson, Gregory J. Exarhos, Wendy S. Frydrych, and Charles B. Duke, Pacific Northwest Laboratory, Richland, WA 99352

Nancy J. Hess, University of Washington, Department of Geology, Seattle, WA 98195

The optical response of a dielectric film is perturbed from that of the analogous bulk material by the inherent film microstructure. A mean field approach has been developed for modelling the real part of the dielectric constant in terms of film microstructure. On this basis, eventual determination of film microstructure parameters such as void density and grain size could be determined from the measured optical response of the film. A semiempirical 'fragment' method has also been used to model the imaginary part of the refractive index for titania. Differences in the electronic transition energies for the anatase and rutile phases of titania are ascribed to dielectric field variation rather than changes in the localized chemical bonding around the titanium site.

Keywords: Dielectric Function; Electronic Structure; Microstructure; Optical Properties

## 1.0 Introduction

The optical response of dielectric films is influenced by phase homogeneity, interfacial strain, grain morphology, and the presence and distribution of voids. Different film deposition techniques have been found to generate distinct microstructures which perturb physical properties from their bulk single crystal values. For example, recent transmission electron microscopy (TEM) results for sol-gel prepared thin films of  $\text{TiO}_2$  have identified the presence of spherical grains, with nearly the same size as the film thickness [1]. In contrast, plasma vapor deposited (PVD) materials are characterized by columnar grain growth [2]. Variation in film microstructure also influences phase transformation phenomena as seen in Raman studies of  $\text{TiO}_2$  films at high pressures [3]. Thus, the optical properties of these materials may not be equivalent to those of a pure phase single crystal. However, knowledge of the microstructure will allow optical properties to be modelled in terms of perturbation of single crystal values. The aim of this paper is to correlate film microstructure and the dielectric properties of single crystal materials to the optical response of dielectric films.

The optical properties of materials are classically defined by an optical response function (equation 1), where  $n'$  represents the measured refractive index, and  $k$  the extinction coefficient.

$$n = n' - ik \quad [1]$$

Both the real and imaginary parts of the optical response are wavelength dependent, particularly in the region of anomalous dispersion. As a first approximation in the absence of strong absorption,



the dielectric constant is simply the square of the refractive index. Ideally, one would like to describe dielectric films in terms of their optical response. Our approach has been to relate the real part of the refractive index to the microstructure of the dielectric films, and the imaginary part to the electronic structure of model systems.

Based upon microstructural results such as those mentioned above, thin films can be treated as a composite material containing grains and voids. Previously, a white light model (equation 2) of the optical response has been used for an approximation of the microstructure in terms of packing fraction. This model provides a first approximation of the microstructure. Serious discrepancies can result since it is assumed that the measured refractive indices can be represented by an average property, and are often compared to values determined at single wavelengths.

$$f = \frac{n(\lambda)}{n(\text{theory})} \quad [2]$$

Quasi-static models offer the incorporation of finer details into the dielectric response. The classical models for dielectric function define limits for the measured dielectric response. Commonly cited examples of these methods are the Wiener [4] and Hashin-Shtrikman [5] limits which define bounds for both the real and imaginary parts of the dielectric response. The upper Wiener limits (equation 3a) are the linear combination of the component systems, where  $f_i$  is defined as the volume fraction of component  $i$  and  $\epsilon_i$  as its dielectric constant, providing no screening and the boundaries parallel to the applied field. The lower limits (equation 3b) are defined by the maximum screening condition. The Hashin-Shtrikman limits are simply the volume defined limits in the Wiener formalism.

$$\epsilon = f_a \epsilon_a + f_b \epsilon_b \quad [3a]$$

$$\frac{1}{\epsilon} = \frac{f_a}{\epsilon_a} + \frac{f_b}{\epsilon_b} \quad [3b]$$

Bruggeman extended these models to include an effective medium (equation 4) in which models (EMA) can effectively describe the optical dielectric response of the material if packing fraction is desired, but offer no new insight into the material science of the film itself. The implicit

$$\epsilon_h = \frac{q\epsilon_a\epsilon_b + (1-q)\epsilon_h(f_a\epsilon_a + f_b\epsilon_b)}{(1-q)\epsilon_h + q(f_a\epsilon_b + f_b\epsilon_a)} \quad [4]$$

assumptions to this model are that the particle size in the microstructure remains small compared to the wavelength of light, and also that the properties of a bulk solid can be used to describe the individual grain properties. In keeping with the effective medium approximation, the  $\epsilon_h$  value is determined from self-consistency.

Nearing  $d/\lambda \sim 0.25$  ( $d$ -particle size,  $\lambda$ - light wavelength), waveguiding and propagation effects can become significant. For dielectric films prepared by PVD, TEM results indicate that the microstructure spans the film thickness, with grains growing in a columnar fashion. Dielectric films for optical applications have thicknesses less than  $1 \mu$ , and thus will require specific corrections for finite wavelength effects.

$$\sum f_i \left[ \frac{\epsilon_i - \epsilon}{\epsilon_i + 2\epsilon} + \frac{1}{30} (\pi d_i / \lambda_i)^2 (\epsilon_i - \epsilon) \right] = 0 \quad [5]$$

Stroud and Pan [6] have proposed the dynamic effective medium approximation (DEMA - equation 5) which incorporates corrections for magnetic dipole effects. This model for the microstructure uses a composite solid consisting of spherical grains and voids, in which  $d_i$  is a spherical diameter, and  $\lambda_i$  is the wavelength of the probe light source.

A simple view of the absorption spectra of solids is a system of coupled oscillators, in which the characteristic resonance frequency of a single mode is coupled to the electric field [7]. Electronic structure methods are often used to determine the nature of allowed transitions in molecules, and by extension, the band structure in condensed phases. However, *ab initio* molecular orbital calculations typically are both storage and computationally intensive, which restrict their utility in problems of this magnitude. Semiempirical methods such as the INDO/S approximation [8] are commonly used to circumvent these problems, and have been shown to give good agreement with experimental results for a number of inorganic systems [8]. Basically, these methods solve the electronic Schrodinger equation, assuming the Born-Oppenheimer approximation, using a linear combination of atom centered orbital functions to approximate the molecular orbitals. The optical excitation spectra are generated from excitations of electrons in high lying occupied molecular orbitals to low lying unoccupied ones, allowing for configuration mixing of orbitals with the same electronic symmetry.

## 2.0 Methods

Modelling of the microstructure was performed using the above outlined mathematical relationships on an Apple Macintosh computer. Packing and particle size parameters determined for the effective medium and dynamic effective medium models were found by minimizing the least squares differences from experimental values. Experimental data for pure phase  $Al_2O_3$  were taken from reference 9, for  $Al_2O_3$  composite media reference 10. The wavelength dependence to the optical response of  $TiO_2$  materials was determined on a Hewlett-Packard HP8451A spectrophotometer; optical parameters were obtained using ellipsometry.

LCAO-MO-SCF calculations using the INDO/S approximations were performed on a VAX 11/780 minicomputer at Pacific Northwest Laboratory. All calculations reported here were made using the default values for empirical two-electron repulsion integrals [11] and spectroscopic parameterization for  $\beta$ . Beta resonance parameters for Ti and O were -7.5 (s,p) and -21.0 (d), and -27.0 (s,p), respectively. The electronic spectrum of the  $[TiO_6]^{8-}$  molecular fragments was used to simulate the response of single crystal material and were assigned from the spectroscopic transition energies composed of single excitations from the 5 highest occupied molecular orbitals, to the 5

lowest energy virtual orbitals. A 10x10 configuration interaction calculation was performed for both crystalline phases (anatase and rutile) of titania to verify that sufficient excitations were included in the interaction scheme. These results indicated no significant lowering in the transition energies with increased number of configurations.

### 3.0 Results and Discussion

Modelling of the optical properties of thin films occurred in two separate efforts, involving microstructure and electronic absorption considerations. The microstructural information provided by dielectric function measurements, along with known properties of ideal crystals were used to model the dielectric function of  $\text{Al}_2\text{O}_3$  composite media and rutile phase titania films. In a later section, the electronic structure of molecular fragments as model systems for  $\text{TiO}_2$ , and their optical excitation spectra will be discussed.

#### 3.1 Effects of Microstructure on the Real Refractive Index

In order to better understand the optical properties of dielectric films, we evaluated the various dielectric function models discussed previously. Our ultimate goal is to parameterize these models, and use them as predictive tools for the microstructure of dielectric films. In Table 1, we list the measured dielectric values for  $\text{Al}_2\text{O}_3$  composite media as reported by Egan and Aspnes [10] along with the values estimated from the various effective medium models at the experimental packing density.

The performance of the various models improved only with the development of a model for microstructure in the composite media. The dielectric values for the effective medium model (EMA) proposed by Bruggeman markedly (15-31%) underestimate the experimental values. Using the dynamic effective medium models proposed by Stroud and Pan, we can introduce microstructure into our model of the composite media in terms of spherical particles. Assuming that the diameter of  $\text{Al}_2\text{O}_3$  particles was maintained in the compressed pellet, the predicted values (DEMA-1) noticeably overestimated (26-45%) the experimental values. On the other hand, using spherical voids (DEMA-2) severely underestimates the experimental values (45-61%).

Table 1 - Dielectric Values for Composite  $\text{Al}_2\text{O}_3$  Media using Dynamic Effective Medium Model

<u>Wavelength</u>	<u>Experimental</u>	<u>EMA</u>	<u>DEMA-1</u>	<u>DEMA-2</u>	<u>DEMA-3</u>	<u>DEMA-3'</u>
5000 Å	2.19	1.856	3.12	1.199	2.064	2.377
4000 Å	2.531	1.870	3.248	1.144	2.093	2.429
2800 Å	2.762	1.914	3.469	1.082	2.166	2.541
2000 Å	2.654	2.015	3.846	1.047	2.325	2.761

Packing fraction = 0.46, 1 $\mu$  particle diameter

The DEMA-3 model has incorporated both spherical  $\text{Al}_2\text{O}_3$  particles and voids (both  $1.0\ \mu$  in diameter) and does markedly better in predicting the dielectric value (6-22%) even though it is physically unrealistic. When we refine this model by estimating a void size ( $0.732 \times d_i$ ) based upon available volume in a unit box containing a spherical particle, the DEMA-3' model gives even better agreement ( $\pm 8\%$ ). Thus, as a result of incorporating microstructural information into our dielectric models, we have been able to significantly improve on the performance of the model using only particle size and the dielectric values of the pure phase material. In Table 2, we show that the incorporation of this simple refinement could lead to predictions of packing fraction. One reason for the poor performance of the EMA model is the sizeable wavelength effects found when the wavelength of probe light is within an order of magnitude of the particle size.

Table 2 - Calculated Packing Fractions for Composite Media ( $\text{Al}_2\text{O}_3$ )

	<u>1.0 <math>\mu</math> Sample</u>	<u>3.0 <math>\mu</math> Sample</u>
Experimental	0.46	0.62
EMA	0.68	0.86
DEMA-3	0.62	-----
DEMA-3'	0.46	0.71

Using this same approach, we measured the dielectric values for  $\text{TiO}_2$  films with film thickness as indicated in Table 3. We had characterized these films (prepared via ion assisted plasma vapor deposition) as polycrystalline, randomly oriented rutile phase material by Raman spectroscopy. The quasi-static limits as noted by the Hashin-Shtrikman model would estimate the packing fractions for these films between 0.80 and 1.0, the upper bound is physically unlikely considering TEM micrographs and also provides little structural detail. Using the DEMA-3' model, satisfactory fits of the experimental data could be obtained as shown in Figure 3 with trends similar to those for the earlier  $\text{Al}_2\text{O}_3$  dielectric models. Packing fractions in the dielectric films decreased as the models incorporate microstructural features, and also with increasing film thickness. In addition, by assuming microstructural details, we are able to reduce the limits of the packing fraction, now being bound by the small particle limit (EMA) and a DEMA model which assumes spherical grains and voids.

Table 3 - Calculated Packing Fractions for PVD-prepared  $\text{TiO}_2$  Thin Films

<u>Sample</u>	<u>d(<math>\mu</math>)</u>	<u>EMA</u>	<u>DEMA-3</u>	<u>DEMA-3'</u>
112F	0.926	0.80	0.72	0.59
112A	0.159	0.76	0.71	0.68
112E	0.710	0.80	0.73	0.61
114E	0.450	0.76	0.71	0.69

Refractive indices for rutile phase  $\text{TiO}_2$  taken from reference 12.



These results have demonstrated two significant points. First, the dielectric properties of the composite media are sensitive to particle size. Second, by introducing a rough approximation of the microstructure to the model, the quality of the predicted dielectric values improved significantly. Sizeable errors in packing fraction were noted for models which did not include microstructure. It is also worth noting that the small particle limit to the dynamic effective medium model ( $d_i \rightarrow 0$ ) is simply the effective medium values.

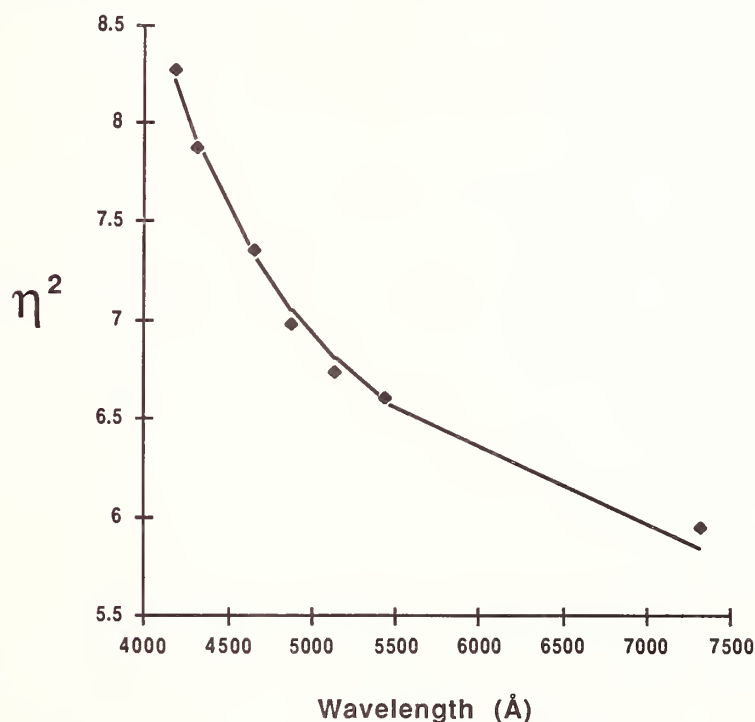


Figure 3 - Comparison of Experimental and Predicted(DEMA-3') Dielectric Function of PVD prepared TiO<sub>2</sub> dielectric films.

### 3.2 Electronic Structure Calculations on Model Systems for TiO<sub>2</sub>

The absorption spectra of TiO<sub>2</sub>, manifested in the imaginary part of the dielectric function, can be represented as a linear combination of oscillators resonating at their absorption maxima, in the electric field generated by the remaining solid. We performed LCAO-MO-SCF calculations using the INDO/S approximations on model complexes of anatase and rutile phase forms of TiO<sub>2</sub> in order to clarify two issues: 1) the sensitivity of the electronic transitions to the local molecular geometry changes as models for the molecular distortions of the complex under mechanical stress, and 2) the effect of the dielectric field on the electronic structure. In previous work, we had noted large vibrational band shifts in the Raman spectra for both anatase and rutile forms of TiO<sub>2</sub> under local stress and at high pressures. As Raman spectroscopy probes the chemical bonding in

dielectric films, the correlation of the electronic structure with lattice distortions of the metal oxide film could potentially provide a sensitive predictor for molecular structure via the dielectric function.

In order to separate the effects of the dielectric field represented by the solid and the molecular nature of the electronic transition, we used the molecular fragment  $[\text{TiO}_6]^{8-}$  as a first order model for the metal oxide surface. Recent work by Burdett [13] on metal oxides has shown that the phase stability of the rutile form of  $\text{TiO}_2$  can be reproduced by a  $[\text{TiO}_6]^{8-}$  molecular complex, and is determined by the anionic field generated by the oxygen sites. Such results are in agreement with the experimental evidence for the absorption maxima for rutile and anatase phase  $\text{TiO}_2$  using diffuse reflectance measurements [14]. These results indicated that the absorption

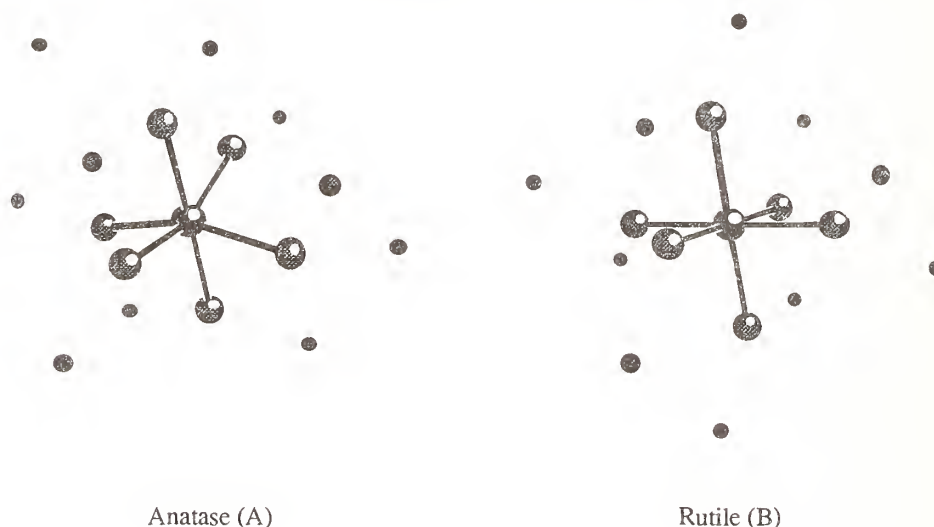


Figure 4 -  $[\text{TiO}_6]^{8-}$  molecular fragment models used to simulate electronic transitions of anatase (A) and rutile (B) phases of  $\text{TiO}_2$ . Molecular geometries were taken from experimental data in reference 17. Noticeably smaller spheres represent second nearest neighbor sites around titanium.

maximum for rutile is approximately  $36400 \text{ cm}^{-1}$  and for anatase approximately  $40000 \text{ cm}^{-1}$ . The observed electronic transition corresponds to a charge transfer where an electron localized on an oxygen p orbital is promoted to a titanium d-orbital. As seen in Figure 4 above, the anatase crystal structure is angularly distorted from the ideal octahedral symmetry, while the rutile phase is axially distorted. In crystal field terms [15], the observed energy difference has been explained in that the axial distortion found in the rutile phase breaks the degeneracy of the  $t_{1u}$  orbital levels to even a greater extent than the anatase form. It is expected that the electronic transition energy would shift to lower energy in response to the dielectric field in the solid [16].

The results of the electronic structure calculations of  $[\text{TiO}_6]^{8-}$  are given in Table 4. The geometry for the anatase and rutile phase  $\text{TiO}_2$  models was derived from the experimental geometry [17], and was taken as the Ti site with its six nearest neighbor oxygen atoms. As a first approximation to the effect of the dielectric field represented by the solid, point charges were located at the the next nearest neighbor Ti sites. The point charge value used in these calculations

corresponded to the Mulliken [18] charge on the Ti sites from the isolated molecular complex calculations. The values given in this table correspond to the lowest 5 eigenvalues from a singly excited, 5 x 5 configuration interaction. The oxygen lone pair p orbital to titanium d orbital transitions have been labelled for clarity.

There are several interesting points illustrated in these results. First, the local geometry changes around the titanium site have only a minor effect on the electronic transition energies. The observed optical transition energies show only a small difference between the anatase and rutile forms; however, the rutile form lies 784  $\text{cm}^{-1}$  lower than the anatase. Thus, the angular distortion

Table 4 - Calculated Electronic Transition Energies for  $[\text{TiO}_6]^{8-}$  ( $\text{cm}^{-1}$ )

<u>Anatase</u>	<u>Rutile</u>	<u>Anatase + Pt.Charges</u>	<u>Rutile + Pt. Charges</u>
45212( $\text{O}_p \rightarrow \text{Ti}_d$ )	45996( $\text{O}_p \rightarrow \text{Ti}_d$ )	34462	35887 ( $\text{O}_p \rightarrow \text{Ti}_d$ )
45212	48251	38065 ( $\text{O}_p \rightarrow \text{Ti}_d$ )	37496
46767	49149	43117	38828
50948	50164	45438	42678

Using the INDO/1 approximation, 5x5 configuration interaction.

for anatase distorts the crystal field to a greater extent than rutile contrary to past expectations. In the bulk solid, rutile phase  $\text{TiO}_2$  requires  $\sim 3600 \text{ cm}^{-1}$  less energy than anatase, making the shift from discrete units to periodic solid over  $4000 \text{ cm}^{-1}$ .

The obvious cause for these effects are the dielectric field represented by the solid. After modelling the next nearest neighbor interactions with point charges, these same calculations split the optical transition energies with the rutile form being  $\sim 2200 \text{ cm}^{-1}$  lower in energy than the anatase form. Another result of this model 'dielectric field' was that the first electronic transition in the anatase model changed from having a major component of d-orbital character to only a minor constituent (making the second eigenvalue the  $\text{O}_p \rightarrow \text{Ti}_d$  transition); while the rutile form remained nearly the same. Thus, we note that the differences in the electronic transitions for these materials arise mostly from the dielectric field generated by the solid, rather than geometric differences in the first coordination sphere around the titanium site.

In summary, we have found that a model of the optical transitions for  $\text{TiO}_2$  dielectric films based solely upon local molecular geometry is insufficient. As a result of the electronic structure calculations, the essential element will be a model of the dielectric field of the solid as incorporated with a molecular subunit. Such observations are in agreement with the proposals of Wemple and Di Domenico [19] who proposed a linear correlation between band gap and dielectric field. An interesting observation is that the differences in phase stability between anatase and rutile forms of  $\text{TiO}_2$  noted by Burdett and coworkers are not reproduced for optical transitions of the  $[\text{TiO}_6]^{8-}$  subunits. However, it is important to note that these models have served as only a first

approximation to the electronic structure of metal-oxide systems, and one possible cause for the poor performance of the INDO/S method would be the use of small rather than extended molecular fragments. Further work using both a tight-binding approach to the electronic band structure and Kirkwood-Onsager models for dielectric effects is currently underway in order to better understand the electronic structure of TiO<sub>2</sub> optical transitions.

#### 4.0 Conclusions

Dielectric function offers a bridge between microstructure and electronic structure. By modelling the real portion of the refractive index using effective medium models of composite media, microstructural information can result from simple optical measurements. Single wavelength methods which are often used to estimate the packing fraction can overestimate the packing fraction, and offer little detail into either the microstructure or molecular structure of the dielectric film. Such shortcomings are commonplace when finite wavelength effects become significant ( $d/\lambda \rightarrow 0.25$ ). Electronic absorption information can be obtained from the imaginary part of the dielectric function and offers similar promise. For TiO<sub>2</sub> materials, the variations in the optical transition energies between anatase and rutile forms of TiO<sub>2</sub> are caused by the extended crystal structure of the material, and not by the localized chemical bonding around titanium. Electronic structure methods such as INDO/S can provide structural and electronic information at the molecular level when incorporated with a model of the dielectric field as simple as point charges located at the next nearest neighbor sites. Knowledge of the dielectric function for dielectric films can potentially be utilized to quickly characterize the microstructural and electronic properties of dielectric films. Such information will require fairly accurate optical data, but is within the realm of conventional techniques such as ellipsometry.

---

Pacific Northwest Laboratory is operated by Battelle Memorial Institute for the U.S.  
Department of Energy, Office of Basic Energy Sciences under Contract DE-AC06-76-RLO 1830.

#### 5.0 References

- [1] W.S. Frydrych, G.J. Exarhos, K.F. Ferris, N.J. Hess, Proc. Mat. Res. Soc. Symp. 121, 343 (1988).
- [2] R. E. Klinger and P. Swab, Proc. of SPIE, R.I. Seddon: Ed., Vol. 678, 41 (1986).
- [3] G.J. Exarhos, K.F. Ferris, W.S. Frydrych, and N.J. Hess in Laser Induced Damage in Optical Materials: 1987, NBS Special Publication.
- [4] D.E. Aspnes, Thin Solid Films 85 249, (1982).
- [5] Z. Hashin and S. Shtrikman, J. Appl. Phys. 33 3125, (1962).
- [6] D. Stroud and F.P. Pan, Phys. Rev. B 17 1602, (1978)



- [7] P.A. Cox, *Electronic Structure and Chemistry of Solids*, (Oxford, New York, 1987).
- [8] a) M.C. Zerner, *Ann. N.Y. Acad. Sci.* 367, 35 (1981); b) W.P. Anderson, W.D. Edwards, and M.C. Zerner, *Inorg. Chem.* 25, 2728 (1986).
- [9] W.G. Egan and T.W. Hilgeman, *Optical Properties of Inhomogeneous Materials* (Academic Press, New York, 1979).
- [10] W.G. Egan and D.E. Aspnes, *Phys. Rev. B* 26, 5313 (1982).
- [11] N. Mataga and K. Nishimoto, *Z. Phys. Chem.* 13, 140 (1957).
- [12] J.R. DeVore, *J. Opt. Soc. Amer.* 41, 416 (1951).
- [13] a) J.K. Burdett and T. Hughbanks, *Inorg. Chem.* 24, 1741 (1985); b) J.K. Burdett, *Inorg. Chem.* 24, 2244, (1985).
- [14] H. Bevan, S.V. Dawes, and R.A. Ford, *Spect. Acta* 13, 43 (1958).
- [15] a) A.L. Companion and R.E. Wyatt, *J. Phys. Chem. Solids* 24, 1025 (1963); b) V.N. Pak and N.G. Ventov, *Zh. Fiz. Khim.* 49, 2538 (1975).
- [16] W.A. Harrison, *Solid State Theory*, (Dover, New York, 1980).
- [17] D.T. Cromer and K. Herrington, *J. Amer. Chem. Soc.* 77, 4708 (1955).
- [18] R.S. Mulliken, *J. Chem. Phys.* 23, 1833 (1955).
- [19] S. H. Wemple and M. DiDomenico, *Phys. Rev. Lett.* 23, 1156 (1969).

- Question: Paul Levy from Brookhaven. I'd like to point out that your curves of reflectivity loss versus exposure and time are in quite accurate accord with well known curves for radiation damage in a number of different materials. And once you start out with a defect precursor, during a radiation, you convert that defect precursor to something which is observed in your reflectivity loss. In addition to that, the curves describe the kind of process where you are introducing these defects and-or their precursors. Also, the defects and-or their precursors are being destroyed by some sort of back reaction. One of your plots at different levels is in very good accord with the mechanism that I just described. I should also point out that the dK which you observed is often attributed to the thermal conversion of the defect back to the precursor.
- Answer: Well, the experiment wasn't designed to identify the damage mechanisms, but we hope to go in that direction.
- Question: I believe that titania, especially at 248 nanometers is almost black, and it definitely isn't absorbing at 351, why would you even consider using a titania material coating for a reflector in these wavelengths?
- Answer: We wanted to first of all measure the reflectivity loss on a coating we know is not a good coating for UV reflectors and we wanted to have a range of coatings starting from those which are considered UV resistant to those which tend to be readily damaged by UV.
- Question: I'd like to follow up a little bit on Paul Lovey's comment about radiation induced damage in a material. Sometimes in UV irradiated or even harder irradiated materials, we see color centers forming that can be annealed out thermally. I wonder if you had treated any of your samples thermally.
- Answer: Well, just before I left to the meeting, we did take one of the TiO<sub>2</sub> samples. We exposed it to 248 nanometer light at a fluence of 45 millijoules per centimeter squared. We did a standard run with a 65 minute exposure followed by a 35 minute recovery. We did see similar recoveries from what you've seen on the data. And then proceeded to apply heat to the sample. It's not a highly controlled experiment but I was interested to see what happens. The sample was heated to about 100° centigrade for a short period of time, about 15 minutes, allowed to cool, and then re-measured. The loss at the end of recovery period that you see on the data is effective permanent. At least for that short period of time that we heated the sample at that temperature, we saw no recovery.
- Question: The loss in reflectance that you saw was actually, if I'm correct, a loss in specular reflectance; it should not necessarily be equated to a loss in absorption. It could well be scattered light. And, in line with that, I wondered if you did any scattering measurements on these wavelengths on the samples?
- Answer: The scattering measurements that we attempted were quite crude, it's a matter of exposing the site that was UV damaged with the heating beam. And just a look with a microscope to see if any scattered visible light could be seen and that we did not see any in any of the experiments, other than the ones that were close to catastrophic damage or had catastrophically damage. Again, it's a crude study, but it indicates that the scattering losses are not major.
- Question: May I respond to the question about why you would ever put 248 on titanium. One of the components in the burst FBL has titania in the coating. We wanted to find out, among other things, how big a trouble we were in.
- Answer: Well, I know that the FBL at Orsay did quite a bit of study on harmonic damage on titanium. They had used titanium for their cavity mirrors. I thought it would be interesting to follow up on some of their work, which they had expectedly exposed these mirrors to the harmonics within their FBL for long periods of time. They've seen similar losses the order of 2%.

Smoothing of Optical Surfaces with Dielectric Thin Films  
Produced by Reactive Ion Plating Deposition

Francis J. Boero  
Newport Corporation, Fountain Valley, CA 92708

Russel A. Chipman  
University of Alabama, Huntsville, AL 35899

Karl H. Guenther  
CREOL, University of Central Florida, Orlando, FL 32826

In this paper we report investigations into a suspected surface smoothing capability of dielectric thin films deposited by low voltage reactive ion plating deposition. This investigation was motivated by preliminary results reported in 1987 at the Boulder Damage Symposium which showed 0.2 nm rms roughness for RIPD  $\text{TiO}_2$  single layers of up to 500 nm thickness on regular sheet glass substrates.

Key words: dielectric multilayers; electron microscopy; ion plating; surface profiling; surface roughness;  $\text{TiO}_2$ ;  $\text{ZrO}_2$

While titania thin films deposited by standard reactive evaporation grow in the well known columnar microstructure [1] (fig. 1), and consequently show a significant increase in surface roughness [2] (fig. 2), low voltage reactive ion plating produces titania films with a constant roughness as low as 0.2 nms rms over a whole range of thicknesses up to 500 nm [3] (fig. 3). This extremely smooth surface can also be seen in the transmission electron micrograph of a direct cross section of that particular specimen (fig 4). Figure 3 shows the actual Talystep surface profile of the same specimen.

We have made some dedicated experiments for investigating and verifying this smoothing behavior. Substrates were used which were precharacterized using either a TALYSTEP or WYKO TOPO 2-D surface profilometer, and a variety of dielectric thin films were deposited, both single layers and multilayers, by low voltage reactive ion plating deposition. The surface roughness of the completed films was again measured with either of the two instruments.

Low voltage reactive ion plating deposition has been described elsewhere in some detail [4-6]. The coatings were deposited in a commercially available Balzers BAP 800 high vacuum box coater, specifically equipped for low voltage reactive ion plating deposition (Fig. 5). The principal difference of this technique, as compared with other ion assisted deposition techniques, is the ionization of the coating material in a ratio of 10 to 20 percent and the self biasing of the dielectric substrates mounted in the insulated rotary dome to -5 to -10 eV with respect to the plasma. Therefore, the substrates and the growing films are bombarded with both argon ions and evaporant ions in a favorable low energy range, with a large spatial uniformity of the ion supply. Further, because of the electrostatic nature of the attraction of the ionized accelerated particles, they arrive at trajectories ending normal on the substrate surface. This leads to a uniform densification over the whole substrate carrier, wholly independent of the orientation of the substrate surface with respect to the vapor source. The materials deposited and the process parameters are summarized in Table 1. Because of conductivity requirements, the starting materials are the metal or a suboxide of the desired oxide film. Therefore, a fairly high oxygen partial pressure of about  $10^{-3}$  mbar is necessary to achieve full oxidation of the coatings. This high pressure violates the usual mean free path condition for high vacuum evaporation, and



the resulting gas phase collisions of the evaporated molecules and atoms contribute to a better thickness uniformity of the growing films over the whole useful area of the rotary dome. The collisions in the plasma also allow for additional ionization of the evaporated material and of the reactive gas by electron transfer processes as indicated in fig. 5.

The surface roughness measurements were carried out with a commercially available WYKO TOPO 2-D optical profilometer at Newport Corporation, and with a digitized stylus-type Talystep profilometer [7] initially set up by Jean M. Bennett and Charles W. Fellows at the University of Alabama in Huntsville. Figures 6 and 7 give examples of surface profiles typically obtained with these two instruments. In order to obtain information on the film formation and film roughness on a microscale, we choose scan lengths of 100 to 250 micrometers, excluding particulate disturbances of the surfaces (spatters and pin holes).

In a dedicated experiment, we deposited  $\text{TiO}_2$  single layers of 3 different thicknesses on precharacterized substrates in 3 different  $90^\circ$  sectors, so as to have these 3 different layer thicknesses (1, 7, and 13 quarterwave optical thickness at 630 nanometers) on one sample. Table 2 gives the result of the surface roughness measurements of this particular experiment. It shows that for the 1 and 7 quarterwave thicknesses the  $\text{TiO}_2$  films maintain the starting substrate surface roughness within the accuracy of the Talystep measurement. The 13 quarterwave  $\text{TiO}_2$  layer, however, shows a catastrophic increase of the surface roughness, which was clearly noticeable in a Nomarski differential interference contrast microscope also. The nature of this catastrophic increase is not yet known, however, we believe that it was an exception since we found smooth surfaces with rather thick  $\text{TiO}_2$  layers in other cases [3]

Table 3 gives a summary of all of the results obtained in this study. The results listed in the first line are particularly interesting. The TOPO 2-D, an optical surface profilometer, yielded a comparable surface roughness after the coating had been deposited, as for the bare substrate. The TALYSTEP, a contacting surface probe, yields a ten times smaller rms surface roughness, although in all other cases the TALYSTEP values are about twice those obtained with the TOPO 2-D. This result suggests that the TOPO 2-D did not really measure the surface roughness of the coating, but rather that of the substrate. This is easily understandable in that the optical thickness of that particular single layer was 4 QWOT at the measurement wavelength of 633 nm. The coating acts as an absentee layer in this case for the probing light, so that the substrate surface is being measured through the coating.

In summary, we have found that low voltage reactive ion plating deposition preserves the surface roughness of well polished substrates ( $\delta \text{ rms} \leq 1 \text{ nm}$ ), but apparently smoothens rougher surfaces. This appears to be true for both single layer coatings of  $\text{ZrO}_2$ ,  $\text{TiO}_2$ , and  $\text{Ta}_2\text{O}_5$  and multilayer coatings of these materials in combination with  $\text{SiO}_2$  for the low index layers. Admittedly, these results have been obtained with a limited number of experiments.

The surface smoothing capabilities of low voltage reactive ion plating deposition may, when reproducibly obtained, ridicule existing or future superpolishing efforts. A single event of catastrophic roughening observed with a rather thick  $\text{TiO}_2$  single layer needs further investigations in order to eliminate this uncertainty.

We would like to acknowledge the contribution of David H. Burns and Josephine Edgell of the University of Alabama in Huntsville for their Raman and Talystep investigations; of Paul Sachdeva, Harald Schink and Zeev Taubenfeld of CREOL for their work in coatings; Rick Seboldt of the Newport Corporation for his work in optical surface profilometry using the WYKO TOPO 2-D; and finally,



Gauthier Fanmuy, Visiting Scholar from the Ecole Nationale Supérieure de Physique de Marseille, France, for his help in developing this manuscript. Harald Schink and Zeev Taubenfeld were also International Visiting Scholars on leave from the Institute of Quantum Optics, University of Hanover, Germany, and the Armament Development Authority (Rafael), Haifa, Israel, respectively.

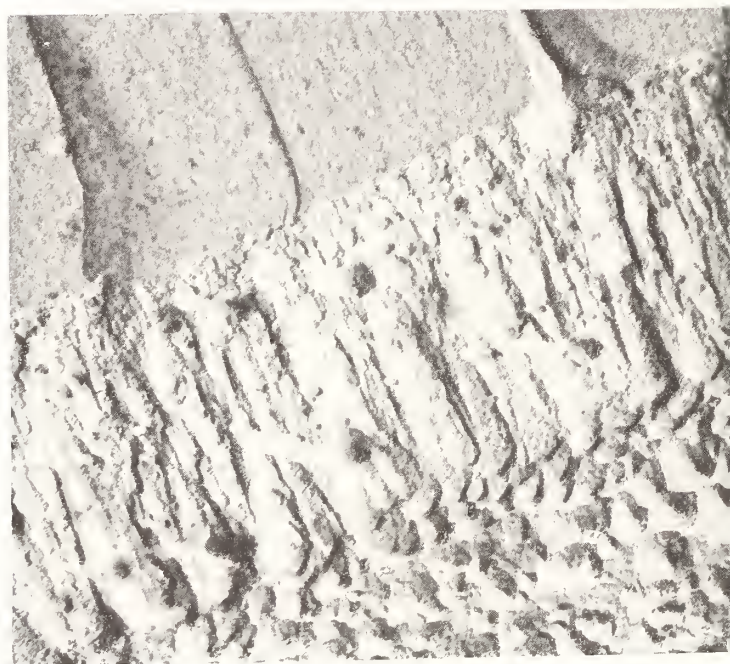
## References

- [1] K.H. Guenther and H.K. Pulker, Appl. Opt. 15, 2992 (1976).
- [2] K.H. Guenther, Appl. Opt. 23, 3806 (1984).
- [3] K.H. Guenther, Boon Loo, Hans K. Pulker, Andreas Saxer and Steven C. Seitel, "Comparative Study of Reactively Evaporated vs. Ion-Plated  $\text{TiO}_2$  Thin Films", paper presented at the 19th Boulder Laser Damage Symposium, Boulder, CO, Oct. 26-28, 1987.
- [4] E. Moll, R. Buhl, and H. Daxinger, U.S. Patent Nr. 4,448,802 (1985).
- [5] H.K. Pulker, W. Haag, and E. Moll, U.S. Patent Nr. 4,619,748 (1986).
- [6] K.H. Guenther *et al.*, J. Vac. Sci. Technol. A 7, in the press (May/June 1989).
- [7] J.M. Bennett, J.H. Dancy, Appl. Opt., 20, 1785 (1981).

## Comments

Question: Let me ask one first. The example that you showed of smoothing was for plate glass as I understood. And we went from 30 some angstroms down to 4 angstroms. In all of the other examples the roughness were of the order of 4 angstroms. So I wonder if you have any data on the auto covariance function of the plate glass? What sort of roughness are we looking at? Do you expect the same sort of smoothing behavior for different sorts of auto covariance functions?

Answer: The auto co-variance functions. Very good question, in fact. We did look at the auto-co-variance function of all the samples characterized. And the plate glass had essentially a zero auto co-variance function after about 100 microns on the surface. After reactive ion beam plating, the auto co-variance fell to zero within 20 microns. So we were bringing that down to a truly amorphous surface. The other samples tested had auto co-variance lengths after polish on the order of 30 to 20 nanometers. So again, there the auto co-variance length was preserved, we did not see an improvement. I didn't show that data because with all the scatter it looked like a diamond turned mirror, just spikes all over the spectrum.



9 QWOT @ 633 nm

Figure 1.  $\text{TiO}_2$  single layer coatings by Reactive Evaporation: evolution of columnar microstructure and surface roughness with film thickness (TEM replicas).

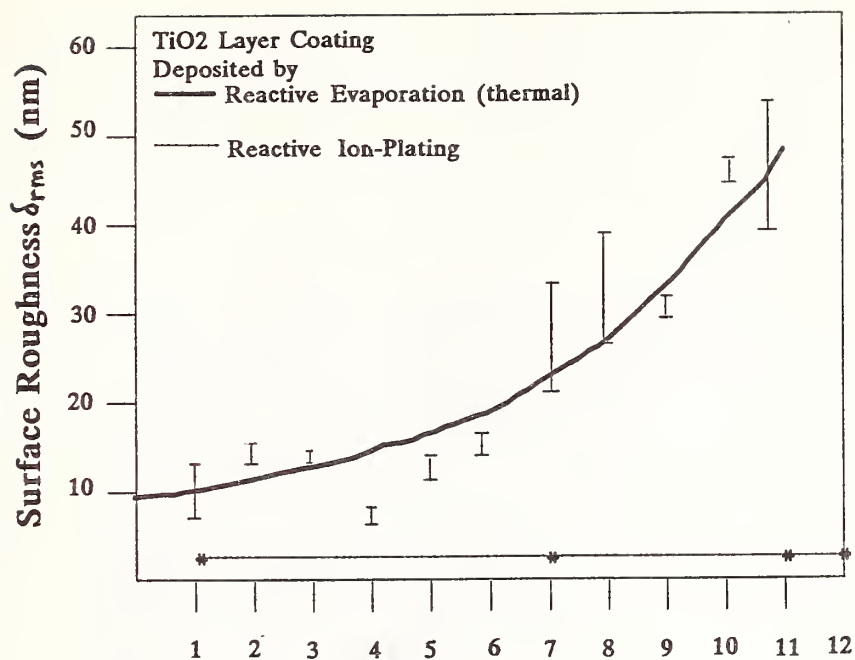


Figure 2. Optical thickness (QW @ 633 nm)

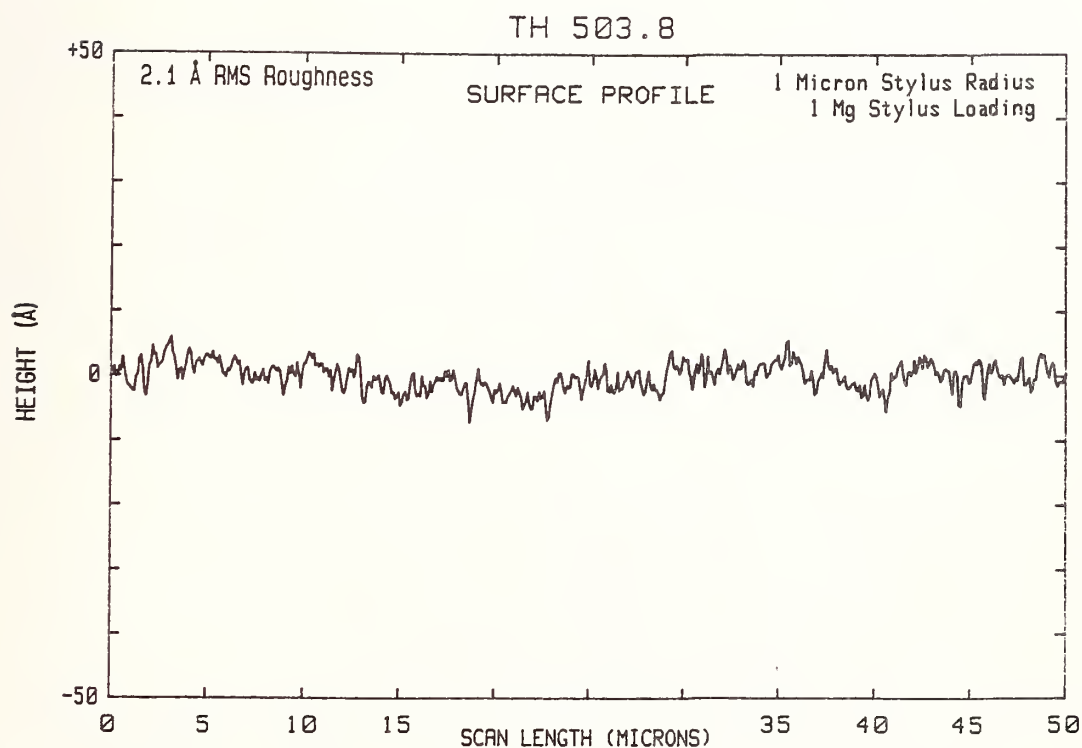


Figure 3. TALYSTEP surface profile taken from an about 50 nm thick  $\text{TiO}_2$  single layer coating, deposited by reactive ion plating: 0.21 nm rms surface roughness (J. Edgell).

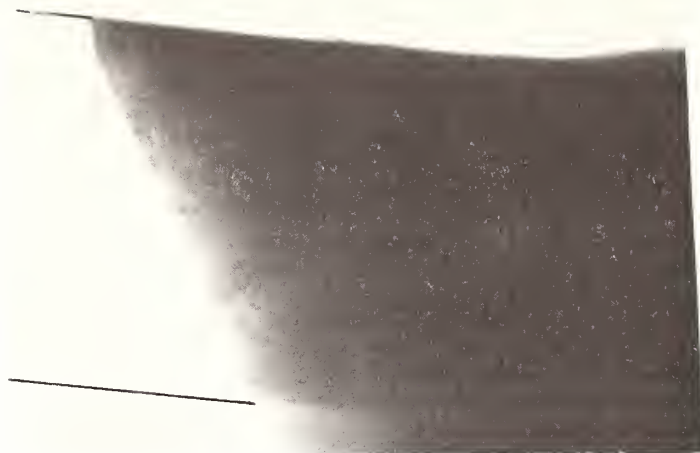


Figure 4.  $\text{TiO}_2$  single layer coating by reactive ion plating (11 QWOT @ 514 nm): Direct transmission electron micrograph (TEM) of a microtome-sliced cross-section. (D. Windham)

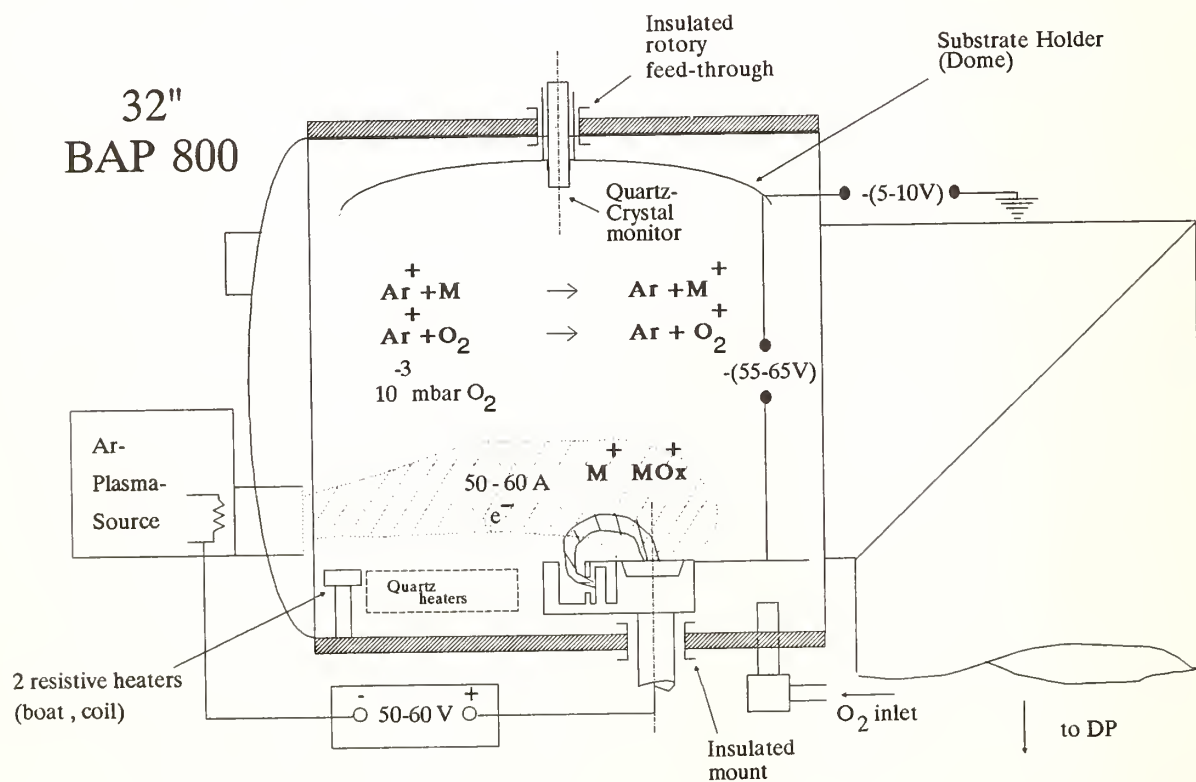


Figure 5. BALZERS BAP 800 high vacuum box coater



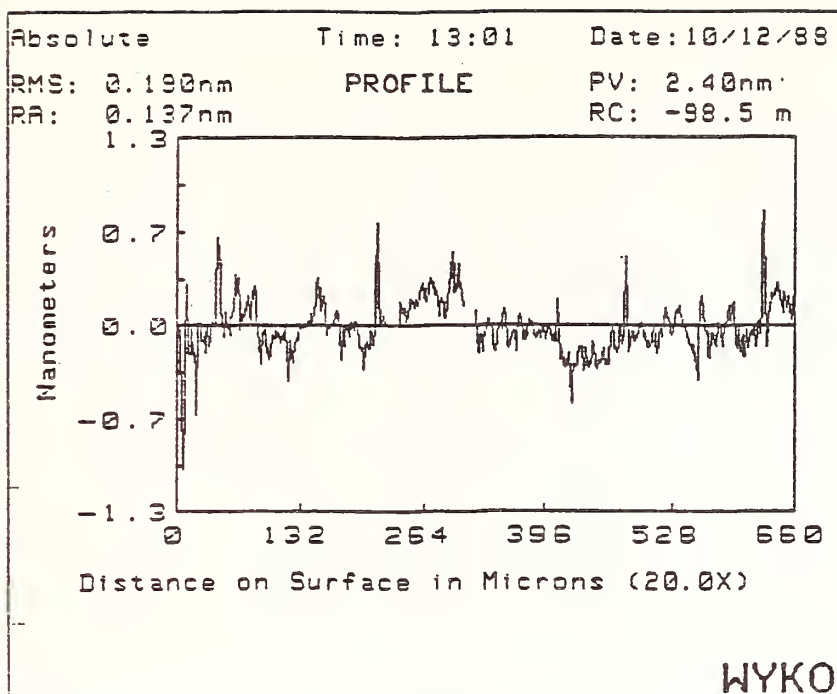


Figure 6. TOPO 2-D Surface profile of RIPD  $\text{ZrO}_2/\text{SiO}_2$  multilayer (HL)<sup>12</sup> @ 1060nm

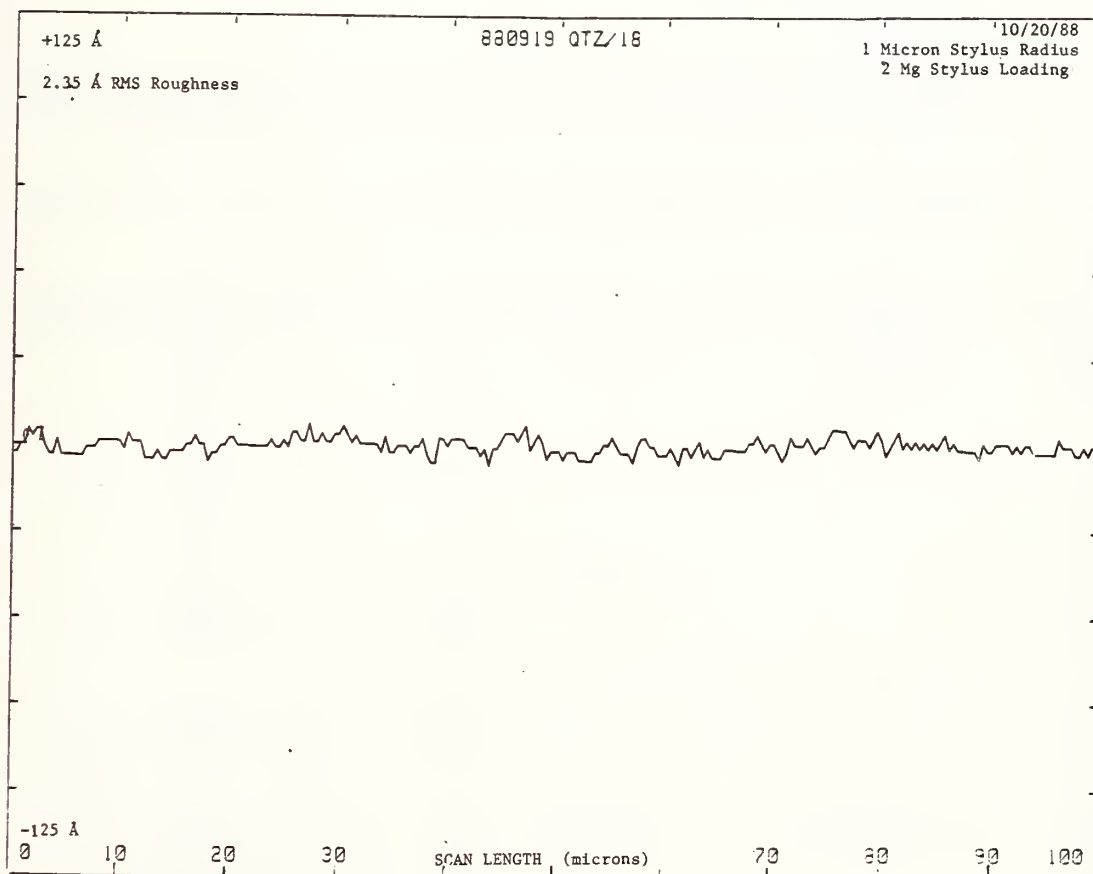


Figure 7. TALYSTEP Surface profile of RIPD  $\text{ZrO}_2/\text{SiO}_2$  multilayer (HL)<sup>12</sup> @ 520nm

Table 1. Thin film materials used for RIPD

starting material	film deposited	index of refraction (@ 550nm)	plasma current (A)	anode voltage (V)	deposition rate (nm/s)	oxygen pressure (10 <sup>-3</sup> mbar)
Si	SiO <sub>2</sub>	1.49	55	55	0.5	1.1
TiO	TiO <sub>2</sub>	2.45	55	70	0.25	1.5
Ta <sub>2</sub> O <sub>5</sub>	Ta <sub>2</sub> O <sub>5</sub>	2.31	55	65	0.3	0.9
Zr	ZrO <sub>2</sub>	2.27	55	80	0.4	1.3

Table 2. TALYSTEP Surface Roughness [nm] of TiO<sub>2</sub> Single Layers Deposited by Low-Voltage Reactive Ion Plating (BALZERS BAP 800)

	Suppl.	I.D. #	TALY	Run #	QWOT	TALY
BK 7	Newport 10B10	1	0.664	17	1	0.732
				18	7	0.846
				19	13	4.746
		2	0.507	17	1	0.354
				18	7	0.402
				19	13	5.086
		3	0.542	17	1	0.653
				18	7	0.562
				19	13	4.625
	OMI	4	0.662	17	1	0.733
				18	7	0.638
				19	13	4.940
	Average		0.594	17	1	0.618
				18	7	0.612
				19	13	4.849

Table 3. Summary of Surface Roughness Measurements on RIPD Thin Films  
Performed with TALYSTEP and WYKO TOPO 2-D Instruments

Substr.	Suppl.	TALY	TOPO	Mat.	QWOT	lambda	TALY	TOPO
Sheet Glass	Kodak	n/a	3.59	ZrO2	(H) 4	650	0.47	4.76
	(2"x2")	n/a	3.24	ZrO2/SiO2	(HL) 11	1,064	1.11	0.40
	Corning	n/a	0.73	TiO2/SiO2	(2H3L) 11	850	n/a	1.40
BK 7	Newport & OMI	0.66	n/a	TiO2	(H) 1	633	0.62	n/a
		0.66	n/a	TiO2	(H) 7	633	0.61	n/a
		0.66	n/a	TiO2	(H) 13	633	4.85	n/a
	LPO	1.69	n/a	Ta2O5/SiO2	(HL) 10	1,064	1.91	n/a
		0.40	n/a	Ta2O5	(H) 4	600	0.68	n/a
	Newport	n/a	0.34	Ta2O5/SiO2	(HL) 12	520	0.56	0.29
		n/a	0.27	Ta2O5/SiO2	(HL) 12	1,064	n/a	0.49
		n/a	0.23	TiO2/SiO2	(HL) 10	520	n/a	0.31
	Newport	n/a	0.15	ZrO2/SiO2	(HL) 12	1,064	0.62	0.19
		n/a	0.17	ZrO2/SiO2	(HL) 12	520	0.26	0.20

Measurement of Thermal Expansion Coefficients  
of Optical Thin Films

Wu Zhouling    Tang Jinfa    Shi Baixuan

Zhejiang University, Hangzhou, PRC

Thermal expansion coefficients of optical thin films can be measured by means of the combination of photothermal displacement optical beam deflection technique (PDOBD) and transverse photothermal optical beam deflection technique (TPOBD). In this paper, single layers of SiO<sub>2</sub>, TiO<sub>2</sub>, ZrO<sub>2</sub>, MgF<sub>2</sub> and ThF<sub>4</sub> are taken as examples to show the experimental methods and results.

Key Words: optical thin films; photothermal deflection; thermal expansion coefficients.

## 1. Introduction

Precise measurements of thermophysical properties like thermal conductivity and thermal expansion coefficient of optical thin films are very important for thermal modeling of laser-induced damage to optical coatings [1,2]. In this paper, we report our recent measurements of thermal expansion coefficients of optical thin films by means of the combination of PDOBD [3,4] and TPOBD [5-8]. The experimental results show that this method is quite versatile and very simple.

## 2. Experimental Procedure

Based on PDOBD and TPOBD, we have built up an apparatus for the measurement of thermal expansion coefficients of optical thin films. Details of the detection system are given in figure 1.

PDOBD was firstly reported by M.A.Olmstead et al [3] in 1983. The physical basis of it was shown in figure 2, and it can be briefly described as follows: when a solid sample is illuminated by an intensity-modulated light beam, the absorption of the energy will cause a thermal wave inside the sample and



hence a corresponding displacement on sample surface. By probing this corresponding surface displacement with a second laser beam, one can relate its deflection to the related properties of the sample.

TPOBD was firstly developed by A.C.Boccara et al [5] in 1980, and its physical basis was shown in figure 3. Defferent from PDOBD, here the reason for the optical beam deflection is the photothermal gradient index.

Optical thin films are usually thermally thin when the modulation frequency is relatively low [7]. In this case, the PDOBD signal  $S_1$ [3,4] and TBOBD signal  $S_2$  [5-8] satisfy

$$S_1 = C_1 \alpha \alpha_l P(1-R) \quad (1)$$

and

$$S_2 = C_2 \alpha_l P(1-R) \quad (2)$$

where  $C_1, C_2$ ---constants, decided by experimental parameters;  
 $\alpha$  ---thermal expansion coefficient of the sample;  
 $\alpha_l$  ---optical absorption coefficient of the sample;  
 $l$  ---thickness of the sample;  
 $P$  ---incident power of the pump laser;  
 $R$  --- reflectance of the sample.

From eq.(1) and eq.(2) we can get with ease

$$S_1/S_2 = (C_1/C_2) \alpha \quad (3)$$

Let  $S=S_1/S_2$ ,  $C=C_1/C_2$ , then we have

$$S = C \alpha \quad (4)$$

where  $C$  is a constant dependent on experimental conditions and the properties of the substrate of the sample.

From eg.(4) we can see that the ratio of PDOBD signal over TPOBD signal is proportional to the thermal expansion coefficient of an optical thin film under the thermally-thin-sample approximation [7]. This is in fact the basis of our measurements of thermal expansion coefficients of optical thin films.

To calibrate the experimental system, we use Au film as calibrating sample, of which the thermal expansion coefficient was already known. The principle of this calibration method is as follows:

Equation (4) is also valid for calibrating sample if the substrate and

the experimental conditions remain unchanged, i.e.

$$S_c = C \alpha_{th-c} \quad (5)$$

where the index c indicates calibrating sample.

From eq.(4) and eq.(5) we can get

$$\alpha_{th} = (S / S_c) \alpha_{th-c} \quad (6)$$

### 3. Experimental Results

Table 1 showed our measured thermal expansion coefficients of several single-layer films and their comparison with those of previous work and related bulk materials. From this table we can find:

(1). Except that of the relatively unstable  $ZrO_2$  single layer film, our results are in good agreement with those previously reported. This fact approves the applicability of the combination of PDOBD and TPOBD in the measurements of thermal expansion coefficients of optical thin films.

(2). Except that of  $SiO_2$  single layer film, the thermal expansion coefficients of the thin films investigated showed apparent differences from those of the related bulk materials. A possible explanation of these differences might be changes in structures of the materials after vacuum deposition.

### 4. Discussion

#### 4.1 Repeated Precision of the Experimental Setup

Ten measurements of  $TiO_2$  film showed an average  $\alpha_{th}$  of  $2.2 \times 10^{-6} \text{ deg}^{-1}$  and a maximum deviation of  $0.3 \times 10^{-6} \text{ deg}^{-1}$ . This corresponds to a relative error smaller than 14%.

#### 4.2 Limits of Our Method in the Measurement of

##### 4.2.1 Film Thickness Limit

Because of the thermally-thin-sample approximation, our method is only applicable to samples with  $l \ll (10-100) \mu m$ , which, fortunately, can be satisfied in most optical thin films.

##### 4.2.2 Optical Absorption Limit

Limited by the sensitivity of TPOBD [8], our apparatus is only applicable to films with  $A \geq 10^{-5}$ , which, fortunately again, is satisfiable in most optical coatings.

#### 4.2.3 Thermal Coefficient Limit (Sensitivity)

Under the condition that the optical absorption limit mentioned above is satisfied, the sensitivity of our method for measuring  $\alpha$  is mainly decided by PDOBD technique. In our experiment, measurement of  $\text{SiO}_2$  thin film sample ( $A \sim 10^{-4}$ ,  $\alpha \leq 10^{-6}$ ,  $Ax \alpha \leq 10^{-10}$ ) showed a PDOBD signal  $S_1 = 0.2^{\text{mV}} / 2.53^{\text{V}}$  and a noise level  $S_{1\text{noise}} \leq 1^{\text{um}} / 2.53^{\text{V}}$ . From this result we can deduce that the sensitivity of the experimental setup is  $(Ax \alpha) \sim 10^{-12}$ . Thus, for optical thin films with absorption losses  $A = 10^{-4} \sim 10^{-3}$ , our method approves a sensitivity of  $\alpha = 10^{-8} \sim 10^{-9} \text{deg}^{-1}$ .

#### 5. Conclusion

The combination of PDOBD and TPOBD is a quite versatile and very simple method for measuring thermal coefficients of optical thin films. Our current apparatus, with a sensitivity of  $\alpha = 10^{-8} \sim 10^{-9} \text{deg}^{-1}$  (when  $A = 10^{-4} \sim 10^{-3}$ ) and the repeated error  $\leq 14\%$ , is applicable to most optical thin films.

---

The authors wish to acknowledge the help and support of Profs. Z.X.Fan and Z.J.Wang.

#### 6. References

- [1] Scott M.L. A review of UV coating material properties. Nat.Bur.Stad.(U.S.) Spec.Publ. 688; 1985. 329.
- [2] Bennet H.E.; Guenther A.H.; Milam D.; Newnam B.E. Laser-induced damage in optical materials sixteenth ASTM symposium. Appl. Opt. 26(5): 813;1987.
- [3] Olmstead, M.A.; Amer, N.M. A new probe of the optical properties of surfaces. J.Vac.Sci.Tech-nol. 1(3): 751;1983.
- [4] Olmstead M.A.; Amer N.M.; Kohn S.; Fournier D.; Boccara A.C. Photothermal displacement spectroscopy: an optical probe for solid and surface. Appl.Phys.A32:141;1983.
- [5] Boccara A.C.; Fournier D.; Badoz J. Thermal-optical spectroscopy: detection by the " mirage effect". Appl.Phys.Lett.36(2):130;1980.
- [6] Jackson W.B.; Amer N.M.; Boccara A.A.; Fournier D. Photothermal deflection spectroscopy and detection. Appl.Opt.20(8): 1333;1981.

- [7] Murphy J.C.; Aamodt L.C. Photothermal spectroscopy using optical beam probing: mirage effect  
J.Appl.Phys. 51(9): 4580;1980.
- [8] Wu Z.L.;Tang J.F.; Shi B.X. Measurement of weak absorption in optical coatings by trans-  
verse photothermal deflection technique. Accepted by Acta Optica Sinica.
- [9] Sparks M.; Duthler C.J. Theoretical studies of high-power ultraviolet and infrared materials  
8th Technical Report, Dec.1976, DARPA Contract No. DAHC 15-73-c-0127,pp.72-96.



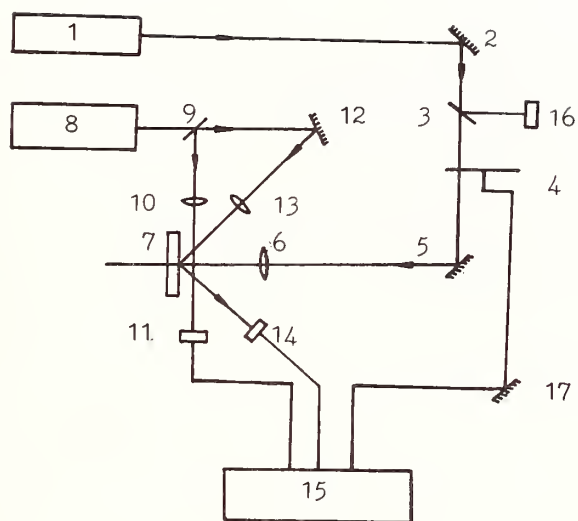


Figure 1. Details of the experimental setup:

- 1--He-Ne pump beam ( $6328\text{\AA}$ ,  $120\text{ mW}$ )
- 2, 5, 12, 17--mirrors; 3, 9--B.S.
- 4--chopper; 6, 10, 13--lens
- 11, 14--position detectors
- 15--lock-in amplifier
- 16--power detector.

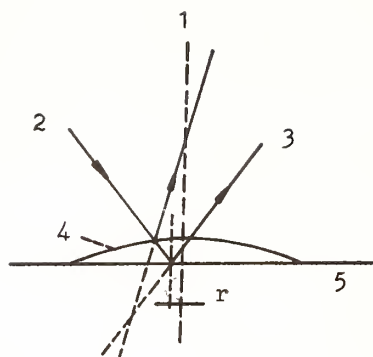


Figure 1. Diagram of the physical principle of PDOBD:

- 1--modulated pump beam
- 2--probe beam
- 3--deflected beam
- 4--thermoelastic deformation
- 5--sample

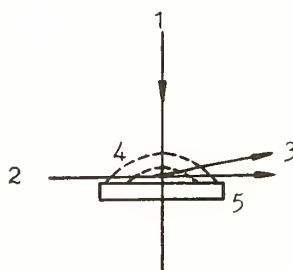


Figure 2. Diagram of the physical principle of TPOBD:

- 1--modulated pump beam
- 2--probe beam
- 3--deflected beam
- 4--gradient refractive index
- 5--sample

Table 1. Measured thermal expansion coefficients of several single-layer optical coatings and their comparison with those of previous work and related bulk materials.

<u>Material</u>	Thermal Expansion Coefficient ( $\times 10^6$ ), $^{\circ}\text{C}^{-1}$		
	<u>our results</u>	<u>previous data</u> <sup>[1]</sup>	<u>bulk</u> <sup>[9]</sup>
$\text{SiO}_2$	$0.81 \pm 0.2$	0.70	0.55
$\text{TiO}_2$	$2.8 \pm 0.5$	2.1	7--9
$\text{ZrO}_2$	$2.5 \pm 0.3$	1.1	4.2
$\text{MgF}_2$	$38 \pm 8.9$	30	13.7
$\text{ThF}_4$	$3.2 \pm 0.6$	2.9	-2.5

Takatomo SASAKI, Atsushi YOKOTANI, Kana FUJIOKA,  
Kunio YASHIDA, Tatsuhiko YAMANAKA and Sadao NAKAI

Institute of Laser Engineering, Osaka University  
2-6 Yamada-oka, Suita, Osaka 565 Japan

We are investigating a new nonlinear crystal for higher harmonic generator in laser fusion experiments. L-Arginine Phosphate Monohydrate (LAP) crystal is a promising nonlinear organic crystal in place of KDP crystal. In order to avoid a large absorption at  $1.06\ \mu\text{m}$  in LAP crystal, deuterated LAP (DLAP) crystals were grown. The deuterization rate was approximately 90 %. We have investigated the laser properties of LAP and DLAP.

The results are as follows. DLAP is less hygroscopic and easier to handle than KDP. Effective optical nonlinear coefficient  $d_{\text{eff}}$  of DLAP is almost twice than that of KDP. Angular acceptance angle is almost half of KDP but temperature acceptance is almost 1.5 times larger. Bulk laser damage threshold of LAP and DLAP against  $1.06\ \mu\text{m}$  laser pulse is more than  $30\ \text{J}/\text{cm}^2$ , whereas that of usual KDP is about  $10\ \text{J}/\text{cm}^2$ . LAP and DLAP are thermally durable against average power density of several hundreds  $\text{W}/\text{cm}^2$  of high repetition laser. These results suggest that LAP and DLAP crystals can be used as a more promising harmonic generator not only for fusion laser but also for high average power laser.

Key Words: organic crystal; crystal growth; frequency conversion; ultraviolet generation; deuterated L-arginine phosphate monohydrate; bulk laser damage threshold; laser fusion;

## 1. INTRODUCTION

We are investigating the improved harmonic generator for laser fusion experiments in place of the conventional KDP crystals.

Organic L-Arginine Phosphate Monohydrate (LAP) is a new nonlinear optical material which was presented in 1983 by Shangdon University, China [1] and is a promising material for laser fusion experiments[2]. Its chemical formula is  $(\text{H}_2\text{N})_2\text{CNH}(\text{CH}_2)_3\text{CH}(\text{NH}_3^+)\text{COO}^-\cdot\text{H}_2\text{PO}_4\cdot\text{H}_2\text{O}$  and consists of L-Arginine, Phosphoric acid and water molecules. Fig. 1 shows the solubilities in water of various kinds of materials, which proves that LAP is more non-deliquescent than KDP.

The problem is that LAP has considerable absorption at  $1.06\ \mu\text{m}$  due to overtones of molecular vibration of the hydrophilic functional groups such as  $-\text{OH}$ ,  $-\text{NH}_3^+$ ,  $=\text{NH}$ ,  $-\text{NH}_2$ ,  $=\text{NH}_2$  etc. The absorption can be reduced by deuterizing of these functional groups. We grew deuterated LAP (DLAP) crystals and investigated the properties of second harmonic generation and laser damage in order to estimate whether it is capable for frequency conversion of high power lasers.

## 2. GROWTH OF DLAP CRYSTAL

The growth solution was prepared by adding deuterated ortho-phosphoric acid ( $\text{D}_3\text{PO}_4$ ) to L-Arginine, which was dissolved in 99.8 %  $\text{D}_2\text{O}$  so that the mole-ratio of L-Arginine and  $\text{D}_3\text{PO}_4$  was 1 to 1. The solution was maintained at the temperature of  $60\ ^\circ\text{C}$  for two hours after mixing to react completely. The reaction was performed in the gloved box in which dry nitrogen gas was filled to prevent the deuterium in the solution from being replaced with the hydrogen in the atmospheric moisture.

The vessel for crystal growth was made of acrylic resin and had a volume of  $1.5\ \text{l}$ . The magnetically sealed mechanics was adopted to isolate the solution in the vessel from the atmosphere and to rotate the seed crystal and the stirrer.



The crystal was grown by the temperature reduction method (temperature range 45 - 20 C). The reduction rate was 0.1 C/day on average. The crystal of which size were  $1.5 \times 4.0 \times 4.5 \text{ cm}^3$  ( $a \times b \times c$  axes) was obtained after twenty days. Fig. 2 shows the photograph of the DLAP crystal. The growth rate of  $c$  axis showed the largest in three axes and the maximum speed of the growth rate without degradation of crystal quality was 1.2 mm/day.

DLAP crystal was usually colorless and transparent but we occasionally obtained the yellowish crystals regardless of the same growth conditions. The investigation of inorganic impurities by an ICP quantometer and a fluorescent X-ray spectroscopy showed no difference between these crystals. We found that when the solution was irradiated by ultra-violet (UV) light, both the solution itself and the resultant grown crystal became yellowish. It is considered that this phenomenon was induced by decomposition of the constituent organic substances. The same thing occurred in LAP crystals.

We estimated the deuterium concentration rate  $\sigma$  by NMR (Nuclear Magnetic Resonance) method [3]. By NMR method, two kinds of  $\sigma$  can be measured separately for hydrophilic ( $-\text{NH}_2$ ,  $=\text{H}_2\text{N}^+$ ,  $-\text{NH}$ ,  $-\text{NH}_3$ ,  $-\text{OH}$ ) and hydrophobic ( $-\text{CH}$ ) groups of LAP. As it was observed that the hydrogen in the hydrophobic groups were not substituted with deuterium, we defined the degree of hydrogen substitution with deuterium in hydrophilic groups as  $\sigma$ . The measured  $\sigma$  was  $89 \pm 1 \%$ .

### 3. EXPERIMENTS OF SECOND HARMONIC GENERATION

#### 3.1. Transmittance Spectra

The samples of 5mm thick obtained from cleavage surfaces were used for measuring the transmittance spectra. Fig. 3 shows the IR spectra of DLAP, LAP and KDP crystals. The yellowish and the colorless crystals showed the same spectra. The transmittance at  $1.06 \mu\text{m}$  ( $\omega_1$ ) of LAP was improved by deuterization.

Figure 4 illustrates the UV spectra. The cut-off wavelength was  $0.26 \mu\text{m}$  for both LAP and DLAP. But the yellowish crystals showed bad transmittance. We can use a DLAP crystal for fourth harmonic generation of Nd:YAG laser (FHG,  $0.265 \mu\text{m}$ ).

#### 3.2. Measurement of loss factor at $1.06 \mu\text{m}$

The precise absorption coefficient was estimated by measuring the temperature increase of the crystal by means of laser irradiation. The CW YAG laser of 5 W was irradiated on the samples of LAP and DLAP. The beam diameter was 2.5 mm and the size of the samples were  $20 \text{ mm} \times 20 \text{ mm}$  in cross section, 4 mm thick. The temperature distribution was measured by a thermoviewer (Nippon-denshi JTG-3210). The maximum temperature 60 C was obtained at the center of the LAP crystal, on the other hand, 28 C in the case of the DLAP, where the room temperature was 23 C.

The estimated absorption coefficients were  $0.09 \text{ cm}^{-1}$  and  $0.02 \text{ cm}^{-1}$  for LAP and DLAP, respectively.

#### 3.3. Experiment of Second Harmonic Generation

DLAP is a negative monoclinic and biaxial crystal. The angle between  $a$  and  $c$  axes is reported to be  $98^\circ$  [5]. Fig. 5 shows the relation between the crystal axes ( $a, b, c$ ) and the principal axes of refractive index ellipsoid ( $x, y, z$ ). This relation was determined by using two optical axes (OA1, OA2) and the cleavage surface which contains  $c$  and  $b$  axes of the crystal. The angle between two optical axes was obtained by crossed Nicol method and was  $37.2 \pm 0.5^\circ$ . The direction of  $x$  axis was determined by dividing this angle by two. K illustrates the propagation direction of laser light. There exist many combination of angles  $\theta$  and  $\phi$  which satisfy the phase matching condition. We calculated the phase matching angles of Type I and Type II for  $\theta$  and  $\phi$  by using measured refractive indices  $n_x$ ,  $n_y$  and  $n_z$  at  $\omega_1$  ( $\lambda=1.06 \mu\text{m}$ ) and  $\omega_2$  ( $\lambda=0.53 \mu\text{m}$ ). Table 1 shows these refractive indices. The calculated results are shown in Fig. 6.

The Q-switched YAG laser was used for SHG experiment. For a given angle  $\phi$ , the angle  $\theta$  was determined to obtain the maximum output of SHG. The experimental data are shown by the dots in Fig. 6. They agreed fairly well with the calculation. The angular tuning curves were obtained by tilting the crystal surface in the direction normal to the calculation curves in Fig. 6. The crystal length was 6 mm. The temperature acceptance was also measured.

The measured results of LAP and DLAP with the data of KDP, DKDP and beta barium borate (BBO) are summarized in Table 2.  $d_{\text{eff}}/d_{\text{eff}}(\text{KDP})$  in Table 2 indicates a relative nonlinear coefficient normalized by that of KDP (Type II) and was obtained from the square root of the SHG peak intensity of angular tuning curves.

The acceptance angle of DLAP is almost a half of KDP, on the other hand,  $d_{\text{eff}}$  is approximately twice. The acceptance temperature is the largest in Table 2.

#### 4. LASER DAMAGE EXPERIMENTS

##### 4.1 Bulk laser damage threshold by 1-on-1 test.

Measurement of the bulk laser damage threshold was performed using a  $\text{Nd}^{3+}:\text{LiYF}_4$  (YLF) laser (wavelength  $1.053\mu\text{m}$ ) in a transverse and longitudinal single mode with a 1-ns pulse. The pulse was focused at the point of 5 mm from a cleavage surface of LAP and DLAP samples by a lens with focal length of 3.5 cm. The focal point moved shot by shot. The damage was observed by eye. A He-Ne was also used to identify small damage spots by utilizing the scattering from the damage spots. Before a laser shot, the scattering centers by a He-Ne laser could be hardly observed inside these samples. Fig. 7 summarizes the results. The damage threshold of LAP was more than  $30\text{ J/cm}^2$  and that of DLAP was extremely higher and was over  $100\text{ J/cm}^2$ , whereas that of usual KDP showed about  $10\text{ J/cm}^2$ . The sample numbers were two, respectively. The reason that the damage threshold of LAP is lower than that of DLAP may be due to the fact that the absorption coefficient at  $1.06\mu\text{m}$  wavelength is bigger than that of DLAP. At this moment we do not understand at all why LAP or DLAP can have such a high damage threshold.

##### 4.2 Thermal durability of LAP.

The thermal durabilities of LAP and KDP were examined by using high average power density of high repetition laser. The normal oscillated Alexandrite laser of which repetition rate was 10 Hz, energy per pulse was 3.8 J, and wavelength was  $0.755\mu\text{m}$  was focused into 2 mm in diameter on the crystal surface. The Alexandrite laser was used because the absorption coefficient of LAP and KDP at the laser wavelength of  $0.755\mu\text{m}$  were almost the same. The maximum average power density was  $1.2\text{ kW/cm}^2$ . The entrance surface of KDP had suffered severe damage just after the irradiation of two to three laser pulses. But LAP did not show any damage, until after fifteen minutes the rear surface began to burn with smoke. This is maybe due to a thermal self-focusing in LAP crystal. This result shows LAP or DLAP is more thermally durable against high power density of high repetition laser than KDP.

#### 5. CONCLUSIONS

The obtained results are;

1. DLAP is less hygroscopic and easier to handle than KDP.
2. Effective optical nonlinear coefficient  $d_{\text{eff}}$  of DLAP is almost twice than that of KDP.
3. Angular acceptance angle is almost half of KDP but temperature acceptance is almost 1.5 times larger.
4. Bulk laser damage threshold of LAP and DLAP against 1ns,  $1\mu\text{m}$  laser pulse is more than  $30\text{ J/cm}^2$ , whereas that of usual KDP is about  $10\text{ J/cm}^2$ .
5. LAP and DLAP are thermally durable against average power density of several hundreds  $\text{W/cm}^2$  of high repetition laser.

These results suggest that LAP and DLAP crystals can be used as a more promising harmonic generator not only for fusion laser but also for high average power laser in ultraviolet region which is useful for lithography, medicine *et al.*

#### 6. REFERENCE

- [1] Xu, D.; Jiang, M.; Tan, Z. : A new phase matchable nonlinear optical crystal L-arginine phosphate monohydrate, *Acta Chemica Sinica* **41**; 1983. 570p.
- [2] Velsko, S.P.; Eimerl, D. : Evaluation of LAP and  $\text{LA}^*\text{P}$  as frequency conversion materials for high power lasers, IQEC'86 (1986) San Francisco, TuJJ5, Monaco, S.B.; Davis, L.E.; Velsko, S.P.; Wang, F.T.; Eimerl, D.; Zalkin, A.: Synthesis and Characterization of chemical analogs of L-arginine phosphate, *J. Crystal Growth* **85**; 1987. 252p, Sasaki, T.; Yokotani, A.; Fujioka, K.; Yamanaka, T.; Nakai, S. : Synthesis and second harmonic generation of deuterated L-arginine phosphate monohydrate crystal, *Technol Repts. Osaka University*, **39**; 1989. March.
- [3] Silverstein, R.M.; Bassler, G.C.; Monill, T.C. ed. *Spectrometric Identification of Organic Compounds*, John Wiley & sons, Inc. 1981.
- [4] Aoki, K.; Nagano, K.; Iitaka, Y. : The crystal structure of L-arginine phosphate monohydrate, *Acta Cryst.* **27**; 1971 11p.

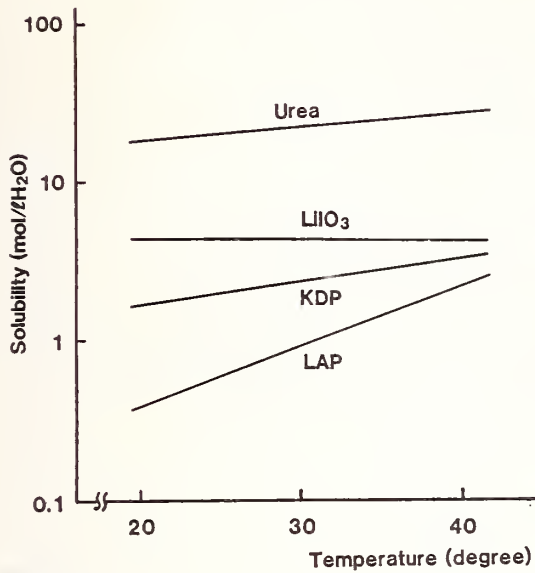


Fig. 1 Solubility curves of water Soluble Crystals.



Fig. 2 DLAP crystal, as grown.  
 $1.5 \times 4.0 \times 4.5 \text{ cm}^3$  ( $\alpha, \beta, \text{c}$  axes)

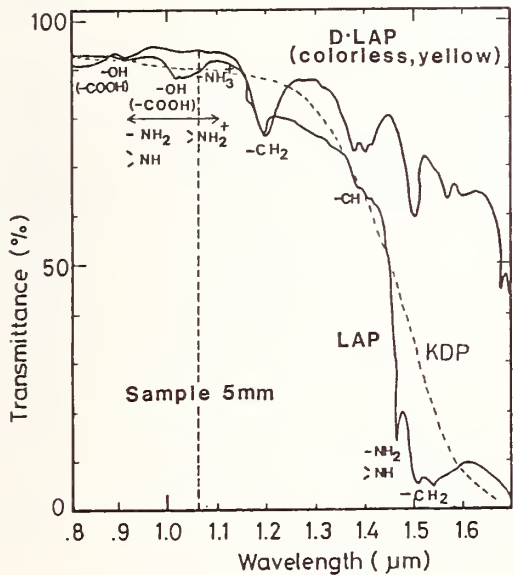


Fig. 3 Infrared transmission curves of DLAP, LAP, and KDP.

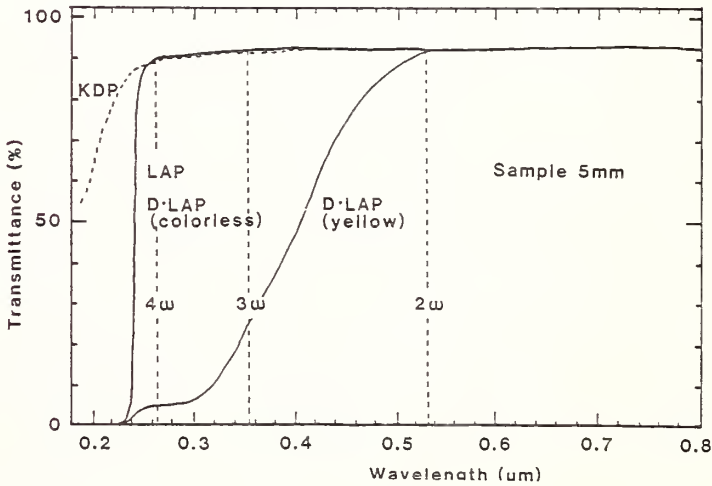
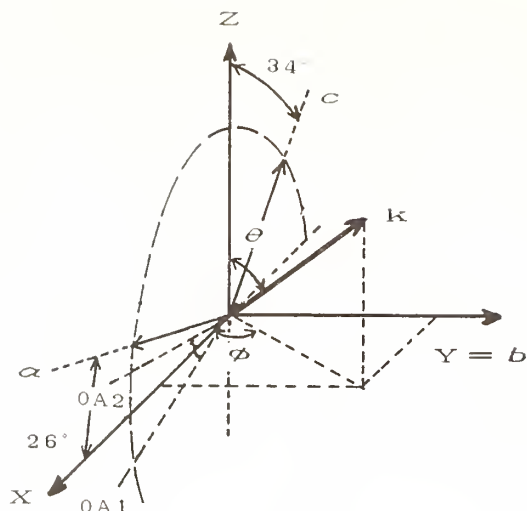
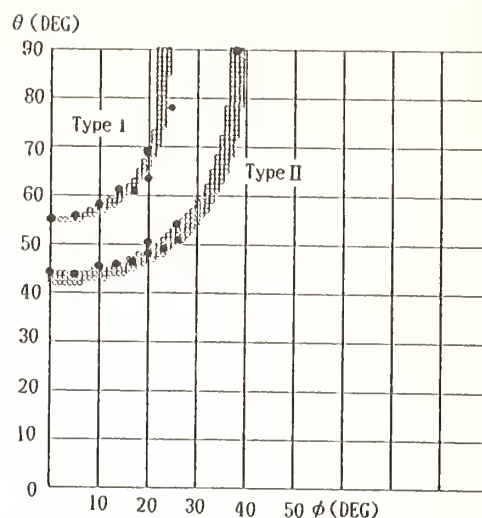


Fig. 4 Ultra-violet transmission curves of LAP and DLAP with yellowish DLAP.



**Fig. 5** Relation between crystal axes ( $a, b, c$ ) and principal axes of refractive index ellipsoid ( $x, y, z$ ) in DLAP crystal.  $\theta$  and  $\phi$  are measured angles from  $z$  and  $x$  axes.  $K$  shows the propagation direction of laser light.



**Fig. 6** Phase matching angles of second harmonic generation for DLAP. Curves show calculations. Dots illustrate experimental data.

**Fig. 7** Bulk laser damage threshold of LAP and DLAP crystals. (1-on-1 test, wavelength:  $1.053\mu\text{m}$ , pulse width: 1ns)

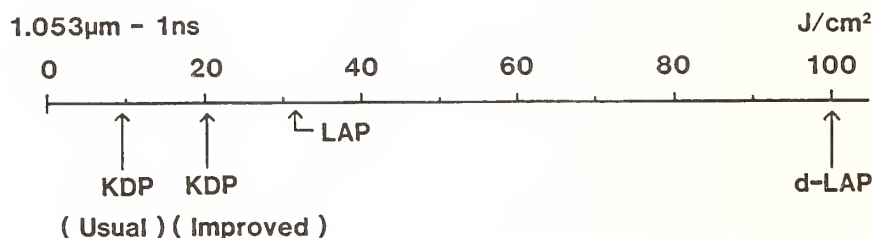


**Table 2** Laser properties of DLAP, LAP, KDP and BBO crystals.

**Table 1** Refractive indices of DLAP crystal.

	Wavelength	
	$1.064\mu\text{m}$	$0.53\mu\text{m}$
$n_x$	1.49769	1.50855
$n_y$	1.55952	1.57672
$n_z$	1.56864	1.5850

		DLAP	LAP	DKDP	KDP	BBO
Absorbance at $1.06\mu\text{m}$ ( $\text{cm}^{-1}$ )		0.02	0.09	0.003	0.05	0.001
UV Cut-off, 95% for $5\text{mm}^2$ ( $\mu\text{m}$ )		0.26	0.26	0.2	0.2	0.198
Angular Acceptance of $2\omega$ (mrad·cm)	Type I	0.52	-	-	1.1	0.52
	Type II	1.1	0.84	2.2	2.1	-
Change of Matching Angle against Temperature (mrad/°C)	Type I	-	-	-	-	0.023
	Type II	0.04	0.06	0.11	0.12	-
Temperature Acceptance of $2\omega$ (°C·cm)	Type I	-	-	-	-	23
	Type II	27	14	20	18	-
$d_{\text{eff}}/d_{\text{eff}}(\text{KDP Type II})$	Type I	1.5 $\theta = 60^\circ$ $\phi = 16^\circ$	-	-	0.75 $\theta = 42^\circ$ $\phi = 45^\circ$	4.4 $\theta = 22^\circ$ $\phi = 0^\circ$
	Type II	1.8 $\theta = 43^\circ$ $\phi = 0^\circ$	1.9 $\theta = 43^\circ$ $\phi = 0^\circ$	0.92 $\theta = 57^\circ$ $\phi = 0^\circ$	1 $\theta = 59^\circ$ $\phi = 0^\circ$	-



## Free vibration pulse laser-induced damage in optical thin films

Fan Zhengxiu, Jin Linfa and Luo Miaohong  
Shanghai Institute of Optics and Fine Mechanics  
Academia Sinica

Some experiments on damage in optical coatings induced by Free vibration pulse laser were performed in SIOFM. It is found that the laser induced damage in optical coatings is mainly due to the pulse peak, and repeated pulses quicken the damage process. The effect of thin film structure and the role of overcoating in laser induced damage are also discussed in this paper.

Key words: damage; laser; microstructure; optical thin film; overcoat

### 1. Introduction

Free vibration pulse laser can generate a very large energy output. It can be applied into laser processing, laser medicine and be used for research purposes. It is of great interest and importance to probe the essence of the interaction between this kind of laser and optical material, and the damage induced by this laser in optical thin films. Some experiments on laser induced damage in optical thin films made in SIOFM are reported here.<sup>1</sup>

### 2. Experimental Results and Discussions

#### 2.1 The pulse structure of the Free vibration pulse laser

Experiments were performed on Nd-glass free vibration pulse laser with its maximum output wavelength  $1.06\ \mu$  and its maximum output energy 1000 J. The pulse structure of this laser is very complex. Figure 1 shows its pulse structure. It is composed of several hundreds of subpulse peaks with each duration several microseconds. The whole pulse duration is about three milliseconds.

#### 2.2 The accumulated effect of laser induced damage in optical thin films

The effect of free vibration laser on optical thin films is the same as that of repeatability laser. The induced damage on optical thin films depends either on the peak power of each subpulse peak or on the accumulated effect of the multipulse repetition.

The accumulated effect relates not only to the pulse structure of laser but to the material of thin film. Figure 2 and figure 3 give the power damage threshold and energy damage threshold of the  $\text{TiO}_2$  thin films and  $\text{ZrO}_2$  thin films vs. laser acting time respectively.

To show clearly the accumulated effect of laser induce damage, the laser pulse was cut and divided by a sector which rotated with a very high rate. There was a narrow slit, which could be varied in its width, in this sector to change laser acting time. The wider the slit width, the longer the laser acting time was and also the more frequently the subpulse peak acted on thin films on condition that the rotation rate be definite.

Comparing two curves in figure 2, it is evident that the accumulated effect of  $\text{TiO}_2$  thin film is very different from that of the  $\text{ZrO}_2$  thin film. With the laser acting time going on, the power damage threshold reduced quickly for the  $\text{TiO}_2$  thin film. But for the  $\text{ZrO}_2$  thin film, the power damage threshold varied slightly as the laser acting time varied from 0.2 ms to 2 ms. The special properties of  $\text{ZrO}_2$  thin film make it be successfully used in the repeatability laser.

### 2.3 The effect of thin film structure on laser induced damage

The damage resistance of thin film depends greatly on the structure of thin film. Table I is the experimental results of laser induced damage in ZnS thin film which possesses grains of various size. It is shown in the table that the smaller the grain, the higher the damage threshold is. The damage tests of  $\text{ZrO}_2$  thin film also lead to the same conclusion.

Listed in table II are the experimental results of laser induced damage in  $\text{ZrO}_2$  thin films with various structure. It is shown that the damage threshold of  $\text{ZrO}$  thin film is the highest for cubic crystallinity and the lowest for monoclinic crystallinity.

### 2.4 The effect of $\text{SiO}_2$ overcoating on laser induced damage in $\text{ZrO}_2/\text{SiO}_2$ multilayers

It is well known that half wavelength  $\text{SiO}_2$  overcoating on  $\text{TiO}_2/\text{SiO}_2$  multilayers can enhance the damage threshold.<sup>2</sup> We have researched this phenomenon and go a step further. It is found that the level of the damage resistance of the  $\text{ZrO}_2/\text{SiO}_2$  multilayers with  $\text{SiO}_2$  overcoating is related to the thickness of  $\text{SiO}_2$  overcoating. Table III shows the results of the damage tests on  $\text{ZrO}_2/\text{SiO}_2$  reflecting coating with  $\text{SiO}_2$  overcoating of various thickness. It is shown that the damage threshold of  $\text{ZrO}_2/\text{SiO}_2$  multilayers increases with increase of the overcoating thickness and reaches a maximum when the thickness of  $\text{SiO}_2$  overcoating approximates to twice the wavelength.

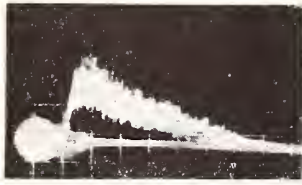
The damage resistance of  $\text{ZrO}_2/\text{SiO}_2$  multilayers is related to its microstructure. We can see from figure 4 some electrographies of  $\text{ZrO}_2/\text{SiO}_2$  multilayers with and without  $\text{SiO}_2$  overcoating, that the surface morphology becomes finer and more smooth with the increase in thickness of  $\text{SiO}_2$  overcoating, but roughness when the overcoating thickness exceeds  $5/2$  the wavelength.

## 3. Conclusion

The damage induced by free vibration pulse laser in optical thin films depends on both the pulse structure of laser and the intrinsic properties of thin films. The accumulated effect of thin film damage depends on the material of thin film. The damage threshold of thin film is related to its structure. In general, the smaller the grains, the higher the damage threshold. The damage threshold of the optical thin film can be enhanced by a  $\text{SiO}_2$  overcoating on it. The level of resistance to laser radiation is related to the thickness of the overcoating. There exists an optimum thickness of the overcoating for the damage threshold to reach a maximum.

## 4. References

- [1] Fan Zhengxiu, Laser Journal, Vol. 9, No. 9, 582; 1982
- [2] W. H. Lowdermilk, SPIE, Vol. 541, 124; 1985



a



b

Figure 1. The pulse structure of Free vibration laser. Time scale: (a) 0.5ms/measure, (b) 5μs/measure.

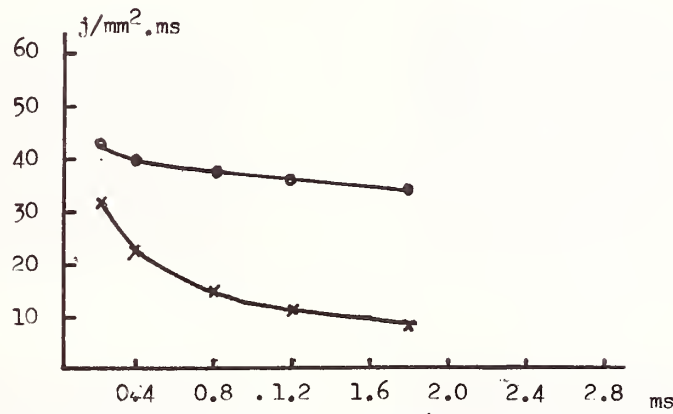


Figure 2. The power damage threshold of the optical coating vs. laser acting time.

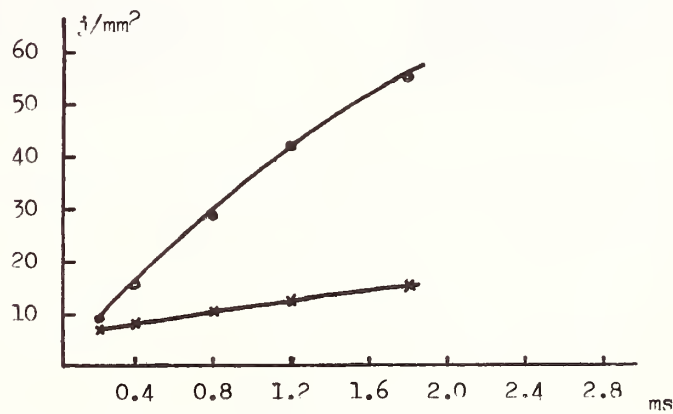
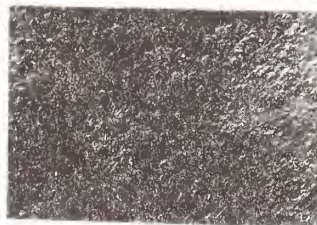


Figure 3. The energy damage threshold of the optical coating vs. laser acting time.

● — ZrO<sub>2</sub>      × — TiO<sub>2</sub>



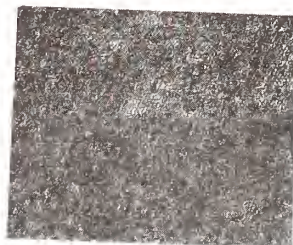
a.



b.



c.



d.



e.



f.

Figure 4. The surface morphologies of the  $\text{ZrO}_2/\text{SiO}_2$  reflecting coating with  $\text{SiO}_2$  overcoating of different thickness.  $\lambda = 1.06 \mu$  (20000x)



Table I. The damage resistance of ZnS thin films with different grain size

Grain size (Å)	200	240	260	300
Damage threshold (j/mm <sup>2</sup> )	50	46	44	36

Table II. The damage resistance of ZrO<sub>2</sub> thin films with different crystallinity

Crystallinity	amorphous	cubic	monoclinic
Damage threshold (j/mm <sup>2</sup> )	19	36	14

Table III. The damage resistance of ZrO<sub>2</sub>/SiO<sub>2</sub> HR multilayers with SiO<sub>2</sub> overcoatings of different thickness

Thickness of SiO <sub>2</sub> overcoating (λ)	0	0.5	1	1.5	2	2.5	3	3.5
Damage threshold (j/mm <sup>2</sup> )	8	10	14	25	31	36	30	20

λ=1.06μ

## Ion-Beam Sputtered $\text{MgF}_2$ and $\text{CaF}_2$ Thin Films

M. F. Dafoe, B. J. Pond, C.K. Carniglia and T. Raj

Martin Marietta Astronautics Group, Laser Systems Technology  
P.O. Box 9316, International Airport, Albuquerque, New Mexico 87119

The optical and mechanical properties of single-layer  $\text{MgF}_2$  and  $\text{CaF}_2$  films deposited by ion-beam sputtering have been investigated and compared with films of the same materials deposited by evaporation from a resistance source. Environmental testing of the ion-beam sputtered (IBS) and evaporated  $\text{MgF}_2$  films has also been done.

For IBS  $\text{MgF}_2$  films, the index of refraction  $n$  is between 1.40 and 1.43 at 633 nm, compared to  $n = 1.38$  for the evaporated films. The extinction coefficient  $k$  is similar to that of conventionally deposited  $\text{MgF}_2$  when oxygen is added to the deposition environment. IBS  $\text{MgF}_2$  films exhibit a small degree of inhomogeneity, with the index of refraction larger at the air/film interface. Mechanical stress in the IBS coatings is compressive, in contrast to the tensile stress commonly found in evaporated coatings. Single-layer  $\text{MgF}_2$  films with a quarter-wave optical thickness of  $18\ \mu\text{m}$  have been deposited on fused silica and zinc sulfide substrates. The transmission band for the IBS  $\text{MgF}_2$  extends from the UV out to approximately  $9\ \mu\text{m}$ , with absorption present at the  $2.8\ \mu\text{m}$  water band.

The index of refraction  $n$  is 1.47 at 633 nm for IBS  $\text{CaF}_2$ , and the degree of inhomogeneity is small, with  $n$  larger at the film/substrate interface. The extinction coefficient is similar for both methods of deposition. Stress in the IBS  $\text{CaF}_2$  films is high and compressive.

Key Words: calcium fluoride; ion-beam sputtering; magnesium fluoride; optical coatings; refractive index; stress

### 1. Introduction

In ion-beam sputter deposition, a beam of ions is used to sputter atoms and/or molecules of a target composed of an atomic or compound material onto a substrate. Ion-beam sputtering is usually done with a beam of neutralized inert gas ions -- argon being the most commonly used. The stoichiometry of the condensing films can often be influenced through the addition of a reactive gas to the deposition environment [1].

Films deposited by ion-beam sputtering generally exhibit excellent optical properties such as low scatter and low absorption. The refractive index in ion-beam sputtered (IBS) optical thin films may approach the values of the bulk materials. Many of the improved properties are attributed to the higher energies of the condensing particles. The average energy of a particle sputtered from a target is typically 5 to 10 eV, compared to 0.1 to 0.3 eV for evaporated particles [2]. The larger energy of the sputtered particles results in higher film densities and the inclusion of fewer contaminants.

A number of materials have been deposited by ion-beam sputtering for use in optical coatings. The list includes many oxides such as  $\text{SiO}_2$ ,  $\text{TiO}_2$ ,  $\text{Al}_2\text{O}_3$ ,  $\text{Ta}_2\text{O}_5$ , and some nitrides such as  $\text{Si}_3\text{N}_4$  and  $\text{AlN}$  [3-6]. Thin film optical coatings of  $\text{ZnS}$  and  $\text{MgF}_2$  have also been successfully deposited by ion-beam sputtering [7,8].

This paper presents the results of a study of IBS  $\text{MgF}_2$  and  $\text{CaF}_2$  thin films. The optical properties (refractive index and extinction coefficient  $k$ ) and some mechanical properties (stress and surface roughness) have been measured for a number of films. These properties are compared for films deposited using various ion-beam energies and for films made with and without the addition of oxygen to the deposition environment as a reactive

gas. In the case of  $\text{MgF}_2$ , tetrafluoromethane ( $\text{CF}_4$ ) and nitrogen were also used as backfill gases, and neon was tried as a sputter gas. These data are compared with data collected from  $\text{MgF}_2$  and  $\text{CaF}_2$  films prepared by thermal evaporation.

## 2. Experimental

The IBS  $\text{MgF}_2$  and  $\text{CaF}_2$  coatings were made in a diffusion pumped, 0.75 meter box coater equipped with a liquid-nitrogen trap. The ion-beam sputtering apparatus consisted of a 2.5 cm Ion Tech Kaufman type ion-beam source, a water cooled target, and a rotating substrate holder [1]. Both the  $\text{MgF}_2$  and  $\text{CaF}_2$  targets were made of hot pressed material. Deposition was monitored on an oscillating-quartz-crystal monitoring system. The approximate temperature of the substrates was measured with an iron-constantan thermocouple placed on the back side of the substrate rack. Due to radiative heating from the ion source, the temperature of the substrates rose from ambient to the 30-40°C range during deposition. Total pressure in the chamber was measured using a standard ion-gauge tube calibrated to nitrogen. The base pressure of the system was typically  $2 \times 10^{-6}$  torr or lower. The argon sputter gas was bled into the system through the ion-beam source to give a total pressure of  $6 \times 10^{-5}$  torr. When oxygen was used as a reactive gas, it was added after the argon pressure had been established, to give a total pressure of  $8 \times 10^{-5}$  torr. The flow of oxygen had to be adjusted during the run to keep the total pressure in the chamber at  $8 \times 10^{-5}$  torr. When  $\text{CF}_4$  and  $\text{N}_2$  were used as backfill gases, their partial pressures were  $4 \times 10^{-5}$  torr and  $2 \times 10^{-5}$  torr, respectively.

$\text{MgF}_2$  and  $\text{CaF}_2$  films were prepared by evaporation from a resistance source for comparison to the IBS films. They were deposited in a diffusion-pumped 18-inch bell jar equipped with a liquid-nitrogen trap. Typical base pressure for the system was  $2.5 \times 10^{-6}$  torr. These depositions were done without the addition of reactive gases to the chamber. The  $\text{MgF}_2$  films were made at a temperature of 150°C, measured by a bimetallic strip thermometer placed on a substrate in the rotating fixture. The  $\text{CaF}_2$  films were deposited without additional heat supplied to the substrates. The radiative heating from the resistance source resulted in a substrate temperature approximately 10°C above ambient. Film thicknesses were controlled by an optical system which monitored the front surface reflection of a part during deposition.

The envelope method was used to determine the optical constants  $n$  and  $k$ , as well as the physical thickness, of each film. This method is based on the analysis of spectral scans of the reflectance and transmittance of a single layer film deposited on a transparent substrate [9-11]. The method has been modified to allow for the determination of the degree of inhomogeneity  $\Delta n/n$  of slightly absorbing films. In some cases  $n$  was determined directly from the reflection measurements and  $k$  was determined from both the reflectance and transmittance measurements by an empirical method [11]. The precision in  $n$  was estimated to be 0.02. The precision in  $k$  was estimated to be 0.0002 at 350 nm for most of the films analyzed. The physical thickness was determined from the optical thickness and the refractive index, with a standard deviation of approximately 10 nm or less.

Established procedures were used for making the transmittance and reflectance measurements necessary for the determination of  $n$ ,  $k$  and  $\Delta n$  [11]. The films used for these measurements were deposited on UV-grade fused silica substrates having a 2.54-cm diameter and a 1-mm thickness. The reference scan for the transmittance measurements was made with an uncoated UV-grade fused silica substrate in each of the sample and reference beams of a dual-beam Varian spectrophotometer. The uncoated piece in the sample beam was then replaced by a coated sample to be measured. The resulting transmittance scan determined the ratio of transmittance of the coated part to an uncoated substrate. The reference for the reflection measurements was made by scanning an uncoated fused silica substrate with a frosted second surface. In this way, the single-surface reflection of fused silica was obtained. When the coated substrates were measured, the second surface reflection of the substrates was removed by using an index matching oil to join the back of the coated sample to the fused silica substrate with a frosted second surface.

Stress in the film was measured by coating one side of a very thin 2.54-cm diameter fused silica disc. The nominal thickness of the discs used was either 0.38 mm or 0.5 mm, depending on the thickness of the applied coating. The curvature of the coated discs was measured on a Fizeau interferometer using either the cadmium 508.6-nm line or the cadmium F' line at 480 nm [12]. The precision in the stress measurements was estimated to be 6 kpsi.

A measurement of the total integrated scatter (TIS) was used to estimate the surface roughness of the films. This technique was used to measure the diffuse and specular



reflectance of a surface, and the results were converted into an equivalent RMS surface roughness [13]. The TIS measurements were made on coated 2-in diameter semiconductor-grade silicon wafers at a wavelength of 633 nm. The uncoated silicon wafers had an RMS surface roughness of 1-2 Å.

Chemical composition of a few selected coatings was determined by Electron Spectroscopy for Chemical Analysis (ESCA), performed with a Perkin-Elmer 548 spectrometer.

Environmental testing was done on fused-silica and silicon-wafer substrates coated with IBS and conventionally deposited  $\text{MgF}_2$ . Environmental testing was not done on the  $\text{CaF}_2$  coatings. The environmental test consisted of subjecting the samples to several 24-hour humidity cycles. Conditions for the humidity cycle were a 50°C temperature and a 95% relative humidity. A visual inspection of each sample was made after each cycle.

Single-layer films were deposited in various thicknesses for the optical, mechanical and environmental test measurements. Most of the spectral and environmental tests were done on films with an optical thickness that was one quarter of 2500 nm. Such a film is described as having a quarter-wave optical thickness (QWOT) of 2500 nm. The evaporated films were prepared with a QWOT of 1300 nm. Thicker films of  $\text{MgF}_2$  could not be deposited without tensile stress fractures. Very thick films of IBS  $\text{MgF}_2$ , having QWOT's of 10-20  $\mu\text{m}$ , were prepared to demonstrate the mechanical superiority of these films over evaporated films. Very thin layers, having a physical thickness of 50-100 nm, were deposited for surface analysis using ESCA.

### 3. Results for $\text{MgF}_2$

The data collected from the IBS and conventionally deposited  $\text{MgF}_2$  films are shown in table 1. The data are labeled by coating run number and grouped according to backfill gas; a dash in the backfill gas column indicates that a reactive gas was not added to the chamber during deposition. Within each backfill-gas grouping, the data are arranged by increasing beam voltage, and within each beam voltage by increasing physical thickness. Data from a thermally evaporated  $\text{MgF}_2$  coating is shown at the bottom of table 1. The value of the optical constants  $n$  and  $k$  at 633 nm and 350 nm, respectively, are listed for each coating. Also listed is the degree of inhomogeneity in each film at 633 nm, as represented by the quantity  $\Delta n/n$ . Positive values for  $\Delta n/n$  correspond to an index that is increasing with distance from the substrate. Negative values of  $\Delta n/n$  correspond to a index that is decreasing with distance from the substrate. Measured values of the compressive stress and average surface roughness are listed for each film.

For the IBS  $\text{MgF}_2$  films, the refractive-index data at 633 nm indicate a nominal value for  $n$  of  $1.42 \pm 0.02$ . This value is slightly higher than the value of 1.38 for the conventionally deposited  $\text{MgF}_2$  coating (run number C2) [14-15]. Figure 1 depicts the dispersion of IBS and evaporated films of  $\text{MgF}_2$ . The dispersion of an IBS  $\text{MgF}_2$  coating with a QWOT of 18  $\mu\text{m}$  is shown in curve (a) of figure 1 (see table 1, run number 43). This particular coating was deposited in the presence of an oxygen backfill. The index data from the film were used to determine the coefficients  $A$ ,  $B$ , and  $C$  of the Conrady dispersion equation  $n(\lambda) = A + B/\lambda + C/\lambda^3$ . The values obtained for these coefficients were  $A = 1.405$ ,  $B = 0.015$  and  $C = 0$ . This dispersion relation was then plotted to produce curve (a). Curve (b) in figure 1 is a plot of the index data obtained from a film produced by thermal evaporation. The higher index of the IBS coating is apparent from the figure.

The higher index of IBS  $\text{MgF}_2$  coatings may be due in part to higher film densities. In addition, the higher refractive index may be due to the inclusion of oxygen in the coatings. Bulk  $\text{MgF}_2$  has an index of approximately 1.38, and bulk magnesium oxide ( $\text{MgO}$ ) has a index of approximately 1.7. A film stoichiometry of the general form  $\text{MgO}_x\text{F}_{2-y}$  would explain the intermediate index value of 1.42. This conclusion is confirmed by an ESCA analysis performed on two  $\text{MgF}_2$  coatings, one made with a  $\text{O}_2$  backfill and the other without any backfill. ESCA was performed at (1) the surface of the coatings and (2) after a very slight sputter-etching to remove surface contaminants. Both of the coatings are comprised of principal elemental components of Mg, F and O. The ratio of F/O was approximately 5.5 for both the coatings. This does not necessarily suggest that the two coatings are identical. The oxygen could be present in chemical bond formation as an oxide, water, carbonaceous material or other hydrocarbons present in the vacuum chamber.



Table 1. Data for IBS and thermally evaporated thin films of MgF<sub>2</sub>.

Run #	Back fill Gas	Beam Voltage (V)	Deposition Rate (Å/min)	Physical Thickness (nm)	Refractive Index at 633 nm	$\frac{\Delta n}{n}$ <sup>a</sup> at 633 nm	Extinction coefficient at 350 nm ( $\times 10^4$ )	Compressive Stress <sup>b</sup> (kpsi)	Average Surface Roughness (Å rms)
8	--	600	21	469	1.40	--	1	36	4
7	--	800	28	321	1.42	--	6	33	3
6 <sup>c</sup>	--	1000	50	370	1.40	--	27	23	5
45	--	1000	23	383	1.41	0.01	21	45	3
64	--	1000	27	500	1.42	--	25	37	2
63	--	1000	20	3360	1.43	--	35	70	15
66 <sup>d</sup>	--	1000	9	360	1.42	0.02	41	43	5
18	O <sub>2</sub>	600	18	414	1.41	--	1	51	2
17	O <sub>2</sub>	800	28	407	1.41	0.01	1	56	4
31	O <sub>2</sub>	1000	41	376	1.41	--	1	68	3
41	O <sub>2</sub>	1000	22	434	1.42	0.01	1	72	2
33	O <sub>2</sub>	1000	38	619	1.42	0.01	1	76	5
9	O <sub>2</sub>	1000	31	651	1.42	--	1	57	3
42	O <sub>2</sub>	1000	21	1730	1.43	--	1	63	5
32	O <sub>2</sub>	1000	39	1800	1.43	--	1	66	7
43	O <sub>2</sub>	1000	19	3330	1.43	--	1	60	10
70	CF <sub>4</sub>	1000	21	327	1.40	0.01	52	67	4
71	CF <sub>4</sub>	1000	27	2550	1.40	-0.02	22	55	15
72	N <sub>2</sub>	1000	26	467	1.42	--	6	58	3
C2 <sup>e</sup>	--	--	708	262	1.38	--	1	-23	2

a - Positive  $\Delta n/n$  values correspond to a higher index at the air/film interface. Negative  $\Delta n/n$  values correspond to a higher index at the film/substrate interface. A dash in this column indicates that the inhomogeneity in a film is less than the uncertainty in the measurement.

b - Negative values correspond to tensile stress.

c - 50 mA beam current. The beam current for all other runs was 30 mA.

d - Neon used as sputter gas.

e - Deposited by thermal evaporation.

The ESCA spectra collected for both coatings after sputter-etching are shown in figure 2(a) and (b). The intensity of photoelectrons is presented along the vertical axis and the energy is presented along the horizontal axis. It is clear that the spectra for MgF<sub>2</sub> deposited with and without oxygen backfill are essentially identical.

There is a small variation in the index of the IBS films, although the variation does not appear to depend on either the beam voltage or the sputter gas. However, it does appear that there may be a dependence of the index on the backfill gas added to the chamber. The films deposited with a backfill gas of CF<sub>4</sub> have low indices, whereas the films deposited with a backfill gas of oxygen or nitrogen have slightly higher indices.

There appears to be a trend toward increasing index with increasing film thickness. This observation is consistent with the small positive values of inhomogeneity measured for some of the films. This trend is more apparent among those films deposited with an oxygen backfill, or deposited without the addition of a backfill gas to the chamber. Index data from the two coatings made with the use of a CF<sub>4</sub> backfill (coating run numbers 70 and 71) depart from this trend in that the two coatings differ markedly in thickness and have the same refractive index. Note that the thicker coating made with a CF<sub>4</sub> backfill has a lower index than the coatings of similar thicknesses produced with an oxygen backfill or without any backfill.

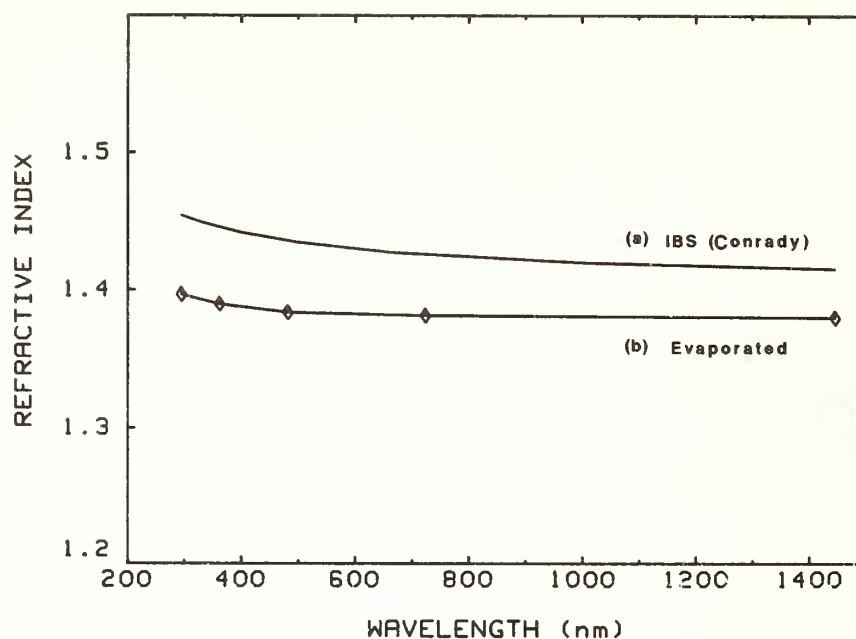


Figure 1. (a) Plot of the Conrady dispersion equation for IBS MgF<sub>2</sub>. The coefficients in the equation were derived from index data taken from a coating with a QWOT of 18  $\mu$ m, and deposited with the use of an oxygen backfill (see table 1, run number 43). (b) Dispersion of an evaporated MgF<sub>2</sub> coating.

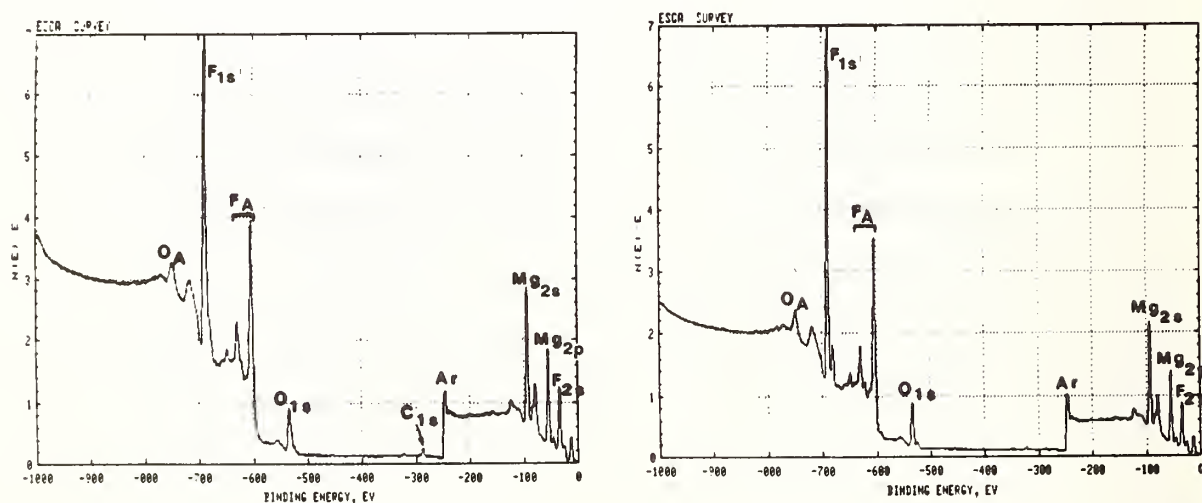


Figure 2. (a) ESCA spectrum taken after a slight sputter etching for an IBS MgF<sub>2</sub> coating deposited without any backfill. (b) ESCA spectrum taken after a slight sputter etching for an IBS MgF<sub>2</sub> coating deposited with an O<sub>2</sub> backfill. The two spectra are essentially identical.

The degree of inhomogeneity, expressed as  $\Delta n/n$ , is very small for the IBS  $\text{MgF}_2$  coatings. The thermally evaporated  $\text{MgF}_2$  film does not have a measurable amount of inhomogeneity. With one exception, those films exhibiting a measurable degree of inhomogeneity have a positive  $\Delta n/n$  value, i.e. a higher index at the air film interface. A positive degree of inhomogeneity has also been observed in IBS oxide films [5].

The extinction coefficient  $k$  at 350 nm in the IBS  $\text{MgF}_2$  films depends on the type of backfill gas, and the beam voltage used during a run. Those coatings made with an oxygen backfill have consistently low  $k$  values of approximately  $10^{-4}$ . The use of  $\text{CF}_4$  or  $\text{N}_2$  as a backfill gas resulted in higher  $k$  values than did oxygen.

In the cases that backfill gases were not added to the chamber,  $k$  at 350 nm was found to depend on beam voltage. As can be seen from table 1,  $k$  increases with increasing beam voltage from a value of  $10^{-4}$  when a beam voltage of 600 V is used, to approximately  $2-3 \times 10^{-3}$  when a beam voltage of 1000 V is used. The observed dependence of  $k$  on beam voltage implies that it is possible to influence film stoichiometry by varying the energy of the ion beam.

The thickest coating made using argon as the sputter gas and without the use of a backfill (run number 63) has the highest  $k$  value. It is suspected that a reduction in the amount of available background gases due to gettering over the course of time is responsible for the higher  $k$  value produced in the coatings from that run. This effect seems plausible considering that the run took approximately 28 hours to complete, and that the base pressure following the run was approximately  $4 \times 10^{-7}$  torr.

Some insight as to the role of the backfill gases in the determination of film properties can be gained by examining the infrared transmittance spectra of the thickest  $\text{MgF}_2$  coatings. Figure 3 shows the transmittance spectra of coatings with QWOT's of 10  $\mu\text{m}$  to 20  $\mu\text{m}$  (from run numbers 42, 43, 63 and 71), deposited on ZnS substrates. These scans were made on a Perkin-Elmer dual-beam spectrophotometer. As can be seen from figure 3, there are two prominent absorption peaks in the spectra of each film at approximately 2.8  $\mu\text{m}$  and 10  $\mu\text{m}$ . The peak at 2.8  $\mu\text{m}$  is due to the presence of hydroxyl ( $-\text{OH}$ ) groups in the film, and the peak at 10  $\mu\text{m}$  suggests the formation of  $\text{MgO}_x$  in the film [16]. Bulk  $\text{MgO}$  displays a similar absorption peak at 10  $\mu\text{m}$  [17].

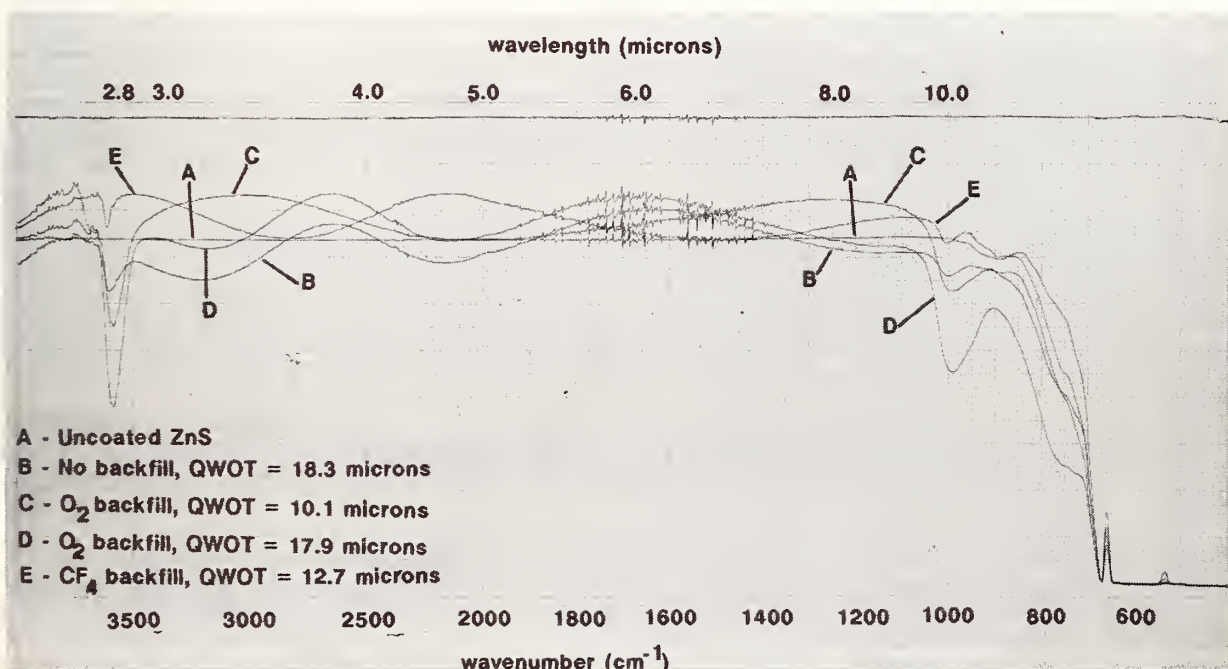


Figure 3. Infrared transmittance spectra of the thickest IBS  $\text{MgF}_2$  coatings. The two absorption peaks at 2.8  $\mu\text{m}$  and 10  $\mu\text{m}$  are due to water and  $\text{MgO}$ , respectively.

An estimate of the absorption at each peak is given in table 2. These estimates were arrived at by approximating the percent absorption at each peak from the spectral scans; the uncertainty in the estimates is about  $87 \text{ cm}^{-1}$  or less depending on the physical thickness of the film. From the data in table 2, it can be seen that those coatings prepared with an oxygen backfill (run numbers 42 and 43) have approximately three times more absorption than the other coatings. This observation indicates that an abundance of oxygen in the deposition environment contributes to the amount of water in the coatings and tends to raise the oxide content through the formation of  $\text{MgO}_x\text{F}_{2-y}$ . Conversely, the coatings which were prepared without a backfill and with a  $\text{CF}_4$  backfill (run numbers 63 and 71, respectively) show less evidence of the inclusion of oxygen.

Table 2. Loss at  $2.8 \mu\text{m}$  and  $10 \mu\text{m}$  absorption peaks in IBS  $\text{MgF}_2$

Run Number	Backfill Gas	Absorption coefficient ( $\text{cm}^{-1}$ )	
		$2.8 \mu\text{m}$ peak	$10.0 \mu\text{m}$ peak
42	$\text{O}_2$	1511	674
43	$\text{O}_2$	1436	785
63	--	281	122
71	$\text{CF}_4$	327	160

Neon was employed as a sputter gas in run number 66 to investigate its effects on film properties. The deposition rate was much lower ( $9 \text{ \AA}/\text{min}$ , compared to  $20\text{--}50 \text{ \AA}/\text{min}$  for films sputtered with argon). The low rate is to be expected, due to the lower sputter efficiency of the lighter gas. The film also exhibited a higher  $k$  value at  $350 \text{ nm}$  than films deposited under similar conditions with argon as the sputter gas.

Stress in the IBS  $\text{MgF}_2$  films is compressive. The use of a backfill gas during deposition produces stress values approximately 10 to 20 kpsi higher than the values produced when the films are deposited without a backfill gas. In general, the large variation in measured stress values cannot be correlated to any of the deposition parameters. The unusually high stress produced in the thickest coating made without a backfill (run number 63) may be the result of a changing deposition environment during the long coating run. Although the compressive stress in the IBS films is high, greater film thicknesses are possible with this process because the stress is compressive rather than tensile and because the adhesion of sputtered films is superior to that of evaporated films.

Several of the  $\text{MgF}_2$  films were subjected to 24-hour humidity cycles as described in section 2. The results indicate that the IBS films are more stable than the thermally-evaporated film. No visible defects were observed on any of the IBS films after the completion of four 24-hour humidity cycles. Inspection of the films with a Nomarski differential-interference-contrast microscope revealed signs of small defect formation in several of the IBS films. They had an approximate diameter of  $150 \mu\text{m}$ . These defects appeared to be associated with nodules resulting from cleaning residue or substrate irregularities.

On the other hand, visible failure of a thermally evaporated  $\text{MgF}_2$  film on a silicon wafer was observed after two 24-hour humidity cycles. The crazed region was approximately  $2 \text{ cm}$  by  $1 \text{ mm}$ , located at one edge of the part.

#### 4. Results for $\text{CaF}_2$

Table 3 documents the results of the  $\text{CaF}_2$  study. The principle parameters were  $\text{O}_2$  partial pressure and beam voltage.



Table 3. Data for IBS and thermally evaporated thin films of CaF<sub>2</sub>

Run #	Back fill Gas	Beam Voltage (V)	Deposition Rate (Å/min)	Physical Thickness (nm)	Refractive Index <sup>a</sup> at 633nm	$\frac{\Delta n^b}{n}$ at 633 nm	Extinction Coefficient <sup>c</sup> at 350 nm ( $\times 10^4$ )	Compressive Stress (kpsi)	Average Surface Roughness (Å rms)
55	--	600	22	490	1.46	-0.01	3	126	2
54	--	1000	29	430	1.46	--	4	136	4
48	O <sub>2</sub>	600	17	274	1.47	-0.01	4	126	15
49	O <sub>2</sub>	600	19	541	1.48	--	4	109	35
53 <sup>d</sup>	O <sub>2</sub>	1000	24	470	1.47	-0.01	2	155	13
47	O <sub>2</sub>	1000	25	608	1.47	-0.01	1	110	33
C3 <sup>e</sup>	--	--	B90	266	1.21	-0.07	2	0	4

a - Limits of error for n are  $\pm 0.02$ .

b - Negative  $\Delta n/n$  values indicate a higher index at the film/substrate interface. Precision in this quantity is 0.01. A dash in this column indicates that the inhomogeneity in a film is less than the uncertainty in the measurement.

c - Limits of error for k are  $\pm 0.0002$  at 350 nm.

d - Foil change and system bake preceded this run.

e - Conventionally deposited film.

For IBS CaF<sub>2</sub>, n at 633 nm and k at 350 nm are  $1.47 \pm 0.02$  and  $0.0003 \pm 0.0002$ , respectively. These optical constants appear to be insensitive to either beam voltage or oxygen partial pressure. The index of refraction at 633 nm is slightly lower in the films deposited without the use of an oxygen backfill, but this difference is within the uncertainty in the measurement. The dispersion of an IBS CaF<sub>2</sub> film is shown in figure 4(a). The curve is a plot of the Conrady dispersion equation, for a coating deposited using an oxygen backfill (see table 3, run number 47). The values for the Conrady dispersion coefficients are A = 1.44B, B = 0.010 and C = 0. The extinction coefficient k does vary slightly from run to run, but the variation cannot be correlated with the deposition parameters.

The index of refraction for IBS CaF<sub>2</sub> at 633 nm is slightly higher than the value of 1.43 for naturally occurring CaF<sub>2</sub> [18]. This may be due to the inclusion of oxygen in the coatings. CaO has an index of approximately 1.84 [19]. A film stoichiometry of the general form CaO<sub>x</sub>F<sub>2-y</sub> would explain the intermediate index value of 1.47. This conclusion is confirmed by an ESCA analysis performed on two CaF<sub>2</sub> coatings, one deposited with an oxygen backfill and the other deposited without any backfill. The analysis procedure used was similar to that used for MgF<sub>2</sub> coatings. Both CaF<sub>2</sub> coatings have the same elemental composition: Ca, F and O. Thus, a general formula of the type CaO<sub>x</sub>F<sub>2-y</sub> provides a good representation of the IBS coatings obtained from a CaF<sub>2</sub> target. As an example of ESCA analysis, figure 5 shows an ESCA spectrum taken near the top surface of the CaF<sub>2</sub> coating deposited with an O<sub>2</sub> backfill. It can be seen that the principal components of the coating are Ca, F and O.

There is a small amount of inhomogeneity present in the CaF<sub>2</sub> films prepared by ion-beam sputtering. All of the coatings with a measurable degree of inhomogeneity have a negative value for  $\Delta n/n$ , indicating a slightly higher index at the film/substrate interface.

The data for a CaF<sub>2</sub> film prepared by thermal evaporation is presented at the bottom of table 3. The most notable feature of this film is its low refractive-index value of 1.21. It should be noted that these results agree with those found in the literature [14,15,20]. The dispersion and inhomogeneity of an evaporated CaF<sub>2</sub> film are represented by curve (b) in figure 4. The bars on the dispersion curve indicate the extent of the index inhomogeneity of the film. The value at the upper end of the bars indicates the index at the film/substrate interface. The value at the lower end indicates the index at the film/air interface. In comparison with the IBS film, the evaporated coating has a lower index and a slightly lower absorption and it is more inhomogeneous.

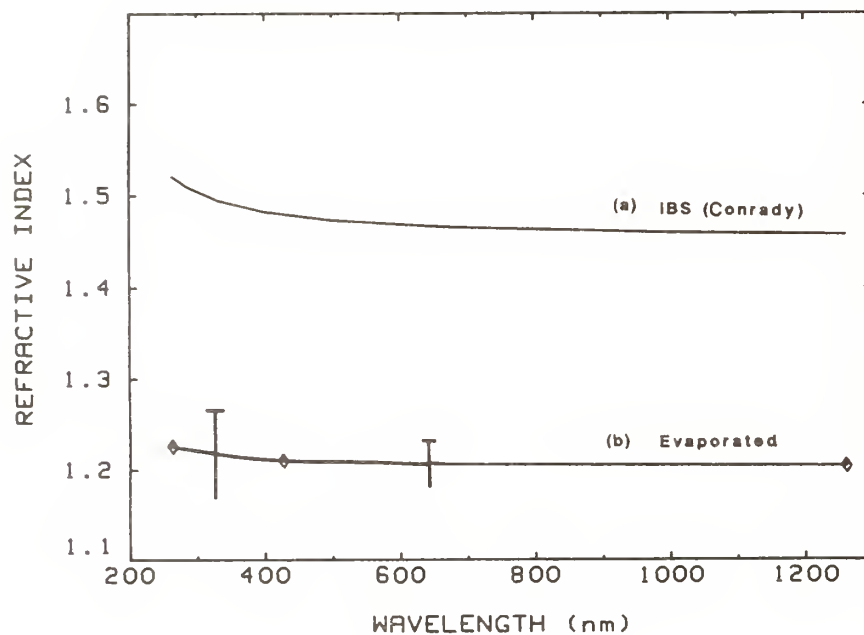


Figure 4. (a) Plot of the Conrady dispersion equation for an IBS  $\text{CaF}_2$  film. The coating from which the index data were taken was deposited using an oxygen backfill (see table 3, run number 47). (b) Dispersion of an evaporated  $\text{CaF}_2$  film. The bars on the dispersion curve indicate the extent of the index inhomogeneity of the film. The value at the upper end of the bars indicates the index at the film/substrate interface. The value at the lower end indicates the index at the film/air interface.

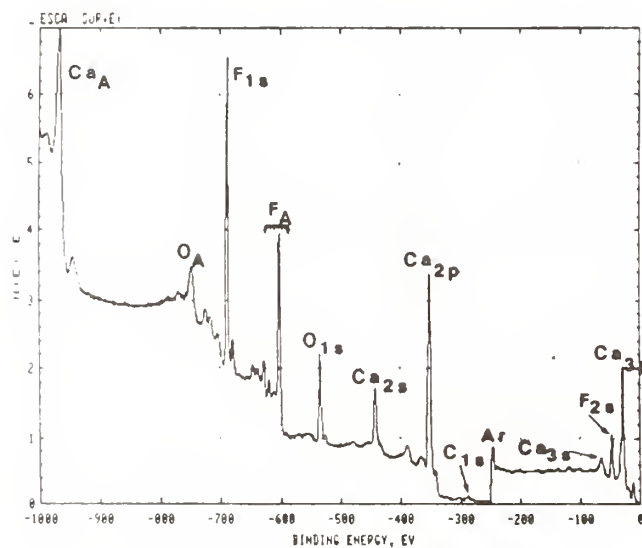


Figure 5. ESCA spectrum taken after a slight sputter etching for an IBS  $\text{CaF}_2$  coating deposited with an  $\text{O}_2$  backfill.

Surface roughness of IBS  $\text{CaF}_2$  coatings depends on oxygen partial pressure. The IBS  $\text{CaF}_2$  films deposited without an oxygen backfill have a much lower surface roughness than those deposited with an oxygen backfill. Surface roughness in the IBS  $\text{CaF}_2$  films does not appear to be related to beam voltage. Thermally evaporated  $\text{CaF}_2$  has a low surface roughness, comparable to that of the IBS coatings prepared without an oxygen backfill.

Compressive stress values for all of the ion-beam sputtered films in table 3 are high. Although there is a large variation in stress from run to run, the variation cannot be correlated to the deposition parameters. However, as noted in table 3, run number 53 was done immediately after a foil change and system bake. The unusually high stress produced in the run may be related to a different film composition in this film deposited in a clean chamber. In contrast to the high stress in the IBS coatings, the stress in the evaporated film was less than the uncertainty in the measurement.

Perhaps the greatest difference between the two methods of deposition can be seen when the mechanical properties of IBS and conventionally deposited  $\text{CaF}_2$  are compared. Evaporated  $\text{CaF}_2$  is very fragile, and extreme care must be taken when handling films prepared by this method. The IBS  $\text{CaF}_2$  coatings are still relatively soft coatings because of the inherent nature of the material. However, they are much more resistant to damage by handling than the evaporated  $\text{CaF}_2$  films.

An IBS  $\text{CaF}_2$  coating was deposited on a substrate with a temperature of  $150^\circ\text{C}$  to investigate whether or not the film properties could be improved by increasing the substrate temperature. An oxygen backfill was not used during this run, and the beam voltage was 1000 V. The result was a highly absorbing film.

An IBS  $\text{CaF}_2$  coating having an approximate QWOT of  $20\mu\text{m}$  was prepared. Deposition was done without an oxygen backfill, and with a beam voltage of 1000 V. The coating was dark brown in color. Computer modeling of a transmission scan of the film indicated an approximate value for  $k$  of 0.03 at 633 nm. This value for  $k$  is about two orders of magnitude higher than  $k$  values for films produced in any other  $\text{CaF}_2$  run deposited at ambient temperature. The reason for the high  $k$  value produced in the thick  $\text{CaF}_2$  coating is most likely a reduction in the amount of available background gases due to gettering over time during the 27.5 hour run. This correlates with the low base pressure of  $2.8 \times 10^{-7}$  torr observed immediately after the long run.

## 5. Conclusions

The results presented here demonstrate that ion-beam sputtering can be used to deposit films of  $\text{MgF}_2$  and  $\text{CaF}_2$  with mechanical properties superior to those of thermally-evaporated films of the same materials. Ion-beam sputtering allows the deposition of  $\text{MgF}_2$  films with significantly greater thicknesses than are possible using conventional deposition methods. In the case of  $\text{CaF}_2$ , film durability is greatly improved by the ion-beam sputtering process.

Ion-beam sputtering has been shown to produce single layer films of  $\text{MgF}_2$  and  $\text{CaF}_2$  with good optical properties. There is evidence that films sputtered from  $\text{MgF}_2$  and  $\text{CaF}_2$  targets contain oxygen. This oxygen tends to increase the refractive index of the films to a value above the bulk index for the materials. Films of  $\text{MgF}_2$  deposited with an oxygen backfill had lower absorption in the visible and near UV spectral regions than films deposited without an oxygen backfill. However,  $\text{MgF}_2$  films deposited with oxygen had IR absorption bands.

---

The authors wish to thank Willy Kunzler, Wayne Wasson and Dan O'Shea of the AFWL/Technical Services Division, Metrology Laboratory, Kirtland AFB, New Mexico, for making the spectral measurements and conducting the environmental tests. The authors also acknowledge the help of Loretta Mascarenas and Jennifer Richberger of Rockwell Power Systems, Optical Component Evaluation Laboratory, Kirtland AFB, New Mexico, for making the TIS measurements.

In addition, the authors are grateful for the efforts of Cathy Madison, Chris Andrews, Jeanette DeBar and Joe Sobczak of Martin Marietta Astronautics Group, Laser Systems Technology, Developmental Optics Facility, Kirtland AFB, New Mexico, in the preparation of the films and in the reduction of the spectral data. The authors also acknowledge the help of Garry Marions and Anthony Hanson, also of Martin Marietta, in making the stress measurements.

This effort was sponsored by the Air Force Weapons Laboratory, Air Force Systems Command, United States Air Force, Kirtland AFB, New Mexico 87117.

## 6. References

- [1] Harper, James M.E. Ion Beam Deposition, chapter II-5 in Thin Film Processes, J.L. Vossen and W. Kern, eds. New York: Academic Press; 1978.
- [2] Wehner, G.K.; Anderson, G.S. The nature of physical sputtering, chapter 3 in Handbook of Thin Film Technology, L.I. Maissel and R. Glang, eds. New York: McGraw-Hill; 1978.
- [3] Sites, J.R.; Gilstrap, P.; Rujkorakarn, R. Ion beam sputter deposition of optical coatings. Opt. Eng. 22: 447-449; 1983.
- [4] Demiryont, H.; Sites, J.R. Oxygen threshold for ion-beam sputter deposited oxide coatings. Nat. Bur. Stand. (U.S.) Spec. Publ. 727: 180-186; 1984.
- [5] Allen, T.H. Reactive ion beam sputtered optical coatings. Proceedings of the 30th Annual Technical Conference of the Society of Vacuum Coaters: 27-41; 1987.
- [6] Pond, B.; Schmell, R.A.; Carniglia, C.K.; Raj, T. Comparison of the optical properties of some high-index oxide films prepared by ion-beam sputter deposition with those of electron beam evaporated films. NIST Spec. Publ. 752: 410-417; 1986.
- [7] Varitimos, T.E.; Tustison, R.W. Ion beam sputtering of ZnS thin films. Thin Solid Films 151: 27-33; 1987.
- [8] Allen, T.H.; Lehan, J.; McIntyre, L.C. Ion beam sputtered magnesium fluoride. Optical Interference Coatings, 1988 Technical Digest Series, Vol. 6, 1988 April 12-15; Tucson, AZ. 293.
- [9] Mouchart, J.; Lagier, G.; Pointu, B. Determination des constantes optiques  $n$  et  $k$  de matériaux faiblement absorbents. Appl. Opt. 24: 1808-1814; 1985.
- [10] Manifacier, J.C.; Gasiot, J.; Fillard, J.P. Determination of the optical constants  $n$ ,  $k$  and the thickness of a weakly absorbing thin film. J. of Phys. E9: 1002-1004; 1976.
- [11] Arndt, D.P. et al. Multiple determination of the optical constants of thin film coating materials. Appl. Opt. 23: 3571-3596; 1984.
- [12] Campbell, D.S. Mechanical properties of thin films, chapter 12 in Handbook of Thin Film Technology, L.I. Maissel and R. Glang, eds. New York: McGraw-Hill; 1970.
- [13] Guenther, K.H.; Wierer, P.G.; Bennett, J.M. Surface roughness measurements of low-scatter mirrors and roughness standards. Appl. Opt. 23: 3820-3836; 1984.
- [14] Heavens, O.S.; Smith, S.D. Dielectric thin films. J. Opt. Soc. Am. 47: 469-472; 1957.
- [15] Pulker, H.K. Characterization of optical thin films. Appl. Opt. 18: 1969-1977; 1979.
- [16] Plyler, E.K.; Griff, N. Absolute absorption coefficients of liquid water at 2.95 $\mu$ , 4.7 $\mu$ , and 6.1 $\mu$ . Appl. Opt. 4: 1663-1662; 1965.
- [17] Willmott, J.C. The infrared spectrum of magnesium oxide. Proc. Phys. Soc. 63: 389-402; 1950.
- [18] Malitson, I.H. A redetermination of some optical properties of calcium fluoride. Appl. Opt. 2: 1103-1107; 1963.
- [19] Handbook of Chemistry and Physics, R.C. Weast, M.J. Astle, W.H. Beyer, eds. Boca Raton, FL: Chemical Rubber Company Press; 1988.
- [20] Heavens, O.S. Optical properties of thin films. Rep. Prog. Phys. 23: 1-65; 1960.



Localization of Absorption Losses in Optical Coatings

Wu Zhouling      Fan Zhengxiu

Shanghai Institute of Optics and fine Mechanics  
Academia Sinica, P.O.Box 8211, Shanghai, PRC

Absorption measurements performed by means of photothermal deflection technique in suitably prepared samples permit a localization of absorption losses in optical coatings.

For single layers, wedge-shaped  $ZrO_2$ ,  $MgF_2$ ,  $ZnS$ ,  $TiO_2$ ,  $Ta_2O_5$  and  $SiO_2$  films are measured. The experimental results show that in  $ZrO_2$ ,  $MgF_2$  and  $ZnS$  films investigated, the film-substrate interface absorption and the air-film interface absorption are nearly the same, while in  $TiO_2$ ,  $Ta_2O_5$  and  $SiO_2$  films, the film-substrate interface absorption dominates over the air-film interface absorption, being the main source of the total absorption loss.

For multilayers, a separate evaluation of the volume and interface absorption of  $TiO_2/SiO_2$  laser mirrors was carried out by means of an appropriate variation in the thickness of the high and low refracting components, and the measured results show a predominance of interface absorption over volume absorption in the multilayer system under investigation.

Key Words, bulk and interface absorption; optical coating; photothermal deflection.

## 1. Introduction

For many systems in modern optics, the reduction of losses in dielectric thin films is extremely important. The absorption loss causes laser-induced damage in dielectric layers, thus limits the radiation intensity of many lasers. To reduce the absorption loss in dielectric thin films, it is necessary to understand the physical origin of absorption in the concerned coatings.

This paper reports our recent local characterization of absorption losses in dielectric thin films. Total absorption measurement was carried out by transverse photothermal deflection technique [1-3], while the separate evaluation of the bulk and interface absorption portions was realized with the help of suitably prepared samples [4,5].

## 2. Preparation of the samples

All of the samples were produced in conventional high vacuum evaporation plants equipped with oil diffusion pumps. For single layers, the samples were made wedge-shaped [4], as shown in fig.1. For multilayers, an appropriate variation in the thickness of the high and low refracting components was introduced [5], as shown in fig.2. The deposition methods and the related characterizations of the samples under investigation is given in table 1.

## 3. Experimental procedure and related theory

### 3.1 Total absorption measurement

Total absorption measurement of the samples investigated was carried out by transverse photo-

thermal deflection technique. The physical basis for this technique [1,2] and a detailed description of our apparatus [3] have been published earlier. Here we introduce the measurement by simply giving

$$A = A_0 S / S_0$$

where  $A_0$  and  $S_0$  are the absorptance and the photothermal deflection amplitude signal of the calibrating sample, while  $A$  and  $S$  those of the sample being measured.

### 3.2 Separate evaluation of volume and interface absorption of single layers

To investigate the absorption of single-layer films deposited on glass-substrates we need to separate four absorption portions, the air-film interface (af), the bulk of the film (f), the film-substrate interface (fs), and the bulk of the substrate (s). Hence, the measured total absorption  $A$  of the sample investigated consists of an air-film as well as a film-substrate interface term and bulk absorption of the film as well as of the substrate [5],

$$A = A_{af} + A_f + A_{fs} + A_s \quad (1)$$

$$= P_{af} a_{af} + \bar{P}_f \bar{\alpha}_f d_f + P_{fs} a_{fs} + \bar{P}_s \bar{\alpha}_s d_s \quad (2)$$

where  $a_{af}$  ( $a_{fs}$ ) — the specific absorption at the air-film (film-substrate) interface;  
 $\bar{\alpha}_f$  ( $\bar{\alpha}_s$ ) — the spatially averaged film (substrate) absorption coefficient;  
 $P_{af}$  ( $P_{fs}$ ) — the relative light power density at the air-film (film-substrate) interface;  
 $\bar{P}_f$  ( $\bar{P}_s$ ) — the spatially averaged relative light power density inside the film (substrate).

In our experiment, to separate  $A_{af}$ ,  $A_f$ ,  $A_{fs}$  and  $A_s$ , we employ the following procedure,

First, measure  $\bar{\alpha}_s$ . This can be carried out by direct measurement of the bare substrate absorptance in the wedge-shaped sample, as shown in fig.1.

Second, separate  $\bar{\alpha}_f$ ,  $a_{af}$  and  $a_{fs}$ . Here, in dependence of the light beam position on the layer, and, hence, of the actual film thickness, the relative power densities at both interfaces and within the film volume will be changing in a characteristic pattern, ranging from a quarter-wave to a half wave optical thickness, tabled by indices (1) and (2), respectively. Measuring wedge-shaped film up to an optical thickness at least of  $2\lambda$ , the rise in  $A^{(1)}$  or  $A^{(2)}$  versus the optical thickness permits a determination of  $\bar{\alpha}_f$ :

$$\bar{\alpha}_f = \frac{1}{\bar{P}_f} \frac{A^{(2)} - A^{(1)}}{d^{(2)} - d^{(1)}} = \frac{1}{\bar{P}_f} \frac{\Delta A}{\Delta d} \quad (3)$$

The specific interface absorption  $a_{af}$  and  $a_{fs}$  are yielded from measured data extrapolated to zero thickness. By rewriting equation (2) for quarterwave as well as halfwave thickness we have

$$a_{af} = \frac{(A^{(1)} - \bar{P}_f^{(1)} \bar{\alpha}_f d_f^{(1)} - \bar{P}_s^{(1)} \bar{\alpha}_s d_s) - (A^{(2)} - \bar{P}_f^{(2)} \bar{\alpha}_f d_f^{(2)} - \bar{P}_s^{(2)} \bar{\alpha}_s d_s) (P_{fs}^{(1)} / P_{fs}^{(2)})}{P_{af}^{(1)} - P_{af}^{(2)} (P_{fs}^{(1)} / P_{fs}^{(2)})} \quad (4)$$

$$a_{fs} = \frac{(A^{(1)} - \bar{P}_f^{(1)} \bar{\alpha}_f d_f^{(1)} - \bar{P}_s^{(1)} \bar{\alpha}_s d_s) - (A^{(2)} - \bar{P}_f^{(2)} \bar{\alpha}_f d_f^{(2)} - \bar{P}_s^{(2)} \bar{\alpha}_s d_s) (P_{af}^{(1)} / P_{af}^{(2)})}{P_{fs}^{(1)} - P_{fs}^{(2)} (P_{af}^{(1)} / P_{af}^{(2)})} \quad (5)$$

Third, calculate  $A_{a,r}$ ,  $A_r$ ,  $A_{r,s}$  and  $A_s$  by comparing eq.(1) and eq.(2). This can be realized in a direct way.

### 3.3 Separate evaluation of volume and interface absorption for multilayer samples

For a multiple layer as shown in fig.2. we have

$$A = A_a + A_{a,r} + A_{r,s} + A_{s,r} + A_r + A_s \quad (6)$$

where  $A$  indicates total absorptance while  $A$  with indices indicate related absorptance portions.

To simplify the analysis, we take quarter-wave-stack HR coatings as examples, thus

$$\begin{aligned} d_1 = d_3 = \dots = d_{2n-1} &= \lambda_0 / (4n_H) \\ d_2 = d_4 = \dots = d_{2n} &= \lambda_0 / (4n_L) \end{aligned}$$

where  $d_i$  is the geometrical thickness of the  $i$ -th layer. Then we have [6]

$$A = A_v + A_{HL} \quad (7)$$

$$= \frac{\lambda_0}{2} (\bar{\alpha}_L + \bar{\alpha}_H) \frac{1}{n_H^2 - n_L^2} + 4 a_{HL} \frac{1}{n_H^2 - n_L^2} \quad (8)$$

where  $\bar{\alpha}$  is the spatially averaged absorption coefficient of low (high) refracting component and  $a_{HL}$  the specific absorption at the H-L interface.

To make a separate evaluation of the volume and interface absorption of the HR coatings, an appropriate variation in the thickness of the high and low refracting components is necessary [5]. Thus, if we have

$$\begin{aligned} n_H l_H &= (2p+1)\lambda_0/4 \\ n_L l_L &= (2q+1)\lambda_0/4 \end{aligned} \quad \begin{matrix} p, q=1, 2, \dots \\ (9) \end{matrix}$$

Then eqs. (6)-(8) may be rewritten as

$$\begin{aligned} A(q, p) &= \frac{4 a_{HL}}{n_H^2 - n_L^2} + \frac{(2q+1)\lambda_0 \bar{\alpha}_L}{2(n_H^2 - n_L^2)} + \frac{(2p+1)\lambda_0 \bar{\alpha}_H}{2(n_H^2 - n_L^2)} \quad (10a) \\ &= A_{HL} + A_V(q) + A_V(p) \\ &= A_{HL} + A_V(q, p) \quad (10b) \end{aligned}$$

where  $A(q, p)$  is the total absorption corresponding  $(q, p)$ ,  $A_v(q)$  and  $A_v(p)$  are the respective volume absorptions. By measuring  $A(q, p)$  with different  $(q, p)$  and then fitting the results to eq. (10), we can get  $a_{HL}$ ,  $\bar{\alpha}_L$  and  $\bar{\alpha}_H$ , and hence  $A_{HL}$  and  $A_v(q, p)$ .

## 4. Experimental results and discussion

### 4.1 Single-layer Samples

Table 2 shows our experimental results of single layers. From these results we can see,

(1). A separate evaluation of bulk and interface absorption of single-layer optical thin films has been realized by means of the combination of transverse photothermal deflection tech-

nique and wedge-shaped samples.

(2). For samples No.1~No.3 ( $ZrO_2$ ,  $MgF_2$ ,  $ZnS$ ), the three absorption portions are nearly the same ( $A_{rs} \approx A_{si} \approx A_{fs}$ ), whereas for samples No.4~No.6 ( $TiO_2$ ,  $Ta_2O_5$ ,  $SiO_2$ ), the film-substrate interface absorption  $A_{rs}$  dominates over the air-film interface absorption  $A_{si}$ , being the main source of the total absorption loss.

(3) Though deposited under the same conditions, the localized absorption losses of samples No.1~3 and No.4~6 show a great difference. This implies that the kind of material plays an important role in the distribution of absorption losses in optical coatings.

#### 4.2 Multilayer Samples

Table 3 shows our calculated  $\bar{\alpha}_L$ ,  $\bar{\alpha}_{H,L}$  and  $A_{nL}/A_0(q,p)$  of the investigated  $TiO_2/SiO_2$  coatings from experimental data and their comparison with those reported previously [5]. From this table we can see,

(1) For the  $TiO_2/SiO_2$  coatings investigated we have  $A_{nL} \approx A_0(q,p)$  and  $\bar{\alpha}_H \gg \bar{\alpha}_L$ . Thus, in the coatings the absorption of the H-L interface and that of the high refracting components make most contributions to the total absorption loss.

(2). Though no consideration of the "intra-interface" [6] absorption was taken into account during processing the experimental data, our calculated results show a good agreement with those reported previously with  $\delta=0.75$  [5]. This indicates that the "intra-interface" absorption is negligible for the coatings investigated in this paper.

#### 5. Conclusions

By means of the combination of photothermal deflection technique and a suitable preparation of the samples, a separate determination of volume and interface absorption is realized for both single-layer and multilayer optical coatings. Experimental results show that in  $ZrO_2$ ,  $MgF_2$  and  $ZnS$  single layers investigated, the film-substrate interface absorption and the air-film interface absorption are nearly the same, whereas in  $TiO_2$ ,  $Ta_2O_5$  and  $SiO_2$  thin films, the film-substrate interface absorption dominates over the air-film interface absorption, being the main source of the total absorption loss.

For the  $TiO_2/SiO_2$  multilayer samples under investigation, the H-L interface is the main source of the absorption loss, though the high refracting components also show a considerable contribution.

---

The authors are grateful to Prof. Zhou J.L. and Shi B.X. for their helpful advices and fruitful discussions.

#### 6. References

- [1] Jackson, W.B.; Amer, N.M.; Boccara, A.C.; Fournier D. Photothermal deflection spectroscopy and detection. Appl. Opt. 20(8), 1333; 1981.
- [2] Murphy, J.C.; Aamodt, L.C. Photothermal spectroscopy using optical beam probing, mirage effect J. Appl. Phys. 51(9), 4580; 1980.



- [3] Wu, Z.L.; Tang, J.F.; Shi, B.X. Measurement of weak absorption in optical coatings by transversal photothermal deflection technique. Accepted by Optica Acta Sinica (Chinese).
- [4] Temple, P.A. Experimental and theoretical considerations in thin-film laser calorimetry. Opt. Eng. 23(2), 325; 1984.
- [5] Walther, H.G.; Welsch E. Calculation and measurement of the absorption in multilayer films by means of photoacoustics. Thin Solid Films 142, 27; 1986.
- [6] Bennet, H.E. Simple expressions for predicting the effect of volume and interface absorption and scattering in high reflectance or antireflectance multilayer coatings. J. Opt. Soc. Am. 70(3), 268; 1980.
- [7] Roche, P. Antiscattering transparent monolayers, theory and experiment. J. Opt. Soc. Am. A. 1(10), 1032; 1984.

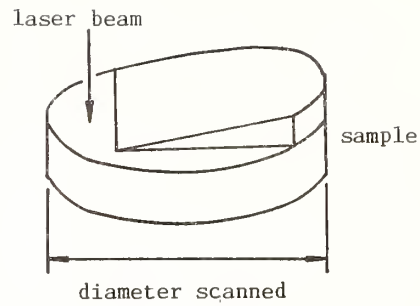


Figure 1. Sample configuration showing a thin wedge of material which has been deposited on the entrance surface of the substrate. The bare region to the left is used to measure  $A_s$  and the step in the foreground is used to determine the film thickness profile.

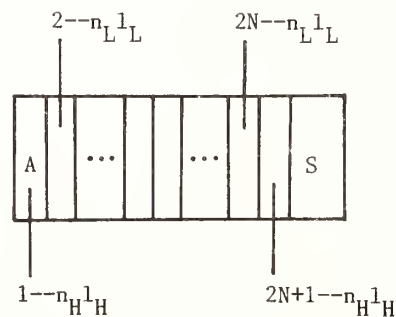


Figure 2. Schematic diagram of the dielectric multilayer sample, consisting of  $2N+1$  layers deposited on the substrate S:

$$n_H^1_H = (2p+1)\lambda/4; \quad n_L^1_L = (2q+1)\lambda/4.$$

Table 1. Deposition methods and related characterizations of the samples investigated( $\lambda$ :6328Å, substrate: K<sub>9</sub>).

Samples	Coating design	Deposition method	Refractive index
S <sub>1</sub> ZrO <sub>2</sub>		EB evaporation	1.90
S <sub>2</sub> MgF <sub>2</sub>			1.38
S <sub>3</sub> ZnS	Wedge-shaped	R evaporation	2.30
S <sub>4</sub> TiO <sub>2</sub>	single layer		2.40
S <sub>5</sub> Ta <sub>2</sub> O <sub>5</sub>		EB evaporation	2.00
S <sub>6</sub> SiO <sub>2</sub>			1.46
S <sub>7</sub> --S <sub>12</sub>	A/[(2p+1)H	EB evaporation	n <sub>H</sub> =2.40
(TiO <sub>2</sub> /	(2q+1)L] <sup>m</sup> /	T=250 C	n <sub>L</sub> =1.46
SiO <sub>2</sub> )	(2q+1)H/S	P=(2--3)x10 <sup>-5</sup> torr	

EB--electron beam; R--risitance; T--substrate temperature; P--deposition pressure.

Table 2. Calculated bulk and interface absorption of single-layer films from measured data at  $\lambda$  =6328Å.

Sample	S <sub>1</sub>	S <sub>2</sub>	S <sub>3</sub>	S <sub>4</sub>	S <sub>5</sub>	S <sub>6</sub>
$\bar{\alpha}_f(\text{cm}^{-1})$	11.8±2	10.3±2	25.0±5	1.2±0.2	3.3±0.4	1.0±0.1
K <sub>f</sub> x10 <sup>5</sup>	5.9±1	5.2±1	12.6±3	0.6±0.1	1.7±0.2	0.5±0.05
$\alpha_{if}$ x10 <sup>4</sup>	1.2±.2	1.5±.3	7.2±1	0.1±.02	0.3±.03	0.1±.02
$\alpha_{fs}$ x10 <sup>4</sup>	0.9±.2	2.3±.4	14.0±2	5.0±0.8	3.9±0.4	1.8±0.2
$\bar{\alpha}_s(\text{cm}^{-1})$	--0	--0	--0	--0	--0	--0
$A_f^{(2)} \times 10^4$	1.9±.3	2.2±.4	3.6±.9	0.2±.03	.55±.05	.2±.02
$A_{if}^{(2)} \times 10^4$	1.2±0.2	1.5±.3	7.2±1	0.1±.02	0.3±.03	0.1±.02
$A_{fs}^{(2)} \times 10^4$	1.1±.2	1.7±.3	19.0±3	6.8±0.8	4.5±0.4	1.5±0.2
A <sub>s</sub> x10 <sup>4</sup>	--0	--0	--0	--0	--0	--0

Table 3. Calculated  $\bar{\alpha}_L$ ,  $\bar{\alpha}_H$ ,  $a_{HL}$  and  $A_{HL}/A_V(q,p)$  of the investigated TiO<sub>2</sub>/SiO<sub>2</sub> coatings in comparison with previous data [5].

Parameter	Our Results	=0 <sup>[5]</sup>	=0.75 <sup>[5]</sup>
$\bar{\alpha}_L(\text{cm}^{-1})$	1.32±0.2	1.1±2	1.1±2
$\bar{\alpha}_H(\text{cm}^{-1})$	18±3.6	52±4	23±10
$a_{HL} \times 10^4$	4.7±0.5	1.1±0.3	2.0±0.6

$A(0,0) \times 10^4$	$6.9 \pm 0.6$	---	$6.0 \pm 0.6$
$A_{HL} \times 10^4$	$5.2 \pm 0.5$	---	$4.3 \pm 0.4$
$A_v(0,0) \times 10^4$	$1.7 \pm 0.3$	---	$1.7 \pm 0.2$
$A_v(0,1) \times 10^4$	$4.8 \pm 0.9$		
$A_v(1,0) \times 10^4$	$1.9 \pm 0.3$		
$A_v(1,1) \times 10^4$	$5.1 \pm 1.0$		
$A_v(0,2) \times 10^4$	$8.0 \pm 1.6$		
$A_v(2,0) \times 10^4$	$2.1 \pm 0.4$		
$A_{HL}/A_v(0,0)$	$3.1 \pm 0.8$		
$A_{HL}/A_v(0,1)$	$1.1 \pm 0.3$		
$A_{HL}/A_v(1,0)$	$2.7 \pm 0.7$		
$A_{HL}/A_v(1,1)$	$1.0 \pm 0.3$		
$A_{HL}/A_v(0,2)$	$0.7 \pm 0.2$		
$A_{HL}/A_v(2,0)$	$2.5 \pm 0.7$		

---

$\delta = 0$ ---Taking no account of the intra-interface;

$\delta = 0.75$ --Taking account of the intra-interface [7].



Measurement of Weak Absorption in Optical Coatings  
by Means of Photothermal Deflection Technique

Wu Zhouling   Tang Jinfa   Shi Baixun  
Zhejiang University, Hangzhou, PRC

An experimental setup has been built up to measure weak absorption in optical coatings based on transverse and collinear photothermal optical beam deflection technique (TPOBD and CPOBD). To calibrate the setup, a C film is used as the calibrating sample and an appropriate approximation is made based on the fact that optical coatings are usually thermally thin when the modulation frequency is relatively low. The sensitivity of weak absorption measurement of this experimental setup is assessed to be  $10^{-5}$  for TPOBD and  $10^{-6}$  for CPOBD, with the He-Ne pump power being about  $100^{\text{mw}}$  and the He-Ne probe beam about  $2^{\text{mw}}$ . Some experimental results are given in this paper. The absorption losses of  $\text{SiO}_2$ ,  $\text{ZrO}_2$  and  $\text{MgF}_2$  single-layers are found to be  $1.73 \times 10^{-4}$ ,  $5.29 \times 10^{-4}$  and  $5.94 \times 10^{-4}$  by TPOBD and  $1.82 \times 10^{-4}$ ,  $5.70 \times 10^{-4}$  and  $6.27 \times 10^{-4}$  by CPOBD. These results are in good agreement with those measured by laser-calorimeter-method.

Key Words: absorption; optical coating; photothermal deflection.

## 1. Introduction

There is more or less absorption in all dielectric materials. Laser-induced damage of optical coatings is often attributed to the weak absorption existing in the films. It is essential to precisely measure weak absorption in dielectric thin films to improve the deposition process and raise the laser damage resistance. Generally, the absorption of high quality optical thin films is of the  $10^{-4}$ - $10^{-5}$  order of magnitude. photothermal deflection technique [1,2] is a suitable one for measuring such weak absorption.

In this paper we report our recent measurements of weak absorption in optical thin films by an experimental setup based on photothermal deflection technique. The experimental results, which showed a good agreement with those measured by laser-calorimeter-method [3], approved the technique quite versatile and very simple.

## 2. Apparatus and Principles

TPOBD and CPOBD are two kinds of photothermal deflection technique. Their geometry is shown in figure 1. The physical basis of it can briefly described as follows: when a solid sample is illuminated by an intensity-modulated laser beam, the absorption of the energy will cause thermal waves in the sample and media adjacent to the sample, and hence corresponding index-of-refraction gradient in these media. By probing this index-of-refraction gradient with a second laser beam, one can relate its deflection to the optical absorption of the sample.

Based on TPOBD and CPOBD, we have built up an apparatus for the measurement of optical absorption of optical thin films. Details of the detection system are given in figure 2.

To calibrate the apparatus, we employ thermally-thin-sample approximation [2] and C film calibrating sample[4,5]. The absorptance of the measured sample is then given by

$$A = (S/S_C) A_C$$

where  $S$ ---OBD amplitude signal of the sample;

$S_C$ ---OBD amplitude signal of the calibrating C film;

$A_C$ ---absorptance of the calibrating C film measured with high precision and accuracy by photometrical method [6].

### 3. Experimental Results and Discussion

Some single layer- and multilayer coatings were measured by both TPOBD and CPOBD. The results and their comparison with those by laser-calorimeter-method are summarized in table 1. Obviously, the results obtained by the three methods agree reasonably well.

Sources of error in our experiments include thermally-thin-approximation, measurement error of calibrating C film and precision of the apparatus. Although accurate analysis of these errors is not ready now, a primary evaluation of them is summarized in table 2, where the precision of the apparatus is derived from ten measurements of  $ZrO_2$  single layers.

The sensitivity of an experimental system is determined by its total noise level. In our experiment, measurements of  $ZrO_2$  single layer ( $A \sim 10^{-4}$ ) showed  $S_{noise} < 1^{uv}$  while  $S_{CPOBD} = 0.4^{mv}$ , and measurements of Au single layer ( $A \sim 30\%$ ) showed  $S_{noise} < 1^{uv}$  while  $S_{TPOBD} = 70^{mv}$ . From this results, the sensitivity of the experimental system is assessed to be  $A \sim 10^{-6}$  for CPOBD and  $A \sim 10^{-5}$  for TPOBD. This is satisfying for most optical coatings.

---

The authors wish to acknowledge Prof. J.L.Zhou and Mr. K.Hu for their fruitful discussions.

### 4. References

- [1] Jackson, W.B.; Amer, N.M.; Boccara, A.C.; Fournier, D. Photothermal deflection spectroscopy and detection. Appl. Opt. 20(8):1333; 1981.

- [2] Murphy, J.C.; Aamodt, L.C. Photothermal spectroscopy using optical beam probing: mirage effect  
J.Appl.Phys. 51(9):4580; 1980.
- [3] Jin S.Z.; Tang J.F. Measurement of weak absorption in optical thin films. Appl.Opt. 26(7):  
2407;1987.
- [4] Wu Z.L.; Tang J.F.; Shi B.X. measurement of weak absorption in optical coatings by trans-  
verse photothermal deflection technique. Accepted by Optica Acta Sinica.
- [5] Wu Z.L.; Tang J.F.; Shi B.X. Measurement of weak absorption in optical coatings by colli-  
near photothermal deflection technique. Accepted by Acta Optica Sinica.
- [6] Deutsch, T.F. J.Opt.Soc.Am. 4(3):663; 1975.

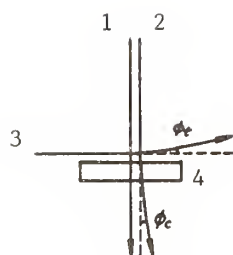


Figure 1. Geometry of TPOBD and CPOBD: 1--pump beam; 2--probe beam of CPOBD;  
3--probe beam of TPOBD; 4--sample;      --probe beam deflection angles.

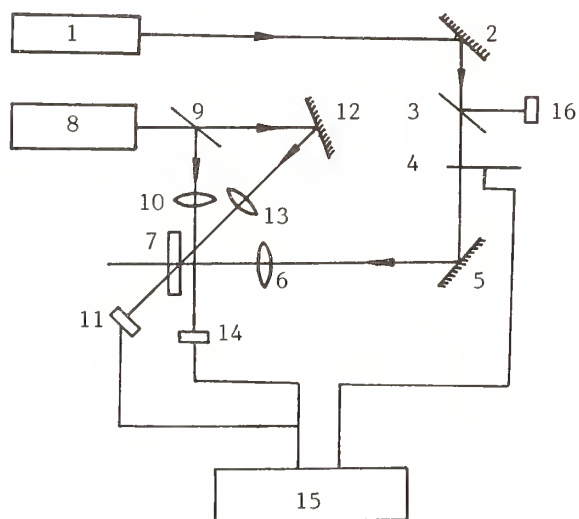


Figure 2. Schematic depiction of experimental configuration used in weak absorption measurements: 1--He-Ne pump beam ( $6328\text{\AA}$ ,  $120\text{ mW}$ ); 2, 5, 12--mirrors; 3, 9--B.S. 4--chopper; 6, 10, 13--lens; 7--sample; 11, 14--position detectors; 15--lock-in amplifier; 16--power detector.



Table 1. Measured results of some samples by TPOBD and CPOBD ( $\lambda_0=6328\text{\AA}$ ) and their comparison with those by laser-calorimeter-method (LCM;  $\lambda_0=5145\text{\AA}$ ).

Sample	<u>SiO<sub>2</sub></u>	<u>ZrO<sub>2</sub></u>	<u>MgF<sub>2</sub></u>	<u>ZnS</u>	<u>Au</u>	<u>Gyro AR</u>	<u>V-AR</u>
A <sub>1</sub> x10 <sup>4</sup>	1.73	5.29	5.94	2.90	3058	6.5	9.8
K <sub>1</sub> x10 <sup>4</sup>	.283	1.05	0953	6.22	--	--	--
A <sub>2</sub> x10 <sup>4</sup>	1.82	5.70	6.23	3.15	--	6.7	10.0
K <sub>2</sub> x10 <sup>4</sup>	.298	1.13	1.00	6.76	--	--	--
K <sub>3</sub> x10 <sup>4</sup>	.310	1.21	1.10	--	3241 <sup>[a]</sup>	6.8 <sup>[a]</sup>	10.4 <sup>[a]</sup>

A<sub>1</sub>, K<sub>1</sub>--data by TPOBD; A<sub>2</sub>, K<sub>2</sub>--data by CPOBD; K<sub>3</sub>--data by LCM<sup>[3]</sup>.  
[a]--the magnitude of absorptance(x10<sup>4</sup>).

Table 2. A primary evaluation of the error sources in our experiments.

Error source	<u>TTA</u>	<u>MEC</u>	<u>RP</u>	<u>Total</u>
Data	<10-18%	<0.5%	<4%	<=14-22%

TTA--Thermally-thin-approximation;

MEC--Measurement error of the calibrating C film;

RP --Repeated precision of the experimental setup.

## RECENT WORK IN THE THEORY OF LASER-INDUCED DAMAGE IN SOLIDS<sup>#</sup>

V. M. Kenkre, V.I. Kovanis and J.K. McIver

Department of Physics, University of New Mexico, Albuquerque, NM 87131

and

A.H. Guenther

Los Alamos National Laboratory, Los Alamos, NM 87545

### Abstract

We describe some recent work in the theory of laser-induced damage in solids. Two aspects of the laser-matter interaction are addressed: an investigation of the initiation of the electron avalanche phenomenon involved in the absorption of intense electromagnetic radiation by a solid, and the construction of a theoretical scheme for the description of laser damage under multiple pulse irradiation.

<sup>#</sup> work supported in part by the AFWL under contract no. F29601-86-K-0207

## 1. INTRODUCTION

The absorption of intense electromagnetic radiation by a solid and the resulting damage processes in the solid<sup>1-6</sup> present a number of interesting problems in the theory of solid state optics. In the following we discuss two lines of investigation; the first deals with a basic model we have constructed<sup>7</sup> for the description of the electron avalanche process in laser damage, and the second with a scheme developed recently<sup>8</sup> for the description of damage under multiple pulse excitation.

## 2. THE AVALANCHE PROCESS

It is generally believed that the anomalously high absorption constant observed under high intensity laser irradiation arises from the sequential occurrence of two processes, the first being the excitation of an electron from the valence to the conduction band, and the second, in its initial stage, of the rapid acquisition of energy by the electron in the conduction band from its nonlinear interaction with the electromagnetic field. This latter process leads to an electron avalanche and is thought responsible for the enormous amount of energy absorbed by the solid from the electromagnetic field.

We approach the avalanche process from basic and quite general considerations. We began by asking whether it was possible to devise a natural mechanism whereby high intensities of electromagnetic radiation result in the explosive acquisition of energy by an electron. We found out that indeed we could, with the help of a simple and compelling model of the process. We describe that model below.

In a two-state system which possesses states differing in energy by  $\Delta$ , and which interacts with a collection of phonons at temperature  $T$ , the application of the Fermi Golden Rule results in the following standard expressions for the excitation rate  $F^\uparrow$  and the deexcitation rate  $F^\downarrow$ :

$$F^{\uparrow} = f(\Delta) n(\Delta) \quad (1)$$

$$F^{\downarrow} = f(\Delta) [n(\Delta) + 1] \quad (2)$$

Here  $f(\Delta)$  is the value at  $\omega = \Delta$  of the function  $f(\omega)$  which is proportional to the product of the phonon density of states and the square of the matrix element for the interaction between the two states, and  $n$  is the Bose distribution.

The rates  $F^{\uparrow}$  and  $F^{\downarrow}$  obey detailed balance. This balance - generally equations (1), (2) - holds in the absence of an electromagnetic field. Our explanation of the avalanche process is based on the possibility of defeating the detailed balance relation as a result of a modification of (1), (2) brought about by an intense electromagnetic field. In the presence of a sinusoidally varying field, the rates  $F^{\uparrow}$  in (1), (2) include<sup>7</sup> a summation of an infinite number of terms labelled by the integer  $m$ , each term being proportional in strength to  $J_m^2(b/\Omega)$  where  $J_m$  is the ordinary Bessel function of order  $m$ ,  $b$  is proportional to the magnitude of the electromagnetic field, and  $\Omega$  is the frequency of the field. The argument of the appropriate  $\delta$ -function in (1) is  $\pm\Delta - \omega - m\Omega$  in a phonon-absorption process and  $\pm\Delta + \omega - m\Omega$  in a phonon-emission process.

By assuming (for simplicity) that the field intensity and therefore the magnitude of  $b$  (or  $b/\Omega$ ) is small enough to allow us to retain only the first two terms in the  $m$  summation, we obtain

$$F^{\uparrow} = F_0^{\uparrow} + F_{1a}^{\uparrow} + F_{1b}^{\uparrow}; \quad \text{and} \quad F^{\downarrow} = F_0^{\downarrow} + F_{1a}^{\downarrow} + F_{1b}^{\downarrow} \quad (3)$$

The subscripts "0" and 1 refer to the order of the process and the explicit expressions are

$$F_0^{\uparrow} = [J_0^2(b/\Omega)] f(\Delta) n(\Delta); \quad F_0^{\downarrow} = [J_0^2(b/\Omega)] f(\Delta) [n(\Delta) + 1] \quad (4)$$

$$F_{1a}^{\uparrow} = [J_1^2(b/\Omega)] f(\Delta + \Omega) n(\Delta + \Omega); \quad F_{1a}^{\downarrow} = [J_1^2(b/\Omega)] f(\Delta + \Omega) [n(\Delta + \Omega) + 1] \quad (5)$$

$$F_{1b}^{\uparrow} = [J_1^2(b/\Omega)] f(-\Delta + \Omega) [n(-\Delta + \Omega) + 1]; \quad F_{1b}^{\downarrow} = [J_1^2(b/\Omega)] f(-\Delta + \Omega) n(-\Delta + \Omega) \quad (6)$$



While the "0" process is the only one present in the absence of the electromagnetic field, in the presence of the field, the 1b process, which possesses the characteristic of population inversion rather than detailed balance, could dominate the interaction. The possible sources of this domination are two: the function  $J_0$  is larger than  $J_1$  for small argument but can be smaller than  $J_1$  for values of the argument which are not too small; and the phonon density of states and/or the interaction matrix element can have values at  $\omega = \Omega + \Delta$  which are negligible with respect to those for  $\omega = \Omega - \Delta$ . For an intensity of the electromagnetic field which is large enough, the  $F_0$ 's can thus be smaller than, and even negligible compared to, the  $F_1$ 's. Under such conditions, the kinetics of the two-state system are described by the Master equation

$$dP_e/dt = F^\uparrow P_g - F^\downarrow P_e; \quad dP_g/dt = F^\downarrow P_e - F^\uparrow P_g \quad (7)$$

the value of the ratio of the probabilities of the excited and ground state for large times, viz.  $P_e(\infty)/P_g(\infty)$ , being

$$P_e(\infty)/P_g(\infty) = \exp(\beta \Delta_{eff}); \quad \Delta_{eff} = \Omega - \Delta \quad (8)$$

Our model thus shows, in a quite natural manner, that (i) in the absence of the field or for small field frequencies, the probability ratio obeys detailed balance, and (ii) in the presence of the field, provided  $\Delta_{eff}$  is positive, it is possible for the system to acquire energy from the field (with the help of its interaction with phonons) and undergo a population inversion. Indeed, if the system has many (rather than two) states, it can move towards its high energy states explosively.

We have analyzed other systems such as the harmonic oscillator with Landau-Teller transition rates to illustrate the above concepts and have calculated quantities such as the critical field from our theory. The reader is referred to ref. 7 for those descriptions.

### 3. MULTIPLE-PULSE LASER DAMAGE

In order to understand the basic characteristics of the observations involved in multiple pulse laser damage, we first address<sup>8</sup> the qualitative behavior of the observed dependence<sup>9-14</sup> of  $N$ , the number of exposures (shots) required for damage under multiple pulse excitation on the ratio of the intensity  $I$  to the one-shot threshold intensity  $I_0$ . The simplest model<sup>8</sup> employs the evolution equation:

$$dE/dt + \alpha E = I \sum_n \delta(t - nT) \quad (9)$$

where  $E$  is (except for constant factors) the energy acquired locally by the solid from the electromagnetic field,  $\alpha$  is a dissipation coefficient which would arise from such processes as thermal conduction or energy transfer to other locations in the solid,  $T$  is the time between pulses, and the summation runs from  $n = 0$  to  $n = N-1$ .

The consequence of (9) is that, at the incidence of every pulse,  $E(t)$  increases by the amount  $I$  and decreases exponentially in the period between pulses. The peak value of  $E(t)$  thus increases after  $N$  pulses to the value  $E_{max}$  given by

$$E_{max} = I (1 - x^N) / (1 - x); \quad x = \exp(-\alpha T) \quad (10)$$

When this  $E_{max}$  reaches a critical value damage occurs. It has been shown<sup>8</sup> that (10) results directly in the following expression for the  $N$ - $I$  dependence:

$$N = - (1/\alpha T) \ln [1 - (I_c/I)] \quad (11)$$

The multiple-pulse critical intensity  $I_c$  is related to the single-shot critical intensity  $I_0$  through

$$I_c = I_0 [1 - \exp(-\alpha T)] \quad (12)$$

Equation (11) with (12) provides an excellent qualitative description of the observed dependence of the number of exposures (shots)  $N$  on the intensity  $I$  which includes the asymptote at  $I/I_0 = 1 - \exp(-\alpha T)$ .

Equation (9) incorporates a highly simplified model. It assumes an exponential response of the quantity  $E(t)$ . As a generalization of that simple model, we have replaced<sup>8</sup> the exponential  $I \exp(-\alpha t)$  by a general response function  $I \phi(t)$  and obtained the relation

$$I_0/I = \sum_n \phi(nT) \quad (13)$$

where the summation, as in (9), is from  $n = 0$  to  $n = N - 1$ . In simple cases, such as when  $\phi$  is an exponential, the summation in (13) can be performed and simple results such as (10) can be obtained. In others the corresponding sums have to be done numerically.

We have explored the consequences of various phenomenological response functions  $\phi$ , incorporating, in some cases, oscillatory dissipation characteristic of coherent energy transfer. We have also derived the response functions from microscopic starting points and are in the process of applying this general scheme of multiple pulse damage theory to existing observations. Suggestions for new observations have been generated by this application. A prescription has also been given to extract the response function  $\phi$  directly from the observed dependence of the number of shots required for damage on the intensity. The prescription is based on considering the summation in (13) as an integration. The derivative of the observed  $(I_0/I)$  with respect to  $N$ , carried out numerically, provides the response function. The extraction is very useful as a precursor to detailed construction of models. This theoretical scheme may be found in ref. 8.

#### 4. CONCLUSION

This study of two different aspects of the laser-induced damage has led to several insights and proposals for new experiments. The model of avalanche ionization<sup>7</sup> that we have described above is much simpler in form than that of Epifanov et al<sup>4, 5</sup> but it preserves the essential physics such as the importance of electron-phonon coupling. Because of its simplicity, it is possible to explore the dependence of avalanche ionization on intensity, frequency, electron-phonon coupling strengths etc. in a straight-forward manner.

The problem of understanding multiple-pulse laser damage has divided the damage-community for years. The work we have described above presents a method not only for attacking the problem but also for comparing multiple-pulse damage measurements made on different materials and carried out by different experimental groups. Instead of comparing the damage thresholds directly, a comparison of the response functions would, firstly indicate whether the same relaxation processes are at work in the two materials and, secondly, permit an extrapolation to other repetition frequencies. Furthermore, a set of response functions for different materials would provide a good starting point for modelling multiple-pulse damage.

#### REFERENCES

1. M. Sparks, D.L. Mills, R. Warren, T. Holstein, L.J. Sham, E. Loh, Jr. and D. F. King, *Phy. Rev. B* 24, 3519(1981)
2. T.W. Walker, A.H. Gunther and P. Nielsen, *IEEE J. Quantum Electron.* QE17, 2053 (1981)
3. A.A. Manekov and A.U. Prokhorov, *Sov. Phys. Uspekhi* 29, 104 (1986)
4. A.S. Epifanov, A.A. Manenkov and A.M. Prokhorov, *Sov. Phys. JETP* 43, 377 (1976)
5. N. Blomebergen, *IEEE J. Quantum Electron.* Vol. QE10, 375 (1974)
6. M.R. Lange, J.K. McIver and A.H. Gunther, *Thin Solid Films* 125, 143 (1985)



7. V.M. Kenkre and J.K. McIver, "Theory of Electron Avalanche in Laser-Induced Damage In Solids", University of New Mexico preprint; see also V. M. Kenkre, J.K. McIver, and V.I. Kovanis, Bull. Am. Phys. Soc. 32, FQ 11(1987)
8. V.M. Kenkre, "A Theoretical Approach to Laser-Induced Damage Under Multiple Pulses", University of New Mexico preprint
9. L. D. Merkle, M. Bass, R.T. Swimm, Opt. Eng. 22, 405 (1983), 25, 196 (1986)
10. L. D. Merkle, N. Koumvakalis and M. Bass, J. Appl. Phys 55, 772 (1984), 59, 2957(1986).
11. R.M. Wood, S.K. Sharma and P. Waite, NBS (US) Spec. Pub. 669, 44 (1984)
12. S.K. Balitskas and E.K. Maldutis, Sov. J. Quant. Electronics 11, 541 (1981)
13. R.M. O'Connell, A.B. Romberger, A.A. Shaffer, T.T. Saito, T.F. Deaton, and K.E. Seigenthaler, J. Opt. Soc. of Am. B 1, 853 (1984)
14. Y.K. Jhee, M. F. Becker and R.M. Walser, J. Opt. Soc. of Am. B 2, 1626 (1985)

MANUSCRIPT NOT RECEIVED

---

VARIATION, VARIABILITY AND DIFFERENCES IN THE MEASUREMENT  
OF LASER-INDUCED DAMAGE THRESHOLDS

R.M. Wood and R.J. Chad  
GEC Hirst Research Centre  
East Lane, Wembley  
Middlesex, HA9 7PP

ABSTRACT

The published literature on the subject of laser induced damage is full of well measured values which disagree with what other workers have found. This paper attempts to distinguish between the variations (described by physical laws and historical/statistical laws) and differences (values measured on similar samples at different laboratories). Examples will be presented of the three types of variance taken from recent measurements. In particular the variability of the damage threshold value versus percent of sites damaged curves will be presented for a series of coated substrates.

MANUSCRIPT NOT RECEIVED

---

THE CONSEQUENCE OF DOPING OPTICAL MATERIALS WITH  $D_2O$

J.B. Franck, J.O. Porteus, L.F. Johnson, J.M. Pentony, and W.N. Faith  
Physics Division, Research Department  
Naval Weapons Center  
China Lake, CA 93555-6001

and

H. Angus Macleod  
Optical Sciences Center  
University of Arizona  
Tucson, AZ 85721

ABSTRACT

In general, water is ubiquitous in nature. In the production of optical thin films the point in the coating process at which the water is incorporated into the film often is unknown. In an attempt to produce a unique sample set for laser-induced desorption experiments, optical thin films were grown in the presence of copious quantities of  $D_2O$ . The results indicate that the uptake of water in optical thin films may not take place in the coating process as might be expected. Preliminary findings indicate that the laser-damage threshold can be improved significantly using this  $D_2O$ -doping process.

## Some Studies of Thin Film Distributed Bragg Reflectors

K L Lewis, I T Muirhead\*, A M Pitt, A G Cullis and G M Williams

RSRE, Malvern, Worcs WR14 3PS, UK  
\* OCLI, Dunfermline, Fife KY11 5FR, UK

The Distributed Bragg Reflector (DBR) is of interest for a range of optical applications. This work is concerned with a study of the problems influencing the fabrication of such structures using molecular beam techniques. Many of the issues involved are concerned with the achievement of stable structures that do not shift under temperature cycling or laser irradiation. These centre around the fundamental properties of the coating materials selected, the degree of perfection of the films, and the control of microstructure and interface interdiffusion. Results have been obtained which show the effect of varying the thickness of the reflecting interfaces on the bandwidth and intensity of the fundamental reflection band. The degree of interface perfection in such structures has been examined using cross-sectional transmission electron microscopy, and correlated with the results of depth profiling X-ray photoelectron spectroscopy studies.

### 1. Introduction

The relationship between laser damage threshold and electric field distribution in thin film coatings has been the subject of many studies reported in the literature. Evidence has been obtained which suggests that coating designs which avoid high values of electric field intensity within layers, or at interfaces, tend to have significantly improved damage thresholds. In antireflection designs, the most vulnerable interface is generally that between the coating and substrate, since this is the likely site for incorporation of impurities. Apfel et al [1] found that the addition of a silica barrier layer between a glass substrate and first layer of a four-layer AR coating improved the average  $1.06\ \mu\text{m}$  damage threshold. Previously, Newman et al [2] had studied the influence of electric field distribution on the damage resistance of thin films of between  $\lambda/4$  and  $5\lambda/4$  in thickness at  $1.06\ \mu\text{m}$ . For high index materials such as  $\text{TiO}_2$ , the damage thresholds for odd  $\lambda/4$  thicknesses were greater than for even  $\lambda/4$  thicknesses, as expected from calculated field values. This was further developed in a subsequent study of  $1.06\ \mu\text{m}$  reflectors [3], where increases in damage threshold were obtained by using non-quarter wave thicknesses for the top few layers of a  $\lambda/4$  stack. The designs were developed to minimise the standing wave field in the high index layer, which also served to reduce the field values at the interfaces between the successive layers. Reflectors incorporating 11  $\lambda/4$  layers of  $\text{TiO}_2/\text{SiO}_2$  were found to have thresholds of about  $1\text{J}/\text{cm}^2$  for 30ps pulses at  $1.06\ \mu\text{m}$ , whilst those with non-quarter wave layers added to the top of the reflector were able to resist twice these fluence levels. The optimum thicknesses for the top layers were derived by Apfel [4].

Similar improvements in damage threshold were found at other wavelengths. For example Newnam et al [5] showed the significant increase in damage resistance at 248nm (8 nsec pulses) possible in scandia/magnesium fluoride reflectors, with thresholds increased from about  $3\text{J}/\text{cm}^2$  to  $5\text{J}/\text{cm}^2$ . A discussion was also presented highlighting the role that laser pulse width may have in determining the degree of enhancement in damage threshold, and the role that coating defects would have in masking any such effect. Carniglia et al [6] assessed the enhancement possible at 355nm using such suppressed electric field designs in scandia/magnesium fluoride, reporting a 40% increase in threshold compared with the basic HR stack. However a variant of the suppressed field design, in which the thickness ratio of the top two HL pairs was reversed, performed no better than the standard design, since the peak electric field in the high index scandia layer was equivalent to that in the standard case.

The role of interfaces in such designs was not fully explored. In many fabrication processes it is not possible to guarantee a perfect interface, that is, one that is free from impurity species. Furthermore, due to the high coating temperatures frequently employed for oxide and fluoride materials, the possibility of interdiffusion effects between adjacent layers is increased, with the ensuing formation of hetero-species. Such effects can be explored by depth profiling techniques, providing that the specific analytical technique used is



sufficiently sensitive to thin sections of material and also to different chemical environments for the constituent elements.

The distributed Bragg reflector (DBR) design is an ideal candidate for distinguishing electric field and interface effects within multilayer structures. DBR structures are usually found in waveguide devices, but advanced growth and thin film deposition techniques such as molecular beam deposition [7] now make it possible to fabricate these from a range of materials to allow assessment at a variety of wavelengths. In general Bragg reflection arises from periodic variations in the dielectric constant of a medium. Various refractive index profiles can produce reflection bands. One example is that of the sinusoidal profile, which produces only one significant reflection band. The particular DBR structure considered in this work is characterised by an essentially uniform refractive index, with very thin, sharp discontinuities incorporated at  $\lambda/2n$  intervals. The electric field distribution in such a structure is compared in figure (1) for a partial reflector design with that of a quarter wave stack, fabricated on a glass substrate. It can be seen that the peak electric field in the quarter wave case is situated at the interface between the high and low index layers, whereas in the DBR design, the peak field is within the high index layer. The relative position of the peak within the high index layer can be shifted simply by altering the phase of the structure by adding to, or subtracting a small amount of material from the multilayer at the air/film interface. For example the peak field can be placed close to an interface, allowing its resulting effect in laser damage threshold to be assessed. Alternatively, the peak field may be allowed to remain close to the centre of the high index layer, allowing an option of exploring the effect on laser damage threshold of incorporating a few atomic layers of different material at this position.

The above arguments have largely been centred on a design based on material with a high average refractive index. Similar effects also occur in the reverse case, where the optical medium is primarily of a low index material, such as barium fluoride, with the periodic profile produced by  $\lambda/2n$  disposition of a small amount of high index material. This latter design is likely to be closest to the ideal for ensuring maximum laser damage resistance, due to the wide energy gap of such fluorides.

This DBR structure gives a reflection peak whose magnitude varies in intensity with total number of periods and with the average refractive index change  $\Delta n$  introduced at each  $\lambda/2$  position. The bandwidth of the reflection peak varies inversely with  $\Delta n$ . The design is therefore fairly flexible, and has the added advantage of allowing the use of techniques for preventing the propagation of columnar microstructure [8].

This work considers the case of partial reflector designs, as may be used in laser cavity mirrors, and highlights some of the results so far achieved.

## 2. Experimental

The reflectors were grown in a three chambered, load-locked UHV/MBE system, fitted with 3 Knudsen sources and in situ surface diagnostics (Auger, XPS) as described previously [7]. Substrates are cleaned before film growth using a raster scanned beam of argon ions (0.5 to 3KeV as appropriate). For film deposition, the substrates were transferred to the growth chamber where growth was arranged to occur from molecular beams of the constituent materials required for the multilayer. The availability of in-situ analysis techniques allows the examination of inter-film reaction at film-film interfaces. The analysis system incorporates a computer controlled depth-profiling facility, allowing continuous or discrete sputter-etching during XPS analysis and is capable of a depth resolution of about 10-20nm under ideal conditions. The assessment facilities have been supplemented by other techniques to provide further information on the structure and morphology of the films, including cross-sectional transmission electron microscopy (XTEM). Cross-sections were prepared by cleaving, epoxy mounting and abrasive thinning to 100  $\mu\text{m}$  in thickness. Further thinning was carried out using argon ions before changing to reactive gases (iodine) for the final stages. This prevents any extrinsic dislocation loops and other ion-beam damage artefacts appearing in the thickness of the specimen being examined.

Optical properties were determined by conventional transmission/reflection spectrophotometry. Laser damage thresholds were determined at the GEC Hirst Research Centre, Wembley, Middlesex using a Nd:YAG laser of pulse length 10 nsec. The laser beam was focussed to a spot of  $1/e^2$  radius 59  $\mu\text{m}$  at 1064nm. Measurements were made on a single shot basis as described in the paper by Wood et al at this conference [9].

### 3. Interface Effects

The perfection of interfaces in the DBR structures was assessed in two different ways. In the first, a multilayer of BaF<sub>2</sub>/ZnSe was specially produced with 10nm thickness of each individual layer. This was then ion beam profiled, and the chemical composition of the layers determined at discrete intervals. Problems that can arise with such measurements are normally due to non-uniformities in the ion beam raster, preventing the formation of flat-bottomed etch pits, which can make the interface appear to more diffuse than it actually is. However the actual binding energies measured for constituent elements are a sensitive indicator of the chemical environment of those elements and are not critically dependant on whether the etching is absolutely uniform or not.

Three spectral scans, expanded in the region of the Zn 2p state are shown in figure (2). The upper trace was measured at the interface between a ZnSe and BaF<sub>2</sub> layer, near the edge of the ZnSe, whilst the lower was measured near the edge of the adjacent BaF<sub>2</sub> layer. It is clear that a shoulder, present on the low energy side of the Zn 2p<sub>3/2</sub> line, increases in intensity as the higher energy peak falls. The second peak is indicative of a different chemical environment for the Zn atom, with the spectral shift comparable to that expected for Zn in ZnF<sub>2</sub>.

The second method used for the assessment of interface perfection involved fabricating DBR designs with increasingly thinner  $\lambda/2$  distributor layers. The actual designs used were as listed in table (1) and were chosen to give a resonance near the band edge of the ZnSe. This would allow any change in position of the absorption edge to be revealed.

Table 1. Details of DBR Designs used for Interface Studies

ZnSe thickness nm	BaF <sub>2</sub> thickness nm	Number of periods	Theoretical OD	Expt OD
100	20	20	2.80	2.03
100	10	20	1.42	0.70
100	5	20	0.72	0.52

The transmission spectra for the three reflectors are shown in figure (3), and values of optical density at the transmission minima are compared in intensity with those calculated for the different designs using conventional matrix techniques in table (1). It is found that agreement is not good, particularly in the 10nm distributor case. This suggests that the interface may not be as clearly delineated as expected, and that the optical properties are being significantly influenced by physical imperfection or chemical reaction. Examination of XTEM micrographs of the related system BaF<sub>2</sub>/ZnS as shown in figure (4a), shows that the interface 'roughness' is of the order of 25Å with a period of about 150-300Å. This is largely fixed by the crystallite diameter of the ZnS layers of about 100Å. Since the morphology of ZnSe and its behaviour during growth is similar to that of ZnS, with similar crystallite diameters of about 100-200Å (figure 4(b)), it is reasonable to assume that an interface spread of approximately 25Å in amplitude also occurs for ZnSe/BaF<sub>2</sub> structures.

The effect of this interface spread on optical transmission at the Bragg resonance can be explored using a model in which the interface is approximated by a simple linear grading of refractive index from the ZnS to the BaF<sub>2</sub> and vice-versa over the distance of 25Å referred to above. For the case of the DBR fabricated using 10nm BaF<sub>2</sub> distributors, this means as a first approximation that half of the BaF<sub>2</sub> layer is graded as shown in figure (5). Here the basic  $\lambda/2$  period has been divided into nine discrete sublayers layers of differing thickness. Layer 1 is the high index material which forms the major part of the filter (ZnSe in this case), whilst layers 5 and 6 are the unaffected parts of the BaF<sub>2</sub> low index material. Layers 2-4 and 7-9 are layers of intermediate refractive index chosen to represent the rough interface. In the first approximation referred to above, the discrete layer profile becomes as shown in table (2), column A.

Table 2. Refractive Indices of Discrete Sublayers for Basic  $\lambda/2$  Cycle in Filters with Varying Degrees of Interface Grading

Layer	Perfect t/nm	Structure n	A		B		C	
			t/nm	n	t/nm	n	t/nm	n
1	100	2.5	95	2.5	90	2.5	90	2.5
2	1	1.5	2	2.3	4.5	2.3	4.5	2.45
3	1	1.5	2	1.9	2.5	1.9	2.5	2.3
4	1	1.5	1	1.6	2	1.6	2	2.1
5	2	1.5	2.5	1.5	1	1.5	1	2.0
6	2	1.5	2.5	1.5	1	1.5	1	2.0
7	1	1.5	1	1.6	2	1.6	2	2.1
8	1	1.5	2	1.9	2.5	1.9	2.5	2.3
9	1	1.5	2	2.3	4.5	2.3	4.5	2.45
Optical density at minimum for 20 periods			1.42	1.52	1.66		0.72	

The predicted optical density (OD) at the transmission minimum for profile A is slightly higher than that of the perfect structure, and even increasing the extent to which the grading propagates into the ZnSe as in case B only serves to produce a slight increase in the intensity of the resonance. This implies that the design is comparatively insensitive to the degree of refractive index grading provided that the principle of material conservation about the interface is obeyed. The major change necessary to bring about agreement with the measured spectrum is to reduce the effective width of the low index layer, and/or increase its refractive index, as shown in example C. On the basis of the physical model, this implies a high degree of chemical reaction between the film materials. This is in accord with the indications of the depth profiling experiments. The products of chemical reaction at the interface are likely to be  $\text{ZnF}_2$  and  $\text{BaSe}$ . These have refractive indices of approximately 1.5 and 2.27 respectively. A 50% mixture of the two would have an approximate index of 1.9 - 2.0, a value of not too dissimilar to that assumed in example C in table 2.

Clearly the detail of interlayer morphology and interdiffusion is important in determining reflector performance and in practical devices it is advisable to reduce individual layer thicknesses in such polycrystalline structures to below 10nm. A more practical limit would be about 15 - 20nm, and if it was necessary to utilise thinner layers, then designs would have to be centred on structures containing interfaces of even higher perfection, such as those produced between amorphous or epitaxial films.

Some improvement occurs in the case of polycrystalline layers of  $\text{PbF}_2/\text{ZnS}$ . Here, because of the higher surface mobility of the  $\text{PbF}_2$  during growth, the microcrystallites of  $\text{PbF}_2$  are some 3000Å wide, as shown by the cross TEM micrograph of figure (6). Within the  $\text{PbF}_2$  crystallites, a high degree of lattice ordering is apparent, but this does not contribute towards a particularly smoother interface. The measured transmission spectrum of a 25 period example containing 15nm thick  $\text{PbF}_2$  distributor layers is plotted in figure (7). Here the thickness of each ZnS layer has been increased to 145nm to produce a peak reflectance close to 710nm. This also allows the first harmonic to be revealed at  $\sim 395\text{nm}$ . The measured optical density at the reflection maximum is 1.3 which is if anything slightly in excess of the theoretical value of 1.13. This suggests that the extent of interdiffusion and reaction at the interface is considerably reduced compared with the case of  $\text{ZnS}/\text{BaF}_2$ , as would be expected from a consideration of the relative atomic diameters of barium and lead.

#### 4. Fundamental Stability of the DBR Structure

Since the DBR design has a comparatively narrow bandwidth, it is necessary to ensure that its position does not shift with change of external conditions such as humidity level and environmental temperature. Shifts with humidity levels would be expected to arise from residual porosity in the material forming the major part of each  $\lambda/2$  period and would be revealed by heating samples to temperatures in excess of 100°C which would be sufficient to drive any absorbed water from the layer. This would be sufficient to drive any absorbed water from the layer. This would be expected to give rise to a reduction in refractive index of the ZnS and a shift of the Bragg resonance to shorter wavelengths. Figure (8) clearly shows that this does not occur in an example based on  $\text{ZnS}/\text{BaF}_2$ , rather the observed spectral shift is to longer wavelengths due to the positive temperature dependence of refractive index. The shift is quite



reproducible, and the position of  $\lambda_{\max}$  returns to its equilibrium value immediately on cooling to room temperature.

## 5. Laser Damage Threshold of ZnS/BaF<sub>2</sub> Designs

The original objective of this study was to explore the potential of DBR designs as partial reflectors for a variety of applications including intra-cavity optics. Since the design allows the peak electric field to be shifted away from film interfaces, it is expected that the laser damage threshold may be enhanced, and possibly limited only by the properties of the material selected for the majority of each  $\lambda/2$  period.

A preliminary study of the response to laser irradiation has been made in a DBR structure based largely on the high index material ZnS. This is not expected to be the ideal candidate structure, but can give valuable information on the general levels of performance achievable. The damage probabilities determined in 1 on 1 experiments at 1.06  $\mu\text{m}$  are plotted in figure (9) for a DBR fabricated to give a peak reflectivity of 60% at 1.06  $\mu\text{m}$ . The zero probability threshold is close to 20 J/cm<sup>2</sup> and is very similar to values determined on films of the component materials (figure (10)). It was found that damage initiated at the glass substrate in all cases. This is significant since it implies that the high peak fields within the  $\lambda/2$  ZnS layers do not themselves appear to initiate damage. This may be a consequence of the relatively higher perfection of these MBE grown structures, with high crystallinity and absence from absorbing inclusions.

The films assessed had been deposited on float glass substrates, which are not expected to be ideal from the point of view of their laser damage resistance. In the case of the DBR reflector it is difficult to understand how incident radiation, sufficient to cause damage in the glass substrate, propagated through the filter to the glass. A possible explanation may have been that at fluences close to 20 J/cm<sup>2</sup> the incident energy density may have been sufficient to drive a spectral shift of the Bragg resonance away from the laser wavelength. This can be explored in principle by using time resolved techniques.

The stability of the DBR structure may be improved by adopting the reverse design discussed in section 1, with  $\lambda/2$  periods of primarily low index materials such as the fluorides. These have large energy gaps, with smaller values of  $\partial n/\partial T$ , which in DBR designs results in reduced electric field intensities.

## 6. Conclusions

A study has been carried out of some of the critical issues involved in the fabrication of distributed Bragg reflectors. Attention has been focussed on the role of interface perfection in controlling the optical properties of the structures at the resonance wavelength. Both chemical reaction and layer interdiffusion contribute towards a reduction in reflection band intensity. Preliminary laser damage studies on partial reflector designs indicate that high damage thresholds can be realised, limited by the substrate when reflectivities are low. It is argued that alternate designs incorporating primarily low index fluoride materials will provide improved performance in high reflectivity designs.

## 7. Acknowledgements

The authors are indebted to R M Wood and R J Chad of the GEC Hirst Research Centre for carrying out the pulsed laser measurements.



### 3. References

- [1] Apfel, J. H. Boulder Damage Symposium, NBS Special Publ 509 255 (1977).
- [2] Newman, B. E.; Gill, D. H. and Faulkner, G. Boulder Damage Symposium, NBS Special Publ 435, 254 (1975).
- [3] Gill, D. H.; Newman, B. E. and McLeod, J. Boulder Damage Symposium, NBS Special Publ 509, 260 (1977).
- [4] Apfel, J. H. Appl Optics 16, 1880 (1977).
- [5] Newman, B. E.; Foltyn, S. R.; Jolin L. J.;, and Carniglia, C. K. Boulder Damage Symposium, NBS Special Publ 638, 363 (1983).
- [6] Carniglia, C. K.; Tuttle Hart, T.; Rainer, F. and Staggs, M. C. Boulder Damage Symposium. NBS Special Publ 688, 347 (1985).
- [7] Lewis, K. L.; Savage, J. A.; Cullis, A. G.; Chew, N. G.; Charlwood, L. and Craig, D. W. Boulder Damage Symposium, NBS Special Publ 727, 162 (1986).
- [8] Lewis, K. L.; Pitt, A. M.; Chew, N. G.; Wyatt-Davies, T. J.; Charlwood, L.; Dosser, O. D. and Muirhead, I. T. Boulder Damage Symposium, NIST Special Publ 752, 365 (1988).
- [9] Wood, R. M. and Chad, R. J. Proc 1988 Boulder Damage Symposium, NIST Special Publ (to be published).

HMSO, London (1988)

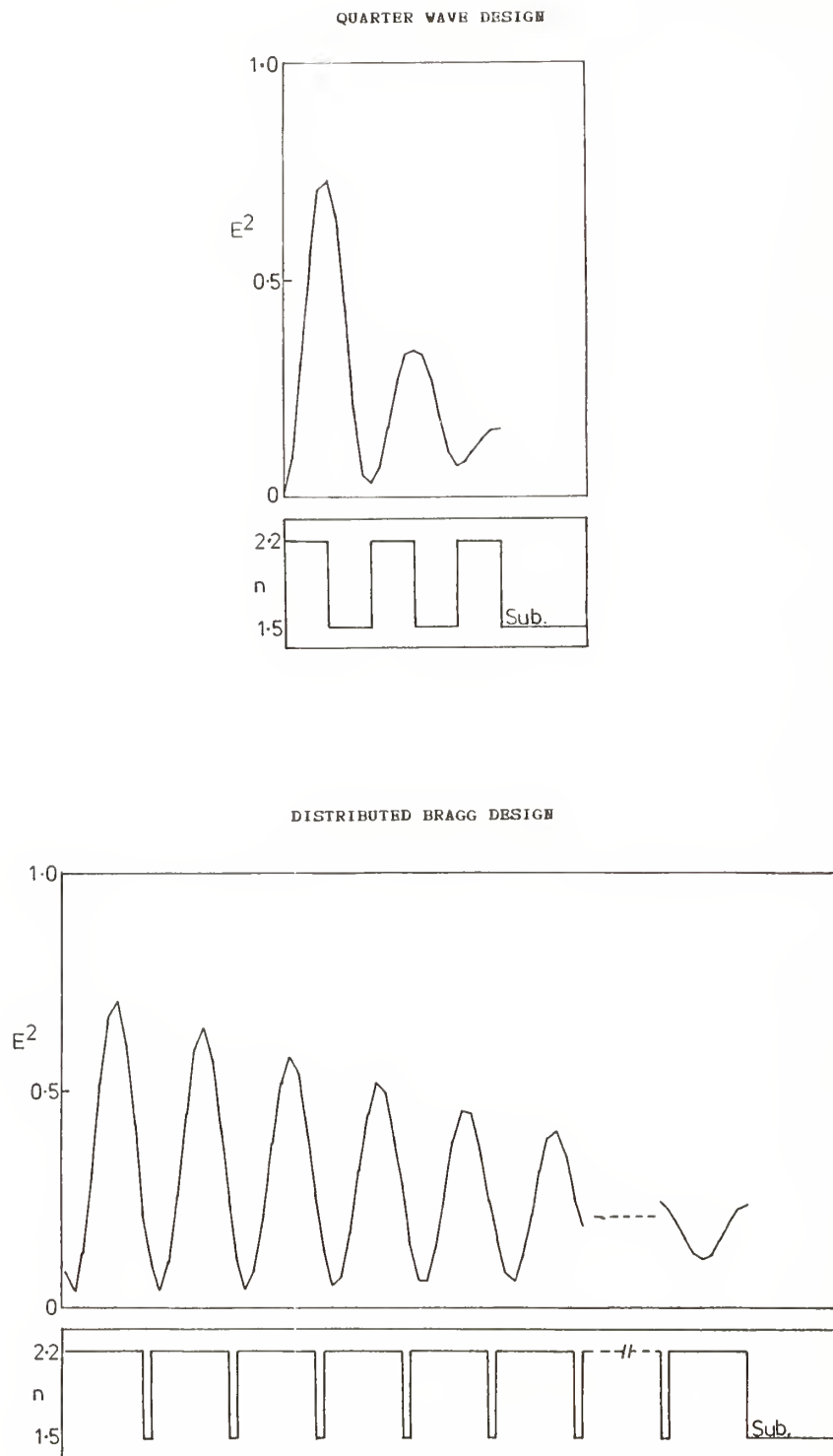


Figure 1. Comparison of electric field distributions in designs for partial reflectors

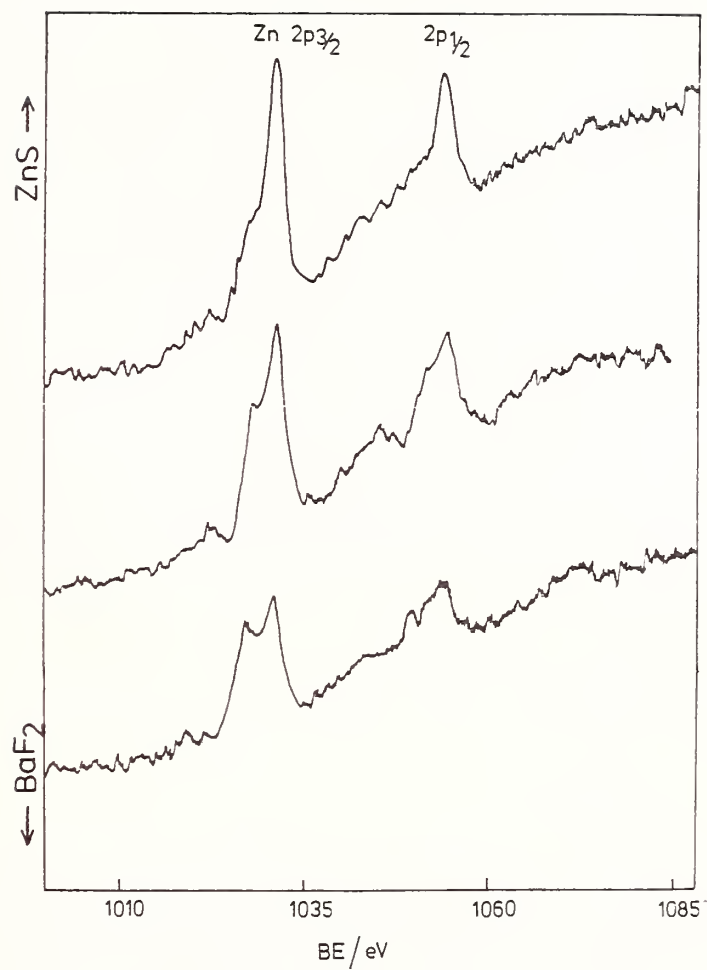


Figure 2. Evidence for change in chemical environment of zinc atoms at interface between ZnS and BaF<sub>2</sub>.

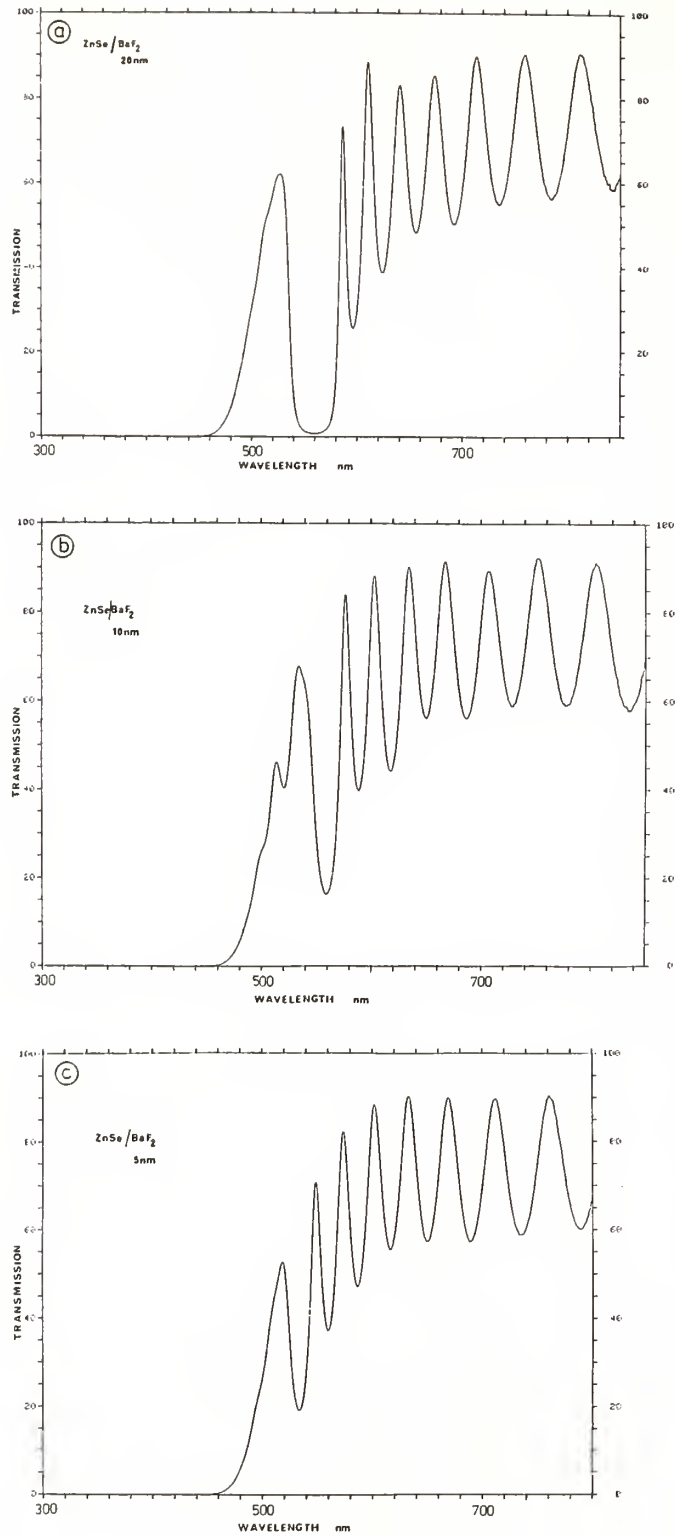


Figure 3. Transmission spectra of distributed Bragg reflectors containing periodic structures of 100nm ZnSe and

- (a) 20nm BaF<sub>2</sub>
- (b) 10nm BaF<sub>2</sub>
- (c) 5nm BaF<sub>2</sub>



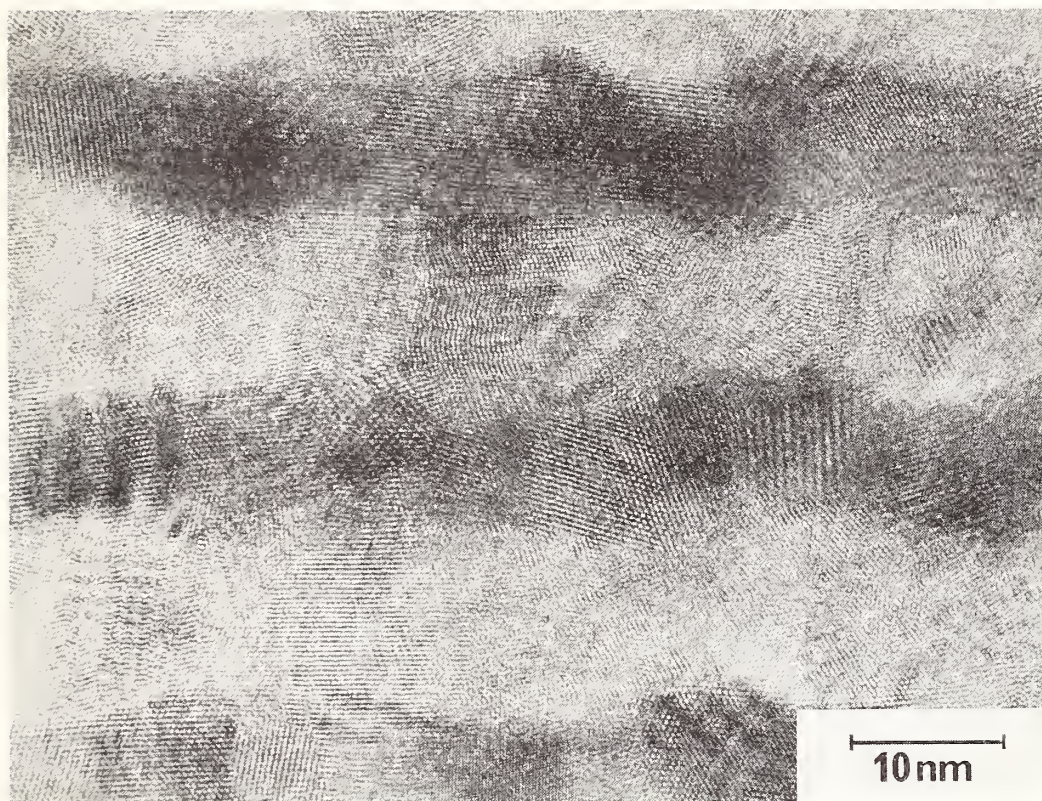


Figure 4(a). Lattice image of a section of a ZnS/BaF<sub>2</sub> periodic structure showing the high degree of lattice ordering in the component microcrystallites, but highlighting the apparent roughness of each interface, to the extent of about 25Å.

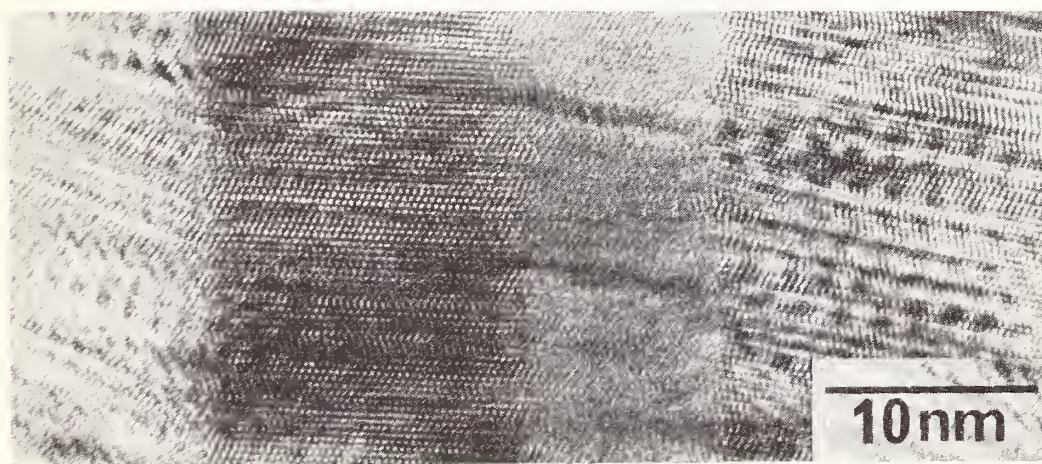


Figure 4(b). Lattice image of a polycrystalline ZnSe film showing detail of the columnar microstructure.

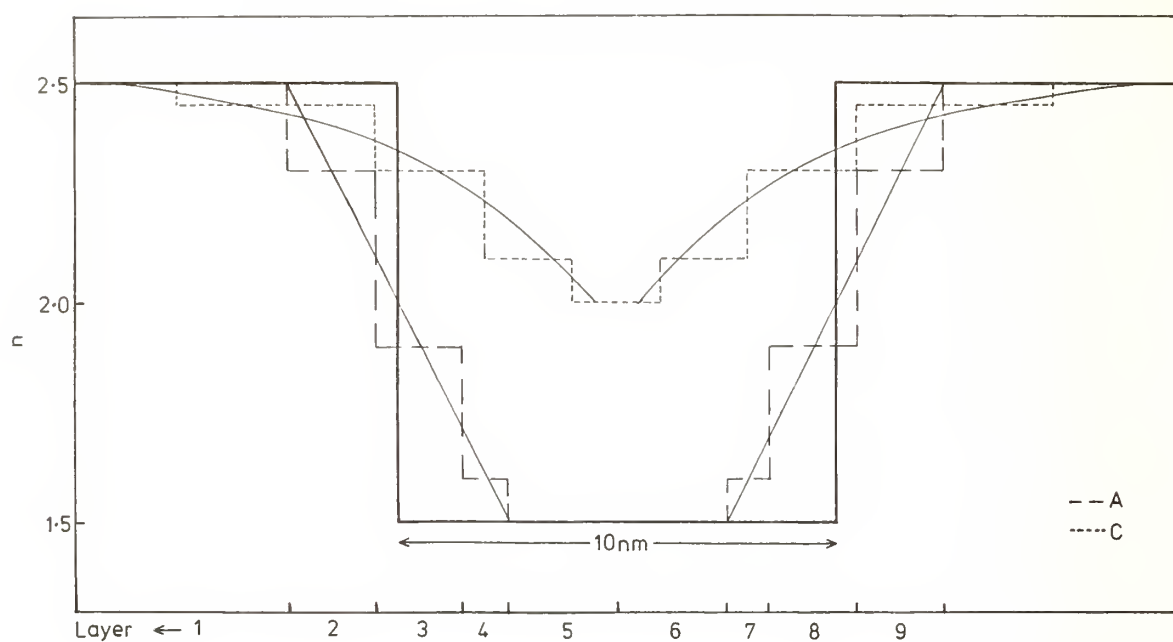


Figure 5. Digital approximation of refractive index grading around 10nm BaF<sub>2</sub> distributor layers.

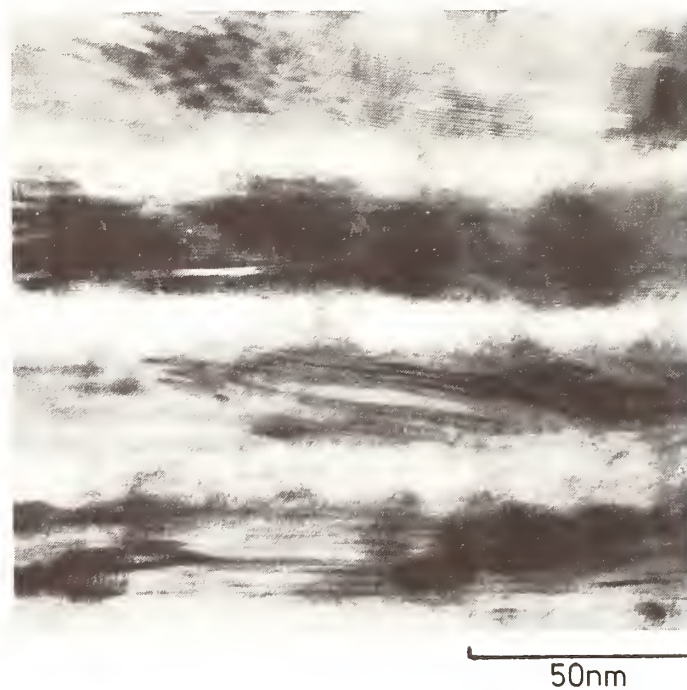


Figure 6. High resolution cross-sectional TEM micrograph of a ZnS/PbF<sub>2</sub> periodic structure showing the enhanced degree of lateral crystallite dimension compared with that of figure 4(a).



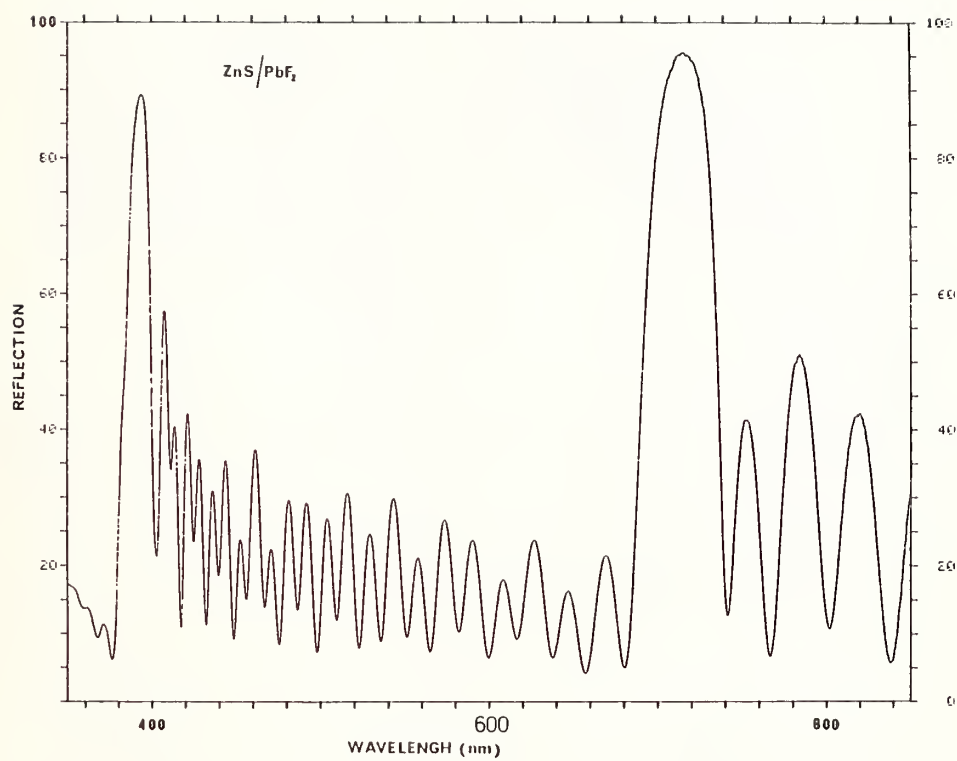


Figure 7. Reflection spectrum of a 25 period ZnS/PbF<sub>2</sub> Bragg reflector, showing both the fundamental and first order lines.

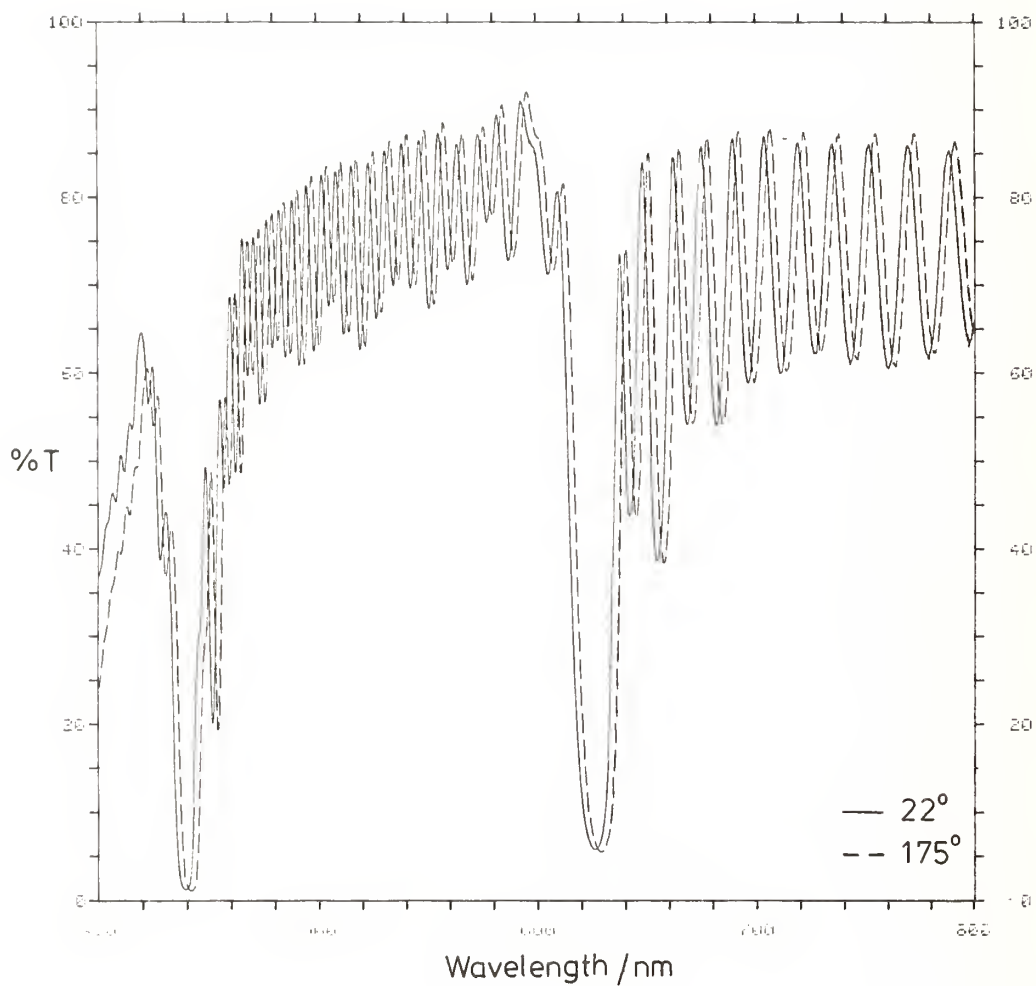


Figure 8. Transmission spectra of 25 period ZnS/PbF<sub>2</sub> DBR design centred near 1250nm, measured at room temperature and at 175°C. The transmission minima shown are the second and third order resonances.



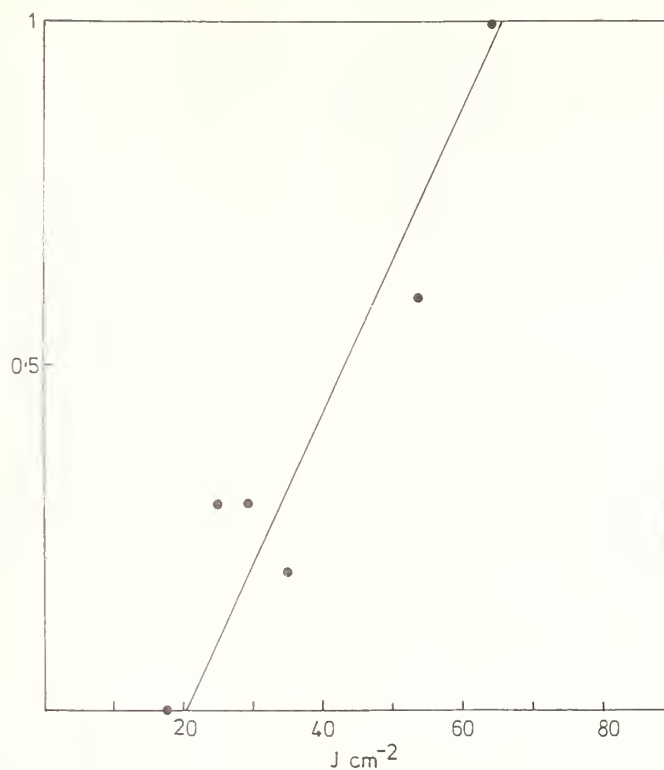


Figure 9. Laser damage probabilities of a ZnS/BaF<sub>2</sub> partial reflector at 1.06  $\mu$ m

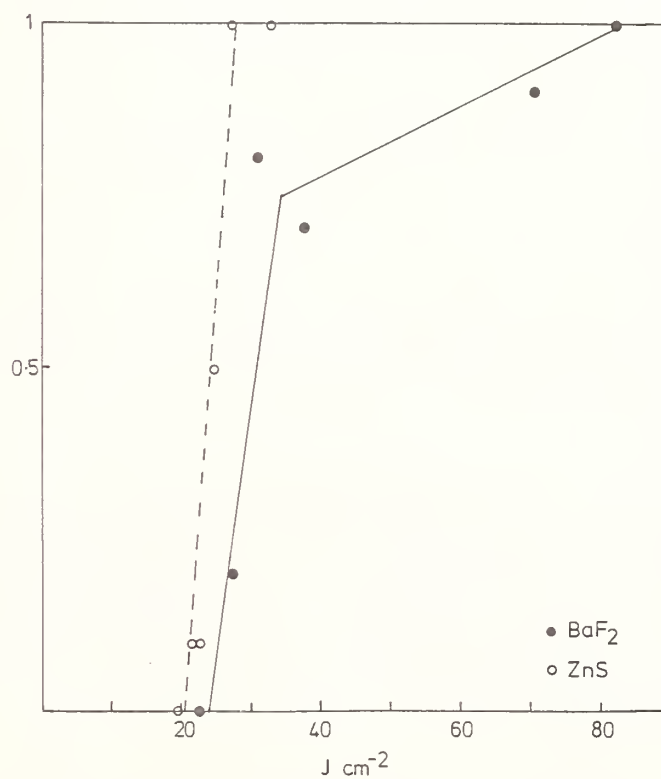


Figure 10. Laser damage probabilities of thin films of the component materials of the design used for the tests in figure (9).

# Laser-Induced Damage of Dielectric Systems with Gradual Interfaces at 1.064 $\mu\text{m}$

D. Ristau, H. Schink, F. Mittendorf, J. Akhtar<sup>o</sup>, J. Ebert and H. Welling

Institut für Quantenoptik, Universität Hannover  
Welfengarten 1, 3000 Hannover, Germany-W.

## ABSTRACT

Previous work has shown that laser induced damage thresholds of e-beam deposited multilayer systems can be increased by codeposition. We have investigated in gradual interfaces between  $\text{SiO}_2$  as low index material and  $\text{Ta}_2\text{O}_5$ ,  $\text{HfO}_2$ ,  $\text{ZrO}_2$  and  $\text{CeO}_2$  as high index materials.

A microprocessor controlled coevaporation technique is used for the production of high reflective and antireflective coatings. Damage thresholds and absorption data of these systems are compared to the performance of conventional systems. An increase of damage thresholds of up to 20% is observed for some materials. This improvement is discussed by comparing the influence of intense laser radiation on gradual and abrupt interfaces.

key words: damage thresholds, gradual interfaces, codeposition, absorption, antireflective coatings, highreflecting mirrors, oxide materials.

## 1 Introduction

From the standpoint of laser induced damage the e-beam process is still of current interest for the production of dielectric layer systems. At present only sol gel processes [1] are proven to produce coatings for special applications, which can withstand higher laser power levels than e-beam deposited coatings. In future, ion processes [2] like IAD (ion assisted deposition), IBS (ion beam sputter deposition) or IPD (ion-plating deposition) are expected to surpass the potentiality of the e-beam process because these techniques yield coatings with an improved microstructure. But, although extensive research has been done on ion processes, the aspect of laser induced damage thresholds (LIDT) has not totally been clarified [3]. Compared to the conventional process ion processes are more complicated, less economic, and up to now, they found only limited application in production. Therefore, e-beam deposition is still a major process in the field of high power coatings and its potentiality should be totally explored.

---

<sup>o</sup>) Optics Laboratory, Pinstech, Islamabad, Pakistan

In the past several years the technique of coevaporation is discussed as a means to improve the properties of e-beam deposited coatings. In preceding studies [4] the technique of coevaporated interfaces has been demonstrated to decrease the total losses in e-beam deposited stacks with alternating materials. In some cases [5] also damage thresholds were higher in gradual 2-QWOT-stacks than in conventional systems with abrupt interfaces.

In this paper an extension of the technique to practical systems like high reflecting mirrors and antireflective coatings is described. For high reflecting mirrors we tested  $\text{TiO}_2$ ,  $\text{Ta}_2\text{O}_5$ ,  $\text{HfO}_2$  and  $\text{ZrO}_2$  in conjunction with  $\text{SiO}_2$ . Damage thresholds of gradual quarterwave stacks and gradual designs with adapted standing wave field distribution were measured and compared to data of the corresponding abrupt systems. Antireflective coatings are double layer systems of  $\text{Ta}_2\text{O}_5$ ,  $\text{HfO}_2$  and  $\text{ZrO}_2$  in combination with  $\text{SiO}_2$  and a system of  $\text{CeO}_2/\text{MgF}_2$ . A comparison of damage thresholds and absorption data for gradual and abrupt systems with the same designs are presented.

## 2 Experimental

In the past, several techniques have been tested for the production of inhomogeneous layers. One of the eldest methods is the evaporation of materials with different evaporation temperatures from a single source [6,7]. During the production of the inhomogeneous region the mixing ratio is varied by adjusting the evaporation temperature. This technique does not need any mechanical alterations in the coating plant, but it suffers from the disadvantages that the properties of the layers are very sensitive to production parameters and the technique is restricted to soft coatings. A more sophisticated technique is based on an e-beam which is alternately switched between the crucibles containing the different materials [8]. The mixing ratio can be adjusted by the exposure times of the materials to the e-beam.

For the production of coatings with gradual interfaces it is sufficient to regulate the deposition rates of the two materials forming the adjacent layers. If coating designs are restricted to types involving two materials, only two evaporation sources with separate rate regulation circuits are necessary. In such an arrangement each source is working with constant rate during most of the deposition time. Solely for depositing the interface regions both sources have to be operated simultaneously with varying deposition rates.

### 2.1 Experimental setup

The experimental setup for simultaneous deposition of two materials with arbitrary rates is shown in figure 1. A quartz crystal monitor head is attached to each e-beam source. Each monitor head is shielded against the evaporation flux of the adjacent source with the aid of an aperture. Thermal radiation from the sources is also kept off the monitor heads by these apertures.

The rate regulation is carried out by a microprocessor system which registers the deposition rates and controls the emission currents of both sources. In order to achieve a sufficient accuracy for the rate measurements the fundamental frequency of the quartz crystals is multiplied by a factor of 16 with the aid of a PLL-circuit. During rate regulation the frequency is

counted digitally and latched into the microprocessor after every 200 ms. The processor calculates appropriate emission current values which are converted by a D/A-converter into steering voltages for the e-beam power supplies. In conjunction with a control panel the microprocessor is a complete rate control system.

For the benefit of more flexibility a desk computer is linked to the microprocessor system. The computer is executing the regulation and calculation tasks meanwhile the sub-system is processing the measurement and control signals. Thus the programs for the regulation, steering, controlling and presenting of the process could be developed on the level of a higher programming language (BASIC). The process software also contains routines for recording the momentary rates and process data on floppy disc for further evaluation after completion of the process.

For the production of defined index profiles a calibration and the determination of regulation parameters are necessary. Single layer samples with defined film thicknesses were used in order to calibrate the crystal monitor. The thickness measurement was performed by using an optical thickness monitor (Leybold OMS 2000) during the process and by evaluation of spectrophotometric data. Regulation parameters were optimized with the aid of a trial and error method utilizing an optional third crystal monitor head. Thus, compared to regulation by emission current the regulation errors of the deposition rate could be decreased by a factor of three. JACOBSSON [9] showed by calculating the refractive index as a function of deposition rates that the index profile is minor influenced by rate variations. For example, a rate error of 20 % results in aberration of approximately 8 % for the refractive index.

## 2.2 Interfaces

In order to keep the expense low for the production, design and examination of the systems with gradual interfaces we restricted ourselves to interfaces with temporal linear variations; i.e. during the deposition of the interface the rate of one material is decreased linearly down to zero meanwhile, in the same time-period, the rate of the other material is increased up to the optimum value. This results in refractive index profiles as shown in figure 2 for a gradual interface between  $\text{HfO}_2$  and  $\text{SiO}_2$ . Depending of the theoretical model used for the calculation the index of refraction as a function of geometrical position shows a slight curvature. In case of figure 2 calculations are based on the Lorentz-Lorenz-theory [9].

The actual profiles realized by the codeposition process can be approximately calculated with the aid of the momentary rates recorded on floppy disc during the process. As an example, an index profile for a sample of  $\text{TiO}_2$  and  $\text{SiO}_2$  is depicted in figure 3. Circles in figure 3 indicate refractive index values determined by an AES depth profile of the same sample. The deviations of the index data range from 10 % to 20 %. Calculations of the spectral behavior of systems with gradual interfaces yield only small variations for different interface depths. Therefore, spectral characteristics are not usable for the determination of an index profile. Hence, summarizing the experience from our setup, the index profiles of gradual interfaces are merely reproducible with errors in the range of 20 %.



### 2.3 Design and production

The v-coating design is best suited for antireflective coatings in high power applications. Two layer coatings of this type yield zero reflectance for any substrate material and they have minimum optical losses. They commonly consist of a thin high index layer next to the substrate which is followed by a thicker low index layer. This design guarantees low optical losses, because the high index material usually has higher absorption and scatter losses than the low index material.

Material	Depth [nm]	Thickness H/L [QWOT]
Ta <sub>2</sub> O <sub>5</sub> /SiO <sub>2</sub>	31	0.38/1.30
HfO <sub>2</sub> /SiO <sub>2</sub>	28	0.46/1.26
ZrO <sub>2</sub> /SiO <sub>2</sub>	28	0.55/1.22
CeO <sub>2</sub> /MgF <sub>2</sub>	74	0.50/1.21

*Table 1: Designs and interface depths for antireflective coatings.*

According to this, we choose for antireflective systems two-layer-designs of four material combinations (table 1). The material combinations were determined by preceding studies on conventional v-coatings [10] and on 2-QWOT gradual systems [4]. For each combination three sets of gradual and conventional systems were deposited on fused silica substrates. The interface depth was kept constant for samples of one combination by choosing constant time intervals for the codeposition periods. Values for the interface depths are calculated by using the momentary rate data of the crystal monitor heads. The high average depth for the CeO<sub>2</sub>/MgF<sub>2</sub>-systems results from a high optimum deposition rate for MgF<sub>2</sub>.

Three types of designs for high reflecting mirror were chosen (table 2) for a total of four material combinations. The first design type (type N) is a standard quarterwave stack (qw stack) with one gradual interface between the first layer pair. The other two design types (type E and D) are non-qw systems optimized [11] for low standing wave field values at the interfaces. In type E the thickness of the upper high index layer is decreased meanwhile the thickness of the adjacent low index layer is increased in a way that the total optical thickness of the layer pair remains constant. Thus, the electric field at the interface between the layer pair next to the air can be adjusted to a value equal to that at the second HL-interface. The maximum intensity at the interfaces is accordingly reduced in the system. The ratio of the maximum intensity in a standard qw stack and the corresponding intensity in the adapted stack is given by the last column (gain) in table 2. In type D the first two layer pairs are adapted leading to increased gain values. Adjusting more than two layer pairs results in a less drastic increase of the gain values. Therefore, taking also into account the additional difficulties in production, a study of these systems should not reveal any new fundamental aspects. Design type E contains gradual interfaces in the first and second

Material	N <sub>0</sub>	Type	Design		Absorption [ppm]	Gain
			Pair N <sub>0</sub> +1	Pair N <sub>0</sub> +2		
TiO <sub>2</sub>	23	N	1.00/1.00	1.00/1.00	679	1.00
TiO <sub>2</sub>	23	E	1.00/1.00	1.57/0.58	566	1.27
TiO <sub>2</sub>	23	D	1.57/0.58	1.68/0.47	512	1.49
Ta <sub>2</sub> O <sub>5</sub>	25	N	1.00/1.00	1.00/1.00	197	1.00
Ta <sub>2</sub> O <sub>5</sub>	25	E	1.00/1.00	1.49/0.61	183	1.22
Ta <sub>2</sub> O <sub>5</sub>	25	D	1.49/0.61	1.60/0.50	182	1.41
HfO <sub>2</sub>	27	N	1.00/1.00	1.00/1.00	199	1.00
HfO <sub>2</sub>	27	E	1.00/1.00	1.46/0.63	189	1.20
HfO <sub>2</sub>	27	D	1.46/0.63	1.57/0.52	189	1.37
ZrO <sub>2</sub>	29	N	1.00/1.00	1.00/1.00	201	1.00
ZrO <sub>2</sub>	29	E	1.00/1.00	1.43/0.64	193	1.18
ZrO <sub>2</sub>	29	D	1.43/0.64	1.54/0.54	190	1.34

Table 2: Design and gain data of high reflecting mirrors.

layer pair. Design type D has three gradual interfaces in the upper three layer pairs. For mechanical protection and stabilization an additional 2-QWOT SiO<sub>2</sub>-overcoating is deposited on each mirror.

For every design type samples with gradual and abrupt interfaces were deposited on BK7-substrates. The gradual interfaces were produced in the same way as used for the antireflective coatings. As depicted in figure 4, spectra of the corresponding gradual and conventional systems are nearly equal in the significant wavelength range. Spectra of the produced systems of TiO<sub>2</sub>/SiO<sub>2</sub> deviates essentially more from the predicted behavior. However, for practical use this deviation is unimportant.

### 3 Analysis

The two stage Nd-YAG-laser system used for the measurement of laser induced damage thresholds is described elsewhere [12]. All measurements were carried out with a pulse width of 14 ns and a beam diameter of 300 μm (FWHM) in 1 on 1 tests at a wavelength of 1.064 μm. Irradiation sites on the sample surface were arranged in form of a rectangular matrix containing typically 20 to 30 shots. For damage detection a scatter measurement system was used during the tests. The samples were inspected by Nomarski microscopy or in difficult cases by a scanning electron microscope after the measurement. Damage thresholds were determined by the average value of the highest energy level without damage and the lowest energy level with damage.

For absorption measurements a thermographic laser calorimeter [13] was used in conjunction with a 200 W Nd-YAG-laser. The absorption data of the antireflective coatings were determined with the assumption that the two layers forming the coating can be combined to a single layer with thermal properties equal to the mean value of the involved films. According to this, the experimental uncertainty of the calorimeter amounts to approximately ±15 %.

#### 4 Results

Absorption data and damage thresholds for the antireflective coatings are summarized in table 3. The main result is an increase of damage thresholds in the range of 5 to 15 % for gradual systems with SiO<sub>2</sub> as low index material. With the exception of CeO<sub>2</sub>/MgF<sub>2</sub> absorption is clearly lower in gradual antireflective systems. The deviating behavior of the system with MgF<sub>2</sub> is probably a consequence of chemical reactions between fluorine and CeO<sub>2</sub> in the interface region. A similar characteristic could be observed for other oxides combined with MgF<sub>2</sub> in preceeding studies [4].

Material	Depth [nm]	Reflection [%]		Absorption [ppm]		Damage Threshold [J/cm <sup>2</sup> ]	
		abr.	gra.	abr.	gra.	abr.	gra.
Ta <sub>2</sub> O <sub>5</sub> /SiO <sub>2</sub>	31	0.39	0.20	935	881	42 ± 6	49 ± 12
HfO <sub>2</sub> /SiO <sub>2</sub>	28	0.15	0.10	1072	219	42 ± 17	44 ± 9
ZrO <sub>2</sub> /SiO <sub>2</sub>	28	0.12	0.08	1083	470	45 ± 10	51 ± 14
CeO <sub>2</sub> /MgF <sub>2</sub>	74	0.12	0.11	940	984	37 ± 6	31 ± 6

Table 3: Damage thresholds and absorption data of anti-reflective coatings with abrupt and gradual interfaces.

For the high reflecting mirrors (tab. 4) a clear tendency is only visible for the standard quarterwave stack of Ta<sub>2</sub>O<sub>5</sub>, HfO<sub>2</sub> and ZrO<sub>2</sub>. A maximum increase of 20 % in damage thresholds is achievable by the codeposition process. An adaption of the standing wave field pattern in gradual systems yields only for ZrO<sub>2</sub> a slight increase of damage thresholds. Conversely, with the excep-

Material Type		Damage Thresh. [J/cm <sup>2</sup> ]	
		abrupt	gradual
TiO <sub>2</sub>	N	34 ± 10	22 ± 7
TiO <sub>2</sub>	E	43 ± 17	6 ± 1
TiO <sub>2</sub>	D	23 ± 4	5 ± 1
Ta <sub>2</sub> O <sub>5</sub>	N	32 ± 6	46 ± 8
Ta <sub>2</sub> O <sub>5</sub>	E	35 ± 7	33 ± 7
Ta <sub>2</sub> O <sub>5</sub>	D	34 ± 10	28 ± 11
HfO <sub>2</sub>	N	43 ± 1	48 ± 17
HfO <sub>2</sub>	E	43 ± 5	39 ± 13
HfO <sub>2</sub>	D	37 ± 13	34 ± 6
ZrO <sub>2</sub>	N	30 ± 8	33 ± 6
ZrO <sub>2</sub>	E	27 ± 8	36 ± 9
ZrO <sub>2</sub>	D	33 ± 8	42 ± 5

Table 4: Damage thresholds of high reflecting mirrors with abrupt and gradual interfaces.

tion of  $\text{ZrO}_2$  conventional systems with design type E have higher thresholds than the standard conventional systems. In case of most of the material combinations damage thresholds of standard qw stacks with one gradual interface have highest damage thresholds among the design types tested. The inconsistent behavior of  $\text{TiO}_2$ -systems is due to an incompatibility of the production parameters for  $\text{TiO}_2$  and  $\text{SiO}_2$  for the codeposition process.

## 5 Discussion

Summarizing the experimental findings, there is evidence that gradual systems of oxide materials have higher damage thresholds than corresponding conventional systems. To explain the better performance of gradual systems the following mechanisms are to be discussed:

### 5.1 Adhesion

Interface regions are objected to high mechanical stress due to different mechanical and thermal properties of the layers building up a system. During exposure to laser radiation this stress may be increased due to heating, leading finally to an ablation of adjacent layers in the interface region. Damage spots of the type shown in figure 5 can be considered as an experimental confirmation. In codeposited film systems mixing of layers should cause a better adhesion. According to this, ablation of adjacent layers is less probable and the system should have a higher damage threshold. During damage tests of gradual systems a morphology similar to that in figure 5 was never observed.

### 5.2 Interface absorption

Interface absorption may play an important role in laser induced damage because it causes the incident laser energy to be dominantly deposited into the sensitive regions of the system. As indicated [4], interface absorption is decreased in gradual systems with  $\text{SiO}_2$  as low index material, and therefore, a better damage resistance can be expected for these systems.

### 5.3 Temperature distribution

Another aspect related to interface absorption is the temperature distribution [12] in the coating. In figure 6 temperature curves in a gradual and a conventional interface of the first layer pair in a standard stack of  $\text{HfO}_2/\text{SiO}_2$  are compared. Assuming a constant absorption in each layer and thermal conductivities given in [12] the calculation yields a 20 % lower temperature in the codeposited interface region. Thermal, mechanical and optical properties at a distinct position of the gradual interface region are assumed to be distributed according to the fraction of the mixed materials at that position. Based upon this model, the conventional interface has even the disadvantage that there is a sharp temperature drop at the interface. This temperature drop may result in additional mechanical loads of the interface during exposure to laser radiation. Thus, regarding the temperature distribution, systems with gradual interfaces are clearly superior to conventional systems.



#### 5.4 Microstructure and packing density

The microstructure of the involved dielectric films influences the damage threshold of a layer system [14]. Therefore it is necessary to investigate in the growth behavior of codeposited interfaces. But, presently no technique is known which permits a spatial resolution high enough to resolve features of the microstructure at the interfaces. So far, studies of microstructure in interfaces are totally depending on models for thin film growth. The packing density curves shown in figure 7 and 8 were calculated by a modified version [15] of the thin film growth model developed by DORYLAND [16]. The calculations are based on simulation of the growth of an abrupt and a codeposited interface between two layers with different particle mobilities and particle sizes. For the conventional layer pair each layer was built up by calculating the position of 9000 evaporant particles. The layers and the codeposited region in figure 8 consist of 6000 particles respectively. Due to the surface roughness of the first layer the packing density of the abrupt interface is linearly decreasing in a small transition region. In figure 8 no particular behavior of the packing density in the codeposited layer is visible. As expected, there is a linear alteration of the density according to the fraction of the involved material components.

However in contrast to this simple model increased packing density have been observed in mixtures. For example FARABAUGH [17] reported enhanced optical properties in layers with a certain mixing ratio of  $\text{ZrO}_2/\text{SiO}_2$ . Therefore, an influence of the microstructure at the gradual interface region can not be excluded.

#### 6. Conclusions

Thresholds of gradual antireflective and highreflective coatings deposited by e-beam evaporation were compared to data of the corresponding conventional systems. With the exception of  $\text{TiO}_2/\text{SiO}_2$ -coatings threshold values range between 30 to 50 J/cm<sup>2</sup>. Experimental data show evidence, that an improvement in damage resistance is achievable for most of the material combinations with  $\text{SiO}_2$  as low index material. Compared to conventional systems, an increase of damage thresholds of up to 20 % could be observed for systems with codeposited interfaces. As possible reasons for this improvement adhesion of adjacent layers, temperature distribution in the layer system and interface absorption were discussed. A modelling of the microstructure in the coevaporated region was not successful in explaining the experimental findings.

## References

- [1] I.N. Thomas: High damage threshold porous silica antireflective coatings. NBS. Spec. Publ. No. 727 p.205 1984
- [2] P.J. Martin: Ion based methods for optical thin film deposition. J. Mater. Sci. Vol. 21 No 1 p.1
- [3] R. Iscoff: Ion assisted deposition. Lasers & Optronics. Feb. 1988 p.53
- [4] F.T. Mittendorf: Die kontrollierte Herstellung inhomogener dielektrischer Schichten. MS-thesis, Universität Hannover 1986
- [5] D. Ristau, X.C. Dang und J. Ebert: Interface and bulk absorption of oxide layers and correlation to damage threshold at 1.064  $\mu\text{m}$ . NBS. Spec. Publ. No. 727 p.298 1984
- [6] S. Fujiwara:Refractive indices of evaporated Cerium Fluoride-Zinc Sulfide films. J. Opt. Soc. Am. Vol.53 p.880 1963
- [7] S. Fujiwara:Refractive indices of evaporated Cerium Fluoride-Zinc Sulfide films. J. Opt. Soc. Am. Vol.53 p.1317 1963
- [8] Vakuum Information 13. Ausgabe VEB Hochvakuum Dresden 1985
- [9] R. Jacobson: Inhomogeneous and coevaporated homogeneous films for optical applications. in G. Hass und R.E. Thun, Herausgeber "Physics of thin films" Springer Verlag, Berlin p.51 1966
- [10] S.M.J. Akhtar: Laserinduzierte Zerstörung dielektrischer Einfach- und Antireflexschichten. PhD-thesis, Universität Hannover 1988
- [11] G. DeBell: PhD-thesis, University of Rochester, University Microfilms, Ann Arbor, Michigan 1971
- [12] D. Ristau: Erhöhung der Zerstörschwellen dielektrischer Schichtsysteme für den Nd-Laser. PhD-thesis, Universität Hannover 1988
- [13] D. Ristau und J. Ebert: Development of a thermographic laser calorimeter. Appl. Opt. Vol.25 No.24 p.4571 1986
- [14] K.H. Guenther: Microstructure of vapor deposited optical coatings. Appl. Opt. Vol.23 No.21 p.3806 1984
- [15] H. Schink: Zerstörschwellen dielektrischer Schichtsysteme mit inhomogenen Schichten. MS-thesis, Universität Hannover 1987
- [16] D.J. Doryland: An improved model of thin film growth. MS-Thesis, Air Force Institute of Technology 1985
- [17] F.N. Farabaugh et.al.: A study of thin film growth in the  $\text{ZrO}_2/\text{SiO}_2$ -System. NIST Spec. No.752 p.321 1986

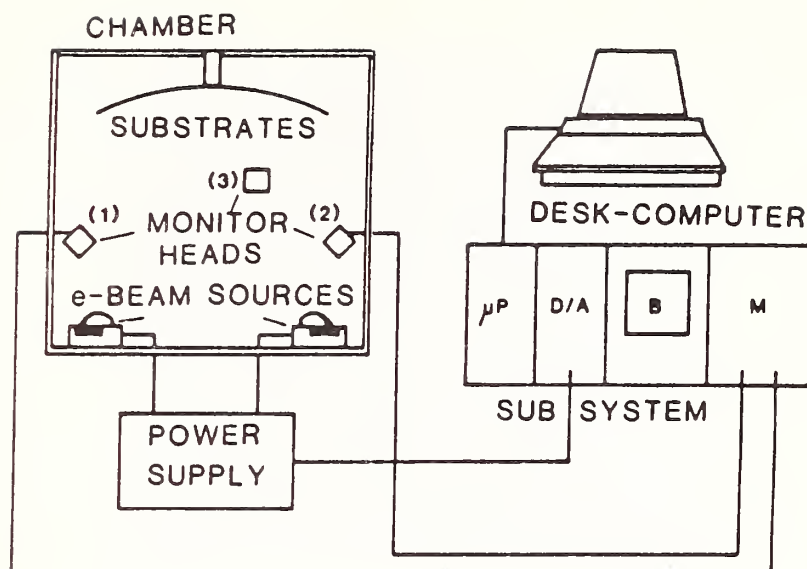


Figure 1: Set up for the production of layers with arbitrary index profiles. The subsystem consists of the microprocessor board ( $\mu P$ ), the D/A converter board (D/A), the control panel (B) and the rate measurement system (M).

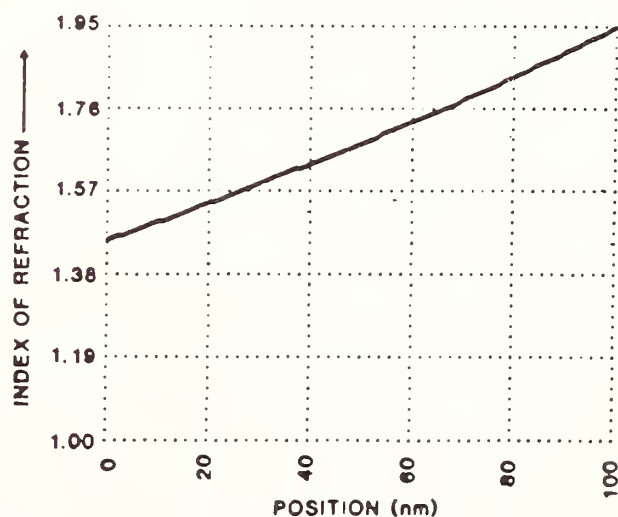


Figure 2: Index of refraction as a function of layer thickness for a gradual interface between  $\text{SiO}_2$  and  $\text{HfO}_2$ . The horizontal scale indicates the layer thickness in units of geometrical thickness.

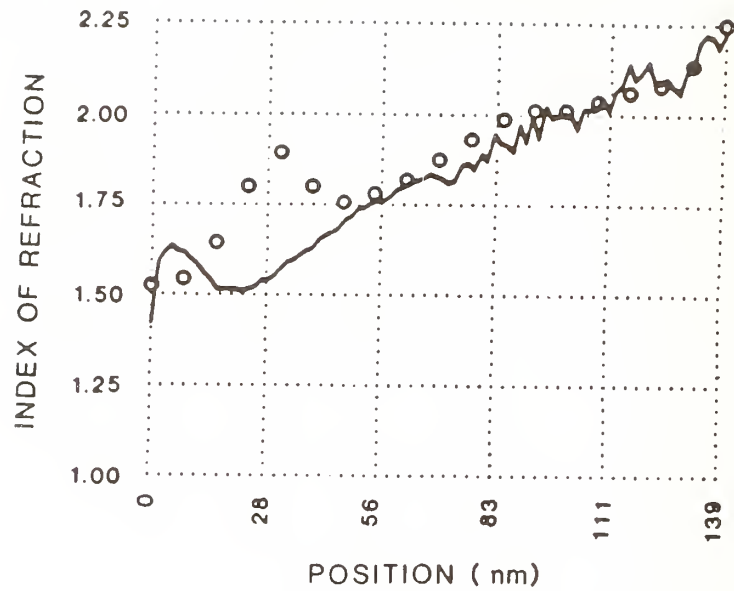


Figure 3: Index profile of a gradual interface between  $\text{TiO}_2$  and  $\text{SiO}_2$  produced by codeposition. Circles indicate index of refraction data calculated with the aid of an AES-profile of the sample.

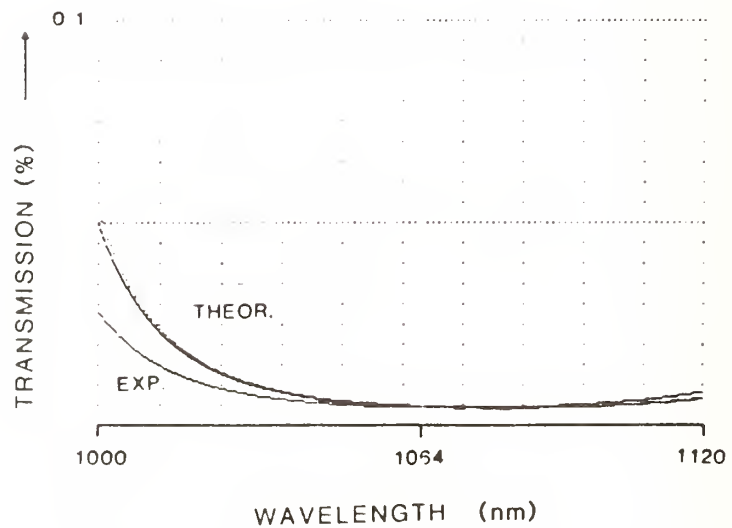


Figure 4: Transmission spectra of high reflecting coatings of  $\text{TiO}_2$  and  $\text{SiO}_2$ . The dashed curve corresponds to the gradual system. EXP. indicates the experimental curve.



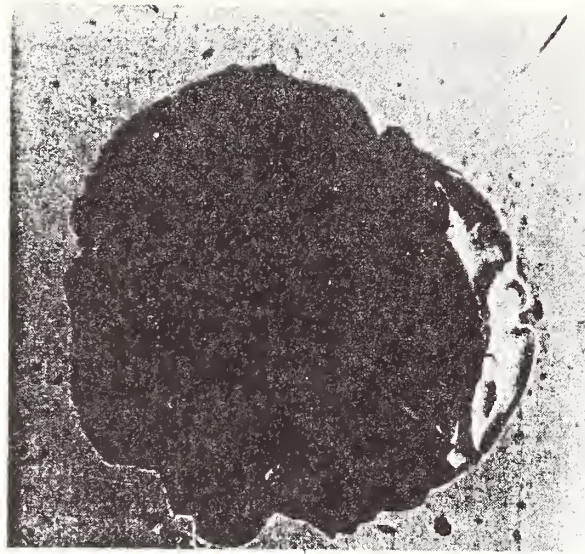


Figure 5: Damage site on a halfwave layer system of  $\text{HfO}_2/\text{SiO}_2$ . The first layer is totally ablated.

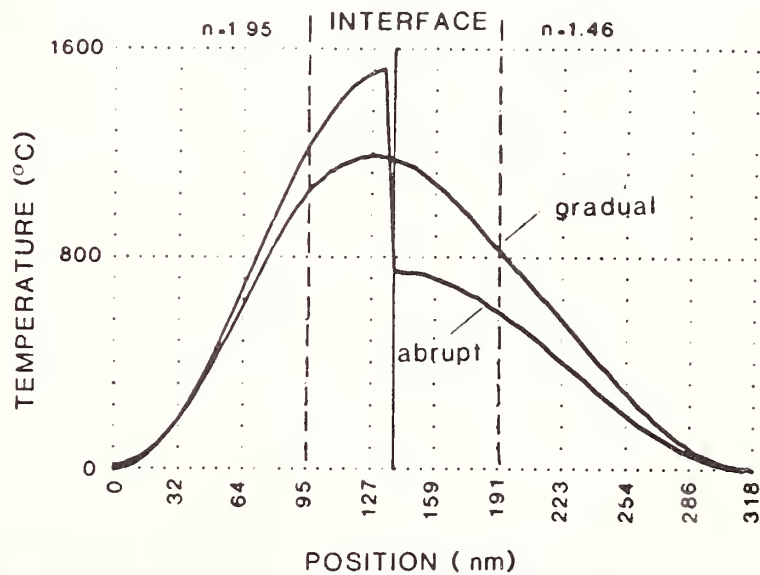


Figure 6: Calculated temperature distribution in the first layer pair of a qw stack of  $\text{HfO}_2/\text{SiO}_2$  for  $1.064 \mu\text{m}$ . The calculation was carried out with a laser pulse duration of 15 ns, an input energy of 30 mJ and a spot diameter of  $300 \mu\text{m}$ . The horizontal scale indicates the position in units of geometrical thickness.

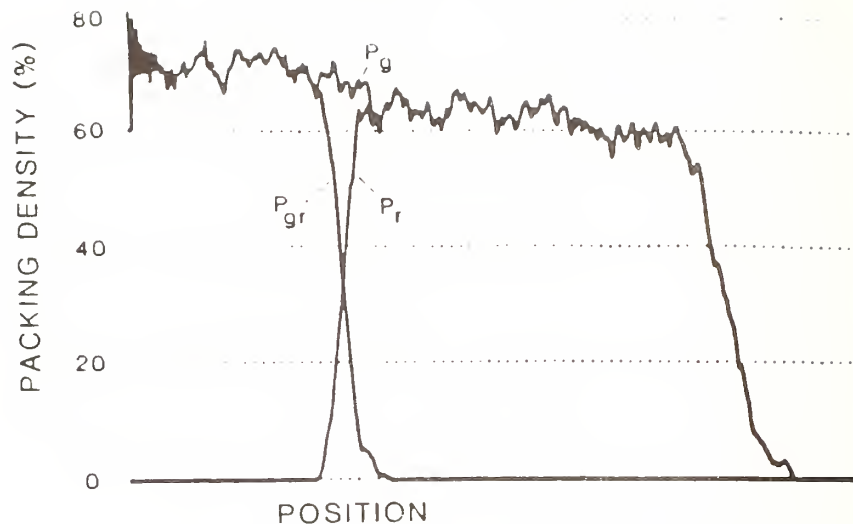


Figure 7: Simulated packing density in a layer system consisting of a dense layer ( $P_{gr}$ , particle diameter 1.5, mobility value 1.3) and layer with lower packing density ( $P_r$ , particle diameter 1.2, mobility value 1.1). A density of 100 % corresponds to the closest packed structure.  $P_g$  is the sum of  $P_r$  and  $P_{gr}$ .

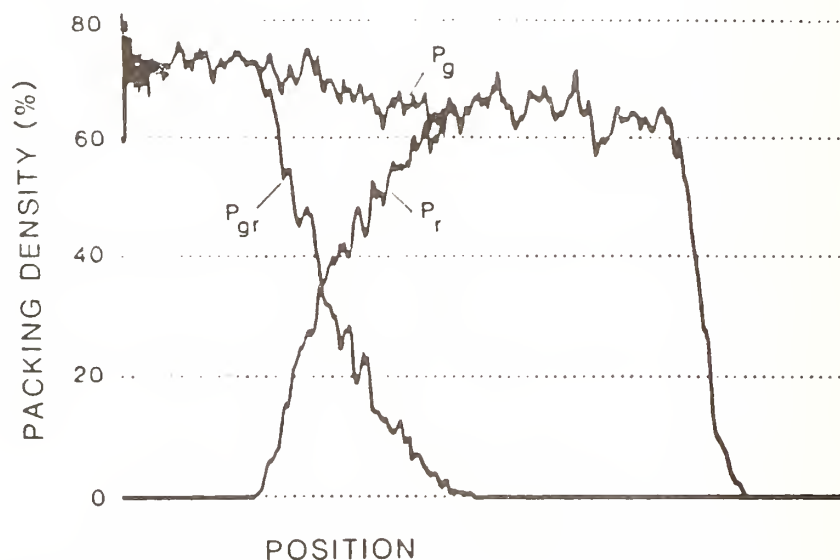


Figure 8: Simulated packing density of two layers with properties equal to figure 7. The interface between the layers is codeposited. It consists of 6000 particles which are concentrated according to a linear alteration of the deposition rate in the interface region.

## Measurements of Pulse Damage Thresholds of AR Coated CdTe at 10.6 $\mu$ m

J. G. Grimm, R. S. Eng, C. Freed, N. W. Harris

Massachusetts Institute of Technology  
Lincoln Laboratory  
P.O. Box 73  
Lexington, MA 02173-0073

R. G. O'Donnell  
Ford Aerospace Corp., Lexington, MA 02173

Laser induced damage thresholds (LIDT) measurement results on AR-coated single and polycrystalline CdTe samples using 35 $\mu$ s flat top pulses from a CO<sub>2</sub> laser MOPA system are reported. Single-shot LIDT's are in excess of 50 J/cm<sup>2</sup>. The LIDT's for cumulative pulses in the 50k shots regime and pulse repetition frequency in the 1-5Hz range have been measured. The LIDT has been found to be dependent approximately on the square root of the pulse width. The problem of protecting AR-coatings from aqueous solution has also been investigated.

Key Words: anti-reflection coatings; cadmium telluride; CO<sub>2</sub> laser MOPA; laser induced damage threshold; pulse repetition frequency effect.

### 1. Introduction

The laser induced damage thresholds of a number of semiconductor materials transparent in the IR spectral region have been measured and reported in the open literature. Despite this there are still many unanswered questions on the dependence of laser induced damage threshold (LIDT) of anti-reflection coatings on pulse length, pulse repetition frequency (prf), and cumulative number of shots. We would like to report our method of generating nearly flat-top medium energy CO<sub>2</sub> laser pulses of large width and our measurements of the damage thresholds of a number of AR-coated CdTe samples using these wide laser pulses. Single-shot laser induced damage thresholds of AR coated samples exceeding 50J/cm<sup>2</sup> have been observed. We have investigated prf and cumulative laser pulse effects on LIDT. Some of the samples have been tested successfully for many thousand laser shots without any observable surface damage.

### 2. Experimental Setup

There are three major components for the damage test measurement setup, namely, the laser beam from a laser master oscillator-power amplifier (MOPA) system, the damage test sample holder, and the damage monitoring instruments. The CO<sub>2</sub> laser beam used in the damage testing station basically comes out of a small laser MOPA system. The output pulse width can be adjusted from 5 $\mu$ s to 80 $\mu$ s prior to any measurements. For the 35 $\mu$ s wide pulse, in particular, the available output energy is about 230mJ. Mode matching this output pulse to a spot size ( $1/e^2$  diameter) of about 0.79mm produces a peak energy density of over 90J/cm<sup>2</sup> at the center of the damage test housing for LIDT testing of CdTe crystals (or other infrared optical components). The pulse energy is approximately proportional to the pulse width. Based on our previous work,<sup>1</sup> this level of energy should be sufficient for LIDT measurements of AR-coated crystals available at this time.

The main components of the CO<sub>2</sub> laser MOPA system are shown in a block diagram in figure 1. A low-pressure hybrid TE CO<sub>2</sub> laser, consisting of a cw dc-discharge gain cell in series with a custom made commercial pulsed-discharge gain cell (Pulse Systems, Inc. Model Dual LP-30 laser gain cell) sharing the same stable resonator configuration laser cavity,<sup>2</sup> produces a smooth single TEM<sub>00</sub> mode, 80mJ pulsed

---

This work was sponsored by the Department of the Navy for SDIO under contract F19628-85-C-0002.

"The views expressed are those of the author and do not reflect the official policy or position of the U.S. Government."

output with a pulse width of about 70 $\mu$ s (FWHM). Within limits, some degree of pulse width control can be achieved by varying the pressures and mixing ratios of the gas constituents, charging voltages and energy storage capacitors.

The output beam size of the hybrid laser is focussed to a beam waist between two acousto-optics (A-O) cells. They are arranged so that there is no resultant frequency shift of the beam. The output beam of the second modulator is next transformed to a beam waist of about 5mm at the entrance plane of the 5:1 beam expander. The output of the beam expander goes to the pulsed low-pressure CO<sub>2</sub> laser amplifier, a modified version of a Model LP-140 from Pulse Systems, Inc. The modified version incorporates electronic triggering circuits for sequentially initiating the dual discharges. This pulsed amplifier has an active gain length of 140cm. The output from the laser amplifier is about 400mJ (full unsliced pulse).

Part of this beam is split off with a 95% beamsplitter and used as an energy monitor. The rest of this beam is focussed by a combination spherical mirror and a lens to a beam spot diameter of 0.79mm at the center of the damage test housing shown in figure 2. The housing is purged constantly with dry filtered N<sub>2</sub> during the damage test measurements. The windows are two inch diameter Ge plates with both sides AR coated.

A photomultiplier tube (PMT) is situated looking into the housing at the front surface of the test sample to detect any visible emissions given off as a precursor to damage. A variable attenuator consisting of a rotatable half wave plate and a polarizer is placed before the housing, providing convenient adjustment of the laser pulse energy. The beam expands as it comes out of the damage test housing and ~3% of the beam is split off and is focussed down to a spot less than 1mm in diameter for temporal envelope detection with a high-speed photoelectromagnetic detector. The pulse energy is measured with an energy meter made by Gentec Inc. with a 1 inch diameter sensitive area. A 2 inch x 2 inch Gentec energy meter is used behind the beamsplitter to monitor the output of the LP-140 laser amplifier. Both of these meters have been calibrated with a Scientech power meter operating in the energy mode before the start of the pulse energy measurements.

All the pulsed systems are synchronized through appropriately timed trigger pulses from a pulse generator, Berkeley Nucleonic Model BNC-8010, which drives several pulse delay generators, Ortec Model 416A, for optimization of time delays to the various trigger inputs.

Figure 3a shows a photograph of 50 consecutive energy pulses superimposed measured at the output of the hybrid TE laser. The pulse repetition frequency was 1Hz. Thus we can estimate that the peak-to-peak fluctuation in the output pulse energy is less than  $\pm 10\%$ . Figure 3b shows the nearly flat top pulse at the output of the laser amplifier. The pulse width is about 35 $\mu$ s (FWHM).

The spatial profile of the laser output was measured at several locations in the optical path using a 32 x 32 pyroelectric detector array, Spiricon Mode LMP-32 x 32. This was to check the quality of the beam insuring a proper spot at the focus on the test sample. Figure 4 shows two views of the laser beam spatial profile at the output of the pulsed amplifier. Figure 4a is an isometric view of this, and figure 4b shows a slice of data taken through the center which also has a Gaussian curve fitted to it. The solid curve is the data recorded by the array, and dashed curve represents the fitted data. From this it can be seen that we operated with a very nearly Gaussian beam. Based on the above plots of the beam profile, the following formula, which is appropriate for a Gaussian beam, is then used to determine the beam energy density,  $J$ , at the center of the beam:

$$J(r=0) = \frac{2E_t}{\pi w^2} \quad (1)$$

where  $E_t$  is the total pulse energy and  $w$  is the beam spot radius. By measuring the beam size and pulse energy, the peak or on-axis energy density was determined.

The input beam to the LP-140 is about 2.5cm in diameter at the  $1/e^2$  point, therefore, no beam truncation is expected for the 4 x 4 cm<sup>2</sup> clear aperture of gain cross section. By examining the input and output beam profiles recorded with the Spiricon 32 x 32 array detector, we see that the beam profile changes very little and remains essentially Gaussian after going through the amplifier for this level of energy extraction. Table I lists the trigger delays used to achieve the highest energy output for a 35 $\mu$ s pulse with minimum temporal variation of pulse energy.



Table I. Trigger Delays Used in MOPA

Name of trigger pulse	Delay ( $\mu$ s)
Pulsed amplifier, primary	0.00
Pulsed amplifier, secondary	+20
Dual LP-30 gain cell	+116
A-O cell	+140 <sup>a</sup>

a: For 35 $\mu$ s pulse width, the leading edge of the sliced hybrid TE laser pulse is about 15 $\mu$ s ahead of the peak of the unsliced hybrid TE laser output pulse.

### 3. Results and Discussion

#### 3.1 Damage Test Procedures

Typically at the start of each measurement, the area of the sample to be targeted was set up and a transmission measurement was made to check the quality of the sample. A series of conditioning runs were made at prf = 1Hz. For each of these conditioning runs the sample was irradiated up to 1000 shots before increasing the fluence level (in general by 5J/cm<sup>2</sup> steps). At the start of each level of conditioning visible emissions were often observed (by the photomultiplier) but they gradually grew weaker as time increased. The emissions usually stopped within the first 100 shots. Upon the completion of each conditioning level the sample was removed and inspected under a microscope. No damage was observed in relation to the PMT signals that faded within a hundred shots. This was continued until threshold was reached.

#### 3.2 Results

##### 3.2.1 Single-Shot Damage Thresholds

Table II shows some typical results of LIDT values measured on both polycrystalline and single crystal CdTe test samples. As can be noted there is a large variation in thresholds of the polycrystalline substrate tested. Originally this was thought to be due to the irradiation of crystal boundaries. The mechanism here was that at the boundary of a single crystal cell impurities would collect and/or the boundary layer would be tellurium-rich and absorb more incident radiation. This would lead to a damage center forming perhaps in the interior of the substrate.

Table II. Single-Shot LIDT Summary

Crystal*	LIDT J/cm <sup>2</sup>	Type of Damage	Damaged Surface	No. of shots at Threshold	Total No. of Shots
P-1	20	Substrate	Output	100	5,000
P-1	30	Substrate	Output	365	13,365
P-1	58	Substrate	Output	2	16,000
P-1	30	Substrate	Output	210	2,210
P-1	65	Coating	Input	5	17,000
S-1	30	Coating	Input	10	5,000

\*P-1 stands for a polycrystalline witness sample; S-1 stands for a single crystal test sample

We observed two different types of damage, believed to be caused by different damage mechanisms. A typical damage site of the first type is shown in figure 5a, it occurs at the AR-coating only. A typical damage site of the second type is shown in figure 5b, it occurs in the substrate. The typical sizes of the two types are

approximately 1/3mm and 1mm, respectively. The damage sites for both types of damage were identified during the testing by lower transmission associated with large signals from the PMT.

Figures 6a and 6b show the times of damage corresponding to the first and second types of damage, respectively. In both figures, the damages had already occurred during the preceding laser pulses and the transmission through the sample as shown are relatively low. Since the second type of damage was of more catastrophic nature, the drop in transmission as shown in figure 6b is nearly 90% which is more severe than that for the first type of damage. The comparatively late occurrence of the PMT signal may be due to a higher required energy to heat the substrate to the damage threshold. The PMT signals associated with the second type of failure were always larger than those of the first type.

These two types of damage were strongly correlated with a particular surface. The failure of the AR coating in the first type of damage occurred more often on the input surface and there were fewer of these failures altogether. This may imply that this type of failure is due to random imperfections in the AR coating. The second type of damage occurred exclusively on the output surface. Moreover, these damage sites are conically shaped pointing back into the substrate up to a millimeter in depth.

### 3.2.2 Contamination due to Protective Coating

In the course of routine handling, these crystals were given a protective optical coating of Microstop® to keep contaminants and solvents from the AR coating that could possibly damage or remove it. We set out to take a series of measurements to find if the application of this coating had any effect on the LIDT after it was removed. These results can be seen in Table III. On average the sample P-1 damaged at lower fluence levels than the pre-treatment surface. The method of cleaning for the above series was to dissolve off the protective coating using several baths of acetone, changing the acetone each time. Then after the surface appeared to be free of the material to the naked eye there was a final rinse with clean acetone and this was then blotted off the surface before being allowed to dry. We are also trying another rinse of ethyl alcohol which is then blown off with dry N<sub>2</sub>.

Table III. Contamination Series

Crystal*	LIDT J/cm <sup>2</sup>	Type of Damage	Damaged Surface	No. of shots at Threshold	Total No. of Shots
P-1	15	Coating	Input	1000	2,000
P-1	40	Substrate	Output	2	7,000
P-1	20	Coating	In + Out	5	3,000
P-1	30	Substrate	Output	50	5,050

\*P-1 stands for a polycrystalline witness sample.

### 3.2.3 Variation of LIDT with Pulsewidth

We have measured the laser-induced damage thresholds of several AR coated CdTe samples a function of pulse width in the long pulse regime. Figure 7 shows the plot of the LIDT's of the CdTe samples vs. laser pulse width ranging from 1ns to several tens of microseconds. At the long pulse regime are our measurement results using the method just described; they represent the first of its kind in LIDT measurements using truly flat-top CO<sub>2</sub> laser pulses, against the method of averaging the power of multiple sub-damage-level picosecond pulses from the free electron lasers recently reported.<sup>3,4</sup> At the short and intermediate pulse width regime, LIDT data from several sources are included.<sup>5,6,7,8</sup> We see that the plot tends to confirm that the dependence of LIDT on the pulse width ( $\tau$ ) for CdTe is approximately proportional of  $\tau^{1/2}$  out to the long pulse regime. This probably can be explained by the fact that the thermal diffusivity of CdTe is among the poorest in semiconductors; that is the thermal heating process is diffusion dominated. The present result on the pulse width dependence implies that the most appropriate damage model for AR-coated CdTe samples is that of impurity inclusion in the AR-coated layers. The square root of the pulse width dependence for the LIDT presently obtained allows designers in laser modulator or related fields, for the first time, to scale the LIDT in the long pulse regime with a much higher degree of confidence.

### 3.4 PRF Dependence of LIDT

The results shown in Table II represent the single-shot laser damage thresholds. In many practical applications, the damage thresholds for multiple shots and/or prf operation are required. Table IV shows results done at a prf of 5Hz.

Table IV. Cumulative Shot Series at 5Hz

Crystal*	LIDT J/cm <sup>2</sup>	Type of Damage	Damaged Surface	No. of shots at Threshold§
S-2	15	None	--	50K
S-2	15	Substrate	Output	46K
S-2	15	Coating	Input	50K
S-3	13	None	--	200K
S-3	13	None	--	200K
S-3	13	Coating	In + Out	150K

\*S-2, S-3 stands for single crystal test samples.

§ Each series started and finished at 15 (or 13) J/cm<sup>2</sup>, there was no conditioning at lower fluence levels

On the single crystal sample S-2, the work done was to target the site, then simply to start testing the sample at 15J/cm<sup>2</sup>. This particular sample was only tested to 50,000 shots. During the testing it was normal to stop to check for damage approximately every 15,000 shots. The situation was similar for sample S-3 except that the peak energy density was lower and the sample was tested for up to 200,000 shots. This sample was checked for damage only if excessive PMT signal was observed.

Due to considerably more complex nature of the multiple shot/prf operation, experimental data are much harder to come by. Among the existing experimental data on semiconductor materials, Wood et al.<sup>9</sup> showed that the LIDT's of small band-gap semiconductor materials were strongly dependent on prf heating, presumably due to nonlinear absorption and other mechanisms such as the thermal run-away effect, which is notoriously large in germanium. For other materials with larger band gaps, the prf effect has been found to be very weak.<sup>9</sup> In another investigation in the YAG laser wavelength region,<sup>10</sup> the effect of prf was also found to be negligible or non-detectable. Based on the above finding, it appears that the prf effect of CdTe samples should be determined by laboratory measurements, especially for long pulse widths, where there is no data. The prf dependence has its origin in multiple-pulse transient heating of a solid.<sup>11,12</sup> The simplest theory on transient repetitive pulse heating is that of the semi-infinite, one dimensional model given below:

$$T_N(0,t) = 2F_0 \sqrt{\frac{T}{\rho c k \pi}} \left[ 1 + \frac{\sqrt{T/T_1}}{2} \sum_{n=1}^{N-1} \frac{1}{\sqrt{n}} \right] \text{ for } N \geq 2 \quad (2)$$

- $T_N(0,t)$  is the temperature at the surface of the solid as a function of time  $t$  measured at the end of the  $N$ th pulse;
- $F_0$  is the absorbed fluence in  $W \cdot cm^{-2}$ ;
- $T$  is the pulsewidth in seconds;
- $T_1$  is the period in seconds;
- $t$  is the time in seconds,  $t = (N - 1)T_1 + T$ ;



- $k$  is the thermal conductivity in  $W \cdot cm^{-1} \cdot ^\circ C^{-1}$ ;
- $c$  is the heat capacitance in  $J \cdot g^{-1} \cdot ^\circ C^{-1}$ ; and
- $\rho$  is the density of the solid in  $g \cdot cm^{-3}$ .

When the summation is not included the result is the temperature rise due to single pulse heating. As time increases, the temperature at the surface gradually builds up because the temperature due to heating from the previous pulse has not decreased to the original level. The cumulative effect due to repetitive pulse heating on the surface temperature is illustrated in figure 8. It shows that the average temperature on the CdTe surface rises as the number of pulses increases for several prf's ranging from 1 to 10Hz. For a single 30 $\mu$ s pulse, in particular, the temperature rise at the end of the pulse is as high as 56 $^\circ$ C for a peak fluence of 15J/cm<sup>2</sup>. As the number of pulses increases, the surface temperature can thus rise by several times that of the temperature rise due to single-pulse heating. Remembering that this is a one-dimensional model in which lateral heat diffusion and other cooling effects have been neglected, the ultimate surface temperature is likely to be much below that predicted here. Nevertheless, the overall picture (or at least the trend) in surface temperature rise is illustrated here in that as the prf goes up, the LIDT vs. the number of pulses is expected to decrease. Armed with the above concept, we have performed measurements on the LIDT of AR-coated CdTe samples at several prf's and at different laser fluences while keeping the thermal diffusion parameters such as the beam spot, sample size, and thickness constant. The results are shown in figure 9. The experimental data points were obtained for 1Hz and 5Hz. The theoretical curves were obtained by multiplying the inverse of the curves in figure 8 by 37J/cm<sup>2</sup>. This value corresponding to the average single-shot damage threshold.<sup>1</sup> It can be seen that the overall trend tends to confirm the strong prf dependence of LIDT for semiconductors such as CdTe in the long pulse regime. The results may have important implications in the design of other high energy/power optical components for operation in the long laser pulse regime.

By performing measurements at different prf and at different fluences described above, we hope that the results can shed light on the dependence of LIDT on the total number of laser shots being different from that of prf. For example, at very low prf, the effect of surface temperature rise can be neglected. The LIDT level reached at the final number of laser shots should represent the effect of cumulative shots independent of prf. On the other hand, the cumulative shot effect can perhaps be extrapolated to the "zero" prf regime by plotting the LIDT vs. shot number using prf as the parameter for the same fluence. This experiment can also be repeated for different fluence levels. Doubtless, this will take considerable amount of time, but at the present level of understanding of LIDT, there is no substitution for hard laboratory data. We are planning to perform more of the measurements in the near future to bolster our understanding of multiple shot/prf effect in this area.

### Summary and Conclusions

We have conducted LIDT measurements on AR-coated CdTe samples, both single crystal and polycrystalline, and have observed a variety of effects relating to the single-shot damage threshold, prf, and cumulative number of shots. There is a large scatter in the single-shot LIDT's of the polycrystalline samples and further work is being done to determine the cause of this. We can see a good agreement with the theory of the  $\tau^{1/2}$  threshold dependence for CdTe when this data is compared to other work done. In the range of prf's investigated and modelled in theory the effects of prf for low number of shots may be negligible but at higher number of shots (>5000) and prf's more measurements are needed to improve the reliability of the prf dependence.



## References

- [1] R. S. Eng, J. G. Grimm, J. Greene, J. A. Daley, and N. W. Harris, "Measurements of Ultra-wide Pulse Damage Thresholds of Anti-reflection Coated IR Materials at 10.6  $\mu\text{m}$ ," Paper presented at the Eighteenth Annual Symposium on Optical Materials for High Power Lasers, Oct. 26-28, 1987, Boulder, Colorado.
- [2] C. Freed, "Ultrastable Carbon Dioxide ( $\text{CO}_2$ ) Lasers," SPIE Proceedings on Laser Research and Development in the Northeast, SPIE Vol. 709, pp. 36-45 (1986).
- [3] B. E. Newnam, "Operational Limits of  $\text{ZnSe}/\text{ThF}_4$  Resonator Mirrors in the Los Alamos Free-electron Laser," Paper presented at the Eighteenth Annual Symposium on Optical Material for High Power Lasers, Oct. 26-28, 1987, Boulder, Colorado.
- [4] S. V. Benson, E. B. Szarnes, B. A. Hooper, E. L. Dotter, and J. M. J. Madey, "Laser Damage on Zinc Selenide and Cadmium Telluride using the Stanford Mark II Infrared Free Electron Laser," Paper presented at the Eighteenth Annual Symposium on Optical Materials for High Power Lasers, Oct. 26-28, 1987, Boulder, Colorado.
- [5] B. E. Newnam and D. H. Gill, "Damage Resistance of  $\text{CO}_2$  Fusion Laser Optics," Optical Engineering, 18, 579 (1979).
- [6] B. E. Newnam and D. H. Gill, "Damage Resistance of AR-coated Germanium Surfaces for Nanosecond  $\text{CO}_2$  Laser Pulses," Laser Induced Damage in Optical Materials: 1977, NBS Spec. Pub. 509 pp. 298-31, 1977.
- [7] S. J. Thomas, Los Alamos National Laboratory, Reported damage threshold exceeding 7 J/cm<sup>2</sup> (4J on 1.2 cm beam spot diameter) on AR-coated CdTe for 1  $\mu\text{s}$   $\text{CO}_2$  laser pulses, private communications.
- [8] Avco Everett Research Laboratory, Inc., "Radiation Damage Tests of Anti-reflection-coated Cadmium Telluride Modulator Crystals," Final Report, Contract No. F19628-85-C-0002, November 1985, prepared for MIT/Lincoln Laboratory, Lexington, MA.
- [9] R. M. Wood, P. Waite, and S. K. Sharma, "Single-shot, Cumulative and PRF Dependent Laser Induced Damage Thresholds," NBS Special Publication 688 p. 174;  
R. M. Wood, S. K. Sharma, P. Waite, E. K. Gorton, and K. Lewis, "Time of Damage and the Effect of the Pulse Repetition Frequency on the Laser Induced Damage Thresholds," Paper presented at the Sixteenth Annual Symposium on Optical Materials for High Power Lasers, Oct. 26-28, 1985, Boulder, Colorado;  
R. M. Wood, P. Waite, and S. K. Sharma, "Variation of Laser Induced Damage Threshold with Laser Pulse Repetition Frequency," NBS Special Publication 669 p. 44.
- [10] P. M. Fauchet and A. E. Siegman, "Surface Damage Mechanisms in Nontransparent Media," NBS Special Publication 727 p. 147.
- [11] W. J. Oosterkamp, "The Heat Dissipation in the Anode of an X-ray Tube," Phillips Res. Rep. 3, 49-59 and 161-173 (1948).
- [12] J. C. Jaeger, "Pulsed Surface Heating of a Semi-infinite Solid," Quarterly Appl. Math. 11, 132-137 (1953).

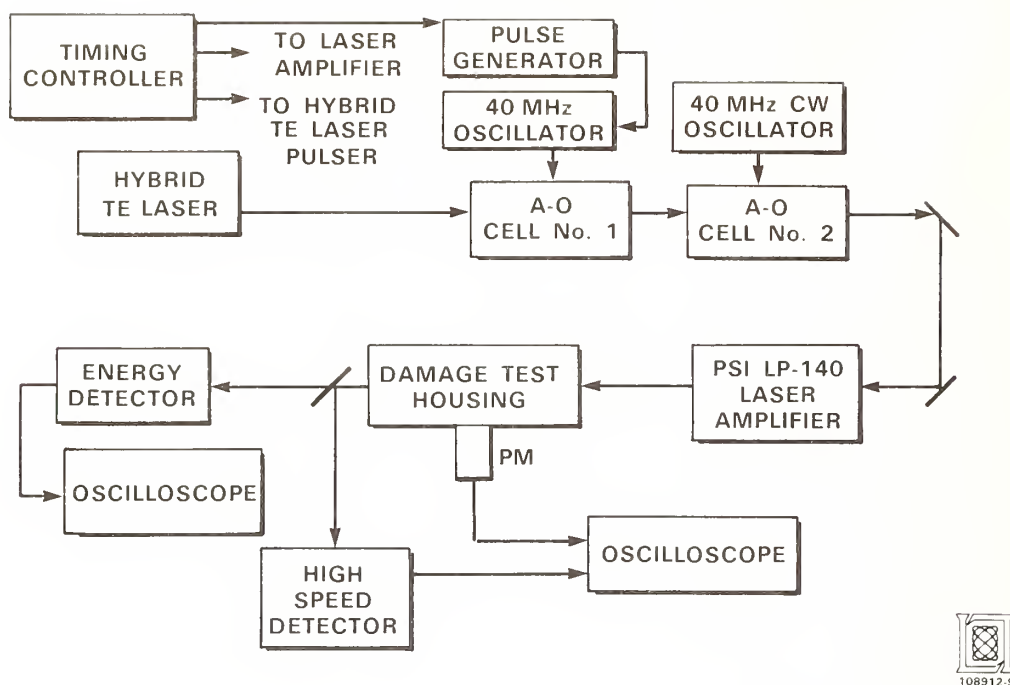


Figure 1. Block diagram of CO<sub>2</sub> laser MOPA system showing hybrid TE laser, pulse controlling A-O cells, pulsed laser amplifier and damage testing diagnostics.

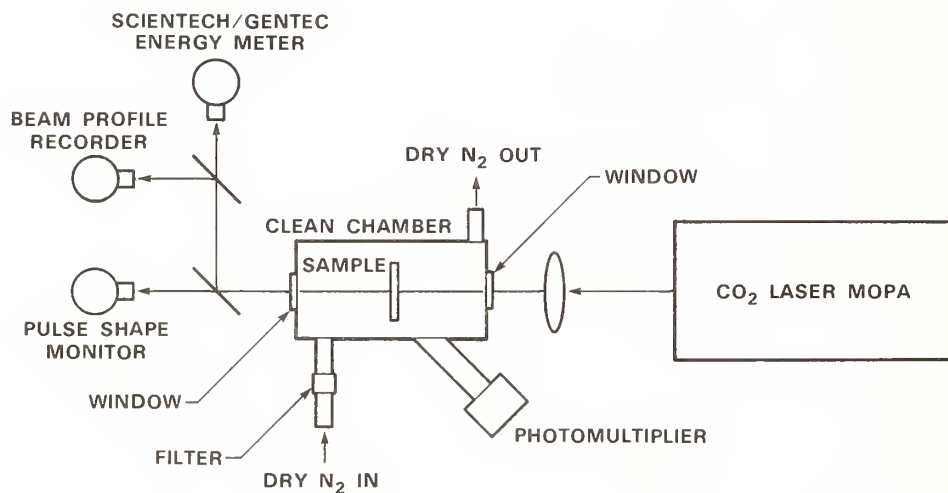


Figure 2. Diagram of the laser induced damage test housing which holds sample under test, shows various diagnostics used. Beam diameter at center of housing is 0.8mm diameter.

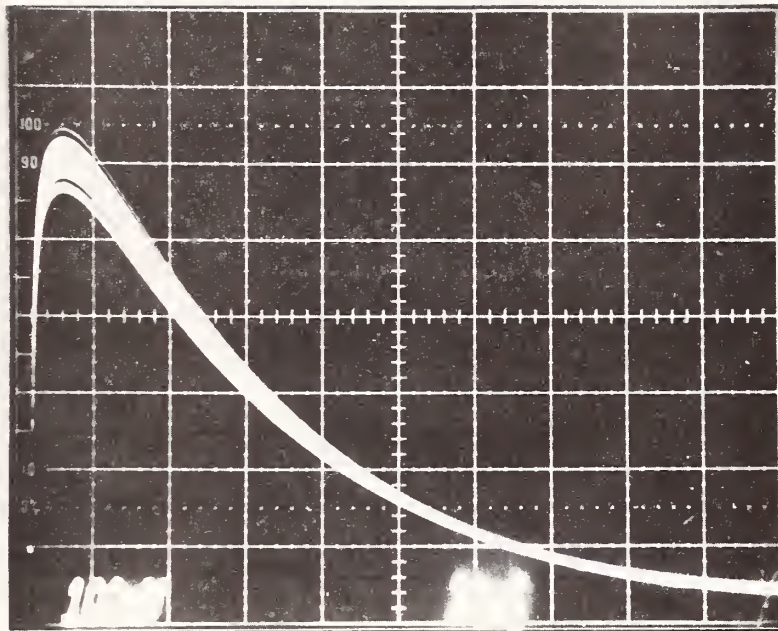
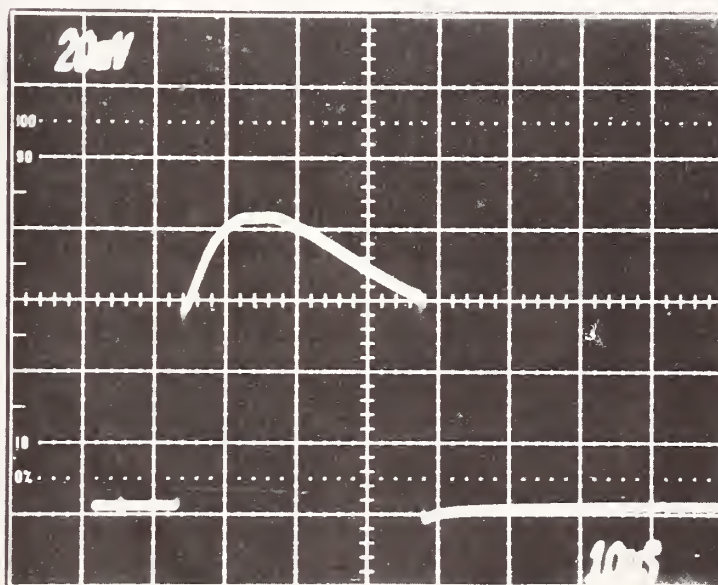


Figure 3a. Pulsed energy readouts of 50 consecutive laser pulses at output of hybrid TE laser.



114902-4  
114902-4

Figure 3b. Temporal profile of laser pulse after amplification by LP-140 pulse laser amplifier showing 35 $\mu$ s pulse width.

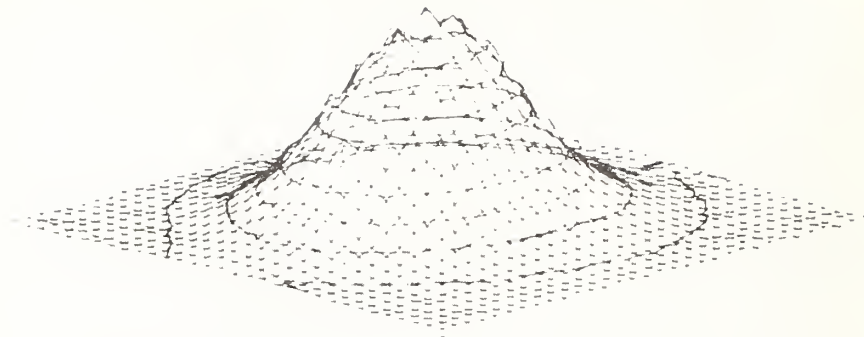
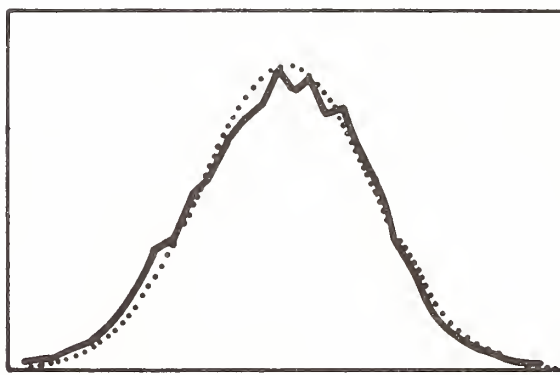


Figure 4a. Isometric view of spatial profile of laser pulse at output of LP-140 pulse laser amplifier.



114902-5

Figure 4b. Slice of data from above view. Solid line is actual data, the dotted line is a fitted Gaussian curve showing good agreement.



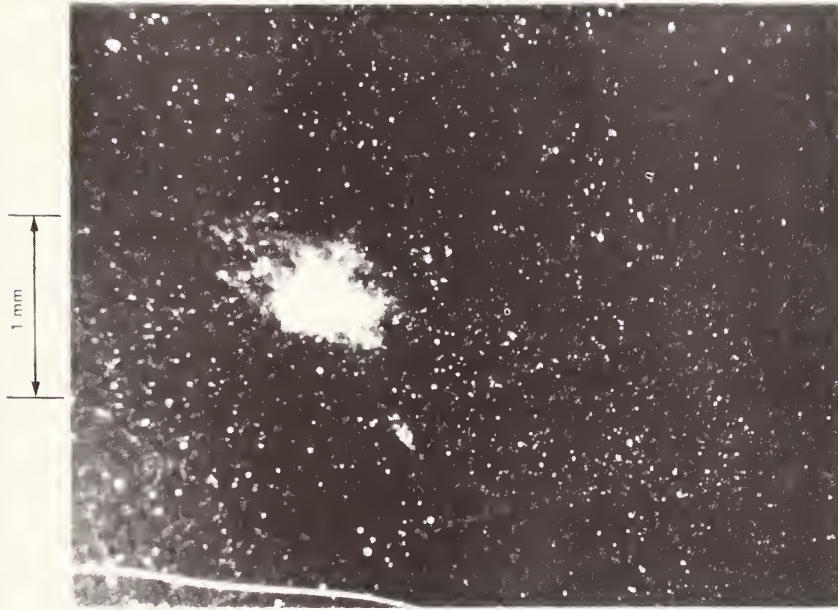


Figure 5a. One type of damage seen. Damage site is small compared to laser beam diameter and penetrates little or none into substrate.



114902-3

Figure 5b. Substrate damage. Occurs on output surface of sample and extends into substrate. Note nearly same size as laser beam diameter.

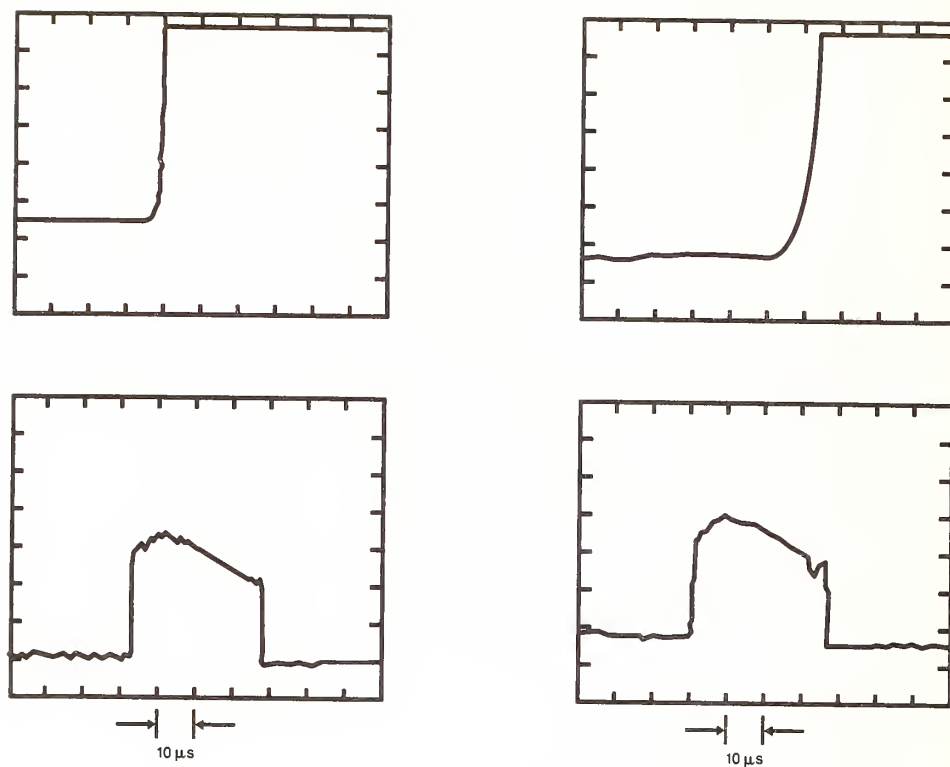
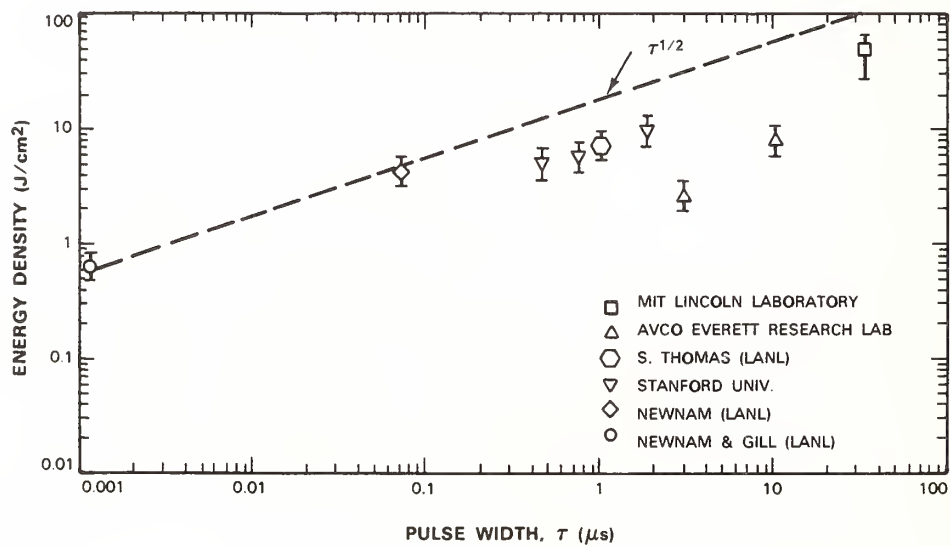


Figure 6. Occurrence of photomultiplier signal (top row) versus time corresponding to laser pulse shape in time; (a) corresponds to coating damage, (b) corresponds to substrate damage.



114902-1

Figure 7. Laser induced damage thresholds of CdTe samples versus laser pulse width

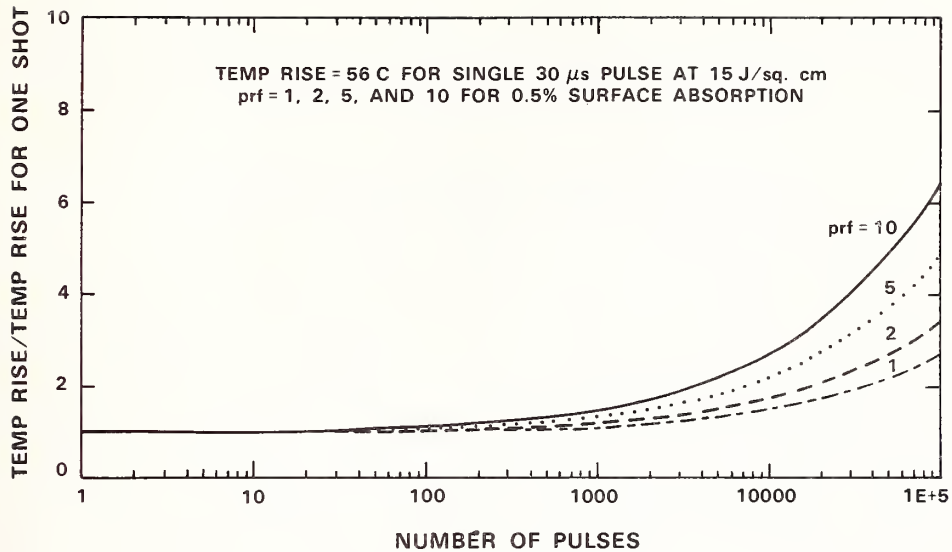


Figure 8. Plot showing temperature rise of sample relative to single shot heating versus number of laser pulses for different pulse repetition frequencies.

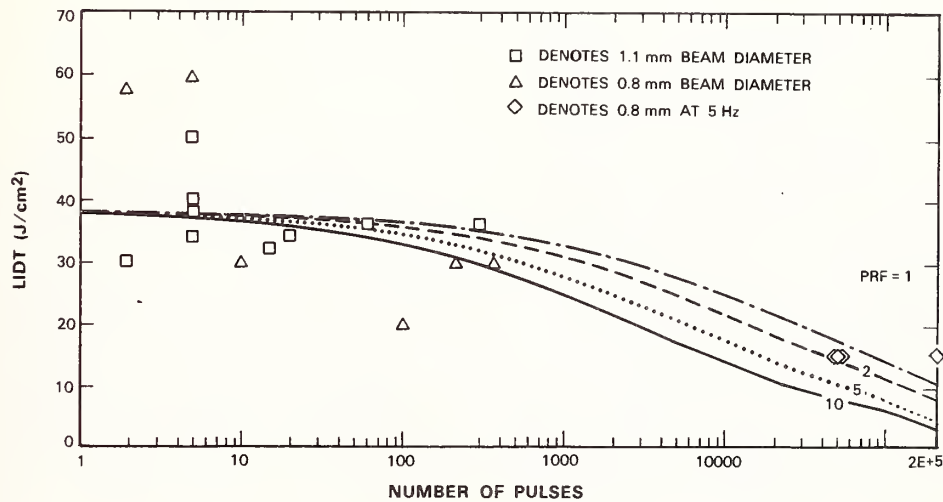


Figure 9. LIPT of AR-coated CdTe versus number of laser pulses, theoretical curves show four different PRF's starting at a mean LIPT of 37J/cm<sup>2</sup>. The different symbols denote different beam sizes and PRF's. All work was done at 1Hz except those noted at 5Hz.

## Microcomputer Finite Difference Modeling of Laser Heating and Melting\*

J. O. Porteus

Physics Division, Research Department  
Naval Weapons Center, China Lake, CA 93555-6001

An existing method of microcomputer finite difference modeling has been adapted to laser-heating and melt-threshold computations. Versatility compared to exact-solution methods permits various applications of moderate complexity with arbitrary pulse waveform and an optional axisymmetric or one-dimensional spatial profile. Thermal diffusion is modeled in two dimensions based on optical and thermal transport properties that can vary with temperature, time, and space. Simplicity and freedom from mainframe requirements make the method accessible, flexible, and easily learned. Examples presented here were performed on XT- and AT-type PC-compatible computers equipped with floating-point math coprocessor running Turbo Pascal 4.0. Comparisons are given with previously reported surface melt thresholds of diamond-turned Cu and Au measured and calculated by earlier methods. Other examples are pulsed-laser bulk heating of semiconductors, including a GaAs coating on a quartz substrate and a comparison of flashlamp heating of laser glass in rod and slab configurations.

Key words: diffusion; GaAs; heating; laser damage; melting; metal mirror; thermal model.

### 1. Introduction

Calculation of temperatures produced by laser heating of optical materials is a common requirement in damage testing and other areas of laser technology. Simple analytic thermal models such as those provided in Carslaw and Jaeger [1]<sup>1</sup> are capable of representing only the most elementary experimental situations. On the other hand, more powerful numerical models such as SINDA [2] are often too formidable for the casual user, or may not be readily available. This paper presents examples of a very capable microcomputer finite-difference modeling (MFDM) method [3] that offers a compromise between these two extremes. The new method is applied to melt thresholds of Cu and Au surfaces with intrinsic properties. Comparisons are made with previously computed results and laboratory measurements on essentially defect-free samples. Other examples include laser damage of a highly absorbing semiconductor, bulk heating of a semiconductor film, and flashlamp heating of laser glass. Computations were performed on XT- and AT-type PC-compatible computers equipped with floating-point math coprocessors. The typical computation time for heating a Cu surface to melt by single-pulse absorption, using 12x12 nodes, is about 5 minutes.

The mathematical basis for the method and the general finite-difference code in BASIC is available in a monograph and on disk [3]. The computations performed for this paper were

\*This work was supported in part by Navy Independent Research funds.

<sup>1</sup>Numbers in brackets indicate the literature references at the end of the paper.



executed in a Turbo Pascal 4.0 version of the code that was adapted specifically to heating by optical absorption and was extended to include temperature-dependent material properties. The temperature dependence of absorption is especially important in laser heating of metal surfaces. Surface absorption of laser flux is treated in terms of a surface transfer coefficient ( $\text{W cm}^{-2} \text{ }^{\circ}\text{C}^{-1}$ ) with an arbitrary surface temperature drop of  $10^5 \text{ }^{\circ}\text{C}$ , which is large compared to any calculated temperature excursions. Bulk absorption is treated as a decrement of transmitted laser flux at each internal node (calculation point representing a space cell in the beam path). An internal heat source at each node is equivalent to the absorbed energy in the corresponding cell. The model accepts any waveform and any axisymmetric or linear spatial profile, expressed either in tabular form or as mathematical formulas. Thermal diffusion can be treated in either one or two dimensions of space.

## 2. Metal Surface Melting

Comparisons were made with melt thresholds of diamond-turned Cu and Au surfaces previously measured at the Naval Weapons Center and calculated by other methods [4-6]. The surfaces were sufficiently free of defects that intrinsic laser-induced melt thresholds could be measured [5]. Results of absorptance measurements on these metals at ambient and elevated temperatures are reproduced from reference 6 in table 1. A linear correction to the ambient absorptance  $A$ , represented as a fraction of  $A$  in the table by  $A^{-1} dA/dT$ , was applied at time intervals of 1 to 10 ns, depending on the laser waveform.

Table 1. Metal surface absorptance

Wavelength ( $\mu\text{m}$ )	Metal	$A \times 10^3$ (@20°C)	$A^{-1} dA/dT \times 10^3$
2.7	Cu	7.90	2.61
	Au	11.2	2.24
3.8	Cu	7.55	2.71
	Au	9.45	2.62
10.6	Cu	6.50	2.77
	Au	8.15	2.66

Thermal properties used here correspond closely to inputs used in the previously reported calculations. Constant values of conductivity  $K$ , density  $\rho$ , and specific heat  $C$  are equivalent to inputs used in reference 4, while  $dK/dT$ , the linear approximation to the temperature dependence of conductivity, is based on tabulated values of  $K$  [7]. Dependence of  $\rho$  and  $C$  on temperature are neglected. Thermal property inputs are summarized in table 2.

Table 2. Metal thermal properties

Property	Cu	Au
K(W m <sup>-1</sup> °C <sup>-1</sup> )	400	315
dK/dT(W m <sup>-1</sup> °C <sup>-2</sup> )	-5.9 x 10 <sup>-2</sup>	-5.3 x 10 <sup>-2</sup>
C(J kg <sup>-1</sup> °C <sup>-1</sup> )	385	130
ρ(kg m <sup>-3</sup> )	8960	19320
M.P. (°C)	1083	1064

Initial comparisons involved the energy density for melting Cu by a 100-ns rectangular pulse of 2.7 μm (HF) wavelength neglecting dK/dT. The MFDM approach produced a value of 53.2, the same as an earlier SINDA result [5], and in excellent agreement with a value of 52.2 computed by Sparks and Loh, who used an analytic model [4]. Further comparisons between MFDM and later SINDA computations [6] use actual waveforms and include dK/dT. The waveforms were approximated by a sequence of linear segments as illustrated for the HF pulse in figure 1. The original waveform data entered into SINDA were unavailable, requiring use of figures reproduced from reference 6. Computed and measured energy densities (J cm<sup>-2</sup>) required to melt Cu and Au with the HF pulse are given in table 3.

Table 3. HF damage calculations

One dimension						
		<u>SINDA</u>		<u>MFDM</u>		
	Cu	173	164 J/cm <sup>2</sup>			
	Au	100	94			
Two dimensions (axial symmetry)						
		53.4-μm spot			151-μm spot	
	<u>D&amp;U<sup>a</sup> &amp; 1D SINDA</u>	<u>D&amp;U<sup>a</sup> &amp; 1D MFDM</u>	<u>2D MFDM</u>	<u>Expt</u>	<u>2D MFDM</u>	<u>Expt</u>
Cu	234	175	176	194	166	155
Au	138	101	101	124	96	100

<sup>a</sup>Spot-size correction from Dobrovolskii and Uglov [8] applied to one-dimensional results.

Results of one-dimensional (infinite spot size) computations shown in the upper part of the table are in very good agreement, the small differences being easily accounted for by the approximate waveform used for MFDM. Two-dimensional results for two different spot sizes are compared in the lower part of table 3. The previously published computational results given in the first column at the lower left were obtained by applying a spot-size correction [8] for the  $53.4\text{-}\mu\text{m}$   $D(1/e^2)$  spot to the one-dimensional SINDA result. Application of the correction involves converting the thermal diffusion length for the actual waveform of figure 1 to that of an "equivalent" rectangular waveform, using the computed one-dimensional temperature-versus-depth profile as described in reference 6. The second column at the lower left of table 3 contains results of applying the spot-size correction procedure to the one-dimensional MFDM results. The third column gives the results of the full two-dimensional MFDM computation, while the fourth column contains corresponding measured melt thresholds [6]. The two columns at the lower right give comparisons of two-dimensional MFDM computed results with recently measured melt thresholds at a larger spot size of  $151\text{ }\mu\text{m}$   $D(1/e^2)$ .

The values in lower columns two and three of table 3 are in excellent agreement, demonstrating the consistency of the two-dimensional MFDM computation with the spot-size correction of reference 8. However, the disagreement with column one is substantial and clearly resulted from applying the wrong spot-size correction to the one-dimensional SINDA result. Figure 2 shows the Cu temperature-versus-depth profiles inferred from SINDA for a rectangular pulse (solid line) and for the actual HF pulse (dashed line), as given in figure 5 of reference 6. Recomputation by MFDM produces the crosses and solid dots, respectively, corresponding to the two waveforms. While the crosses properly fall on the solid line, there is a wide deviation of the dots from the dashed line, evidently from using the wrong SINDA-computed data in this case. The resulting discrepancies between inferred thermal diffusion lengths  $l_B$  and  $l'_B$  produce the large computational discrepancies in table 3. This example demonstrates the potential hazard of complex computations such as SINDA that are not under the user's immediate control.

Temperature profiles provided by the two-dimensional MFDM computation are shown in figure 3 as a function of the radial dimension at each of three depths below the Cu surface. The time corresponds to that of the peak surface temperature computed using the melt-threshold energy density.

Further MFDM computations of metal surface melt thresholds were carried out at  $3.8$  (DF) and  $10.6\text{ }\mu\text{m}$  ( $\text{CO}_2$ ) wavelengths with the waveforms indicated in figures 4 and 5, respectively, which are reproduced from reference 6. The DF and hybrid TEA laser waveforms again were approximated with linear segments. However, for the ordinary TEA waveform, an analytic expression [9] identical to that used in the SINDA computation [6] was used, permitting a more precise comparison between MFDM and SINDA in this case. Results of all of the one-dimensional computations are summarized in table 4.

In order to show the effect of neglecting the dependence of conductivity on temperature, the MFDM results are presented here both without and with inclusion of  $dK/dT$  in columns three and four, respectively. The % deviation of the MFDM from the SINDA results (column five) are shown in column six. For the  $\text{CO}_2$  TEA laser, where the waveform input is identical for both methods, the deviation is essentially zero. The DF case gives fortuitously good agreement, while the HF and  $\text{CO}_2$  hybrid MFDM computations, which also use approximate waveforms, produce modest discrepancies.

Table 4. One-dimensional MFDM versus SINDA

Melt thresholds (J/cm <sup>2</sup> )					
Pulse	Metal	MFDM <sup>a</sup>	MFDM	SINDA	%Dev
HF	Cu	171	164	173	-5.2
	Au	99	94	100	-6.0
DF	Cu	202	194	194	0
	Au	124	118	118	0
CO <sub>2</sub> TEA <sup>b</sup>	Cu	77	74	74	0
	Au	47	45	45	0
CO <sub>2</sub> Hybrid	Cu	357	342	384	-10.9
	Au	219	209	235	-11.1

<sup>a</sup>dK/dT = 0.<sup>b</sup>Identical waveform inputs for SINDA and MFDM.

In table 5, melt thresholds computed by two-dimensional MFDM (including dK/dT) are compared with measured thresholds reported in reference 6. The agreement indicated in

Table 5. Two-dimensional MFDM versus experiment

Melt Thresholds (J/cm <sup>2</sup> )					
Pulse	Spot(μm) <sup>a</sup>	Metal	MFDM	Measured <sup>b</sup>	%Dev
HF	53.4	Cu	176	194	-9.3
		Au	101	124	-18.5
DF	63.2	Cu	224	178	25.8
		Au	138	120	15.0
CO <sub>2</sub> TEA	242	Cu	74	69.8	6.0
		Au	45	43.4	3.7
CO <sub>2</sub> Hybrid	238	Cu	359	476	-24.5
		Au	220	276	-20.3

<sup>a</sup>Gaussian D(1/e<sup>2</sup>).<sup>b</sup>Porteus *et al.* [6].

the last column is acceptable in all cases, considering the inherent lack of precision in calibration and possible instability in the laser waveforms. Calibration errors are largely due to errors in the spatial profiles, which are measured by pinhole scans in the focal plane where the sample is tested. Pinhole-scan data are generally more precise for larger spots;



this probably is why the agreement at HF is better for the 151- $\mu\text{m}$  spot size (table 3, bottom right). The HF waveform tends to be more stable than the double-peaked DF pulse (fig. 4), possibly accounting for the larger average deviation from calculated values with the latter pulse. In the case of the  $\text{CO}_2$  hybrid pulse, there is considerable uncertainty in the relative amount of energy under the long tail at the end of the pulse (fig. 5). The comparatively low computed values of the thresholds (column four) suggest that the effective pulse length is longer than represented in the approximation.

### 3. Semiconductor Bulk Heating

As an example of bulk absorption in a nonlinear thermal medium, the heating of GaAs by a pulsed 0.69- $\mu\text{m}$  ruby laser is considered. In general, semiconductors present a much more complex problem than metals or insulators because the absorbed laser energy can be redistributed significantly by hot carriers or secondary photons before thermalization occurs [10]. However, MFDM shows that immediate local thermalization can provide a good approximation when the photon energy is somewhat greater than the band gap. Multiphoton absorption is also negligible here. These simplifications were assumed in the present computations, where the following empirical relationships are used for the temperature-dependent bulk absorption coefficient of GaAs [10]:

$$\begin{aligned}\alpha &\approx 1 \times 10^3 \exp[149 \text{ eV}^{-1}(E' - 1.38 \text{ eV})] \text{ m}^{-1} & ; E' < 1.48 \text{ eV} \\ &\approx 2.91 \times 10^6 \exp[3.22 \text{ eV}^{-1}(E' - 1.79 \text{ eV})] \text{ m}^{-1} & ; 1.426 < E' < 1.83 \text{ eV} \\ &\approx 3.48 \times 10^6 \exp[1.71 \text{ eV}^{-1}(E' - 1.83 \text{ eV})] \text{ m}^{-1} & ; 1.83 < E' < 2.5 \text{ eV},\end{aligned}\quad (1)$$

where  $E' \equiv h\nu + E_g(300^\circ\text{K}) - E_g(T)$ ,  $h\nu$  being the photon energy and  $E_g$  the band gap energy. The temperature dependence of  $E_g$  is obtained from [11]

$$E_g(T)(\text{eV}) = 1.519 - 5.405 \times 10^{-4} T(^{\circ}\text{K})^2/[T(^{\circ}\text{K}) + 204] \quad (2)$$

The Fresnel transmission of the GaAs surface in air at normal incidence is 0.662, based on the tabulated refractive index of 3.78 at 0.69  $\mu\text{m}$  [12]. The temperature dependence is probably quite small and is neglected.

The temperature-dependent thermal conductivity and specific heat of GaAs are expressed, respectively, as [11]

$$K(T) \approx 54 [300/T(^{\circ}\text{K})]^{1.2} \text{ W m}^{-1} ^{\circ}\text{C}^{-1} \quad (3)$$

and

$$C(T) \approx 307 + 0.0725T(^{\circ}\text{K}) \text{ J kg}^{-1} ^{\circ}\text{C}^{-1} \quad (4)$$

The density is taken as 5230  $\text{kg m}^{-3}$ , independent of  $T$ .

Using the above inputs MFDM was applied to compute surface melt thresholds of bulk GaAs, which were then compared with experimental values reported in the literature [13-15]. One-dimensional modeling was used, which is an excellent approximation for times far longer than the reported pulse lengths, provided the spot size is  $\sim 1$  mm or larger (reported only in ref. 14). Reported pulse lengths were assumed to correspond to the full width at half maximum (FWHM) of the Gaussian waveform used in the computation. Results are summarized in table 6.

Table 6. GaAs melt thresholds

Pulse (ns) <sup>a</sup>	MFDM (MW cm <sup>-2</sup> ) <sup>b</sup>	Measured (MW cm <sup>-2</sup> ) <sup>b</sup>	%Dev.	Reference
20	9.4	8 ± 2	+13	[13]
30	7.4	12.2	-39	[14]
40	6.1	4.9	+24	[15]

<sup>a</sup>FWHM of Gaussian pulse<sup>b</sup>Peak power density

Clearly, computed values fall within the experimental scatter. The magnitude of the scatter is typical of results on different samples measured in different laboratories.

To demonstrate application of MFDM to layered structures, the above modeling was applied to a 1- $\mu$ m-thick GaAs film on a fused quartz substrate. Since less than 1% of the incident 0.69- $\mu$ m light is reflected at the GaAs/quartz interface, interference effects and heating of the film by back-reflected light may be neglected. Thermal properties of fused quartz used in the computation are summarized in table 7 [16,17].

Table 7. Fused quartz

Property	Value
K(W m <sup>-1</sup> °C <sup>-1</sup> )	1.37
dK/dT(W m <sup>-1</sup> °C <sup>-2</sup> )	3.0 x 10 <sup>-3</sup>
C(J kg <sup>-1</sup> °C <sup>-1</sup> )	782
dC/dT(J kg °C <sup>-2</sup> )	0.6
$\rho$ (kg m <sup>-3</sup> )	2100

The two-component structure was modeled in one dimension using a 30-ns FWHM Gaussian pulse with a peak power density of 5 MW/cm<sup>2</sup>. The temporal behavior is shown at three positions within the structure in figure 6. Time zero is taken arbitrarily at 42 ns before the peak of the laser pulse. Figure 7 shows the temperatures plotted as a function of depth referenced to the GaAs/quartz interface for three successive times on the time scale of figure 6. The maximum temperature of 748°C occurs on the front surface approximately 18 ns after the peak of the pulse. Because of the relatively fast thermal diffusion within the GaAs, the temperatures within this material rapidly reach a quasi-equilibrium value; the temperature gradient in the quartz moderates much more gradually. Further development of MFDM to deal with absorption of standing waves in multilayer structures is planned.

#### 4. Flashlamp Heating of Water-Cooled Laser Glass

To demonstrate the potential of MFDM for design of water-cooled systems, the final example considers repetitive pulsed flashlamp heating of water-cooled NS-0835 laser glass in three configurations. The material properties (assumed constant) can be found in reference 18. The input flashlamp pulse is 7  $\mu$ s long and has a repetition frequency of 10 Hz. The glass is assumed to absorb 9 J of energy per pulse distributed uniformly within its volume.

A 3/16-in.-diameter by 3-in.-long rod is the first configuration considered. It is cooled with 20°C water on its outer curved surface. A value of 1 W cm<sup>-2</sup> °C<sup>-1</sup> was assumed for the surface transfer coefficient at the glass-water interface, based on information on page 20 of reference 1. Figure 8 shows computed temperatures at the center and on the surface opposite the center of the rod for three pulses. The low rate of diffusion prevents cooling of the center and return to ambient temperature at the surface after each pulse. Figure 9, which is presented on a longer time scale, shows the slow recovery to ambient if the heating is terminated after the third pulse. These results are consistent with observations in our laboratory.

Temperature profiles along a radius of the rod for increasing numbers of repetitive pulses up to 16 are shown in figure 10. The central temperature continues to increase to unacceptably high levels with little tendency toward equilibration. The two other configurations considered are slab geometries with the same water cooling on both of the larger slab faces. The thicker slab has a cross section of 1/8 x 7/32 in., and the thinner one is 1/16 x 7/16 in. Both slabs, like the rod, are 3 in. long, and the volume of material is very nearly the same in all three configurations. With the same uniform heat load for 16 pulses, the temperature profiles across the shortest dimension in each case are as indicated in figure 11. It is apparent that central temperatures are not reduced appreciably in the thicker slab compared to the rod, but a significant reduction is achieved with the thinner slab geometry.

#### 5. Conclusion

A capable method for microcomputer finite-difference modeling of laser heating and melting has been validated by reproducing results previously obtained by other methods. As demonstrated by examples, the method is flexible and does not require a mainframe computer or a computer specialist to implement. The discovery of an error in an earlier published result illustrates the hazards of computations that cannot be adequately verified. Laser-induced melt thresholds of metal surfaces computed by the newer method are in satisfactory agreement with experiments on diamond-turned samples. A realistic representation of the actual waveform is found to be important if accuracy is to be maintained. Computed thresholds for surface melting of GaAs by pulsed ruby lasers fall within the scatter of measured values without the added complication of thermal redistribution mechanisms. Application to problems involving layered optical components was demonstrated.

#### 6. Acknowledgments

The author is indebted to Avraham Amith of ITT Electro-Optical Products Division and to Teri L. Cole of the Naval Weapons Center for providing references and information on GaAs.

## 7. References

- [1] Carslaw, H. S.; Jaeger, J. C. *Conduction of heat in solids*. 2nd ed. Oxford; Oxford University Press; 1959.
- [2] Gaski, J. D.; Fink, L. C.; Ishimoto, T. "Systems improved numerical differencing analyzer," TRW Systems Rep. 11027-6003-RO-00; Sept. 1970.
- [3] Reece, G. *Microcomputer modeling by finite differences*. New York; John Wiley & Sons; 1986.
- [4] Sparks, M.; Loh, E., Jr. "Temperature dependence of absorption in laser damage of metallic mirrors: I. Melting," *J. Opt. Soc. Am.* **69**; 847-858; 1979.
- [5] Porteus, J. O.; Decker, D. L.; Grandjean, D. J.; Seitel, S. C.; Faith, W. N. "Defect-damage-resistant copper mirrors," in *Laser induced damage in optical materials: 1979*. Bennett, H. E.; Glass, A. J.; Guenther, A. H.; Newnam, B. E., ed. 1979 October 30-31; Boulder, CO. Nat. Bur. Stand. (U.S.) Spec. Publ. 568; 1980 July. Pp. 175-186.
- [6] Porteus, J. O.; Decker, D. L.; Faith, W. N.; Grandjean, D. J.; Seitel, S. C.; Soileau, M. J. "Pulsed laser-induced melting of precision diamond-machined Cu, Ag, and Au at infrared wavelengths," *IEEE J. Quantum Electron.* **QE-17**; 2078-2085; 1981.
- [7] Weast, R. C. ed. *CRC handbook of chemistry and physics*, 64th ed. Boca Raton, FL; CRC Press, Inc.; 1983-1984. P. E-9.
- [8] Dobrovolskii, I. P.; Uglov, A. A. "Analysis of the heating of solids by laser radiation allowing for the temperature dependence of the absorptivity," *Sov. J. Quantum Electron.* **4**, 788-790; 1974.
- [9] Porteus, J. O.; Soileau, M. J.; Bennett, H. E. "Laser damage measurements at CO<sub>2</sub> and DF wavelengths," in *Laser induced damage in optical materials: 1975*, Glass, A. J.; Guenther, A. H., ed. 1975 July 29-31; Boulder, CO. Nat. Bur. Stand. (U.S.) Spec. Publ. 435; 1976 April. Pp. 207-215.
- [10] Meyer, J. R.; Kruer, M. R.; Bartoli, F. J. "Optical heating in semiconductors: Laser damage in Ge, Si, InSb, and GaAs," *J. Appl. Phys.* **51**; 5513-5522; 1980.
- [11] EMIS Group. *Properties of gallium arsenide: Data review series No. 2*. London and New York; Inspec Publishers; 1986. Section 1.
- [12] Palik, E. D., ed. *Handbook of optical constants of solids*. New York; Academic Press, Inc.; (1985). P. 439.
- [13] Smith, J. L.; Tanton, G. A. "Intense laser flux effects on GaAs," *Appl. Phys.* **4**; 313-315; 1974.
- [14] Birnbaum, M.; Stocker, T. L. "Reflectivity enhancement of semiconductors by Q-switched ruby lasers," *J. Appl. Phys.* **39**; 6032-6036; 1968.
- [15] Blinov, L. M.; Vavilov, V. S.; Galkin, G. N. "Changes in the optical properties and carrier density in Si and GaAs due to strong photoexcitation with a ruby laser," *Soviet Phys.—Semicon.* **1**; 1124-1129; 1967.



- [16] Weast, R. C., ed. *CRC handbook of chemistry and physics*, 64th ed. Boca Raton, FL; CRC Press; 1983-1984. P. E-6.
- [17] Knoll, M. *Materials and processes of electron devices*. New York; Springer-Verlag; 1959. P. 224.
- [18] Pressley, R. J., ed. *CRC handbook of lasers*. Boca Raton, FL; CRC Press; 1971. Pp. 362, 363.

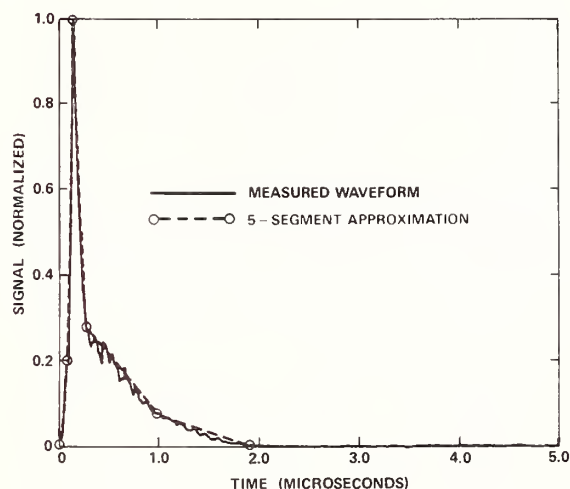


Figure 1. HF waveform used for melt-threshold measurements with linear-segment approximation used in MFDM computation of thresholds.

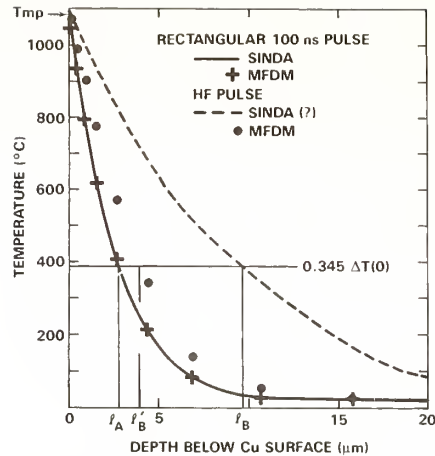


Figure 2. One-dimensional profiles of temperature versus depth in Cu at HF computed at the surface melt threshold when the surface has reached the melting point. Different curves/points correspond to different input waveforms or computational methods. Significance of the thermal diffusion lengths indicated on the depth axis is explained in the text.

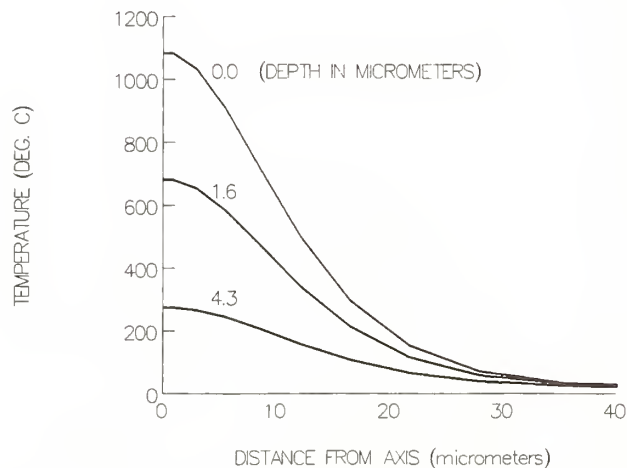


Figure 3. Two-dimensional profiles of temperature - versus - radial distance from the beam axis in Cu at HF computed by MFDM. Different curves represent different depths below the surface. The energy density on axis is at the surface melt threshold ( $176 \text{ J cm}^{-2}$ ), and the surface is at the melting point. The spot size is  $53.4 \text{ } \mu\text{m } D(1/e^2)$ .

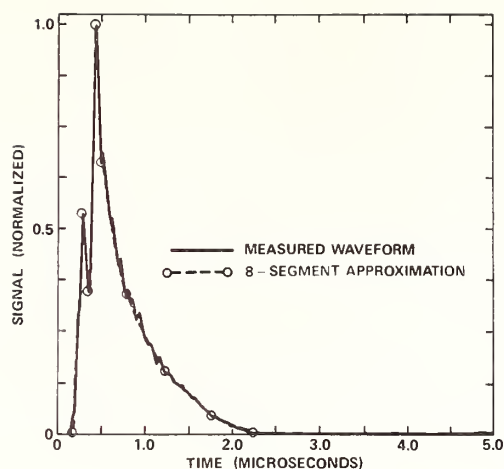


Figure 4. DF waveform used for melt-threshold measurements with linear-segment approximation used in MFDM computation of thresholds.

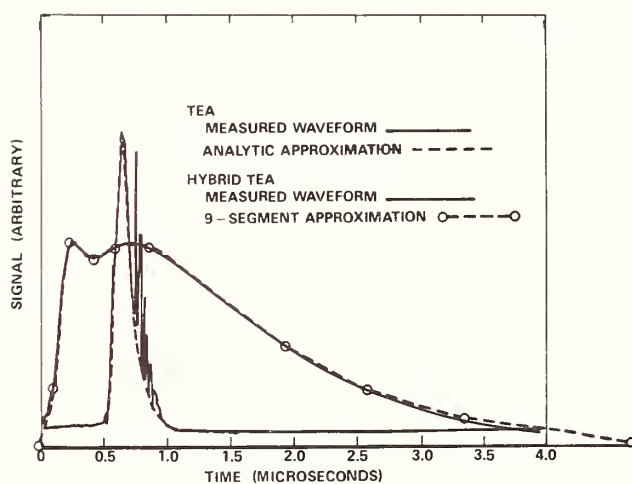


Figure 5.  $\text{CO}_2$  waveforms used for melt-threshold measurements. For computation with both SINDA and MFDM, the TEA waveform was approximated by an analytic function with linear rise and exponential decay [9]. The linear-segment approximation indicated was used in MFDM computation of thresholds measured with the hybrid TEA waveform.

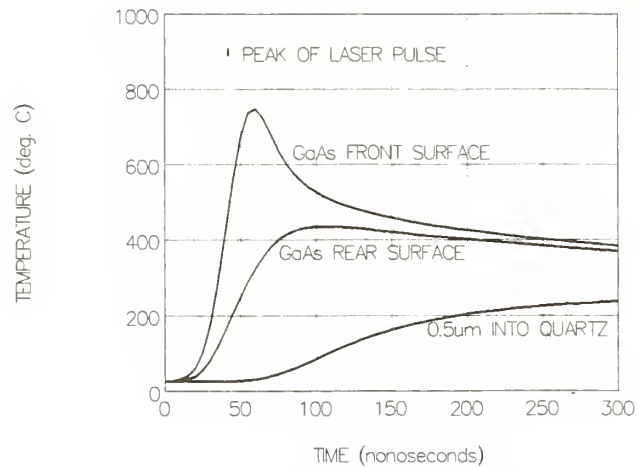


Figure 6. Dependence of temperature on time at three depths in GaAs on quartz computed by MFDM. The laser pulse peaks at the time indicated by the short vertical bar.

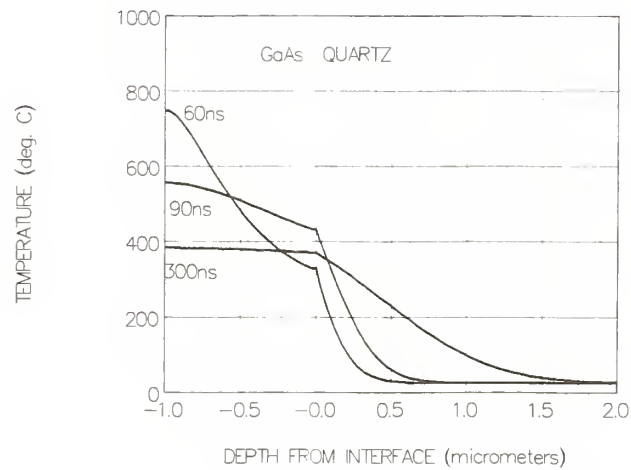


Figure 7. Dependence of temperature on depth measured from the substrate interface in GaAs on quartz. The curves represent three different instants of time on the time scale of figure 6.



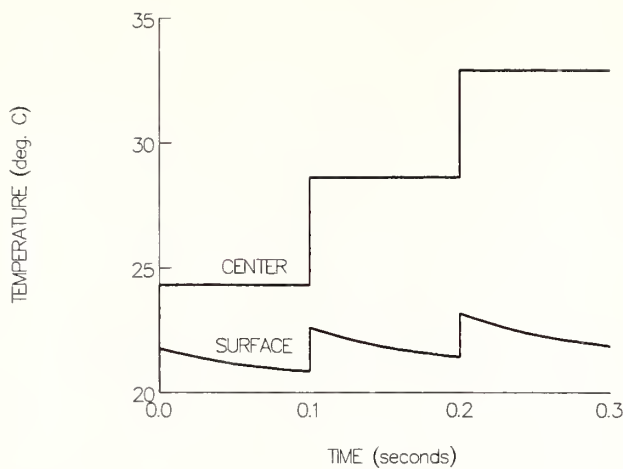


Figure 8. Computed temperature rise of a flashlamp-heated, water-cooled NS-0835 glass rod at its center and surface during a sequence of three flashlamp pulses.

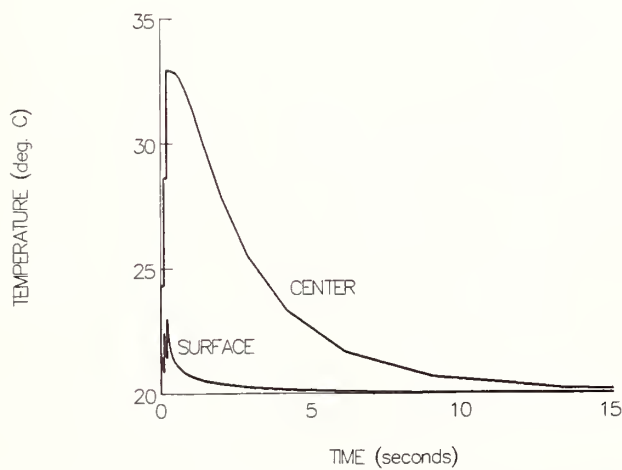


Figure 9. Computed temperature rise and fall of the flashlamp-heated, water-cooled NS-0835 glass rod during and after a sequence of three flashlamp pulses. The time scale is 50 times longer than in figure 8.

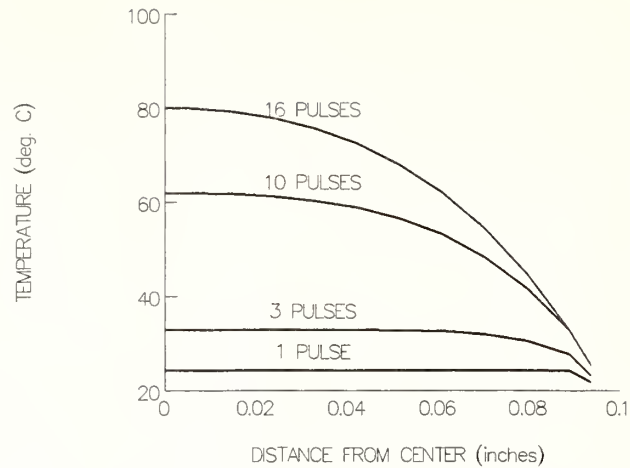


Figure 10. Computed profiles of temperature-versus-radial distance from the center in the flashlamp-heated, water-cooled NS-0835 glass rod. Different curves correspond to pulse trains of different lengths.

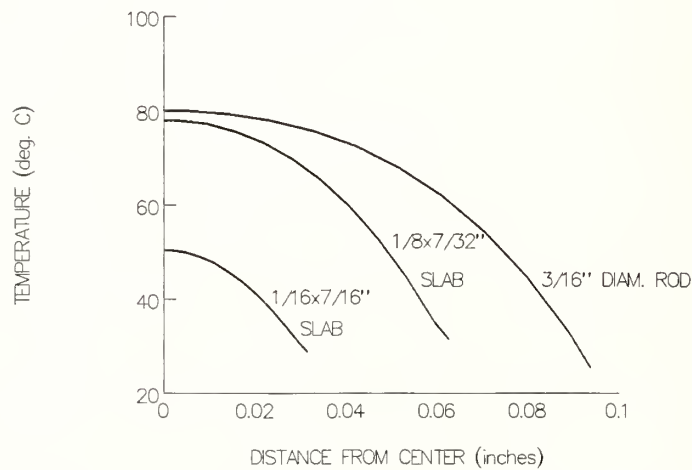


Figure 11. Computed profiles of temperature versus distance from the center in the flashlamp-heated, water-cooled NS-0835 glass rod and slabs of the same volume for a train of 16 pulses. Curves correspond to the three different cross-sectional configurations.

Accumulated Surface Damage on ZnS Crystals Produced by Closely Spaced  
Pairs of Picosecond Laser Pulses\*

L. L. Chase and H. W. H. Lee

Lawrence Livermore National Laboratory  
Livermore, CA 94550

Excitation of a transparent ZnS crystal by repetitive picosecond dye laser pulses causes an accumulated surface modification leading to optical damage. The onset of the damage is detected by an abrupt increase in the emission of neutral Zn (and possibly  $S_2$ ) from the surface. Comparison of the neutral emission thresholds with pulse-pair and single-pulse excitation shows that linear absorption is the dominant laser-surface interaction. In general, this measurement technique shows considerable promise for investigating the possible influence of nonlinear absorption or excitation processes on damage mechanisms. The data suggest that heating of small absorbing regions produces the surface modification that leads to the observed surface ablation. The nature of the damage observed at fluences above the threshold suggests that it is caused by heating of a relatively large ( $\sim 10 - 100 \mu\text{m}$ ) surface region that has been modified by the accumulation pulses.

Key words: surface damage; accumulation; picosecond; neutral species emission

## 1. Introduction

The interaction of intense laser beams with the surfaces of transparent optical materials can involve linear and nonlinear absorption caused by surface states, defects and impurities. Direct measurement and characterization of these interactions is very difficult. It is known, however, that laser excitation of many materials causes the emission of charged and neutral surface constituents and impurities. The characteristics of the emitted products, such as the identity of the emitted species, velocity distributions, absolute and relative yields, and internal excitations, provide useful information regarding the laser-surface interaction[1,2]. In previous work on ZnS with nanosecond lasers at wavelengths above and below the interband absorption threshold, it was found that Zn, S, and possibly  $S_2$  were emitted at laser fluences below the threshold for observable optical damage[1]. In this work we measured the yield of neutral Zn and S from surfaces of ZnS single crystals caused by multiple-pulse excitation with a picosecond dye laser at a wavelength of 580 nm, which is much longer than the interband absorption threshold of about 330 nm. This wavelength is, however, well within the region of two-photon bulk absorption[3]. In this circumstance two photon absorption involving bulk, surface, or defect levels may be a significant factor in optical damage mechanisms, particularly for picosecond pulses, which have high peak intensities at the damage threshold.

## 2. Experimental Procedure

The experimental setup is shown in figure 1. The sample was irradiated in a vacuum system at a pressure of about  $10^{-9}$  torr using a picosecond dye laser operating at 10 Hz with a pulsewidth of 1.5 ps and a pulse energy of up to 300  $\mu\text{J}$ . The laser was focused to a spot diameter of about 150  $\mu\text{m}$ , yielding fluences of up to about 1.3  $\text{J}/\text{cm}^2$ . A quadrupole mass spectrometer was used with a reduced mass resolution to detect the emitted Zn at masses 64 - 68 amu. It is also possible that  $S_2$  (mostly mass 64 amu and some at 66 amu) is detected, although its presence in the emission is not established with certainty because of its mass overlap with Zn. The output of the mass spectrometer was sampled by a gated integrator for a time interval of 1 ms following the laser pulse. The polished surface of the crystal was cleaned in methanol and heated in vacuum to 300 C to desorb contaminants. Data were collected using multiple excitation on each of a grid of spots separated by about 1 mm on the sample surfaces.

\*Work performed under the auspices of the Division of Materials Sciences of the Office of Basic Energy Sciences, U.S. Department of Energy by the Lawrence Livermore National Laboratory under Contract No. W-7405-ENG-48.

### 3. Experimental Results and Discussion

At low fluences with 10 Hz excitation the neutral emission from the surface is very weak and is not detectable at the sensitivities used for this work. This is consistent with the behavior of the Zn emission yields observed below the optical damage threshold in our previous experiments[1], which showed that the surface sites from which atoms are desorbed at low fluences are bleached after a few laser pulses. At a rather well-defined threshold fluence, however, a large flux of neutrals is observed after several hundred pulses, and the number of pulses required to initiate the emission decreases very rapidly with increasing fluence. This is illustrated in figures 2 and 3. In figure 2 the emission yields from each of several different sites are plotted as a function of time in traces (a) - (e). The abscissa is labeled by the cumulative number of excitation pulses. The fluence per pulse was increased at successive spots. At the lowest fluence,  $0.38 \text{ J/cm}^2$ , no emission was observed for up to 3800 pulses. On the next site, the fluence per pulse was increased to  $0.4 \text{ J/cm}^2$ , and emission was observed after about 300 pulses. Traces (c) - (e) show that the number of pulses required to initiate emission decreases rapidly with increasing fluence. This is evident in figure 3, where the number of required pulses is plotted as a function of pulse fluence for a series of initially virgin spots. This procedure was repeated several times, and it was found that the threshold fluence was repeatable to within about 20 - 30 percent. For this case of excitation by a single pulse every 100 ms, we define the single-pulse threshold fluence  $F_t(1)$  for which the emission increase is observed after at most 1000 pulses. We found visible damage on each grid spot for which the threshold fluence was attained. The form of this damage will be discussed below. The important point is that the neutral emission threshold corresponds to the multiple-pulse optical damage threshold.

The threshold fluence was measured for excitation by pairs of identical picosecond pulses separated by various time delays,  $\tau$ .  $F_t(2,\tau)$  is defined as the sum of the fluences of the two pulses. The threshold fluence for the pulse pair (twice the fluence of each pulse) was compared with the threshold fluence for a single pulse. The ratio  $R = F_t(2,\tau)/F_t(1)$  is plotted in figure 4 as a function of  $\tau$ . For  $\tau < 2 \text{ ps}$ , the two pulses form interference fringes on the surface, and the peak fluence in the fringe maxima is twice as large as for a single pulse of the same fluence. This accounts for the value of  $R \sim 0.5$  for small time delays.

For  $2 \text{ ps} < \tau < 1 \text{ ns}$ ,  $R$  is approximately unity. This result implies that the threshold is determined by the total fluence of the pulse pair. When the pulses have no temporal overlap, which is the case in this range of time delays, emission resulting from multiphoton or other superlinear interaction processes would occur at a higher fluence than for a single pulse, since the intensity of each pulse of the pulse pair is half as large as for the single pulse. For example, the total absorbed energy due to two-photon absorption is proportional to the number of pulses times the square of the peak intensity. If this absorbed energy determines the emission threshold, we should find  $R = \sqrt{2}$ . For nonlinear absorption proportional to  $I^n$  the appropriate value of  $R$  is  $R = 2^{1-1/n}$ .

For  $\tau > 1 \text{ ns}$ , the ratio  $R$  increases toward the value  $R = 2$  that is expected if the pulses act independently on the surface, and each pulse must exceed the single-pulse threshold fluence. The simplest model that accounts for the changes with pulse separation is that the cooperative effects caused by the two pulses decay exponentially with increasing pulse separation with a time constant  $\tau_m$ . This is equivalent to assuming that the relevant surface excitation produced by the first pulse decays with this time constant and its effective fluence is reduced by  $\exp(-\tau/\tau_m)$ . Then the ratio  $R$  is determined from the condition that the effective fluence of the two pulses at the emission threshold be equal to that of the single pulse threshold:

$$F_t(2,\tau) \exp(-\tau/\tau_m)/2 + F_t(2,\tau)/2 = F_t(1) \quad (1)$$

The ratio  $R$  obtained from eq. (1) is

$$R = [1 + \exp(-\tau/\tau_m)]^{-1}. \quad (2)$$



The dotted curve in figure 4 gives a reasonable fit of this function to the data for a "memory time"  $\tau_m = 5$  ns.

Heating is a possible explanation for this "memory time" in the double-pulse threshold behavior. The approximate distance over which heat diffuses in a time  $\tau_m$  is  $d = (\kappa\tau_m)^{1/2}$ , where  $\kappa$  is assumed to be the bulk thermal diffusivity of ZnS. For  $\tau_m = 5$  ns, this assumption yields  $d = 0.1$   $\mu\text{m}$  as the approximate dimension of the heated regions of the sample surface. This could correspond to the size of absorbing inclusions or it could be the depth of an absorbing region near the surface produced by damage introduced in the polishing process. It is possibly significant that a similar size estimate was made based on surface temperatures obtained from Doppler shifts of ablated Zn atoms caused by laser excitation above the bandgap of ZnS<sup>2</sup>. In ref. 2, much higher effective particle temperatures were observed than could be accounted for using the known interband absorption coefficient and the bulk thermal diffusivity of ZnS. It was suggested that these high temperatures resulted from heating of a thermally isolated region of 0.1  $\mu\text{m}$  dimensions by the interband absorption. In the present experiments, bulk interband absorption does not, of course, play a role. It is possible that some form of surface absorption, rather than bulk interband absorption, is also responsible for the emission observed in ref. 2.

How can heating account for the progressive surface modification implied by the accumulation effect involved in the multiple-pulse damage? It is known that ZnS sublimates at the relatively low temperature of 1200 C. Since the sublimation rate increases very rapidly with increasing temperature, the degree of surface modification caused by this process would have a threshold-like behavior as a function of laser fluence. If the sublimation process is not congruent, it will lead to the production of surface defects through loss of stoichiometry. In our previous experiments with excitation by single nanosecond pulses, we did in fact find evidence that the Zn emission was delayed relative to the S emission following a laser pulse[1]. This time delay provides evidence that the two constituents desorb at different rates, with the likely result being a surface that is deficient in sulfur. This anion deficiency could result in the production of color centers, such as F centers, near the surface. This type of surface modification could produce enough defects to cause a catastrophic runaway in the cycle of absorption of light and the consequent production of additional absorbing defects.

There are other possible causes for the memory effect implied by the data in figure 4. Electronic excitation can exist for several nanoseconds after a short pulse, either in the form of localized excitations or as free carriers. Deeply trapped carriers form color centers which could enhance the absorption of the second pulse. Free carriers produced by the first pulse could likewise cause additional absorption and heating during the second pulse. An accumulation effect would appear to be unlikely in either case, since the original absorbing site would be bleached, leading to no net increase in the absorbing sites. A second possibility involves the emitted neutrals produced by the first laser pulse, which travel only a few microns from the surface within the 5 ns memory time. Ionization and heating of these neutrals by the second laser pulse could lead to surface bombardment, resulting in ablation or heating. This process is not a likely cause of the accumulation effect since the ionization of Zn or S requires about 10 eV of energy and would involve a four-photon absorption, which is not consistent with the observed value of R.

After the sample was removed from the vacuum chamber, it was investigated using Nomarski microscopy. A typical damage site is shown in figure 5. At this site, laser excitation was halted very soon (several tens of pulses) after neutral emission was observed. The damage spot, which appears elongated because of the excitation at 45° to the surface normal, covers a sizeable fraction of the laser focal spot. We saw no evidence of clearly defined nucleation sites for the damage at most irradiated spots on the crystal. Either the damaged regions spread very rapidly on successive shots or the damage is initiated over a rather large area. The damaged surface acquires a granular structure, which suggests that material is removed either by plasma ablation or by sublimation, rather than by melting.

The accumulation effects observed in this work may well be related to damage caused by single and multiple-pulse excitation at much longer pulse lengths than we have used. Since total fluence is the important parameter determining the threshold for the accumulation process, the same surface modification must also proceed during excitation by longer laser pulses. The important point is that when either prolonged or repetitive excitation creates a critical level of surface defects, optical damage will occur either during a long pulse or on a subsequent short pulse.

#### 4. Conclusions

These experiments show that nonlinear excitation of any type is not involved in the accumulation effect leading to multiple-pulse damage on ZnS despite the very large intensities,  $> 50 \text{ Gw/cm}^2$ , of the picosecond pulses at the threshold fluence. The total fluence of the pulses is the important parameter. It is most likely that the accumulation is caused by the heating of either small absorbing defects or by a thin surface layer, with a typical dimension of  $0.1 \mu\text{m}$  in either case. Efforts are underway to detect changes in surface composition resulting from laser excitation in order to characterize the accumulated surface modification. The use of picosecond pulse-pair excitation to investigate the duration of surface excitations leading to optical damage is a promising technique that is currently being applied to other materials.

We are grateful to M. D. Perry and O. L. Landen for the use of their Short Pulse Laser Facility and to Robert Hughes for assistance with the experiments.

#### 5. References

- [1] Chase, L. L.; Smith, L. K., Laser Induced Surface Emission of Neutral Species and its Relationship to Optical Surface Damage Processes. Nat. Bur. Stand. (U.S.) Spec. Publ.; (Laser Induced Damage in Optical Materials: 1987) - to be published.
- [2] Arlinghaus, H. F.; Calaway, W. F.; Young, C. E.; Pellin, M. J.; Gruen, D. M.; Chase, L. L., High Resolution Multiphoton Laser-induced Fluorescence Spectroscopy of Zinc atoms Ejected from Laser-irradiated ZnS Crystals. Journ. Appl. Phys., to be published.
- [3] Bae, Y.; Song, J. J.; Kim, Y. B., Photoacoustic Study of Two-photon Absorption in Hexagonal ZnS. J. Appl. Phys. 53, 615 (1982).

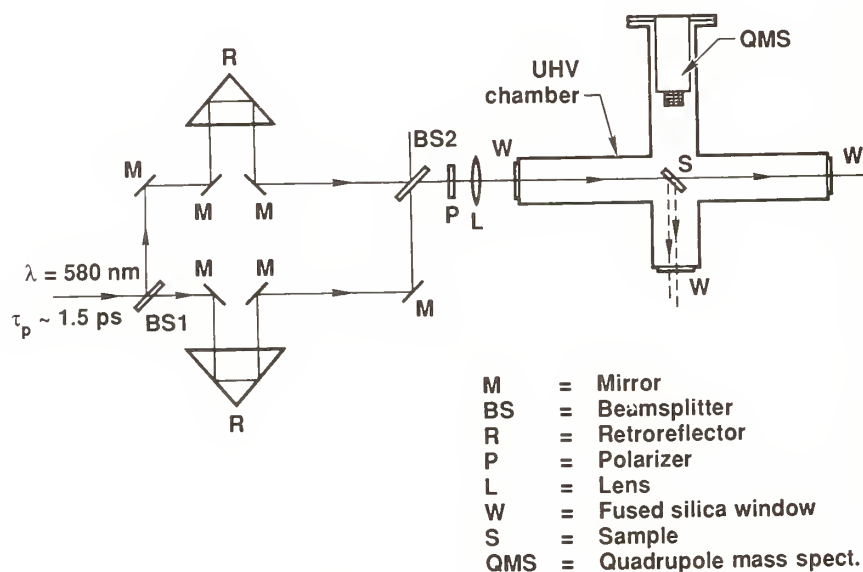


Figure 1. Schematic of UHV system and picosecond pulse pair excitation setup.

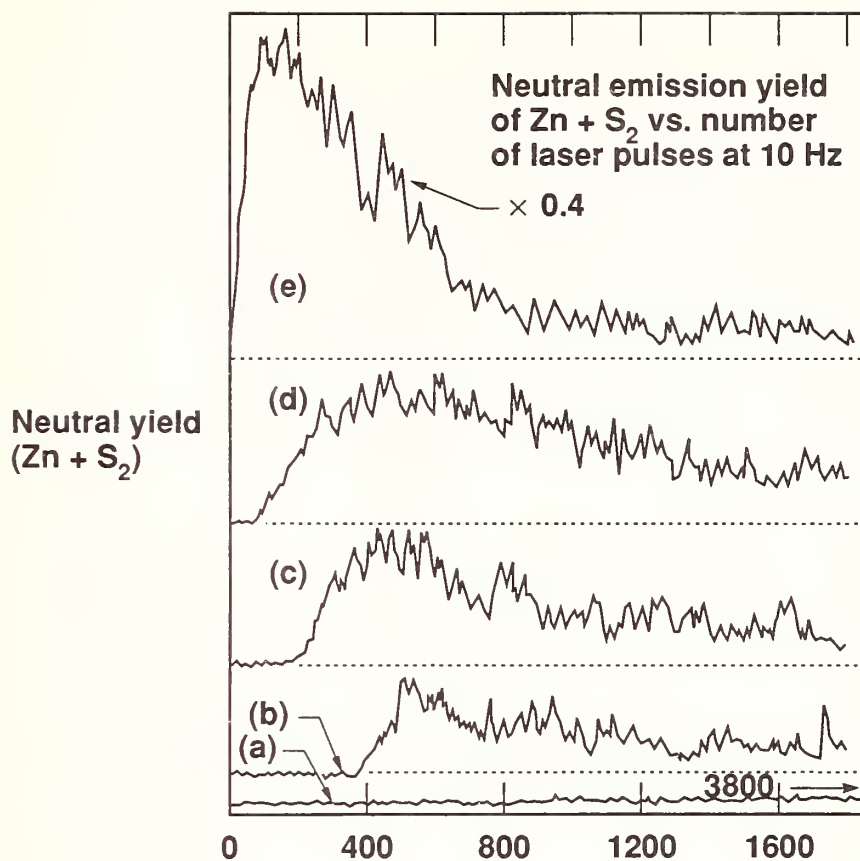


Figure 2. Neutral emission yield for picosecond pulse excitation of ZnS at a 10 Hz repetition rate. Approximate fluences (J/cm<sup>2</sup>) are: (a) 0.38, (b) 0.4, (c) 0.43, (d) 0.56, (e) 1.35.

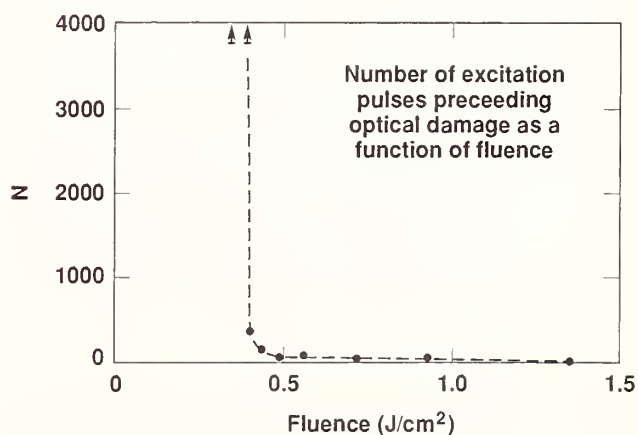


Figure 3. Number of pulses required to produce neutral emission and damage as a function of pulse fluence.

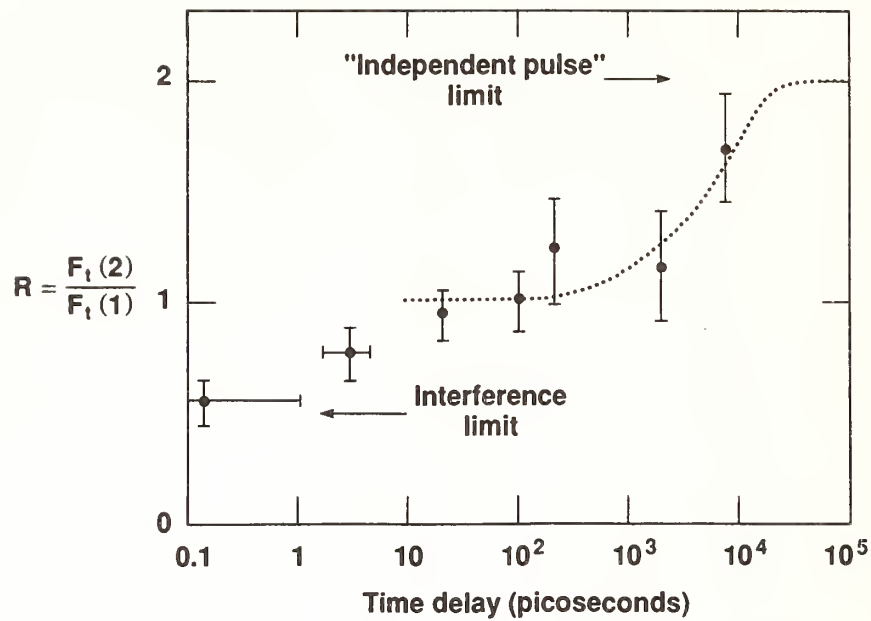


Figure 4. Ratio of threshold fluences for pulse-pair and single-pulse excitation as a function of pulse-pair separation. The dotted line is calculated from eq. (2) with  $\tau_m = 5$  ns.

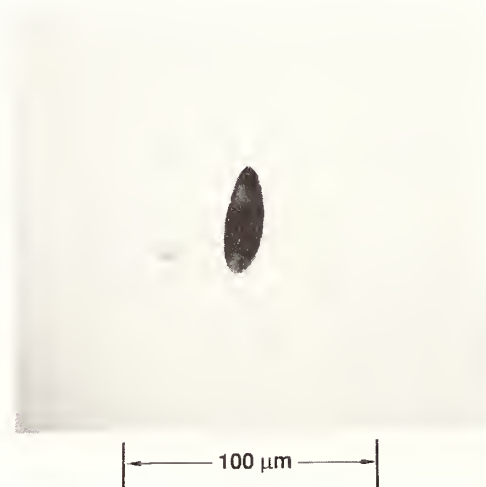


Figure 5. Nomarski micrograph of optical damage observed at the threshold fluence.



#### DISCLAIMER

This document was prepared as an account of work sponsored by an agency of the United States Government. Neither the United States Government nor the University of California nor any of their employees, makes any warranty, express or implied, or assumes any legal liability or responsibility for the accuracy, completeness, or usefulness of any information, apparatus, product, or process disclosed, or represents that its use would not infringe privately owned rights. Reference herein to any specific commercial products, process, or service by trade name, trademark, manufacturer, or otherwise, does not necessarily constitute or imply its endorsement, recommendation, or favoring by the United States Government or the University of California. The views and opinions of authors expressed herein do not necessarily state or reflect those of the United States Government thereof, and shall not be used for advertising or product endorsement purposes.

## 1053-nm High-Field Effect in Monomeric and Polymeric Conjugated Systems

M. Guardalben, A. Bevin, K. Marshall, and A. Schmid

Laboratory for Laser Energetics  
University of Rochester  
Rochester, NY 14623-1299

and

F. Kreuzer

Consortium f. Elektrochemische Industrie GmbH  
D-8000 Munchen  
Federal Republic of Germany

Organic liquids and solids, i.e., monomeric and polymeric liquid crystals, of varying aromaticity have been investigated for their 1053-nm, 0.8 ns optical survival strength in high-power laser fields. We report that the higher a material's degree of delocalization the lower its near-IR damage threshold. This is in accordance with earlier reports of third-order nonlinear susceptibilities being tied to the degree of charge delocalization in aromatic molecules. Laser damage in aromatic materials is therefore driven more by  $\chi^{(3)}$  and less by extrinsic effects such as absorbing impurities. The importance of these findings in selecting liquid-crystalline optical devices for high peak-power, near-IR laser systems is pointed out.

Key words: aromaticity; conjugation; laser-induced damage; liquid crystals; pi-bonds; third-order nonlinear susceptibility

### 1. Introduction

Organic, conjugated  $\pi$ -electron molecular and polymeric materials offer great promise for high-power laser applications. Their advantage over conventional materials lies in the flexibility that organic synthesis offers for their design. By the same approach that leads to the design of other organic compounds, especially pharmaceutical ones, organic materials with specific linear or nonlinear optical properties can now be defined, designed, and characterized in terms of optical response. The most important properties in this regard are absorption at certain wavelengths, nonlinear susceptibilities, fast response times, and high-power laser-damage thresholds.

The OMEGA laser is among the first to employ organic optical devices in significant numbers [1]. The majority of these devices are liquid-crystal-based circular polarizers developed and manufactured in-house.

Other devices use the linear birefringence of monomeric liquid-crystal molecules and usually comprise an eutectic mixture of several types of such molecules. In preparing devices for  $5 \text{ J cm}^{-2}/1\text{-ns}$  applications, the question arises whether an improved laser-damage threshold can be engineered in an acceptable tradeoff with other parameters by changing the eutectic's composition. After elimination of compounds because of unsuitable linear absorption properties, the choice is between highly conjugated and more saturated compounds.

There are predictions that the nonlinear optical susceptibilities of organic systems are affected by the degree of conjugation. For  $\chi^{(2)}$ , ample experimental evidence [2] supports this contention. For  $\chi^{(3)}$ , less data exist. Because  $\chi^{(3)}$  affects self-focusing, and because in the absence of extrinsic impurities self-focusing is a dominant mechanism for laser damage in many transparent materials, we tested the extent to which the damage threshold in some organic materials is affected by the degree of conjugation.

## 2. Experiments

Three model compounds were chosen for this test: two monomers and one polymer. We report first on the nematic monomers and then on the cholesteric polymer. One monomeric,  $\pi$ -electron-rich compound was 4-octyl-cyanobiphenyl, which is a liquid crystal with a nematic mesophase at room temperature. Its saturated counterpart, 4-octyl-cyanobicyclohexyl, was also tested. As shown in figure 1, the two compounds differ structurally only in their aromatic and saturated cores. The bicyclohexyl compound is commercially available under the trade name ZLI-S-1185 and has a nematic phase starting at  $62^\circ\text{C}$  [3]. Laser

**Damage Threshold Comparison of Two Model Compounds**  
(800-ps pulse length, 100- $\mu\text{m}$  path length, 5-mm spot size, linear polarization)

Compound	K-15	ZLI-1185
Structure	$\text{CH}_3-(\text{CH}_2)_4-\text{C}_6\text{H}_4-\text{C}_6\text{H}_4-\text{CN}$	$\text{CH}_3-(\text{CH}_2)_4-\text{C}_6\text{H}_{10}-\text{C}_6\text{H}_{10}-\text{CN}$
Mesophase	nematic ( $22^\circ\text{C}$ )	nematic ( $62^\circ\text{C}$ )
1-on-1 ( $\text{J}/\text{cm}^2$ )	$9.6 \pm 2.4$	$>16.6^*$
N-on-1 ( $\text{J}/\text{cm}^2$ )	$5.4 \pm 1.3$	$14.6 \pm 0.5$

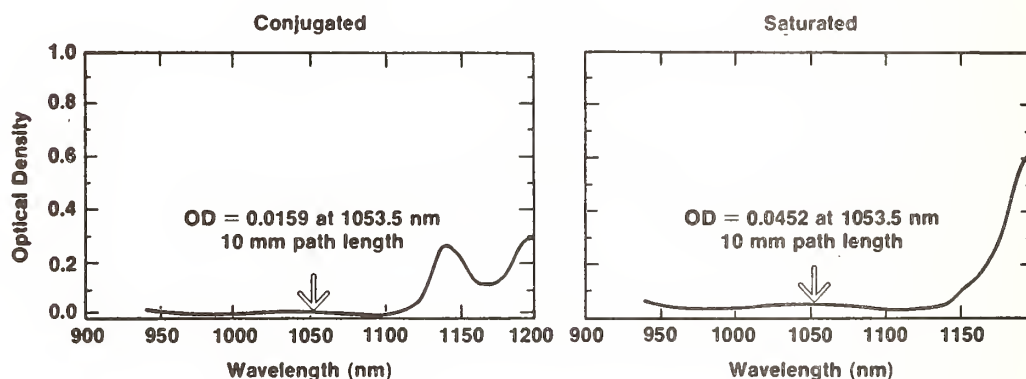
• Liquid crystals unaligned; alignment layers usually lower threshold

\* for given spot size, transport optics damage at  $20 \text{ J}/\text{cm}^2$

G2247

Figure 1. A comparison between a highly conjugated and an equivalent highly saturated liquid-crystal system shows that the polarizability of the saturated system raises the near-IR laser damage threshold.

interaction tests were conducted at 1053 nm (fundamental of Nd:phosphate glass laser), where neither material exhibits any resonance. This is substantiated by the two absorption scans in figure 2, obtained from 1-cm-path length cells at elevated temperatures keeping the compounds in their respective isotropic phases. The 1053-nm absorption coefficient for the biphenyl compound was  $3.6 \times 10^{-2} \text{ cm}^{-1}$ . For the saturated compound, the residual absorption was three times larger. Absorption measurements were done in the isotropic phase to minimize the scattering contribution to the extinction.



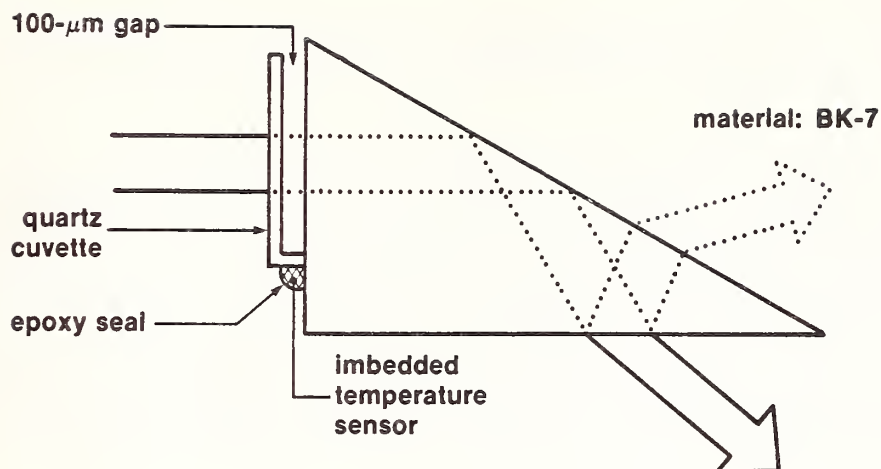
G2322

Figure 2. The damage-test experiments were carried out at a wavelength where neither of the liquid-crystal samples exhibits any resonances. The residual linear absorption at 1053 nm of the saturated compound is higher than that of the conjugated one, and yet its damage threshold is also higher.

Tests with linearly polarized incident pulses of 800-ps length were conducted identically for both monomeric materials. Unaligned cells of 100- $\mu\text{m}$  path length were prepared from 30-60-90 borosilicate prisms and uncoated, fused-quartz cuvette covers and were sealed by high-temperature epoxy. This sample geometry is illustrated in figure 3. Cells were filled, by capillary action, with the liquid crystalline materials in their isotropic phase. Because this involves elevated temperatures, cells were not equipped with the organic alignment layers that are often used in aligning liquid crystals in either homeotropic or homogeneous configurations. It is also important to note that to date we have not found an alignment material that by itself shows a damage threshold in excess of those reported here for liquid crystals. What is frequently measured in tests of liquid-crystal/alignment-layer systems is therefore not the damage threshold of the liquid crystal but that of the alignment layer. A project currently under way aims at sorting out the alignment materials with the highest damage threshold.

Irradiation by high-peak-power laser pulses occurred at normal incidence. The beam was weakly focused to a spot size of about 5 mm.





- For materials with high-temperature nematic phase, use high-temperature epoxy
- Ohmic-heating pads affixed to prism side walls

G2406

Figure 3. Sample geometry used for laser damage tests of monomers eliminated back reflection and interference effects in the tested layer, thereby permitting accurate threshold determination. For each polymeric sample, a 100- $\mu\text{m}$ -thick polymer layer was sprayed directly onto the face of the prism.

Laser-induced sample changes that in liquid crystals usually appear as small bubbles can be observed with a long-working-distance microscope. The detectability of bubbles was limited by the lifetime of bubbles that redissolve into the liquid matrix. One-on-one and N-on-1 irradiation modes were chosen. In N-on-1 testing, each separate sample site was irradiated by a series of ten pulses each (8% pulse-to-pulse energy stability). In that mode, occurrence of damage was checked after each shot. After the appearance of a bubble, irradiation was terminated even if that bubble happened to redissolve. In N-on-1 testing, the interval between pulses was 5 s. A record of peak fluence and its location within the beam was obtained for each shot.

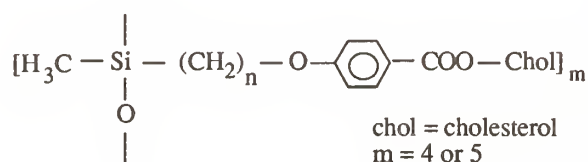
### 3. Results

Results for the monomeric materials are listed in figure 1. For both the aromatic and saturated compounds, the N-on-1 threshold is lower than the 1-on-1 threshold. This is in general agreement with many other monomeric liquid-crystal compounds tested earlier. However, in both 1-on-1 and N-on-1 results, a significant difference is apparent between the  $\pi$ -electron-rich and the fully saturated nematic. In fact, the beam transport optics for this experiment suffered damage before any site of the saturated compound showed single-shot bubble formation. The

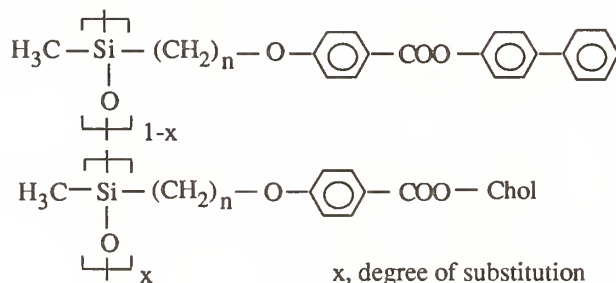
corresponding fluence level is twice that of the single-shot threshold average for the aromatic compound. The N-on-1 threshold comparison shows an improvement over the aromatic compound by nearly a factor of 3.

To eliminate from consideration that impurities may cause these threshold differences, the purity of the sample stock was determined by combined gas chromatography-Fourier Transform Infrared Spectroscopy (GC-FTIR). At the one-part-in- $10^5$  sensitivity level, no extraneous signals were observed from either compound. The only unusual feature was an isomer signature from the bicyclohexyl material. Within the stated sensitivity limit, impurities must be ruled out as a damage-dominating mechanism. Similarly, the opposing trends of damage thresholds and linear-absorption coefficients between the two nematics make linear absorption an unlikely damage mechanism.

The polymeric material was tested in a different approach. Here, the  $\pi$ -electron-rich phenyl functional group was removed in the preparation of the control-sample polymer. The liquid-crystal polymer comprised a polysiloxane backbone with lateral, mesogenic side groups. The structure of the repeat unit is shown below:



The cholesterol functional group with its alkyl tail introduces chirality into the polymer, offering interesting optical properties. Among them is the coupling between the molecular helix and the proper-handed, circularly polarized light of a wavelength  $\lambda$  that matches the pitch of the helix. By varying the pitch of the chiral structure, tuned optical devices can be prepared [4]. One method for varying the pitch of a chiral nematic polymer is to prepare a variable-weight copolymer of the design



in which the density (1-x) of interleaved copolymer pendants determines the degree of pitch dilation along the backbone direction. By virtue of the  $\pi$ -electron distribution in the copolymer, changing this density results in an increase or decrease in the nonlinear optical susceptibility of the total system in accordance with copolymer content. Testing the damage threshold of chiral copolymer samples tuned to different (nonresonant

with regard to the 1053-nm incident wavelength) wavelengths provides further corroboration for the postulated link between  $\chi^{(3)}$  and the degree of conjugation.

Damage-test samples of the copolymer were prepared by dissolving the material in toluene and spraying about 100- $\mu$ m-thick films onto carefully cleaned, 30-60-90 borosilicate glass prism surfaces. Film thicknesses were uniform to better than 10% across individual samples but varied by up to 20% from sample to sample. The three copolymers reported here had cholesteric weight percents of 14%, 21%, and 35%, corresponding to tuned-response peak wavelengths of 1170 nm, 760 nm, and 450 nm, respectively. In 1-on-1 tests conducted in the same way as for monomeric materials, an important trend emerged: the copolymer with the highest cholesterol content—i.e., that with the lowest volume density of conjugation—showed the highest damage threshold; the one with the lowest cholesterol content and therefore the highest volume density of conjugation showed the lowest threshold. This trend is evident in table 1.

Table 1. Damage Thresholds of Cholesteric Copolymers

Weight % Cholesteric	Peak Wavelength (nm)	Film Thickness ( $\mu$ m)	1-on-1 Threshold (J/cm <sup>2</sup> )
14	1170	108	0.8 $\pm$ 0.1
21	760	104	2.4 $\pm$ 0.3
35	450	83	5.1 $\pm$ 1.2
Smectic-C	not applicable	105	5.8 $\pm$ 0.3

G2414

Catalysts used in the synthesis of these polymers were thought to affect these thresholds through platinum trace residues. Platinum inclusions in laser glass have been widely acknowledged as prime damage-inducing impurities [5]. However, tests with especially purified copolymer samples yielded only marginally higher damage thresholds than those listed in table 1. We surmise that the role of impurities in the IR laser damage of these materials is as insignificant as in the monomeric compounds. The damage morphology in polymers differed from monomers in that no bubbles were observed. Damage was monitored at the same spatial resolution as in the case of bubbles, except that here permanent structural modifications in the form of microscopic pits were recorded.

Finally, a cholesteric polymer was prepared that totally lacked the copolymer pendants used in the previous examples for wavelength tuning and the phenyl group in the cholesteric pendant. Except for one conjugated bond on the cholesterol itself, this system was entirely  $\pi$ -electron free. These reductions affected not only the laser damage threshold but other physical properties as well. The polymer glass transition temperature, affecting the material's processability, was raised

and its mesogenic phase behavior changed. The chiral nematic room-temperature phase changed to smectic-C. Again, special efforts were made to keep this compound platinum-free. The platinum content was verified to be <1 ppm. When films of this material were prepared from a toluene solution in the same manner as for previous polymer samples, laser-damage thresholds could be measured. The 1053-nm, 1-on-1 threshold was  $5.8 \pm 0.3$  J/cm<sup>2</sup>, a 10% improvement over the best copolymer mentioned earlier. These measured thresholds compare well with the ones obtained for traditional, dielectric thin films [6].

#### 4. Summary

To summarize, we conclude that, once impurities have been removed as a major cause of damage in organic optical materials, the volume density of conjugation in a compound becomes the dominant laser-damage factor. Because of this link, a reformulation of liquid-crystal polarizer compositions is under way that will enhance the damage resistance of liquid-crystal optical elements used in the OMEGA laser. The guiding principle here is to substitute, wherever possible, highly saturated compounds for conjugated ones. One trade-off in this case is a drop in birefringence associated with the loss in conjugation, a trade-off easy to accommodate. The same principle will also help make other liquid-crystal devices high-power compatible, such as soft apertures [7], cholesteric laser end mirrors [8,9], or active devices, such as shutters and modulators [10].

---

Dr. F. Kreuzer of Consortium fur Elektrochemische Industrie, Munich, West Germany, kindly provided the polymeric sample materials and their analytical characterization. He also offered valuable advice.

This work was supported by the U.S. Department of Energy Office of Inertial Fusion under agreement No. DE-FC03-85DP40200, the U.S. Army Research Office under contract DAAL03-86-K-0173, the New York State Center for Advanced Optical Technology at the Institute of Optics, and by the Laser Fusion Feasibility Project at the Laboratory for Laser Energetics which has the following sponsors: Empire State Electric Energy Research Corporation, New York State Energy Research and Development Authority, Ontario Hydro, and the University of Rochester. Such support does not imply endorsement of the content by any of the above parties.

#### 5. References

- [1] Jacobs, S. D.; Cerqua, K. A.; Marshall, K. L.; Schmid, A.; Guardalben, M. J.; and Skerrett, K. J. *J. Opt. Soc. Amer. B* 5(9): 1962; 1988.
- [2] Nicoud, J. F. *Mol. Cryst. Liq. Cryst.* 156: 257; 1988; Katz, H. E.; Singer, K. D.; Sohn, J. E.; Dirk, C. W.; King, L. A.; and Gordon, H. M. *J. Amer. Chem. Soc.* 109: 6561; 1987.
- [3] Materials supplied by EM Chemicals, 5 Skyline Drive, Hawthorne, NY 10532.



- [4] Il'Chisin, I. P.; Tikhonov, E. A.; Tishchenko, V. G.; and Shpak, M. T. JETP Lett. 32: 24; 1980.
- [5] Milam, D.; Hatcher, C. W.; and Campbell, J. H. in Seventeenth Annual Symposium on Optical Materials for High Power Lasers, Nat. Bur. Stand. (U.S.), Spec. Publ. 746; 1985.
- [6] Walker, T.; Guenther, A.; and Nielsen, P. IEEE J. Quantum Electron. QE-17: 2041; 1981.
- [7] LLE Review 24: 188; 1985.
- [8] Denisov, Yu. V.; Kizel', V. A.; Orlov, V. A.; and Perevozchikov, N. F. Sov. J. Quantum Electron. 10: 1447; 1980.
- [9] Lee, J. C.; Jacobs, S. D.; Gingold, R. J. Advances in Nonlinear Polymers and Inorganic Crystals, Liquid Crystals, and Laser Media (1987), SPIE Vol. 824: 7; 1987.
- [10] Soref, R. A. Opt. Lett. 4: 155; 1979.

#### COMMENTS

Question: I was convinced that the impurities are not playing a big role but I guess I'm not convinced that it is Type 3 driven. Did you measure Type 3 in these materials?

Answer: We have not yet, we are presently setting up an experiment using nearly degenerate for mixing process that will measure  $\text{Chi}^3$ . We have measured in our laboratory Type 3 not necessarily those same materials but very similar materials and found it to be really quite small.

Question: These were shift basis?

Answer: Shift basis, yes. I believe those materials at least for our applications are chemically unstable. I understand the problems with them is bistability. But the point about the conjugation and the large  $\text{Chi}^3$ . In our measurements it wasn't that  $\text{Chi}^3$  was actually small, as small as ethanol for example. We will wait for  $\text{Chi}^3$  measurements. The purpose of these experiments was to find a pure model system where we could hopefully very clearly correlate  $\text{Chi}^3$  with damage.

Question: Let's assume it is  $\text{Chi}^3$  and you have a 100 micron thick cell. You've got a relatively large beam, you are not going to get much in the way of beam concentration in that small propagation distance. Are you speculating that it is two photon absorption, the imaginary part of the  $\text{Chi}^3$ , or do you really think it is a self-focusing kind of effect?

Answer: Well, at this point I can't say exactly what it may be.

# Thermally Induced Phase-Retardance Degradation in Laser-Irradiated Liquid Crystal Cells

Claude A. Klein, Terry A. Dorschner, Douglas S. Hobbs, and Daniel P. Resler

Raytheon Company, Research Division  
Lexington, MA 02173

The optical birefringence is the key performance parameter for liquid-crystal based wave plates and other liquid-crystal electro-optical devices. This paper reports experimental and theoretical work relating to the degradation of the phase retardance that can occur in laser-irradiated liquid crystal cells at moderate intensity levels. Experiments were carried out with a continuous-wave CO<sub>2</sub>-laser beam normally incident on a cell containing the nematic mixture BDH-E7. To better understand beam-induced phenomena in liquid crystals, which are very sensitive to temperature changes, a simple procedure for obtaining peak temperatures and temperature distributions has been developed. For this purpose, the steady-state thermal response is best described in terms of the average temperature increment of the cell and the radial temperature profile of the liquid crystal layer. Predictions based on this model are found to be in good agreement with experimental results, which is significant because it demonstrates that, for irradiances of less than 1 kW/cm<sup>2</sup>, the degradation originates entirely from the temperature-induced reduction of the birefringence.

**Keywords:** laser irradiance, liquid crystal, nematic compound, optical birefringence, phase retardance, thermally induced.

## 1. Introduction

The optical anisotropy of liquid crystals (LCs) plays a critical role in the operation of electro-optic devices that use LC cells. With nematic LCs, in particular, incident light experiences a refractive index that can vary from the ordinary index  $n_o$  to the extraordinary index  $n_e$ , depending upon polarization, for propagation directions transverse to the molecular long axis. The birefringence,

$$\Delta n = n_e - n_o, \quad (1)$$

is positive and ranges from 0.04 to 0.4 depending on composition, alignment, and wavelength [1], which makes it possible to fabricate nematic LC devices for manipulating the polarization of laser beams. Specifically, if the LC layer is such that the phase retardance,<sup>1</sup>

$$\phi = (2\pi/\lambda) \Delta n, \quad (2)$$

or difference in phase shifts for ordinary and extraordinary polarized light propagating through a homogeneously aligned cell, becomes equal to  $\pi$ , the cell becomes a half-wave plate and can be used to rotate the plane of polarization of linearly polarized light. The LC birefringence originates from an anisotropic molecular polarizability and can be expressed in a manner such as [2]

$$\Delta n = G(T) \frac{\lambda^2 \lambda^{*2}}{\lambda^2 - \lambda^{*2}}, \quad (3)$$

where  $\lambda^*$  refers to a mean resonance wavelength located in the ultraviolet; the birefringence thus exhibits little dispersion in the infrared. With regard to temperature, however, Eq. (3) suggests that the birefringence always has some temperature dependence, which can be of consequence in the context of high-power applications and may lead to large optical non-linearities [3].

<sup>1</sup>The symbols are identified in Appendix.

In this paper, we report on experimental and theoretical work relating to the degradation of the phase retardance that can occur in laser-irradiated LC cells at intensity levels in excess of a few Watts per square centimeter. Our experiments were carried out with a CO<sub>2</sub>-laser beam that impinges on a cell containing the eutectic nematic mixture E-7 produced by BDH Chemicals, Ltd. We will demonstrate that the primary mechanism causing the degradation is of a thermal nature in the sense that the degradation reflects the heating of the LC layer resulting from some finite absorption of the incident light. In this connection, key information can be extracted from the tabulation of nematic birefringences presented in Ref. 1. Figure 1 illustrates both the spectral dispersion and the temperature sensitivity of the BDH-E7 birefringence: The thermal birefringence coefficient,  $d(\Delta n)/dT$ , is seen to be negative and to increase rapidly as the temperature approaches the nematic-to-isotropic phase-transition point. Consequently, we may expect the retardance of laser-irradiated nematic LC cells to decrease as the temperature rises and to drop off abruptly at high-irradiance levels unless new mechanisms intervene, such as optical field-induced reorientation of the LC molecules [4].

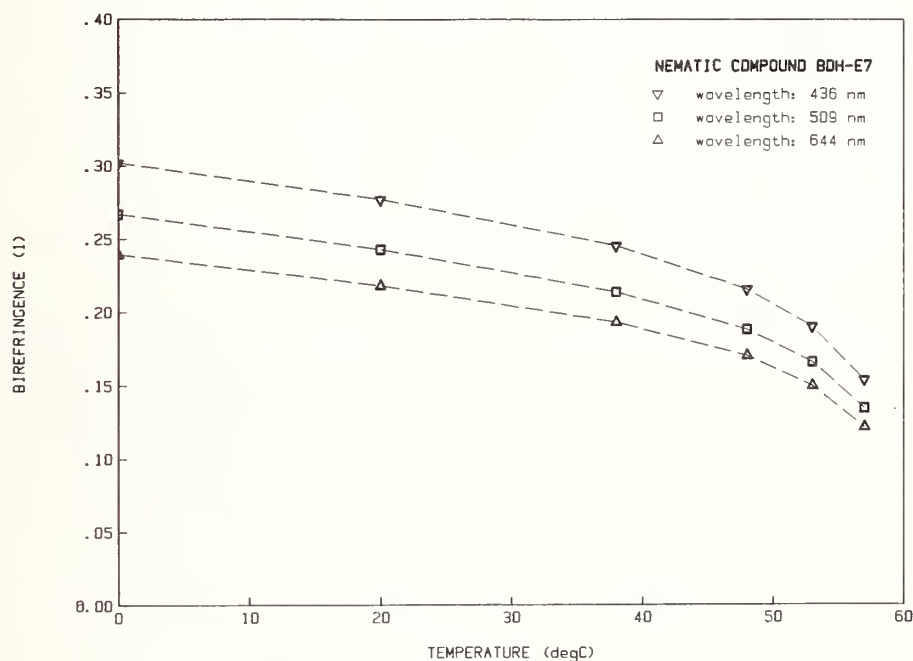


Figure 1. Nematic birefringence of the liquid-crystal compound E-7 produced by BDH Chemicals, Ltd. This plot, which is based on data compiled in Ref. 1, encompasses three wavelengths in the visible and covers most of the operating temperature range.

Temperature affects not only the birefringence of liquid crystals but also the viscosity, which may enhance the response and, thus, improve the performance in some applications [2]. Furthermore, temperature variations induced by Gaussian beams can give rise to thermal lensing effects, which result in self-defocusing and causes a reduction in focal intensity [5]. To understand and describe such beam-induced phenomena, which are very sensitive to temperature changes, it is essential to develop a procedure for obtaining peak temperatures and temperature distributions in laser-irradiated LC cells.

For this purpose, we consider an axially-symmetric laser beam of Gaussian intensity impinging normally on a cylindrical LC cell that operates in a transmissive mode. We assume that surfaces and interfaces are perfectly anti-reflection (AR) coated and, in addition, that absorptions are sufficiently low so that beam-intensity losses can be ignored. In a steady-state regime, that is, for continuous laser

illumination, the thermal response of the cell can be expressed in the same manner as for laser windows [6], i.e.,

$$T(r, z) - T_A = [T(r, z) - T(r)] + [T(r) - T_A] , \quad (4)$$

where  $T_A$  refers to the ambient temperature, and  $T(r)$  represents the axially-averaged cell temperature:

$$T(r) = \frac{1}{L} \int_0^L T(r, z) dz . \quad (5)$$

We are primarily concerned with the beam-induced temperature increase of the LC layer. Because this layer is usually very thin compared to the cell's dimension, we may disregard the  $z$ -dependence and rely on the relation

$$\Delta T_{LC}(r) = [T_{LC}(r) - T(r)] + [T(r) - T_A] \quad (6)$$

to carry out the thermal analysis. In effect, Eq. (6) provides an appropriate "roadmap" in the sense that it delineates the two major steps required to complete this investigation. Specifically, Secs. 2 and 3 concern the term  $T(r) - T_A$ , which describes the average temperature increase of the cell and its radial variation. The temperature increment of the LC layer,  $T_{LC}(r) - T(r)$ , is the subject of Sec. 4, which leads to the temperature profile  $\Delta T_{LC}(r)$  that allows us to evaluate the phase-retardance degradation. In Sec. 5, we show that our measurements agree very well with predictions, which is significant because it demonstrates that, for incident irradiances of less than  $1 \text{ kW/cm}^2$ , the degradation is attributable solely to thermal processes; these conclusions are restated in Sec. 6.

## 2. Thermal Model: LC Cell

In a transmissive mode of operation, practical applications of liquid crystals require that the fluid be contained in a cell comprised of two transparent substrates (or windows) separated by means of "spacers" of appropriate thickness. Figure 2 depicts a simple LC cell of the type used in our experiments: The two windows, which are AR coated on both sides, are a few millimeters thick, but the LC layer sandwiched between them is much thinner (typically, 10 to 50  $\mu\text{m}$ ).<sup>2</sup> The cell is mounted on a rigid support structure, which is made of insulated copper and provides a cooling interface; a thermocouple affixed at the edge allows us to monitor the temperature of the cell without creating significant interference.

Returning now to Eq. (6), we may first consider the term  $T(r) - T_A$ , which concerns the radial dependence of the cell's temperature. For this purpose, we are postulating that the LC layer is sufficiently thin so that heat flow into the windows dominates; in other words, from a heat-transfer point of view, we assume that the LC layer behaves in the manner of a coating. As noted in the Introduction, we are also assuming that the depletion of the laser beam, which is caused by absorptions and reflections as the beam passes through the cell, is in fact minimal. If this is acceptable, the steady-state temperature of the cell, when illuminated by an axially-symmetric beam of intensity  $I(r)$ , obeys an equation such as

$$K_W \left[ \frac{\partial^2 T(r, z)}{\partial r^2} + \frac{1}{r} \frac{\partial T(r, z)}{\partial r} + \frac{\partial^2 T(r, z)}{\partial z^2} \right] + \beta(z) I(r) = 0 , \quad (7)$$

where  $K_W$  is the thermal conductivity of the two windows, and  $\beta(z)$  refers to the local absorption

<sup>2</sup>Note that there are no electrodes since the measurements of interest here do not require any voltage.



# TRANSMISSION-MODE LIQUID CRYSTAL CELL

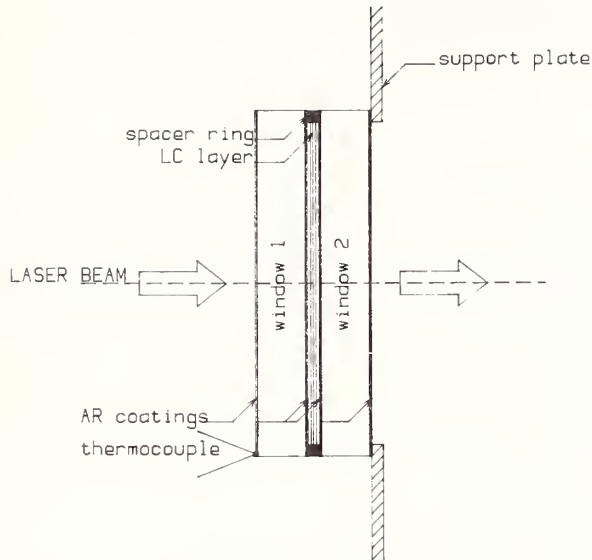


Figure 2. Sketch of an elemental liquid-crystal cell operating in a transmissive mode. The support plate acts as a heat sink; the thermocouple measures the edge-temperature increase under laser illumination.

coefficient. We now apply the operator  $(1/L) \int_0^L dz$  to generate the differential equation that controls the radial diffusion and, thus, governs the radial dependence of the  $z$ -averaged temperature, or mean temperature through the thickness of the cell; this yields [5]

$$\frac{d^2 T(r)}{dr^2} + \frac{1}{r} \frac{dT(r)}{dr} + \frac{1}{L} \left[ \frac{\partial T(r,z)}{\partial z} \Big|_L - \frac{\partial T(r,z)}{\partial z} \Big|_0 \right] + \frac{\beta_{eff}}{K_W} I(r) = 0 \quad (8)$$

if  $\beta_{eff}$  represents an effective absorption coefficient defined as follows:

$$\beta_{eff} = \frac{1}{L} \int_0^L \beta(z) dz = \frac{1}{L} (4\beta_S + 2L_W \beta_W + \alpha_l) . \quad (9)$$

This expression takes into account the absorption of light by the two AR-coated windows as well as the absorption by the LC layer. Much simplification can be achieved if one considers the thermal boundary condition at the front and back faces,

$$\frac{\partial T(r,z)}{\partial z} \Big|_{z=0} = \frac{h_F}{K_W} [T(r,0) - T_A] \quad (10a)$$

$$\frac{\partial T(r,z)}{\partial z} \Big|_{z=L} = - \frac{h_F}{K_W} [T(r,L) - T_A] , \quad (10b)$$

and assumes that, because of the symmetry of the configuration and because the windows are expected to be made of high-thermal-conductivity material, axial temperature variations can be disregarded. In this light, it is seen that, if  $\delta T(r)$  designates the mean temperature increment,

$$\delta T(r) \equiv T(r) - T_A, \quad (11)$$

Eq. (8) reduces to an ordinary second-order differential equation,

$$\frac{d^2[\delta T(r)]}{dr^2} + \frac{1}{r} \frac{d[\delta T(r)]}{dr} - \frac{2h_F}{LK_W} \delta T(r) + \frac{\beta_{eff}}{K_W} I(r) = 0, \quad (12)$$

which is amenable to analytical or numerical treatment [5]. Regarding the parameter  $h_F$ , it is understood to represent a heat-transfer coefficient that combines the effects of heat losses associated with thermal radiation and natural convection; for surfaces a few centimeters in size and temperature differentials of a few degrees, we estimate that an  $h_F$  of about  $6 \times 10^{-4} \text{ W cm}^{-2} \text{ K}^{-1}$  should be a good number [7].

Applicable solutions of Eq. (12) must satisfy appropriate boundary conditions. On axis, and on account of the azimuthal symmetry, we have

$$\left. \frac{d}{dr} \delta T(r) \right|_0 = 0. \quad (13a)$$

At the edge, we take it that (a) conduction into the support structure dominates the heat-loss process, and (b) the rate of heat loss is proportional to the temperature difference between the two media; in other words, we are postulating that the following holds:

$$\left. \frac{d}{dr} \delta T(r) \right|_{D/2} = - \frac{h_E}{K_W} \delta T(D/2), \quad (13b)$$

where  $h_E$  represents an appropriate (empirical) heat-transfer coefficient. Equation (12), together with the boundary conditions (13), provides a simple model for the radial temperature profile of continuously illuminated LC cells of the type displayed in Fig. 2. The model applies to configurations that make use of thin LC slabs sandwiched between two identical windows that are highly transparent and possess good thermal conductivity. The edge heat-transfer coefficient  $h_E$  characterizes the efficiency of the diffusion-assisted cooling into the support plate and must be obtained from a set of relevant data; we will address this task in the next section.

### 3. Edge Temperature Increment

All our experiments were carried out on the same liquid crystal cell (serial number .5LC-17) with a single-mode  $\text{CO}_2$ -laser source emitting at  $\lambda = 10.6 \mu\text{m}$  and having a maximum CW output power of about 3.5 W. Relevant characteristics of this cell are listed in Table 1.<sup>3</sup> The cell is nominally a half-wave retarder,

$$(2\pi/\lambda) \Delta n \approx \pi, \quad (14)$$

based on the reported birefringence of a homogeneously aligned, parallel oriented BDH-E7 LC compound. The two windows are made of AR-coated germanium and exhibit good transparency in the infrared. Bulk absorption coefficients of BDH-E7 at  $10.6 \mu\text{m}$  are known [2] to be ca.  $55 \text{ cm}^{-1}$  and ca.  $40 \text{ cm}^{-1}$  for

<sup>3</sup>Details concerning cell preparation and experimental setup will be reported elsewhere [8].

extraordinary and ordinary rays, respectively; for our purposes, we ignore the dichroism and use an average liquid-crystal absorption coefficient of  $50 \text{ cm}^{-1}$ . In conjunction with Ge absorptivities and coating absorptances as given in Table 1, this leads [see Eq. (9)] to an effective absorption coefficient  $\beta_{\text{eff}} \approx 0.35 \text{ cm}^{-1}$ , which implies that about 13% of the incident power is dissipated in traversing the cell. As indicated earlier, our model does not take into account the insertion loss, which may include additional reflection losses. With  $h_F \approx 6 \times 10^{-4} \text{ Wcm}^{-2}\text{K}^{-1}$  (see Sec. 2), and  $L$  and  $K_W$  as listed in Table 1, Eq. (12) reduces to

$$\frac{d^2[\delta T(r)]}{dr^2} + \frac{1}{r} \frac{d[\delta T(r)]}{dr} - 5.05 \times 10^{-3} \delta T(r) + 0.593 I_0 \exp(-2r^2/r_0^2) = 0 \quad (15)$$

for an incident Gaussian beam of peak intensity  $I_0$  (in Watts per square centimeter) and  $1/e^2$ -radius  $r_0$  (in centimeters), which yields the radial temperature profile if the boundary conditions

$$\left. \frac{d}{dr} \delta T(r) \right|_0 = 0 \quad (16a)$$

and

$$\left. \frac{d}{dr} \delta T(r) \right|_{D/2} = - \frac{h_E}{0.59} \delta T(D/2) \quad (16b)$$

are satisfied.

Table 1. Key parameters relating to configuration and performance of liquid-crystal cell # .5LC-17.

Cell aperture	$D$	=	1 in. (2.54 cm)
Window thickness	$L_W$	=	2 mm
LC layer thickness	$l$	=	25 $\mu\text{m}$
Cell thickness	$L$	=	0.4035 cm(a)
LC birefringence	$\Delta n_0$	=	0.205(b)
Relative thermal coefficient	$(1/\Delta n_0)d(\Delta n)/dT$	=	-0.0065 $^{\circ}\text{C}^{-1}$ (c)
LC absorption coefficient	$\alpha$	$\approx$	50 $\text{cm}^{-1}$ (b)
LC thermal conductivity	$K_{LC}$	$\approx$	$5 \times 10^{-4} \text{ cal}^{-1}\text{s}^{-1}\text{cm}^{-1}\text{K}^{-1}$ (d)
Window thermal conductivity	$K_W$	=	0.59 $\text{Wcm}^{-1}\text{K}^{-1}$ (e)
Window absorption coefficient	$\beta_W$	$\approx$	0.03 $\text{cm}^{-1}$ (e)
Coating absorptance	$\beta_S$	$\approx$	0.1% (typical)
Spacer expansion coefficient	CTE	<	$1 \times 10^{-5} ^{\circ}\text{C}^{-1}$ (f)

(a) Two windows plus LC layer and AR coatings.

(b) BDH-E7 room temperature/10.6- $\mu\text{m}$  value (see Ref. 2).

(c) Derived from birefringences tabulated in Ref. 1.

(d) Tentative value for nematics (see Ref. 3).

(e) Germanium at 25 $^{\circ}\text{C}$  (see Ref. 12).

(f) Low-thermal-expansion-coefficient dielectric.

Equation (16b) involves an edge heat-transfer coefficient,  $h_E$ , whose magnitude cannot be readily estimated considering the geometry of the device and its support structure. With a laser beam focused to a spot size of 2 mm ( $1/e^2$  diameter) on target, the edge temperature recorded by the thermocouple was found to increase linearly with beam intensity,<sup>4</sup>

$$T_E = (24.00 \pm .16) + (0.0383 \pm .0014) I_0, \quad (17)$$

which is as expected since solutions of Eq. (15) "scale" with  $I_0$ . At a peak intensity of 200 W/cm<sup>2</sup>, for instance, the "true" edge-temperature increment is therefore  $\delta T_E = (7.66 \pm .28)^\circ\text{C}$  as indicated by the least-squares fit. This result should allow us to extract an appropriate  $h_E$  value with reasonable confidence. On using a fourth-order Runge-Kutta algorithm, the relevant differential equation,

$$\frac{d^2[\delta T(r)]}{dr^2} + \frac{1}{r} \frac{d[\delta T(r)]}{dr} - 5.05 \times 10^{-3} \delta T(r) + 119 \exp(-200r^2) = 0, \quad (18)$$

yields the correct edge-temperature increment ( $\delta T_E = 7.66$ ) for initial values as follows:  $\delta T(0) = 8.60$  and  $d(\delta T)/dr|_0 = 0$ , the latter on account of the boundary condition (16a). At the edge, the solution has a slope of  $-0.211^\circ\text{C/cm}$ , which says that (a) the temperature of the cell is almost uniform, essentially because of the high thermal conductivity of the windows, and (b) the heat-transfer coefficient  $h_E$  is equal to  $0.016 \text{ Wcm}^{-2}\text{K}^{-1}$ , as derived from the boundary condition (16b), and appears to be acceptable from the point of view of characterizing the cooling efficiency [9]. Returning now to the system (15, 16a, 16b), and inserting the values  $r_0 = 0.1 \text{ cm}$  and  $h_E = 0.016 \text{ Wcm}^{-2}\text{K}^{-1}$ , the solution yields edge-temperature increments as a function of the incident peak intensity that fit available experimental data remarkably well (see Fig. 3). We also show solutions obtained for  $h_E = 0.001, 0.01$ , and  $0.1 \text{ Wcm}^{-2}\text{K}^{-1}$ , which demonstrate that the temperature rise is indeed highly dependent upon the edge heat-transfer coefficient. Throughout the rest of this paper, we assume that the heat-loss rate at the edge of the cell can be modeled by means of a conventional heat-transfer coefficient set equal to  $0.016 \text{ Wcm}^{-2}\text{K}^{-1}$ .<sup>5</sup>

At this point, we may wish to examine how the power absorbed by the cell,

$$P_A = \beta_{eff} L (\pi r_0^2 I_0 / 2), \quad (19)$$

which amounts to 0.443 W at the 200-W/cm<sup>2</sup> irradiance level for a 2-mm diameter beam, will be channeled into the environment as a result of the combined effects of face- and edge-cooling. In a steady-state regime, conduction into the support plate dissipates the power

$$P_E = (\pi D L) h_E \delta T_E, \quad (20)$$

whereas radiation and convection dissipate the fraction

$$P_F = 4 \pi h_F \int_0^{D/2} \delta T(r) r dr \quad (21)$$

if  $\delta T(r)$  describes the temperature rise induced by the beam. On inserting our numbers, these equations yield  $P_E = 0.401 \text{ W}$  and  $P_F = 0.047 \text{ W}$ , which is indeed compatible with the total absorbed power and

<sup>4</sup>  $T_E$  is in degrees centigrade and  $I_0$  in Watts per square centimeter; the measured ambient laboratory temperature was close to  $24^\circ\text{C}$  (August 1988).

<sup>5</sup> Note that the present cell has not been optimized for thermal efficiency. Its purpose is strictly to facilitate development of an adequate model to describe thermal effects in LC devices. A well-engineered cell may have edge heat-transfer coefficients as large as  $0.1 \text{ Wcm}^{-2}\text{K}^{-1}$ , which would substantially reduce the magnitude of the effects reported here.



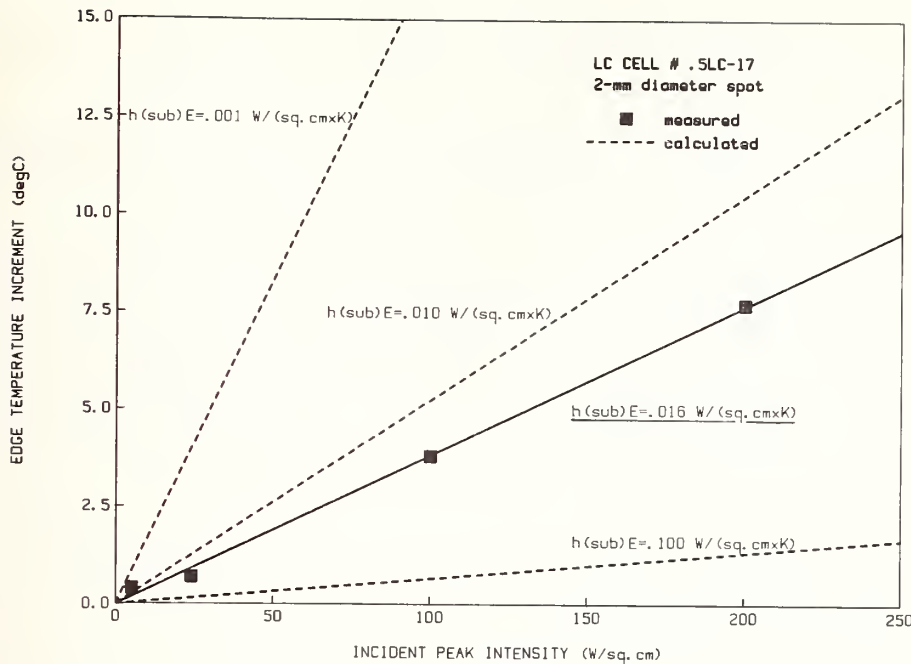


Figure 3. Laser-induced edge-temperature increment of the liquid-crystal cell sketched in Fig. 2 and characterized in Table 1. The measurements imply an edge heat-transfer coefficient  $h_E$  of  $0.016 \text{ Wcm}^{-2}\text{K}^{-1}$ .

suggests that the loss of heat at the front and back faces is small but not negligible by comparison with the loss experienced at the edge.<sup>6</sup>

#### 4. Thermal Model: LC Layer

As outlined in connection with Eq. (6), the formalism we have adopted now calls for an evaluation of the term  $T_{LC}(r) - T(r)$ ,  $T_{LC}(r)$  referring to the  $z$ -averaged temperature of the thin LC layer, and  $T(r)$  to the  $z$ -averaged cell temperature. For this purpose, we proceed as in Sec. 3: We write down the relevant steady-state heat-diffusion equation, i.e.,

$$K_{LC} \left[ \frac{\partial^2 T(r, z)}{\partial r^2} + \frac{1}{r} \frac{\partial T(r, z)}{\partial r} + \frac{\partial^2 T(r, z)}{\partial z^2} \right] + \alpha I(r) = 0, \quad (22)$$

and then average over the axial variable, which yields

$$\frac{d^2 T_{LC}(r)}{dr^2} + \frac{1}{r} \frac{dT_{LC}(r)}{dr} + \frac{1}{L} \left[ \frac{\partial T(r, z)}{\partial z} \right]_{L_W+L} - \frac{\partial T(r, z)}{\partial z} \Big|_{L_W} \Big] + \frac{\alpha}{K_{LC}} I(r) = 0. \quad (23)$$

Note that we are assuming that the LC layer is thermally isotropic, thus disregarding available experimental evidence on anisotropic heat diffusivities in nematics [11]. The boundary conditions at the

<sup>6</sup>Since there is some uncertainty regarding the proper value of  $h_F$ , numerical simulations using finite-difference techniques [10] were performed to assess the impact of varying  $h_F$ : In a worst-case situation ( $h_F \equiv 0$ ), we find that  $h_E$  as obtained from Eq. (16b) increases to  $0.018 \text{ Wcm}^{-2}\text{K}^{-1}$ , in accord with Eq. (20) when  $P_E$  is set equal to  $P_A$ .

layer/window interfaces,

$$\left. \frac{\partial T(r, z)}{\partial z} \right|_{L_W + l} = - \frac{h_{LC}}{K_{LC}} [T_{LC}(r, L_W + l) - T_W(r, L_W + l)] \quad (24a)$$

$$\left. \frac{\partial T(r, z)}{\partial z} \right|_{L_W} = \frac{h_{LC}}{K_{LC}} [T_{LC}(r, L_W) - T_W(r, L_W)] , \quad (24b)$$

involve an appropriate heat-transfer coefficient,  $h_{LC}$ , and the local temperatures on both sides of the interfaces. Since the LC layer is very thin, we take it that axial temperature variations within the layer are minimal and assume that  $T_{LC}(r, L_W + l)$  and  $T_{LC}(r, L_W)$  are both equal to the average temperature  $T_{LC}(r)$ ; moreover, we have seen in Sec. 3 that the Ge windows are practically thermal isotherms, which implies that we may set  $T_W(r, L_W + l)$  and  $T_W(r, L_W)$  equal to  $T(r)$ . On introducing now the notation  $\delta T_{LC}(r)$  for the LC layer temperature increment relative to the windows,

$$\delta T_{LC}(r) \equiv T_{LC}(r) - T(r) , \quad (25)$$

and keeping in mind that  $dT(r)/dr$  is very small, we conclude that, in a first approximation, the LC layer temperature increment obeys the differential equation

$$\frac{d^2 [\delta T_{LC}(r)]}{dr^2} + \frac{1}{r} \frac{d [\delta T_{LC}(r)]}{dr} - \frac{2h_{LC}}{K_{LC}l} \delta T_{LC}(r) + \frac{\alpha}{K_{LC}} I(r) = 0 . \quad (26)$$

A priori, the heat-transfer coefficient  $h_{LC}$  is unknown. If, however, we consider that the thermal conductivity of the LC layer is much smaller than that of the windows (see Table 1), it appears justified to treat the LC layer as a "thin skin" in the sense of Carslaw and Jaeger [7], which says that the rate of heat flow through each interface, per unit area and unit time, is  $(1/R)(\theta - \theta_0)$ ,  $\theta$  and  $\theta_0$  designating the temperatures inside and outside the skin, and  $R$  representing the thermal resistance of the skin; in other words, we may set the heat-transfer coefficient  $h_{LC}$  equal to the inverse thermal resistance of the LC layer, i.e.,

$$h_{LC} = K_{LC}/l . \quad (27)$$

Hence, we may rewrite Eq. (26) as follows:

$$\frac{d^2 [\delta T_{LC}(r)]}{dr^2} + \frac{1}{r} \frac{d [\delta T_{LC}(r)]}{dr} - \frac{2}{l^2} \delta T_{LC}(r) + \frac{\alpha}{K_{LC}} I(r) = 0 , \quad (28)$$

and obtain the temperature profile of the LC layer without injecting any *ad hoc* parameter.

Expressed in non-dimensional variables [5], a heat-diffusion equation of this type calls for consideration of the Nusselt number, which reduces to

$$Nu = (2/l^2)(D/2)^2 \quad (29)$$

for the configuration of interest here. For a layer thickness  $l$  of 25  $\mu\text{m}$  and a device aperture  $D$  of 1 in., the Nusselt number is very large ( $Nu = 5.16 \times 10^5$ ), which indicates that the diffusion of heat within the layer should be negligible compared to the loss of heat that occurs at the two interfaces, thus substantiating our initial postulate that the totality of heat generated in the LC layer will be collected by the windows. In a steady-state regime, the LC layer temperature increment therefore "images" the incident beam shape; if this beam has a Gaussian intensity distribution,  $I(r) = I_0 \exp(-2r^2/r_0^2)$ , it follows immediately that the solution of Eq. (28) is also a Gaussian,

$$\delta T_{LC}(r) = \frac{\alpha I_0 l^2}{2K_{LC}} \exp \left[ -2 \left( \frac{r}{r_0} \right)^2 \right], \quad (30)$$

which yields peak temperatures, at the center of the spot, that are strongly dependent upon the layer thickness  $l$  and control the useful operating temperature range of a laser-irradiated LC cell.

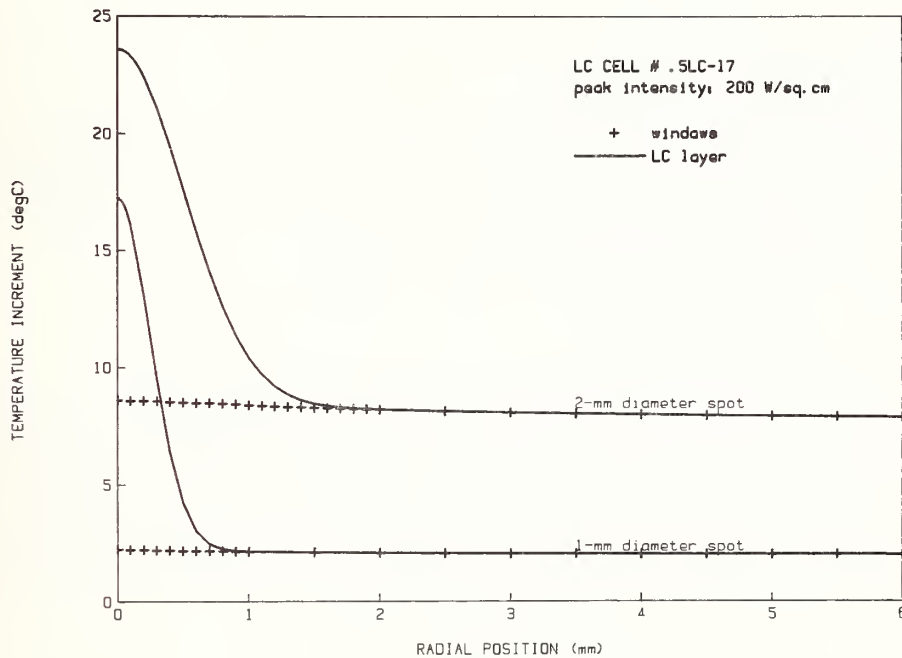


Figure 4. Laser-induced temperature profile of the liquid-crystal cell sketched in Fig. 2 and characterized in Table 1, for spot sizes of 1- and 2-mm diameter, at incident CW peak intensities of 200 W/cm<sup>2</sup>. The two windows are at almost uniform temperature while the liquid-crystal layer temperature mirrors the beam shape.

Returning now to Eq. (6), and making use of the notations introduced earlier [Eqs. (11) and (25)], we may express the steady-state beam-induced temperature rise of the LC layer simply as follows,

$$\Delta T_{LC}(r) = \delta T(r) + \delta T_{LC}(r), \quad (31)$$

and perform all relevant calculations using Table 1 as a data base and setting the edge heat-transfer coefficient equal to 0.016 Wcm<sup>-2</sup> (see Sec. 3). Figure 4 illustrates the results of this procedure for spot sizes of 1- and 2-mm diameter, the incident Gaussian beam having a peak intensity  $I_0$  of 200 W/cm<sup>2</sup>. These temperature increments are linearly dependent upon  $I_0$ , which has important implications in terms of tolerable irradiances since LC temperatures in excess of 60 °C will induce a phase transition to the isotropic state [1], thus causing a catastrophic deterioration of the device's performance. The key indicator in this respect is the "net" temperature averaged over the beam spot size ( $r \leq r_0$ ),

$$\overline{T}_{LC} = T_A + \overline{\Delta T}_{LC} \approx T_A + \delta T(0) + \overline{\delta T}_{LC}, \quad (32)$$

considering that the windows are effectively isotherms (see Fig. 4). The average LC layer temperature increment,  $\overline{\delta T}_{LC}$ , can be easily obtained from Eq. (30),

$$\overline{\delta T}_{LC} = [\delta T_{LC}(0)/2][1 - \exp(-2)], \quad (33)$$

which yields  $\overline{\delta T_{LC}} = 6.5\text{ }^{\circ}\text{C}$  irrespective of the spot size and, thus, points to  $\Delta T_{LC}$ 's of 14.9 and 8.7  $^{\circ}\text{C}$  for 1- and 2-mm spot sizes, at peak irradiances of 200 W/cm<sup>2</sup> as in Fig. 4. In terms of our measurements, these calculations suggest that the 2-mm spot size experiments, which were carried out at an ambient temperature of 24  $^{\circ}\text{C}$  and peak irradiances of no more than 200 W/cm<sup>2</sup>, did not cause the average LC layer temperature to exceed 38.9  $^{\circ}\text{C}$ ; our 1-mm spot size experiments, however, which involve substantially higher irradiance levels (see Fig. 5), may have given rise to average temperatures (over the beam spot area) that approach the transition temperature of BDH-E7 liquid crystals.<sup>7</sup>

##### 5. Phase-Retardance Degradation

Figure 5 documents the results of our phase-retardance measurements; the experimental uncertainty is estimated on the order of  $\pm 1\%$ . The retardance decreases monotonically as the incident beam intensity increases and obeys a linear dependence with an index of correlation of 0.992 and 0.999 for spot sizes of 1 and 2 mm, respectively; the least-squares fits,

$$\phi_1 = (178.25 \pm .75) - (0.0532 \pm .0020) I_0 \quad (34a)$$

for the 1-mm diameter run and

$$\phi_2 = (174.05 \pm .09) - (0.0902 \pm .0008) I_0 \quad (34b)$$

for the 2-mm diameter run, demonstrate that our LC cell does not quite satisfy the half-wave plate condition (180 deg) at zero irradiance. As mentioned earlier, the 2-mm diameter run was performed in the summer of 1988 at an ambient temperature of 24  $^{\circ}\text{C}$ , whereas the "1-mm" data points plotted in Fig. 5 are the results of later experiments that were made at a laboratory temperature of 22  $^{\circ}\text{C}$ . Since the retardance of an LC wave-plate is known to exhibit a strong temperature sensitivity [1], we may assess the dependence in the light of Eq. (2), that is,

$$\frac{d\phi}{\phi} = \frac{d(\Delta n)}{\Delta n} + \frac{d\ell}{\ell}, \quad (35)$$

keeping in mind that  $d(\Delta n)/\Delta n$  is independent of wavelength [see Eq. (3)],

$$\frac{d(\Delta n)}{\Delta n} = \frac{d[G(T)]}{G(T)}, \quad (36)$$

and approximately equal to  $-0.0065\text{ }^{\circ}\text{C}^{-1}$ , at room temperature, based on the BDH-E7 birefringences recorded in Fig. 1. Since the spacer has an expansion coefficient of less than  $1 \times 10^{-5}\text{ }^{\circ}\text{C}^{-1}$ , it follows that any temperature-induced degradation of the phase retardance is essentially due to the birefringence alone and that the relation  $\Delta\phi/\phi_0 = \Delta(\Delta n)/\Delta n_0$  holds. The observed phase-retardance difference of  $(4.2 \pm .84)\text{ deg}$  is therefore explainable by an ambient temperature difference of 3.7  $^{\circ}\text{C}$ , which is somewhat larger than the recorded 2  $^{\circ}\text{C}$ ; we suspect that the ambient temperature measurements were not sufficiently accurate.

The task of describing the intensity dependence of the cell retardance requires some care because the measured degradation as evidenced in Fig. 5 represents a spatially averaged effect, the relevant phenomena occurring within the confine of the Gaussian-shaped CO<sub>2</sub>-laser beam impact area. On assuming that the degradation originates entirely from thermal effects, a proper "Ansatz" must reflect

<sup>7</sup>In this connection, it is noteworthy that experiments that were carried out at a peak intensity of 900 W/cm<sup>2</sup> ( $T_{LC} \approx 61\text{ }^{\circ}\text{C}$  at an ambient temperature of 22  $^{\circ}\text{C}$ ) showed evidence of an abrupt falloff of the phase retardance.



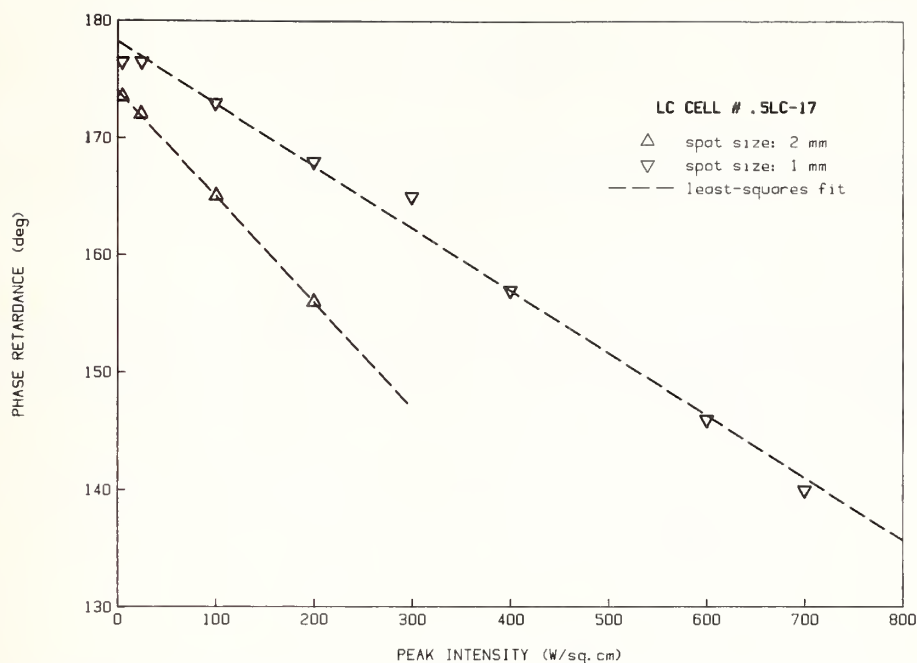


Figure 5. Beam-intensity dependence of the 10.6- $\mu$ m phase retardance measured for the liquid-crystal cell sketched in Fig. 2 and characterized in Table 1. The 1- and 2-mm diameter spot-size runs were carried out at a laboratory temperature of 22 and 24  $^{\circ}$ C, respectively.

the radial dependence of the temperature, which translates into

$$\frac{\Delta\phi}{\phi_0} = \frac{\int_0^{D/2} [\Delta\phi(r)/\phi_0] I(r) r dr}{\int_0^{D/2} I(r) r dr}, \quad (37)$$

where  $\Delta\phi(r)/\phi_0$  is the relative change in retardance experienced by an incident ray that traverses the cell at a distance  $r$  from the axis. If  $\Delta n(r)$  denotes the  $r$ -dependent temperature-induced variation of the birefringence, we already know that the following holds:

$$\frac{\Delta\phi(r)}{\phi_0} = \frac{\Delta n(r)}{n_0}, \quad (38)$$

$\Delta n(r)$  relating to the LC-layer temperature increase in this manner:

$$\Delta n(r) = \int_0^{\Delta T_{LC}(r)} \frac{d(\Delta n)}{dT} dT. \quad (39)$$

Upon inserting these relations into Eq. (37), it is seen that the thermally induced phase-retardance degradation can be expressed in a compact form,

$$\frac{\Delta\phi}{\phi_0} = \frac{(1/n_0) \int_0^{D/2} \int_0^{\Delta T_{LC}(r)} [d(\Delta n)/dT] dT \times I(r) r dr}{\int_0^{D/2} I(r) r dr}, \quad (40)$$

which convolves the temperature dependence of the birefringence, the beam-induced temperature rise, and the shape of the incident beam. In a first step, we take it that (a) the thermal birefringence

coefficient is temperature independent, and (b) the beam covers only the central part of the cell's aperture. In that case, Eq. (40) reduces to

$$\frac{\Delta\phi}{\phi_0} \approx \frac{d(\Delta n)/dT}{\Delta n_0} \times \frac{\int_0^\infty \Delta T_{LC}(r) I(r) r dr}{\int_0^\infty I(r) r dr} \quad (41)$$

and becomes amenable to analytic evaluation if a functional expression can be formulated for the beam-induced temperature rise. In Sec. 4, we have seen that, over the spot area, it is a good approximation to write

$$\Delta T_{LC}(r) \approx \delta T(0) + \delta T_{LC}(r), \quad (42)$$

where  $\delta T(0)$  refers to the  $r=0$  solution of the differential equation (12), and  $\delta T_{LC}(r)$  is as given in Eq. (30). Consequently, Eq. (41) leads to the result that, for Gaussian beams of moderate intensity, the retardance degrades in accord with

$$\frac{\Delta\phi}{\phi_0} \approx \frac{d(\Delta n)/dT}{\Delta n_0} \left\{ \delta T(0) + \delta T_{LC}(0) \times \frac{\int_0^\infty \exp[-4(r/r_0)^2] r dr}{\int_0^\infty \exp[-2(r/r_0)^2] r dr} \right\}, \quad (43)$$

which yields

$$\frac{\Delta\phi}{\phi_0} \approx \frac{d(\Delta n)/dT}{\Delta n_0} \left[ \delta T(0) + \delta T_{LC}(0)/2 \right] \quad (44)$$

and, thus, defines an effective laser-induced temperature increase,  $\Delta T_{eff} \equiv \delta T(0) + \delta T_{LC}(0)/2$ . Since  $\delta T(0)$  and  $\delta T_{LC}(0)$  are both linear functions of the peak intensity  $I_0$ , and since  $d(\Delta n)/dT$  is always negative and relatively constant at temperatures up to 40 °C (see Fig. 1), we conclude that the pattern exhibited in Fig. 5 substantiates this analysis and justifies some of the approximations.

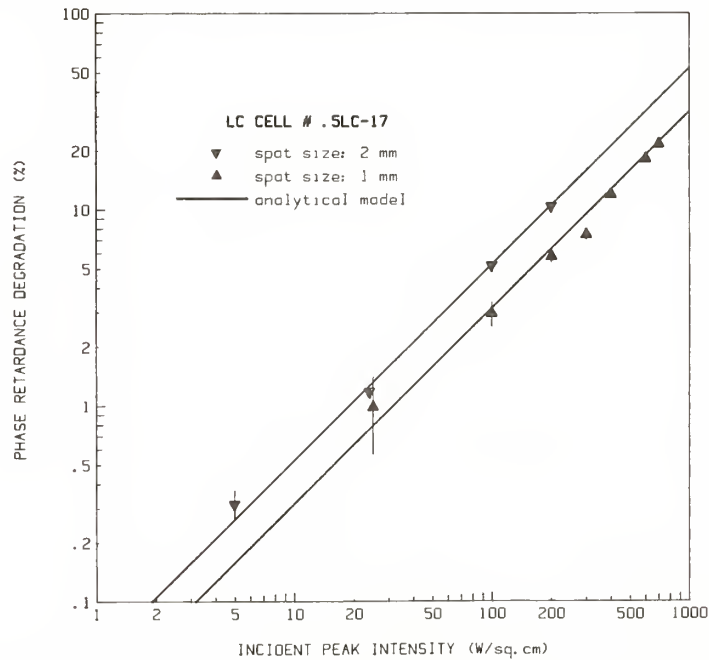


Figure 6. Phase-retardance degradation as a function of the CO<sub>2</sub>-laser intensity, for spot sizes of 1- and 2-mm diameter. Data points are as derived from the measurements recorded in Fig. 5; the straight lines illustrate the results of model calculations and do not involve any adjustable parameter.

For temperatures ranging from 20 to 38 °C, the relative thermal birefringence coefficient,  $(1/\Delta n_0)d(\Delta n)/dT$ , of the BDH-E7 nematic mixture is equal to  $-0.0065\text{ }^{\circ}\text{C}^{-1}$  based on data listed in Ref. 1 (see also Fig. 1). In conjunction with effective temperature increments as derived in Sec. 4, Eq. (44) predicts that the degradation experienced by cell # .5LC-17 when illuminated by a CO<sub>2</sub>-laser beam of intensity  $I_0$  (in Watts per square centimeter) obeys the relations

$$|\Delta\phi_1/\phi_{1,0}| = 3.16 \times 10^{-4} I_0 \quad (45a)$$

and

$$|\Delta\phi_2/\phi_{2,0}| = 5.25 \times 10^{-4} I_0 \quad (45b)$$

for spot sizes of 1- and 2-mm diameter, respectively. These two "predictions" are depicted in Fig. 6, on a log-log scale, and compared with the results of our measurements, the error bars reflecting uncertainties in the reference (zero-intensity) retardance as determined by means of least-squares fits [see Eq. (34)]. There is good agreement, which validates our analytical model and provides rather conclusive evidence that the physical mechanism responsible for the retardance degradation observed in our experiments relates to laser-induced heating of the liquid crystal.

## 6. Conclusion

The interaction of laser light with liquid crystals is currently a subject of considerable importance, from a fundamental as well as an applied point of view. In this paper, we have examined the degradation of the phase retardance of a nematic LC cell operating in a transmissive mode and subjected to continuous CO<sub>2</sub>-laser radiation of less than 1 kW/cm<sup>2</sup> peak intensity. The degradation was found to be linearly dependent on the peak intensity and to reflect the loss of birefringence caused by thermal effects. The laser-induced temperature rise resulting from the absorption of incident light thus constitutes the primary physical mechanism responsible for the performance degradation of an LC cell and, therefore, requires special attention. The task of modeling the temperature distribution is not straightforward for several reasons; these have been addressed in detail and solved in a reasonably consistent manner. The agreement with experimental observations is encouraging and suggests that our analytical procedure merits further consideration in the context of investigating high-power laser applications of LC devices.

At this point, we may state specific conclusions as follows:

- If the LC layer is very thin compared to the windows, Eq. (31) provides a suitable model for the radial temperature distribution in the sense that  $\delta T(r)$  describes the average temperature increase of the windows [ $\delta T(r) = T(r) - T_A$ ], whereas  $\delta T_{LC}(r)$  refers to the additional temperature increment of the LC layer [ $\delta T_{LC}(r) = T_{LC}(r) - T(r)$ ]; both are linearly dependent upon incident irradiances.
- Solutions of Eq. (12), in conjunction with the boundary conditions (13) and the results of edge-temperature measurements, demonstrate that a conventional heat-transfer coefficient can be utilized to characterize the efficiency of diffusion-assisted cooling through the support plate; the beam-induced temperature rise of high-thermal-conductivity substrates then turns out to be almost uniform (see Fig. 4).
- The temperature profile of the LC layer derives from the differential equation for face-cooled slabs [Eq. (26)] upon setting the heat-transfer coefficient equal to the reciprocal thermal resistance of the LC layer; for thin layers, this leads to very large Nusselt numbers, which implies that the LC layer temperature increment,  $\delta T_{LC}(r)$ , mirrors the incident beam shape.

- Figure 5 documents the results of our phase-retardance measurements; the retardance decreases monotonically as the beam intensity increases and obeys a linear dependence at irradiance levels up to 800 W/cm<sup>2</sup>.
- The measured retardance degradation reflects spatially-averaged beam-induced effects; for Gaussian beams, the model predicts that the retardance degrades in accord with Eq. (44), which involves the relative thermal birefringence coefficient,  $(1/\Delta n_0)d(\Delta n)/dT$ , and the effective laser-induced temperature increase  $\Delta T_{\text{eff}} = \delta T(0) + \delta T_{\text{LC}}(0)/2$ .
- As evidenced in Fig. 6, the model predicts the laser-induced degradation of the phase retardance with good accuracy, thus confirming that heating is the causative mechanism; in this connection, we note that nematic LCs having small  $d(\Delta n)/dT$ 's are of particular promise for high-power applications.

#### Acknowledgement

This work was supported in part by AFWAL under Contract No. F33615-87-C-1507.

#### Appendix/Glossary

D	: cell aperture	$T_{\text{LC}}(r)$	: LC layer temperature
G(T)	: function of temperature	$\overline{T_{\text{LC}}}$	: spot-averaged LC layer temperature
$h_E$	: edge heat-transfer coefficient	z	: axial coordinate
$h_F$	: face heat-transfer coefficient	$\alpha$	: LC absorption coefficient
$h_{\text{LC}}$	: LC layer heat-transfer coefficient	$\beta_S$	: coating absorptance
I(r)	: beam intensity	$\beta_W$	: window absorption coefficient
$I_0$	: peak intensity	$\beta_{\text{eff}}$	: effective absorption coefficient
$K_{\text{LC}}$	: LC thermal conductivity	$\delta T_E$	: edge temperature increment
$K_W$	: window thermal conductivity	$\delta T(r)$	: window/cell temperature increment
l	: LC layer thickness	$\delta T_{\text{LC}}(r)$	: LC layer temperature increment
L	: cell thickness	$\overline{\delta T_{\text{LC}}}$	: spot-averaged LC layer temperature increment
$L_W$	: window thickness	$\Delta n$	: liquid crystal birefringence
$n_e$	: extraordinary refractive index	$\Delta n_0$	: fiducial LC birefringence
$n_o$	: ordinary refractive index	$\Delta T_{\text{LC}}(r)$	: LC layer temperature increase
Nu	: Nusselt number	$\overline{\Delta T_{\text{LC}}}$	: spot-averaged LC layer temperature increase
$P_A$	: power absorbed	$\Delta \Delta n(r)$	: local birefringence variation
$P_E$	: power removed, edge	$\Delta \phi$	: operational retardance variation
$P_F$	: power removed, faces	$\Delta \phi(r)$	: local retardance variation
r	: radial coordinate	$\lambda$	: laser wavelength
$r_0$	: $1/e^2$ spot radius	$\lambda^*$	: resonance wavelength
$T_A$	: ambient temperature	$\phi$	: phase retardance
$T_E$	: edge temperature	$\phi_0$	: fiducial retardance
$T(r, z)$	: local temperature	$\phi_1$	: measured retardance, 1-mm spot size
$T(r)$	: axially-averaged temperature	$\phi_2$	: measured retardance, 2-mm spot size
$T_W(r)$	: window temperature		



## References

- [1] Jacobs, S.D., "Liquid crystals for laser applications," in *CRC Handbook of Laser Science and Technology*, Vol. IV/Pt. 2 (CRC Press, Cleveland/OH, 1986), pp. 409-65.
- [2] Wu, S.T., "Infrared properties of nematic liquid crystals: an overview," *Optical Engineering*, Vol. 26 (1987), pp. 120-8.
- [3] Richard, L., Maurin, T., and Huignard, J., "Phase conjugation with gain at CO<sub>2</sub> laser line  $\lambda = 10.6 \mu\text{m}$  from thermally induced gratings in nematic liquid crystals," *Optics Communications*, Vol. 57 (1986), pp. 365-70.
- [4] Wu, S.T., and Hess, L.V., "Nonlinear rotatory power of 90° twisted nematic liquid crystals," in *Laser-Induced Damage in Optical Materials: 1984* (NBS Special Publication 727, Washington/DC, 1986), pp. 23-9.
- [5] Klein, C.A., "Beam-induced spherical aberration in cooled CW laser light transmitting components," in *Laser-Induced Damage in Optical Materials: 1986* (NBS Special Publication 752, Washington/DC, 1988), pp. 96-126.
- [6] Klein, C.A., "Methodology for designing high-energy laser windows," in *Proceedings of the International Conference on Lasers: 1978* (STS Press, McLean/VA, 1979), pp. 283-95.
- [7] Carslaw, H.S., and Jaeger, J.C., *Conduction of heat in solids: second edition*, Oxford University Press, Oxford/UK, 1959.
- [8] Sharp, R.C., Resler, D.P., Hobbs, D.S., and Dorschner, T.A., "An electrically tunable liquid crystal wave plate in the IR," to be published.
- [9] Halley, J.M., and Midwinter, J.E., "Thermal analysis of optical elements and arrays on thick substrates with convection cooling," *Journal of Applied Physics*, Vol. 62 (1987), pp. 4055-64.
- [10] Mason, T.C., and Stocks, D.C., *BASIC differential equations*, Butterworths and Co., London/UK, 1987.
- [11] Urbach, W., Hervet, H., and Rondelez, F., "Thermal diffusivity in mesophases: a systematic study in 4-4'-di-(n-alkoxy) azoxy benzenes," *Journal of Chemical Physics*, Vol. 78 (1983), pp. 5113-24.
- [12] Musikant, S., *Optical materials: an introduction to selection and application*, Marcel Dekker, Inc., New York/NY, 1985.

FUNDAMENTAL MECHANISMS OF LASER-INDUCED DAMAGE IN TRANSPARENT  
SOLIDS: UP-TO-DATE STATUS OF RESEARCH AND UNDERSTANDING\*

A.A. Manenkov

General Physics Institute of the USSR Academy of Sciences  
Moscow, USSR

Work on the investigation of damage mechanisms in transparent solids under IR, visible and UV laser pulsed radiation are reviewed. Basic theoretical models and regularities of laser damage associated with impact and multiphoton ionization (intrinsic processes), thermal explosion of absorbing inclusion and thermal radiation induced photoionization of surrounding matrix, and with mechano-chemical reactions of absorbing "hot" radical formation (extrinsic processes) are described. Experimental data confirming laser damage mechanisms discussed for optical materials of different classes, including crystals, glasses and polymers are analyzed.

Key words: absorbing inclusions; electron avalanche; "hot" radicals; impact ionization; laser damage mechanisms; mechano-chemical reactions; multiphoton ionization; polymers; thermal radiation produced photoionization

## 1. INTRODUCTION

A little more than 20 years have passed since the first observations in 1964 of optical breakdown in transparent solids /1,2, thus the present 20th Anniversary of the Boulder Damage Symposium virtually coincides with the age of systematic studies of the laser damage problem.

The laser damage research field is enormous and includes physical problems of the interaction of high-power laser radiation with matter and various physical, chemical, mechanical, optical, and other aspects of material technology for high-power laser optics. Therefore, it is impossible to present in one report, even briefly, the major results achieved for a 20 year period of research in this field.

For this reason I confine myself in this report to reviewing the main progress in investigations of fundamental mechanisms of laser induced damage to transparent optical materials. From the very beginning of the laser damage research a large number of possible mechanisms and models of damage under high-power laser radiation have been discussed in the literature, including light pressure, electrostriction, hypersound generated at stimulated Mandelstam-Brillouin light scattering (SMBS), impact ionization (electron avalanche), multi-photon ionization, different types of thermal effects (thermoelastic stresses, thermal ionization, photoionization by thermal radiation of heated inclusions, thermo-chemical and mechano-chemical reactions, etc) initiated by absorbing inclusions and defects in optical materials. The thermal effects give rise to a so called extrinsic breakdown, since its characteristics are essentially determined by different types of inclusions and defects in a material, unlike the processes mentioned at the beginning, which are inherent in the material matrix and are responsible for intrinsic breakdown.

A great number of works have been carried out to study the intrinsic and extrinsic mechanisms. Below I dwell on some of the works which, in my opinion, develop most consistently the theoretical concepts of laser damage mechanisms and present most convincing experimental investigations on their realizability in optical materials of different classes under various experimental conditions.

---

\* The review paper presented at the 20th Symposium on Optical Materials for High Power Lasers, Boulder, Colorado, October 26-28, 1988.

Before presenting the results on damage mechanism studies I would like to point out two effects, self-focusing and accumulation effect, playing an important role in the laser damage processes and appreciably influencing the possibility of establishing real damage mechanisms as well as practically attainable laser resistance of optical materials. These effects have been considered in a great number of works, but I will not discuss their results in this paper and refer to reader to review papers /3,4/ recently published.

## 2. INTRINSIC DAMAGE MECHANISMS

A nature of intrinsic damage mechanisms of laser damage is of special interest, since it determines ultimate resistance of optical materials to laser damage. Among the intrinsic mechanisms mentioned above, most probable are impact and multiphoton ionization. Other intrinsic mechanisms discussed in the literature and related to light pressure, electrostriction, and hypersound generation by SMBS turn out to be insufficiently efficient to induce damage /5,6/. Moreover, SMBS even hampers the formation of damage, as it reduces local intensity of the laser beam propagating in a sample due to back scattering /7/.

### 2.1 Impact Ionization (electron avalanche).

The process of impact ionization as a mechanism of laser damage has been discussed and theoretically investigated by many researchers (see /8-18/ and references therein). Its essence consists of an avalanche multiplication of the electrons due to impact ionization of a dielectric, which heats the crystal lattice through electron-photon interaction. A high temperature of the lattice, leading to thermoelastic stresses or irreversible phase transitions (melting, etc.), is reached at the electron concentration in the conduction band of an order of  $10^{18} \text{ cm}^{-3}$ .

Sufficient concentration of the initial (seeding) electrons in the conduction band has an essential influence upon the development of electron avalanche and determines the probability of laser damage. Seed electrons may appear through photoionization of the impurities and defects, or multiphoton ionization of the host atoms of the crystal lattice.

A consistent theory of laser damage caused by avalanche impact ionization has been developed by Epifanov et. al. /11,12,14,16,17,18/ on the basis of solving the quantum kinetic equation for the electrons in the conduction band. The theory enabled the establishment of the major regularities of the laser damage associated with avalanche ionization: the dependence of damage threshold intensity (or critical field) upon laser frequency, pulse duration, material parameters, and initial temperature of a crystal.

The statistical regularities of laser damage have also been established, which are associated with suppression of avalanche ionization because of insufficient concentration of the seed electrons. The most important results of the theory developed are as follows.

The breakdown critical field is determined by the expressions /11,12/:

$$E_c^2 = \frac{Im^2 V_s^2}{2K Te^2} \left( \Omega^2 + \frac{I}{m \ell_{ac}^2} \right) \quad (1)$$

for high initial temperatures,  $T$ , of a crystal and relatively low frequencies of the laser field  $\Omega$ , when the conditions hold:

$$\hbar\Omega/I \leq 0.2, \quad KT > \frac{1}{2} V_s (2 mI)^{1/2}$$

here  $V_s$  is the sound velocity,  $I$  is the ionization potential,  $m$  and  $e$  are the electron effective mass and charge, respectively,  $\ell_{ac}$  is free path of an electron associated with acoustic phonons;

$$E_c^2 = \frac{mV_s(2mI)^{1/2}}{2e^2} \left( \Omega^2 + \frac{2I}{5m \hbar_0^2} \right) \quad (2)$$

for low temperatures  $KT < 1/2 V_s(2mI)^{1/2}$  and low frequencies  $\hbar\Omega/I \gtrsim 0.2$ .

Also established was the character of the dependences of the breakdown critical field upon frequency and pulse duration for high frequencies  $\Omega/I \gtrsim 0.2$  /17/.

These results indicate significantly different dependences of the breakdown threshold upon frequency, pulse duration and temperature for different frequency and pulse duration regions. Figures 1, 2, and 3 illustrate these specific differences. The predicted characteristic frequency and temperature dependences of the critical field have been used in our experimental studies to verify the realizability of avalanche laser damage mechanism in wide-band gap crystals. The results will be presented below.

The above theoretical results pertained to the case where in the interaction region where there is sufficient concentration,  $n_0$  of seed electrons to initiate avalanche impact ionization. In this case the breakdown critical field is determined by the rate of the electron avalanche development which weakly depends on  $n_0$  /11,14/. In the opposite case, when the concentration is small ( $n_0 V < 1$ ), the critical field increases and is determined by the rate of seed electron creation, rather than by that of the avalanche development. Analysis of the peculiarities of laser induced damage due to impact ionization under conditions when electron avalanche is deterred because of insufficient concentration of seed electrons has shown that in this case the damage process acquires a statistical character: the breakdown threshold is determined by the probability of appearance of seed electrons. The latter, as mentioned above, may be generated through the impurity ionization or multiphoton ionization of host atoms. Naturally, under these conditions not only does the value of the breakdown threshold increase, compared to that of the undeterred avalanche, but there are also essential changes in the characteristic dependences of the threshold upon frequency, temperature, and interaction volume. For instance, if the seed electrons are generated by multiphoton ionization, the breakdown threshold does not depend on temperature. A spot-size dependence of the breakdown threshold is determined by the probability of the appearance of an electron in the interaction region and this depends upon the geometry of the laser beam and ionization rate, which, in turn, depends on the radiation intensity. In particular, when the seed electron generation is associated with multiphoton ionization of the impurities, the spot-size of the damage threshold is calculated from the relationship /19/:

$$V_{\text{eff}} \sum_i S_i = -\ln(1-P) \quad (3)$$

where  $V_{\text{eff}}$  is an effective interaction volume for a Gaussian laser beam

$$V_{\text{eff}} = \frac{4}{3} \pi k B^4 \int_0^{[(I_m/I_a)-1]^{1/2}} \frac{\xi^2(\xi^2 + 3)}{(\xi^2 + 1)\chi - 1} d\xi$$

$I_a$  is the avalanche breakdown critical intensity,  $I_m$  is the maximum intensity in the beam of radius  $b$ ,  $k = \frac{2}{\lambda} \pi$  is the wave number,  $S_i$  is the density of the impurities and defects of the  $i$ -type,  $P$  is the breakdown probability,  $\chi$  is the degree of the multiphoton process.

## 2.2 Multiphoton Ionization

Multiphoton ionization was considered above as an auxiliary process providing a delivery of seed electrons necessary for the development of impact ionization. If,



however, the probability of multiphoton ionization  $W_n$  is high, the rate of the electron generation in the conduction band through this process may exceed that caused by impact ionization and, hence, the process may become dominant in damage.

A series of works have been concerned with theoretical analysis of the conditions for realization of this situation /17, 20-23/. For instance, Epifanov et al /17/ have analyzed the relative roles of multiphoton and impact ionization on the basis of rate equations for the electron concentration and lattice heating due to both processes of electron generation:

$$\frac{dN}{dt} = \gamma N + W_n - R(N) \quad (4)$$

$$\frac{d\theta}{dt} = \beta \theta^2 N \quad (5)$$

here  $\gamma$  is the rate parameter of the electron avalanche,  $R(N)$  is the term describing the carrier recombination,  $\theta = T/T_0$ ,  $T_0$  is the initial temperature of the lattice,  $\beta$  and  $\alpha$  are the parameters determined by the mechanism of electron-photon interaction.

As a result of this analysis, the criteria for breakdown have been obtained for both impact and multiphoton ionization processes and cleared up the question which of them is dominating in determining the laser damage threshold depending on pulse duration,  $T$ . In particular, the pulse duration dependence of the damage threshold was shown to be appreciably different for the two processes /17/. Figure 4 illustrates pulse duration dependences of the breakdown critical field for the NaCl crystal. The competition of impact and multiphoton ionization is discerned, which depends on the values  $W_n$  and  $T$ . In a particular pulse duration region multiphoton ionization may become a dominating mechanism for breakdown. Since the rates of impact and multiphoton ionizations depend on many characteristic material constants and on the frequency of electromagnetic radiation /14,23/, it is rather difficult to predict theoretically which of the two mechanisms would become dominant in particular regions of frequencies and pulse durations. For this reason experimental investigations based on studying the regularities inherent in both processes and predicted by the theory become decisive in elucidating this problem. The results of these studies will be presented below.

### 2.3 Damage Mechanisms Associated with Heating of Absorbing Inclusions

Various defects and inclusions in transparent solids may possess considerable absorption coefficients; they may include strong local heating and initiate different processes in the surrounding matrix (thermoelastic and thermochemical processes, ionization, and etc.) which lead to macrodamage of a material in the vicinity of the defects. Some theoretical models of thermal damage associated with the above processes have been discussed in the literature.

The first models of laser damage due to absorbing inclusions were suggested in 1970 by two groups of authors /24,25/. They analyzed laser induced heating of an absorbing inclusion assuming parameters of the inclusion and dielectric to be independent of temperature. Those models qualitatively account for some observed regularities of laser induced damage (for instance, the pulse width dependence of a damage threshold /24/), but they are, however, not adequate to describe the physics of laser damage. First of all, they are based on the assumption that the thermal parameters of the inclusions and ambient optical medium are independent of temperature, which is hardly valid. Indeed, at the laser radiation intensities close to the threshold, the temperature in the inclusion region may reach a value of  $10^4$ K (in particular, this is indicated by a high-temperature glow observed at damage), and when analyzing laser heating of an inclusion up to those high temperatures one could hardly neglect the temperature dependence of such thermophysical parameters as the inclusion absorption coefficient and heat conductivity of the inclusion and ambient medium.

Besides, in the framework of the models considered in /24,25/, a criterion for a critical temperature choice at which damage must occur remains groundless because of the difficulty of estimation of such phase transition parameters as melting temperature and ultimate tensile stress under pulsed heating. This particularly refers to the case of damage by short (for instance, nanosecond) laser pulses when the heating process has an essentially nonstationary character.

A principally new approach to the problem of laser damage initiated by absorbing inclusions was offered in 1972 /26/ to show that an account of the temperature dependence of thermophysical parameters of a medium leads to a qualitative change of the heating process -- it acquires an explosion character.

The damage threshold in this model is determined by an asymptotically sharp temperature increase in the inclusion region. The thermal explosion model is attractive because it naturally accounts for the observed features of laser damage: the presence of a sharp threshold and high temperature glow (spark) accompanying damage.

The next principal step in the development of inclusion damage concepts was made in 1978 /27/, when photoionization by thermal radiation emitted by a laser heated inclusion was proposed as an efficient damage mechanism. It was shown that photoionization inevitably occurring at a high-temperature explosion of an absorbing inclusion (at  $T \sim 10^4\text{K}$  the maximum of the Planck thermal radiation lies in the UV spectrum region), is an efficient source of additional absorption in the surrounding dielectric. It should be emphasized that the presence of additional absorption in the mechanism of laser damage is particularly required when the energy absorbed only by the inclusion is insufficient to induce (for instance, through thermoelastic stresses or melting) macrodamage in the ambient matrix.

A detailed consideration of the thermal photoionization mechanism was carried out recently /28,29/ to clear up the conditions for the inclusion thermal explosion and thermal instability produced by photoionization in the ambient matrix and to determine the damage thresholds corresponding to both processes. It was shown that photoionization may be a decisive process in laser induced damage to optical materials containing absorbing inclusions.

Note here one more mechanism of additional absorption in the ambient matrix -- thermal ionization of a dielectric /30/, but it may evidently be effective enough only in narrow-band gap materials.

Specific damage mechanisms may take place in polymers featuring physical-chemical properties substantially different from those of inorganic materials (crystals and glasses).

Several mechanisms of laser-induced damage to polymers have been discussed in the literature: multiquantum photodestruction of macromolecules, thermochemical reaction to form elemental carbon, mechanochemical reactions leading to formation of "hot" radicals, etc. /31/. Among them the mechanochemical mechanism is evidently the most realistic one: it provides an explanation for regularities of laser damage in polymers.

Below, in Sections 3.1 and 3.2, I describe in some detail the two most adequate, in our opinion, inclusion initiated damage mechanisms in optical materials associated with thermal explosion and mechanochemical reactions.

### 3. THERMAL EXPLOSION OF THE ABSORBING INCLUSION

A detailed analysis of the laser heating of an absorbing inclusion has been performed by Koldunov et al. /28,29/ by solving the heat conductivity equation with a nonlinear thermal source (with an assumed temperature dependence of the inclusion absorption cross section):

$$\frac{C_k \rho_k}{t_k(T)} \frac{\partial \theta_k}{\partial t} = \nabla^2 \theta_k + \frac{\sigma(T, w) q}{\frac{4}{3} \pi R^3} f(t) \eta(R \cdot r) \quad (8)$$

where  $\theta_k = \theta_k(T(r, t))$  is the potential of the heat flow determined by the relationships:

$$\theta_k(T(r, t)) = \int_0^{T(r, t)} \chi_k(y) dy, \quad \theta_k(T, T_0) = \theta_k(T) - \theta_k(T_0)$$

$T_0$  is the inclusion initial temperature,  $C_k$ ,  $\rho_k$ ,  $\chi_k(T)$  are heat capacity, density and heat conductivity (index  $k=1$  refers to the inclusion, and  $k=2$  to the ambient dielectric),  $q$  is the maximal intensity of the laser pulse with a temporal shape  $f(t)$ ,  $R$  and  $\sigma(T, w)$  are radius and cross-section of the inclusion absorption,  $\eta(R-r)=1$  at  $r < R$ ,  $\eta(R-r)=0$  at  $r \geq R$ .

It was shown that the temperature dependence of the inclusion absorption cross section leads to an explosive character of its heating. The thermal explosion threshold is determined from the condition of loss of thermal stability of a solution of equation (8). For a semiconductor-type inclusion, whose absorption cross section temperature dependence is described by the relationship

$$\sigma(T) = \sigma_0 + \sigma_1 \exp(-A/T) \quad (9)$$

where  $\sigma_0$  and  $\sigma_1$  are constants,  $A$  is activation energy, the explosion threshold is expressed by (in the limit  $\sigma_0 = 0$ ):

$$q_n = \frac{3 \chi_2 T_0}{2 \epsilon x_1 A R^2} \exp(A/T_0) (1 + \chi_2/2\chi_1)^{-1} \quad (10)$$

for the laser pulse width

$$t_0 \gg T_2 = \frac{C_2 \rho_2 R^2}{3\chi_2}$$

( $x_1$  is the inclusion absorption coefficient corresponding to  $\sigma_1$ ).

Analysis of the inclusion heating with the absorption cross section given by (9) has shown that, due to absorption saturation, the inclusion temperature becomes stabilized at the level

$$T_1 \approx \frac{q R^2 x_1}{3 \chi_1} \quad (11)$$

Estimates using the formulas (10) and (11) for an inclusion with  $R=10^{-5}$  cm,  $x_1=10^3$  cm $^{-1}$ ,  $A=10^3$  K in glass,  $\chi_2=3 \cdot 10^{-3}$  cal. cm $^{-1}$  s $^{-1}$  K $^{-1}$  yield  $q_n=10^9$  W/cm $^2$  and, at  $q \leq q_n$ ,  $T_1 \approx 10^4$  K.

At such a temperature  $\sim 10^4$  K, photoionization of the ambient matrix by thermal radiation plays an important role in laser heating. The electrons generated by photoionization are an additional source of absorption of laser radiation with a cross-section

$$\sigma_{ph} = \frac{16 \pi \beta \omega T^3}{C^3} \tau_r R^2 I_m(\alpha(\omega, T)) \int_{E/T}^{\infty} \frac{x^2 dx}{\exp(x) - 1} \quad (12)$$

where  $\alpha(\omega, T)$  is the electron polarizability,  $\omega$  is the laser radiation frequency,  $\beta$  is the refractive index of the dielectric,  $E$  is the band gap energy,  $C$  is the light velocity,  $\tau_r$  is the electron recombination time. Absorption photoionized by electrons leads to thermal instability in a medium, which has a character of thermal explosion similar to that of inclusion heating.

The kinetic analysis of thermal instability due to both processes - nonlinear heating of an inclusion and photoionized electrons, has allowed the determination of the pulse width dependence of the damage threshold [29]. For a rectangular shaped pulse this dependence has a form:

$$q(t_0) = q_n \left[ 1 - \exp \left( - \xi \frac{t_0}{2\tau} \right) \right]^{-1} \quad (13)$$

where

$$\tau = \frac{C_1 \rho_1 R^2}{3\chi_2}$$

is the temperature relaxation time of the inclusion,  $\xi$  is the temperature nonlinearity parameter of the absorption cross-section associated with photoionization:

$$\sigma_{ph} = \sigma(T_{ph}) \exp \left( \xi \frac{T - T_{ph}}{T_{ph}} \right) \quad (14)$$

$T_{ph}$  is the threshold temperature of the photoionization produced instability. The expression (14) is the approximation of (12) at  $T \approx T_{ph}$  with  $\xi = 1.2 - 2$ . For a pulse with a Gaussian temporal shape the pulse width dependence differs but slightly from (13).

### 3.1 The Mechanochemical Mechanism of Laser-Induced Damage in Polymers

A specific model of laser induced damage in polymers is based on the following idea [31,32]. Laser produced pulsed thermoelastic stresses in the polymer matrix around the absorbing inclusions and defects initiate mechanochemical reactions of formation of vibrationally excited ("hot") radicals having an absorption in a wide spectral region from IR to UV. Thus, hot radicals are a source of additional absorption in the matrix, like free photoionized carriers discussed in chapter 3.1.

Mathematical analysis of the mechanochemical damage mechanism based on solving the heat conduction equation with a nonlinear thermal source associated with the absorbing radical generation, led to the derivation of a simple expression for the laser damage threshold intensity [31]

$$I_d = \frac{D E_a}{\tau_a} \quad (15)$$

where  $D$  is the thermoelastic parameter,  $E_a$  is the activation energy for the hot radical formation,  $\tau_a$  is the vibrational relaxation time of the chemical bonds from which hot radicals are formed.

This formula explains the accumulation effect in the multishot laser damage which is strongly pronounced in polymers. Indeed, the hot radical lifetime increases with increasing elastic stress,

$$\tau_a(\sigma_s) = t_0(1 + \delta\sigma_s) \quad (16)$$

(here  $t_0$  and  $\delta$  are parameters) and, hence, due to accumulation from pulse to pulse of thermoelastic stresses in the vicinity of the absorbing defects, the  $N$ -pulse damage threshold decreases.

Another effect in laser damage to polymer materials, the influence of the low-molecular weight additives upon the laser resistance, is also clear in the framework of the radical damage mechanism. This influence is due to decreasing relaxation time  $T_a$ , since the energy of the excited vibrational states of the polymer macromolecules is transferred to the vibrational levels of the low-molecular weight additives.



A simple analysis /31/ has shown that, due to energy transfer, (which we call vibrational cross-relaxation) reduction in the relaxation time  $T_a$  is expressed by a relationship:

$$\tau_a^{-1} = \frac{\tau_a}{1 + W_{cr}\tau_a} \quad (17)$$

where  $W_{cr}$  is the vibrational cross-relaxation rate.

From (15) and (17) it is seen that the damage threshold is essentially determined by the value of the parameter  $W_{cr}$ , i.e. by the efficiency of the interaction of the additive molecule with the polymer macromolecules. Thus, the developed theoretical concepts of the laser damage mechanism in polymers predict a way to increase their laser resistance, that is insertion into a polymer of suitable low molecular weight additives which efficiently suppress the generation of hot radicals through vibrational cross-relaxation.

#### 4. EXPERIMENTAL CONFIRMATION OF LASER DAMAGE MECHANISMS

A great number of works have been published in the literature making attempts to interpret the experimental results on the basis of the above theory and some other mechanisms of laser induced damage in different type optical materials. However, a lot of conclusions on the realizability of either mechanism turned out to be doubtful or, at least, not convincing, because they have not been backed by reliable theoretical models. This particularly refers to the confirmation of intrinsic breakdown mechanisms such as electron avalanche and multiphoton ionization. Not dwelling here on many controversial discussions reflected in the literature of the last 20 years<sup>1</sup>. I present only some major experimental results, which confirm most reliably, in our opinion, the role of the laser damage mechanisms discussed above, both intrinsic and extrinsic ones.

##### 4.1. Electron-Avalanche Mechanism

Detailed investigations of frequency and temperature dependences of laser-induced damage threshold have been performed in alkali-halide crystals /33-35/ (see, also /3,15/). The experiments were carried out on a great number of the NaCl, KCl, KBr, LiF, NaF samples, and others, in a wide frequency range using single-mode lasers with well controlled radiation parameters (CO<sub>2</sub> lasers ( $\lambda=10.6 \mu\text{m}$ ), YAG:Nd ( $\lambda=1.06 \mu\text{m}$  and second harmonic  $\lambda=0.53 \mu\text{m}$ , ruby laser ( $\lambda=0.69 \mu\text{m}$ ), CaF<sub>2</sub>:Er ( $\lambda=2.76 \mu\text{m}$ )) and temperatures ( $T=100-900 \text{ K}$ ).

Figures 5 and 6 present for example temperature and frequency dependences of the damage threshold for the most damage resistant samples of NaCl, in which one could expect intrinsic breakdown. Analysis of these data has indicated that the dependences observed are in a good agreement with the theoretically predictions of the electron-avalanche breakdown mechanism. This mechanism also accounts for some "anomalies" in the temperature dependence of the breakdown threshold observed for the long-wave length radiation ( $\lambda=10.6 \mu\text{m}$  and  $\lambda=2.76 \mu\text{m}$ ). These anomalies turned out to be associated with the suppression of an avalanche because of the lack of seed electrons. This effect was directly confirmed in a special experiment with two crossed laser beams at different frequencies /35/: one with  $\lambda 10.6 \mu\text{m}$ , caused damage, the other with  $\lambda 0.337 \mu\text{m}$ , generated seed electrons through photoionization. A 6-fold decreasing of the damage threshold was detected in the damage region illuminated with the UV laser beam ( $\lambda=0.337 \mu\text{m}$ ). The observed decrease is explained by the deterrence of the avalanche ionization (and, hence, by a higher breakdown threshold), by insufficient seed electrons in the absence of preionization by UV radiation.

Thus, both types of experiments, studying frequency and temperature dependences and influence of the UV illumination, convincingly confirmed that the electron-avalanche mechanism is realized in high-purity crystals.

<sup>1</sup> On some of these discussions see reference /3, 15/.

#### 4.2. Multiphoton Ionization

Some attempts have been made in the literature to analyze experimental laser damage data on the basis of the multiphoton ionization mechanism (see /3,36,37/ and references therein). However, conclusive experimental studies have not yet been done (in particular, searching for typical dependences, for this mechanism, of damage threshold upon, for instance, frequency and pulse duration), which would unambiguously confirm a dominating role of this mechanism in laser damage. Perhaps the most substantive investigations on elucidation of the role of multiphoton ionization in laser damage, particularly of wide-band gap optical materials, were direct measurements of the multiphoton absorption coefficients /38-40/ and estimation of the temperature in the interaction region due to this kind absorption in alkali-halide crystals /37/.

The picosecond photoconductivity method used in /39,40/ turned out to be rather reliable for detecting and identifying multiphoton ionization processes in wide-band gap crystals, and it is precise enough for measuring the corresponding absorption coefficients, as well as such important parameters as mobility and lifetime of electrons.

It was revealed that the 2-nd, 3-rd, and 4-th harmonics of the YAG:Nd-laser rather efficiently excite free carriers in the KCl, NaCl, KBr, and KI crystals as a result of multiphoton ionization up to the 4-th order. For instance, the estimates of the effective absorption coefficients associated with the 2-nd, 3-rd, and 4-th photon processes of carrier excitation in KCl and NaCl at the intensities close to the damage threshold ( $I \approx 5 \cdot 10^{12} \text{ W/cm}^2$ ) turned out to be rather large:  $\sim 10^4 \text{ cm}^2$  at  $\lambda = 0.266 \text{ }\mu\text{m}$ ,  $\sim 10^2 \text{ cm}^2$  at  $\lambda = 0.355 \text{ }\mu\text{m}$  and  $\sim 5 \cdot 10^2 \text{ cm}^2$  at  $\lambda = 0.532 \text{ }\mu\text{m}$ . This absorption may cause an essential heating of a crystal and result in damage /40/.

In /37/ the temperature dependence of the luminescence intensity of a self-trapped exciton in KBr was measured in order to estimate the heating of the interaction region associated with free carrier absorption. At the intensities close to the damage threshold this heating turned out to be close to the crystal melting temperature. This enabled the authors to conclude that free carrier absorption in KBr due to 4-photon ionization is a dominating process in the laser induced damage under the experimental conditions ( $\lambda = 0.532 \text{ }\mu\text{m}$ ,  $\tau = 100 \text{ ps}$ ).

The published results of experiments of both types - on photoconductivity and exciton luminescence - undoubtedly indicate a considerable role of multiphoton ionization in the interaction of high-power short (picosecond) laser pulses with wide-band gap dielectrics. But in our opinion, to conclude more reliably if multiphoton ionization is a dominant damage mechanism, further purposeful investigations have to be made.

#### 4.3 Damage Mechanisms Associated with Absorbing Inclusions

A great number of investigations confirm a decisive role of the absorbing defects in the laser damage to optical materials of various classes. Two most demonstrative experimental facts support this statement: spatial variation of the damage thresholds inside a sample or on the surface, and the influence of the material production technology and successive treatment (polishing, annealing, etc.).

The other facts, such as morphology, statistical character of damage (spot size dependence of the damage threshold, the breakdown probability dependence upon intensity) are also often considered as proofs of the extrinsic mechanism of breakdown. However, the latter fact may also be associated with intrinsic damage mechanisms. For instance, the spot-size dependence of the damage threshold due to avalanche ionization may be associated with the diffusion of the electrons from the interaction region. Therefore, to make unambiguous conclusions on the realizability of either damage mechanism, a thorough analysis of the experimentally observed regularities has to be made by comparison with those predicted by the theory.

Such analysis aimed at elucidation of the damage mechanisms due to the heating of absorbing defects is usually hampered by the lack of data on the nature and characteristics of the defects<sup>2</sup>. The problem is that there are no simple and reliable

---

<sup>2</sup>Except for the trivial cases, where harmful defects of large enough size, for instance, platinum metallic inclusions in glasses, are apriori known.

investigation techniques developed for small-size (submicron) defects in solids, which usually initiate the laser damage in high-quality materials of laser optics. The variety and complexity of the defects which may be formed in optical materials during the technological process of their production make much more complex even the problem of their identification, not to mention the measurement of their optical, thermal and other characteristics (for instance, absorption coefficient and its temperature dependence) important for the theory of laser damage. Besides, not only may original defects (inclusions, impurity clusters) play an important role in the laser damage processes, but also new defects developing under high-power laser irradiation (such as color centers in crystals and glasses, radicals in polymers).

All this strongly hampers analysis of experimental laser damage data on the basis of sufficiently simple theoretical models. Nevertheless, the experimental data obtained up to now on laser induced damage in crystals, glasses, and polymers lead to the conclusion that the above mentioned mechanisms of thermal explosion and mechanochemical reactions are realized in these types of optical materials under various experimental conditions.

For instance, a sharply expressed threshold character and continuous spectrum of the glow (spark) accompanying laser damage in crystals and glasses are qualitatively explained by the photoionization thermal explosion mechanism and are not consistent with the other models such as, for instance, the thermoelastic model /25/. No correlation of damage threshold observed for crystals and glasses with their mechanical properties is either in agreement with the thermal explosion mechanism, but contradicts to the predictions of the thermoelastic damage model.

The observed dependence of the damage threshold upon the pulse duration /24/ is also qualitatively consistent with the predictions of the thermal explosion theory, though more detailed investigations of this dependence are required for different materials to draw reliable conclusions.

The mechano-chemical mechanism developed for explanation of the peculiarities of the laser damage in polymers is confirmed by much experimental data (see /31,32/ and references therein). For instance, this mechanism enables to explain well the dependence of the damage threshold upon temperature, most sharply pronounced in the vicinity of the glass transition temperature, and upon plasticizer insertion, which is associated with variation in visco-elastic properties of the polymer matrix characterized by elastic stress parameter,  $\sigma_g$  (see formulas (15) and (16)). The mechanism also explains the influence of the low-molecular weight additives upon the polymer damage resistance; this influence is associated with the efficiency of vibrational cross-relaxation between the additive molecules and macromolecules characterized by cross-relaxation rate parameter  $W_{cr}$  (see formulas (15) and (17)).

Analysis of the discussed theoretical model made it possible to devise ways to physically modify the polymers with a view to increasing their laser damage resistance: 1) insertion of plasticizers which decrease the induced elasticity limit of the matrix; 2) introduction of low-molecular weight additives hampering the formation of absorbing radicals due to vibrational cross-relaxation. Realization of these ideas enabled the development of modified polymers of the acryl series with high laser damage resistance, comparable with that of the most damage resistant crystals and glasses. For instance, at  $\lambda=1.06 \mu\text{m}$ ,  $\tau=10 \text{ ns}$  the damage threshold for modified PMMA is  $I_d=5.10^{11} \text{ W/cm}^2$ , as compared to  $I_d=7.10^{11} \text{ W/cm}^2$  / 32/ for silicate glass  $K_8$  and fused quartz.

## 5. CONCLUSION

From the above analysis of the up-to-date status of the fundamental research of laser damage mechanisms in transparent optical materials one can conclude that the main theoretical concepts have already been developed and related to intrinsic processes (avalanche and multiphoton ionization), as well as extrinsic processes associated with the absorbing defects (thermal explosion of an absorbing inclusion, matrix photoionization by thermal radiation emitted by an inclusion, mechanochemical reactions of the absorbing radical formation). These mechanisms account well enough for the experimental data on laser damage in optical materials of different classes by nanosecond pulses. There are some experimental results indicating an important role of multiphoton ionization in the



laser damage of wide-band gap dielectric crystals by picosecond pulse radiation at short (visible and near UV) wavelengths. But further theoretical and experimental studies have to be performed to make more definite conclusions about conditions in which the multiphoton ionization mechanism is dominating.

Special attention should be given to studies of laser-induced damage in extreme ultrashort (femtosecond) laser pulse range. This field is almost completely open to study (only first observations were reported /41/).

## 6. REFERENCES

- [1] Guliano, C.R. Appl. Phys. Lett., 5, 137 (1964).
- [2] Cullom, G.H., Waynant, R.W. Appl. Opt. 3, 989 (1964).
- [3] Manenkov, A.A., Prokhorov, A.M. Uspekhi Physicheskikh Nauk 148, 179 (1986).
- [4] Manenkov, A.A., Matyushin, G.A., Nechitailo, V.S., Prokhorov, A.M. Izvestiya AN SSSR, ser. Phys. 52, No.9, 1788 (1988).
- [5] Ritus, A.I., Manenkov, A.A. Pis'ma JETP, 6, 349 (1967).
- [6] Sharma, B.S., Rieckhoff, K.E. Canad. J. Phys. 48, 117 (1979).
- [7] Bel'kyavichus, P.Y., Kosenko, E.K., Lukoshyus, Y.P., Maldutis, E.K. Kvantovaya Elektronika 5, 2032 (1978).
- [8] Zverev, G.M., Mikhailova, G.N., Pashkov, V.A., Soloviev N.M. Soviet JETP, 53, 1849 (1967).
- [9] Molchanov, A.G. Physika Tverdogo Tela 12, 954 (1970).
- [10] Bloembergen, N. IEEE J. Quant. Electr. QE-10, 375 (1974).
- [11] Epifanov, A.S. Soviet JETP, 167, 1805 (1974).
- [12] Epifanov, A.S., Manenkov, A.A., Prokhorov, A.M. Pis'ma JETP, 21, 483 (1975).
- [13] Zakharov, S.I. Soviet JETP, 68, 2167 (1975).
- [14] Epifanov, A.S., Manenkov, A.A., Prokhorov, A.M. Soviet JETP, 70, 728 (1976).
- [15] Manenkov, A.A. Proc. 9-th Symposium on Opt. Materials for High Power Lasers, Boulder, CO, 1977, NBS Spec. Publ. 503, p.455 (1977).
- [16] Epifanov, A.S., Manenkov, A.A., Prokhorov, A.M. Proc. of Lebedev Physical Inst. Acad. Sci. USSR, v. 101, 87 (1978).
- [17] Gorshkov, B.G., Epifanov, A.S., Manenkov, A.A. Soviet JETP, 76, 617 (1979).
- [18] Epifanov, A.S. IEEE J. Quant. Electr. QE-17, 2018 (1981).
- [19] Epifanov, A.S., Garnov, S.V. IEEE J. Quant. Electron. QE-17, 2023 (1981).
- [20] Braunlich, P., Schmid, A., Kelley, P. Appl. Phys. Lett., 26, 150 (1975).
- [21] Schmid, A., Kelley, P., Braunlich, P. Phys. Rev. B, 16, 4569 (1977).
- [22] Kelley, P., Schmid, A., Braunlich, P. Phys. Rev. B, 20, 815 (1979).
- [23] Vinogradov, A.V., Faizulov, F.S. Kvantovaya Elektronika 4, 1144 (1977).
- [24] Danileiko, Yu.K., Manenkov, A.A., Prokhorov, A.M., Khaimov-Malkov, V. Ya. Soviet JETP, 58, 31 (1970).



- [25] Hopper, R.W., Uhlman, D.R. J. Appl. Phys. v. 41, p. 4023 (1970).
- [26] Danileiko, Yu.K., Manenkov, A.A., Prokhorov, A.M., Khaimov-Malkov, V.Ya. Soviet JETP, 63, 1032 (1972).
- [27] Danileiko, Yu.K., Manenkov, A.A., Nechitailo, V.S. Kvantovaya Elektronika 5, 194 (1978).
- [28] Koldunov, M.F., Manenkov, A.A., Pokotilo, I.L. Kvantovaya Elektronika, 15, 544 (1988).
- [29] Koldunov, M.F., Manenkov, A.A., Pokotilo, I.L. "The Theory of Inclusion-Initiated Damage in Optical Materials: the Thermal Explosion Mechanism". A paper presented at the 20-th Symposium on Optical Materials for High-Power Lasers, Boulder, Colorado, October 26-28, 1988, submitted to this Symposium Proceedings.
- [30] Anisimov, S.I., Makshantsev, B.I. Physika Tverdogo Tela, 15, 1090 (1973).
- [31] Dyumaev, K.M. Manenkov, A.A., Maslyukov, A.P., Matyushin, G.A., Nechitailo, V.S., Prokhorov, A.M. Izvestiya AN SSSR, 49, No. 6, 1084 (1985).
- [32] Dyumaev, K.M., Manenkov, A.A., Maslyukov, A.P., Matyushin, G.A., Nechitailo, V.S., Prokhorov, A.M. "Recent Progress in Understanding Fundamental Mechanisms of Laser-Induced Damage in Optical Polymers". Submitted to the Proceedings of the 19-th Symposium on Optical Materials for High-Power Lasers, Boulder, Colorado, 1987.
- [33] Gorshkov, B.G., Danileiko, Yu.K., Epifanov, A.S., Lobachev, V.A., Manenkov, A.A., Sidorin, A.V. Soviet JETP, 72, 1171 (1977).
- [34] Gomelauri, G.V., Manenkov, A.A. Kvantovaya Elektronika, 6, 45 (1979).
- [35] Gorshkov, B.G., Danileiko, Yu.K., Epifanov, A.S., Manenkov, A.A., Prokhorov, A.M., Sidorin, A.V. Kvantovaya Elektronika, 8, 155 (1981).
- [36] Walker, T.W., Guenther, A.H., Nielsen, P.E. IEEE J. Quant. Electr., QE-17, 2053 (1981).
- [37] Shen, X.A., Braunlich, P., Jones, S.C., and Kelley, P. Phys. Rev. Lett. 5, No. 14, 1605 (1987).
- [38] Liu, P., Yen, R., Smith, W.L., Lotem, H., Bechtel, J.H., Bloembergen, N., Adhar, R.S. Phys. Rev. B17, 4620 (1978).
- [39] Garnov, S.V., Epifanov, A.S., Klimentov, S.M., Manenkov, A.A., Prokhorov, A.M. JETP Letters, 45, 399 (1987).
- [40] Garnov, S.V., Epifanov, A.S., Klimentov, S.M., Manenkov, A.A., Prokhorov, A.M. "Multiphoton Photoconductivity and Laser-Induced Damage in Alkali halide Crystals under Picosecond Pulses from RAG:Nd Laser and its Harmonics", submitted to the Proceedings of the 19-th Symposium on Optical Materials for High-Power Lasers, Boulder, Colorado, 1987.
- [41] Gordienko, V.M., Magnitsky, S.A., Platonenko, V.T. "Optical Breakdown of Gases and Solids by Femtosecond Pulses Radiation". Abstracts of the VII All-Union Conference on Optical Radiation "Interaction with Matter", p. 20, Leningrad, March 14-18, 1988.

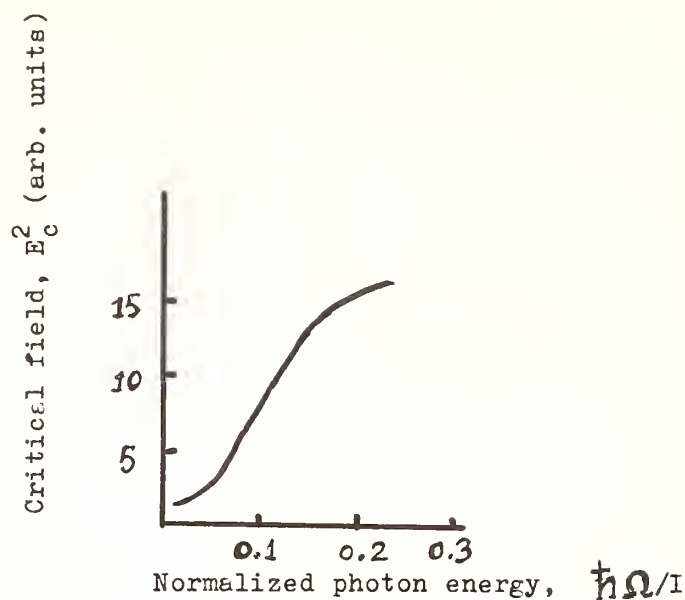


Fig.1. Frequency dependence of critical field predicted<sup>/11,12,14/</sup> by electron avalanche theory for relatively small photon energies,  $\hbar\Omega/I \lesssim 0.2$  ( $\Omega$  is laser frequency,  $I$  is ionization potential).

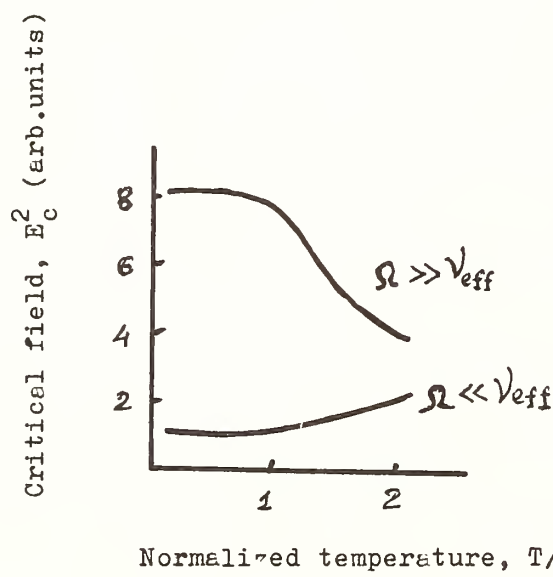


Fig.2. Temperature dependence of critical field predicted<sup>/12/</sup> by electron avalanche theory for various frequency ranges:  $\Omega \gg \nu_{eff}$  and  $\Omega \ll \nu_{eff}$  ( $\Omega$  is laser frequency,  $\nu_{eff}$  is electron-photon collision frequency).  
 $T_n = 1/2 v_s (2mI)^{1/2}$  (see text for denotations).

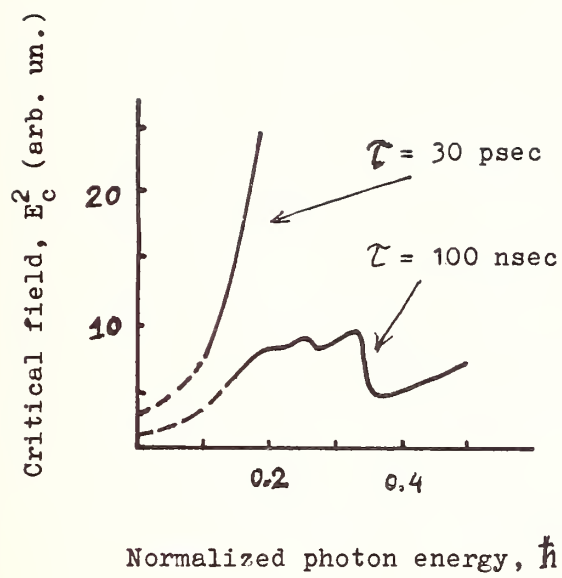


Fig.3. Frequency dependence of critical field predicted<sup>/17/</sup> by electron avalanche theory for picosecond and nanosecond pulse width regions (  $\Omega$  is laser radiation frequency,  $I$  is ionization potential).

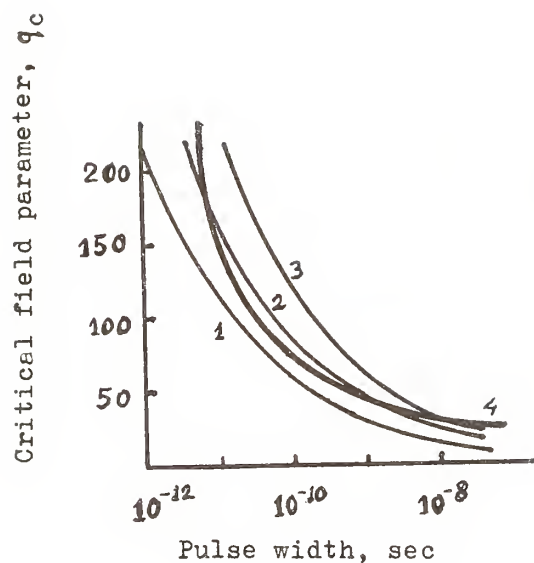


Fig.4. Critical field parameter,  $q_c \propto E^2$ , versus pulse width for NaCl predicted [97] by multiphoton (curves 1,2,3) and electron avalanche (curve 4) mechanisms. Curves 1, 2 and 3 were calculated taking various value of the multiphoton rate parameter  $W_n$  ( $n=5$ ):  
 $W_n^{(1)} > W_n^{(2)} > W_n^{(3)}$



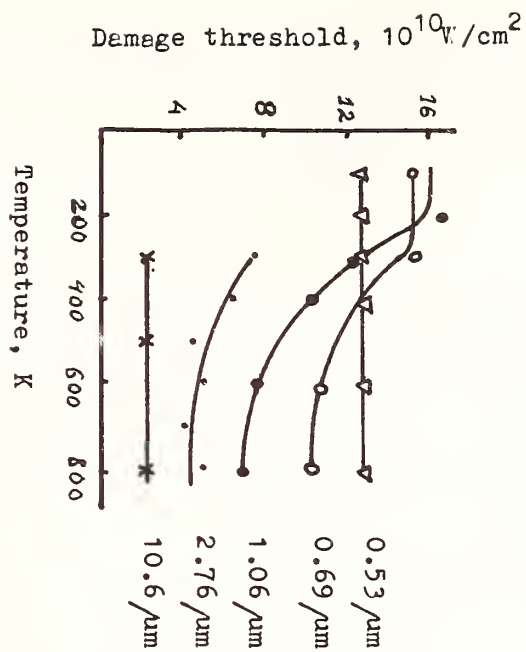


Fig.5. Damage threshold versus temperature in NaCl at various wavelengths /33,34/.

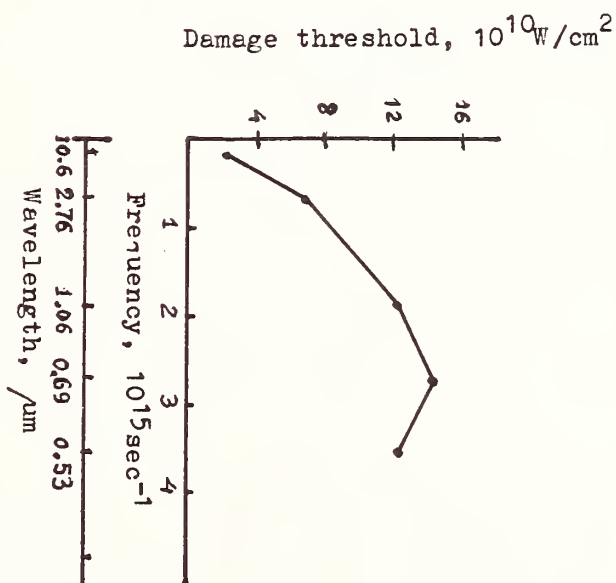


Fig.6. Frequency dependence of damage threshold in NaCl at 300 K /33,34/.

# THE THEORY OF INCLUSION-INITIATED LASER DAMAGE IN OPTICAL MATERIALS: THE THERMAL EXPLOSION MECHANISM

M.F. Koldunov, A.A. Manenkov, and I.L. Pokotilo  
General Physics Institute of the USSR  
Academy of Sciences  
Moscow, USSR

A model of laser induced damage based on the mechanism of thermal explosion of absorbing inclusions is analyzed. Conditions for occurrence of the thermal explosion are formulated. The influence of saturation of the absorption of laser radiation and the role of photoionization of a dielectric matrix by absorbing inclusion on thermal radiation in explosion development are considered. The kinetics of the thermal explosion are analyzed, and the pulse width dependence of the damage threshold is found. Numerical estimates of the damage thresholds for typical cases are presented, showing that the thermal explosion model considered is a rather realistic one for describing the laser-induced damage in optical materials containing absorbing inclusions.

Key words: absorbing inclusions, damage threshold, laser induced damage, photoionization, pulse-duration dependence, thermal explosion, thermal radiation.

## I. INTRODUCTION

The important result of the numerous experimental investigations which have been carried out until recently consists of the fact that absorbing inclusions strongly affect the laser-induced damage in dielectric materials /1/. Many laser damage features (low damage threshold of the dielectric surface as compared with its bulk, variation of the damage threshold in a sample and from one sample to another, damage statistics and so on) are explained from this standpoint.

The pioneering theoretical investigations of laser damage due to absorbing inclusion were carried out in papers /2,3/ where laser heating of the absorbing inclusion was analyzed under the assumption that the material parameters, such as absorption and thermal conductivity coefficients, are independent of temperature. Expressions were found for a laser damage threshold in terms of different criteria of the critical temperature,  $T_n$ , corresponding to the melting point /2/ and the mechanical breakdown /3/.

The models considered in papers /2,3/ qualitatively explain some important regularities of laser induced damage, such as the dependence of the damage threshold on pulse duration /2/, but they do not sufficiently correspond to physical processes of laser damage. First of all, the assumption that the material parameters are independent of temperature cannot be correct, since the temperature in an inclusion region can reach  $10^4$  °K, when the intensity is equal to the damage threshold /1/. Besides, in a framework of the thermoelastic model /3/ the value and physical sense of the critical temperature remain indefinite because of difficulty in estimating critical stresses at which the mechanical breakdown occurs. Finally, from the viewpoint of the thermoelastic stress model a correlation between the damage threshold of the materials and their physical-mechanical parameters should take place, which does not agree with the experimental data.

A substantially new approach to the laser damage problem has been proposed in paper /4/, where it was shown that an allowance for the temperature dependence of the material parameters yields a qualitative change in the character of laser-produced heating of the absorbing inclusions. In this case there is a threshold intensity  $q_n$  (or an associated critical temperature  $T_n$ ) which if exceeded, leads to thermal explosion of the absorbing inclusion. The thermal explosion model explains the catastrophic character of laser-induced damage with a strictly defined damage threshold. If the energy absorbed by the inclusion is not sufficient to produce a macrodamage in the material (it can take place for inclusions of very small submicron size), the thermal explosion can serve as a source of absorption in the surrounding material through photoionization by thermal radiation. This mechanism was proposed in Ref. /5/ and developed in detail in Ref. /6/. Another mechanism of additional absorption is associated with thermal-ionization /7/ but it, obviously, may be effective only for the narrow bandgap materials.

The aim of the present paper is to report a consistent treatment of the laser-induced damage model related to thermal explosion of the absorbing inclusions. In Section 2 there is an analysis of the conditions for the occurrence of thermal instability and the role of the absorption saturation in the inclusion and the conditions of thermal instability in the material associated with photoionization. In Section 3 we consider the kinetics of thermal explosion and the pulse-width dependence of damage threshold. In Section 4 major results obtained are discussed and numerical estimations of the damage threshold predicted by a thermal explosion mechanism are presented for a typical case.

## II. LASER HEATING OF ABSORBING INCLUSIONS

The laser-induced damage in optical materials is related, as a rule, with the absorbing inclusion of a small size  $R \lesssim 10^{-5}$  cm ( $R$  is the inclusion radius). For this reason, it is rather difficult to control them in optical materials. Typically, they are the foreign material particles of metallic or oxide nature.

The inclusions usually have very high absorption and in spite of their small size they can create high temperature in their vicinity. It is important that the absorption coefficient depends on temperature. For example, in the case of a semiconductor-type inclusion the temperature dependence of the absorption coefficient is described by

$$x(T) = x_0 + x_1 \exp\left(-\frac{A}{T}\right) \quad (1)$$

where  $A$  is the activation energy,  $x_0$  and  $x_1$  are the constants. This example illustrates the principle laws of  $T$ -dependence of  $x(T)$  in the general case: at low temperatures  $x(T)$  is independent of  $T$ ;  $x(T)$  increases rapidly in the region of  $T \sim A/2$  and  $x(T)$  no longer increases at high temperatures. The specific feature of the behavior of  $x(T)$  defines a physical picture of the inclusion laser heating: increase of  $x(T)$  can give a thermal instability of the inclusion with rapid growth of its temperature (thermal explosion). The saturation of absorption leads to limitation of the temperature rise, temperature stabilization, and the suppression of thermal explosion.

Below we shall analyze laser heating of the absorbing inclusions on the basis of solution of the thermal conductivity equation, taking into account the temperature dependence of absorption coefficient of the conclusion and surrounding dielectric. As was mentioned above, the increase of  $x(T)$  with increasing  $T$  results in thermal explosion of the inclusion and in sharp temperature increase in its vicinity. In such conditions  $q_n$  is defined as the laser light intensity above which the thermal explosion occurs. For this reason, in the framework of the thermal explosion theory the mechanical properties of the material do not play any role in defining  $q_n$ , and its value is determined completely by the nonlinear characteristics of absorption and some other material parameters related to thermal conductivity.

### Basic Equations

Heating of inclusion with the radius  $R$  by a laser pulse with the maximum intensity  $q$  and temporal shape  $f(t)$  is described by the thermal conductivity equation:

$$\frac{\partial}{\partial t} (C_k \rho_k T(r, t)) = \nabla^2 \theta_k + \frac{\sigma(T) q f(t)}{\frac{4}{3} \pi R^3} \eta(R-r) \quad (2)$$

where  $\theta_k = \theta_k(r, t)$  is the heat flow potential which is defined by

$$\theta_k(r, t) = \theta_k(T(r, t)) = \int_0^{T(r, t)} \chi_k(y) dy,$$

$C_k$  is the heat capacity,  $\rho_k$  is the density,  $\chi_k(T)$  is the thermal conductivity of the inclusion and matrix (subscript  $K = 1$  refers to the inclusion, and  $K = 2$  - to the matrix),  $\eta(x) = 1$  at  $x > 0$ ,  $\eta(x) = 0$  at  $x \leq 0$ , and  $\sigma(T)$  is the absorption cross-section of the inclusion at temperature  $T$ . Hereinafter the inclusion temperature is considered as a surface temperature. It is a good approximation for the inclusion with a strong thermal conductivity for which

$$\frac{\Delta T}{T} \lesssim \frac{\chi_2}{2\chi_1} < 1,$$

where  $\Delta T$  is the temperature difference in the inclusion center and on its surface. For pulse duration

$$\tau_0 \gg \tau_2 = \frac{c_2 \rho_2 R^2}{3\chi_2}$$

and intensity  $q \leq q_n$  ( $q_n$  is the damage threshold) the stationary temperature distribution around the inclusion is arranged, and the maximum heat flow potential is satisfied by the following equation:

$$\nabla^2 \theta_k = - \frac{\sigma(T)q}{\frac{4}{3} \pi R^3} \eta(R-r) \quad (3)$$

Its solution, satisfying the physically reasonable conditions

$$\theta_k < +\infty \text{ and } \theta_2(r) \rightarrow \theta_2(T_0)$$

at  $r \rightarrow \infty$  ( $T_0$  is the initial temperature of dielectric), is

$$\theta_1(r) = \frac{1}{2} \theta_2(T, T_0) \left( 1 - \frac{r^2}{R^2} \right) + \theta_1(T) \quad (4)$$

$$\theta_2(r) = \frac{R}{r} \theta_2(T, T_0) + \theta_2(T_0) \quad (5)$$

where

$$\theta_2(T, T_0) = \theta_2(T) - \theta_2(T_0).$$

Heat flow potentials which are determined by Eqs.(4) and (5) depend on the inclusion temperature. Its value is defined by  $\sigma(T)$  which depends on the temperature itself. Its self-coordination value is determined from the condition of equality of heat flow potentials at the inclusion surface ( $r = R$ ). It gives:

$$q = \Phi(T) \quad (6)$$

where

$$\Phi(T) = \frac{4\pi R \theta_2(T, T_0)}{\sigma(T)}.$$



## Thermal Instability

The laser heating character of the absorbing inclusion for laser pulse duration  $\tau_0 \gg \tau_2$  is determined by the  $\Phi(T)$  function, which, therefore, determines the solution behavior of Eq.(2). When Eq.(6) has a solution, it gives maximum temperature of the inclusion corresponding to the stationary temperature distribution around the inclusion.

The function  $\Phi(T)$  has a maximum if the absorption cross-section grows rapidly with temperature. It can be found from the equation

$$\left\{ \frac{1}{\chi_2(T)} \int_{T_0}^T \chi_2(y) dy \right\} \frac{d}{dT} \{ \ln \sigma(T) \} = 1 \quad (7)$$

When Eq.(7) has the only solution  $T_n$ , the function  $\Phi(T)$  has single maximum  $q_n = \Phi(T_n)$  (see Fig.1, plot 1). Equation (6) has a solution only in the region  $q \leq q_n$ . At  $q > q_n$  Eq.(6) has no solution, i.e. the stationary temperature distribution around the inclusion cannot occur; then, a thermal explosion develops. So the temperature at which  $\Phi(T)$  is maximum is the inclusion critical temperature, which, if exceeded, leads to thermal instability. The maximum of  $\Phi(T)$  gives the threshold intensity  $q_n$ . For this reason, the function  $\Phi(T)$  will be called the threshold function.

It is of great interest to consider the influence of the saturation of absorption on the development of thermal instability. Let us investigate this influence for the semiconductor-type inclusion, the absorption cross-section of which is given by

$$\sigma(T) = \sigma_0 + \sigma_1 \exp\left(-\frac{A}{T}\right).$$

(see (1)). Let  $\chi_2$  be independent of  $T$ ; then Eq.(7) has the following form:

$$\frac{A}{T} \left( 1 - \frac{T_0}{T} \right) = \frac{\sigma_0}{\sigma_1} \exp\left(\frac{A}{T}\right) + 1. \quad (8)$$

In order to find the parameter region of this model where the explosion takes place, we shall follow the theory of catastrophes /9/. The region boundary is

$$\frac{\sigma_0}{\sigma_1} = \frac{1}{e^2} \left( 1 - \frac{4 T_0}{A} \right). \quad (9)$$

For the inclusion in a dielectric with parameters  $\frac{\sigma_0}{\sigma_1}$  and  $\frac{A}{T_0}$  from region I (see Fig. 2) Eq. (9) has no real solution. The threshold function  $\Phi(T)$  increases monotonically with the temperature rise and, hence, there is no thermal instability.

For the inclusion with the parameters from region II (see Fig.2), eq.(7) has two solutions. In this case the threshold function is shown in Fig.1 (plot 2). At  $q > q_n$  the thermal instability occurs and the temperature grows up to  $T_I$  due to saturation of inclusion absorption.

In the limiting case when  $\sigma_0 = 0$ , Eq.(8) has an exact solution, substitution of which into Eq.(6) at  $A \gg T_0$  yields the threshold intensity:

$$qn = \frac{3 \chi_2 T_0^2}{e \tilde{\chi}_1 A R^2} \exp \left( \frac{A}{T_0} \right) \left( 1 + \frac{\chi_2}{2 \chi_1} \right)^{-1} \quad (10)$$

where  $\tilde{\chi}_1$  is the absorption coefficient of the dielectric. For an inclusion with  $R=10^{-5}$  cm,  $\tilde{\chi}_1=10^3$  cm $^{-1}$ ,  $A=10^3$  cmK in the glass, and  $\chi_2=3 \cdot 10^{-3}$  cal.cm $^{-1}$ sec $^{-1}$  K $^{-1}$ , Eq.(10) yields  $q_n \approx 10^9$  W/cm $^2$ . The temperature  $T_1$  in the inclusion region corresponding to this threshold intensity  $q_n$ , reaches the value

$$T_1 \approx \frac{q_n R \tilde{\chi}_1}{3 \chi_1} \approx 10^4 \text{ K.}$$

At such a high temperature of the absorbing inclusion an important role in the laser damage process should be played by the thermal radiation, which produces photoionization in the surrounding medium. An absorption in the vicinity of the inclusion due to photoionized electrons increases the temperature and creates the thermal instability. We consider this process below in more detail.

#### Photoionization Instability

The absorption cross-section associated with both the inclusion and the photoionized electrons in the surrounding dielectric can be presented as follows /6/:

$$\sigma(T) = \frac{4\pi}{c\beta} \omega \operatorname{Im}\{\alpha(T)\} \int_V n(r,T) d^3r \quad (11)$$

where  $c$  is the light velocity,  $\alpha(T)$  is the electron polarizability, and  $n(r,T)$  is the electron density.

The integral is taken over the volume of the dielectric and the inclusion. By dividing the integral into two parts - the dielectric and inclusion - we derive:

$$\sigma(T) = \sigma_1(T) + \sigma_{ph}(T)$$

where  $\sigma_1(T)$  is the inclusion absorption cross-section,  $\sigma_{ph}(T)$  is the absorption cross-section related with the electron absorption in a dielectric due to photoionization.

The electron density  $n(r,t)$  is determined by generation, recombination, and diffusion processes and can be found from the following equation:

$$\frac{\partial n}{\partial t} = D \nabla^2 n - \frac{n}{\tau_r} + g(T,r) \quad (12)$$

where  $D$  is the diffusion coefficient,  $\tau_r$  is the electron recombination time,  $g(T,r)$  is the rate of electron generation. The latter term due to photoionization is determined by:

$$g(T,r) = \left( \frac{R}{r} \right)^2 \int_{\frac{E}{\hbar}}^{\infty} \frac{\mu(\Omega) e^{-\mu(\Omega)(r-R)}}{\Omega} I(\Omega, T) d\Omega \quad (13)$$

where  $\mu(\Omega)$  is the absorption coefficient of a dielectric at the frequency  $\Omega$ ,  $E$  is the optical band gap of a dielectric,  $I(\Omega, T)$  is the spectral density of thermal radiation intensity at frequency  $\Omega$  and temperature  $T$  emitted by a laser heated inclusion.

By integrating Eq.(12) over the dielectric volume, and multiplying the result by

$$\frac{4}{c\beta} \omega \operatorname{Im}(\alpha(T))$$

we can derive the following equation for  $\sigma_{ph}(T, t)$ :

$$\frac{d\sigma_{ph}(T, t)}{dt} = -\frac{\sigma_{ph}(T, t)}{\tau_r} + \frac{16\pi^2\omega}{c\beta} \operatorname{Im}(\alpha(T)) \int_R^\infty g(r, T) dr \quad (14)$$

The stationary solution of Eq.(14) which is satisfied at  $q \leq q_n$  and  $\tau_0 \gg \tau_r$  is:

$$\sigma_{ph}(T) = \frac{16\pi\omega}{c\beta} \tau_r \operatorname{Im}(\alpha(T)) R^2 \int_R^\infty \int_E^\infty \frac{\mu(\Omega) e^{-\mu(\Omega)(r-R)}}{\Omega} I(\Omega, T) d\Omega \quad (15)$$

Assuming that  $I(\Omega, T)$  is determined by the Planck distribution, we find

$$\sigma_{ph}(T) = K \left( \frac{T}{E} \right)^3 \int_{E/T}^\infty \frac{x^2 dx}{\exp(x) - 1} \quad (16)$$

where

$$K = \frac{16\beta\omega}{c^3} \tau_r R^2 \operatorname{Im}(\alpha(T)) E^3.$$

Additional absorption due to photoionization leads to thermal explosion in a dielectric in the vicinity of the inclusion. Its threshold temperature is found from Eq.(7). By substituting  $\sigma(T) = \sigma_1(T) + \sigma_{ph}(T)$  into Eq.(7), and assuming that the parameters  $\sigma_1$  and  $\chi_2$  are independent of temperature we obtain:

$$S(Z) = \frac{2}{Z^3} \int_Z^\infty \frac{x^2 dx}{\exp(x) - 1} + \frac{1}{\exp(Z) - 1} = \Lambda \quad (17)$$

where  $Z = E/T$ ,  $\Lambda = \sigma_1/K$ .

The plot of  $S(z)$  obtained by numerical calculation is shown in Fig.3. It enables one to determine  $T_{ph}$  when  $\Lambda$  is known. According to the previous consideration the threshold intensity is determined by the relationship:

$$q_{ph} = \Phi(T_{ph})$$

In the general case, the absorption cross-section can be represented in the form:

$$\sigma(T) = \sigma_0 + \sigma_1 \exp \left( - \frac{A}{T} \right) + \sigma_{ph}(T)$$

where the first and the second terms are related to the inclusion and the third term is due to photoionization of the surrounding dielectric. A threshold function has two maxima in this case (see Fig.1, plot 3). One of them corresponds to absorption of laser radiation increasing in the inclusion region, and another one to  $\sigma(T)$  growth due to photoionization in a dielectric. Thus, the model of thermal explosion of an absorbing inclusion has two thresholds: one of the thresholds arises from thermal instability in the inclusion vicinity. The former determines intensity for damage, if the absorbing energy in the inclusion is enough for a failure in the dielectric. But for the energy deficit (for instance, when inclusion is small) the macroscopic failure arises when the intensity is equal to the photoionization threshold.

### III. KINETICS OF THERMAL EXPLOSION

The purpose of this section is to study the development of thermal instability. It is important to find the induction time of thermal explosion, since it gives the dependence of the damage threshold on laser pulse duration.

During the induction time  $\tau_i$ , the inclusion temperature is a little over its threshold. Hence, the solution of Eq.(2) can be found in the form (4), when the inclusion temperature  $T=T(t)$  depends on the time.

Submitting  $\theta_1(T(r,t))$  into Eq.(2), and deriving it with respect to  $r$ , as well as substituting  $r=R$  and taking into account the relationship

$$x_2 \frac{d\theta_1}{dt} = x_1 \frac{d\theta_2}{dt} ,$$

it gives

$$\frac{d\theta_2(T, T_0)}{dt} = \frac{1}{\tau} \theta_2(T, T_0) + \frac{1}{4\pi R\tau} \sigma(T) qf(t) . \quad (18)$$

The kinetics of the photoionization instability are very complicated for a consistent study, since it requires solving two coupled equations (14) and (18). We shall analyze two limited cases  $\tau > \tau_0 \gg \tau_r$  and  $\tau_r > \tau_0 \gg \tau$ .

In the former case we can neglect the time derivative in Eq.(14), and therefore  $\sigma_{ph}(T)$  is determined by Eq.(15). Within the region  $T \sim T_{ph}$  it can be approximated by the expression

$$\sigma(T) = \sigma(T_{ph}) \exp \left( \xi \frac{T - T_{ph}}{T_{ph}} \right)$$

as the numerical calculations have shown with  $\xi = 1.2 \div 2$ . Using the dimensionless variable

$$y = \frac{\theta_2(T, T_{ph})}{\theta_2(T_{ph}, T_0)}$$

Eq.(18) is transformed to



$$\frac{dy}{dt} = -\frac{1}{\tau} - \frac{1}{\tau} y + \frac{1}{\tau} \frac{q}{q_n} f(t) \exp(\delta y) \quad (19)$$

where

$$\delta = \frac{\xi \theta_2(T_{ph}, T_0)}{\chi_2(T_{ph}) T_{ph}}, \quad \tau = \frac{c_1 \rho_1 R^2}{3\chi_2}.$$

Equation (19) should be solved with the initial condition, which can be chosen as  $y(t) = 0$  at  $qf(t) = q_n$ , since in the region of  $qf(t) \leq q_n$ , the heat flow potential coincides with its stationary value. Neglecting the second term in Eq.(19) we derive:

$$y(t) = -\frac{t}{\tau} - \frac{1}{\delta} \ln \left\{ 1 - \frac{\delta}{\tau} \frac{q}{q_n} \int_0^t f(x) \exp\left(-\frac{\delta x}{\tau}\right) dx \right\} \quad (20)$$

When the induction time is long, it may be found with a high degree of accuracy from the condition  $y(\tau_1) = \infty$ , which gives

$$\frac{\delta}{\tau} \frac{q}{q_n} \int_0^{\tau_1} f(x) \exp\left(-\frac{\delta x}{\tau}\right) dx = 1 \quad (21)$$

For a rectangular-shaped pulse we derive from equation (21):

$$\tau_1 = \frac{\tau}{\delta} \ln \frac{q}{q - q_n}. \quad (22)$$

For the Gaussian pulse, analytic solution of Eq.(21) cannot be obtained. For this reason we have used the numerical calculation, the results of which are represented in Fig.4. It is seen that the induction time of thermal explosion is greatly different for Gaussian and rectangular pulses at the same laser light intensity. In the case of a rectangular pulse, we can speak about instantaneous damage in the region of high intensity. On the contrary, in the case of a Gaussian pulse the induction time of thermal explosion decreases very slowly with increasing intensity. This takes place because thermal explosion in this case occurs at the front part of the laser pulse, and the remaining portion of the pulse does not affect the development of thermal instability.

For Gaussian and rectangular pulses having the same maximum intensity, the dependence of  $\tau_1$  on  $\tau_0$  is different. For a rectangular pulse it is very simple: in the region

$$\tau_0 \geq 2\tau \ln \frac{q}{q - q_n}$$

the magnitude of  $\tau_1$  is independent of  $\tau_0$ , and in the region

$$\tau_0 < 2\tau \ln \frac{q}{q - q_n}$$

thermal explosion does not occur. The results of numerical calculation of  $\tau_1 = \tau_1(\tau_0)$  for Gaussian pulses are shown in Fig.5.

In the case  $\tau_r \gg \tau$  we can neglect time derivative in Eq.(18). Then, assuming that  $\chi_2$  does not depend on T for the rectangular shape of the laser pulse we derive from Eqs.(14) and (18):

$$\frac{dT}{dt} = -\frac{1}{\tau} (T-T_0) + \frac{\tau}{\tau_r} \frac{\sigma(T)q}{c} \quad (23)$$

The replacements

$$\theta_2 \rightarrow T \text{ and } t \rightarrow t \frac{\tau_r}{\tau}$$

transform Eq.(23) into Eq.(18). For this reason, their solutions coincide, and the induction time of thermal explosion has a form of Eq.(22), where the substitution  $\tau \rightarrow \tau_r$  is performed.

#### Pulse width dependence of damage threshold

In the framework of the thermal explosion theory, failure of a material is realized when thermal explosion is developed during the laser pulse. In accordance with the definition the induction time,  $\tau_i$ , is the time during which the inclusion temperature increases from  $T_n$  to  $\infty$ . Taking into account that at  $(q-q_n) \ll q_n$ , the increase of inclusion temperature from  $T_0$  to  $T_n$  is also equal to  $\infty$  we can write the following condition for laser damage

$$\tau_0 = 2\tau_i \quad (qd) \quad (24)$$

which determines the pulse width dependence of the damage threshold intensity.

In the case of a rectangular-shaped laser pulse,  $\tau_i$  is given by Eq.(22) and hence, from Eq.(24), we find:

$$q_d = q_n \left\{ 1 - \exp \left[ -\xi \frac{\tau_0}{2\tau} \right] \right\}^{-1} \quad (25)$$

For the Gaussian pulse, the dependence  $q=q(\tau_0)$  is found by numerical calculation and is shown in Fig.6.

One can see that the pulse width dependences of the damage threshold for the Gaussian and rectangular pulses are not essentially different in spite of the big difference in  $\tau_i$  for these two cases. For this reason, Eq.(25) gives a qualitative picture of the pulse width dependence of the damage threshold for pulses with arbitrary shape.

According to Eq.(25) the character of the thermal instability depends on the value of

$$\xi \frac{\tau_0}{\tau} . \quad \text{If} \quad \xi \frac{\tau_0}{\tau} \gg 1$$

then  $q_d = q_n$ , and the thermal instability has the explosion character. If

$$\xi \frac{\tau_0}{\tau} \ll 1 \text{ then } q_d \approx \frac{2}{\xi} \frac{\tau}{\tau_0} q_n$$

and the laser threshold is determined by the thermal instability kinetics. In this case the damage is determined by laser pulse energy

$$W_d \approx \frac{2}{\xi} \frac{\tau q_n}{d} .$$

#### IV. DISCUSSION AND CONCLUSIONS

The theory presented here of laser-induced damage mechanism associated with thermal explosion of the absorbing inclusion is applicable for pulse duration

$$t_0 \gg t_2 = \frac{C_2 P_2 R^2}{3 \xi_2}$$

For absorbing inclusions with radius  $R = 10^{-5}$  cm in a glass with  $\chi_2 = 3 \cdot 10^{-3}$  cal.  $\text{cm}^{-1} \text{sec}^{-1} \text{K}$ ,  $t_2 = 5$  nsec and therefore the theory is applicable when  $t_0 > 10$  nsec.

For the semiconductor-type inclusions the explosion threshold intensity estimated from Eq.(10) is  $q_n \approx 10^9 \text{ W/cm}^2$ .

The threshold intensity for photoionization induced thermal explosion depending on the relaxation time,  $t_r$ , of the conduction band electrons, which ranges from  $10^{-5}$  sec to  $10 \text{ nsec}/10/$ . Assuming that  $t_r = 10$  nsec, we get  $T_{ph} \approx 5 \cdot 10^8 \text{ W/cm}^2$ .

The increase of  $t_r$  results in a decrease of the photoionization explosion threshold, for example for  $t_r = 10^{-7}$  sec,  $q_{ph} = 8 \cdot 10^7 \text{ W/cm}^2$ .

Therefore, the above estimations indicate that for the laser pulse widths  $t_0 > t_r$  the photoionization mechanism has a rather low initiation threshold, and this mechanism may be the major one in the laser-induced damage to transparent optical materials with absorbing inclusions.

In the case of pulse widths  $t_0 < t_r$  the damage threshold is given by (see eq.(25)):

$$q_d = \frac{2 t_r}{\xi \frac{dt_r}{dt_0}} q_{ph}$$

Then, for  $t_0 = 10$  nsec and  $t_r = 100$  nsec we get  $q_d = 10^9 \text{ W/cm}^2$ . So, the damage threshold connected with photoionization increases appreciably when the pulse width decreases.

The pulse width dependence for the damage mechanism discussed here is determined by Eq.(25) which coincides, for the limiting cases  $t_0 \ll t$  and  $t_0 \gg t$ , with the results of linear theory of thermal damage /2/, but differs significantly from the diffusion-type dependence  $q_d \sim t_0^{-1/2}$  discussed often in literature /II/ and from the dependence  $q_d \sim t_0^{-2/3}$  predicted by thermoionization model /8/. For this reason the investigation of pulse width dependence of the damage threshold gives a good possibility for elucidating the damage mechanism initiated by absorbing inclusions.

In conclusion, we point out the most important features of the theory developed in this paper:

- o Nonlinear increase of the absorption coefficient of the inclusion with the temperature due to explosion character of inclusion heating results in the initiation of laser damage in a dielectric. The saturation of absorption stabilizes the inclusion temperature and can protect the dielectri from laser damage.
- o The analysis of thermal instability in a dielectric due to photoionization by thermal radiation from the heated inclusion has shown that photoionization thermal explosion can be a dominating mechanism in laser damage.
- o In the general case, laser-induced damage initiated by the absorbing inclusion has a two-threshold character. One threshold is related to thermal explosion in the inclusion region, the other one to photoionization instability.
- o The dependence of the damage threshold on pulse duration which is revealed from the thermal instability kinetics is determined by the inclusion and dielectric parameters. The induction time of the thermal explosion, which is observed with a cut off the propagating laser pulse, strongly depends on the temporal shape of the pulse, whereas the pulse width dependence of the damage threshold slightly depends on pulse shape.

The concepts considered present a rather full picture of laser damage by absorbing inclusions. They give a basis for experimental investigation of laser damage mechanism. The numerical estimations show that thermal explosion of absorbing inclusions is a real mechanism of laser-induced damage in optical materials.

# REFERENCES

1. A.A. Manenkov, A.M. Prokhorov. Uspekhi Fizicheskikh Nauk, v.145, p.179, 1986 (in Russian)
2. Yu.K. Danileiko, A.A. Manenkov, A.M. Prokhorov, V.Ya. Khaimov-Mal'kov. JETP, v.58, p.31, 1070 (in Russian)
3. R.W. Hopper, D.R. Uhlman. J. Appl. Phys., 41, 4023 (1970)
4. Yu.K. Danileiko, A.A. Manenkov, V.S. Nechitailo, A.M. Prokhorov, V.Ya. Khaimov-Mal'kov. JETP, v.63, p.1031, 1972 (in Russian)
5. Yu.K. Danileiko, A.A. Manenkov, V.S. Nechitailo. Kvant. Electron., 5, p.194, 1978 (in Russian)
6. M.F. Koldunov, A.A. Manenkov, I.L. Pokotilo. Kvant. Electron.,15, p.544, 1988 (in Russian)
7. S.I. Anisimov, B.I. Makshantsev. FTT, v.15, p.1090, 1973 (in Russian)
8. B.I. Makshantsev, P.S. Kondratenko, G.M. Gandel'man. FTT, v.16, p.173, 1974.
9. R. Gilmore. Catastrophe theory for scientists and engineers. A Wiley-Interscience Publication, 1981.
10. A.I. Ansel'm. Introduction into a semiconductor theory. M. Nauka, 1987 (in Russian)
11. Th.W.Walker, R.H. Guenther, R.E. Nielsen. d EEE, Journal of Quant. Electr., QE-17, No 10, p.2041 (1981).



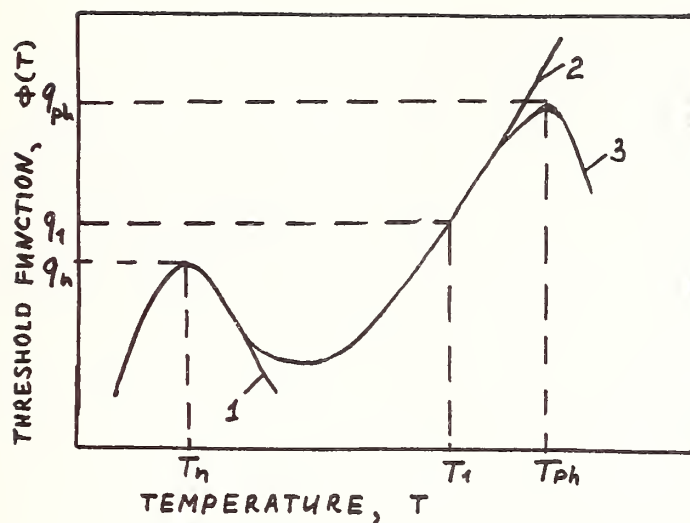


Fig.1. Thermal explosion threshold function,  $\Phi(T)$  for no various behaviour of absorption coefficient: I - saturation, 2 - semiconductor-type saturation, 3 - semiconductor-type inclusion plus photoionization

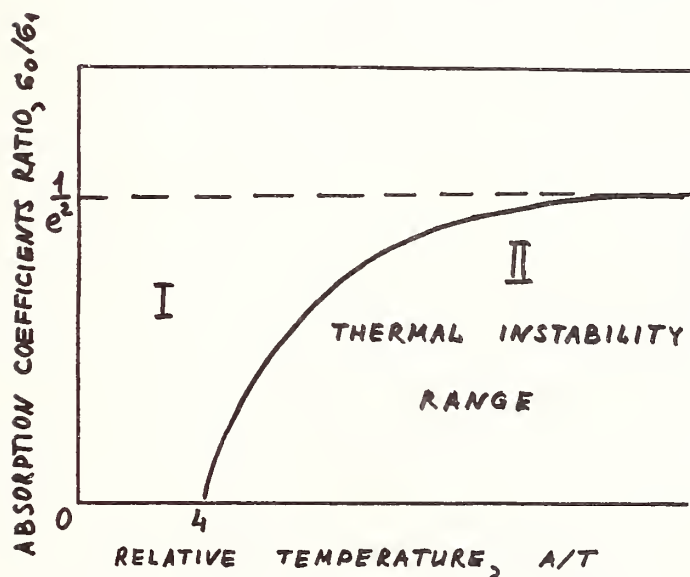


Fig.2. Parametric presentation of thermal instability for semiconductor-type inclusion.

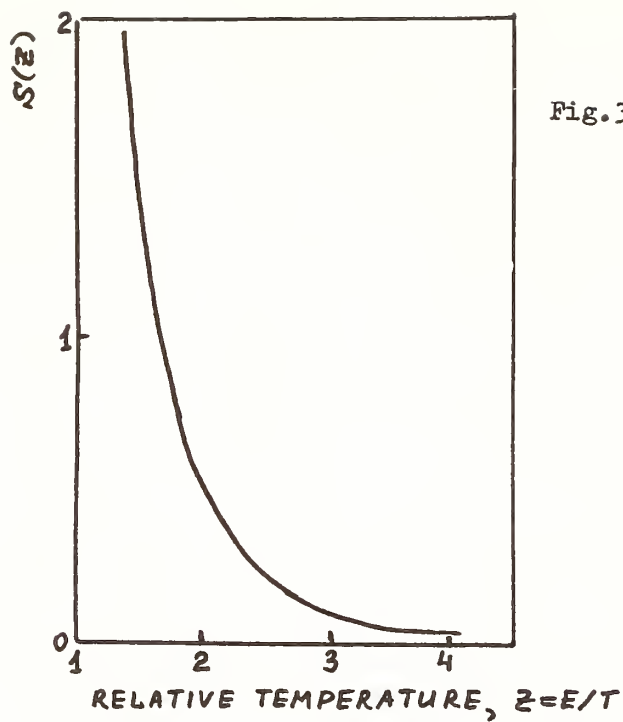


Fig.3.  $S(z)$  function (see eq.(I7)) which determines photoionization critical temperature

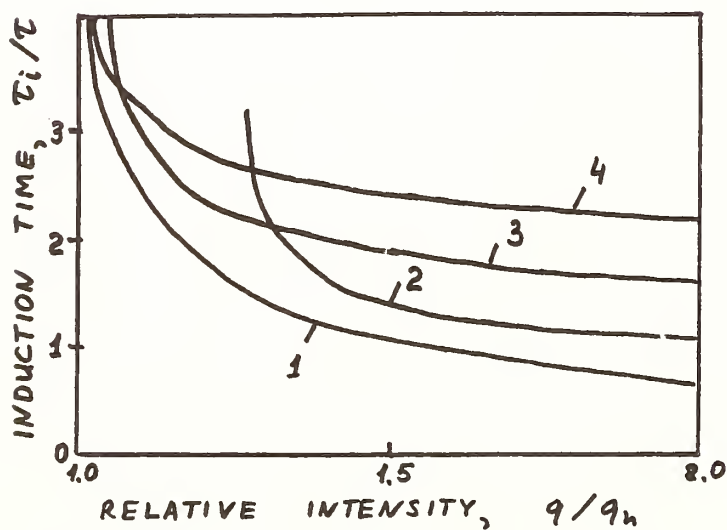


Fig.4. Explosion induction time versus laser intensity for step-like (1) and Gaussian (2,3,4) pulses.  
 2 -  $\tau_0 = \tau$ , 3 -  $\tau_0 = 3\tau$ , 4 -  $\tau_0 = 7\tau$

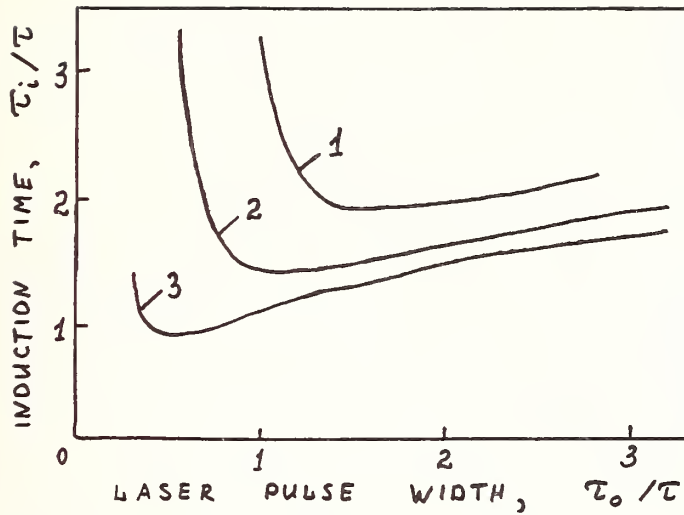


Fig.5. Explosion induction time versus Gaussian pulse width for various laser intensity: 1 -  $q=1,3q_n$ , 2 -  $q=1,5q_n$ , 3 -  $q=2q_n$ , where  $q_n$  is explosion threshold intensity.

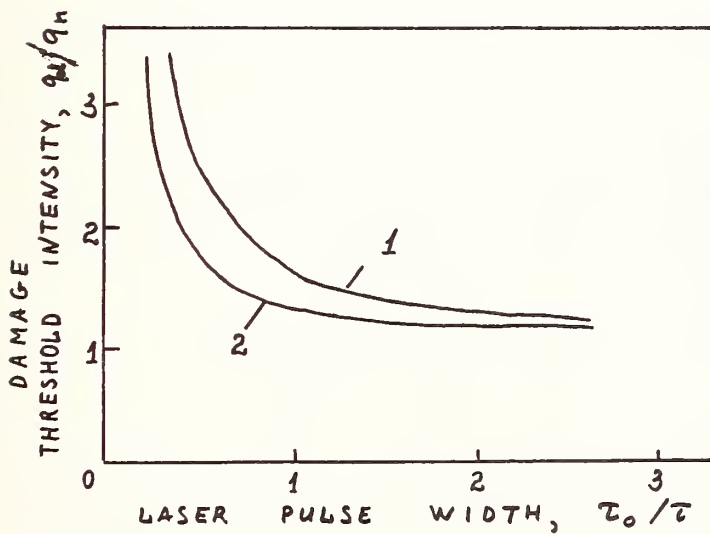


Fig.6. Pulse width dependence of damage threshold intensity for rectangular (1) and Gaussian (2) pulses.

Manuscript Received  
4-24-89

Experimental Investigation on the Role of Wavelength in the  
Laser Conditioning Effect

J.W. Arenberg and D.W. Mordaunt

Hughes Aircraft Company  
Electro-Optical and Data Systems Group  
El Segundo, California 90245-0902

This paper reports on an experimental investigation regarding the role of the wavelength in the laser conditioning effect. In this investigation, the threshold enhancement due to conditioning by irradiation at fluence levels below the damage threshold at  $1.06\mu\text{m}$  is measured at  $1.06\mu\text{m}$  and  $0.53\mu\text{m}$ . Conditioning of the optic at  $1.06\mu\text{m}$  is followed by testing at both  $1.06\mu\text{m}$  and  $0.53\mu\text{m}$ , to determine the threshold for the onset of enhancement at each wavelength due to conditioning at  $1.06\mu\text{m}$ .

This experiment also allows for some comments to be made regarding the properties for the main actor in the laser conditioning effect.

Key words: laser conditioning effect; preconditioning, prepulsing, laser cleaning, water in coatings.

## 1. Introduction

This paper reports on an experiment carried out to collect phenomenological data on the laser conditioning effect. The present effort continues in the vein of earlier experiments.<sup>1,2</sup> The laser conditioning effect is the enhancement of the laser damage threshold due to subthreshold irradiation. Previous efforts have been directed at quantifying the magnitude and duration of the threshold enhancement due to conditioning when the conditioning and test wavelength are the same. The experiment reported on herein compares the threshold enhancement at due to conditioning at one wavelength,  $1.06\mu\text{m}$  and two different test wavelengths,  $1.06\mu\text{m}$  and  $0.53\mu\text{m}$ .

The experiment will shed some light on the nature of the major actor in the laser conditioning effect. Water has been hypothesized to be the major actor at longer wavelengths,  $\lambda > 1.06\mu\text{m}$ , and the desorption of water has been correlated to threshold enhancement in recent work.<sup>3</sup>

This paper reports on threshold enhancement due to conditioning at  $1.06\mu\text{m}$  at test wavelengths  $1.06\mu\text{m}$  and  $0.53\mu\text{m}$  for double-V ( $1.06\mu\text{m}/0.53\mu\text{m}$ ) antireflection (AR) coated glass. The first item of data collected was the unconditioned and conditioned thresholds at  $1.06\mu\text{m}$  and  $0.53\mu\text{m}$ .<sup>4</sup> This sets the magnitude of the threshold enhancement at each wavelength. Next, the threshold for the onset for the conditioning effect was estimated. The estimation was made by plotting damage probability versus conditioning fluence. The damage probability as a function of conditioning fluence was generated by irradiating a grid at three subthreshold (unconditioned  $1.06\mu\text{m}$  threshold) fluences and then irradiating half of the grid at the  $1.06\mu\text{m}$  conditioned threshold and the other half at the  $0.53\mu\text{m}$  conditioned threshold and recording the number of sites damaged out of the total irradiated.

Finally, the thresholds for the onset of conditioning at  $1.06\mu\text{m}$  and  $0.53\mu\text{m}$  due to conditioning at  $1.06\mu\text{m}$  are compared. The conditioning threshold data is then analyzed to yield some information about the properties of the main actor in the laser conditioning effect.

## 2. Experimental Conditions

A sketch of the test facility is given as figure 1. The test laser is Nd:YAG source for the generation of  $1.06\mu\text{m}$  and a second harmonic generator crystal for the  $0.53\mu\text{m}$  light. The nominal test conditions are given in table 1.



Table 1

Parameter	Value
1.06 $\mu$ m pulse width (FWHM)	15 nsec
1.06 $\mu$ m spot size (1/e <sup>2</sup> diam.)	0.5 mm
0.53 $\mu$ m pulse width (FWHM)	15 nsec
0.53 $\mu$ m spot size (1/e <sup>2</sup> area)	0.5 mm
Pulse repetition frequency	1 Hz
1.06 $\mu$ m transverse mode	TEM <sub>00</sub>
Number of shots per site per fluence level	16

### 3. Experimental Procedure

As a baseline, the unconditioned and conditioned thresholds were measured for both 1.06 $\mu$ m and 0.53 $\mu$ m. The unconditioned threshold is the minimum fluence causing catastrophic failure of the optical surface when each site is exposed to only one test fluence. Damage is denoted by flashes, noise and definite cratering. The test set shown in figure 1 allows for the surface to be observed through a microscope (20X magnification) during irradiation, thus making the association of flashes and the onset of cratering possible. The conditioned threshold was the lowest fluence at which a conditioned site was seen to fail. The irradiance history of the conditioned site was exposure to a slowly increased fluence level, dwelling for 16 shots at each level. The typical conditioned exposure consisted of 5 to 7 fluence levels separated by 4-5 J/cm<sup>2</sup>. As the conditioned threshold became better defined, smaller fluence steps were taken in the neighborhood of the threshold to attain higher resolution.

Following the identification of the 1.06 $\mu$ m and 0.53 $\mu$ m conditioned thresholds, a grid was laid out. The grid consisted of 3 rows of 16 spots. Each row was conditioned at a different level. The irradiation levels were 25%, 50% and 75% of the 1.06 $\mu$ m conditioned threshold. Half of the spots in each row were irradiated at the 1.06 $\mu$ m conditioned threshold and the other half at the conditioned threshold at 0.53 $\mu$ m. The frequency of damage was recorded for each test wavelength and conditioning fluence, resulting in a plot of the frequency of damage versus the conditioning fluence at 1.06 $\mu$ m.

### 4. Results and Discussion

The conditioned and unconditioned damage thresholds measured for the coating are given in table 2.

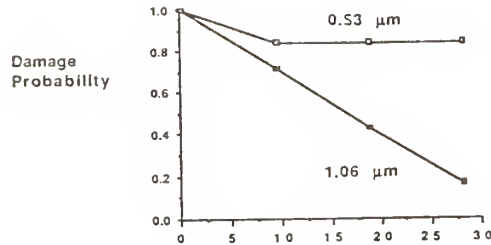
Table 2

Test Type	0.53 $\mu$ m	1.06 $\mu$ m
Conditioned	13 $\pm$ 1 J/cm <sup>2</sup>	38 $\pm$ 4 J/cm <sup>2</sup>
Unconditioned	13 $\pm$ 1 J/cm <sup>2</sup>	30 $\pm$ 3 J/cm <sup>2</sup>

From the test results, it is clear that the coating does not condition at 0.53 $\mu$ m due to subthreshold exposure at 0.53 $\mu$ m, while the coating undergoes a noticeable increase, 8 $\pm$ 5 J/cm<sup>2</sup> when conditioned and tested at 1.06 $\mu$ m.

The damage frequency plotted as a function of the 1.06 $\mu$ m conditioning fluence is given in figure 2. In figure 2 there is no sharp onset of conditioning associated with threshold enhancement, as has been noted in other work.<sup>2,3</sup> In the case of 1.06 $\mu$ m conditioning, there was a continuous decrease in the probability of damage with increasing conditioning fluence. At 0.53 $\mu$ m

test wavelength, there was no conditioning noted, as the probability does not decrease for increasing 1.06 $\mu$ m conditioning exposure.



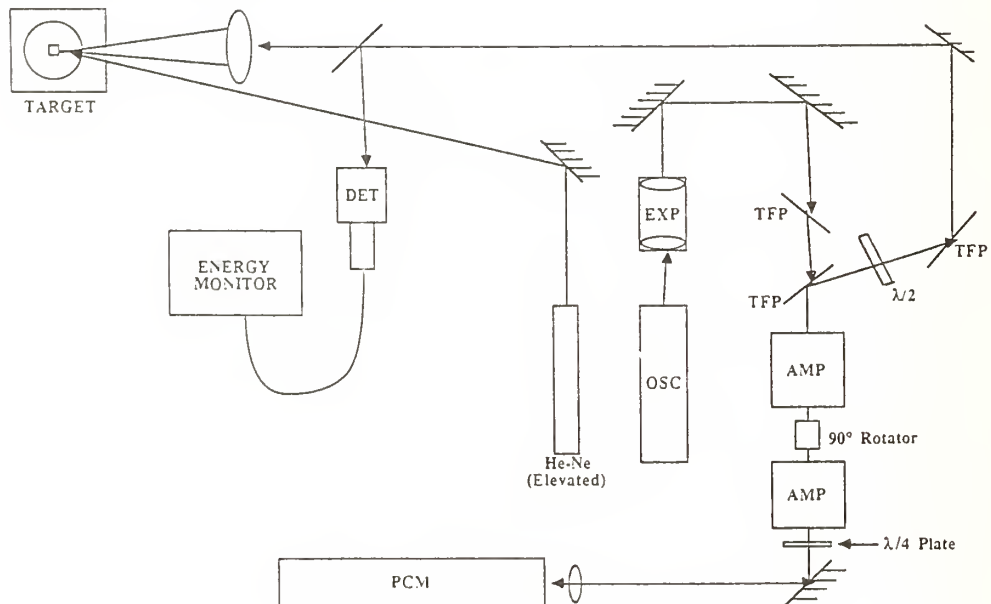
1.06 $\mu$ m Conditioning Fluence in J/cm<sup>2</sup>

The coating did not condition at 0.53 $\mu$ m, due to subthreshold exposure at either 1.06 $\mu$ m or at 0.53 $\mu$ m, but did condition at 1.06 $\mu$ m. Since the laser damage threshold is monotonically related to the reciprocal of the absorption of the coating, all other factors equal, it may be inferred that the conditioning of the optic reduced the absorption of the coating at 1.06 $\mu$ m and not at 0.53 $\mu$ m. Thus, it is concluded that the main actor in the laser conditioning effect has the property of being more absorbant of laser radiation at 1.06 $\mu$ m than at 0.53 $\mu$ m.

Liquid water has absorptive properties that are in qualitative agreement with the inferred properties of the actor in the conditioning effect.<sup>5</sup>

This experiment contributes to present body of evidence identifying the removal of water from coatings, which results in decreased coating absorption, as the mechanism of threshold enhancement in the laser conditioning effect.<sup>2,3,6,7,8</sup>

Figure 1. The laser damage test facility consists of a Nd:YAG oscillator/amplifier configuration. The abbreviations are defined as follows: OSC = oscillator; AMP = amplifier; EXP = beam expanding telescope; TFP = thin film polarizer;  $\lambda/4$  = quarter wave plate;  $\lambda/2$  = half wave plate; and DET = energy detector.



## 5. References

- [1] Arenberg, J.W.; Frink, M.E. On the role of adsorbed water in the conditioning of coated optics at  $1.06\mu\text{m}$ . 19th symposium on optical materials for high power lasers; 1987 October; Boulder, CO.
- [2] Frink M.E.; Arenberg, J.W.; Mordaunt, D.S.; Seitel, S.C.; Babb, M.T.; Teppo, E.A. Temporary laser damage threshold enhancement by laser conditioning of anti-reflection coated glass. Appl. Phys. Lett. 51:415; 1987 August 10.
- [3] Wilson, D.R.; Gibson, A.D.  $\text{CO}_2$  laser induced damage in a model thin film system: ZnS on GE in laser induced damage in optical materials. Nat. Bur. Stand. (U.S.) Spec. Publ. 746; 1988. 460 p.
- [4] Arenberg, J.W.; Frink, M.E.; Mordaunt, D.W.; Lee, G; Seitel, S.C.; Teppo, E.A. Correlation of laser damage tests at  $1.06\mu\text{m}$  varying modal content and irradiance history. Nat. Inst. Stand. Tech. (U.S.) Spec. Publ. 752; 1988. 352 p.
- [5] Hulbert, E.O. Optics of distilled and natural water. J. Opt. Soc. Am. 35(11): 698; 1945 November.
- [6] Kovalev, V.I.; Morozov, V.V.; Faizullov, F.S. Appearance of opacity and damage of optical materials by carbon dioxide laser pulses. Soviet Journal of Quantum Electronics. 4(10): 1208; 1975 April.
- [7] Kovalev, V.I.; Faizullov, F.S. Influence of absorbed water on the optical strength of infrared optical elements. Soviet Journal of Quantum Electronics. 7(3): 326; 1977 March.
- [8] Zverev, G.M.; Sidoryuk, O.E.; Skvortsov, L.A. Influence of water absorption processes on the optical strength of dielectric titanium dioxide coating. Soviet Journal of Quantum Electronics. 11(10): 1393; 1981 October.

APPENDIX I  
BOULDER DAMAGE SYMPOSIUM  
OCTOBER 26-28, 1988

LIST OF ATTENDEES

Joseph A. Abate  
Hampshire Instruments  
10 Carlson Road  
Rochester, NY 14510  
(716) 482-4070

M. A. Acharekar  
Litton Laser Systems  
1666 Providence Cr.  
Orlando, FL 32818  
(407) 297-4450

Bradford G. Ackerman  
Cornign Glass Works  
MP-21-04-2  
Walnut Street  
Corning, NY 14831  
(607) 974-7578

John Allen  
OMITEC Electro-Optics  
Totnes  
Devon  
ENGLAND

Claude Amra  
E.N.S.P.M.  
University of Marseille  
D.U. St. Jerome  
13397 Marseille Cedex 13

Jonathan W. Arenberg  
Hughes Aircraft Company  
P.O. Box 902  
Bldg. El M/S D127  
El Segundo, CA 90245-0902 FRANCE  
(213) 616-3090

Heinrich F. Arlinghaus  
Atom Sciences, Inc.  
114 Ridgeway Center  
Oak Ridge, TN 37830  
(615) 483-1113

Mira H. Bakshi  
Deacon Research  
900 Welch Road, Ste 203  
Palo Alto, CA 94304  
(415) 326-1520

Steve Barnes  
Oxford Instruments Ltd.  
Eynsham  
Oxford OX8 1TL  
UNITED KINGDOM  
(0865) 882855

Donald Barnes  
W.J. Schafer Assoc.  
1901 N. Fort Myer Dr.  
Arlington, VA 22209  
(703) 558-7900

William T.(Pat) Beauchamp  
Optical Coating Lab., Inc.  
2789 Northpoint Parkway  
Santa Rosa, CA 95407  
(707) 525-7649

Philip Beck  
Martin Marietta  
Denver Astronautics Group  
P.O. Box 179, M/S L-8005  
Denver, CO 80201  
(303) 971-5075

Michael F. Becker  
University of Texas at Austin  
Elec. Engineering Dept.  
Austin, TX 78712  
(512) 471-3628

Ray Bell, Jr.  
Lockheed  
3251 Hanover Street  
Palo Alto, CA  
(415) 424-3396



Harold E. Bennett  
Naval Weapons Center  
Code 38101  
China lake, CA 93555  
(619) 939-1440

Jerry R. Bettis  
Rocketdyne  
6633 Canoga Ave.  
Canoga Park, CA 91304  
(818) 700-6616

Charlie Bice  
USASDC-GBL  
GBL-PO  
WSMR, NM 88002  
(505) 674-6358

Norman Boling  
Deposition Sciences Inc.  
386 Tesconi Ct.  
Santa Rosa, CA 95401  
(707) 579-2008

Jim Boyer  
CLS-6, MS J-564  
Los Alamos Nat'l Lab  
Los Alamos, NM 87545  
(505) 667-7102

Arthur J. Braundmeier  
Southern Illinois University  
Physics Department  
Box 1654  
Edwardsville, IL 62026  
(618) 692-2359

Ernie Braunschweig  
R & D Associates  
P.O. Box 9377  
Albuquerque, NM 87119  
(505) 842-8911

Mike Bristow  
EPA  
P.O. Box 93478  
Las Vegas, NV 89193  
(702) 798-2272

Raymond M. Brusasco  
Lawrence Livermore Nat'l Lab  
P.O. Box 5508, L-483  
Livermore, CA 94550  
(415) 423-3896

John H. Campbell  
Lawrence Livermore Nat'l Lab  
P.O. Box 5508, L-490  
Livermore, CA 94550  
(415) 422-6497

Dr. Charles Carniglia  
Martin Marietta  
P.O. Box 9316  
Albuquerque, NM 87119  
(505) 844-1064

R. Thomas Casper  
Physics Department  
Washington State University  
Pullman, WA 99164-2814  
(509) 335-8613

Jack P. Chambers  
II-VI, Inc.  
Saxonburg Blvd.  
Saxonburg, PA 16056  
(412) 352-4455

Lloyd L. Chase  
Lawrence Livermore Nat'l Lab  
P.O. Box 5508, L-490  
Livermore, CA 94550  
(415) 447-3659

Charles Cockrum  
Rocky Mountain Instrument Co.  
Waswing Ct.  
Longmont, CO 80501  
(303) 449-6652

Ben Contreras  
Martin Marietta  
Denver Astronautics Group 6349  
P.O. Box 179, M/S L-8005  
Denver, CO 80201  
(303) 977-0584

Michael Creighton  
Perkin-Elmer  
761 Main Ave.  
Norwalk, CT 06859-0420  
(203) 834-4511

Mark Dafoe  
Martin Marietta  
P.O. Box 9316  
Albuquerque, NM 87119  
(505) 844-1064

William J. Davis  
ITEK/Litton  
10 Maguire Rd.  
Lexington, MA 02173  
(617) 276-2233

Jeffrey De Natale  
Rockwell Int'l Science Ctr.  
1049 Camino Dos Rios  
Thousand Oaks, CA 91360  
(805) 373-4439

Don Decker  
Naval Weapons Center  
Code 3816  
China Lake, CA 93555  
(619) 939-3247

Frank Demarco  
Lawrence Livermore Nat'l Lab  
P.O. Box 5508, L-491  
Livermore, CA 94550  
(415) 422-3022

John A. Detrio  
University of Dayton  
300 College  
Dayton, OH 45469  
(513) 229-3527

Fred E. Domann  
Univ. of Wisconsin-Platteville  
Dept. of Physics  
Platteville, WI 53818  
(608) 342-1657

Fred W. Doss  
Spectra-Physics Optic Corp.  
1330 West Middlefield Rd.  
Mountain View, CA 94039  
(415) 961-2550

George Dugdale  
Perkin-Elmer  
761 Main Ave.  
Norwalk, CT 06859-0420  
(203) 834-6271

James W. Early  
Los Alamos Nat'l Lab  
P.O. Box 1663  
CLS-6, MS-J564  
Los Alamos, NM 87545  
(505) 665-0810

David F. Edwards  
Lawrence Livermore Nat'l Lab  
Livermore, CA 94550  
(415) 422-0747

Robert V. Ellis  
USAF  
AFWL/AROD  
Kirtland AFB, NM 87117-6008  
(505) 846-3488

David C. Emmony  
Loughborough Univ. of Tech.  
Loughborough  
Leicestershire  
UNITED KINGDOM  
509 22 33 06

Richard S. Eng  
MIT Lincoln Lab  
244 Wood Street  
Rm L-200  
Lexington, MA 02173  
(617) 981-3835

Richard Esposito  
Balzers  
8 Sagamore Park Road  
Hudson, NH 03051  
(603) 889-6888

P. A. Evans  
Oak Ridge Nat'l Lab  
P.O. Box 2009  
Oak Ridge, TN 37831-8039  
(615) 574-9406

Gregory J. Exarhos  
Battelle Northwest  
M/S K2-44  
P.O. Box 999  
Richland, WA 99352  
(509) 375-2440

William Farmer  
US Army Strategic Defense Comm.  
P.O. Box 1500  
Huntsville, AL 35807-3801  
(205) 895-4780

George Ferguson  
Lockheed  
3251 Hanover Street  
Palo Alto, CA 94303  
(415) 424-2319

Bob L. Francis  
United Technologies  
Optical Systems  
1601 Randolph Road SE  
Suite 100 South  
Albuquerque, NM 87106  
(505) 768-1480

Jerome Franck  
Naval Weapons Center  
China Lake, CA 9333555  
(619) 939-3827

Mark Frink  
TRW  
Lawrence Livermore Nat'l Lab  
L-634  
Livermore, CA  
(415) 423-5927

Tatsuo Fukano  
Hoya Corporation  
3-1 Musashino 3-Chome  
Akishima-shi  
Tokyo 196  
JAPAN  
0425-46-2736

Jean-Pierre Gailliard  
CENG-Leti CMM  
85 X  
38041 Grenoble  
FRANCE  
76 88 44 20

Marie Garcia  
Aerojet  
1100 W. Hollyvale St.  
P.O. Box 296  
Azusa, CA 91750  
(818) 812-2351

Dr. Adolf Giesen  
University of Stuttgart  
Pfaffenwaldring 38  
D-7000 Stuttgart 80  
WEST-GERMANY  
0711-6862705

Dennis H. Gill  
Los Alamos Nat'l Lab  
CLS-DO  
M/S J-563  
Los Alamos, NM 87544  
(505) 667-8680

Ray Gonzales  
Lawrence Livermore Nat'l Lab  
P.O. Box 5508, L-272  
Livermore, CA 94550  
(415) 423-3277

Erik Grann  
Union Carbide Corp.  
750 S. 32nd Street  
Washougal, WA 98671  
(206) 835-8566

Joel Grimm  
MIT Lincoln Lab  
244 Wood Street  
Rm L-200  
Lexington, MA 02173  
(617) 981-3835

Mark Guardalben  
University of Rochester  
250 E. River Rd.  
Rochester, NY 14623-1299  
(716) 275-5101

Dr. Arthur H. Guenther  
Los Alamos Nat'l Laboratory  
Mail Stop A-110  
Los Alamos, NM 87545  
(505) 667-8682

Sandra R. Gyetvay  
The Aerospace Corp.  
P.O. Box 92957  
Los Angeles, CA 90009  
(213) 336-8239

Bob Hahn  
Optical Coating Laboratory  
2789 Northpoint Parkway  
Santa Rosa, CA 95407  
(707) 525-7791

Randolph L. Hall  
Rockwell Int'l Science Ctr.  
1049 Camino Dos Rios  
Thousand Oaks, CA 91360  
(805) 373-4203

Francis Harrison  
CLS-6, M/S J-564  
Los Alamos Nat'l Laboratory  
Los Alamos, NM 87545  
(505) 667-7102

Edward A. Hildum  
Lawrence Livermore Nat'l Lab  
P.O. Box 5508, L-490  
Livermore, CA 94550  
(415) 422-8726

Lowell M. Hobrock  
Hughes Aircraft Co.  
2000 E. El Segundo Blvd.  
El Segundo, CA  
(213) 616-9620

L. W. Hodge  
Lockheed  
0/51-50, B/586  
P.O. Box 3504  
Sunnyvale, CA 94088-3504  
(408) 742-6232

Samuel J. Holmes  
Northrop Research and  
Technology Center  
One Research Park  
Palos Verdes Peninsula,  
CA 90274  
(213) 544-5314

Patrick J. Hood  
Rockwell International  
1049 Camino Dos Rios  
Thousand Oaks, CA 91360  
(805) 373-4285

Hamilton T. Hunter  
Oak Ridge Nat'l Laboratory  
Bldg. 6003, M/S 6372  
Oak Ridge, TN 37831-6372  
(615) 576-4295

Guildord J. Hutcheson  
USAMICOM  
AMSML-RD-AS-OG  
Hutcheson  
Redstone Arsenal, AL  
(205) 533-5605

Yoshiaki Ihara  
Ihara Tec Import Co.  
16-6, 3-Chome  
Katayama  
Niiza, Saitama 352  
JAPAN  
0484-79-9271

Linda Johnson  
Naval Weapons Center  
Code 3818  
China Lake, CA 93555  
(619) 939-1422

L. John Jolin  
Los Alamos Nat'l Lab  
CLS-6, M/S J-564  
Los Alamos, NM 87545  
(505) 667-7314

Scott C. Jones  
Physics Department  
Washington State University  
Pullman, WA 99163  
(509) 335-4672



Larry G. Jones  
Litton Laser Systems  
2787 5. Orange Blossom Trail  
Apopka, FL 32703  
(407) 880-8078

Kenneth A. Kaufman  
TRW Space & Defense  
Mail Stop 01-1080  
One Space Park  
Redondo Beach, CA 90278  
(213) 535-1740

Dr. Wayne D. Kimura  
Spectra Technology  
2755 Northup Way  
Bellevue, WA 98004-1495  
(206) 827-0460

Dr. Claude A. Klein  
Raytheon Res. Division  
131 Spring Street  
Lexington, MA 02173  
(617) 860-3113

Theodore Kohane  
Raytheon Res. Division  
131 Spring Street  
Lexington, MA 02173  
(617) 860-3073

G. Edward Kuhl  
W.J. Schafer Assoc., Inc.  
5100 Springfield Pike  
Suite 311  
Dayton, OH 45431-1231  
(513) 253-9572

Ramin Lalezari  
PMS Electro-Optics  
1855 South 57th Court  
Boulder, CO 80301  
(303) 443-7100

Dr. Anthony Leone, Jr.  
Lockheed  
0/92-40 B/205  
3251 Hanover Street  
Palo Alto, CA 94304-1191  
(415) 354-5376

D. R. Jungwirth  
Northrop  
2301 W. 120th Street  
M/S H321/N3  
Hawthorne, CA 90250  
(213) 600-4788

Paul Kelly  
NRC  
CANADA

C. William King  
Harshaw/Filtrol  
6801 Cochran Road  
Solon, OH 44139  
(216) 248-7400

Kent Kogler  
IIT Research Institute  
10 W. 35th Street  
Chicago, IL 60616  
(312) 567-4561

Dr. Wm. A. Koldewyn  
Ball Space Systems Div.  
P.O. Box 1062  
Boulder, CO 80306

Nessim Lagnado  
Hughes Research Center  
75 Coromar Drive  
Goleta, CA 93117  
(805) 562-2615

Thomas A. Leonard  
Ball Systems Eng. Dept.  
Suite 180  
2875 Presidential Dr.  
Fairborn, OH 45324  
(513) 429-5005

Paul W. Levy  
Brookhaven Nat'l Lab  
Bldg. 480  
Upton, NY 11973  
(516) 282-3820

Dr. Keith Lewis  
Royal Signals & Radar Establishment  
St. Andrews Road  
Malvern  
Worcestershire, WR1K 3PS  
UNITED KINGDOM  
0684 892733 Ext. 3062

Bo Ljung  
Kearfott Guidance &  
Navigation Corp.  
1225 McBride Ave.  
Little Falls, NJ 07424  
(201) 785-2761

C. D. Marrs  
Naval Weapons Center  
Code 3817  
China Lake, CA 93555  
(619) 939-2470

Frederick J. McClung  
Hughes Aircraft Co.  
1600 Randolph Ct.  
Albuquerque, NM 87106  
(505) 768-6118

Ted McMin  
McDonnell Douglas  
P.O. Box 516  
St. Louis, MO 63166  
(314) 234-4321

Helmuth E. Meissner  
Hoya Optics, Inc.  
3430 Edison Way  
Fremont, CA 94538  
(415) 490-1880

Jeff Millard  
Jaycor  
11011 Torreyana Road  
San Diego, CA 92421  
(619) 453-6580

John Lester Miller  
Martin Marietta  
MC L8030 SPW11  
P.O. Box 179  
Denver, CO 80201  
(303) 971-6945

Dr. Marie L. Linvill  
The Aerospace Corp.  
Mail Stop M2/241  
P.O. Box 92957  
Los Angeles, CA 90009  
(213) 336-5879

Dr. K. Mann  
Laser Laboratorium Goettingen  
Tammannstr. 6  
3400 Goettingen  
WEST GERMANY  
0551/374645

Prof. Eckart Matthias  
Freie Universitaet Berlin  
Dept. of Physics  
Arnimallee 14  
1000 Berlin 33  
WEST GERMANY  
30-838-3340

Michael McGuirk  
Corion Corporation  
73 Jeffrey Ave.  
Holliston, MA 01746  
(508) 429-5065

Jim McNally  
Dept. of Physics  
USAF/OPF  
USAF Academy, CO 80840  
(719) 472-2240

J. Francois Mengue  
Commissariat a L'Energie Atomique  
B.P. 27  
94190 Villeneuve St. Georges  
FRANCE

David R. Miller  
Univ. of Calif. San Diego  
Dept. of A.M.E.S.  
B-010  
La Jolla, CA 92093  
(619) 534-3182

Osborne Milton, Jr.  
U.S. Govt.  
CSSO-A-FB  
Ground Base Laser Proj. Office  
WSMR, NM 88002  
(505) 678-6260

Kent Moncur  
KMS Fusion  
3621 S. State Rd.  
Ann Arbor, MI 48108  
(313) 769-8500

Mark B. Moran  
Naval Weapons Center  
Code 3817  
China Lake, CA 93555  
(619) 939-3827

Dennis W. Morelli  
OCLI  
2789 Northpoint Parkway  
Santa Rosa, CA 95407  
(707) 525-7011

Yoshiharu Namba  
Chubu University  
1200 Matsumotocho  
Kasugai  
Aichi 487  
JAPAN  
0568-51-1111 XT.2306

Daniel R. Neal  
Sandia Nat'l Laboratory  
Div. 1128  
P.O. Box 5800  
Albuquerque, NM 87815  
(505) 846-1262

Davis B. Nichols  
Boeing Aerospace  
P.O. Box 3999  
M/S 8H-29  
Seattle, WA 98124  
(206) 773-8938

Robert M. O'Connell  
University of Missouri  
Dept. of Electrical Engineering  
Columbia, MO  
(314) 882-8373

Harumichi Okamoto  
Nippon Mining Co.  
708 Nishiya-Machi  
Hodogaya-Ku  
Yokohama 240  
JAPAN  
045-383-1525

Thomas A. Mooney  
Barr Associates, Inc.  
2 Lyberty Way  
Westford, MA 01886  
(508) 692-7513

David W. Mordaunt  
Hughes Aircraft Co.  
Bldg. E1, M/S B-129  
P.O. Box 902  
El Segundo, CA 90245  
(213) 616-5422

Amber J. Morgan  
Lawrence Livermore Nat'l Lab  
P.O. Box 5508, L-249  
Livermore, CA 94550  
(415) 422-6059

Yoshiharu Namba  
Chubu University  
1200 Matsumotocho  
Kasugai  
Aichi 487  
JAPAN  
0568-51-111 EXT 2306

Brian E. Newnam  
Los Alamos Nat'l Laboratory  
MS J-564  
Los Alamos, NM 87545  
(505) 667-7979

N. S. Nogar  
Los Alamos Nat'l Lab  
CLS-2, G-738  
Los Alamos, NM  
(505) 667-9305

Albert Oglozu  
Naval Weapons Center  
China Lake, CA 93555  
(619) 939-3247

Takayuki Okamoto  
Okamoto Optics Work, Inc.  
8-34 Haramachi  
Isogo-Ku  
Yokohama 235  
JAPAN

Yoshiaki Okamoto  
Okamoto Optics Work  
8-34 Haramachi  
Isogo-Ku  
Yokohama  
JAPAN  
045 752-2233

Roger A. Paquin  
Perkin-Elmer  
Applied Science & Technology Ctr.  
100 Wooster Hts Rd.  
M/S 848  
Danbury, CT 06810  
(203) 797-6130

Emile Pelletier  
E.N.S.P.M.  
Univ. of Marseille  
D.U. St. Jerome  
13397 Marseille Cedex 13  
FRANCE  
(33) 91 28 83 28

James R. Place  
Lockheed Missiles & Space Co.  
2309 Renard S.E.  
Suite 301  
Albuquerque, NM 87106  
(505) 842-6724

Bradley Pond  
Martin Marietta  
P.O. Box 9316  
Albuquerque, NM  
(505) 844-1064

Howard T. Powell  
Lawrence Livermore Nat'l Lab  
P.O. Box 5508, L-490  
Livermore, CA 94550  
(415) 422-6149

M. Rahe  
Laser Zentrum-Hannover  
Welfengarten 1  
3000 Hannover 1  
WEST-GERMANY  
0511/762-42265]

Dr. Tilak Raj  
Martin Marietta  
P.O. Box 9316  
Albuquerque, NM 87119  
(505) 844-1064

Roger A. Paquin  
The Perkin-Elmer Corp.  
Research Directorate  
100 Wooster Heights Rd.  
Danbury, CT 06810  
(203) 797-6130

Peter D.S. Parkinson  
General Electric, SCO  
P.O. Box 8355  
M/S 360 V3  
Philadelphia, PA 19701  
(215) 354-5672

John H. Pitts  
Lawrence Livermore Nat'l Lab  
P.O. Box 5508, L-481  
Livermore, CA 94550  
(415) 422-5327

Robert D. Poirier  
Corion Corporation  
73 Jeffrey Ave.  
Holliston, MA 01746  
(508) 429-5065

James O. Porteus  
Naval Weapons Center  
Code 3817  
China Lake, CA 93555  
(619) 939-3827

William P. Proffitt  
Rocketdyne Div.  
6633 Canoga Ave.  
M/S 46  
Canoga Park, CA 91305  
(818) 710-7381

Frank Rainer  
Lawrence Livermore Nat'l Lab  
P.O. Box 5508, L-490  
Livermore, CA 94550  
(415) 422-4376

John H.L. Ranson  
Pilkington P.E.  
Glascoed Road  
St. Asaph Clwyd LL17 0LL  
Wales  
UNITED KINGDOM  
0745 583301



Detlev Ristau  
Institut fur Quantenoptik  
Universitat Hannover  
Welfengarten 1  
3000 Hannover  
WEST GERMANY  
0511/762-4265

Jacquelin A. Ruller  
Naval Research Lab  
Code 6505  
Washington, DC 20375  
(202) 767-3487

Takatomo Sasaki  
Osaka University  
Inst. of Laser Engineering  
Yamadaoka 2-6  
Suita, Osaka 565  
JAPAN  
06-877-5111 x 4562

Harald Schink  
Laser Center, Hannover  
c/o CREOL  
Univ. of Central Florida  
12424 Research parkway  
Orlando, FL 32826  
(407) 658-6800, 6806

Roland D. Seals  
Martin Marietta  
Oak Ridge Nat'l Lab  
P.O. Box 2009  
Oak Ridge, TN 37831-8039  
(615) 574-0936

X. A. Shen  
Dept. of Physics  
Washington State University  
Pullman, WA 99164  
(509) 335-4173

Lin Simpson  
Physics Department  
Washington State University  
Pullman, WA 99164-2814  
(509) 335-8613

James G. Sliney, Jr.  
Rockwell International  
Rocketdyne Div.  
6633 Canoga Ave.  
Mail STop FA03  
Canoga Park, CA 91304  
(818) 710-7184

Denis Riviere  
Laboratoires de Marcoussis  
Route de Nozay  
91460 Marcoussis  
FRANCE  
(1) 64 49 11 09

Virgil E. Sanders  
Los Alamos Nat'l Lab  
P.O. Box 1663  
MS-J564  
Los Alamos, NM 87777545  
(505) 667-7398

Paul Schall  
JAYCOR  
2811 Wilshire Blvd. #690  
Santa Monica, CA 90403  
(213) 829-0584

Marion L. Scott  
Los Alamos Nat'l Laboratory  
M/S E549  
Los Alamos, NM 87545  
(505) 667-7557

Steven C. Seitel  
Montana laser Optics, Inc.  
P.O. Box 4151  
Bozeman, MT 59772  
(406) 586-5100

Wigbert Siekhaus  
Lawrence Livermore Nat'l Lab  
P.O. Box 808, L-357  
Livermore, CA 94550  
(415) 422-6884

Lin Simpson  
Washington State University  
Pullman, WA

Dr. M.J. Soileau  
University of Central Florida  
Center of Research in  
Electro-Optics & Lasers  
12424 Research Parkway  
Orlando, FL 32826  
(407) 658-6800

Rob W. Sparrow  
OPTOVAC  
East Brookfield Road  
North Brookfield, MA 01535  
(508) 867-6444

Michael C. Staggs  
Lawrence Livermore Nat'l Lab  
P.O. Box 5508, L-249  
Livermore, CA 94550  
(415) 422-6059

James L. Stanford  
Naval Weapons Center  
Code 381  
China Lake, CA 93555  
(619) 939-1444

Alan F. Stewart  
Battelle PNL  
P.O. Box 999  
Richland, WA 99352  
(509) 375-6876

J. L. Stiggall  
Lockheed  
O/51-50, B/586  
P.O. Box 3504  
Sunnyvale, CA 94088-3504  
(408) 742-5526

William C. Sweatt  
Sandia Nat'l Laboratories  
P.O. Box 5800  
Albuquerque, NM 87185-5800  
(505) 844-6792

Randall T. Swimm  
Univ. of Southern California  
Los Angeles, CA 90089-1112  
(213) 743-4370

Paul Szczepanski  
Airtron/Litton  
200 East Hanover Ave.  
Morris Plains, NJ 07950  
(201) 539-5500

Izawa Takao  
Showa Optical Co., Ltd.  
804 Hakusancho, Midori-ku  
Yokohama, Kanagawa  
226 JAPAN  
045 (931) 6511

John Taylor  
Lawrence Livermore Nat'l Lab  
P.O. Box 808, L-456  
Livermore, CA 94550  
(415) 422-1345

Dr. Douglas W. Templeton  
US Army Tank-Automotive Command  
AMSTA-RSC  
Warren, MI 48397-5000  
(313) 574-5325

Dr. Douglas Templeton  
U.S. Army  
Tank Automotive Command  
Warren, MI 48397-5000  
(313) 574-5325

Ian M. Thomas  
Lawrence Livermore Nat'l Lab  
P.O. Box 5508, L-483  
Livermore, CA 94550  
(415) 423-3896

Dennis A. Thompson  
Eastman Kodak Co.  
121 Lincoln Ave.  
Rochester, NY 14653-8119  
(716) 253-2684

James Tillotson  
Northrop  
Hawthorne, CA  
(213) 600-3050

Shelle Dawn Tilstra  
GV Medical, Inc.  
3750 Annapolis Lane  
Minneapolis, MN 55447  
(612) 559-4000

Michael J. Treadaway  
Jaycor  
P.O. Box 85154  
San Diego, CA 92138  
(619) 535-3123

Thomas P. Turner  
Los Alamos National Lab  
CLS-6, MS J564  
Los Alamos, NM 87545  
(505) 667-3589

Trudy Tuttle Hart  
OCLI  
2789 Northpoint Parkway  
Santa Rosa, CA  
(707) 525-7192

Gerard Villela  
Laboratoires de Marcoussis  
Route de Nazay  
91460 Marcoussis  
FRANCE  
(1) 64 49 11 84

Richard H. Vogt  
Hughes Optical Products  
2000 S. Wolf Rd.  
Des Plaines, IL 60018  
(312) 699-3551

Brad P. Volkmer  
U.S. Govt.  
CSSO-H-FB  
Ground Base Laser Proj. Office  
WSMR, NM 88002  
(505) 678-6092

Marc von Gunten  
Spectra-Physics Optics Corp.  
1330 West Middlefield Road  
Mail Stop 4-30  
Mountain Valley, CA 94039-7013  
(415) 961-2550 x3008

Bob Wald  
NIST  
MS/724.02  
325 Broadway  
Boulder, CO 80303-3328  
(303) 497-3542

Steve E. Watkins  
University of Texas at Austin  
Elec. Engineering Dept.  
Austin, TX 78712  
(512) 471-3628

R. K. Wedel  
Lockheed  
O/51-50, B/586  
P.O. Box 3504  
Sunnyvale, CA 94088-3504  
(408) 742-6641

Carolyn Weinzapfel  
Lawrence Livermore Nat'l Lab  
7000 East Ave., L-491  
Livermore, CA 94550  
(415) 423-4594

Patricia L. White  
Battelle PNL  
P.O. Box 999  
MS IN: K3-S9  
Richland, WA 99352  
(509) 375-6876

John Wilder  
Lawrence Livermore Nat'l Lab  
P.O. Box 808, L-483  
Livermore, CA 94550  
(415) 423-3896

Theodore C. Willis  
McDonnell Douglas Co.  
MDAC-MDE  
P.O. Box 516  
St. Louis, MO 63166  
(314) 232-1335

G. Richard Wirtenson  
Lawrence Livermore Nat'l Lab  
P.O. Box 808  
Livermore, CA 94550  
(415) 422-1100

Charles V. Woerner  
Nat'l Aeronautics & Space Admin.  
Langley Res. Center  
Mail Stop 356  
Hampton, VA 23665-5225  
(804) 865-2303

C. Robert Wolfe  
Lawrence Livermore Nat'l Lab  
P.O. Box 5508, L-490  
Livermore, CA 94550  
(415) 422-3516

Dr. William C. Womack  
Ball Aerospace Systems Group  
1600 Commerce Street  
Boulder, CO 80301  
(303) 939-4138

R. M. Wood  
G.E.C. Hirst Research Center  
East Lane  
Wembley Middlesex  
HA97PP  
UNITED KINGDOM  
01-908-9127

Laura Ellen Wood  
Martin Marietta Denver Aerospace  
8263 W. Floyd Ave. 6-302  
Lakewood, CO 80227  
(303) 971-6944

Frank J. Woodberry  
Rocketdyne Div.  
6633 Canoga Ave.  
M/S FA-03  
Canoga Park, CA 91303  
(818) 700-4737

Ren-jye Yeh  
Litton/GCS  
5500 Canoga Ave.  
M/S 12  
Woodland Hills, CA 91367  
(818) 888-3415

Yoshiatsu Yokoo  
Hoya Corporation  
3-1, Musashino 3-Chome  
Akishima-shi  
Tokyo 196  
JAPAN  
0425-46-2736

Chen-Zhi Zhang  
University of Texas at Austin  
Materials Science & Engineering  
Austin, TX 78712  
(512) 471-3628

Richard K. Zoborowski  
OCLI  
2789 Northpoint Parkway  
Santa Rosa, CA 95407  
(707) 525-7011

Zygmunt Zubkow  
Ball Aerospace Systems Group  
1600 Commerce Street  
Boulder, CO 80301  
(303) 939-54482



U.S. DEPT. OF COMM. <b>BIBLIOGRAPHIC DATA SHEET</b> <i>(See instructions)</i>	1. PUBLICATION OR REPORT NO. NIST/SP-775	2. Performing Organ. Report No.	3. Publication Date October 1989
4. TITLE AND SUBTITLE Laser Induced Damage in Optical Materials: 1988			
5. AUTHOR(S) Harold E. Bennett (NWC), Arthur H. Guenther (LANL) Brian E. Newnam (LANL), and M.J. Soileau (UCF)			
6. PERFORMING ORGANIZATION <i>(If joint or other than NBS, see instructions)</i> NATIONAL BUREAU OF STANDARDS DEPARTMENT OF COMMERCE WASHINGTON, D.C. 20234		7. Contract/Grant No.	8. Type of Report & Period Covered Final
9. SPONSORING ORGANIZATION NAME AND COMPLETE ADDRESS <i>(Street, City, State, ZIP)</i> National Institute of Standards and Technology (NIST) American Society for Testing and Materials (ASTM) Defense Advanced Research Project Agency (DARPA) Department of Energy (DOE)			
10. SUPPLEMENTARY NOTES Library of Congress Catalog Card Number <input type="checkbox"/> Document describes a computer program; SF-185, FIPS Software Summary, is attached.			
11. ABSTRACT <i>(A 200-word or less factual summary of most significant information. If document includes a significant bibliography or literature survey, mention it here)</i> The Twentieth Annual Symposium on Optical Materials for High Power Lasers (Boulder Damage Symposium) was held at the National Institute of Standards and Technology in Boulder, Colorado, October 26-28, 1988. The Symposium was held under the auspices of the ASTM Committee F-1, Subcommittee on Laser Standards, with the joint sponsorship of NIST, the Defense Advanced Research Project Agency, and the Department of Energy. Over 210 scientists attended the Symposium, including representatives from the United States, the United Kingdom, France, Canada, the People's Republic of China, Japan, Federal Republic of Germany, Lithuania, and the Soviet Union. The Symposium was divided into sessions concerning Materials and Measurements, Surfaces and Mirrors, Thin Films, and Fundamental Mechanisms. As in previous years, the emphasis of the papers presented at the Symposium was directed toward new frontiers and new developments. Particular emphasis was given to materials for high-power apparatus. The wavelength range of prime interest was from 10.6 $\mu\text{m}$ to the uv region. Highlights included surface characterization, thin film-substrate boundaries, and advances in fundamental laser-matter threshold interactions and mechanisms. Harold E. Bennett of the Naval Weapons Center, Arthur H. Guenther of the Los Alamos National Laboratory, Brian E. Newnam of the Los Alamos National Laboratory, and M. J. Soileau of the University of Central Florida were co-chairmen of the Symposium. The Twenty-First Annual Symposium is scheduled for November 1-3, 1989, at the National Institute of Standards and Technology, Boulder, Colorado.			
12. KEY WORDS <i>(Six to twelve entries; alphabetical order; capitalize only proper names; and separate key words by semicolons)</i> laser damage; laser interaction; optical components; optical fabrication; optical materials and properties; thin film coatings			
13. AVAILABILITY <input checked="" type="checkbox"/> Unlimited <input type="checkbox"/> For Official Distribution. Do Not Release to NTIS <input checked="" type="checkbox"/> Order From Superintendent of Documents, U.S. Government Printing Office, Washington, D.C. 20402. <input type="checkbox"/> Order From National Technical Information Service (NTIS), Springfield, VA. 22161		14. NO. OF PRINTED PAGES 576 15. Price	



# **NIST** *Technical Publications*

## **Periodical**

---

**Journal of Research of the National Institute of Standards and Technology**—Reports NIST research and development in those disciplines of the physical and engineering sciences in which the Institute is active. These include physics, chemistry, engineering, mathematics, and computer sciences. Papers cover a broad range of subjects, with major emphasis on measurement methodology and the basic technology underlying standardization. Also included from time to time are survey articles on topics closely related to the Institute's technical and scientific programs. Issued six times a year.

## **Nonperiodicals**

---

**Monographs**—Major contributions to the technical literature on various subjects related to the Institute's scientific and technical activities.

**Handbooks**—Recommended codes of engineering and industrial practice (including safety codes) developed in cooperation with interested industries, professional organizations, and regulatory bodies.

**Special Publications**—Include proceedings of conferences sponsored by NIST, NIST annual reports, and other special publications appropriate to this grouping such as wall charts, pocket cards, and bibliographies.

**Applied Mathematics Series**—Mathematical tables, manuals, and studies of special interest to physicists, engineers, chemists, biologists, mathematicians, computer programmers, and others engaged in scientific and technical work.

**National Standard Reference Data Series**—Provides quantitative data on the physical and chemical properties of materials, compiled from the world's literature and critically evaluated. Developed under a worldwide program coordinated by NIST under the authority of the National Standard Data Act (Public Law 90-396). NOTE: The Journal of Physical and Chemical Reference Data (JPCRD) is published quarterly for NIST by the American Chemical Society (ACS) and the American Institute of Physics (AIP). Subscriptions, reprints, and supplements are available from ACS, 1155 Sixteenth St., NW., Washington, DC 20056.

**Building Science Series**—Disseminates technical information developed at the Institute on building materials, components, systems, and whole structures. The series presents research results, test methods, and performance criteria related to the structural and environmental functions and the durability and safety characteristics of building elements and systems.

**Technical Notes**—Studies or reports which are complete in themselves but restrictive in their treatment of a subject. Analogous to monographs but not so comprehensive in scope or definitive in treatment of the subject area. Often serve as a vehicle for final reports of work performed at NIST under the sponsorship of other government agencies.

**Voluntary Product Standards**—Developed under procedures published by the Department of Commerce in Part 10, Title 15, of the Code of Federal Regulations. The standards establish nationally recognized requirements for products, and provide all concerned interests with a basis for common understanding of the characteristics of the products. NIST administers this program as a supplement to the activities of the private sector standardizing organizations.

**Consumer Information Series**—Practical information, based on NIST research and experience, covering areas of interest to the consumer. Easily understandable language and illustrations provide useful background knowledge for shopping in today's technological marketplace.

*Order the above NIST publications from: Superintendent of Documents, Government Printing Office, Washington, DC 20402.*

*Order the following NIST publications—FIPS and NISTIRs—from the National Technical Information Service, Springfield, VA 22161.*

**Federal Information Processing Standards Publications (FIPS PUB)**—Publications in this series collectively constitute the Federal Information Processing Standards Register. The Register serves as the official source of information in the Federal Government regarding standards issued by NIST pursuant to the Federal Property and Administrative Services Act of 1949 as amended, Public Law 89-306 (79 Stat. 1127), and as implemented by Executive Order 11717 (38 FR 12315, dated May 11, 1973) and Part 6 of Title 15 CFR (Code of Federal Regulations).

**NIST Interagency Reports (NISTIR)**—A special series of interim or final reports on work performed by NIST for outside sponsors (both government and non-government). In general, initial distribution is handled by the sponsor; public distribution is by the National Technical Information Service, Springfield, VA 22161, in paper copy or microfiche form.

**U.S. DEPARTMENT OF COMMERCE**  
National Institute of Standards and Technology  
(formerly National Bureau of Standards)  
325 Broadway  
Boulder, Colorado 80303-3328

---

OFFICIAL BUSINESS  
PENALTY FOR PRIVATE USE, \$300